TOWARDS THE NEXT GENERATION OF DEEP BRAIN STIMULATION THERAPIES: TECHNOLOGICAL ADVANCEMENTS, COMPUTATIONAL METHODS, AND NEW TARGETS

EDITED BY: George C. McConnell, Sabato Santaniello, John Thomas Gale, Rose Taj Faghih, Caleb Kemere, Martin Han and Justin David Hilliard

PUBLISHED IN: Frontiers in Neuroscience

frontiers Research Topics

frontiers

ISSN 1664-8714
ISBN 978-2-88971-464-3
DOI 10.3389/978-2-88971-464-3

About Frontiers

Frontiers is more than just an open-access publisher of scholarly articles: it is a pioneering approach to the world of academia, radically improving the way scholarly research is managed. The grand vision of Frontiers is a world where all people have an equal opportunity to seek, share and generate knowledge. Frontiers provides immediate and permanent online open access to all its publications, but this alone is not enough to realize our grand goals.

Frontiers Journal Series

The Frontiers Journal Series is a multi-tier and interdisciplinary set of open-access, online journals, promising a paradigm shift from the current review, selection and dissemination processes in academic publishing. All Frontiers journals are driven by researchers for researchers; therefore, they constitute a service to the scholarly community. At the same time, the Frontiers Journal Series operates on a revolutionary invention, the tiered publishing system, initially addressing specific communities of scholars, and gradually climbing up to broader public understanding, thus serving the interests of the lay society, too.

Dedication to Quality

Each Frontiers article is a landmark of the highest quality, thanks to genuinely collaborative interactions between authors and review editors, who include some of the world's best academicians. Research must be certified by peers before entering a stream of knowledge that may eventually reach the public - and shape society; therefore, Frontiers only applies the most rigorous and unbiased reviews.
Frontiers revolutionizes research publishing by freely delivering the most outstanding research, evaluated with no bias from both the academic and social point of view. By applying the most advanced information technologies, Frontiers is catapulting scholarly publishing into a new generation.

What are Frontiers Research Topics?

Frontiers Research Topics are very popular trademarks of the Frontiers Journals Series: they are collections of at least ten articles, all centered on a particular subject. With their unique mix of varied contributions from Original Research to Review Articles, Frontiers Research Topics unify the most influential researchers, the latest key findings and historical advances in a hot research area! Find out more on how to host your own Frontiers Research Topic or contribute to one as an author by contacting the Frontiers Editorial Office: frontiersin.org/about/contact

TOWARDS THE NEXT GENERATION OF DEEP BRAIN STIMULATION THERAPIES: TECHNOLOGICAL ADVANCEMENTS, COMPUTATIONAL METHODS, AND NEW TARGETS

Topic Editors:
George C. McConnell, Stevens Institute of Technology, United States
Sabato Santaniello, University of Connecticut, United States
John Thomas Gale, Independent researcher, United States
Rose Taj Faghih, University of Houston, United States
Caleb Kemere, Rice University, United States
Martin Han, University of Connecticut, United States
Justin David Hilliard, University of Florida, United States

Citation: McConnell, G. C., Santaniello, S., Gale, J. T., Faghih, R. T., Kemere, C., Han, M., Hilliard, J. D., eds. (2021). Towards the Next Generation of Deep Brain Stimulation Therapies: Technological Advancements, Computational Methods, and New Targets. Lausanne: Frontiers Media SA. doi: 10.3389/978-2-88971-464-3

Table of Contents

frontiers in Neuroscience

EDITORIAL
published: 19 August 2021
doi: 10.3389/fnins.2021.737737

Editorial: Towards the Next Generation of Deep Brain Stimulation Therapies: Technological Advancements, Computational Methods, and New Targets

Sabato Santaniello[1]*, *George C. McConnell*[2], *John T. Gale*[3], *Rose T. Faghih*[4], *Caleb Kemere*[5], *Justin D. Hilliard*[6] and *Martin Han*[7]

[1] Biomedical Engineering Department and Institute for the Brain and Cognitive Sciences, University of Connecticut, Storrs, CT, United States, [2] Department of Biomedical Engineering, Stevens Institute of Technology, Hoboken, NJ, United States, [3] Gale Neurotechnologies Inc., Smoke Rise, GA, United States, [4] Department of Electrical and Computer Engineering, University of Houston, Houston, TX, United States, [5] Department of Electrical and Computer Engineering, Rice University, Houston, TX, United States, [6] Department of Neurosurgery, University of Florida, Gainesville, FL, United States, [7] Biomedical Engineering Department and Institute of Materials Science, University of Connecticut, Storrs, CT, United States

Keywords: movement disorders, psychiatric disorders, neurostimulation devices, basal ganglia, electrodermal activity, DBS lead, adaptive DBS, DBS surgery

OPEN ACCESS

Edited and reviewed by:
Michela Chiappalone,
Italian Institute of Technology (IIT), Italy

***Correspondence:**
Sabato Santaniello
sabato.santaniello@uconn.edu

Specialty section:
This article was submitted to Neuroprosthetics, a section of the journal Frontiers in Neuroscience

Received: *07 July 2021*
Accepted: *23 July 2021*
Published: *19 August 2021*

Citation:
Santaniello S, McConnell GC, Gale JT, Faghih RT, Kemere C, Hilliard JD and Han M (2021) Editorial: Towards the Next Generation of Deep Brain Stimulation Therapies: Technological Advancements, Computational Methods, and New Targets. Front. Neurosci. 15:737737. doi: 10.3389/fnins.2021.737737

Editorial on the Research Topic

Towards the Next Generation of Deep Brain Stimulation Therapies: Technological Advancements, Computational Methods, and New Targets

Deep Brain Stimulation (DBS) has matured into a staple of modern therapeutics for movement disorders and is considered a promising tool toward the treatment of psychiatric conditions (Vedam-Mai et al., 2021). More importantly, DBS has been the engine propelling the development of a diverse ecosystem of technological innovations, ranging from surgical navigation systems that incorporate connectome data (Li et al., 2020) to algorithms that predict the therapeutic outcomes of brain stimulation (Gonzalez-Escamilla et al., 2019; Reich et al., 2019), and implantable neurostimulators that integrate chronic monitoring and real-time modulation of neural activity (Stanslaski et al., 2018; Topalovic et al., 2020).

With the wealth of technological advancements accrued in recent years, two key questions have rapidly gained interest: (1) How do stimulation targets and settings affect the therapeutic efficacy of DBS? and (2) How can we minimize the burden associated with DBS programming while maximizing the clinical efficacy? In this Research Topic we gathered original research studies from experts in the field who addressed these questions and provided cutting-edge solutions toward the next generation of DBS therapies.

Despite advancements in neuro-navigation and planning, the decision about precisely where to stimulate (i.e., *which electrode contact should be activated on a DBS array?*) remains challenging, in part because intraoperative feedback on lead placement often relies on expert interpretation of intra-operative multiunit recordings. To cope with this limitation, Ozturk et al. reported a double-blinded pilot study that showed the potential of novel intra-operative analyses based on local field potentials. The authors demonstrated that the analysis can be done online in the operating

room and enhanced the therapeutic outcomes of DBS through improved target localization compared to current methods using multiunit recording. Li and McConnell reported interesting work in rats that mapped the heterogeneity of the electrophysiology in the substantia nigra (SNr) and the ventral tegmental area, which are promising new targets for DBS. The authors reported the existence of distinct electrophysiological features in these areas and showed how these features can help precisely target SNr subregions during DBS surgery.

To further enhance the therapeutic outcomes of DBS, Anderson et al. developed a novel directional DBS lead with thousands of microscale contacts. The new design dramatically increased the spatial resolution of stimulation steering and improved the selectivity in targeting small diameter fibers, which promises to significantly widen the window of therapy for DBS. Furthermore, Zheng et al. investigated the effects that can be induced on the therapeutic outcomes of DBS by changing the appearance order of the intervals between consecutive pulses. They showed that a random arrangement of inter-pulse intervals (IPI) can recruit more neurons to fire in synchrony following specific sub-sequences of pulses compared to gradual IPI, thus providing a paradigm to widen the neuronal recruitment in response to DBS.

A general consensus has been that the burden of DBS programming will be lowered by introducing closed-loop control algorithms. However, studies so far have mainly assessed the feasibility of closed-loop DBS over short periods (Little et al., 2013; Arlotti et al., 2018) and have been limited to control algorithms that lack sensitivity and specificity over long durations. Because symptom fluctuations are a hallmark of various movement disorders, occurring on multiple time scales, there is an unmet need for algorithms that can self-adapt as symptoms and biomarkers evolve with time. In this Research Topic, we presented work related to this need with respect to the fluctuations of pathological beta-band in Parkinson's disease (PD). Fleming, Dunn, et al. evaluated the resilience of traditional PI controllers against beta-band fluctuations, and Fleming, Orlowski, et al. proposed a novel, self-tuning controller that tracks beta-band fluctuations over time and adjusts the closed-loop DBS strategy accordingly. Also, Su et al. proposed a hierarchical control architecture, where the closed-loop DBS is based on an autoregressive (AR) model of the input-output relationship between DBS pulses and pathological beta-band oscillations. As the AR model is updated periodically through the day, the control strategy is automatically adjusted to efficiently cope with the daily fluctuations of beta-band oscillations. Finally, Cutsuridis expanded the model-based framework to develop DBS strategies for chronic memory loss treatment.

With regard to PD, DBS therapies have been traditionally focused on motor symptoms such as akinesia (Moro et al., 2010), even though cognitive symptoms are a significant contributor to the severe disability imposed by the disease, diminishing the individual's quality of life. An emerging trend suggests that DBS therapies should be used to satisfy multiple therapeutic goals simultaneously and address both motor and non-motor symptoms. This may necessitate the investigation of new targets, stimulation patterns, and feedback signals. In Bentley et al., authors capitalized on the positive cognitive outcomes of intermittent theta-burst stimulation (iTBS, a TMS paradigm) of the dorsolateral prefrontal cortex (DLPFC) and delivered DBS with iTBS pulse sequences to the globus pallidus of PD patients. They documented the effects of GPi iTBS vs. regular GPi DBS on the neuronal activity in the DLPFC, which is a center for PD cognitive symptoms, and reported evidence of the cognitive effects of DBS. Wickramasuriya et al., on the other hand, proposed the use of sympathetic arousal as a potential biomarker of non-motor symptoms. The authors specifically focused on neuropsychiatric symptoms and developed an innovative approach to efficiently decode psychological arousal from neural activity underlying skin conductance signal variations. Finally, Guo et al. investigated hybrid stimulation protocols to treat disorders of consciousness (DOC) and proposed a combination of deep stimulation and high-density transcranial direct current stimulation of the precuneus to rehabilitate DOC patients.

Altogether, these contributions showed that the next generation of DBS therapies will aim to expand the range of clinical applications and boost therapeutic outcomes through a rapid integration in the design process of wearable sensing modalities, electronic miniaturization, control methods, and electrophysiological exploration.

AUTHOR CONTRIBUTIONS

All authors contributed to edit the manuscript.

FUNDING

This work was partly supported by the Branfman Family Foundation (to GCM), the US National Science Foundation CAREER Awards 1845348 (to SS) and 1942585 (to RTF), the US National Science Foundation CRII Award 1755780 (to RTF), the US Department of Defense Army CDMRP grant W81XWH-17-1-0538 (to MH), and the National Institutes of Health grant R01DC014044 (to MH).

REFERENCES

Arlotti, M., Marceglia, S., Foffani, G., Volkmann, J., Lozano, A. M., Moro, E., et al. (2018). Eight-hours adaptive deep brain stimulation in patients with Parkinson disease. *Neurology* 90, e971–e976. doi: 10.1212/WNL.0000000000005121

Gonzalez-Escamilla, G., Muthuraman, M., Reich, M. M., Koirala, N., Riedel, C., Glaser, M., et al. (2019). Cortical network fingerprints predict deep brain stimulation outcome in dystonia. *Movement Disord.* 34, 1537–1546. doi: 10.1002/mds.27808

Li, N., Baldermann, J. C., Kibleur, A., Treu, S., Akram, H., Elias, G. J. B., et al. (2020). A unified connectomic target for deep brain stimulation

in obsessive-compulsive disorder. *Nat. Commun.* 11:3364. doi: 10.1038/s41467-020-16734-3

Little, S., Pogosyan, A., Neal, S., Zavala, B., Zrinzo, L., Hariz, M., et al. (2013). Adaptive deep brain stimulation in advanced Parkinson disease. *Ann. Neurol.* 74, 449–457. doi: 10.1002/ana.23951

Moro, E., Lozano, A. M., Pollak, P., Agid, Y., Rehncrona, S., Volkmann, J., et al. (2010). Long-term results of a multicenter study on subthalamic and pallidal stimulation in Parkinson's disease. *Movement Disord.* 25, 578–586. doi: 10.1002/mds.22735

Reich, M. M., Horn, A., Lange, F., Roothans, J., Paschen, S., Runge, J., et al. (2019). Probabilistic mapping of the antidystonic effect of pallidal neurostimulation: a multicentre imaging study. *Brain* 142, 1386–1398. doi: 10.1093/brain/awz046

Stanslaski, S., Herron, J., Chouinard, T., Bourget, D., Isaacson, B., Kremen, V., et al. (2018). A chronically implantable neural coprocessor for investigating the treatment of neurological disorders. *IEEE Trans. Biomed. Circuits Syst.* 12, 1230–1245. doi: 10.1109/TBCAS.2018.2880148

Topalovic, U., Aghajan, Z. M., Villaroman, D., Hiller, S., Christov-Moore, L., Wishard, T. J., et al. (2020). Wireless programmable recording and stimulation of deep brain activity in freely moving humans. *Neuron* 108, 322–334 e329. doi: 10.1016/j.neuron.2020.08.021

Vedam-Mai, V., Deisseroth, K., Giordano, J., Lazaro-Munoz, G., Chiong, W., Suthana, N., et al. (2021). Proceedings of the eighth annual deep brain stimulation think tank: Advances in optogenetics, ethical issues affecting DBS research, neuromodulatory approaches for depression, adaptive neurostimulation, and emerging DBS technologies. *Front. Hum. Neurosci.* 15:644593. doi: 10.3389/fnhum.2021.644593

Conflict of Interest: JG was employed by Gale Neurotechnologies Inc.

The remaining authors declare that the research was conducted in the absence of any commercial or financial relationships that could be construed as a potential conflict of interest.

Publisher's Note: All claims expressed in this article are solely those of the authors and do not necessarily represent those of their affiliated organizations, or those of the publisher, the editors and the reviewers. Any product that may be evaluated in this article, or claim that may be made by its manufacturer, is not guaranteed or endorsed by the publisher.

frontiers in Neuroscience

ORIGINAL RESEARCH
published: 30 April 2019
doi: 10.3389/fnins.2019.00412

Effects of Long-Lasting High-Definition Transcranial Direct Current Stimulation in Chronic Disorders of Consciousness: A Pilot Study

Yongkun Guo[1], Yang Bai[2,3], Xiaoyu Xia[4], Jinju Li[1], Xiaoli Wang[1], Yiwu Dai[4], Yuanyuan Dang[4], Jianghong He[4], Chunying Liu[1] and Hui Zhang[1]**

[1] Department of Neurosurgery, Zhengzhou Central Hospital Affiliated to Zhengzhou University, Zhengzhou, China,
[2] International Vegetative State and Consciousness Science Institute, Hangzhou Normal University, Hangzhou, China,
[3] Department of Basic Medical Science, School of Medicine, Hangzhou Normal University, Hangzhou, China,
[4] Department of Neurosurgery, PLA Army General Hospital, Beijing, China

OPEN ACCESS

Edited by:
Sabato Santaniello, University of Connecticut, United States

Reviewed by:
Antonino Naro, Centro Neurolesi Bonino Pulejo (IRCCS), Italy
Tommaso Bocci, Università degli Studi di Messina, Italy

***Correspondence:**
Chunying Liu
liuchunying0302@126.com
Hui Zhang
528zhanghui@sina.cn

Specialty section:
This article was submitted to Neuroprosthetics, a section of the journal Frontiers in Neuroscience

Received: *01 March 2019*
Accepted: *11 April 2019*
Published: *30 April 2019*

Citation:
Guo Y, Bai Y, Xia X, Li J, Wang X, Dai Y, Dang Y, He J, Liu C and Zhang H (2019) Effects of Long-Lasting High-Definition Transcranial Direct Current Stimulation in Chronic Disorders of Consciousness: A Pilot Study. Front. Neurosci. 13:412. doi: 10.3389/fnins.2019.00412

Transcranial direct current stimulation (tDCS) recently was shown to benefit rehabilitation of patients with disorders of consciousness (DOC). However, high-Definition tDCS (HD-tDCS) has not been applied in DOC. In this study, we tried to use HD-tDCS protocol (2 mA, 20 min, the precuneus, and sustaining 14 days) to rehabilitate 11 patients with DOC. Electroencephalography (EEG) and Coma Recovery Scale–Revised (CRS-R) scores were recorded at before (T0), after a single session (T1), after 7 days' (T2), and 14 days' HD-tDCS (T3) to assess the modulation effects. EEG coherence was measured to evaluate functional connectivity during the experiment. It showed that 9 patients' scores increased compared with the baseline. The central-parietal coherence significantly decreased in the delta band in patients with DOC. EEG coherence might be useful for assessing the effect of HD-tDCS in patients with DOC. Long-lasting HD-tDCS over the precuneus is promising for the treatment of patients with DOC.

Keywords: disorders of consciousness, high-definition transcranial direct current stimulation, electroencephalography, Coma Recovery Scale–Revised scores, coherence

INTRODUCTION

Chronic disorders of consciousness (DOC) consist of vegetative state/ unresponsive wakefulness syndrome (VS/ UWS) and minimally conscious state (MCS) (Giacino et al., 2014). MCS is characterized by minimal but definite behavioral evidence of self or environmental awareness (Giacino et al., 2014). Recently, MCS was subcategorized into MCS− describing low-level behavioral responses and MCS+ describing high level behavioral responses (Bruno et al., 2012). Even though many pharmacological (i.e., amantadine, zolpidem) and non-pharmacological interventions (i.e., deep brain stimulation, spinal cord Stimulation, transcranial magnetic stimulation, median nerve electrical stimulation) have been assessed in the last decade, there remain few effective therapies for patients with DOC (Schiff et al., 2007; Giacino et al., 2012; Della Pepa et al., 2013; Yamamoto et al., 2013; Cossu, 2014; Thibaut et al., 2014; Tucker and Sandhu, 2016).

Transcranial direct current stimulation (tDCS) is a promising non-invasive brain stimulation technique for treatment of patients with DOC, which is safe, less uncomfortable and easy to handle (Zhang and Song, 2018). tDCS modulates cortical excitability at stimulation sites via weak current which flows through the brain from the anode to the cathode. Anodal tDCS boost neuronal activation via sub-threshold neuronal membrane polarization, and cathodal tDCS can reduce cortical excitability (Lefaucheur et al., 2017). The effects of tDCS stimulation can be long-lasting, and are connected with the duration of stimulation and current intensity (Zhao et al., 2017). Previous studies illustrated the residual capacity for neural plasticity and recovery of consciousness in some patients with DOC. Our group showed that tDCS can effectively modulate the cortical excitability of patients with DOC, especially in patients with MCS (Bai et al., 2017a,c). Martens et al. found that 4 weeks of home-based tDCS moderately improved the recovery of signs of consciousness in patients with MCS (Martens et al., 2018). Similarly, Zhang and his colleagues reported 20 sessions of tDCS can improve CRS-R scores and modulate the P300 amplitude in patients with MCS. The P300 has been commonly used to detect residual awareness in patients with DOC (Giacino et al., 2018). Several studies have also showed that patients with MCS can benefit from tDCS over the left dorsolateral prefrontal cortex (DLPFC) (Angelakis et al., 2014; Thibaut et al., 2014, 2015, 2017; Dimitri et al., 2017). Except the treatment effect of tDCS in patients with DOC, tDCS induced changes in cortical connectivity and excitability is useful in differentiating MCS from UWS patients (Naro et al., 2015). However, another study discovered that tDCS of the left DLPFC did not have remarkable clinical and EEG effects in patients with DOC (Estraneo et al., 2017). A critical problem of tDCS in patients with DOC is stimulated area. The left DLPFC is common in traumatic brain injury, Huang et al. (2017) chose the posterior parietal cortex as the site of stimulation. Researchers found tDCS of the posterior parietal cortex improves the recovery of clinical signs of consciousness in some patients with MCS (Huang et al., 2017). For researching the mechanism of change of tDCS in patients with DOC, a more focal stimulation is important. However, The main disadvantage of conventional tDCS is that it produces diffuse brain current flow. It is difficult to interpret whether produced effects are due to stimulation of the targeted cortical region or neighboring anatomical area (Bai et al., 2014; To et al., 2016).

High-Definition tDCS using the 4 × 1 smaller compact scalp electrodes, instead of the two large pad electrodes, is a new neuromodulation technique. HD-tDCS improves the spatial precision, resulting in focal neural and specific behavioral changes (Dmochowski et al., 2011; Villamar et al., 2013; Shekhawat and Vanneste, 2018). HD-tDCS has been previously reported to improve motor function, verbal learning, working memory, and pain and tinnitus control (Borckardt et al., 2012; Caparelli-Daquer et al., 2012; Kuo et al., 2013; Donnell et al., 2015; Nikolin et al., 2015; Shekhawat et al., 2016). It has been shown to reliably target specific brain areas and produce plastic changes that may outlast conventional tDCS (Kuo et al., 2013; Hogeveen et al., 2016). There is no study has examined the impact of HD-tDCS on DOC to date.

The CRS-R is a standardized behavioral assessment measure that has been widely used for diagnostic assessment and outcome measurement in patients with DOC (Gerrard et al., 2014). However, the rate of clinical misdiagnosis based on the CRS-R remains high (Xie et al., 2017). Previous results have demonstrated EEG can detect and analyze brain activity in clinical practice (Lehembre et al., 2012; Bai et al., 2017a,b). Our previous research has found the quantitative EEG was useful for assessment of the effect of tDCS and rTMS in patients with DOC (Bai et al., 2017a,c; Xia et al., 2017). EEG coherence has been applied to evaluate the effective connectivity of DOC, a high coherence hints at an increased functional interplay between the underlying neuronal networks (Rampil, 1998; Davey et al., 2000; Bai et al., 2017a,c).

We applied resting state EEG and CRS-R scores for assessing the effect in patients with DOC treated with long-lasting HD-tDCS. We aim to confirm that HD-tDCS applied to the precuneus on patients with DOC could produce clinically useful behavioral modifications. We also want to find direct EEG evidence to demonstrate the efficacy of HD-tDCS in patients with DOC.

MATERIALS AND METHODS

Patients

We enrolled medically stable 18 patients with DOC hospitalized in Department of Neurosurgery, Zhengzhou Central Hospital Affiliated to Zhengzhou University, between October 2016 and June 2017. Due to pulmonary infection, phlebothrombosis, and other clinical interferences, 11 patients (5 VS and 6 MCS, mean age:52.8 years, range: 30.0–71.0 years, 4 females, and 7 males) completed the entire experiment (**Table 1**). Inclusion criteria were VS/UWS or MCS patients, according to the JFK CRS-R scores. We excluded patients with DOC who had precuneus lesions, have had tDCS treatment before or last less than 3 months to avoid the spontaneous recovery period. Participants who had pacemakers, aneurysm clips, other devices implanted or other treatments and drugs which modifying cortical-excitability were also eliminated. The present study was approved by the ethics committee of the Zhengzhou Central Hospital Affiliated to Zhengzhou University.

Design and HD-tDCS: Stimulation Protocol

All patients received HD-tDCS modulation (2 mA, 20 min, anode centered over the precuneus) for two session per day over 14 consecutive days (**Figure 1**). The CRS-R assessments were conducted at four time points: before the experiment (T0), after a single session of HD-tDCS (T1), after the treatment of 7 days (T2), and 14 days (T3). In this study, any side effects of HD-tDCS were monitored and reported.

HD-tDCS

4 x1-Ring high-definition electrodes with an anode center electrode overlying the targeted brain area surrounded by four cathodal electrodes were used to deliver direct current to the

TABLE 1 | Demographic details of the patients included in the study.

Patient	Age	Etiology	MRI findings	Duration (months)	CRS-R						
					A	V	M	OM	C	Ar	Total
MCR1	66–70	Hemorrhage	Left frontal-parietal lesions, diffuse atrophy	3	2	3	3	1	0	2	11
MCR2	51–55	Hemorrhage	Left frontal-temporal lesion	3	2	2	2	1	0	1	8
MCR3	56–60	Hemorrhage	Left hemisphere lesion, diffuse cortical atrophy	3	2	3	2	1	0	2	10
MCR4	26–30	Hemorrhage	Left parietal-temporal-thalamus lesion	6	1	2	2	1	0	1	7
MCR5	71–75	Hemorrhage	Left frontal-temporal-parietal lesions	4	2	2	3	1	0	2	10
MCR6	51–55	Hemorrhage	Right frontal-parietal-thalamus lesions	3	1	2	2	1	0	2	8
VS1	36–40	Hemorrhage	Left frontal -temporal cortical atrophy	6	1	1	2	0	0	2	6
VS2	61–65	Hemorrhage	Left hemisphere lesion	3	1	1	2	1	0	1	6
VS3	51–55	Hemorrhage	Right frontal-temporal cortical atrophy	3	1	1	2	1	0	1	6
VS4	36–40	TBI	Bilateral frontal and diffuse cortical atrophy.	8	1	1	2	1	0	1	6
VS5	51–55	TBI	Left frontal-temporal, diffuse cortical atrophy	6	1	0	2	0	0	1	4

CRS-R, Coma Recovery Scale–Revised scores; A, auditory; V, visual; M, motor; OM, oromotor; C, communication; Ar, arousal.

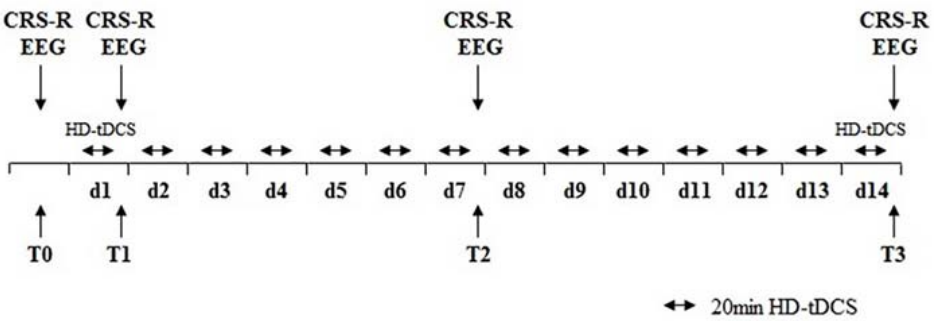

FIGURE 1 | Protocol of the study. HD-tDCS, high-definition transcranial direct current stimulation; CRS-R, Coma Recovery Scale–Revised scores; EEG, electroencephalography.

scalp with the application of Ag/AgCl ring electrodes (Model 4x1-C2: Soterix Medical Inc., New York, NY, United States). HD-tDCS enables a more restricted cortical neuromodulation and leads to higher electric fields. Electrodes were held in place by specially designed plastic casings embedded in a 32-channel EEG recording cap. The center electrode (anode) was placed at Pz according to the international 10–20 EEG system, and four cathodal electrodes were placed approximately 3.5 cm radially from Pz; corresponding roughly to locations Cz, P3, P4, and POz (**Figure 3A**).

EEG Recording and Pre-processing

We used 32 EEG recorder (Nicolet EEG V32, Natus, United States). EEG recorded at four time points: before the experiment (T0), after a single session of HD-tDCS (T1), after the treatment of 7 days (T2), and 14 days (T3). EEG signals were continuously recorded from 32 channels at positions of the International 10/20 system. The electrodes with the setting of a band-pass filtered at DC to 1000 Hz in the recorder. The EEG signal was digitized at a sampling rate of 2.5 kHz. The skin impedance was maintained below 5 kΩ. EEG recordings were carried out while patients were behaviorally awake.

Off-line analysis was carried out using EEGLAB 12.0.2.5b, running in a MATLAB environment (version 2013b, Math Works Inc., Natick, Massachusetts, United States). The 50-Hz power signal was removed by a notch filter. The independent component analysis function was used to identify and remove the artifact-relevant components. The EEG data were down-sampled to 500 Hz and average referenced. Then, the EEG date were divided into epochs of 10 s with 50% overlap in each patient.

EEG Analysis

Coherence was measured using spectral cross-correlation and normalized power spectra of signals obtained from two electrodes with the following equation:

$$\mathrm{Coh}_{xy}(f) = \frac{|P_{xy}(f)|^2}{P_{xx}(f)\,P_{yy}(f)}$$

where $P_{xy}(f)$ was the cross-power spectral density and $P_{xx}(f)$ and $P_{yy}(f)$ were the respective auto-power spectral densities of the signals.

As shown in **Figure 2A**, the frontal region included electrodes Fp1, Fp2, Fz, F3, F4, Fc5, Fc6, Fc1, FC2, F7, and F8; the central

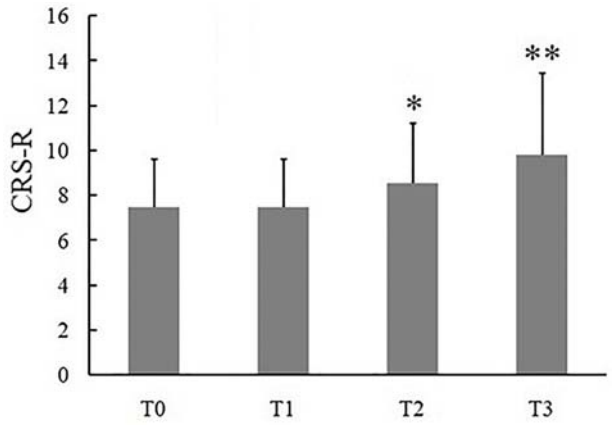

FIGURE 2 | Effects of long-lasting HD-tDCS treatments evaluated with CRS-R in patients with DOC. Asterisk indicates significant differences (*$P < 0.05$, **$P < 0.01$).

TABLE 2 | Clinical evaluation of the patients on day 7 and 14.

Patient	CRS-R improvement (day 7/14)							Changes of diagnosis
	A	V	M	OM	C	Ar	Total	
MCR1	0/1	0/0	0/0	0/0	0/0	0/0	0/1	MCS− elevated to MCS+
MCR2	0/0	1/1	1/1	0/0	0/0	1/1	3/3	Remained MCS−
MCR3	0/1	0/0	1/2	0/1	0/1	0/0	1/5	MCS− elevated to MCS+
MCR4	0/2	1/1	0/1	0/0	0/1	1/1	2/6	MCS− elevated to MCS+
MCR5	0/0	0/1	0/0	0/0	0/0	0/0	0/1	Remained MCS−
MCR6	1/2	1/1	1/1	1/2	0/0	0/0	4/6	MCS− elevated to MCS+
VS1	0/0	0/0	0/0	0/0	0/0	0/0	0/0	Remained VS
VS2	0/0	1/1	0/0	0/0	0/0	0/1	1/2	Remained VS
VS3	0/0	0/1	0/0	0/0	0/0	0/0	0/1	Remained VS
VS4	0/0	0/0	0/0	0/0	0/0	1/1	1/1	Remained VS
VS5	0/0	0/0	0/0	0/0	0/0	0/0	0/0	Remained VS

CRS-R, Coma Recovery Scale–Revised scores; A, auditory; V, visual; M, motor; OM, oromotor; C, communication; Ar, arousal.

region included electrodes CZ, C3,C4,Cp1,Cp2,Cp5, and Cp6; the parietal region included electrodes Pz, P3, P4, and Poz. Central-parietal coherence was calculated using pairwise electrodes from the central and parietal regions. The frontal inter-hemisphere and central inter-hemisphere coherences were also calculated.

Statistics

The statistics were performed via SPSS for Windows, version 17.0. The Wicoxon signed-rank test was used to analyze the effects of HD-tDCS on CRS-R. And the Kolmogorov–Smirnov test was utilized to observe the coherence between different regions at the delta bands. Bonferroni correction was conducted after multiple comparisons. $P < 0.05$ was regarded as statistically significant.

RESULTS

Effects of the HD-tDCS Treatment as Measured by CRS-R

Eleven (6 MCS and 5 VS) patients with chronic DOC completed the treatment, with no specific side effects, such as redness of the skin, signs of discomfort or epilepsy. 9/11 (72%) patients (54% of responders, 6 MCS and 3 VS) showed the CRS-R scores increased after 14 days of stimulation (**Table 2**). The CRS-R scores increased with the treatment going on, compared with the baselines, and the CRS-R score at the 7 day was significantly higher than the baseline (**Figure 2**, $P < 0.05$). It demonstrated that long-lasting HD-tDCS treatment can improve the recovery of consciousness in patients with DOC, whereas behavioral changes were not observed at just one session of stimulation.

Effects of the HD-tDCS Treatment as Measured by EEG

The coherence in the delta bands between the defined central and parietal regions was calculated (**Figure 3B**). Results showed that it decreased with the treatment going on, and the coherence index at T3 was higher significantly than that at T0 ($P < 0.05$). **Figure 3C** showed behavioral improvement was not discovered after the first stimulation. But the delta band coherence changed in the frontal inter -hemisphere regions in some patients with DOC. Besides, it reduced remarkably at day 7 ($P < 0.05$). Similarly, as shown in **Figure 3D**, the coherence between the central inter- hemisphere regions reduced after stimulation, and especially on day 7 and 14 ($P < 0.05$).

DISCUSSION

Several studies have reported effectiveness of conventional tDCS over the left DLPFC in patients with DOC (Angelakis et al., 2014; Thibaut et al., 2014, 2015, 2017; Dimitri et al., 2017). Patients with MCS but not VS are more easily benefit from tDCS at the left DLPFC. Recently, a sham-controlled randomized clinical trial investigated that 9/37 (27%) patients with MCS showed improvements after conventional tDCS over the posterior parietal cortex (Huang et al., 2017). A randomized double-blinded sham-controlled cross-over study didn't support effectiveness of conventional tDCS over the left DLPFC in patients with DOC (Estraneo et al., 2017). Estraneo et al.'s (2017) study didn't observe relevant behavioral and EEG changes in the single or repeated stimulation over the left DLPFC. What's more, owing to low spatial resolution of conventional tDCS, it was difficult to explain causality between stimulation of target brain region and the behavioral changes (Kuo et al., 2013). In addition, many studies only used CRS-R to evaluate treatment effects of conventional tDCS. In fact behavioral changes are not always observed in patients with DOC, particularly in short-term modulation. The precuneus as known to be involved in conscious processes plays an important role in consciousness recovery (Laureys and Schiff, 2012). Therefore, we targeted anodal HD-tDCS at the precuneus to evaluated modulation clinical effects and EEG oscillation in patients with DOC. We found that long-lasting HD-tDCS improved the recovery of consciousness

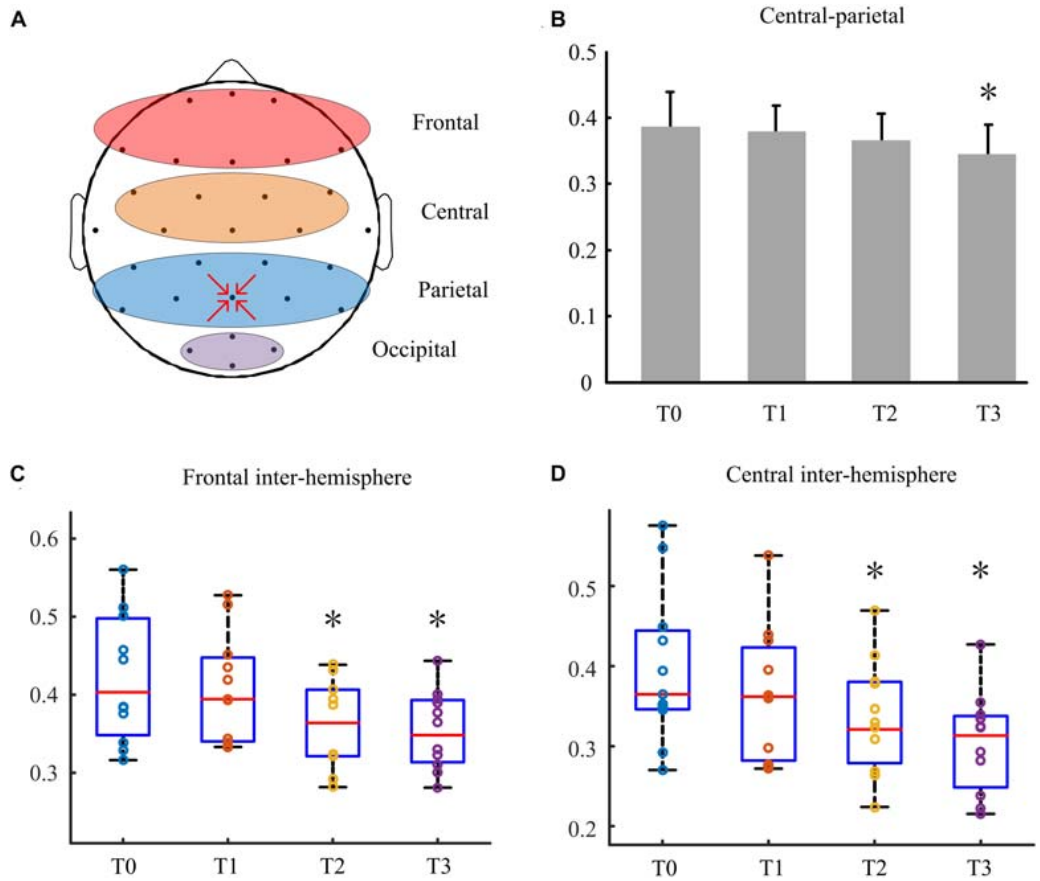

FIGURE 3 | The coherence between different regions in the delta bands. **(A)** Defined different regions of brain. **(B)** The coherence between central and parietal regions. **(C)** The frontal inter-hemisphere coherence. **(D)** The central inter-hemisphere coherence. Asterisks indicate statistically significant differences (*$P < 0.05$).

in patients with MCS and some patients in VS. Resting state EEG showed a significant reduction of the coherence between the central and parietal region at the delta band. Significant decreasing of coherence was also found at inter-hemisphere of frontal and central. These changes occurred in different time windows and brain regions for patients with DOC. No side effects such as discomfort, skin burn, and seizures were observed after any of the stimulation.

High-Definition tDCS delivery system was developed to enhance the spatial accuracy of tDCS, which is believed to enhance the clinical effects of this therapeutic tool. HD-tDCS uses the 4 × 1 montage of stimulating electrodes, which generates in maximal focused electric field strength under the target electrode with brain current flow constrained by the ring radius (Kuo et al., 2013; Gbadeyan et al., 2016; Hogeveen et al., 2016). Thus, it produced more spatially restricted electric field, as compared to the conventional electrode placement. HD-tDCS has the characteristics of high spatial resolution and more focused electric field than conventional tDCS protocols, which may offer the opportunity to explore the contribution of stimulation cortical target to consciousness. The efficacy of HD-tDCS for investigating motor cortex excitability, conscious movement intention, fibromyalgia, pain, tinnitus, verbal learning, and memory functioning have been reported (Borckardt et al., 2012; Caparelli-Daquer et al., 2012; Kuo et al., 2013; Donnell et al., 2015; Nikolin et al., 2015; Shekhawat et al., 2016). To our knowledge, there is no study has examined the impact of HD-tDCS on DOC. Targeting the precuneus using HD-tDCS will help probably to understand the recovery mechanisms of clinical sign of consciousness better.

The site of stimulation is also a critical scientific issue (Xia et al., 2017). The left DLPFC, cerebellum and the posterior parietal cortex were selected as the stimulation sites in DOC frequently. Cerebellum involves in short- and long-term habituation of unconditioned responses (Naro et al., 2016; Bocci et al., 2018), but it is not essential for consciousness. Cerebellar tDCS may be useful for ameliorating the level of consciousness (Naro et al., 2016). Both Left DLPFC and the precuneus are involved in conscious processes (Schiff, 2010; Xia et al., 2017). Conventional tDCS of the DLPFC have shown promising results in patients with MCS, which requires gray matter integrity (Thibaut et al., 2015). The probability of damage in DLPFC is higher than the posterior parietal cortex in DOC, the latter seems a better stimulation site in clinic (Pandya and Seltzer, 1982). The precuneus is associated with memory retrieval, controlling spatial aspects of behavior and Visual-spatial

visualization (Wenderoth et al., 2005; Ionta et al., 2014; Blanke et al., 2015; Kragel and Polyn, 2016; Rissman et al., 2016). The precuneus plays an important role in the mesocircuit model. Thibaut et al. (2015) found the precuneus metabolism and behavioral level supporting the fronto-parietal network correlate with outcomes in DOC (Thibaut et al., 2015). Moreover, the precuneus seems to be a brain region that can differentiate patients with MCS from VS.

As mentioned in the introduction, a single session of tDCS over the left DLPF transiently improves CRS-R total scores in patients with MCS (Giacino et al., 2012). Results of another study suggest that repeated tDCS improves the recovery of consciousness in 56% patients with DOC (Thibaut et al., 2017). In this study, We didn't observe any patient showed behavioral response to HD-tDCS after the first session of stimulation. Interestingly, we observed that 6/11 patients (54% of responders,4 MCS and 2 VS) showed the CRS-R scores significant improvement after 7 days of stimulation. The improvement was observed in 6 patients with MCS and 3 patients with VS after 14 days of stimulation. Four patients with MCS – rose from MCS − to MCS +. These results suggested that repeated HD-tDCS daily could promote consciousness level in MCS, whereas all VS remained previous consciousness state. These results suggested that the first session is not predictive of a future positive effect of the stimulation on the level of consciousness. Stimulation term is another critical issue, long-lasting stimulation possible improves neuroplasticity and strengthen the effect of the stimulation. In the future, longer-term stimulations (such as 20,30, or 60 days) should be considered to discover the potential of recovery effects in patients with DOC. MCS patients have more prominent potential of neural plasticity, which attain more benefit from HD-tDCS.

To reveal the mechanism of action and clinical effects of HD-tDCS over the precuneus of patients with DOC, functional connectivity of coherence was investigated using based resting state EEG. Previous studies have shown that the severity of DOC was correlated with increased low-frequency band power and decreased high-frequency band power (Bai et al., 2017a,b,c; Xia et al., 2017). Our data showed the significant reduction of short-range central-parietal coherence at the delta band after long-lasting HD-tDCS modulation. The long-range frontal-parietal coherence in the delta band did not decrease. But the frontal inter-hemisphere coherence significantly decreased in the delta band with increasing stimulation sessions. Besides, remarkably decrease compared to baseline was first shown at day 7. Similar results were observed in the central inter-hemisphere. Behavioral improvement was not discovered after the first stimulation. But the delta band coherence changes in brain implied a cortical response to the stimulation. Some patients who had no response to the first stimulation CRS-R scores improved after the whole stimulation session. These indicated that HD-tDCS could effectively alter the brain electrical activity. Accordingly, HD-tDCS induced variation of delta band coherence negatively correlated with the patients' CRS-R scores to some extent.

Studies demonstrated that the degree of DOC may be correlated with increased low-frequency band power in EEG patients (Bai et al., 2017a,b,c; Xia et al., 2017). The alteration of delta oscillations is accompanied by function alterations in the brain (Cavinato et al., 2015). The rationale for performing HD-tDCS in consciousness recovery remains unclear, but we found the trend of changes in the delta band in the frontal central and parietal regions. These changes can be summarized in a modulation of cortical coherence in short-range central-parietal and long-range frontal-parietal areas within a delta frequency range. Therefore, we considered that the changes occurring in the delta bands may provide evidence for supporting the modulating effects of HD-tDCS in patients with DOC.

Our study has several limitations. Firstly, the sample size was small. In the following research, we need recruit more patients with DOC to confirm and validate tDCS effectiveness. Secondly, this study lacked a randomized cross-over design and follow-up assessment, for long-term effect needs to be verified to determine its clinical effect. Thirdly, initial level of consciousness varied from VS/UWS to MCS. Therefore, future clinical trials should set up MCS and VS groups based on larger samples. In addition, we did not utilize neurophysiological and neuroimaging technology (e.g., event-related potential ERP, mainly the P300 component, functional MR), which would allow to better understand the treatment effects and mechanisms of HD-tDCS in patients with DOC (Zhang et al., 2017; Ragazzoni et al., 2019). What's more, P300 recording reflecting residual levels of awareness can assist in prognostication regarding 12-month recovery of consciousness for patients with DOC (Giacino et al., 2018). In future study, Multi-Modality technology should be applied together to provide a broader and more holistic evaluation of therapeutic efficacy.

CONCLUSION

In this study, we found that Long-lasting HD-tDCS over the precuneus could improve the recovery of consciousness in patients with DOC. EEG changes in the delta band were observed in fronta-central-parietal cortex, which provides direct evidence of the HD-tDCS protocol effects on the patients with DOC. Further studies are needed to verify the clinical effect of HD-tDCS on larger numbers of patients and expound the mechanism of the recovery of consciousness of HD-tDCS protocol.

DATA AVAILABILITY

All datasets generated for this study are included in the manuscript and/or the supplementary files.

ETHICS STATEMENT

This study was carried out in accordance with the recommendations of the ethics committee of the Zhengzhou Central Hospital with written informed consent from all subjects. All subjects gave written informed consent in accordance with the Declaration of Helsinki. The protocol was approved by the ethics committee of the Zhengzhou Central Hospital.

AUTHOR CONTRIBUTIONS

YWD, JH, CL, and HZ designed the study. YG, JL, and XW collected the data. YB, XX, and YYD analyzed the data. YB and CL created the figures and tables. YG wrote and edited the manuscript.

FUNDING

This research was supported by the Key Scientific Research Projects of Henan Province Universities and Colleges (19A320041 and 18B310037) and the Medicine and Health Science and Technology Project of Zhejiang Province (2019RC254).

REFERENCES

Angelakis, E., Liouta, E., Andreadis, N., Korfias, S., Ktonas, P., Stranjalis, G., et al. (2014). Transcranial direct current stimulation effects in disorders of consciousness. *Arch. Phys. Med. Rehabil.* 95, 283–289. doi: 10.1016/j.apmr.2013.09.002

Bai, S., Dokos, S., Ho, K. A., and Loo, C. (2014). A computational modelling study of transcranial direct current stimulation montages used in depression. *Neuroimage* 87, 332–344. doi: 10.1016/j.neuroimage.2013.11.015

Bai, Y., Xia, X., Kang, J., Yang, Y., He, J., and Li, X. (2017a). TDCS modulates cortical excitability in patients with disorders of consciousness. *Neuroimage Clin.* 15, 702–709. doi: 10.1016/j.nicl.2017.01.025

Bai, Y., Xia, X., Li, X., Wang, Y., Yang, Y., Liu, Y., et al. (2017b). Spinal cord stimulation modulates frontal delta and gamma in patients of minimally consciousness state. *Neuroscience* 346, 247–254. doi: 10.1016/j.neuroscience.2017.01.036

Bai, Y., Xia, X., Wang, Y., Guo, Y., Yang, Y., He, J., et al. (2017c). Fronto-parietal coherence response to tDCS modulation in patients with disorders of consciousness. *Int. J. Neurosci.* 128, 587–594. doi: 10.1080/00207454.2017.1403440

Blanke, O., Slater, M., and Serino, A. (2015). Behavioral, neural, and computational principles of bodily self-consciousness. *Neuron* 88, 145–166. doi: 10.1016/j.neuron.2015.09.029

Bocci, T., Ferrucci, R., Barloscio, D., Parenti, L., Cortese, F., Priori, A., et al. (2018). Cerebellar direct current stimulation modulates hand blink reflex: implications for defensive behavior in humans. *Physiol. Rep.* 6:e13471. doi: 10.14814/phy2.13471

Borckardt, J. J., Bikson, M., Frohman, H., Reeves, S. T., Datta, A., Bansal, V., et al. (2012). A pilot study of the tolerability and effects of high-definition transcranial direct current stimulation (HD-tDCS) on pain perception. *J. Pain* 13, 112–120. doi: 10.1016/j.jpain.2011.07.001

Bruno, M. A., Majerus, S., Boly, M., Vanhaudenhuyse, A., Schnakers, C., Gosseries, O., et al. (2012). Functional neuroanatomy underlying the clinical subcategorization of minimally conscious state patients. *J. Neurol.* 259, 1087–1098. doi: 10.1007/s00415-011-6303-7

Caparelli-Daquer, E. M., Zimmermann, T. J., Mooshagian, E., Parra, L. C., Rice, J. K., Datta, A., et al. (2012). "A pilot study on effects of 4x1 high-definition tDCS on motor cortex excitability," in *Proceedings of the Annual International Conference of the IEEE Engineering in Medicine and Biology Society*, (San Diego, CA: IEEE), 735–738.

Cavinato, M., Genna, C., Manganotti, P., Formaggio, E., Storti, S. F., Campostrini, S., et al. (2015). Coherence and consciousness: study of fronto-parietal gamma synchrony in patients with disorders of consciousness. *Brain Topogr.* 28, 570–579. doi: 10.1007/s10548-014-0383-5

Cossu, G. (2014). Therapeutic options to enhance coma arousal after traumatic brain injury: state of the art of current treatments to improve coma recovery. *Br. J. Neurosurg.* 28, 187–198. doi: 10.3109/02688697.2013.841845

Davey, M. P., Victor, J. D., and Schiff, N. D. (2000). Power spectra and coherence in the EEG of a vegetative patient with severe asymmetric brain damage. *Clin. Neurophysiol.* 111, 1949–1954.

Della Pepa, G. M., Fukaya, C., La Rocca, G., Zhong, J., and Visocchi, M. (2013). Neuromodulation of vegetative state through spinal cord stimulation: where are we now and where are we going? *Stereotact. Funct. Neurosurg.* 91, 275–287. doi: 10.1159/000348271

Dimitri, D., De Filippis, D., Galetto, V., and Zettin, M. (2017). Evaluation of the effectiveness of transcranial direct current stimulation (tDCS) and psychosensory stimulation through DOCS scale in a minimally conscious subject. *Neurocase* 23, 96–104. doi: 10.1080/13554794.2017.1305112

Dmochowski, J. P., Datta, A., Bikson, M., Su, Y., and Parra, L. C. (2011). Optimized multi-electrode stimulation increases focality and intensity at target. *J. Neural. Eng.* 8:046011. doi: 10.1088/1741-2560/8/4/046011

Donnell, A. D., Nasciment, T., Lawrence, M., Gupta, V., Zieba, T., Truong, D. Q., et al. (2015). High-definition and non-invasive brain modulation of pain and motor dysfunction in chronic TMD. *Brain Stimul.* 8, 1085–1092. doi: 10.1016/j.brs.2015.06.008

Estraneo, A., Pascarella, A., Moretta, P., Masotta, O., Fiorenza, S., Chirico, G., et al. (2017). Repeated transcranial direct current stimulation in prolonged disorders of consciousness: a double-blind cross-over study. *J. Neurol. Sci.* 375, 464–470. doi: 10.1016/j.jns.2017.02.036

Gbadeyan, O., McMahon, K., Steinhauser, M., and Meinzer, M. (2016). Stimulation of dorsolateral prefrontal cortex enhances adaptive cognitive control: a high-definition transcranial direct current stimulation study. *J. Neurosci.* 36, 12530–12536. doi: 10.1523/JNEUROSCI.2450-16.2016

Gerrard, P., Zafonte, R., and Giacino, J. T. (2014). Coma recovery scale-revised: evidentiary support for hierarchical grading of level of consciousness. *Arch. Phys. Med. Rehabil.* 95, 2335–2341. doi: 10.1016/j.apmr.2014.06.018

Giacino, J. T., Fins, J. J., Laureys, S., and Schiff, N. D. (2014). Disorders of consciousness after acquired brain injury: the state of the science. *Nat. Rev. Neurol.* 10, 99–114. doi: 10.1038/nrneurol.2013.279

Giacino, J. T., Katz, D. I., Schiff, N. D., Whyte, J., Ashman, E. J., Ashwal, S., et al. (2018). Practice guideline update recommendations summary: disorders of consciousness: report of the guideline development, dissemination, and implementation subcommittee of the american academy of neurology; the american congress of rehabilitation medicine; and the national institute on disability, independent living, and rehabilitation research. *Neurology* 91, 450–460. doi: 10.1212/wnl.0000000000005926

Giacino, J. T., Whyte, J., Bagiella, E., Kalmar, K., Childs, N., Khademi, A., et al. (2012). Placebo-controlled trial of amantadine for severe traumatic brain injury. *N. Engl. J. Med.* 366, 819–826. doi: 10.1056/NEJMoa1102609

Hogeveen, J., Grafman, J., Aboseria, M., David, A., Bikson, M., and Hauner, K. K. (2016). Effects of high-definition and conventional tDCS on response inhibition. *Brain Stimul.* 9, 720–729. doi: 10.1016/j.brs.2016.04.015

Huang, W., Wannez, S., Fregni, F., Hu, X., Jing, S., Martens, G., et al. (2017). Repeated stimulation of the posterior parietal cortex in patients in minimally conscious state: a sham-controlled randomized clinical trial. *Brain Stimul.* 10, 718–720.

Ionta, S., Martuzzi, R., Salomon, R., and Blanke, O. (2014). The brain network reflecting bodily self-consciousness: a functional connectivity study. *Soc. Cogn. Affect. Neurosci.* 9, 1904–1913. doi: 10.1093/scan/nst185

Kragel, J. E., and Polyn, S. M. (2016). Decoding episodic retrieval processes: frontoparietal and medial temporal lobe contributions to free recall. *J. Cogn. Neurosci.* 28, 125–139. doi: 10.1162/jocn_a_00881

Kuo, H. I., Bikson, M., Datta, A., Minhas, P., Paulus, W., Kuo, M. F., et al. (2013). Comparing cortical plasticity induced by conventional and high-definition 4 x 1 ring tDCS: a neurophysiological study. *Brain Stimul.* 6, 644–648. doi: 10.1016/j.brs.2012.09.010

Laureys, S., and Schiff, N. D. (2012). Coma and consciousness: paradigms (re)-framed by neuroimaging. *Neuroimage* 61, 478–491. doi: 10.1016/j.neuroimage.2011.12.041

Lefaucheur, J. P., Antal, A., Ayache, S. S., Benninger, D. H., Brunelin, J., Cogiamanian, F., et al. (2017). Evidence-based guidelines on the therapeutic use of transcranial direct current stimulation (tDCS). *Clin. Neurophysiol.* 128, 56–92. doi: 10.1016/j.clinph.2016.10.087

Lehembre, R., Marie-Aurelie, B., Vanhaudenhuyse, A., Chatelle, C., Cologan, V., Leclercq, Y., et al. (2012). Resting-state EEG study of comatose patients: a connectivity and frequency analysis to find differences between vegetative and minimally conscious states. *Funct. Neurol.* 27, 41–47.

Martens, G., Lejeune, N., O'Brien, A. T., Fregni, F., Martial, C., Wannez, S., et al. (2018). Randomized controlled trial of home-based 4-week tDCS in chronic minimally conscious state. *Brain Stimul.* 11, 982–990. doi: 10.1016/j.brs.2018.04.021

Naro, A., Calabro, R. S., Russo, M., Leo, A., Pollicino, P., Quartarone, A., et al. (2015). Can transcranial direct current stimulation be useful in differentiating unresponsive wakefulness syndrome from minimally conscious state patients? *Restor. Neurol. Neurosci.* 33, 159–176. doi: 10.3233/rnn-140448

Naro, A., Russo, M., Leo, A., Cannavo, A., Manuli, A., Bramanti, A., et al. (2016). Cortical connectivity modulation induced by cerebellar oscillatory transcranial direct current stimulation in patients with chronic disorders of consciousness: a marker of covert cognition? *Clin. Neurophysiol.* 127, 1845–1854. doi: 10.1016/j.clinph.2015.12.010

Nikolin, S., Loo, C. K., Bai, S., Dokos, S., and Martin, D. M. (2015). Focalised stimulation using high definition transcranial direct current stimulation (HD-tDCS) to investigate declarative verbal learning and memory functioning. *Neuroimage* 117, 11–19. doi: 10.1016/j.neuroimage.2015.05.019

Pandya, D. N., and Seltzer, B. (1982). Intrinsic connections and architectonics of posterior parietal cortex in the rhesus monkey. *J. Comp. Neurol.* 204, 196–210. doi: 10.1002/cne.902040208

Ragazzoni, A., Di Russo, F., Fabbri, S., Pesaresi, I., Di Rollo, A., Perri, R. L., et al. (2019). "Hit the missing stimulus". A simultaneous EEG-fMRI study to localize the generators of endogenous ERPs in an omitted target paradigm. *Sci. Rep.* 9:3684. doi: 10.1038/s41598-019-39812-z

Rampil, I. J. (1998). A primer for EEG signal processing in anesthesia. *Anesthesiology* 89, 980–1002.

Rissman, J., Chow, T. E., Reggente, N., and Wagner, A. D. (2016). Decoding fMRI signatures of real-world autobiographical memory retrieval. *J. Cogn. Neurosci.* 28, 604–620. doi: 10.1162/jocn_a_00920

Schiff, N. D. (2010). Recovery of consciousness after brain injury: a mesocircuit hypothesis. *Trends Neurosci.* 33, 1–9. doi: 10.1016/j.tins.2009.11.002

Schiff, N. D., Giacino, J. T., Kalmar, K., Victor, J. D., Baker, K., Gerber, M., et al. (2007). Behavioural improvements with thalamic stimulation after severe traumatic brain injury. *Nature* 448, 600–603.

Shekhawat, G. S., Sundram, F., Bikson, M., Truong, D., De Ridder, D., Stinear, C. M., et al. (2016). Intensity, duration, and location of high-definition transcranial direct current stimulation for tinnitus relief. *Neurorehabil. Neural Repair* 30, 349–359. doi: 10.1177/1545968315595286

Shekhawat, G. S., and Vanneste, S. (2018). High-definition transcranial direct current stimulation of the dorsolateral prefrontal cortex for tinnitus modulation: a preliminary trial. *J. Neural Transm.* 125, 163–171. doi: 10.1007/s00702-017-1808-6

Thibaut, A., Bruno, M. A., Ledoux, D., Demertzi, A., and Laureys, S. (2014). tDCS in patients with disorders of consciousness: sham-controlled randomized double-blind study. *Neurology* 82, 1112–1118. doi: 10.1212/wnl.0000000000000260

Thibaut, A., Di Perri, C., Chatelle, C., Bruno, M. A., Bahri, M. A., Wannez, S., et al. (2015). Clinical response to tDCS depends on residual brain metabolism and grey matter integrity in patients with minimally conscious state. *Brain Stimul.* 8, 1116–1123. doi: 10.1016/j.brs.2015.07.024

Thibaut, A., Wannez, S., Donneau, A. F., Chatelle, C., Gosseries, O., Bruno, M. A., et al. (2017). Controlled clinical trial of repeated prefrontal tDCS in patients with chronic minimally conscious state. *Brain Inj* 31, 466–474. doi: 10.1080/02699052.2016.1274776

To, W. T., Hart, J., De Ridder, D., and Vanneste, S. (2016). Considering the influence of stimulation parameters on the effect of conventional and high-definition transcranial direct current stimulation. *Expert Rev. Med. Devices* 13, 391–404. doi: 10.1586/17434440.2016.1153968

Tucker, C., and Sandhu, K. (2016). The effectiveness of Zolpidem for the treatment of disorders of consciousness. *Neurocrit. Care* 24, 488–493. doi: 10.1007/s12028-015-0227-5

Villamar, M. F., Volz, M. S., Bikson, M., Datta, A., Dasilva, A. F., and Fregni, F. (2013). Technique and considerations in the use of 4x1 ring high-definition transcranial direct current stimulation (HD-tDCS). *J. Vis. Exp.* 77:e50309. doi: 10.3791/50309

Wenderoth, N., Debaere, F., Sunaert, S., and Swinnen, S. P. (2005). The role of anterior cingulate cortex and precuneus in the coordination of motor behaviour. *Eur. J. Neurosci.* 22, 235–246. doi: 10.1111/j.1460-9568.2005.04176.x

Xia, X., Liu, Y., Bai, Y., Liu, Z., Yang, Y., Guo, Y., et al. (2017). Long-lasting repetitive transcranial magnetic stimulation modulates electroencephalography oscillation in patients with disorders of consciousness. *Neuroreport* 28, 1022–1029. doi: 10.1097/wnr.0000000000000886

Xie, Q., Ni, X., Yu, R., Li, Y., and Huang, R. (2017). Chronic disorders of consciousness. *Exp. Ther. Med.* 14, 1277–1283. doi: 10.3892/etm.2017.4639

Yamamoto, T., Katayama, Y., Obuchi, T., Kobayashi, K., Oshima, H., and Fukaya, C. (2013). Deep brain stimulation and spinal cord stimulation for vegetative state and minimally conscious state. *World Neurosurg.* 80, S30.e1–S30.e9. doi: 10.1016/j.wneu.2012.04.010

Zhang, Y., and Song, W. (2018). Transcranial direct current stimulation in disorders of consciousness: a review. *Int. J. Neurosci.* 128, 255–261. doi: 10.1080/00207454.2017.1381094

Zhang, Y., Song, W., Du, J., Huo, S., Shan, G., and Li, R. (2017). Transcranial direct current stimulation in patients with prolonged disorders of consciousness: combined behavioral and event-related potential evidence. *Front. Neurol.* 8:620. doi: 10.3389/fneur.2017.00620

Zhao, H., Qiao, L., Fan, D., Zhang, S., Turel, O., Li, Y., et al. (2017). Modulation of brain activity with noninvasive transcranial direct current stimulation (tDCS): clinical applications and safety concerns. *Front. Psychol.* 8:685. doi: 10.3389/fpsyg.2017.00685

Conflict of Interest Statement: The authors declare that the research was conducted in the absence of any commercial or financial relationships that could be construed as a potential conflict of interest.

frontiers in Neuroscience

PERSPECTIVE
published: 04 July 2019
doi: 10.3389/fnins.2019.00667

Memory Prosthesis: Is It Time for a Deep Neuromimetic Computing Approach?

*Vassilis Cutsuridis**

School of Computer Science, University of Lincoln, Lincoln, United Kingdom

Memory loss, one of the most dreaded afflictions of the human condition, presents considerable burden on the world's health care system and it is recognized as a major challenge in the elderly. There are only a few neuromodulation treatments for memory dysfunctions. Open loop deep brain stimulation is such a treatment for memory improvement, but with limited success and conflicting results. In recent years closed-loop neuroprosthesis systems able to simultaneously record signals during behavioral tasks and generate with the use of internal neural factors the precise timing of stimulation patterns are presented as attractive alternatives and show promise in memory enhancement and restoration. A few such strides have already been made in both animals and humans, but with limited insights into their mechanisms of action. Here, I discuss why a deep neuromimetic computing approach linking multiple levels of description, mimicking the dynamics of brain circuits, interfaced with recording and stimulating electrodes could enhance the performance of current memory prosthesis systems, shed light into the neurobiology of learning and memory and accelerate the progress of memory prosthesis research. I propose what the necessary components (nodes, structure, connectivity, learning rules, and physiological responses) of such a deep neuromimetic model should be and what type of data are required to train/test its performance, so it can be used as a true substitute of damaged brain areas capable of restoring/enhancing their missing memory formation capabilities. Considerations to neural circuit targeting, tissue interfacing, electrode placement/implantation, and multi-network interactions in complex cognition are also provided.

Keywords: deep learning, neuromimetic architecture, neuromimetic computing, closed loop stimulation, memory implants

OPEN ACCESS

Edited by:
John Thomas Gale, Independent Researcher, Smoke Rise, United States

Reviewed by:
Shaun R. Patel, Harvard Medical School, United States
Cory Inman, Emory University, United States

***Correspondence:**
Vassilis Cutsuridis
vcutsuridis@lincoln.ac.uk;
vcutsuridis@gmail.com

Specialty section:
This article was submitted to Neuroprosthetics, a section of the journal Frontiers in Neuroscience

Received: *12 March 2019*
Accepted: *11 June 2019*
Published: *04 July 2019*

Citation:
Cutsuridis V (2019) Memory Prosthesis: Is It Time for a Deep Neuromimetic Computing Approach? Front. Neurosci. 13:667. doi: 10.3389/fnins.2019.00667

Memory is important in our lives. It is our brain's filing system. Without memory we are unable to remember our past experiences and our loved ones, yet be able to think about the future. Without memory we cannot learn anything. Loss of ability to remember is one of the most dreaded afflictions of the human condition and presents considerable and rising social and economic costs on the world's health and social care systems in the context of the increasing aging of the world's population. Brain disorders such as Alzheimer's disease (AD) and Traumatic Brain Injury (TBI) lead to profound memory deficits and are recognized as major challenges and one of the most important causes of disability in the elderly.

Unfortunately, there are only a few non-pharmacological neuromodulation treatments (Guo et al., 2002; Sjögren et al., 2002; Solé-Padullés et al., 2006; Mannu et al., 2011; Suthana et al., 2012) which alter the course and symptoms of these brain disorders.

Direct deep-brain stimulation (DBS) has emerged in the last decade as a neuromodulation technique to treat memory dysfunctions (Hu et al., 2009; Arrieta-Cruz et al., 2010; Laxton et al., 2010; Stone et al., 2011; Boggio et al., 2012; Lyketsos et al., 2012; Suthana et al., 2012; Fell et al., 2013; Hardenacke et al., 2013; Hescham et al., 2013a, 2015; Lee D. J. et al., 2013; Suthana and Fried, 2014; Sweet et al., 2014; Lee et al., 2015; Sankar et al., 2015; Zhang et al., 2015; Jacobs et al., 2016; Lozano et al., 2016; Rezai et al., 2016), but with limited success and contradicting results. A review of all DBS studies is beyond the scope of this article. Interested readers should refer to Bick and Eskandar (2016); Khan et al. (2019); Curot et al. (2017); Ezzyat and Rizzuto (2018) for excellent extensive reviews of the effects of DBS on all memory-related brain areas. Below I briefly review a few of these conflicting studies. In one study DBS at 50Hz applied to human entorhinal cortex (EC) enhanced spatial memory, while hippocampal stimulation did not affect performance (Suthana et al., 2012), whereas in another study DBS at 50 Hz application to both human EC and hippocampus (HC) disrupted spatial and verbal memory (Jacobs et al., 2016). In both studies DBS was applied during the encoding phase, and recall performance was tested when stimulation was off. In another study when 50 Hz DBS was applied between the encoding and recall periods in the left medial temporal lobe (MTL) of patients, then memory recall was impaired (Merkow et al., 2017). Direct electrical stimulation at 50 Hz in HC, parahippocampal regions, prefrontal cortex and lateral temporal cortex (LTC) found that high gamma activity induced by word presentation was decreased in regions where stimulation decreased memory performance, and increased in LTC where memory enhancement was observed (Kucewicz et al., 2018). In other studies, memory impairment was observed when both hippocampi were stimulated simultaneously (Lacruz et al., 2010), but the type of impairment depended on which hippocampus was stimulated (Coleshill et al., 2004). Theta-burst micro-stimulation with physiologic level currents in the right EC during learning significantly improved memory specificity for novel portraits as well as recognition of previously-viewed photos, but not for similar lures (Titiz et al., 2017). On the other hand, theta-burst stimulation of human MTL resulted in spatial memory retrieval impairment (Kim et al., 2018). Theta-burst stimulation in amygdala or fornix (FX) in humans led to visuo-spatial memory enhancement (Miller et al., 2015; Inman et al., 2018). Chronic DBS at 130–450 Hz for several months showed no significant or subtle improvement in memory (Velasco et al., 2007; McLachlan et al., 2010; Boëx et al., 2011; Miatton et al., 2011). Bilateral 20Hz DBS of nucleus basalis of Meynert (NBM) showed memory improvement when stimulation was applied at an earlier stage of dementia and a younger age cohort (Kuhn et al., 2015). Bilateral DBS of anterior thalamic nucleus (ATN) of an epilepsy patient cohort showed greater subjective memory impairment when the stimulation was on and improved word fluency and verbal memory (Fisher et al., 2010; Oh et al., 2012).

Similar conflicting results have been observed in animal studies. Intermittent stimulation in NBM in adult monkeys enhanced working memory, but continuous stimulation led to memory impairment (Liu et al., 2017). EC stimulation in rats promoted neurogenesis in dentate gyrus and enhanced spatial memory in a water maze task in a manner dependent on neurogenesis (Stone et al., 2011). Chronic DBS in Alzheimer's disease (AD) mice improved performance in Morris water maze task with AD-DBS mice spending more time at the novel object and location than with AD-no stimulation mice (Mann et al., 2018). EC, FX, and region CA1 stimulation during a spatial memory study restores performance in a rat scopolamine injection dementia model (Hescham et al., 2013b, 2015), whereas in another study DBS of EC and FX showed significant HC-dependent spatial memory improvement in Morris water maze than in ATN DBS (Zhang et al., 2015). HC-independent recognition memory was also enhanced by EC and FX DBS, but not with ATN DBS (Zhang et al., 2015). Low-current stimulation of rostral intralaminar thalamic nuclei in rats just prior to memory retrieval in a delayed match-to-sample task improved performance, whereas high-current stimulation impaired it (Mair and Hembrook, 2008).

These conflicting results are due to methodological differences across human and animal studies including but not limited to details in participants (age, cognitive, and neurologic abnormalities), animal species (rats, mice, monkeys), behavioral task design, electrode characteristics (e.g., electrode geometry), electrode placements (location), stimulation parameters (amplitude, impedance, frequency, duration, charge density), timing of stimulation (during encoding phase, during retrieval phase, in-between encoding, and retrieval), mode of stimulation (intermittent, chronic, continuous) and statistical analysis methods (Montgomery and He, 2016; Suthana et al., 2018). Open-loop DBS generates only pre-programmed high frequency electrical stimulations without being able to receive feedback from the current brain state. Because of its therapeutic effectiveness, clinical innervations have so far preceded the scientific understanding of its mechanisms of action (McIntyre et al., 2004).

Future advances in memory prosthesis technology should thus address fundamental questions on its therapeutic mechanisms of action. They should also be closed-loop (i.e., receive feedback from the current brain state), capable of online self-adaptation to time-varying environments, and amenable to low-power hardware implementations for memory restoration and rehabilitation (Senova et al., 2018). They should be able to simultaneously record neural signals during behavioral tasks and then with the use of internal factors of the neural state determine the precise timing of stimulation (e.g., stimulating at a particular phase of an ongoing endogenous neural oscillation), or make the decision whether to stimulate at all (Hampson et al., 2013; Deadwyler et al., 2017; Ezzyat et al., 2018). Developments toward the latter direction have already been attempted (Berger et al., 2008, 2011; Deadwyler et al., 2017; Ezzyat et al., 2017, 2018). The Ramp project (Ramp project)[1] examined the efficacy of a biohybrid architecture of tightly coupled natural and neuromorphic hardware neurons. CoroNet (Coronet FP7 project)[2] developed the scientific and technological foundations for future "bio-hybrid" devices that

[1] Ramp project. Available online at: http://www.rampproject.eu
[2] Coronet FP7 Project. Available online at: http://www.coronet-project.eu

will combine biological and artificial nervous tissues. DARPA's RAM project (DARPA RAM project)[3] aims to develop and test a wireless, fully implantable neural-interface medical device for human clinical use. The Human Brain Project (Human Brain Project)[4] although not directly contributing in the biohybrid/implant direction, it indirectly contributes to it with its neuromorphic hardware (1Mio cores Spinnaker machine) and brain simulation platform.

The first stride toward a closed-loop implantable memory prosthesis system was conducted by Berger et al. (Song et al., 2009; Berger et al., 2010, 2011; Hampson et al., 2012) as an artificial bridge between the chemically lesioned CA3 and CA1 synaptic connections in a rat's hippocampus, when the animal was trained to perform a delayed non-matched sample (DNMS) task. The chip consisted of three components: (1) a recording multi-electrode array (MEA), (2) a very large scale integration (VLSI) implemented multi-input multi-output (MIMO) prediction model of neural activity based on the recorded neural signals, and (3) a stimulating MEA driven by the MIMO predicted neural activities. The MIMO predicted spiking neural activity was based on five electrophysiological mechanisms: (i) a feedforward process transforming the input MEA recorded spike train to a synaptic potential, (ii) a feedback process generating an after-potential caused by the output spike, (iii) an intrinsic neuronal noise, (iv) a subthreshold potential dynamics, and (v) a threshold function to generate each output spike. When the chip was tested against the damaged CA3-CA1 connection in the lesioned rat, the animal was able to successfully perform the DNMS task with a success rate of over 90% (the success rate for a lesioned rat without the prosthetic device was $<$50%), demonstrating the chip as a viable memory enhancement device. A second stride toward memory improvement by the chip was made by the same group in non-human primates trained in a delayed match-to-sample (DMS) task (Deadwyler et al., 2017). Despite the chip's successes, it had several limitations. First, it was tested against a single behavioral task on a well-trained animal. That meant the model was "trained" to perform a single input-output mapping. Furthermore, the model was non-adaptive (hard-wired), unable to improve its performance through experience according to a prescribed learning rule. Initial attempts toward the latter direction have been recently made by the same group by incorporating a phenomenological spike timing-dependent plasticity (STDP) rule in an updated MIMO model (Song et al., 2014). However, its synaptic plasticity rule was far too simplistic to capture the complex molecular and biochemical dynamics of synaptic plasticity *in vivo* (Froemke and Dan, 2002; Froemke et al., 2005; Wang et al., 2005). Both MIMO models were completely blind to the CA3 circuit memory computations and processes during their therapeutic courses of action.

A third stride toward a closed-loop memory enhancement/restoration stimulation system was recently made by Ezzyat et al. (2017, 2018) using a machine learning (ML) approach. A set of stimulation-free trials with neural data and labels indicating memory performance was collected from 25 neurosurgical patients undergoing clinical monitoring for epilepsy while they participated in a delayed free recall memory task. A multivariate classifier model was then trained to discriminate patterns of neural activity during encoding for each particular participant. The resulting weight codes from training were then used during testing to map features of iEEG activity to an output probability value, which in turn generated appropriate stimulation patterns during a later word recall phase. Improved memory recall performance was demonstrated particularly when stimulation was timed to periods of poor memory function. Despite its memory improvement success, the closed-loop stimulation system was completely "blind" to the neurobiology of learning and memory offering no insights into the biophysical mechanisms of action of DBS stimulation of the human lateral MTL when participants perform a memory recall task.

With the advent of new and more advanced experimental techniques (Boyden, 2015; Grosenick et al., 2015; Grossman et al., 2017; Kim et al., 2017; Chen et al., 2018; Hardt and Nadel, 2018; Lee and Brecht, 2018), a wealth of knowledge about the anatomical, physiological, molecular, synaptic and connectivity properties of the various cell types in memory-related circuits has accumulated (Cutsuridis et al., 2010a, 2019; Prager et al., 2016; Sprekeler, 2017; Lucas and Clem, 2018). Apart from the numerous different identified classes of interneurons targeting specific parts of excitatory cells (Freund and Buzsáki, 1996; Markram et al., 2004; Klausberger and Somogyi, 2008; Ehrlich et al., 2009; Karnani et al., 2014; Prager et al., 2016; Tremblay et al., 2016; Sprekeler, 2017; Krabbe et al., 2018) and a complex set of intra- and extra-areal excitatory inputs targeting them (Witter, 2019) there is also increasing evidence on the important role of inhibition between interneurons (Chamberland and Topolnik, 2012) in sculpting their activity and entraining them to fire with respect to ongoing network oscillations (Somogyi et al., 2013; Roux and Buzsáki, 2015; Cardin, 2018). Synapses on excitatory and inhibitory cells have been shown to undergo various forms of long-term plasticity (LTP/LTD/STDP, branch potentiation, clustered plasticity, metaplasticity) across different timeframes (ms, seconds, minutes, hours, days, longer) (Govindarajan et al., 2006; Citri and Malenka, 2008; Losonczy et al., 2008; Froemke, 2015; Hattori et al., 2017; Hennequin et al., 2017; Lamsa and Lau, 2019). Hippocampal oriens interneurons display anti-Hebbian long term potentiation, which depends on cholinergic modulation via nicotinic acetylcholine receptors (Griguoli et al., 2013; Rozov et al., 2017). Experimental investigations and compartmental modeling has predicted inhibition of dendritic Ca^{2+} transients modulate the sign and magnitude of synaptic plasticity like long-term potentiation (LTP) or long term depression (LTD) (Cutsuridis, 2011, 2012, 2013; Gidon and Segev, 2012; Jadi et al., 2012; Camiré and Topolnik, 2014) The interaction mechanisms of such molecular, synaptic and cellular components form complex neural circuitries firing at different phases of neuronal oscillations, externally paced or internally generated (Cobb et al., 1995; Buzsaki, 2002; Montgomery et al., 2009), which support different functionalities in health and

[3]DARPA's RAM project. Available online at: http://www.darpa.mil/program/restoring-active-memory

[4]Human Brain Project. Available online at: https://www.humanbrainproject.eu/en/

disease of memory and learning (Marín, 2012; Hangya et al., 2014; Wester and McBain, 2014; Caroni, 2015; Prager et al., 2016; Maffei et al., 2017; Villette and Dutar, 2017; Lucas and Clem, 2018; Vargova et al., 2018). Only by linking this wealth of information into coherent theoretical frameworks (Cutsuridis and Wenneckers, 2009; Cutsuridis et al., 2010b, 2011; Cutsuridis and Hasselmo, 2012; Pendyam et al., 2013; Bezaire et al., 2016) light will be shed into the therapeutic mechanisms of action of any memory enhancement/improvement system. Thus, with the recent exponential increase in computational power, it is thus imperative for the experimental including medical and computational communities to communicate with each other more closely, in order to decipher the molecular, synaptic, cellular, circuit, and systems mechanisms by which closed-loop neuromodulation system operates in memory enhancement, restoration, and rehabilitation and accelerate the progress in memory prosthesis research.

Below, I provide few guidelines on how to construct such a system. I propose that a computational deep (multi-layered) neuromimetic circuit approach empowered with biophysically realistic learning rules mimicking the neural dynamics of memory related circuits amenable to neuromorphic VLSI hardware driven by *in-vivo* MEA recordings, able to decode memory engrams and stimulate memory related populations of neurons should be adopted to move forward the memory prosthesis research. Model components (nodes, synapses, connectivity) should have to mimic the operations of real neurons, synapses and circuits. Several strides toward this direction have already been made (Cutsuridis and Wenneckers, 2009; Cutsuridis et al., 2010b, 2011; Cutsuridis and Hasselmo, 2012; Schneider et al., 2012; Pendyam et al., 2013; Bezaire et al., 2016; Sanjay and Krothapalli, 2019; Yu et al., 2019). One such stride was the Cutsuridis et al. (2010b) microcircuit model of region CA1 dynamics in encoding and retrieval of memories. The study explored the functional roles of somatic, axonic and dendritic inhibition during these processes. It showed how theta modulated inhibition separated encoding and retrieval of memories in the hippocampus into two functionally independent processes. The study predicted: (1) somatic inhibition allowed generation of dendritic calcium spikes that promoted synaptic LTP, while minimizing cell output, (2) proximal dendritic inhibition controlled both cell output and suppressed dendritic calcium spikes, thus preventing LTP, and (3) distal dendritic inhibition removed interference from spurious memories during recall. Some of the Cutsurdis et al. study's predictions have been recently verified by experimental studies (Siegle and Wilson, 2014). The model should also be empowered with biophysically realistic learning rules (LTP/LTD/STDP, branch potentiation, clustered plasticity, metaplasticity, error driven Hebbian learning, etc) mimicking the processes and operations of synaptic plasticity across different timeframes (ms, seconds, minutes, hours, days, longer) in neural cells (Kastellakis et al., 2015, 2016; Li et al., 2016). Once the model's neural dynamics has been extensively validated against experimental data from multiple levels of detail (molecular, synaptic, cellular, dendritic, micro-, meso- and macro-circuit), thus casting it as a faithful representation of a real human/animal tissue (memory circuit), then the model should be trained with real MEA recording and stimulation data from humans or animals while they are performing memory-related behavioral tasks and with verified memory restoration/enhancement effects. Deficits should be in the encoding and/or retrieval of declarative memories (or specific types of declarative memories). Behavioral memory tasks should assess performance metrics across various timeframes (hours, days, weeks, or longer) testing different memory specificities (e.g., memory of an object, event, or context in which it occurs, or high-level semantics of sets of objects/events, or an association of an object and an event linked to one another in a memory occurring either simultaneously or in a temporal sequence). MEA data should be split in training, cross-validation and testing datasets. Model's performance must be tested across individual participants and/or the whole participant population and it must be able to retain functionality across time, situational contexts, and/or experimental settings (tasks). Model robustness and generalization should be validated within and across individual human participant and/or animal and should be demonstrated by the ability of the model to restore memory function when applied to different human participants/animals and in different situational contexts.

Once the model has been computationally trained and its performance have been extensively tested across individuals, experimental settings, memory types and situational contexts, then its structure and weight codes can be transferred to a neuromorphic chip to be implanted or interfaced with indwelling probes for recording and stimulation of human and/or animal neural activity. At this point a number of other outstanding technical difficulties need to be overcome and questions to be answered:

- Electrode Placement and Implantation: The exact placement and trajectory path for the recording and simulation electrodes is of paramount importance to any successful implantable neuroprosthesis system. Any slight deviation from the optimal path to the target due to lead migration or misplacement may result in adverse effects such as hemorrhage, seizures, abnormal sensations, etc or tissue damage (Edwards et al., 2017). Electrode location thus must be adjusted to maximize therapeutic effects, while minimize adverse ones (Edwards et al., 2017). Intra/post-operative imaging (e.g., MRI or CAT) scans can confirm electrode placement (Edwards et al., 2017).
- Neural Circuit Targeting: The electrical field generated by a DBS macroelectrode affects the three-dimensional geometry of the surrounding to the electrode neural processes (i.e., axons and dendrites) (McIntyre et al., 2004). Knowing the anatomical distribution of the DBS electric field and controlling its shape is of utmost importance to maximize the therapeutic effect of stimulation, minimize its adverse effects, and get a deeper understanding of the DBS mechanisms of action (Klooster et al., 2016; Edwards et al., 2017). Electrode design (size, diameter, number of contacts) and directional steering is an active experimental and theoretical research area (Klooster et al., 2016). Mathematical models using finite difference or finite element methods model the electric field induced in the brain during DBS as a function of different

stimulation parameters and delineate the effects the electric field has on the neural tissue. The importance of specific conductivities, encapsulation layers and steering toward the stimulation target are some of the main focuses of these studies (Wei and Grill, 2005; Johnson and McIntyre, 2008; Vasques et al., 2009; Schmidt and van Rienen, 2012a,b; Lempka and McIntyre, 2013). Recently developed neural probes have provided precision in shaping the electrical field generated during stimulation (Klooster et al., 2016). One such probe is the "SureSTIM" (Martens et al., 2011), a 64 disc-shaped electrode array arranged in 16 equally-spaced rows, which allows for both long-term stimulation and local field potential recording, while diminishes the induction of adverse effects by stimulating tissue beyond the stimulation target.

- Neural Tissue Interfacing and Longevity: Brain-chip interfaces allow for chips and nerve tissue to establish a close physical interaction thus allowing the transfer of information in one or both directions (Vassanelli et al., 2012). Major operations, like cognition including memory, are sustained by the concurrent activity of a large number of neurons in complex neural networks located in several interconnected brain structures. To better understand neural circuit operations and to develop powerful brain-machine interfaces, then an interface between a semiconductor chip or an ensemble of chips and the neural tissue of a living animal allowing for bi-directional communication (not only to record but also to control neuronal activity) and high-spatiotemporal resolution sampling of a large number of neurons over the networks, and simultaneously from multiple regions of the brain is needed (Vassanelli et al., 2012). Usually small CMOS chips featuring stimulation and recording sites integrated at high-density implanted in one or in several brain areas, either independently or simultaneously, can lead to an unprecedented control of neuronal activity in the mammalian brain (CyberRat ICT 2007 project)[5] Obtaining such high spatiotemporal resolution enables to explore and control brain information processing with unprecedented detail. The chips are either directly implanted into the tissue or connected through leads that reside permanently in the brain. Wireless transmission is desired to simplify chips connectivity with the monitoring system and to remove interference with animals' movements (Vassanelli et al., 2012). Several bottlenecks are usually faced: power dissipation induced heat generation of the chips, biocompatibility and mechanical-electrical stability, particularly for chronic implantation in the freely behaving animal, chip implantation (and chip design) to match at best the 2D architecture of the array with the 3D architecture of the neuronal networks in the brain while limiting to the minimum tissue damage (Vassanelli, 2018).
- Multi-Network Interactions in Complex Cognition: For a long time, it was hypothesized that DBS worked either via functional ablation by suppressing or inhibiting the structure being stimulated or via activation of the stimulated structure (McIntyre et al., 2004). It is currently accepted that DBS changes network-wide oscillations and there may be coherence between cortical and subcortical brain signals (Wagle Shukla and Okun, 2012; Lee H. et al., 2013). Are these changes though due to a widespread DBS electric field affecting circuits/areas/regions well beyond the stimulated one (global effects) or due to a localized electric field affecting only the DBS brain circuit/region/area, which in turn drives other connected with it brain circuits/regions/areas (local effects)? A notable study on uncovering the mechanisms of whole-brain dynamics of deep brain stimulation has shown that DBS shifts global brain dynamics of patients toward a healthy regime with the effect more pronounced in specific brain areas (Saenger et al., 2017). Higher communicability and coherence in brain areas were measured when DBS was on than then it was off (Saenger et al., 2017).

Overall, to accelerate progress in memory prosthesis technologies then a closed-loop deep neuromimetic circuit computing approach empowered with biophysically realistic learning rules mimicking the neural dynamics of memory related circuits amenable to neuromorphic VLSI hardware driven by *in-vivo* MEA recordings, able to decode memory engrams and stimulate memory related populations of neurons should be adopted. Such software novelties along with multimodal neuroimaging, electrophysiological and electrochemical monitoring technologies and innovative neural probe engineering advances (e.g., SureSTIM) could then act as true substitutes (bridges) of damaged memory-related brain areas capable of restoring/enhancing their missing memory formation capabilities as well as deciphering their mechanisms of action.

DATA AVAILABILITY

No datasets were generated or analyzed for this study.

AUTHOR CONTRIBUTIONS

The author confirms being the sole contributor of this work and has approved it for publication.

ACKNOWLEDGMENTS

Authors would like to thank Stefanos Kollias, Jonathan Erichsen and the two reviewers for comments on earlier versions of the manuscript.

[5]CyberRat ICT 2007 project. Available online at: https://www.vassanellilab.eu/projects/cyberrat/

REFERENCES

Arrieta-Cruz, I., Pavlides, C., and Pasinetti, G. M. (2010). Deep brain stimulation in midline thalamic region facilitates synaptic transmission and short term memory in a mouse model of Alzheimer's disease. *Transl. Neurosci*. 1, 188–194. doi: 10.2478/v10134-010-0023-x

Berger, T. W., Gerhardt, G., Liker, M. A., and Sousou, W. (2008). The impact of neurotechnology in rehabilitation. *IEEE Rev. Biomed. Eng.* 1, 157–197. doi: 10.1109/RBME.2008.2008687

Berger, T. W., Hampson, R. E., Song, D., Goonawardena, A., Marmarelis, V. Z., and Deadwyler, S. A. (2011). A cortical neural prosthesis for restoring and enhancing memory. *J. Neural Eng.* 8:046017. doi: 10.1088/1741-2560/8/4/046017

Berger, T. W., Song, D., Chan, R. H., and Marmarelis, V. Z. (2010). The neurobiological basis of cognition: Identification by multi-input, multioutput nonlinear dynamic modelling. *Proc. IEEE Inst. Electr. Electron. Eng.* 98, 356–374. doi: 10.1109/JPROC.2009.2038804

Bezaire, M. J., Raikov, I., Burk, K., Vyas, D., and Soltesz, I. (2016). Interneuronal mechanisms of hippocampal theta oscillations in a full-scale model of the rodent CA1 circuit. *Elife*. 5:e18566. doi: 10.7554/eLife.18566

Bick, S. K., and Eskandar, E. N. (2016). Neuromodulation for restoring memory. *Neurosurg. Focus* 40:E5. doi: 10.3171/2016.3.FOCUS162

Boëx, C., Seeck, M., Vulliémoz, S., Rossetti, A. O., Staedler, C., Spinelli, L., et al. (2011). Chronic deep brain stimulation in mesial temporal lobe epilepsy. *Seizure* 20, 485–490. doi: 10.1016/j.seizure.2011.03.001

Boggio, P. S., Ferrucci, R., Mameli, F., Martins, D., Martins, O., Vergari, M., et al. (2012). Prolonged visual memory enhancement after direct current stimulation in Alzheimer's disease. *Brain Stimulat.* 5, 223–230. doi: 10.1016/j.brs.2011.06.006

Boyden, E. S. (2015). Optogenetics and the future of neuroscience. *Nat. Neurosci.* 18, 1200–1201. doi: 10.1038/nn.4094

Buzsaki, G. (2002). Theta oscillations in the hippocampus. *Neuron* 33, 325–340. doi: 10.1016/S0896-6273(02)00586-X

Camiré, O., and Topolnik, L. (2014). Dendritic calcium nonlinearities switch the direction of synaptic plasticity in fast-spiking interneurons. *J. Neurosci.* 34, 3864–3877. doi: 10.1523/JNEUROSCI.2253-13.2014

Cardin, J. A. (2018). Inhibitory interneurons regulate temporal precision and correlations in cortical circuits. *TINS* 41, 689–700. doi: 10.1016/j.tins.2018.07.015

Caroni, P. (2015). Inhibitory microcircuit modules in hippocampal learning. *Curr. Opin. Neurobiol.* 35, 66–73. doi: 10.1016/j.conb.2015.06.010

Chamberland, S., and Topolnik, L. (2012). Inhibitory control of hippocampal inhibitory neurons. *Front Neurosci.* 6:165. doi: 10.3389/fnins.2012.00165

Chen, S., Weitemier, A. Z., Zeng, X., He, L., Wang, X., Tao, Y., et al. (2018). Near-infrared deep brain stimulation via upconversion nanoparticle-mediated optogenetics. *Science* 359, 679–684. doi: 10.1126/science.aaq1144

Citri, A., and Malenka, R. C. (2008). Synaptic plasticity: multiple forms, functions, and mechanisms. *Neuropsychopharmacology* 33, 18–41. doi: 10.1038/sj.npp.1301559

Cobb, S. R., Buhl, E. H., Halasy, K., Paulsen, O., and Somogyi, P. (1995). Synchronization of neuronal activity in hippocampus by individual GABAergic interneurons. *Nature* 378, 75–78. doi: 10.1038/378075a0

Coleshill, S. G., Binnie, C. D., Morris, R. G., Alarcón, G., van Emde Boas, W., Velis, D. N., et al. (2004). Material-specific recognition memory deficits elicited by unilateral hippocampal electrical stimulation. *J. Neurosci.* 24, 1612–1616. doi: 10.1523/JNEUROSCI.4352-03.2004

Curot, J., Busigny, T., Valton, L., Denuelle, M., Vignal, J. P., Maillard, L., et al. (2017). Memory scrutinized through electrical brain stimulation: a review of 80 years of experiential phenomena. *Neurosci. Biobehav. Rev.* 78. 161–177. doi: 10.1016/j.neubiorev.2017.04.018

Cutsuridis, V. (2011). GABA inhibition modulates NMDA-R mediated spike timing dependent plasticity (STDP) in a biophysical model. *Neural Netw. [[Inline Image]]*24, 29–42. doi: 10.1016/j.neunet.2010.08.005

Cutsuridis, V. (2012). Bursts shape the NMDA-R mediated spike timing dependent plasticity curve: role of burst interspike interval and GABA inhibition. *Cogn. Neurodynamics* 6, 421–441. doi: 10.1007/s11571-012-9205-1

Cutsuridis, V. (2013). Interaction of inhibition and triplets of excitatory spikes modulates the NMDA-R mediated synaptic plasticity in a computational model of spike timing dependent plasticity. *Hippocampus* 23, 75–86. doi: 10.1002/hipo.22057

Cutsuridis, V., Cobb, S. and Graham, B. P., (2010b). Encoding and retrieval in the hippocampal CA1 microcircuit model. *Hippocampus* 20, 423–446. doi: 10.1002/hipo.20661

Cutsuridis, V., Graham, B. P., Cobb, S., and Vida, I. (2010a). *Hippocampal Microcircuits: A Computational Modeler's Resource Book*, *1st edn.* New York City, NY: Springer. doi: 10.1007/978-1-4419-0996-1

Cutsuridis, V., Graham, B. P., Cobb, S., and Vida, I. (2019). *Hippocampal Microcircuits: A Computational Modeler's Resource Book, 2nd edn*. Cham: Springer. doi: 10.1007/978-3-319-99103-0

Cutsuridis, V., Grahan, B. P., Cobb, S., and Hasselmo, M. E. (2011). "Bio-inspired models of memory capacity, recall performance and theta phase precession," in *Proceedings of the IJCNN* (San Jose, CA: IEEE), 141–148. doi: 10.1109/IJCNN.2011.6033637

Cutsuridis, V., and Hasselmo, M. (2012). GABAergic modulation of gating, timing and theta phase precession of hippocampal neuronal activity during theta oscillations. *Hippocampus* 22, 1597–1621. doi: 10.1002/hipo.21002

Cutsuridis, V., and Wenneckers, T. (2009). Hippocampus, microcircuits and associative memory. *Neural Netw.* 22, 1120–1128. doi: 10.1016/j.neunet.2009.07.009

Deadwyler, S. A., Hampson, R. E., Song, D., Opris, I., Gerhrdt, G. A., Marmarelis, V. Z., et al. (2017). A cognitive prosthesis for memory facilitation by closed-loop function ensemble stimulation of hippocampal neurons in primate brain. *Exp. Neurol.* 287(Pt 4): 452–460. doi: 10.1016/j.expneurol.2016.05.031

Edwards, C. A., Kouzani, A., Lee, k. H., and Ross, E. K. (2017). Neurostimulation devices for the treatment of neurologic devices. *Mayo Clin. Proc.* 92, 1427–1444. doi: 10.1016/j.mayocp.2017.05.005

Ehrlich, I., Humeau, Y., Grenier, F., Ciocchi, S., Herry, C., and Lüthi, A. (2009). Amygdala inhibitory circuits and the control of fear memory. *Neuron* 62, 757–771. doi: 10.1016/j.neuron.2009.05.026

Ezzyat, Y., Kragel, J. E., Burke, J. F., Gorniak, R., Rizzuto, D. S., and Kahana, M. J. (2017). Direction brain stimulation modulates encoding states and memory performance. *Curr. Biol.* 27, 1251–1258. doi: 10.1016/j.cub.2017.03.028

Ezzyat, Y., and Rizzuto, D. S. (2018). Direct brain stimulation during episodic memory. *Curr. Opin. Biomed. Eng.* 8, 78–83. doi: 10.1016/j.cobme.2018.11.004

Ezzyat, Y., Wanda, P. A., Levy, D. F., Kadel, A., Aka, A., Pedisich, I., et al. (2018). Closed-loop stimulation of temporal cortex rescues functional networks and improves memory. *Nat. Commun.* 9:365. doi: 10.1038/s41467-017-02753-0

Fell, J., Staresina, B. P., Do Lam, A. T., Widman, G., Helmstaedter, C., Elger, C. E., et al. (2013). Memory modulation by weak synchronous deep brain stimulation: a pilot study. *Brain Stimulat.* 6, 270–273. doi: 10.1016/j.brs.2012.08.001

Fisher, R., Salanova, V., Witt, T., Worth, R., Henry, T., Gross, R., et al. (2010). Electrical stimulation of the anterior nucleus of thalamus for treatment of refractory epilepsy. *Epilepsia* 51, 899–908. doi: 10.1111/j.1528-1167.2010.02536.x

Freund, T. F., and Buzsáki, G. (1996). Interneurons of the hippocampus. *Hippocampus* 6, 347–470.

Froemke, R. C. (2015). Plasticity of cortical excitatory-inhibitory balance. *Annu Rev Neurosci.* 38, 195–219. doi: 10.1146/annurev-neuro-071714-034002

Froemke, R. C., and Dan, Y. (2002). Spike timing-dependent synaptic modification induced by natural spike trains. *Nature* 416:4330438. doi: 10.1038/416433a

Froemke, R. C., Poo, M. M., and Dan, Y. (2005). Spike timing-dependent synaptic plasticity depends on dendritic location. *Nature* 434, 221–225. doi: 10.1038/nature03366

Gidon, A., and Segev, I. (2012). Principles governing the operation of synaptic inhibition in dendrites. *Neuron* 75, 330–341. doi: 10.1016/j.neuron.2012.05.015

Govindarajan, A., Kelleher, R. J., and Tonegawa, S. (2006). A clustered plasticity model of long-term memory engrams. *Nat. Rev. Neurosci.* 7, 575–583. doi: 10.1038/nrn1937

Griguoli, M., Cellot, G., and Cherubini, E. (2013). In hippocampal oriens interneurons anti-Hebbian long-term potentiation requires cholinergic signaling via α7 nicotinic acetylcholine receptors. *J. Neurosci.* 33, 1044–1049. doi: 10.1523/JNEUROSCI.1070-12.2013

Grosenick, L., Marshel, J. H., and Deisseroth, K. (2015). Closed-loop and activity-guided optogenetic control. *Neuron* 86, 106–139. doi: 10.1016/j.neuron.2015.03.034

Grossman, N., Bono, D., Dedic, N., Kodandaramaiah, S. B., Rudenko, A., Suk, H. J., et al. (2017). Noninvasive deep brain stimulation via temporally interfering electric fields. *Cell* 169, 1029–1041.e16. doi: 10.1016/j.cell.2017.05.024

Guo, Y., Shi, X., Uchiyama, H., Hasegawa, A., Nakagawa, Y., Tanaka, M., et al. (2002). A study on the rehabilitation of cognitive function and short-term memory in patients with Alzheimer's disease using transcutaneous electrical nerve stimulation. *Front. Med. Biol. Eng.* 11, 237–247. doi: 10.1163/156855701321138905

Hampson, R. E., Song, D., Chan, R. H., Sweatt, A. J., Riley, M. R., Gerhardt, G. A., et al. (2012). A nonlinear model for hippocampal cognitive prosthesis: memory facilitation by hippocampal ensemble stimulation. *IEEE Trans. Neural. Syst. Rehabil. Eng.* 20, 184–197. doi: 10.1109/TNSRE.2012.2189163

Hampson, R. E., Song, D., Opris, I., Santos, L. M., Shin, D. C., Gerhardt, G. A., et al. (2013). Facilitation of memory encoding in primate hippocampus by a neuroprosthesis that promotes task specific neural firing. *J. Neural Eng.* 10:066013. doi: 10.1088/1741-2560/10/6/066013

Hangya, B., Pi, H. J., Kvitsiani, D., Ranade, S. P., and Kepecs, A. (2014). From circuit motifs to computations: mapping the behavioral repertoire of cortical interneurons. *Curr. Opin. Neurobiol.* 26, 117–124. doi: 10.1016/j.conb.2014.01.007

Hardenacke, K., Kuhn, J., Lenartz, D., Maarouf, M., Mai, J. K., Bartsch, C., et al. (2013). Stimulate or degenerate: deep brain stimulation of the nucleus basalis Meynert in Alzheimer dementia. *World Neurosurg* 80, S27.e35–S27.e43. doi: 10.1016/j.wneu.2012.12.005

Hardt, O., and Nadel, L. (2018). Systems consolidation revisited, but not revised: The promise and limits of optogenetics in the study of memory. *Neurosci Lett.* 680, 54–59. doi: 10.1016/j.neulet.2017.11.062

Hattori, R., Kuchibhotla, K. V., Froemke, R. C., and Komiyama, T. (2017). Functions and dysfunctions of neocortical inhibitory neuron subtypes. *Nat. Neurosci.* 20, 1199–1208. doi: 10.1038/nn.4619

Hennequin, G., Agnes, E. J., and Vogels, T. P. (2017). Inhibitory plasticity: balance, control, and co-dependence. *Annu. Rev. Neurosci.* 40, 557–579. doi: 10.1146/annurev-neuro-072116-031005

Hescham, S., Jahanshahi, A., Meriaux, C., Lim, L. W., Blokland, A., and Temel, Y. (2015). Behavioral effects of deep brain stimulation of different areas of the Papez circuit on memory- and anxiety related functions. *Behav. Brain Res.* 292, 353–360. doi: 10.1016/j.bbr.2015.06.032

Hescham, S., Lim, L. W., Jahanshahi, A., Blokland, A., and Temel, Y. (2013a). Deep brain stimulation in dementia-related disorders. *Neurosci. Biobehav. Rev.* 37, 2666–2675. doi: 10.1016/j.neubiorev.2013.09.002

Hescham, S., Lim, L. W., Jahanshahi, A., Steinbusch, H. W., Prickaerts, J., Blokland, A., et al. (2013b). Deep brain stimulation of the forniceal area enhances memory functions in experimental dementia: the role of stimulation parameters. *Brain Stimulat.* 6, 72–77. doi: 10.1016/j.brs.2012.01.008

Hu, R., Eskandar, E., and Williams, Z. (2009). Role of deep brain stimulation in modulating memory formation and recall. *Neurosurg Focus* 27:E3. doi: 10.3171/2009.4.FOCUS0975

Inman, C. S., Manns, J. R., Bijanki, K. R., Bass, D. I., Hamann, S., Drane, D. L., et al. (2018). Direct electrical stimulation of the amygdala enhances declarative memory in humans. *PNAS* 115, 98–103. doi: 10.1073/pnas.1714058114

Jacobs, J., Miller, J., Lee, S. A., Coffey, T., Watrous, A. J., Sperling, M. R., et al. (2016). Direct electrical stimulation of the human entorhinal region and hippocampus impairs memory. *Neuron* 92, 983–990. doi: 10.1016/j.neuron.2016.10.062

Jadi, M., Polsky, A., Schiller, J., and Mel, B. W. (2012). Location-dependent effects of inhibition on local spiking in pyramidal neuron dendrites. *PLoS Comput. Biol.* 8:e1002550. doi: 10.1371/journal.pcbi.1002550

Johnson, M. D., and McIntyre, C. C. (2008). Quantifying the neural elements activated and inhibited by globus pallidus deep brain stimulation. *J. Neurophysiol.* 100, 2549–2563. doi: 10.1152/jn.90372.2008

Karnani, M. M., Agetsuma, M., and Yuste, R. (2014). A blanket of inhibition: functional inferences from dense inhibitory connectivity. *Curr. Opin. Neurobiol.* 26, 96–102. doi: 10.1016/j.conb.2013.12.015

Kastellakis, G., Cai, D. J., Mednick, S. C., Silva, A. J., and Poirazi, P. (2015). Synaptic clustering within dendrites: an emerging theory of memory formation. *Prog. Neurobiol.* 126, 19–35. doi: 10.1016/j.pneurobio.2014.12.002

Kastellakis, G., Silva, A. J., and Poirazi, P. (2016). Linking memories across time via neuronal and dendritic overlaps in model neurons with active dendrites. *Cell Rep.* 17, 1491–1504. doi: 10.1016/j.celrep.2016.10.015

Khan, I. S., D'Agostino, E. N., Calnan, D. R., Lee, J. E., and Aronson, J. P. (2019). Deep brain stimulation for memory modulation: a new frontier. *World Neurosurg.* 126, 638–646. doi: 10.1016/j.wneu.2018.12.184.

Kim, C. K., Adhikari, A., and Deisseroth, K. (2017). Integration of optogenetics with complementary methodologies in systems neuroscience. *Nat. Rev. Neurosci.* 18, 222–235. doi: 10.1038/nrn.2017.15

Kim, K., Schedlbauer, A., Rollo, M., Karunakaran, S., Ekstrom, A. D., and Tandon, N. (2018). Network-based brain stimulation selectively impairs spatial retrieval. *Brain Stimul.* 11, 213–221. doi: 10.1016/j.brs.2017.09.016

Klausberger, T., and Somogyi, P. (2008). Neuronal diversity and temporal dynamics: the unity of hippocampal circuit operations. *Science* 321, 53–57. doi: 10.1126/science.1149381

Klooster, D. C., de Louw, A. J., Aldenkamp, A. P., Besseling, R. M., Mestrom, R. M., Carrette, S., et al. (2016). Technical aspects of neurostimulation: focus on equipment, electric field modeling, and stimulation protocols. *Neurosci. Biobehav. Rev.* 65, 113–141. doi: 10.1016/j.neubiorev.2016.02.016

Krabbe, S., Gründemann, J., and Lüthi, A. (2018). Amygdala inhibitory circuits regulate associative fear conditioning. *Biol. Psychiatry* 83, 800–809. doi: 10.1016/j.biopsych.2017.10.006

Kucewicz, M. T., Berry, B. M., Kremen, V., Miller, L. R., Khadjevand, F., Ezzyat, Y., et al. (2018). Electrical stimulation modulates high γ activity and human memory performance. *eNeuro* 5:eNEURO.0369–17. doi: 10.1523/ENEURO.0369-17.2018

Kuhn, J., Hardenacke, K., Lenartz, D., Gruendler, T., Ullsperger, M., Bartsch, C., et al. (2015). Deep brain stimulation of the nucleus basalis of Meynert in Alzheimer's dementia. *Mol. Psychiatry* 20, 353–360. doi: 10.1038/mp.2014.32

Lacruz, M. E., Valentín, A., Seoane, J. J., Morris, R. G., Selway, R. P., and Alarcón, G. (2010). Single pulse electrical stimulation of the hippocampus is sufficient to impair human episodic memory. *Neuroscience* 170, 623–632. doi: 10.1016/j.neuroscience.2010.06.042

Lamsa, K., and Lau, P. (2019). Long-term plasticity of hippocampal interneurons during in vivo memory processes. *Curr. Opin. Neurobiol.* 54, 20–27. doi: 10.1016/j.conb.2018.08.006

Laxton, A. W., Tang-Wai, D. F., McAndrews, M. P., Zumsteg, D., Wennberg, R., Keren, R., et al. (2010). A phase I trial of deep brain stimulation of memory circuits in Alzheimer's disease. *Ann. Neurol.* 68, 521–534. doi: 10.1002/ana.22089

Lee, A. K., and Brecht, M. (2018). Elucidating neuronal mechanisms using intracellular recordings during behavior. *TINS* 41, 385–403. doi: 10.1016/j.tins.2018.03.014

Lee, D. J., Gurkoff, G. G., Izadi, A., Berman, R. F., Ekstrom, A. D., Muizelaar, J. P., et al. (2013). Medial septal nucleus theta frequency deep brain stimulation improves spatial working memory after traumatic brain injury. *J. Neurotrauma.* 30, 131–139. doi: 10.1089/neu.2012.2646

Lee, D. J., Gurkoff, G. G., Izadi, A., Seidl, S. E., Echeverri, A., Melnik, M., et al. (2015). Septohippocampal neuromodulation improves cognition after traumatic brain injury. *J. Neurotrauma* 32, 1822–1832. doi: 10.1089/neu.2014.3744

Lee, H., Fell, J., and Axmacher, N. (2013). Electrical engram: how deep brain stimulation affects memory. *TINS* 17, 574–584. doi: 10.1016/j.tics.2013.09.002

Lempka, S. F., and McIntyre, C. C. (2013). Theoretical analysis of the local field potential in deep brain stimulation applications. *PLoS ONE* 8:e59839. doi: 10.1371/journal.pone.0059839

Li, Y., Kulvicius, T., and Tetzlaff, C. (2016). Induction and consolidation of calcium-based homo- and heterosynaptic potentiation and depression. *PLoS ONE* 11:e0161679. doi: 10.1371/journal.pone.0161679

Liu, R., Crawford, J., Callahan, P. M., Terry, A. V. Jr., and Constantinidis, C. (2017). Intermittent stimulation of the nucleus basalis of Meynert improves working memory in adult monkeys. *Curr. Biol.* 27.−2646.e2644. doi: 10.1016/j.cub.2017.07.021

Losonczy, A., Makara, J. K., and Magee, J. C. (2008). Compartmentalized dendritic plasticity and input feature storage in neurons. *Nature* 452, 436–441 doi: 10.1038/nature06725

Lozano, A. M., Fosdick, L., Chakravarty, M. M., Leoutsakos, J. M., Munro, C., Oh, E., et al. (2016). A phase II Study of fornix deep brain stimulation

in mild Alzheimer's Disease. *J. Alzheimers Dis. J. A. D.* 54, 777–787. doi: 10.3233/JAD-160017

Lucas, E. K., and Clem, R. L. (2018). GABAergic interneurons: the orchestra or the conductor in fear learning and memory? *Brain Res. Bull.* 141, 13–19. doi: 10.1016/j.brainresbull.2017.11.016

Lyketsos, C. G., Targum, S. D., Pendergrass, J. C., and Lozano, A. M. (2012). Deep brain stimulation: a novel strategy for treating Alzheimer's disease. *Innov. Clin. Neurosci.* 9, 10–17.

Maffei, A., Charrier, C., Caiati, M. D., Barberis, A., Mahadevan, V., Woodin, M. A., et al. (2017). Emerging mechanisms underlying dynamics of GABAergic synapses. *J. Neurosci.* 37, 10792–10799. doi: 10.1523/JNEUROSCI.1824-17.2017

Mair, R. G., and Hembrook, J. R. (2008). Memory enhancement with event related stimulation of the rostral intralaminar thalamic nuclei. *J. Neurosci.* 28, 14293–14300. doi: 10.1523/JNEUROSCI.3301-08.2008

Mann, A., Gondard, E., Tampellini, D., Milsted, J. A. T., Marillac, D., Hamani, C., et al. (2018). Chronic deep brain stimulation in an Alzheimer's disease mouse model enhances memory and reduces pathological hallmarks. *Brain Stimul.* 11, 435–444. doi: 10.1016/j.brs.2017.11.012

Mannu, P., Rinaldi, S., Fontani, V., and Castagna, A. (2011). Radio electric asymmetric brain stimulation in the treatment of behavioural and psychiatric symptoms in Alzheimer disease. *Clin. Interv. Aging* 6, 207–211. doi: 10.2147/CIA.S23394

Marín, O. (2012). Interneuron dysfunction in psychiatric disorders. *Nat. Rev. Neurosci.* 13, 107–120. doi: 10.1038/nrn3155

Markram, H., Toledo-Rodriguez, M., Wang, Y., Gupta, A., Silberberg, G., and Wu, C. (2004). Interneurons of the neocortical inhibitory system. *Nat. Rev. Neurosci.* 5, 793–807. doi: 10.1038/nrn1519

Martens, H. C. F., Toader, E., Decré, M. M. J., Anderson, D. J., Vetter, R., Kipke, D. R., et al. (2011). Spatial steering of deep brain stimulation volumes using a novel lead design. *Clin. Neurophysiol.* 122,558–566. doi: 10.1016/j.clinph.2010.07.026

McIntyre, C. C., Savasta, M., Walter, B. L., and Vitek, J. L. (2004). How does deep brain stimulation work? Present understanding and future questions. *J. Clin. Neurophysiol.* 21, 40–50. doi: 10.1097/00004691-200401000-00006

McLachlan, R. S., Pigott, S., Tellez-Zenteno, J. F., Wiebe, S., and Parrent, A. (2010). Bilateral hippocampal stimulation for intractable temporal lobe epilepsy: impact on seizures and memory. *Epilepsia* 51, 304–307. doi: 10.1111/j.1528-1167.2009.02332.x

Merkow, M. B., Burke, J. F., Ramayya, A. G., Sharan, A. D., Sperling, M. R., and Kahana, M. J. (2017). Stimulation of the human medial temporal lobe between learning and recall selectively enhances forgetting. *Brain Stimulat.* 10, 645–650. doi: 10.1016/j.brs.2016.12.011

Miatton, M., Van Roost, D., Thiery, E., Carrette, E., Van Dycke, A., Vonck, K., et al. (2011). The cognitive effects of amygdalo-hippocampal deep brain stimulation in patients with temporal lobe epilepsy. *Epilepsy Behav.* 22, 759–764. doi: 10.1016/j.yebeh.2011.09.016

Miller, J. P., Sweet, J. A., Bailey, C. M., Munyon, C. N., Luders, H. O., and Fastenau, P. S. (2015). Visual-spatial memory may be enhanced with theta burst deep brain stimulation of the fornix: a preliminary investigation with four cases. *Brain* 138, 1833–1842. doi: 10.1093/brain/awv095

Montgomery, E. B., and He, H. (2016). Deep brain stimulation frequency-a divining rod for new and novel concepts of nervous system function and therapy. *Brain Sci.* 6:34. doi: 10.3390/brainsci6030034

Montgomery, S. M., Betancur, M. I., and Buzsaki, G. (2009). Behaviour-dependent coordination of multiple theta dipoles in the hippocampus. *J. Neurosci.* 29, 1381–1394. doi: 10.1523/JNEUROSCI.4339-08.2009

Oh, Y. S., Kim, H. J., Lee, K. J., Kim, Y. I., Lim, S. C., and Shon, Y. M. (2012). Cognitive improvement after long-term electrical stimulation of bilateral anterior thalamic nucleus in refractory epilepsy patients. *Seizure* 21, 183–187. doi: 10.1016/j.seizure.2011.12.003

Pendyam, S., Bravo-Rivera, C., Burgos-Robles, A., Sotres-Bayon, F., Quirk, G. J., and Nair, S. S. (2013). Fear signaling in the prelimbic-amygdala circuit: a computational modeling and recording study. *J. Neurophysiol.* 110, 844–861. doi: 10.1152/jn.00961.2012

Prager, E. M., Bergstrom, H. C., Wynn, G. H., and Braga, M. F. (2016). The basolateral amygdala γ-aminobutyric acidergic system in health and disease. *J. Neurosci. Res.* 94, 548–567. doi: 10.1002/jnr.23690

Rezai, A. R., Sederberg, P. B., Bogner, J., Nielson, D. M., Zhang, J., Mysiw, W. J. et al. (2016). Improved function after deep brain stimulation for chronic, severe traumatic brain injury. *Neurosurgery* 79, 204–211. doi: 10.1227/NEU.0000000000001190

Roux, L., and Buzsáki, G. (2015). Tasks for inhibitory interneurons in intact brain circuits. *Neuropharmacology* 88, 10–23. doi: 10.1016/j.neuropharm.2014.09.011

Rozov, A. V., Valiullina, F. F., and Bolshakov, A. P. (2017). Mechanisms of long-term plasticity of hippocampal GABAergic synapses. *Biochemistry* 82, 257–263. doi: 10.1134/S0006297917030038

Saenger, V. M., Kahan, J., Foltynie, T., Friston, K., Aziz, T. Z., Green, A. L., et al. (2017). Uncovering the underlying mechanisms and whole-brain dynamics of deep brain stimulation for Parkinson's disease. *Sci. Rep.* 7:9882. doi: 10.1038/s41598-017-10003-y

Sanjay, M., and Krothapalli, S. B. (2019). "Modelling epileptic activity in hippocampal CA3," in *Hippocampal Microcircuits: A Computational Modeller's Resource Book, 2nd edn,* eds C. Cutsuridis, B. P. Graham, S. Cobb, and I. Vida (Cham: Springer-Nature Switzerland), 755–775. doi: 10.1007/978-3-319-99103-0_26

Sankar, T., Chakravarty, M. M., Bescos, A., Lara, M., Obuchi, T., Laxton, A. W., et al. (2015). Deep brain stimulation influences brain structure in Alzheimer's disease. *Brain Stimulat.* 8, 645–654. doi: 10.1016/j.brs.2014.11.020

Schmidt, C., and van Rienen, U. (2012a). Modeling the field distribution in deep brainstimulation: the influence of anisotropy of brain tissue. *IEEE Trans. Biomed.Eng.* 59, 1583–1592. doi: 10.1109/TBME.2012.2189885

Schmidt, C., and van Rienen, U. (2012b). Sensitivity analysis of the field distribution indeep brain stimulation with respect to the anisotropic conductivity of braintissue. *Biomed. Tech.* 57 (Suppl. 1), 4266. doi: 10.1515/bmt-2012-4266

Schneider, C. J., Bezaire, M., and Soltesz, I. (2012). Toward a full-scale computational model of the rat dentate gyrus. *Front. Neural Circ.* 6:83. doi: 10.3389/fncir.2012.00083

Senova, S., Chaillet, A., and Lozano, A. M. (2018). Fornical closed-loop stimulation for Alzheimer's disease. *TINS* 41, 418–428. doi: 10.1016/j.tins.2018.03.015

Siegle, J. H., and Wilson, M. A. (2014). Enhancement of encoding and retrieval functions through theta phase-specific manipulation of hippocampus. *Elife* 3:e03061. doi: 10.7554/eLife.03061

Sjögren, M. J., Hellström, P. T., Jonsson, M. A., Runnerstam, M., Silander, H. C., and Ben-Menachem, E. (2002). Cognition-enhancing effect of vagus nerve stimulation in patients with Alzheimer's disease: a pilot study. *J. Clin. Psychiatry* 63, 972–980. doi: 10.4088/JCP.v63n1103

Solé-Padullés, C., Bartrés-Faz, D., Junqué, C., Clemente, I. C., Molinuevo, J. L., Bargalló, N., et al. (2006). Repetitive transcranial magnetic stimulation effects on brain function and cognition among elders with memory dysfunction. A randomized sham-controlled study. *Cereb. Cortex* 16, 1487–1493. doi: 10.1093/cercor/bhj083

Somogyi, P., Katona, L., Klausberger, T., Lasztóczi, B., and Viney, T. J. (2013). Temporal redistribution of inhibition over neuronal subcellular domains underlies state-dependent rhythmic change of excitability in the hippocampus. *Philos. Trans. R. Soc. Lond. B Biol. Sci.* 369:20120518. doi: 10.1098/rstb.2012.0518

Song, D., Chan, R. H., Marmarelis, V. Z., Hampson, R. E., Deadwyler, S. A., and Berger, T. W. (2009). Nonlinear modeling of neural population dynamics for hippocampal prostheses. *Neural Netw.* 22, 1340–1351. doi: 10.1016/j.neunet.2009.05.004

Song, D., Robinson, B.S, Granacki, J. J., and Berger, T. W. (2014). Implementing spiking neuron model and spike timing-dependent plasticity with generalized Laguerre-Volterra models. *Conf. Proc. IEEE Eng. Med. Biol. Soc.* 714–717. doi: 10.1109/EMBC.2014.6943690

Sprekeler, H. (2017). Functional consequences of inhibitory plasticity: homeostasis, the excitation-inhibition balance and beyond. *Curr. Opin. Neurobiol.* 43, 198–203. doi: 10.1016/j.conb.2017.03.014

Stone, S. S., Teixeira, C. M., Devito, L. M., Zaslavsky, K., Josselyn, S. A., Lozano, A. M., et al. (2011). Stimulation of entorhinal cortex promotes adult neurogenesis and facilitates spatial memory. *J. Neurosci.* 31, 13469–13484. doi: 10.1523/JNEUROSCI.3100-11.2011

Suthana, N., Aghajan, Z. M., Mankin, E. A., and Lin, A. (2018). Reporting guidelines and issues to consider for using intracranial brain stimulation

in studies of human declarative memory. *Front. Neurosci.* 12:905. doi: 10.3389/fnins.2018.00905

Suthana, N., and Fried, I. (2014). Deep brain stimulation for enhancement of learning and memory. *Neuroimage* 85, 996–1002. doi: 10.1016/j.neuroimage.2013.07.066

Suthana, N., Haneef, Z., Stern, J., Mukamel, R., Behnke, E., Knowlton, B., et al. (2012). Memory enhancement and deep-brain stimulation of the entorhinal area. *N. Engl. J. Med.* 366, 502–510. doi: 10.1056/NEJMoa1107212

Sweet, J. A., Eakin, K. C., Munyon, C. N., and Miller, J. P. (2014). Improved learning and memory with theta-burst stimulation of the fornix in rat model of traumatic brain injury. *Hippocampus* 24, 1592–1600. doi: 10.1002/hipo.22338

Titiz, A. S., Hill, M. R. H., Mankin, E. A., Aghajan, Z., Elisahi, V, D., Tchemodanov, N., et al. (2017). Theta-burst microstimulation in the human entorhinal area improves memory specificity. *eLife* 6:e29515. doi: 10.7554/eLife.29515

Tremblay, R., Lee, S., and Rudy, B. (2016). GABAergic interneurons in the neocortex: from cellular properties to circuits. *Neuron* 91, 260–292. doi: 10.1016/j.neuron.2016.06.033

Vargova, G., Vogels, T., Kostecka, Z., and Hromadka, T. (2018). Inhibitory interneurons in Alzheimer's disease. *Bratisl Lek Listy*. 119, 205–209. doi: 10.4149/BLL_2018_038

Vasques, X., Cif, L., Hess, O., Gavarini, S., Mennessier, G., and Coubes, P. (2009). Stereotactic model of the electrical distribution within the internal globuspallidus during deep brain stimulation. *J. Comput. Neurosci.* 26, 109–118. doi: 10.1007/s10827-008-0101-y

Vassanelli, S. (2018). "Implantable neural interfaces," in *Living Machines: A Handbook of Research in Biomimetics and Biohybrid Systems,* eds T. J. Prescott, N. Lepora, P. F. M. J. Verschure (Oxford University Press). doi: 10.1093/oso/9780199674923.003.0050

Vassanelli, S., Mahmud, M., Girardi, S., and Maschietto, M. (2012). On the way to large-scale and high-resolution brain-chip interfacing. *Cogn. Comput*. 4, 71–81. doi: 10.1007/s12559-011-9121-4

Velasco, A. L., Velasco, F., Velasco, M., Trejo, D., Castro, G., and Carrillo-Ruiz, J. D. (2007). Electrical stimulation of the hippocampal epileptic foci for seizure control: a double-blind, long-term follow-up study. *Epilepsia* 48, 1895–1903. doi: 10.1111/j.1528-1167.2007.01181.x

Villette, V., and Dutar, P. (2017). GABAergic microcircuits in Alzheimer's Disease models. *Curr. Alzheimer Res.* 14, 30–39. doi: 10.2174/1567205013666160819125757

Wagle Shukla, A., and Okun, M. S. (2012). Personalized medicine in deep brain stimulation through utilization of neural oscillations. *Neurology* 78, 1900–1901. doi: 10.1212/WNL.0b013e318259e2af

Wang, H. X., Gerkin, R. C., Nauen, D. W., and Bi, G. Q. (2005). Coactivation and timing-dependent integration of synaptic potentiation and depression. *Nat. Neurosci.* 8, 187–193. doi: 10.1038/nn1387

Wei, X. F., and Grill, W. M. (2005). Current density distributions, field distributions andimpedance analysis of segmented deep brain stimulation electrodes. *J. Neural Eng.* 2, 139–147. doi: 10.1088/1741-2560/2/4/010

Wester, J. C., and McBain, C. J. (2014). Behavioral state-dependent modulation of distinct interneuron subtypes and consequences for circuit function. *Curr. Opin. Neurobiol.* 29, 118–125. doi: 10.1016/j.conb.2014.07.007

Witter, M. (2019). "Connectivity of the hippocampus," in *Hippocampal Microcircuits: A Computational Modeler's Resource Book, 2nd edn,* eds V. Cutsuridis, B. P. Graham, S. Cobb, I. Vida (Cham: Springer-Nature Switzerland).

Yu, G. J., Hendrickson, P. J., Song, D., and Berger, T. W. (2019). "Spatiotemporal patterns of granule cell activity revealed by a large-scale, biologically realistic model of the hippocampal dentate gyrus," in *Hippocampal Microcircuits: A Computational Modeller's Resource Book, 2nd edn,* eds C. Cutsuridis, B. P. Graham, S. Cobb, and I. Vida (Cham: Springer-Nature Switzerland), 473–508.

Zhang, C., Hu, W. H., Wu, D. L., Zhang, K., and Zhang, J. G. (2015). Behavioral effects of deep brain stimulation of the anterior nucleus of thalamus, entorhinal cortex and fornix in a rat model of Alzheimer's disease. *Chin. Med. J.* 128, 1190–1195. doi: 10.4103/0366-6999.156114

Conflict of Interest Statement: The author declares that the research was conducted in the absence of any commercial or financial relationships that could be construed as a potential conflict of interest.

frontiers in Neuroscience

ORIGINAL RESEARCH
published: 07 August 2019
doi: 10.3389/fnins.2019.00780

Skin Conductance as a Viable Alternative for Closing the Deep Brain Stimulation Loop in Neuropsychiatric Disorders

*Dilranjan S. Wickramasuriya, Md. Rafiul Amin and Rose T. Faghih**

Computational Medicine Laboratory, Department of Electrical and Computer Engineering, University of Houston, Houston, TX, United States

Markers from local field potentials, neurochemicals, skin conductance, and hormone concentrations have been proposed as a means of closing the loop in Deep Brain Stimulation (DBS) therapy for treating neuropsychiatric and movement disorders. Developing a closed-loop DBS controller based on peripheral signals would require: (i) the recovery of a biomarker from the source neural stimuli underlying the peripheral signal variations; (ii) the estimation of an unobserved brain or central nervous system related state variable from the biomarker. The state variable is application-specific. It is emotion-related in the case of depression or post-traumatic stress disorder, and movement-related for Parkinson's or essential tremor. We present a method for closing the DBS loop in neuropsychiatric disorders based on the estimation of sympathetic arousal from skin conductance measurements. We deconvolve skin conductance via an optimization formulation utilizing sparse recovery and obtain neural impulses from sympathetic nerve fibers stimulating the sweat glands. We perform this deconvolution via a two-step coordinate descent procedure that recovers the sparse neural stimuli and estimates physiological system parameters simultaneously. We next relate an unobserved sympathetic arousal state to the probability that these neural impulses occur and use Bayesian filtering within an Expectation-Maximization framework for estimation. We evaluate our method on a publicly available data-set examining the effect of different types of stress on peripheral signal changes including body temperature, skin conductance and heart rate. A high degree of arousal is estimated during cognitive tasks, as are much lower levels during relaxation. The results demonstrate the ability to decode psychological arousal from neural activity underlying skin conductance signal variations. The complete pipeline from recovering neural stimuli to decoding an emotion-related brain state using skin conductance presents a promising methodology for the ultimate realization of a closed-loop DBS controller. Closed-loop DBS treatment would additionally help reduce unnecessary power consumption and improve therapeutic gains.

Keywords: skin conductance (SC), deep brain stimulation (DBS), deconvolution analysis, arousal, state-space (SS) representation

OPEN ACCESS

Edited by:
Cuntai Guan,
Nanyang Technological University, Singapore

Reviewed by:
Julie G. Pilitsis,
Albany Medical College, United States
Nicole Bentley,
University of Alabama at Birmingham, United States

****Correspondence:***
Rose T. Faghih
rtfaghih@uh.edu

Specialty section:
This article was submitted to Neuroprosthetics, a section of the journal Frontiers in Neuroscience

Received: *03 May 2019*
Accepted: *11 July 2019*
Published: *07 August 2019*

Citation:
Wickramasuriya DS, Amin MR and Faghih RT (2019) Skin Conductance as a Viable Alternative for Closing the Deep Brain Stimulation Loop in Neuropsychiatric Disorders. Front. Neurosci. 13:780. doi: 10.3389/fnins.2019.00780

INTRODUCTION

Deep Brain Stimulation (DBS) is a type of therapy involving the application of high frequency electrical stimulation, usually at ∼130 Hz, to specific anatomical structures deep within the brain (Oluigbo et al., 2012; Carron et al., 2013). While the precise mechanics of the therapy are yet to be fully understood, it has been hypothesized that DBS mimics the effect of ablative lesions without causing any tissue damage (Dostrovsky and Lozano, 2002). A second hypothesis suggests that stimulation from the implanted electrodes modulates electrical circuit activity within dysfunctional brain regions (Oluigbo et al., 2012; Cleary et al., 2015). DBS has been approved by the Food and Drug Administration (FDA) for the treatment of Parkinson's disease and essential tremor in the United States. Humanitarian device exemptions have also been granted by the FDA for the use of DBS in the treatment of severe obsessive compulsive disorder and dystonia (Grahn et al., 2014). Meanwhile, the therapy has also been investigated as a treatment option for a host of other medical conditions including major depression (Puigdemont et al., 2012; Merkl et al., 2013), chronic pain (Boccard et al., 2015; Lempka et al., 2017), drug-resistant epilepsy (Vesper et al., 2007; Fisher et al., 2010), anorexia nervosa (Lipsman et al., 2013; Wu et al., 2013), and substance abuse (Zhou et al., 2011; Müller et al., 2013).

Commercially-available DBS systems currently function in an open loop manner. In open-loop DBS, stimulation is delivered continuously until manually re-adjusted. In contrast, a closed-loop DBS (CLDBS) system automatically adjusts stimulation parameters based on sensor feedback recorded from the patient (Herron et al., 2017). The feedback signal is usually based on a symptom-related biomarker (Bouthour et al., 2019). Open-loop systems can require multiple post-operative visits in the months following surgery (Grahn et al., 2014). During visits, different parameters of the electrical stimulation including frequency, amplitude, and pulse width are adjusted for improving therapeutic benefit (Bronstein et al., 2011). Manual adjustment of the parameters in a trial-and-error fashion is time consuming. It is also challenging to explore the complete stimulation parameter space during brief patient visits. Moreover, open-loop DBS systems apply stimulation even if not strictly required. Consider, for instance, two common movement disorders—essential tremor and Parkinson's disease. Motor symptoms for both disorders include rhythmic involuntary movements (tremors). In essential tremor, the tremors occur during volitional movement (Plumb and Bain, 2007) and stimulation may be unnecessary when a patient is not using an affected limb (Herron et al., 2017). The tremors occur at rest in Parkinson's (Chou et al., 2011). However, motor symptoms can fluctuate continually (Rosin et al., 2011; Little et al., 2013). Evidence suggests that local field potential (LFP) β-band oscillations in the subthalamic nucleus correlate with motor impairment in Parkinson's (Little and Brown, 2012). CLDBS systems switching on control based on LFP threshold crossings were shown to have superior performance in treating Parkinson's patients and had substantial gains in reducing stimulation time (Little et al., 2013, 2016). The effectiveness of CLDBS over an open-loop stimulation in Parskinson's was also shown in non-human primates (Rosin et al., 2011). CLDBS systems have thus arisen gradually to eliminate part of the inefficiencies of their open-loop predecessors.

In a recent work describing a theoretical framework for the design of a CLDBS system for treating chronic pain, Shirvalkar et al. (2018) point out two important elements of closing the loop: (i) the extraction of an accurate, relevant, and timely biomarker of the underlying state variable of interest; (ii) a control-theoretic (e.g., state-space) representation of the system relating the biomarker to the unobserved state variable. In their specific application, they suggest using LFPs from the somatosensory cortex, the dorsal anterior cingulate cortex and the orbitofrontal cortex for tracking a multidimensional pain state. Others have similarly suggested neurochemical biomarkers, skin conductance features, and hormone concentrations as a means of feedback for treating a broad range of neuropsychiatric disorders (Grahn et al., 2014; Bina and Langevin, 2018). Following the suggestion of Shirvalkar et al. (2018), we present a proof-of-principle state-space framework that can be used for CLDBS therapy.

DBS has recently emerged as a potentially successful treatment option for patients diagnosed with post-traumatic stress disorder (PTSD) (Koek et al., 2014; Langevin et al., 2016). PTSD is a type of psychiatric disorder that can occur in patients who have experienced traumatic or stressful events in the past. Distressing memories or dreams often persist long after the event (Jetly et al., 2015). Symptoms of PTSD include changes in psychological arousal, reactivity and mood, and are evidenced by factors such as hypervigilance and exaggerated startle responses (American Psychiatric Association, 2013). This state of hyperarousal or hypervigilance in PTSD has been noted in multiple studies (Woodward et al., 2000; Risser et al., 2006; Hellmuth et al., 2012). While the method we present here could find broader applicability to a range of neuropsychiatric disorders, it seems particularly suited to address PTSD with its hyperarousal symptoms.

Bina and Langevin (2018) suggest the possibility of monitoring skin conductance changes as a potential biomarker in a CLDBS system for treating PTSD. Sympathetic nerve fibers innervate the sweat glands (Low, 2012). Consequently, changes in the conductivity of the skin owing to perspiration provide a measure of sympathetic drive or arousal (Critchley et al., 2002). Heightened responsivity in terms of skin conductance has been noted in PTSD patients compared to controls (Orr and Roth, 2000). In a three-group study of Vietnam combat veterans with PTSD, psychiatric Vietnam combat veterans, and psychiatric non-combat Vietnam-era veterans, McNally et al. (1987) reported that PTSD subjects had the largest skin conductance responses (SCRs) in response to combat-related words. In a similar study comprising of Vietnam combat veterans with PTSD, Vietnam combat veterans, and non-combat controls, Goldfinger et al. (1998) reported that PTSD veterans had the highest baseline skin conductance levels. In an affect-toned Rorschach test conducted in the same study, arousal, as measured by skin conductance, was highest in the PTSD group as well. Pole (2007) also noted higher skin conductance baselines, larger SCRs and slower skin conductance habituation in startle and trauma-cue studies in PTSD patients in a meta-analysis study of adults with and without PTSD. Skin conductance changes

also occur in depression. Ward and Doerr (1986) measured skin conductance in patients with depression, parents of firstborn one- to three-month old infants and control subjects, and found that depressed patients had significantly lower skin conductance levels than the other groups. Lin et al. (2011) examined the effects of stress and depression using a series of physiological measures. Participants were first categorized into the normal, low-risk and high-risk depression groups and were assigned to one of two stress treatments. Percentage change in skin conductance between baseline and during the stress treatment periods were significantly dependent on and correlated positively with depression. Both PTSD and depression are potential candidates for DBS therapy when other treatment options have been exhausted. Skin conductance additionally has the advantage of being easily measured with wearable devices such as the Empatica E4 (Koskimäki et al., 2017). Wearable devices afford convenience, seamless integration into clothing and do not involve the risks of surgically implanted sensors.

We develop a state-space model to track an unobserved sympathetic arousal state from skin conductance measurements. The relationship between arousal and skin conductance has been attested to in multiple studies (Boucsein, 2012). Individual SCRs are a notable feature in a skin conductance signal. SCRs accompany psychologically arousing stimuli as the skin's conductivity increases momentarily. We relate arousal to the rate at which SCRs occur. Current methods for detecting SCRs in a skin conductance signal rely on detecting peaks above a threshold set between 0.01 and 0.05 μS (Benedek and Kaernbach, 2010). Inter-subject variability in skin conductance signals is a known phenomena (Dawson et al., 2007). We therefore use a deconvolution strategy for extracting the physiological parameters related to sweat secretion for each individual and detect neural impulses to the eccrine sweat glands that generate the SCRs rather than relying on heuristic peak detection. The following section describes our two-part methodology. We first describe the deconvolution approach that utilizes its own state-space formulation for detecting neural impulses based on sweat diffusion and evaporation dynamics. We next describe the state-space formulation for the CLDBS system that relates the probability of neural impulses to a latent sympathetic arousal state. We present our results thereafter and finally conclude with a discussion of our results, and how our methodology could be used in an experimental CLDBS prototype (e.g., such as in the conceptual architecture depicted in **Figure 1**).

1. MATERIALS AND METHODS

1.1. Data

We use the Non-EEG Dataset for Assessment of Neurological Status (Birjandtalab et al., 2016). The data is publicly available through the PhysioNet database (Goldberger et al., 2000). The data-set contains skin conductance recordings from 20 healthy college students who were exposed to physical, emotional, and cognitive stress during three different time periods. Skin conductance was recorded using the wrist-worn Affectiva Q Curve device. Skin conductance can be contaminated by noise sources such as motion artifacts, range saturation and amplification factor changes (Boucsein, 2012). Many of the signals had to be discarded owing to motion artifact contamination and noise due to bad skin contact. Hence, we only used the data from six subjects. We re-labeled the original subject numbers with corresponding participant numbers (**Table 1**). The physical, cognitive, and emotional stress periods each lasted 5 min and were interspersed by 5 min intervals of relaxation. Subjects were made to stand, walk and jog during the physical stress part of the experiment. We excluded data from this portion

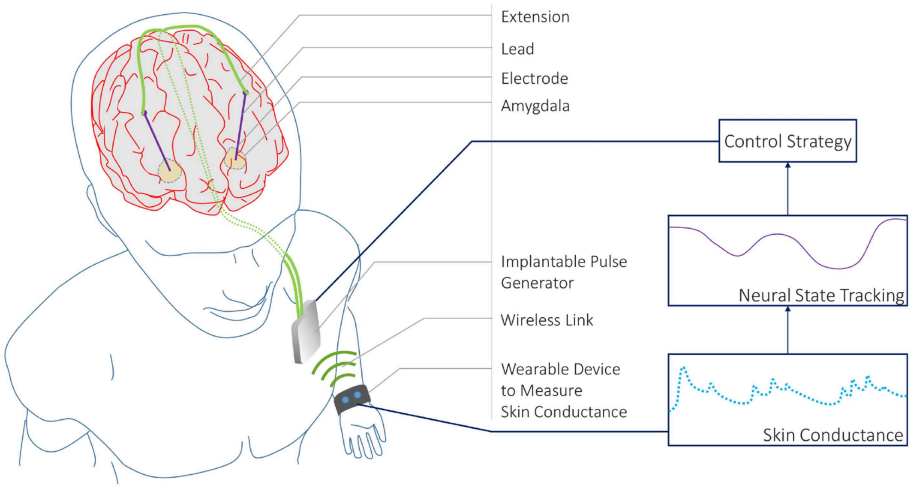

FIGURE 1 | A CLDBS System based on Skin Conductance Measurements. A conceptual CLDBS architecture for treating neuropsychiatric disorders based on tracking a neural state from peripheral skin conductance measurements. Koek et al. (2014) and Langevin et al. (2016) applied stimulation to the amygdala in treatment-refractory PTSD patients. The amygdala plays an important role in emotion processing. In particular, the basolateral nucleus of the amygdala contains cells that are responsive to both fear acquisition and fear extinction (Lüthi and Lüscher, 2014). Koek et al. (2014) and Langevin et al. (2016) targeted this area owing to the partially dysfunctional fear extinction mechanism for trauma-related cues in PTSD patients.

TABLE 1 | Subject information for selected participants.

Participant	Subject ID	Age	Gender	BMI (kgm^{-2})
1	1	30	M	30.00
2	5	30	M	24.75
3	8	27	M	19.32
4	9	25	M	21.70
5	12	32	F	20.20
6	16	24	M	16.66

of the experiment and focus only on the psychological aspects. The cognitive stress portion consisted of two separate tasks. In the first task, subjects had to count backwards in 7's beginning at 2,485 for 3 min and then perform the Stroop test for a further 2 min. In a Stroop test, a subject is shown a word denoting a color and is asked to read it out. However, the color in which the text is written may not necessarily correspond to what it means. A buzzer notified subjects of any errors they made. Emotional stress was induced by means of a horror movie clip. The authors of the data-set noted that many of the volunteers participating in the experiment showed a stress response that was visible to the experiment administrator while they were just being given instructions regarding the cognitive tasks. Hence, they categorized the 40 s interval just prior to the counting task and the Stroop test as a stress period.

1.2. Skin Conductance Deconvolution Using Compressed Sensing

1.2.1. Skin Conductance Model Formulation

A skin conductance signal $y_{SC}(t)$ consists of two distinct parts. The comparatively slow varying part, also known as the tonic level, is primarily related to thermoregulation and is a function of ambient temperature and humidity. The other part, also known as the phasic component, fluctuates much faster and is generated by sympathetic nerve fibers stimulating the sweat glands. Therefore,

$$y_{SC}(t) = y(t) + y_T(t), \tag{1}$$

where $y(t)$ and $y_T(t)$ represent the constituent phasic and tonic components, respectively.

The phasic component $y(t)$ can be extracted from $y_{SC}(t)$ using an algorithm such as cvxEDA (Greco et al., 2016). The physiology leading to the generation of the phasic component—namely the diffusion of sweat from the sweat duct to the stratum corneum, and its subsequent evaporation thereafter—can be modeled using first order dynamics (Alexander et al., 2005; Benedek and Kaernbach, 2010; Boucsein, 2012), and mathematically expressed via the following pair of differential equations:

$$\dot{x}_1(t) = -\frac{1}{\tau_r}x_1(t) + \frac{1}{\tau_r}u(t) \qquad \text{(diffusion)} \tag{2}$$

$$\dot{x}_2(t) = \frac{1}{\tau_d}x_1(t) - \frac{1}{\tau_d}x_2(t) \qquad \text{(evaporation)} \tag{3}$$

where $x_1(t)$ is an internal variable, $x_2(t)$ is the phasic component, and $u(t)$ is the neural stimuli to the sweat glands. $x_1(t)$ is related to the amount of sweat and pressure within the sweat duct. The phasic component consists of a series of SCRs, each of which results from a single neural impulse burst. τ_r and τ_d are the rise and decay times of a single SCR.

The number of SCRs in a phasic skin conductance signal is typically much smaller than the total number of acquired data samples. Consequently, the number of underlying neural impulse bursts causing the SCRs is also small. This enables us to employ a sparsity constraint when solving for $u(t)$. We model $u(t)$ as a finite sum of weighted, shifted delta functions

$$u(t) = \sum_{i=1}^{N} u_i \delta(t - \Delta_i), \tag{4}$$

where u_i represents the amplitude of an impulse occurring at Δ_i, and N is the number of samples in the neural stimuli signal. N is proportional to the recording duration T_d and the input sampling frequency f_u ($N = T_d \cdot f_u$). $\Delta_i = iT_u$ where $T_u = f_u^{-1}$. u_i is positive if there is an impulse at time instance Δ_i and 0 otherwise. The continuous-time phasic skin conductance $y(t)$ contaminated by measurement noise $v(t)$ is

$$y(t) = x_2(t) + v(t). \tag{5}$$

If the signal is periodically sampled at T_y intervals to yield a total of M measurements, we can define the equivalent discrete-time observation y_k as

$$y_k = x_2(kT_y) + v_k \tag{6}$$

where v_k is Gaussian noise. Given all the discrete measurements y_k for $k = 1, 2, \ldots, M$, we would like to recover $u(t)$ and estimate τ_r and τ_d. We take $x_1(0) = 0$ as an initial condition assuming that the sweat duct is empty at the beginning. The state-space solution for $x_2(kT_y)$ leads us to (Faghih et al., 2015b)

$$y_k = a_k y_0 + \mathbf{b}_k \mathbf{u} + v_k, \tag{7}$$

where $a_k = e^{-\frac{kT_y}{\tau_d}}$, $\mathbf{b}_k = \left[\frac{1}{(\tau_r-\tau_d)}(e^{-\frac{kT_y}{\tau_r}} - e^{-\frac{kT_y}{\tau_d}}) \quad \frac{1}{(\tau_r-\tau_d)}(e^{-\frac{kT_y-T_u}{\tau_r}} - e^{-\frac{kT_y-T_u}{\tau_d}}) \quad \frac{1}{(\tau_r-\tau_d)}(e^{-\frac{kT_y-2T_u}{\tau_r}} - e^{-\frac{kT_y-2T_u}{\tau_d}}) \quad \cdots \quad \frac{1}{(\tau_r-\tau_d)}(e^{-\frac{T_u}{\tau_r}} - e^{-\frac{T_u}{\tau_d}}) \quad \underbrace{0 \quad \cdots \quad 0}_{N-\frac{kT_y}{T_u}}\right]$ and $\mathbf{u} = [u_1 \quad u_2 \quad \cdots \quad u_N]^\top$ represents a sparse vector containing all the neural stimuli over the entire signal duration (i.e., very few of the u_i's are non-zero). Concatenating all the measurements into a single vector $\mathbf{y} = [y_1 \quad y_2 \quad \cdots \quad y_M]^\top$ we have,

$$\mathrm{y} = \mathbf{A}_\tau y_0 + \mathbf{B}_\tau \mathbf{u} + \boldsymbol{v} \tag{8}$$

where $\mathbf{A}_\tau = [a_1 \quad a_2 \quad \cdots \quad a_M]^\top$, $\mathbf{B}_\tau = [\mathbf{b}_1^\top \quad \mathbf{b}_2^\top \quad \cdots \quad \mathbf{b}_M^\top]^\top$, $\boldsymbol{v} = [v_1 \quad v_2 \quad \cdots \quad v_M]^\top$ and y_0 is the initial condition of the phasic skin conductance signal. Here, T_y is an integer multiple of T_u.

1.2.2. Deconvolution

We set the sampling interval for the phasic skin conductance signal and neural stimuli to $T_y = 0.5$ s and $T_u = 0.25$ s, respectively. Equation (8) has $M < N$ and represents an ill-posed problem with multiple solutions. The sparsity constraint on $\mathbf{u}$ however, makes it possible to solve the equation via compressed sensing. An l_1-norm penalization term is typically added to the objective function to impose sparsity (Faghih, 2018). We consider l_p-norm penalization in this particular formulation. We further constrain the rise and decay times to $0.1 \leq \tau_r \leq 1.4$ and $1.5 \leq \tau_d \leq 6$ similar to Amin and Faghih (2018, 2019). We impose these constraints based on prior work in the literature to ensure that the solution is identifiable and physiologically plausible (Alexander et al., 2005; Benedek and Kaernbach, 2010; Greco et al., 2016). Letting $\boldsymbol{\tau} = [\tau_r \quad \tau_d]^\top$, we formulate the following constrained optimization problem based on Equation (8) to estimate $\boldsymbol{\tau}$ and $\mathbf{u}$

$$\underset{\substack{\boldsymbol{\tau},\,\mathbf{u} \\ C\tau \leq b,\,\mathbf{u}\geq 0}}{\operatorname{argmin}} \; J(\boldsymbol{\tau},\mathbf{u}) = \frac{1}{2}||\mathbf{y} - \mathbf{A}_\tau y_0 - \mathbf{B}_\tau \mathbf{u}||_2^2 + \lambda||\mathbf{u}||_p^p, \qquad (9)$$

where $C = \begin{bmatrix} -1 & 1 & 0 & 0 \\ 0 & 0 & -1 & 1 \end{bmatrix}^\top$, $b = \begin{bmatrix} -0.1 & 1.4 & -1.5 & 6 \end{bmatrix}^\top$ and λ is the l_p-norm regularization parameter for imposing sparsity on $\mathbf{u}$. λ is chosen to provide a balance between exploiting sparsity and accounting for signal fluctuations (Faghih, 2018). This optimization problem is challenging. We therefore decouple it into two sub-problems. A coordinate descent approach can be formulated similar to Faghih (2014, 2018), Faghih et al. (2014, 2015a,b) by solving the following sub-problems iteratively (for $l = 0, 1, 2, \cdots$) until convergence:

1. $\mathbf{u}^{(l+1)} = \underset{\text{s.t. } \mathbf{u}\geq 0}{\operatorname{argmin}} \; J_\lambda(\boldsymbol{\tau}^{(l)}, \mathbf{u})$
2. $\boldsymbol{\tau}^{(l+1)} = \underset{\text{s.t. } C\boldsymbol{\tau}\leq b}{\operatorname{argmin}} \; J(\boldsymbol{\tau}, \mathbf{u}^{(l+1)})$

The first step represents a sparse recovery problem with a constrained convex optimization formulation. Many different approaches exist to solve this. One of the popular approaches is the iterative re-weighted least squares (IRLS) method. We solve this sparse recovery problem using two IRLS methods called FOCUSS+ (Murray, 2005) and GCV-FOCUSS+ (Zdunek and Cichocki, 2008). FOCUSS+ uses a heuristic approach for increasing λ at each IRLS step. We use FOCUSS+ for obtaining a suitable initialization of $\mathbf{u}$. GCV-FOCUSS+ uses the Generalized Cross-Validation (GCV) technique to update λ at each step (Golub et al., 1979). We initialize GCV-FOCUSS+ with the result from FOCUSS+ and then run the IRLS until convergence. We finally constrain the minimum amplitude of any detected neural impulse to be 0.01 to reduce noisy detections. The second step in the coordinate descent approach represents a system identification problem with a constrained non-convex optimization formulation. We use the interior point method to solve this step.

The overall deconvolution algorithm begins by extracting the phasic skin conductance component using cvxEDA (Greco et al., 2016), then randomly initializing $\boldsymbol{\tau}$ and performing the initialization step for $\mathbf{u}$ using FOCUSS+. Thereafter, we proceed with coordinate descent using GCV-FOCUSS+ and the interior point method. We perform the deconvolution on a small 3 min segment (taken from close to the opening portion of the experimental data we consider) of the signal to obtain the rise and decay times. Once we obtain these parameters, we use them to perform sparse recovery with GCV-FOCUSS+ on the entire skin conductance signal.

1.3. Sympathetic Arousal State Estimation

The autonomic nervous system contains both a sympathetic and a parasympathetic branch. The sympathetic branch mediates the body's "fight or flight" response and causes increases in blood pressure, perspiration and heart rate (Silverthorn, 2009). As pointed out earlier, sympathetic nerve fibers innervate the sweat glands (Low, 2012) and consequently skin conductance provides an index of sympathetic arousal (Critchley et al., 2002). Multiple skin conductance features such as tonic levels, rates of SCR appearance, SCR amplitudes and decay rates have been examined in the context of various behavioral interventions (Dawson et al., 2007; Boucsein, 2012). The rate at which SCRs occur has been shown to be related to cognitive task load (Jennings, 1986; Munro et al., 1987) and is thus a useful biomarker of autonomic arousal (Aikins et al., 2009). Here, we describe our approach of estimating an unobserved sympathetic arousal state based on the appearance of neural impulses underlying SCR generation.

We develop a state-space model relating arousal to the probability that the neural impulses occur (Wickramasuriya et al., 2018). The model is inspired by an earlier work relating a sequence of binary response variables to a latent cognitive learning state (Smith et al., 2004). We first divide the time-axis into bins of T_u duration indexed over j and assign $s_j = 1$ or $s_j = 0$ based on whether or not a neural impulse occurs at the jth time instance. Similar to Smith et al. (2004), we assume that sympathetic arousal z_j follows a random walk with time,

$$z_j = z_{j-1} + \epsilon_j \;\; ; \;\; \epsilon_j \sim \mathcal{N}(0, \sigma_\epsilon^2). \qquad (10)$$

The appearance of neural impulses s_j is a Bernoulli distributed random variable with probability p_j and is taken to be related to z_j via a sigmoid function (Smith et al., 2004),

$$\log\Big(\frac{p_j}{1-p_j}\Big) = \alpha + z_j \implies p_j = \frac{1}{1+e^{-(\alpha+z_j)}}. \qquad (11)$$

The choice of the sigmoid function follows from the theory of generalized linear models (McCullagh and Nelder, 1989). Such logarithmic or exponential transformations are frequently encountered in count or frequency type data. Assuming that a subject's sympathetic arousal state $z_0 \approx 0$ at the outset of the experiment, $\alpha = \log[p_0(1-p_0)^{-1}]$ can be calculated by taking p_0 as the probability that a neural impulse occurs randomly in a time bin for each individual (Smith et al., 2004; Wickramasuriya et al., 2018).

Given the observations $S_{1:J} = \{s_1, s_2, \ldots, s_J\}$ we wish to estimate $z_j \; \forall j$. We use Bayesian filtering and Expectation-Maximization (EM) for estimating the arousal states z_j

and recovering the unknown model parameters z_0 and σ_ϵ^2. The algorithm iterates between the E-step and M-step until convergence.

1.3.1. Expectation Step

The E-step consists of two parts—a forward filter and a backward smoother. The filter first calculates a state estimate $z_{j|j}$ using the observations $S_{1:j}$ available up to the jth time index. The backward smoother determines a second estimate $z_{j|J}$ given all the available observations $S_{1:J}$. A Gaussian approximation is made at the filter formulation step and leads to the following equations at the lth EM iteration (Smith et al., 2004):

Predict:

$$z_{j|j-1} = z_{j-1|j-1} \tag{12}$$

$$\sigma^2_{j|j-1} = \sigma^2_{j-1|j-1} + \sigma_\epsilon^{2(l)} \tag{13}$$

Update:

$$z_{j|j} = z_{j|j-1} + \sigma^2_{j|j-1}\left[s_j - \frac{1}{1+e^{-(\alpha+z_{j|j})}}\right] \tag{14}$$

$$\sigma^2_{j|j} = \left\{\frac{1}{\sigma^2_{j|j-1}} + \frac{e^{\alpha+z_{j|j}}}{\left[1+e^{\alpha+z_{j|j}}\right]^2}\right\}^{-1}. \tag{15}$$

One should note that $z_{j|j}$ appears on both sides of Equation (14) and therefore is numerically solved using Newton's method. We next obtain the smoothed state and variance estimates $z_{j|J}$ and $\sigma^2_{j|J}$ as follows (Mendel, 1995):

$$\mathcal{A}_j = \frac{\sigma^2_{j|j}}{\sigma^2_{j+1|j}} \tag{16}$$

$$z_{j|J} = z_{j|j} + \mathcal{A}_j\left(z_{j+1|J} - z_{j+1|j}\right) \tag{17}$$

$$\sigma^2_{j|J} = \sigma^2_{j|j} + \mathcal{A}_j^2\left(\sigma^2_{j+1|J} - \sigma^2_{j+1|j}\right). \tag{18}$$

1.3.2. Maximization Step

We maximize the complete data likelihood at the M-step to estimate the two unknown model parameters σ_ϵ^2 and z_0. The parameter updates for the $(l+1)$th iteration are as follows (Smith et al., 2004):

$$\sigma_\epsilon^{2(l+1)} = \frac{2}{J+1}\left[\sum_{j=2}^{J}(\sigma^2_{j|J} + z^2_{j|J}) - \sum_{j=2}^{J}(\mathcal{A}_j\sigma_{j|J} + z_{j|J}z_{j-1|J})\right] \tag{19}$$

$$+ \frac{1}{J+1}\left[\frac{3}{2}z^2_{1|J} + 2\sigma^2_{1|J} - (\sigma^2_{J|J} + z^2_{J|J})\right] \tag{20}$$

$$z_0^{(l+1)} = \frac{1}{2}z_{1|J}. \tag{21}$$

Following a criteria similar to Smith et al. (2004), we take the parameters to have converged once their absolute difference between consecutive iterations does not exceed 10^{-8}.

1.3.3. High Arousal Index

Similar to Smith et al. (2004), we calculate the probability that sympathetic arousal state z_j exceeds a specific threshold. We name this the High Arousal Index (HAI). HAI helps express how aroused a person is above a certain baseline. After the EM algorithm has converged, the state z_j at each time instance is taken to be Gaussian distributed $z_j \sim \mathcal{N}(z_{j|J}, \sigma^2_{j|J})$ and we define HAI as follows:

$$\text{HAI} = \Pr(z_j > z_T), \tag{22}$$

where the threshold z_T is set to each subject's median state value across the whole experiment. Recall that the experiment acquired data from subjects during episodes of both stress and relaxation. The high stress induced during the experiment corresponds to a state of high arousal and the relaxation corresponds to low arousal. Therefore, we selected z_T as the median value as an approximation of normal arousal in between the two extremes.

2. RESULTS

2.1. Skin Conductance Deconvolution

Figure 2 shows the skin conductance signals and deconvolution results for the selected participants during the backward counting task. In each sub-figure, the upper sub-panel shows the separation of the tonic and phasic components using cvxEDA (Greco et al., 2016). The lower sub-panel in each sub-figure shows the corresponding neural stimuli recovered using our deconvolution approach along with the reconstructed signal. It is the timings of these neural impulses that are used for estimating sympathetic arousal. Our method detects all significant impulses though it misses a few small ones that are comparable to noise. The number of detected impulses and the estimated SCR rise and decay times τ_r and τ_d are given in **Table 2**. Recall that these numbers are calculated based on data acquired during the backward counting task of the experiment. The τ_r and τ_d values estimated from this portion of the experiment are finally used to solve for the neural impulses over the entire signal. Also given in **Table 2** are the squared multiple correlation coefficients R^2 for the participants. R^2 is an indication of goodness-of-fit and expresses how much of the variance of the data is captured by the model. R^2 is above 0.93 for everyone indicating a good fit to the data. The number of impulses varies considerably from person to person. This is likely due to the fact that each participant responds to stress uniquely, despite being exposed to the same type of external stressor.

To further validate our deconvolution approach, we generated a second set of synthetic data using the $\boldsymbol{\tau}$ and $\mathbf{u}$ already estimated for each participant. We added 25 dB SNR Gaussian noise to corrupt this new simulated phasic skin conductance data and performed deconvolution yet again. **Figure 3** shows the results along with the ground truth. **Table 3** shows the estimated parameters and their errors. Again, all R^2 values are above 0.98 indicating a very good fit to the data.

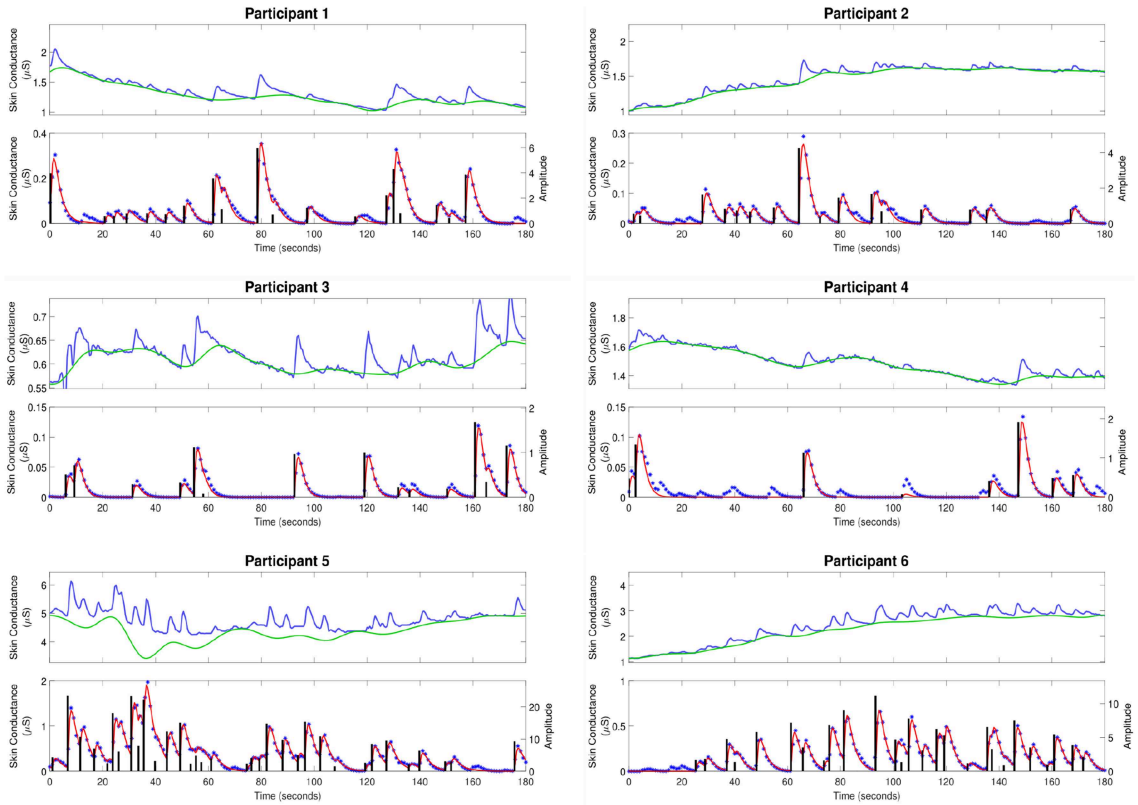

FIGURE 2 | Estimated deconvolution of the experimental skin conductance data. For each of the participants, (i) the upper sub-panel depicts the raw skin conductance data (blue curve) and the separated tonic component of the skin conductance data using cvxEDA (green curve); (ii) the lower sub-panel depicts the separated phasic component (blue stars), the estimated reconstructed signal (red curve), the estimated neural stimuli timings and amplitudes (black vertical lines).

TABLE 2 | Experimental results.

Participant	τ_r (second)	τ_d (second)	$\|\|u\|\|_0$	R^2
1	0.681	2.591	20	0.9629
2	1.398	1.568	17	0.9707
3	1.159	1.505	14	0.9868
4	0.965	1.880	8	0.9399
5	0.604	3.018	35	0.9788
6	0.663	2.617	28	0.9686

The estimated model parameters and the squares of the multiple correlation coefficients (R^2) for the fits of the experimental skin conductance time series.

2.2. Sympathetic Arousal State Estimation

Figure 4 shows the sympathetic arousal state estimation results. For participant 1, arousal as measured by HAI remains above 90% during the cognitive tasks and reduces significantly during relaxation. HAI then increases around the start of emotional stress. Participant 2 has a similar response although the increase in arousal at the start of emotional stress is much less. There is also a notable, though not significantly high, increase right in the middle of the relaxation period. The arousal profile for participant 3 is almost identical to that of participant 1 with a high level at the start, a significant drop during relaxation and a moderate increase at the starting point of emotional stress.

The HAIs are somewhat different for the remaining participants. For participant 4, arousal increases up to or above the 90% threshold a few times during the cognitive tasks, but does not remain high continuously. There is a significant drop during relaxation and an increase above 90% when the horror movie begins. HAI for participant 5 remains high during the cognitive tasks and then drops during relaxation. There are several notable increases during emotional stress, though none of them increase above the 90% threshold. None of the increases however, exceed 90% in this period. Participant 6 is closest to participant 4 although HAI remains more consistently above 90% during cognitive stress with only a slight drop in the middle. Arousal thereafter drops during relaxation and increases above 90% for a brief period at the start of emotional stress. The estimated arousal states $z_{j|J}$ also follow the general trend of the corresponding HAIs for all participants.

3. DISCUSSION

3.1. Skin Conductance Deconvolution

Our method successfully recovers neural impulses associated with phasic SCRs. Between-subject variability in the estimated

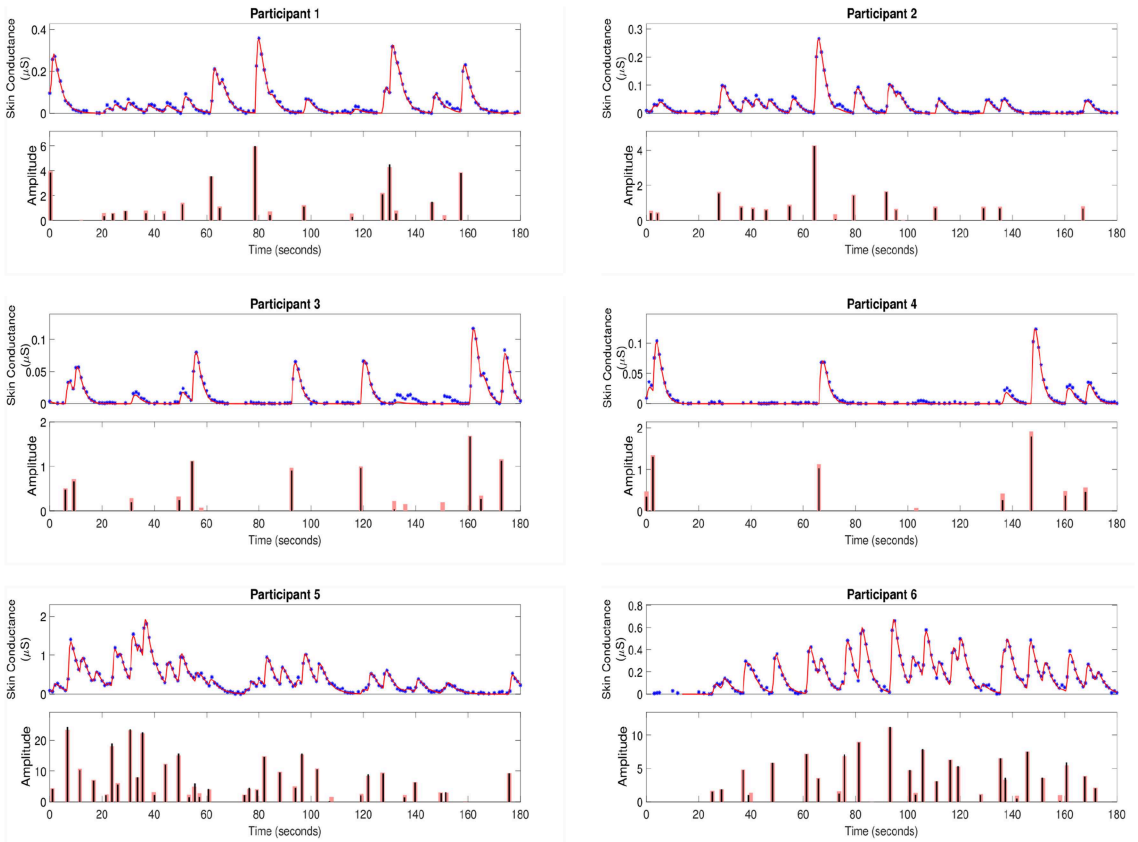

FIGURE 3 | Estimated deconvolution of the simulated phasic skin conductance data in six participants. For each of the participants, (i) the upper sub-panel depicts the simulated phasic component of the skin conductance data samples with 25 dB SNR Gaussian noise (blue stars), the estimated reconstructed signal (red curve); (ii) the lower sub-panel depicts the estimated neural stimuli timings and amplitudes (black vertical lines) and the ground truth of the neural stimuli (red vertical lines) for each of the participants.

TABLE 3 | Results from simulated data.

Participant	$\hat{\tau}_r$ (second)	$\hat{\tau}_d$ (second)	$\|\|\hat{u}\|\|_0$	R^2	$\frac{\|\hat{\tau}_r - \tau_r\|}{\tau_r} \times 100\%$	$\frac{\|\hat{\tau}_d - \tau_d\|}{\tau_d} \times 100\%$	$\|\|u\|\|_0 - \|\|\hat{u}\|\|_0\|$
1	0.664	2.627	19	0.9921	2.49	1.39	1
2	1.348	1.573	16	0.9919	3.58	0.32	1
3	1.128	1.503	11	0.9806	2.67	0.13	3
4	1.139	1.510	7	0.9891	18.03	19.68	1
5	0.5514	3.230	34	0.9936	8.71	7.02	1
6	0.650	2.672	27	0.9918	2.00	2.10	1

The estimated model parameters and the squares of the multiple correlation coefficients (R^2) for the fits of the experimental skin conductance time series.

rise and decay times and the number of impulses is to be noted. The tonic levels also show considerable variations from person to person. These variations clearly highlight the need for determining the physiological parameters τ_r and τ_d on an individual basis rather than relying on fixed values for everyone.

Deconvolution using simulated data (**Figure 3** and **Table 3**) also shows that most impulses are accurately recovered. Only impulses that are comparable to noise peaks are missed. The error percentages in estimating τ_r and τ_d are less than 10% for five of the participants. Participant 4 has a much higher percentage error. Recall that our problem formulation for estimating the rise and decay times is not convex. Consequently, there exists the possibility of stagnating at a local minimum. While we attempt to mitigate this problem through multiple initializations, and then taking the solution with the smallest squared error, there still exists a finite possibility of stagnating at a location other than the global minimum. The number of neural impulses for participant 4 is also much lower than for the others. Consequently, there are less SCRs to fit to and the result is more error-prone.

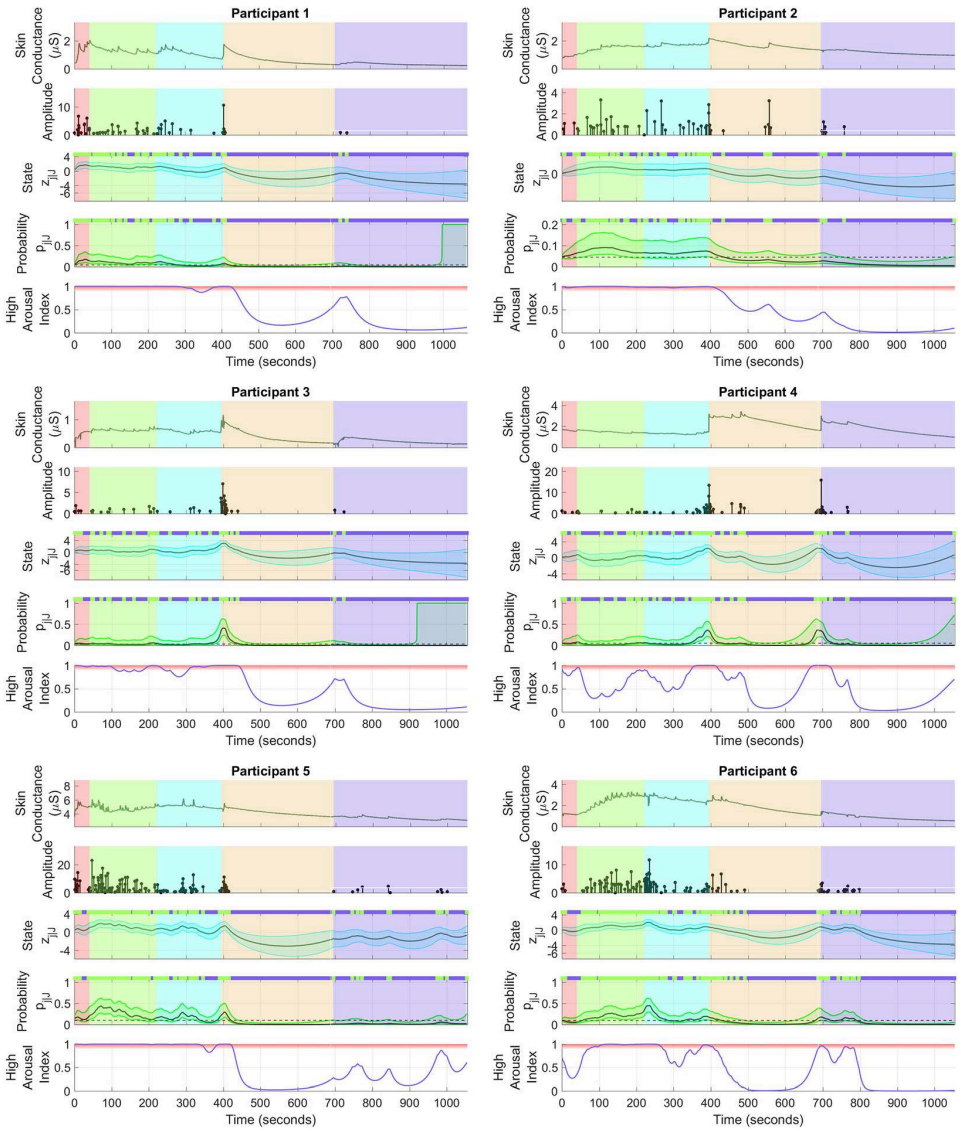

FIGURE 4 | Sympathetic arousal state estimation. For each of the participants, (i) the top sub-panel depicts the skin conductance signal; (ii) the 2nd sub-panel depicts the recovered neural impulses; (iii) the 3rd sub-panel depicts the smoothed sympathetic arousal state $z_{j|J}$ and its confidence intervals; (iv) the 4th sub-panel depicts the smoothed impulse occurrence probability $p_{j|J}$ and its confidence intervals; (v) the lower sub-panel depicts the high arousal index (HAI) with the region above 90% probability highlighted in red. The color-coded backgrounds correspond to the instruction period for the cognitive tasks (red), the backward counting task (green), the Stroop test (cyan) (both the counting task and the Stroop test make up the cognitive stress portion), relaxation (light brown) and emotional stress (violet). Small green rectangles above 3rd and 4th sub-panels depict neural impulse location timings.

Each SCR, resulting from a single neural impulse, is mathematically modeled as a bi-exponential function. Estimating the rise and decay times of an SCR in the presence of noise is challenging due to this sensitive exponential nature. More than one pair of rise and decay times exist that can closely approximate an experimental SCR shape. Results are also heavily dependent on the removal of the tonic part. cvxEDA (Greco et al., 2016) models the tonic part with cubic B-spline basis functions with a 10 s knot size. Greco et al. (2016) used l_2-norm penalization on the cubic spline basis function coefficients to avoid overfitting. They selected the regularization parameter to the penalization term based on prior data they had analyzed. This parameter depends on how the data is scaled in reality and how much of the tonic part it contains. Here, we set the regularization parameter related to the smoothness of the tonic component in cvxEDA at 0.001 instead of the 0.01 default to obtain a better separation of the tonic and phasic components.

Our current implementation of skin conductance deconvolution comprises of the two-step coordinate descent algorithm described earlier. Although it performs well in terms of accuracy, a faster implementation is necessary for a real-time CLDBS system. The physiological parameters τ_r and τ_d usually

remain stable over a prolonged period of time. Therefore, we can perform only the sparse recovery procedure on windows of incoming data after an initial parameter estimation is complete, and thereafter estimate τ_r and τ_d in the background from time-to-time. A faster implementation of the sparse recovery step (e.g., using Greedy algorithms or Bayesian approaches) could further help improve time complexity.

3.2. Sympathetic Arousal State Estimation

A general trend is to be observed in the participant arousal levels in **Figure 4**. In the case of cognitive stress, the subjects' arousal states and HAI remain almost constantly high with the exception of participant 4. In contrast, there is only a moderate increase that dies down at the start of the emotional stress phase. The cognitive tasks required active engagement, i.e., mathematical calculations and active concentration, on the part of the participants. Meanwhile, the emotional stress period only involved passive engagement—the subjects just had to watch a horror movie clip without any significant cognitive effort. The varying level of cognitive activity is a likely reason for the difference in arousal between cognitive and emotional stress. Birjandtalab et al. (2016) used a clip from the horror movie entitled the "The Horde" to generate emotional stress. It is also possible that the movie was insufficient to generate significant emotional stress. The desired stress-generating effect may not have been realized if, for instance, a participant had already watched the movie. A visual inspection of the sub-panels depicting skin conductance in **Figure 4** does not show a significant number of SCRs during emotional stress. It is likely PTSD patients may experience more emotional rather than cognitive stress. However, the emotions they experience may not necessarily be those evoked in healthy subjects for the very same stimuli. For instance, scenes of blood and dead bodies in a horror movie may evoke traumatic memories in PTSD patients leading to higher levels of stress. Further experimentation with a patient population would help validate our methods in detecting elevated levels of arousal in PTSD.

Sympathetic arousal information is not only encoded in how frequently neural impulses to the sweat glands occur, but also in the skin conductance signal amplitudes. Consequently, the amplitude of individual SCRs are taken as indicators of arousal (Bach et al., 2010). The tonic skin conductance level also contains emotion-related information (Braithwaite et al., 2013). Our current state-space formulation only considers the rate at which neural impulses (i.e., binary events) occur. Future work would incorporate the additional amplitude features for estimating sympathetic arousal using augmented state-space models that include both binary and continuous observations (Prerau et al., 2009; Coleman et al., 2011). The addition of heart rate could also help obtain an improved sympathetic arousal estimate (Wickramasuriya and Faghih, 2019).

The current EM approach is also offline and therefore requires modification if it is to be used in real-time in an experimental CLDBS prototype. We suggest running the forward filter in the E-step continuously and performing the full EM procedure in the background from time to time. This is very similar to the approach proposed for deconvolution when adapting to the needs of real-time computation. This may also permit the model parameters to change in adaption to disease progression and changing environmental conditions over time. The steps could also be run in parallel in a multicore processor. Several smartphones are now enabled with multicore processors and one option could be to perform the CLDBS computations on a wearer's phone. Another option would be to stream the data to the internet and perform computations in the cloud. Developing a custom hardware device to accompany the CLDBS implant is yet another option for performing skin conductance deconvolution and arousal state estimation in real-time.

3.3. Study Limitations

As noted earlier, many of the skin conductance recordings were contaminated with noise and had to be discarded. In-band motion artifacts such as those seen in the data-set usually contaminate a signal nonlinearly. Adaptive filtering (Mathews, 1991; Zaknich, 2005) and multi-level wavelet-based thresholding (Chen et al., 2015) are some of the options for suppressing motion artifacts. It is likely that skin conductance will indeed be contaminated with such artifacts in a real-world setting. We leave the development of an accelerometer-based adaptive filter for removing motion artifacts in skin conductance for future work. In another work, Amin and Faghih (2018) illustrated a way of performing concurrent deconvolution from multi-channel skin conductance data to obtain an estimate from noisy data. They included weights in different channels based on the standard deviation of noise in each channel while estimating the neural stimuli. They showed that the multi-channel approach could be more reliable for noisy skin conductance data. Multi-channel approach could potentially be used to achieve a more reliable CLDBS system. Moreover, factors other than sympathetic arousal can also influence skin conductance (e.g., body temperature, hydration, physical activity, and electrolytes). Variations induced by these factors may thus confound sympathetic arousal estimates; this is a limiting factor of using skin conductance alone. Such factors could be taken into account in a real-world setting and their effect canceled to obtain an improved arousal estimate. This would require an extended state-space model incorporating body temperature and hydration levels, for instance, as additional observations.

The present work is a proof-of-principle framework for using skin conductance in closing the DBS loop. As skin conductance relates to sympathetic arousal, and moreover as PTSD patients frequently show symptoms of hyperarousal, we note the suitability of using skin conductance as a CLDBS biomarker. The data-set used here however, does not include any PTSD patients and is a limitation of this study. Further investigation is therefore necessary to validate the use of skin conductance in an experimental CLDBS prototype for PTSD patients. Recall that differences in skin conductance have been reported in the literature between individuals with and without PTSD. The coefficients of the differential equations ($\boldsymbol{\tau}$) in Equations (2) and (3) governing sweat secretion dynamics are determined on a per subject basis. Thus, even if $\boldsymbol{\tau}$ were significantly different between healthy and patient populations, our deconvolution methodology would still adapt to each individual. Furthermore, we only track

a single skin conductance feature—the occurrence of neural impulses. The α coefficient in Equation (11) is calculated from the baseline probability of impulses on a per subject basis. The process noise variance σ_ϵ^2 in Equation (10) is also estimated for each subject individually via the EM algorithm. Therefore, our Bayesian filter for sympathetic arousal estimation is also able to adapt to each individual. Although the present study did not include data from a patient population, we would however expect our methods to generalize to them nevertheless due to the ability of the framework to adapt to each individual.

3.4. Effect of DBS on Skin Conductance

The neural substrates underlying skin conductance have been examined in studies involving functional imaging, brain lesions and direct electrical stimulation (Critchley, 2002). Mangina and Beuzeron-Mangina (1996) applied electrical stimulation to the limbic structures of a group of subjects with intractable epilepsy and measured bilateral skin conductance. When the left sides of the amygdala, posterior hippocampus, anterior hippocampus and cingulate gyrus were stimulated, higher SCR amplitudes on the left hand were observed compared to the right. The reverse was also true when the right sides of the same interior structures were stimulated. They also reported that stimulation intensity increased SCR amplitudes. Lanteaume et al. (2006) examined the effect of electrical stimulation of the amygdala on self-reported emotions and SCRs in a group of patients with drug-resistant partial epilepsy. SCR amplitudes were larger when the stimulation caused a positive emotional change as opposed to a negative change or no change. Our methodology does not make use of the SCR amplitudes but rather the rates at which they occur. Further research would be necessary to quantify the effect on SCR rates when applying direct stimulation via a DBS implant to the limbic structures. A correction for the effect due to the stimulation could be incorporated into the state-space model in this case.

3.5. Closing the DBS Loop

Developing a complete CLDBS system is a challenge. Our approach demonstrates the ability to recover sympathetic arousal from skin conductance measurements using state-space methods. Neural stimuli to the sweat glands originating from the sympathetic nerve fibers encode emotion-related information in how frequently they fire. By relating the probability of neural impulse occurrence to sympathetic arousal through a state-space model, we are able to estimate a continuous state trajectory across different episodes of relaxation and stress.

Different biomarkers have been suggested for closing the loop in DBS therapy. Ideally, the biomarker should enable the real-time tracking of an unobserved brain state. Here, we investigate skin conductance as a viable alternative for a CLDBS as a means of treating neuropsychiatric disorders such as PTSD. While we have sought to address how to estimate an emotion-related state trajectory from peripheral skin conductance measurements, there remains the problem of determining the mapping from the state variable back into the CLDBS stimulation parameter space (i.e., the amplitude, frequency, and width of the electrical stimuli). Determining this mapping will enable sympathetic arousal to be controlled in realtime. Grahn et al. (2014) proposed a novel means of addressing this mapping problem in a CLDBS system they developed for maintaining stable dopamine levels in rodents. They first varied the frequency, amplitude, and pulse width of the electrical stimulation and measured the corresponding dopamine level responses for different parameter combinations. We too could similarly vary the electrical stimulation parameters of a DBS system while measuring skin conductance changes and estimate the corresponding arousal levels. Grahn et al. (2014) next characterized the dopamine responses using a combination of 7th order polynomials and 2nd order exponentials. This required a total of 12 model coefficients. They next trained a neural network having the frequency, amplitude and pulse width as the inputs and the 12 model coefficients as the outputs. Likewise, we could train a neural network mapping stimulation parameters to arousal responses. Thereafter, Grahn et al. (2014) trained a *second* neural network having the model coefficients as inputs and the frequency, amplitude and pulse width as the outputs. They used this inverse model for predicting the stimulation parameters necessary for maintaining specific extracellular dopamine levels. Therefore, a CLDBS system utilizing our method for arousal estimation could utilize a similar neural network characterizing the inverse relationship back into the stimulation parameter space in its feedback path.

A simpler option would be to use on/off control instead of adjusting the stimulation parameters in a continuous manner. Herron et al. (2017) developed an on/off CLDBS controller for a patient suffering from tremor. The controller applied electrical stimulation when β-band power recorded from invasively acquired electroencephalography (EEG) dropped below a certain (manually-tuned) threshold, and switched it off when the power exceeded yet another threshold. Preliminary on/off control could be applied in the case of neuropsychiatric disorders too, for instance when sudden angry outbursts or bouts of depression as detected by abnormally elevated or diminished arousal levels occur.

We wish to point out that not all elevated arousal levels need to be controlled (e.g. high arousal levels due to positive excitement). When proposing a CLDBS framework for the treatment of chronic pain, Shirvalkar et al. (2018) too noted that they did not wish to avoid all feelings of pain *per se*, as pain itself provides a warning of potential tissue damage. Therefore, a fully closed-loop system for the treatment of neuropsychiatric disorders should be able to recognize the positive–negative aspect of emotion as well. This positive–negative or pleasure–displeasure dimension is known by the term emotional valence (Russell, 1980). The CLDBS would ideally need to estimate a vector $\mathbf{z}_j$ containing both arousal and valence. Emotional valence information can be decoded using physiological signals such as scalp EEG, heart rate, electromyography and skin conductance (Koelstra et al., 2012; Soleymani et al., 2012). Stimulation can then be turned on, for instance, only if high arousal is detected and valence is negative.

Finally a control algorithm is necessary in the CLDBS feedback loop when progressing beyond preliminary on/off stimulation. Our state estimation approach relies on a rate of neural firing. Azgomi et al. (2019) developed a fuzzy feedback controller based on the rate of SCR appearances for increasing arousal

during relaxation and decreasing it during periods of cognitive stress. The controller was based on the model proposed in Wickramasuriya et al. (2018) and can directly be used with the method presented here. In a review of CLDBS therapy, Carron et al. (2013) mention two different other works, namely those by Grant and Lowery (2013) and Pasillas-Lépine et al. (2013), that propose a control mechanism based on the rate of neural firing for estimating a state variable. Pasillas-Lépine et al. (2013) proposed a proportional control based on the firing rates of the subthalamic nucleus and global pallidus. Grant and Lowery (2013) developed a similar CLDBS controller based on β-band oscillations in LFPs. An adaptation of one of these methods could also be used for developing a control law for regulating emotion based on peripheral skin conductance measurements.

3.6. Conclusion

DBS has met with success in treating a host of disease conditions where other therapeutic measures have been exhausted. CLDBS systems have been proposed as the future of DBS due to their inherent advantages over the previous generation of open-loop systems. Closing the DBS loop is a challenge. In this work, we present a method for estimating sympathetic arousal from skin conductance measurements as a potential mechanism that could be deployed within a CLDBS system for treating neuropsychiatric disorders. The methodology consists of two parts: (i) the deconvolution of phasic skin conductance to obtain the neural impulses that generate SCRs; (ii) a state-space model for tracking sympathetic arousal based on the frequency at which the SCRs appear. Results are demonstrated on a publicly available data-set. We finally discuss possibilities for developing a controller that could map the state estimates back into the stimulation parameter space for automated closed-loop control. While we mention PTSD as an example scenario here, our approach could be generalized to other disease conditions where any type of impulse-like or pulsatile signal is a biomarker. For instance, if neural spiking or pulsatile cortisol secretions are clinically-relevant features for a particular disease condition, then the Bayesian filter described here could also be used as part of closing the loop. Additionally, the methods presented here are personalized, i.e., the model parameters are estimated for each individual. Differences in skin conductance have been reported in the literature between healthy subjects and patients with anorexia nervosa (Tchanturia et al., 2007) and depression (Ward and Doerr, 1986). If skin conductance biomarkers can be determined for each of these conditions (based on SCR amplitudes, rates of SCR occurrence, skin conductance levels etc.), then an extended state-space model could be developed to track a symptom-related neural state that incorporates both binary and continuous-valued observations (Prerau et al., 2009; Coleman et al., 2011).

DATA AVAILABILITY

Publicly available datasets were analyzed in this study. This data can be found here: https://physionet.org/physiobank/database/noneeg/.

AUTHOR CONTRIBUTIONS

RF conceived and designed the study. DW and MA analyzed data and wrote the manuscript. RF, DW, and MA developed the algorithms and analysis tools.

FUNDING

The work was supported in part by the National Science Foundation grant 1755780 CRII: CPS: Wearable Machine Interface Architectures.

REFERENCES

Aikins, D. E., Johnson, D. C., Borelli, J. L., Klemanski, D. H., Morrissey, P. M., Benham, T. L., et al. (2009). Thought suppression failures in combat PTSD: a cognitive load hypothesis. *Behav. Res. Ther.* 47, 744–751. doi: 10.1016/j.brat.2009.06.006

Alexander, D. M., Trengove, C., Johnston, P., Cooper, T., August, J. P., and Gordon, E. (2005). Separating individual skin conductance responses in a short interstimulus-interval paradigm. *J. Neurosci. Methods* 146, 116–123. doi: 10.1016/j.jneumeth.2005.02.001

American Psychiatric Association. (2013). *Diagnostic and Statistical Manual of Mental Disorders*, 5th Edn. Arlington, VA: American Psychiatric Association.

Amin, M. R., and Faghih, R. T. (2018). "Inferring autonomic nervous system stimulation from hand and foot skin conductance measurements," in *52th Asilomar Conference on Signals, Systems and Computers*. (Pacific Grove, CA).

Amin, M. R., and Faghih, R. T. (2019). Sparse deconvolution of electrodermal activity via continuous-time system identification. *IEEE Trans. Biomed. Eng.* doi: 10.1109/TBME.2019.2892352. [Epub ahead of print].

Azgomi, H. F., Wickramasuriya, D. S., and Faghih, R. T. (2019). "State-space modeling and fuzzy feedback control of cognitive stress," in *41st Annual International Conference of the IEEE Engineering in Medicine and Biology Society (EMBC)* (Berlin).

Bach, D. R., Flandin, G., Friston, K. J., and Dolan, R. J. (2010). Modelling event-related skin conductance responses. *Int. J. Psychophysiol.* 75, 349–356. doi: 10.1016/j.ijpsycho.2010.01.005

Benedek, M., and Kaernbach, C. (2010). Decomposition of skin conductance data by means of nonnegative deconvolution. *Psychophysiology* 47, 647–658. doi: 10.1111/j.1469-8986.2009.00972.x

Bina, R. W., and Langevin, J.-P. (2018). Closed loop deep brain stimulation for PTSD, addiction, and disorders of affective facial interpretation: review and discussion of potential biomarkers and stimulation paradigms. *Front. Neurosci.* 12:300. doi: 10.3389/fnins.2018.00300

Birjandtalab, J., Cogan, D., Pouyan, M. B., and Nourani, M. (2016). "A non-EEG biosignals dataset for assessment and visualization of neurological status," in *2016 IEEE International Workshop on Signal Processing Systems (SiPS)* (Dallas, TX), 110–114.

Boccard, S. G., Pereira, E. A., and Aziz, T. Z. (2015). Deep brain stimulation for chronic pain. *J. Clin. Neurosci.* 22, 1537–1543. doi: 10.1016/j.jocn.2015.04.005

Boucsein, W. (2012). *Electrodermal Activity*. New York, NY: Springer Science + Business Media, LLC. doi: 10.1007/978-1-4614-1126-0

Bouthour, W., Mégevand, P., Donoghue, J., Lüscher, C., Birbaumer, N., and Krack, P. (2019). Biomarkers for closed-loop deep brain stimulation

in Parkinson disease and beyond. *Nat. Rev. Neurol.* 15, 343–352. doi: 10.1038/s41582-019-0166-4

Braithwaite, J. J., Watson, D. G., Jones, R., and Rowe, M. (2013). A guide for analysing electrodermal activity (EDA) & skin conductance responses (SCRs) for psychological experiments. *Psychophysiology* 49, 1017–1034. doi: 10.1111/j.1469-8986.2012.01384.x

Bronstein, J. M., Tagliati, M., Alterman, R. L., Lozano, A. M., Volkmann, J., Stefani, A., et al. (2011). Deep brain stimulation for Parkinson disease: an expert consensus and review of key issues. *Arch. Neurol.* 68, 165–165. doi: 10.1001/archneurol.2010.260

Carron, R., Chaillet, A., Filipchuk, A., Pasillas-Lépine, W., and Hammond, C. (2013). Closing the loop of deep brain stimulation. *Front. Syst. Neurosci.* 7:112. doi: 10.3389/fnsys.2013.00112

Chen, W., Jaques, N., Taylor, S., Sano, A., Fedor, S., and Picard, R. W. (2015). "Wavelet-based motion artifact removal for electrodermal activity," in *37th Annual International Conference of the IEEE Engineering in Medicine and Biology Society (EMBC)* (Milano), 6223–6226.

Chou, K. L., Grube, S., and Patil, P. G. (2011). *Deep Brain Stimulation: A New Life for People With Parkinson's, Dystonia, and Essential Tremor*. New York, NY: Oxford University Press; Demos Medical Publishing.

Cleary, D. R., Ozpinar, A., Raslan, A. M., and Ko, A. L. (2015). Deep brain stimulation for psychiatric disorders: where we are now. *Neurosurg. Focus* 38:E2. doi: 10.3171/2015.3.FOCUS1546

Coleman, T. P., Yanike, M., Suzuki, W. A., and Brown, E. N. (2011). "A mixed-filter algorithm for dynamically tracking learning from multiple behavioral and neurophysiological measures," in *The Dynamic Brain: An Exploration of Neuronal Variability and Its Functional Significance*, eds M. Ding and D. L. Glanzman (New York, NY: Oxford University Press), 1–16.

Critchley, H. D. (2002). Electrodermal responses: what happens in the brain. *Neuroscientist* 8, 132–142. doi: 10.1177/107385840200800209

Critchley, H. D., Melmed, R. N., Featherstone, E., Mathias, C. J., and Dolan, R. J. (2002). Volitional control of autonomic arousal: a functional magnetic resonance study. *Neuroimage* 16, 909–919. doi: 10.1006/nimg.2002.1147

Dawson, M. E., Schell, A. M., and Filion, D. L. (2007). "The electrodermal system," in *The Handbook of Psychophysiology*, eds J. T. Cacioppo, L. G. Tassinary, and G. G. Berntson (New York, NY: Cambridge University Press), 159–181.

Dostrovsky, J. O., and Lozano, A. M. (2002). Mechanisms of deep brain stimulation. *Mov. Disord.* 17, S63–S68. doi: 10.1002/mds.10143

Faghih, R. T. (2014). *System identification of cortisol secretion: characterizing pulsatile dynamics* (Ph.D. thesis). Massachusetts Institute of Technology: Cambridge, MA, United States.

Faghih, R. T. (2018). "From physiological signals to pulsatile dynamics: a sparse system identification approach," in *Dynamic Neuroscience*, eds Z. Chen and S. V. Sarma (Cham: Springer), 239–265.

Faghih, R. T., Dahleh, M. A., Adler, G. K., Klerman, E. B., and Brown, E. N. (2014). Deconvolution of serum cortisol levels by using compressed sensing. *PLoS ONE* 9:e85204. doi: 10.1371/journal.pone.0085204

Faghih, R. T., Dahleh, M. A., Adler, G. K., Klerman, E. B., and Brown, E. N. (2015a). Quantifying pituitary-adrenal dynamics and deconvolution of concurrent cortisol and adrenocorticotropic hormone data by compressed sensing. *IEEE Trans. Biomed. Eng.* 62, 2379–2388. doi: 10.1109/TBME.2015.2427745

Faghih, R. T., Stokes, P. A., Marin, M.-F., Zsido, R. G., Zorowitz, S., Rosenbaum, B. L., et al. (2015b). "Characterization of fear conditioning and fear extinction by analysis of electrodermal activity," in *Engineering in Medicine and Biology Society (EMBC), 2015 37th Annual International Conference of the IEEE* (Milano: IEEE), 7814–7818.

Fisher, R., Salanova, V., Witt, T., Worth, R., Henry, T., Gross, R., et al. (2010). Electrical stimulation of the anterior nucleus of thalamus for treatment of refractory epilepsy. *Epilepsia* 51, 899–908. doi: 10.1111/j.1528-1167.2010.02536.x

Goldberger, A. L., Amaral, L. A., Glass, L., Hausdorff, J. M., Ivanov, P. C., Mark, R. G., et al. (2000). PhysioBank, PhysioToolkit, and PhysioNet: components of a new research resource for complex physiologic signals. *Circulation* 101, e215–e220. doi: 10.1161/01.CIR.101.23.e215

Goldfinger, D. A., Amdur, R. L., and Liberzon, I. (1998). Psychophysiologic responses to the rorschach in ptsd patients, noncombat and combat controls. *Depress. Anxiety* 8, 112–120. doi: 10.1002/(SICI)1520-6394(1998)8:3<112::AID-DA3>3.0.CO;2-U

Golub, G. H., Heath, M., and Wahba, G. (1979). Generalized cross-validation as a method for choosing a good ridge parameter. *Technometrics* 21, 215–223. doi: 10.1080/00401706.1979.10489751

Grahn, P. J., Mallory, G. W., Khurram, O. U., Berry, B. M., Hachmann, J. T., Bieber, A. J., et al. (2014). A neurochemical closed-loop controller for deep brain stimulation: toward individualized smart neuromodulation therapies. *Front. Neurosci.* 8:169. doi: 10.3389/fnins.2014.00169

Grant, P. F., and Lowery, M. M. (2013). Simulation of cortico-basal ganglia oscillations and their suppression by closed loop deep brain stimulation. *IEEE Trans. Neural Syst. Rehabil. Eng.* 21, 584–594. doi: 10.1109/TNSRE.2012.2202403

Greco, A., Valenza, G., Lanata, A., Scilingo, E. P., and Citi, L. (2016). cvxEDA: A convex optimization approach to electrodermal activity processing. *IEEE Trans. Biomed. Eng.* 63, 797–804. doi: 10.1109/TBME.2015.2474131

Hellmuth, J. C., Stappenbeck, C. A., Hoerster, K. D., and Jakupcak, M. (2012). Modeling PTSD symptom clusters, alcohol misuse, anger, and depression as they relate to aggression and suicidality in returning us veterans. *J. Traumat. Stress* 25, 527–534. doi: 10.1002/jts.21732

Herron, J. A., Thompson, M. C., Brown, T., Chizeck, H. J., Ojemann, J. G., and Ko, A. L. (2017). Cortical brain–computer interface for closed-loop deep brain stimulation. *IEEE Trans. Neural Syst. Rehabil. Eng.* 25, 2180–2187. doi: 10.1109/TNSRE.2017.2705661

Jennings, J. R. (1986). "Bodily changes during attending," in *Psychophysiology: Systems, Processes, and Applications*, eds M. G. H. Coles, E. Donchin, and S. Porges (New York, NY: Guilford Press), 268–289.

Jetly, R., Heber, A., Fraser, G., and Boisvert, D. (2015). The efficacy of nabilone, a synthetic cannabinoid, in the treatment of PTSD-associated nightmares: a preliminary randomized, double-blind, placebo-controlled cross-over design study. *Psychoneuroendocrinology* 51, 585–588. doi: 10.1016/j.psyneuen.2014.11.002

Koek, R. J., Langevin, J.-P., Krahl, S. E., Kosoyan, H. J., Schwartz, H. N., Chen, J. W., et al. (2014). Deep brain stimulation of the basolateral amygdala for treatment-refractory combat post-traumatic stress disorder (PTSD): study protocol for a pilot randomized controlled trial with blinded, staggered onset of stimulation. *Trials* 15:356. doi: 10.1186/1745-6215-15-356

Koelstra, S., Muhl, C., Soleymani, M., Lee, J.-S., Yazdani, A., Ebrahimi, T., et al. (2012). DEAP: A database for emotion analysis; using physiological signals. *IEEE Trans. Affect. Comput.* 3, 18–31. doi: 10.1109/T-AFFC.2011.15

Koskimäki, H., Mönttinen, H., Siirtola, P., Huttunen, H.-L., Halonen, R., and Röning, J. (2017). "Early detection of migraine attacks based on wearable sensors: experiences of data collection using Empatica E4," in *Proceedings of the 2017 ACM International Joint Conference on Pervasive and Ubiquitous Computing and Proceedings of the 2017 ACM International Symposium on Wearable Computers* (Maui, HI: ACM), 506–511.

Langevin, J.-P., Chen, J., Koek, R., Sultzer, D., Mandelkern, M., Schwartz, H., and Krahl, S. (2016). Deep brain stimulation of the basolateral amygdala: targeting technique and electrodiagnostic findings. *Brain Sci.* 6:28. doi: 10.3390/brainsci6030028

Lanteaume, L., Khalfa, S., Régis, J., Marquis, P., Chauvel, P., and Bartolomei, F. (2006). Emotion induction after direct intracerebral stimulations of human amygdala. *Cereb. Cortex* 17, 307–1313. doi: 10.1093/cercor/bhl041

Lempka, S. F., Malone D. A. Jr., Hu, B., Baker, K. B., Wyant, A., Ozinga J. G. IV, et al. (2017). Randomized clinical trial of deep brain stimulation for poststroke pain. *Ann. Neurol.* 81, 653–663. doi: 10.1002/ana.24927

Lin, H.-P., Lin, H.-Y., Lin, W.-L., and Huang, A. C.-W. (2011). Effects of stress, depression, and their interaction on heart rate, skin conductance, finger temperature, and respiratory rate: sympathetic-parasympathetic hypothesis of stress and depression. *J. Clin. Psychol.* 67, 1080–1091. doi: 10.1002/jclp.20833

Lipsman, N., Woodside, D. B., Giacobbe, P., Hamani, C., Carter, J. C., Norwood, S. J., et al. (2013). Subcallosal cingulate deep brain stimulation for treatment-refractory anorexia nervosa: a phase 1 pilot trial. *Lancet* 381, 1361–1370. doi: 10.1016/S0140-6736(12)62188-6

Little, S., Beudel, M., Zrinzo, L., Foltynie, T., Limousin, P., Hariz, M., et al. (2016). Bilateral adaptive deep brain stimulation is effective in Parkinson's disease. *J. Neurol. Neurosurg. Psychiatry* 87, 717–721. doi: 10.1136/jnnp-2015-310972

Little, S., and Brown, P. (2012). What brain signals are suitable for feedback control of deep brain stimulation in parkinson's disease? *Ann. N. Y. Acad. Sci.* 1265, 9–24. doi: 10.1111/j.1749-6632.2012.06650.x

Little, S., Pogosyan, A., Neal, S., Zavala, B., Zrinzo, L., Hariz, M., et al. (2013). Adaptive deep brain stimulation in advanced Parkinson disease. *Ann. Neurol.* 74, 449–457. doi: 10.1002/ana.23951

Low, P. A. (2012). "Chapter 51 - sweating," in *Primer on the Autonomic Nervous System, 3rd Edition*, eds D. Robertson, I. Biaggioni, G. Burnstock, P. A. Low, and J. F. Paton (San Diego, CA: Academic Press), 249–251.

Lüthi, A., and Lüscher, C. (2014). Pathological circuit function underlying addiction and anxiety disorders. *Nat. Neurosci.* 17:1635. doi: 10.1038/nn.3849

Mangina, C. A., and Beuzeron-Mangina, J. H. (1996). Direct electrical stimulation of specific human brain structures and bilateral electrodermal activity. *Int. J. Psychophysiol.* 22, 1–8. doi: 10.1016/0167-8760(96)00022-0

Mathews, V. J. (1991). Adaptive polynomial filters. *IEEE Signal Process. Mag.* 8, 10–26.

McCullagh, P., and Nelder, J. A. (1989). *Generalized Linear Models, Vol. 37*. London; New York: Chapman and Hall; CRC Press.

McNally, R. J., Luedke, D. L., Besyner, J. K., Peterson, R. A., Bohm, K., and Lips, O. J. (1987). Sensitivity to stress-relevant stimuli in posttraumatic stress disorder. *J. Anxiety Disord.* 1, 105–116. doi: 10.1016/0887-6185(87)90001-6

Mendel, J. M. (1995). *Lessons in Estimation Theory for Signal Processing, Communications, and Control*. Englewood Cliffs, NJ: Prentice Hall PTR; Pearson Education.

Merkl, A., Schneider, G.-H., Schönecker, T., Aust, S., Kühl, K.-P., Kupsch, A., et al. (2013). Antidepressant effects after short-term and chronic stimulation of the subgenual cingulate gyrus in treatment-resistant depression. *Exp. Neurol.* 249, 160–168. doi: 10.1016/j.expneurol.2013.08.017

Müller, U. J., Voges, J., Steiner, J., Galazky, I., Heinze, H.-J., Möller, M., et al. (2013). Deep brain stimulation of the nucleus accumbens for the treatment of addiction. *Ann. N. Y. Acad. Sci.* 1282, 119–128. doi: 10.1111/j.1749-6632.2012.06834.x

Munro, L. L., Dawson, M. E., Schell, A. M., and Sakai, L. M. (1987). Electrodermal lability and rapid vigilance decrement in a degraded stimulus continuous performance task. *J. Psychophysiol.* 1, 249–257.

Murray, J. F. (2005). *Visual recognition, inference and coding using learned sparse overcomplete representations* (Ph.D. thesis). University of California, San Diego, CA, United States.

Oluigbo, C. O., Salma, A., and Rezai, A. R. (2012). Deep brain stimulation for neurological disorders. *IEEE Rev. Biomed. Eng.* 5, 88–99. doi: 10.1109/RBME.2012.2197745

Orr, S. P., and Roth, W. T. (2000). Psychophysiological assessment: clinical applications for PTSD. *J. Affect. Disord.* 61, 225–240. doi: 10.1016/S0165-0327(00)00340-2

Pasillas-Lépine, W., Haidar, I., Chaillet, A., and Panteley, E. (2013). "Closed-loop deep brain stimulation based on firing-rate regulation," in *2013 6th International IEEE/EMBS Conference on Neural Engineering (NER)* (San Diego, CA), 166–169.

Plumb, M., and Bain, P. (2007). *Essential Tremor: The Facts*. New York, NY: Oxford University Press.

Pole, N. (2007). The psychophysiology of posttraumatic stress disorder: a meta-analysis. *Psychol. Bull.* 133:725. doi: 10.1037/0033-2909.133.5.725

Prerau, M. J., Smith, A. C., Eden, U. T., Kubota, Y., Yanike, M., Suzuki, W., et al. (2009). Characterizing learning by simultaneous analysis of continuous and binary measures of performance. *J. Neurophysiol.* 102, 3060–3072. doi: 10.1152/jn.91251.2008

Puigdemont, D., Pérez-Egea, R., Portella, M. J., Molet, J., de Diego-Adeliño, J., Gironell, A., et al. (2012). Deep brain stimulation of the subcallosal cingulate gyrus: further evidence in treatment-resistant major depression. *Int. J. Neuropsychopharmacol.* 15, 121–133. doi: 10.1017/S1461145711001088

Risser, H. J., Hetzel-Riggin, M. D., Thomsen, C. J., and McCanne, T. R. (2006). PTSD as a mediator of sexual revictimization: the role of reexperiencing, avoidance, and arousal symptoms. *J. Traumat. Stress* 19, 687–698. doi: 10.1002/jts.20156

Rosin, B., Slovik, M., Mitelman, R., Rivlin-Etzion, M., Haber, S. N., Israel, Z.,et al. (2011). Closed-loop deep brain stimulation is superior in ameliorating parkinsonism. *Neuron* 72, 370–384. doi: 10.1016/j.neuron.2011.08.023

Russell, J. A. (1980). A circumplex model of affect. *J. Pers. Soc. Psychol.* 39:1161. doi: 10.1037/h0077714

Shirvalkar, P., Veuthey, T. L., Dawes, H. E., and Chang, E. F. (2018). Closed-loop deep brain stimulation for refractory chronic pain. *Front. Comput. Neurosci.* 12:18. doi: 10.3389/fncom.2018.00018

Silverthorn, D. U. (2009). *Human Physiology: An Integrated Approach, 6th Edn*. Illinois City, IL: Pearson Education, Inc.

Smith, A. C., Frank, L. M., Wirth, S., Yanike, M., Hu, D., Kubota, Y., et al. (2004). Dynamic analysis of learning in behavioral experiments. *J. Neurosci.* 24, 447–461. doi: 10.1523/JNEUROSCI.2908-03.2004

Soleymani, M., Lichtenauer, J., Pun, T., and Pantic, M. (2012). A multimodal database for affect recognition and implicit tagging. *IEEE Trans. Affect. Comput.* 3, 42–55. doi: 10.1109/T-AFFC.2011.25

Tchanturia, K., Liao, P.-C., Uher, R., Lawrence, N., Treasure, J., and Campbell, I. C. (2007). An investigation of decision making in anorexia nervosa using the Iowa Gambling Task and skin conductance measurements. *J. Int. Neuropsychol. Soc.* 13, 635–641. doi: 10.1017/S1355617707070798

Vesper, J., Steinhoff, B., Rona, S., Wille, C., Bilic, S., Nikkhah, G., et al. (2007). Chronic high-frequency deep brain stimulation of the STN/SNr for progressive myoclonic epilepsy. *Epilepsia* 48, 84–1989. doi: 10.1111/j.1528-1167.2007.01166.x

Ward, N. G., and Doerr, H. O. (1986). Skin conductance: a potentially sensitive and specific marker for depression. *J. Nerv. Ment. Dis.* 174, 553–559.

Wickramasuriya, D. S., and Faghih, R. T. (2019). "A novel filter for tracking real-world cognitive stress using multi-time-scale point process observations," in *41st Annual International Conference of the IEEE Engineering in Medicine and Biology Society (EMBC)* (Berlin).

Wickramasuriya, D. S., Qi, C., and Faghih, R. T. (2018). "A state-space approach for detecting stress from electrodermal activity," in *40th Annual International Conference of the IEEE Engineering in Medicine and Biology Society (EMBC)* (Honolulu, HI), 3562–3567.

Woodward, S. H., Murburg, M. M., and Bliwise, D. L. (2000). PTSD-related hyperarousal assessed during sleep. *Physiol. Behav.* 70, 197–203. doi: 10.1016/S0031-9384(00)00271-7

Wu, H., Van Dyck-Lippens, P. J., Santegoeds, R., van Kuyck, K., Gabriëls, L., Lin, G., et al. (2013). Deep-brain stimulation for anorexia nervosa. *World Neurosurg.* 80, S29–se1. doi: 10.1016/j.wneu.2012.06.039

Zaknich, A. (2005). *Principles of Adaptive Filters and Self-Learning Systems*. London: Springer Science & Business Media.

Zdunek, R., and Cichocki, A. (2008). Improved M-FOCUSS algorithm with overlapping blocks for locally smooth sparse signals. *IEEE Trans. Signal Process.* 56, 4752–4761. doi: 10.1109/TSP.2008.928160

Zhou, H., Xu, J., and Jiang, J. (2011). Deep brain stimulation of nucleus accumbens on heroin-seeking behaviors: a case report. *Biol. Psychiatry* 69, e41–e42. doi: 10.1016/j.biopsych.2011.02.012

Conflict of Interest Statement: The authors declare that the research was conducted in the absence of any commercial or financial relationships that could be construed as a potential conflict of interest.

frontiers in Neuroscience

ORIGINAL RESEARCH
published: 10 September 2019
doi: 10.3389/fnins.2019.00956

Model-Based Evaluation of Closed-Loop Deep Brain Stimulation Controller to Adapt to Dynamic Changes in Reference Signal

Fei Su[1,2,3], *Karthik Kumaravelu*[1], *Jiang Wang*[3] *and Warren M. Grill*[1*†]

[1] *Department of Biomedical Engineering, Duke University, Durham, NC, United States,* [2] *School of Mechanical and Electrical Engineering, Shandong Agricultural University, Tai'an, China,* [3] *School of Electrical and Information Engineering, Tianjin University, Tianjin, China*

OPEN ACCESS

Edited by:
Giovanni Mirabella, Sapienza University of Rome, Italy

Reviewed by:
Karim Oweiss, University of Florida, United States
J. Luis Lujan, Mayo Clinic College of Medicine and Science, United States

***Correspondence:**
Warren M. Grill
warren.grill@duke.edu

†ORCID:
Warren M. Grill
orcid.org/0000-0001-5240-6588

Specialty section:
This article was submitted to Neural Technology, a section of the journal Frontiers in Neuroscience

Received: *14 March 2019*
Accepted: *26 August 2019*
Published: *10 September 2019*

Citation:
Su F, Kumaravelu K, Wang J and Grill WM (2019) Model-Based Evaluation of Closed-Loop Deep Brain Stimulation Controller to Adapt to Dynamic Changes in Reference Signal. Front. Neurosci. 13:956. doi: 10.3389/fnins.2019.00956

High-frequency deep brain stimulation (DBS) of the subthalamic nucleus (STN) is effective in suppressing the motor symptoms of Parkinson's disease (PD). Current clinically-deployed DBS technology operates in an open-loop fashion, i.e., fixed parameter high-frequency stimulation is delivered continuously, invariant to the needs or status of the patient. This poses two major challenges: (1) depletion of the stimulator battery due to the energy demands of continuous high-frequency stimulation, (2) high-frequency stimulation-induced side-effects. Closed-loop deep brain stimulation (CL DBS) may be effective in suppressing parkinsonian symptoms with stimulation parameters that require less energy and evoke fewer side effects than open loop DBS. However, the design of CL DBS comes with several challenges including the selection of an appropriate biomarker reflecting the symptoms of PD, setting a suitable reference signal, and implementing a controller to adapt to dynamic changes in the reference signal. Dynamic changes in beta oscillatory activity occur during the course of voluntary movement, and thus there may be a performance advantage to tracking such dynamic activity. We addressed these challenges by studying the performance of a closed-loop controller using a biophysically-based network model of the basal ganglia. The model-based evaluation consisted of two parts: (1) we implemented a Proportional-Integral (PI) controller to compute optimal DBS frequencies based on the magnitude of a dynamic reference signal, the oscillatory power in the beta band (13–35 Hz) recorded from model globus pallidus internus (GPi) neurons. (2) We coupled a linear auto-regressive model based mapping function with the Routh-Hurwitz stability analysis method to compute the parameters of the PI controller to track dynamic changes in the reference signal. The simulation results demonstrated successful tracking of both constant and dynamic beta oscillatory activity by the PI controller, and the PI controller followed dynamic changes in the reference signal, something that cannot be accomplished by constant open-loop DBS.

Keywords: closed-loop deep brain stimulation, Parkinson's disease, beta band activity, proportional-integral controller, Routh-Hurwitz stability analysis

INTRODUCTION

Parkinson's disease (PD) is characterized by degeneration of dopaminergic neurons in the substania nigra pars compacta (SNc) resulting in motor symptoms including bradykinesia, rest tremor, postural instability, and rigidity (Davie, 2008; Jankovic, 2008). High-frequency deep brain stimulation (DBS) of the subthalamic nucleus (STN) or globus pallidus internus (GPi) is a well-established surgical therapy to treat the motor symptoms of PD (Krack et al., 2003; Rodriguez-Oroz et al., 2005; Odekerken et al., 2016). Current clinical DBS technology is open loop—stimulation is always on and the stimulation parameters are tuned periodically through manual adjustments by health care professionals. The process of selection of DBS parameters is challenging due to the large number of parameters (Kuncel and Grill, 2004). Therefore, the efficacy of current open-loop DBS may be suboptimal and patients can experience side effects, including speech deficits and cognitive dysfunction (Deuschl et al., 2006; Okun and Foote, 2010; Massano and Garrett, 2012; Cyron, 2016).

Recent clinical studies suggest that closed-loop DBS (CL DBS) may be more efficient at suppressing PD motor symptoms with reduced side effects as compared to continuous high-frequency STN DBS (Rosin et al., 2011; Carron et al., 2013; Hebb et al., 2014; Rossi et al., 2016). However, the design of CL DBS controllers comes with several challenges including selection of a feedback signal reflecting PD symptoms and the capacity of the controller to adapt to dynamic changes in the reference signal (Hebb et al., 2014; Arlotti et al., 2016a; Parastarfeizabadi and Kouzani, 2017). Concurrent neuronal recordings and behavioral assessments from PD patients and animal models of PD showed a strong correlation between beta band oscillations (13–35 Hz) and PD motor symptoms, especially bradykinesia (Zaidel et al., 2010; Jenkinson and Brown, 2011; Little and Brown, 2012; Hoang et al., 2017), and beta band activity may be an appropriate feedback signal for CL DBS. However, beta oscillations in the basal ganglia desynchronize in preparation and during voluntary movement (Levy et al., 2002; Brittain and Brown, 2014). Therefore, a fixed beta power reference may not be appropriate for control of DBS, and it may be beneficial to include in the controller design the ability to adapt to dynamic changes in the reference signal.

The objective of this study was to design a controller for CL DBS that can adapt to dynamic changes in the reference signal. We evaluated the performance of a proportional integral (PI) controller using a network model of the basal ganglia (BG) (Kumaravelu et al., 2016). The parameters of the PI controller were tuned by coupling a linear controlled auto-regressive (CAR) model with Routh-Hurwitz stability analysis. The PI controller was successful in adapting to dynamic changes in the reference signal, and such a control scheme may be suitable for implementation in CL DBS systems.

METHODS

A block diagram of the proposed CL DBS framework is shown in **Figure 1A**. The signal power of model neuron activity in the beta band was used as the feedback signal $y\left(k\right)$, and the error $e\left(k\right)$ between the actual beta power and the desired beta power $y_{sp}\left(k\right)$ was sent to the PI controller to calculate the stimulation frequency $u\left(k\right)$. Thus, the PI controller calculated the DBS frequency according to the variation of beta oscillatory power. The calculated DBS frequency determined the time of the next stimulation pulse $I_{dbs}\left(t\right)$ delivered to a biophysical network model of the parkinsonian cortex-basal ganglia-thalamus (CTx-BG-Th) network. The selection of appropriate PI controller parameters was required for the actual beta power to track dynamic variations in the desired power. Below we propose a stability analysis method to calculate automatically the PI parameters.

Computational Model of the Cortex-Basal Ganglia-Thalamus Network

We used a model of the CTx-BG-Th network as a test bed to evaluate the performance of the closed-loop control scheme (Kumaravelu et al., 2016), and a implementation of this model in MATLAB can be downloaded from ModelDB (https://senselab.med.yale.edu/modeldb/). The CTx-BG-Th model included the cortex, striatum, STN, globus pallidus externus (GPe), GPi

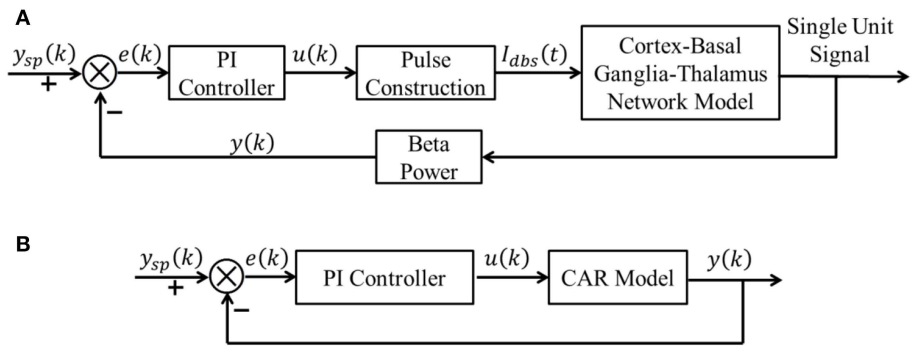

FIGURE 1 | (A) The CL DBS framework. The spike times of model neurons in the GPi were calculated, and the beta band power of these spike times was used as the feedback signal $y\,(k)$. The error term $e\,(k)$ between the desired beta power $y_{sp}\,(k)$ and actual value $y\,(k)$ was input to the PI controller to calculate the stimulation frequency $u\,(k)$. The stimulation signal $I_{dbs}\,(t)$ delivered to the cortex-basal ganglia-thalamus network model was subsequently determined. **(B)** The transformed linear system of the CL DBS system. This transformed linear system was used to determine the appropriate parameters for the PI controller, and the PI parameters were constant once calculated.

and a thalamic nucleus, and each region was comprised of 10 single-compartment Hodgkin-Huxley type neurons. In the original publication, the model was validated extensively, including matching the responses evoked in the basal ganglia by cortical stimulation in rats (Kita and Kita, 2011), model neuron firing rates and patterns that were consistent with parkinsonian rats (Mallet et al., 2008), and responses to STN DBS at different frequencies that matched those measured experimentally (McConnell et al., 2012; So et al., 2012). Model BG neurons exhibited exaggerated low-frequency oscillatory activity in the parkinsonian state compared to the healthy condition, similar to that seen *in vivo*. Since, beta oscillatory activity is well-correlated with PD symptoms (Leventhal et al., 2012; Stein and Bar-Gad, 2013), we chose the beta band (13–35 Hz) power present in the activity of the GPi neurons as the model-based proxy for symptoms (Brocker et al., 2013) to evaluate the effectiveness of the CL DBS controller. There is a strong correlation between single unit firing and LFPs in the beta band in the STN (Levy et al., 2002; Kühn et al., 2005) and in the GP (Goldberg et al., 2004), and the power spectrum calculated from the single unit spike times of GP neurons was correlated with motor symptoms of parkinsonism (McConnell et al., 2012). Simulations were implemented in MATLAB R2016a and equations were solved using the forward Euler method with a time step of 0.01 ms; spectral analyses were performed using the "mtspecgrampt" function of the Chronux neural signal analysis package (chronux.org) (sliding 1 s window, 0.1 s step size and [3 5] tapers (3 is the time-bandwidth product and 5 is the number of tapers)). The spectrum of all 10 GPi neurons spike time series was calculated using the multi-taper spectral estimation method.

Identification of Relationship Between Stimulation Frequency and Beta Band Power of GPi Model Neurons Spike Times

The oscillations within the CTx-BG-Th network were similar across the different parts of the loop (Kumaravelu et al., 2016), for STN, GPi, and GPe both single neuron and local field potentials (LFPs) exhibited excessive beta band oscillation in the PD state, while for thalamus and cortex single neuron oscillation were not dominant (Stein and Bar-Gad, 2013). The beta band power of GPi model neurons spike times was chosen to characterize the model state. The dynamics of the CTx-BG-Th network were highly non-linear and therefore it was inappropriate to use the linear PI controller to control directly the network model of PD. A linear model of the plant between the stimulation frequency and the beta band power of GPi model neuron spike times was first identified using a CAR model. The structure of a CAR model was

$$\begin{aligned}&\left(1+a_1z^{-1}+a_2z^{-2}+\cdots+a_{n_a}z^{-n_a}\right)y\left(k\right)\\&=\left(b_0+b_1z^{-1}+b_2z^{-2}+\cdots+b_{n_b}z^{-n_b}\right)u\left(k\right)+\varepsilon\left(k\right)\end{aligned}\quad(1)$$

where z was the lag operator, $u\left(k\right)$ was the input signal (stimulation frequency) and $y\left(k\right)$ was the output signal (beta power of GPi model neuron spike times), n_b and n_a were the order of input and output sequences, respectively, and $\varepsilon\left(k\right)$ was assumed to be white noise. The identification process included the following steps:

1. Collect input and output data from the CTx-BG-Th network model.
2. Estimate model parameters $a_1\cdots a_{n_a}$ and $b_0\cdots b_{n_b}$.
3. Choose appropriate order parameters n_a and n_b.
4. Quantify the prediction accuracy of the CAR model.

The identification accuracy of the CAR model was highly dependent on the input output data that were selected, because not all data provided an equal amount of information (Ljung, 1999). The designed stimulation sequence was delivered to the CTx-BG-Th model (in the open loop), and the corresponding output data (beta band power) was calculated. To obtain more informative input/output data to identify the CAR model, the frequencies (input data) of the stimulation waveform were chosen randomly between 5 and 200 Hz. **Figure 2A** illustrates the stimulation sequence from 12 to 16 s, illustrating that each frequency continued for 0.4 s to ensure that at least two pulses were delivered for each random frequency. The simulation duration was 400 s, resulting in responses to 1,000 frequency samples. The stimulation sequence was delivered to the computational model of the CTx-BG-Th network, and spiking activity was recorded from GPi model neurons. The time window used to bin the beta power of GPi spike times was sensitive to the temporal dynamics of beta power when the stimulation frequencies were randomly changed (**Figure 2C**). Differences in beta power across time window bins were compared using one-way ANOVA with *post-hoc* Tukey's honestly significant difference (HSD) test, and statistical significance was defined as $\alpha = 0.05$. The beta power varied across different time window bins ($F = 252.54$, $p < 0.0001$). When the time window bin was larger than 0.1 s, the calculated beta power was no <1.6 times the value with time window bin equaled to 0.1 s. The choice of the short 0.1 s bin enabled capture of small dynamic changes in beta power, as our objective was to implement a controller that responded to such changes. Bin sizes of 0.2 s or longer did not reflect the dynamic variation of the beta power, as indicated by the invariance to bin size. Since each frequency was delivered for 0.4 s and the bin used to calculate beta power was 0.1 s, the beta power obtained in **Figure 2B** was the average of four values within 0.4 s.

We used the recursive least squares (RLS) method (Ljung, 1999) to estimate the CAR model parameters. The CAR model was transformed into a standard LS form (Ljung, 1999),

$$\begin{aligned}y\left(k\right)\;=\;&-a_1y\left(k-1\right)-a_2y\left(k-2\right)-\cdots-a_{n_a}y\left(k-n_a\right)\\&+b_0u\left(k\right)+b_1u\left(k-1\right)+b_2u\left(k-2\right)+\cdots\\&+b_{n_b}u\left(k-n_b\right)+\varepsilon\left(k\right)=\boldsymbol{\varphi}^T\left(k\right)\boldsymbol{\theta}+\boldsymbol{\varepsilon}\left(k\right)\end{aligned}\quad(2)$$

where $\boldsymbol{\varphi}\left(k\right)=\left[-y\left(k-1\right),\cdots,-y\left(k-n_a\right),u\left(k\right),\cdots,u\left(k-n_b\right)\right]^T$ was the known sequence of input and output data, and $\boldsymbol{\theta}=\left[a_1,a_2,\cdots,a_{n_a},b_0,b_1,\cdots,b_{n_b}\right]^T$ was the vector of unknown model parameters. From Equation (2), the current value of the output signal was correlated with the past input and output signals as well as the current input signal. Then, unknown model parameters were estimated by the RLS method,

$$y_e\left(k\right)=\boldsymbol{\varphi}^T\left(k\right)\hat{\boldsymbol{\theta}}\quad(3)$$

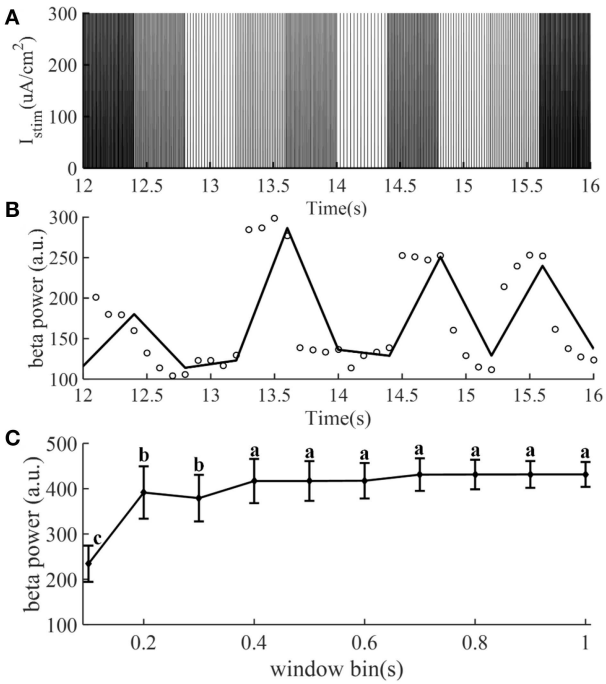

FIGURE 2 | The stimulation sequence **(A)** and beta band power **(B)** obtained from the CTx-BG-Th network model to train the CAR model. Only data from 12 to 16 s are presented to improve visualization. **(A)** The stimulation frequency was randomly selected from 5 to 200 Hz, and for each frequency the corresponding stimulation sequence lasted for 0.4 s. **(B)** Circles represent the beta power value in each 0.1 s, the collected beta power within 0.4 s was the average of four values. **(C)** Mean ± standard deviation of beta power of GPi model neuron spike times plotted as a function of time window bin (50 trials). The mean value of beta power varies across different time window bin values, and values not sharing the same letter were significantly different ($p < 0.05$, Tukey's HSD).

where $\hat{\boldsymbol{\theta}}$ was the estimated parameter vector calculated using the following equations:

$$\begin{cases} \hat{\boldsymbol{\theta}}(k) = \hat{\boldsymbol{\theta}}(k-1) + \mathbf{K}(k)\left[y(k) - \boldsymbol{\varphi}^T(k)\hat{\boldsymbol{\theta}}(k-1)\right] \\ \mathbf{K}(k) = \frac{\mathbf{P}(k-1)\boldsymbol{\varphi}(k)}{1+\boldsymbol{\varphi}^T(k)\mathbf{P}(k-1)\boldsymbol{\varphi}(k)} \\ \mathbf{P}(k) = \left[I - \mathbf{K}(k)\boldsymbol{\varphi}^T(k)\right]\mathbf{P}(k-1) \end{cases} \quad (4)$$

The root mean square error (RMSE) between the actual output signal and the CAR model predicted output signal was used to quantify the prediction accuracy of the CAR model,

$$e_{RMSE} = \sqrt{\frac{1}{N}\sum_{k=1}^{N}\left(y(k) - y_e(k)\right)^2} \quad (5)$$

The e_{RMSE} declined as the CAR model order (n_a and n_b) was increased (**Figure 3A**). Since the purpose of the identified CAR model was to design the PI controller but not to substitute for the original CTx-BG-Th network model, we were not interested in higher-order dynamics. Akaike's information criterion (AIC) was used to select the model order (McQuarrie and Chih-Ling, 1998),

$$\mathrm{AIC} = \frac{2K - 2L}{N} + \frac{2K(K+1)}{N-K-1} \quad (6)$$

where $K = n_a + n_b + 1$ was the number of parameters to be estimated, N was the length of predicted data, and $L = -\frac{N}{2}\ln(2\pi) - \frac{N}{2}\ln\left(\frac{{e_{RMSE}}^2}{N}\right) - \frac{N}{2}$. When $n_a = 3 \quad and\ n_b = 3$ the valued of AIC was minimized, thus, the structure of the CAR model was

$$\begin{aligned} y_e(k) = & -a_1 y_e(k-1) - a_2 y_e(k-2) - a_3 y_e(k-3) \\ & + b_0 u(k) + b_1 u(k-1) + b_2 u(k-2) \\ & + b_3 u(k-3) \end{aligned} \quad (7)$$

and the corresponding estimated CAR model parameters in each iteration are shown in **Figure 3B**.

Selection of PI Controller Parameters

Although a common Proportional-Integral-Differential (PID) controller has three control terms (P, I, and D), we only chose the P and I terms, because the D action is sensitive to the model prediction accuracy (Aström and Hägglund, 1995). With the selected CAR model, $e_{RMSE} = 27.9$, there were still prediction error, and the D term was not used due to these inaccuracies of the CAR model. The transformed system with the CAR model substituted for the network model was used to choose the parameters of the PI controller (**Figure 1B**).

The structure of a discrete PI controller was (Aström and Hägglund, 1995),

$$u(k) = u(k-1) + k_p\left[e(k) - e(k-1)\right] + k_i e(k) \quad (8)$$

and the aim was to select the P term and I term coefficients, k_p and k_i. The Routh-Hurwitz stability criterion (Gopal, 2002) was used to calculate automatically the PI parameters, where the selected PI controller must ensure the stability of the system. The forward transfer function of this system (**Figure 1B**) is given by Equation (9).

$$\begin{aligned} G(z) &= \frac{Y(z)}{E(z)} = \frac{Y(z)}{U(z)} \cdot \frac{U(z)}{E(z)} = \frac{b_0 z^3 + b_1 z^2 + b_2 z + b_3}{z^3 + a_1 z^2 + a_2 z + a_3} \cdot \frac{\left(k_p + k_i\right)z - k_p}{z-1} \\ &= \frac{b_0\left(k_p + k_i\right)z^4 + \left[b_1\left(k_p + k_i\right) - b_0 k_p\right]z^3 + \left[b_2\left(k_p + k_i\right) - b_1 k_p\right]z^2 + \left[b_3\left(k_p + k_i\right) - b_2 k_p\right]z - b_3 k_p}{z^4 + (a_1 - 1)z^3 + (a_2 - a_1)z^2 + (a_3 - a_2)z - a_3} \end{aligned} \quad (9)$$

The closed-loop transfer function was

$$\Phi(z) = \frac{G(z)}{1 + G(z)} \quad (10)$$

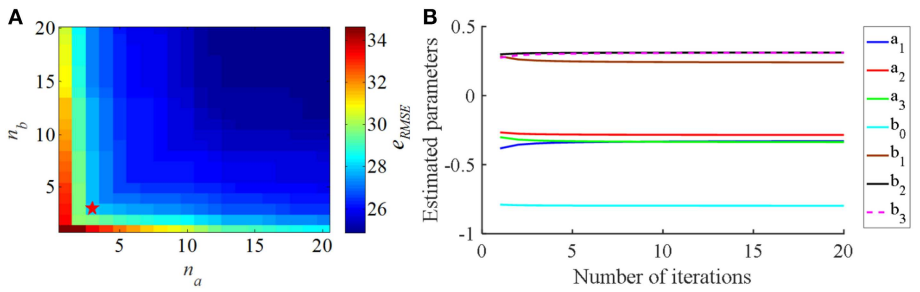

FIGURE 3 | (A) The relationship between the CAR model order parameters (n_a and n_b) and the RMS error (e_{RMSE}) between the actual output signal and the CAR model predicted output signal. **(B)** The estimated CAR model parameters across iterations to minimize e_{RMSE}.

The characteristic equation of this system was

$$\begin{aligned} D(z) &= 1 + G(z) = \left[1 + b_0\left(k_p + k_i\right)\right] z^4 + \left[\left(a_1 - 1\right)\right. \\ &\quad + b_1\left(k_p + k_i\right) - b_0 k_p\left.\right] z^3 + \left[\left(a_2 - a_1\right) + b_2\left(k_p + k_i\right)\right. \\ &\quad - b_1 k_p\left.\right] z^2 + \left[\left(a_3 - a_2\right) + b_3\left(k_p + k_i\right)\right. \\ &\quad - b_2 k_p\left.\right] z - a_3 - b_3 k_p = 0 \end{aligned} \tag{11}$$

According to the Routh-Hurwitz stability criterion, we substituted z with w, where $z = \frac{w+1}{w-1}$, and the variable of the characteristic equation became w.

$$\begin{aligned} \mathrm{D}(w) &= m_4\left(\frac{w+1}{w-1}\right)^4 + m_3\left(\frac{w+1}{w-1}\right)^3 + m_2\left(\frac{w+1}{w-1}\right)^2 \\ &\quad + m_1\left(\frac{w+1}{w-1}\right) + m_0 = 0 \end{aligned} \tag{12}$$

Combining Equations (11) and (12), $m_4 = 1 + b_0\left(k_p + k_i\right)$, $m_3 = \left(a_1 - 1\right) + b_1\left(k_p + k_i\right) - b_0 k_p$, $m_2 = \left(a_2 - a_1\right) + b_2\left(k_p + k_i\right) - b_1 k_p$, $m_1 = \left(a_3 - a_2\right) + b_3\left(k_p + k_i\right) - b_2 k_p$, $m_0 = -a_3 - b_3 k_p$. Then multiplying both sides of Equation (12) by $(w-1)^4$, such that, $(w-1)^4 D(w) = n_4 w^4 + n_3 w^3 + n_2 w^2 + n_1 w + n_0 = 0$, that is,

$$D_1(w) = n_4 w^4 + n_3 w^3 + n_2 w^2 + n_1 w + n_0 = 0 \tag{13}$$

where $n_4 = m_0 + m_1 + m_2 + m_3 + m_4$, $n_3 = -4m_0 - 2m_1 + 2m_3 + 4m_4$, $n_2 = 6m_0 - 2m_2 + 6m_4$, $n_1 = -4m_0 + 2m_1 - 2m_3 + 4m_4$, $n_0 = m_0 - m_1 + m_2 - m_3 + m_4$.

The stability of this system was equivalent to the following conditions:

$$n_i > 0\,(i = 0, 1, 2, 3, 4), n_3 n_2 > n_4 n_1, n_3 n_2 n_1 > n_4 n_1^2 + n_3^2 n_0 \tag{14}$$

Combining Equations (11)–(13), $n_i$could also be described as a function of k_p and k_i, and to ensure that all conditions in Equation (14) were satisfied, we chose $k_p = 0.80$, $k_i = 0.05$.

Closed-Loop Frequency Modulation

Considering the established physiological responses to different pulse repetition frequencies of DBS (Birdno and Grill, 2008), we constrained the calculated stimulation frequency to between 5 and 200 Hz. When the calculated frequency was larger than 200 Hz, it was set to 200 Hz; when the calculated frequency was <5 Hz, it was set to 5 Hz.

$$u(k) = \begin{cases} 5 & u(k) < 5 \\ u(k-1) + k_p\left[e(k) - e(k-1)\right] + k_i e(k) & 5 \le u(k) \le 200 \\ 200 & u(k) > 200 \end{cases} \tag{15}$$

The stimulation frequency was calculated using the PI controller, which required knowledge of the beta power at the k*th* and (k-1)*th* time points. The beta power of the k*th* time point was calculated from (t−0.1) s to t s, the beta power of the (k-1)*th* time point was calculated from (t_1-0.1) s to t_1 s. The time difference between t and t_1 was 0.008 s. Note this was not the time step for the controller to update the DBS frequency, and the controller updated the DBS frequency only after the former interpulse interval ended.

RESULTS

Prediction Performance of the CAR Model

The performance of the CAR model during the model training process is shown in **Figure 4A**. The correlation coefficient between the actual and estimated data in the model training process was $r\left(y, y_e\right) = 0.84$. In addition, we generated different sequences of random stimulation frequencies, and delivered the corresponding stimulation signals to the network model to calculate the resulting sequences of beta power. The same sequences of stimulation frequencies were also delivered to the trained CAR model. The prediction performance of the trained CAR model on two example data sequences is shown in **Figures 4B,C**. In this testing phase, the correlation coefficient between the two outputs were $r\left(y, y_e\right) = 0.82$ and $r\left(y, y_e\right) = 0.80$. Thus, the prediction accuracy of the CAR model was ∼80%.

To create a quantitative comparator for the prediction accuracy of the identified CAR model, we delivered an identical test stimulation signal to the CTx-BG-Th network model five times. The mean correlation coefficient among any two output datasets was 0.95. Since the CTx-BG-Th was highly non-linear,

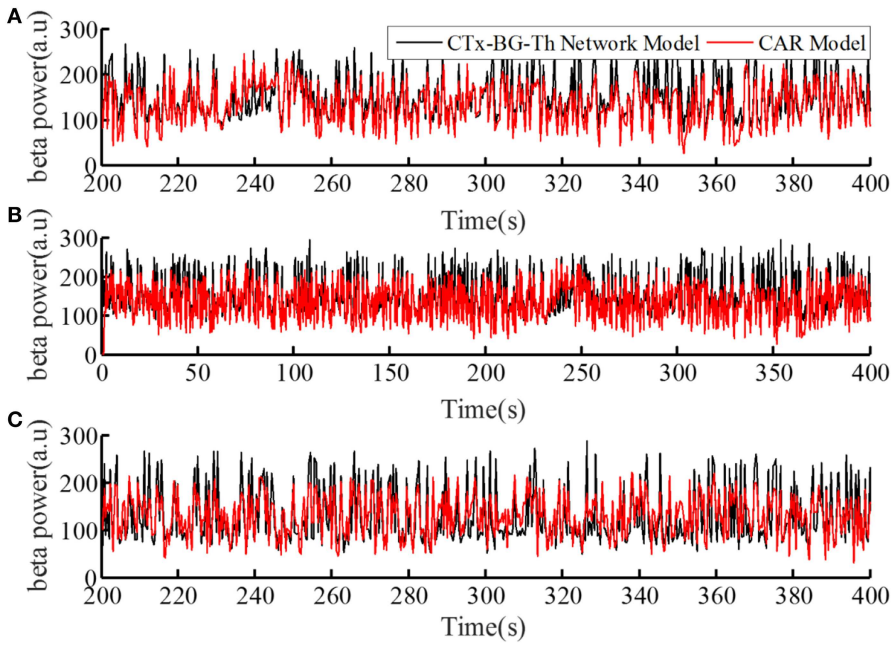

FIGURE 4 | The prediction performance of the CAR model during model training **(A)** and testing **(B,C)**. The datasets used to train and test the CAR model were generated as described in section Computational Model of the Cortex-Basal Ganglia-Thalamus Network. The black line represented the beta power calculated from the original CTx-BG-Th network model, and the red line represented the beta power data predicted by the identified CAR model.

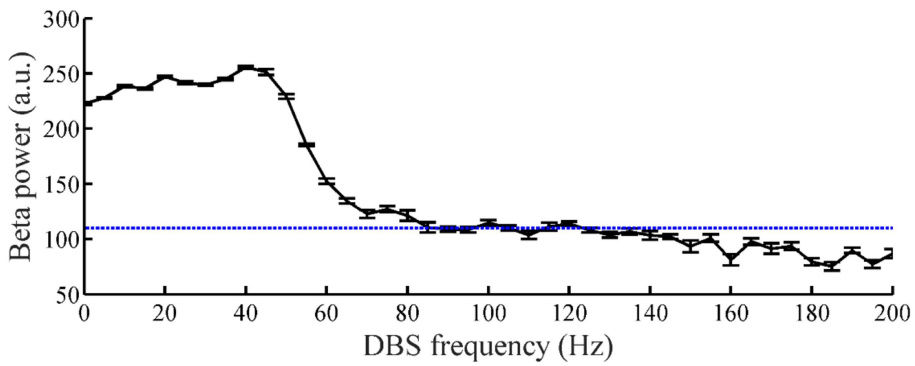

FIGURE 5 | The relationship between DBS frequency and the beta band power of GPi model neuron spike times. Standard error bars are shown for 50 trials. The dotted line labels the 110 target beta power value.

while the structure of the CAR model presented here was linear, the difference between 0.95 and 0.8 may reflect the unmodeled non-linear dynamics between the stimulation frequency and the beta power. However, since our aim in identifying the CAR model was as a tool to design the PI controller, the 80% accuracy was deemed sufficient.

Tracking of Constant Beta Power

The relationship between the DBS pulse repetition frequency and the beta power of GPi model neuron spike times in the CTx-BG-Th model is shown in **Figure 5**. The beta band power in the healthy and PD states of the CTx-BG-Th model were 162 and 222.5, respectively. Similar to the effects of DBS frequency on motor symptoms (Birdno and Grill, 2008), reductions in beta band oscillatory activity were observed only for higher frequencies of DBS. The target beta power was selected to be 110, which was approximately the value generated by DBS at 115 Hz. When the stimulation frequency was larger than 100 Hz, the variations of beta power with changes in frequency were quite small, and the selection of a specific beta power target level had no particular impact on the results.

The spectrograms of the spike times from model GPi, GPe, and STN neurons in the parkinsonian condition, during 115 Hz DBS, and during CL DBS are shown in **Figure 6**. Under the parkinsonian condition, the model neurons in these three nuclei exhibited oscillatory activity around 20 Hz. During the 115 Hz

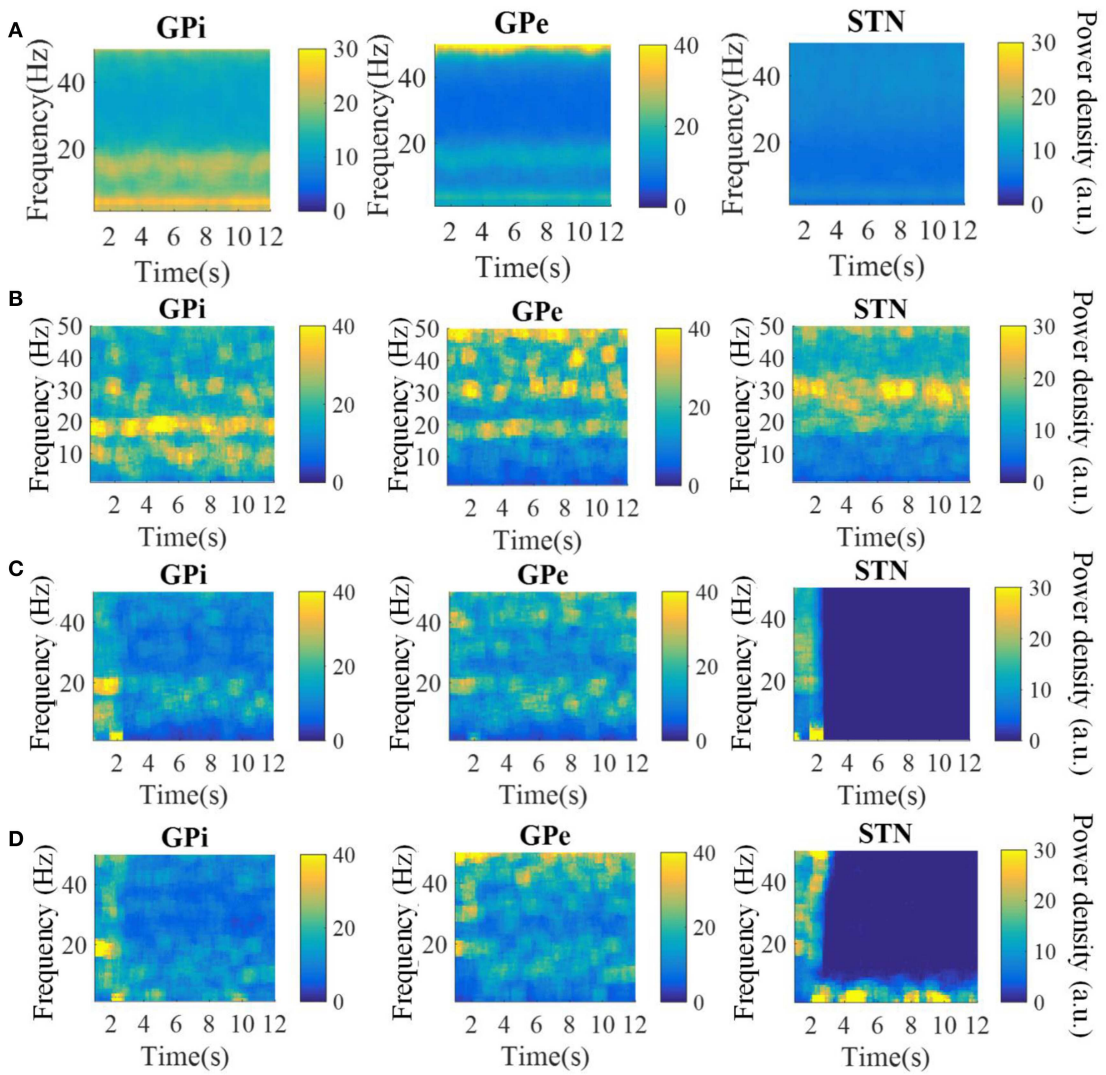

FIGURE 6 | Spectrograms of the spike times from model GPi, GPe, and STN neurons in the normal **(A)**, parkinsonian condition **(B)**, during 115 Hz DBS **(C)**, and during CL DBS **(D)**. In the parkinsonian condition, all neurons exhibited excessive oscillatory activity compared with the normal condition. The 115 Hz DBS and CL DBS began at $t = 2$ s, and greatly reduced the beta band oscillatory activity.

DBS and CL DBS cases, stimulation began at $t = 2$ s, after which the oscillatory activity rapidly diminished. CL DBS produced intermittent oscillatory activity in model STN neurons in the low frequency band (3–12 Hz), which was 6.2 times larger than the lower frequency power present during open loop DBS (OL DBS) at 115 Hz. The dynamic sequence of stimulation frequencies during CL DBS (**Figure 7A**) exhibited peaks in the power spectrum both around 115 Hz and between 3 and 12 Hz. DBS (**Figure 7D**). The stimulation signal power 3–12 Hz generated oscillatory activity in model STN neurons in the low frequency band that was larger than during 115 Hz OL DBS. Thus, although both stimulation methods reduced the power in the beta band, they may act through different mechanisms.

The variations of DBS frequency and the corresponding changes in beta band power in model GPi neurons during CL DBS are shown in **Figures 7A,B**, respectively. The stimulation began at $t = 2$ s, the initial stimulation frequency was set to 5 Hz, and the CL DBS system calculated the subsequent frequencies automatically to drive the beta band power to the target of 110. The mean stimulation frequency from 2 to 30 s was 118.7 Hz, and the mean beta power from 2 to 30 s was 114.3, while the mean beta power during OL DBS from 2 to 30 s was 111.3 (**Figure 7C**). Compared to OL DBS at 115 Hz, the CL DBS controller generated a wider distribution of power in the stimulation frequency sequence (**Figure 7D**), and the power present in the low frequency band of the stimulation signal generated low frequency power in STN model neurons during CL DBS (**Figure 6D**). The response time was shorter for open loop 115 Hz DBS (0.09 s) than for CL DBS (0.66 s); however, the response time was strongly dependent on the initial

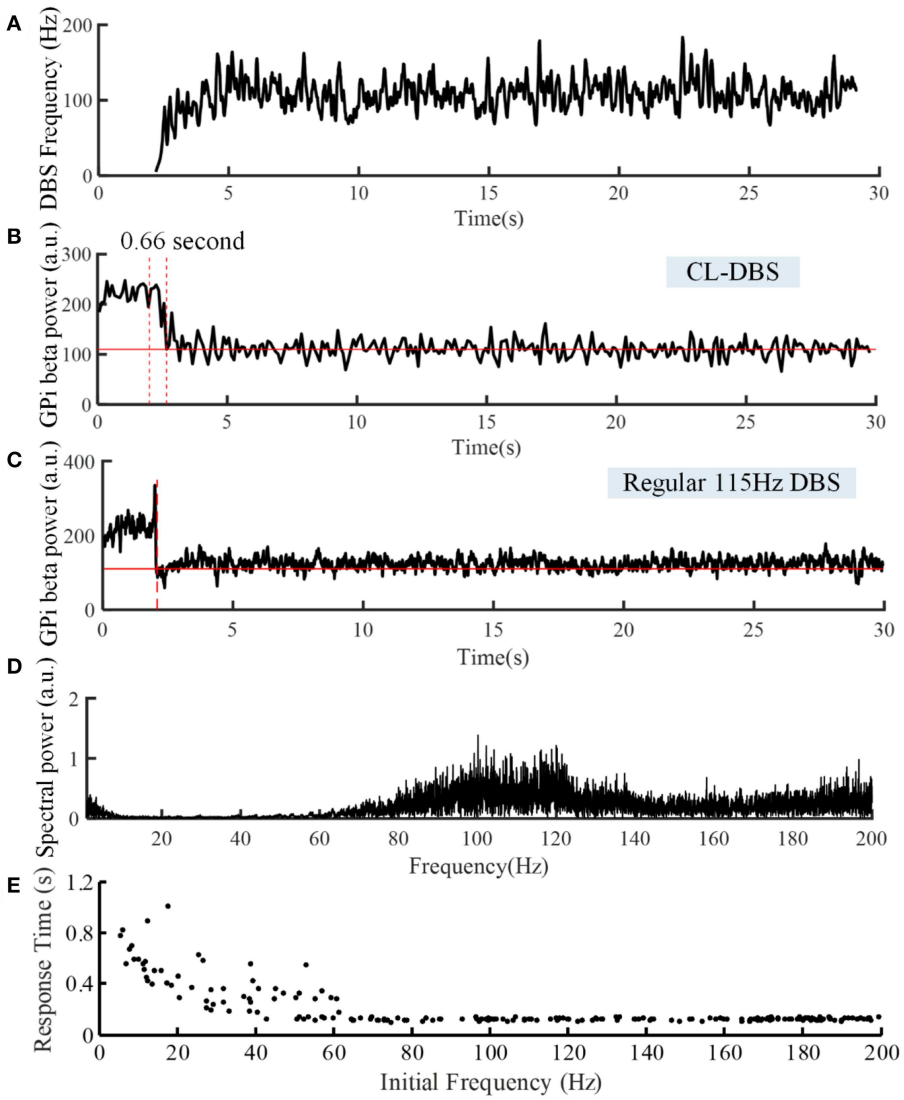

FIGURE 7 | Variations of DBS frequency **(A)** and beta power of spike times from model GPi neurons during CL DBS **(B)** and regular 115 Hz DBS **(C)**. The stimulation signal began at $t = 2$ s, and the beta power converged to the target of 110 at $t = 2.66$ s in **(B)** and at $t = 2.09$ s in **(C)**. **(D)** The corresponding spectral power of the stimulation sequence for this CL DBS example. **(E)** The relationship between the initial frequency of the CL controller and response time in the CL DBS system. The initial frequency of CL DBS was randomly selected from a uniform distribution between 5 and 200 Hz, and the corresponding response time was calculated across 200 trials.

value of frequency during CL DBS (**Figure 7E**). As the initial frequency was increased the response time decreased, and when the initial frequency was ≥60 Hz, the response time for CL DBS was <0.15 s.

To assess the robustness of the PI controller, we changed the target beta power while keeping the PI parameters unchanged (**Figure 8A**). **Figures 8B–E** illustrate the stimulation frequency and beta power variation when the desired beta power was 140 and 180, respectively. When the target beta power was 140, the response time was 0.89 s, and the mean stimulation frequency was 74 Hz. When the target beta power was 150, the response time was 1.15 s, and the mean stimulation frequency was 56 Hz. When the target beta power was larger than 160, the tracking performance declined. Thus, as the desired beta power was larger, the convergence time of GPi beta power became longer. When the target beta power was set to 60 (i.e., a value not achievable with OL DBS, **Figure 5**), the calculated stimulation frequency varied between 155 and 200 Hz (mean = 177.8 Hz), the mean beta power from 2 to 30 s was 82.3, and with OL DBS at 177.8 Hz, the mean beta power was 87.91.

Tracking of Dynamic Changes in Target Beta Power

Beta power in the BG exhibits dynamic changes prior to and during voluntary movement and a fixed target beta power may not be appropriate for functional control of DBS.

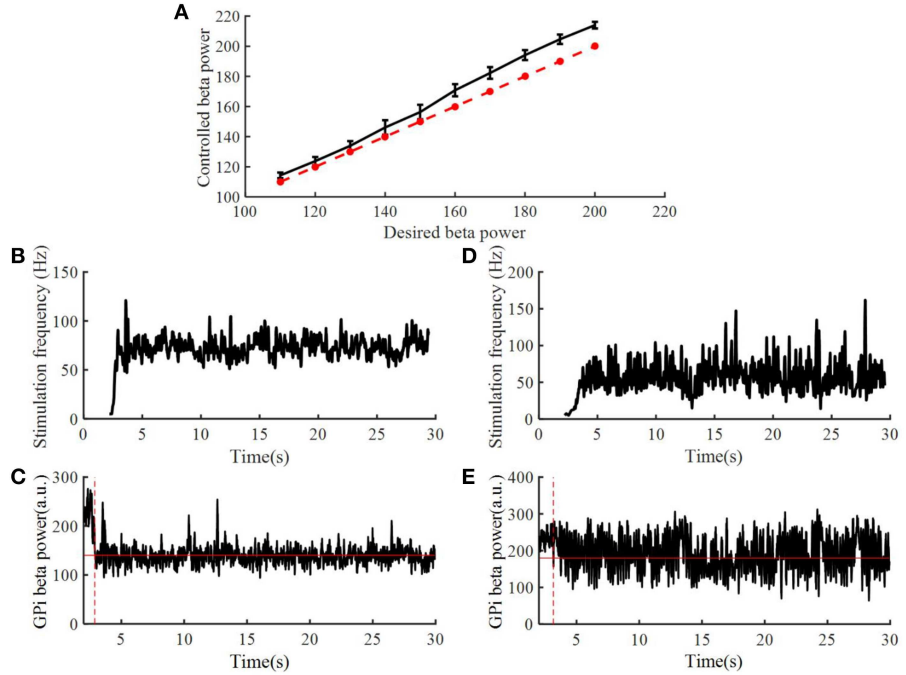

FIGURE 8 | Performance of the PI controller across different levels of target beta power. **(A)** The dotted line represented the value of desired beta power, and the solid line represented the value of controlled beta power; standard error bars are shown for 50 trials. The variation of DBS frequency and beta power of model GPi neuron spike times when the desired beta power was 140 **(B,C)** and 180 **(D,E)**, respectively. The red solid line in **(C,E)** are the desired beta power value. The red dotted line in **(C,E)** indicate the time when the controlled beta power reached the desired beta power.

Therefore, we tested the performance of the control system with time-varying beta power. According to **Figure 5**, when the stimulation frequency of regular DBS increased from 50 to 130 Hz, the GPi beta band power decreased gradually from 220 to 110, and the beta band power tended to saturate at DBS frequencies larger than 130 Hz. Therefore, the target values randomly selected from a uniform distribution between 110 and 220. The duration of the target value varied from 10 to 1 s (**Figures 9a1–h1**). The correlation coefficient between the target beta power and actual beta power between 3.5 and 30 s was calculated, as this mitigated the confounding effects of the initial stimulation frequency. The tracking performance of the CL DBS declined with the duration of the target value, and when the duration was 10, 5, 2, 1, and 0.5 s, the correlation coefficients were 0.83, 0.82, 0.71, 0.69, and 0.49, respectively. Sinusoidal trajectories of target beta power with frequencies ranging from 0.05 to 1 Hz were also tested. The BG model can generate beta power between 90 and 200 during regular DBS, and the minimum and maximum amplitude of the target sinusoidal trajectories were therefore set to be 90 and 200, respectively. The tracking performance and variation of stimulation frequency of the CL DBS system are shown in **Figures 9a2–h2**, and the correlation coefficient between the actual beta power and the target trajectory was used to quantify the tracking accuracy. The tracking performance declined with the increase in target sinusoidal frequency, and the correlation coefficient was 0.85, 0.65, 0.49, and 0.17 for sinusoidal frequencies of 0.05, 0.3, 0.5, and 1 Hz, respectively.

DISCUSSION

Beta band oscillatory activity in the BG is correlated with motor symptoms in PD and may be a suitable biomarker for CL DBS in PD (Little and Brown, 2012; Hoang et al., 2017). For example, Arlotti et al. (2016b) and Little et al. (2013) used the beta oscillation amplitude to control the on time of DBS. DBS was delivered only when the beta-band oscillation amplitude was larger than a pre-set threshold, which reduced energy consumption compared to continuous DBS, while increasing the therapeutic effects on motor symptoms. Subsequently, Dan et al. demonstrated that this approach was also effective in a PD patient with chronically implanted DBS (Piña-Fuentes et al., 2017). In complementary modeling studies, Grant and Lowery designed a CL DBS system to modulate the amplitude of DBS based on beta band oscillations of LFPs, where the coupling strength within the cortico-basal ganglia network was altered to illustrate the ability of CL DBS to respond to changes in network activity (Grant and Lowery, 2013).

However, beta oscillatory activity exhibits dynamic changes (desynchronization) during movement, and Johnson et al. found that a constant beta set point may not be suitable as CL DBS performed poorly during reaching behavior (Johnson et al., 2016). Therefore, if beta power is to be used as a feedback control signal, a constant reference value might not be appropriate. In more recent studies, DBS voltage was adjusted proportionally to the STN LFP beta power, and this adaptive DBS reduced side effects compared to traditional open-loop DBS (Rosa et al., 2015;

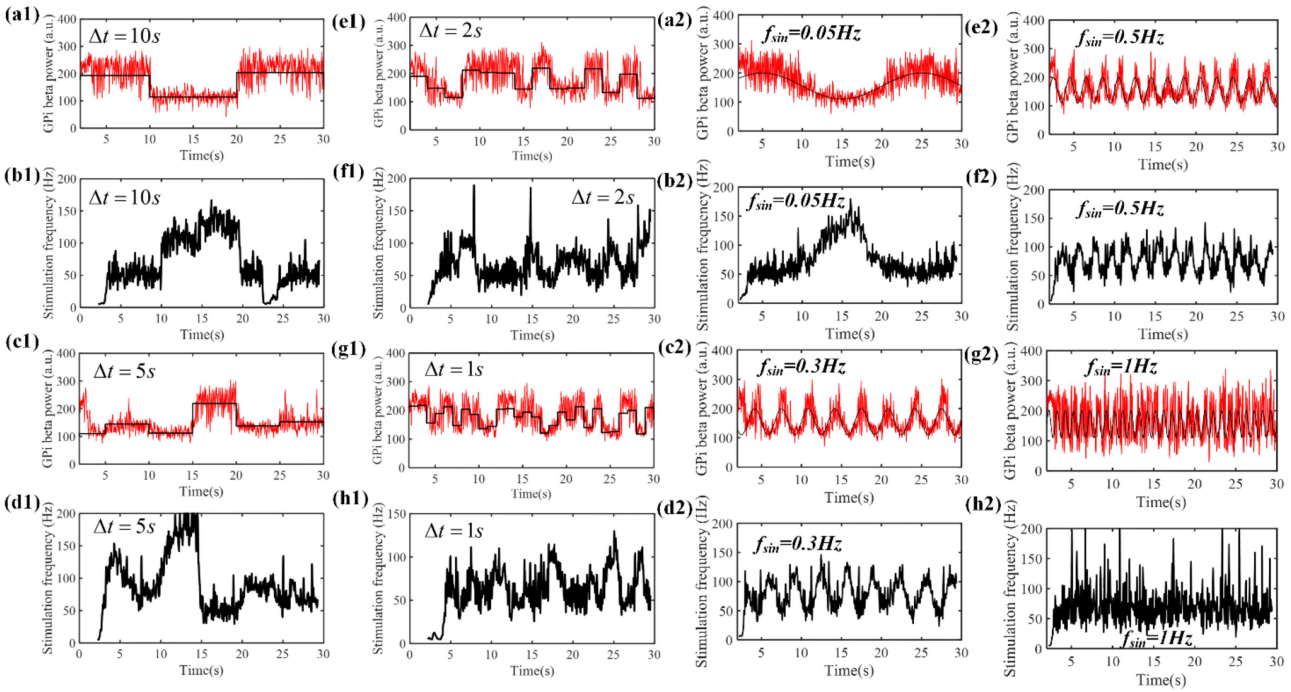

FIGURE 9 | (a1–h1) The performance of the PI controller tracking dynamic changes in target beta power and the corresponding variation in stimulation frequency by the CL DBS system. The duration of the target beta power was 10 s **(a1)**, 5 s **(c1)**, 2 s **(e1)** and 1 s **(g1)**, respectively. The black line represents the desired beta power, and the red line represents the actual beta power during CL DBS. **(b1,d1,f1,h1)** show the respective variations in stimulation frequency during CL DBS. When the duration of target beta power declined from 10 to 0.5 s, the correlation coefficients between the desired and actual beta power were 0.83, 0.82, 0.71, 0.69, 0.49, respectively. **(a2–h2)** The performance of the PI controller tracking sinusoidal trajectories at different frequencies and the associated DBS frequencies determined by the CL controller. The black line in **(a2,c2,e2,g2)** represented the desired beta power, and the red line represented the actual beta power. When the frequency of target sinusoidal trajectories increased from 0.05 to 1 Hz, the correlation coefficients between the desired and actual beta power were 0.85, 0.65, 0.49, and 0.17, respectively. Sinusoidal trajectories of target beta power with frequencies ranging from 0.05 to 1 Hz were also tested. The BG model can generate beta power between 90 and 200 during regular DBS, and the minimum and maximum amplitude of the target sinusoidal trajectories were therefore set to be 90 and 200, respectively. The tracking performance and variation of stimulation frequency of the CL DBS system are shown in **(a2–h2)**, and the correlation coefficient between the actual beta power and the target trajectory was used to quantify the tracking accuracy. The tracking performance declined with the increase in target sinusoidal frequency, and the correlation coefficient was 0.85, 0.65, 0.49, and 0.17 for sinusoidal frequencies of 0.05, 0.3, 0.5, and 1 Hz, respectively.

Arlotti et al., 2018). In another alternative to simply reducing oscillatory activity below a fixed threshold, Santaniello et al. automatically adjusted the stimulation voltage in a mathematical model to match a desired profile of oscillatory neuronal activity (Santaniello et al., 2011). During go/no-go voluntary movements, dynamic changes in beta band power occur at 0.3–1Hz (Sanes and Donoghue, 1993; Zaepffel et al., 2013). The proposed controller could track dynamic changes slower than 1 Hz, and thus such an approach may account for the dynamic changes in beta oscillatory power that occur during movement. Instead of simply switching the stimulation on and off, or adjusting the stimulation amplitude, the controller regulated the stimulation frequency in real time. If the variation in beta band power during a wide range of movements was known a priori, such a closed-loop system that modulates stimulation frequency to track dynamic beta oscillatory activity may facilitate a wide range of individual patient motor behaviors.

The proposed closed-loop stimulation algorithm was simulated using a validated CTx-BG-Th model (Kumaravelu et al., 2016). There are several other potential models of the network effects of DBS, which might be used for development and evaluation of closed-loop controllers. Hahn and McIntyre developed a network model of the effects of DBS in the STN of the parkinsonian non-human primate, and demonstrated that effective DBS suppressed burst activity in the GPi (Hahn and McIntyre, 2010). Subsequently, Holt and Netoff implemented a mean field version of this model and analyzed the effects of different frequencies of DBS (Holt and Netoff, 2014). Similarly, Santaniello et al. (2015) implemented a network model of the effects of STN DBS in the parkinsonian non-human primate and demonstrated the importance of both antidromic and orthodromic activation. We selected the Kumaravelu et al. network model because it replicated a wide range of electrophysiological data from the unilateral 6-OHDA lesioned rat model of PD (Kumaravelu et al., 2016) thereby facilitating subsequent *in vivo* evaluation of the controller.

The proposed CL DBS controller was successful at regulating the beta oscillatory activity of spike times of model GPi neurons to track different beta reference values. The stimulation frequency was automatically calculated by the PI controller, and

PI parameters were calculated using stability analysis of the system rather than trial-and-error adjustment (Gorzelic et al., 2013). However, there were several potential limitations of the proposed CL DBS method. The identified linear CAR model described only 80% of the relationship between the stimulation frequency and the beta power. Therefore, although the PI controller was robust to changes in the reference beta power, the dynamic changes in beta power could be tracked well only at frequencies of $\leq$1 Hz. When the target beta power changed faster than 1 Hz, the tracking error increased, likely as a result of the unmodeled dynamics. In subsequent trial-and-error tuning, it appeared that the best PI controller parameters were different for different beta power targets. Thus, adaptive controllers that modulate the PI controller parameters with the variation of target beta power may improve the tracking performance for dynamic reference signals. The CTx-BG-Th network was highly non-linear, and performance might also be improved using a non-linear controller. The beta oscillatory power was selected as the biomarker in this study, however, other biomarkers such as the spike time entropy (Dorval et al., 2008) and phase amplitude coupling (de Hemptinne et al., 2015) are also correlated with parkinsonian symptoms, and might be suitable feedback control signals. The application of other biomarkers or multiple biomarkers in the design of closed-loop stimulation for PD is worth exploring (Hoang et al., 2017). The controller regulated the stimulation frequency, but the effects of DBS are also dependent on the pulse amplitude, pulse duration, and stimulation pattern (Kuncel and Grill, 2004; Grill, 2018). Further, Holt et al. demonstrated that the effects of burst DBS in a network model of the basal ganglia (Hahn and McIntyre, 2010) were strongly dependent on timing relative to the phase of oscillatory activity (Holt et al., 2016).

We demonstrated successful tracking of different dynamic beta power reference signals, and the simulated dynamic targets could represent different movements of PD patients. Thus, an important challenge to implement the proposed CL DBS approach experimentally or clinically is to determine the relationship between reference beta oscillation power and the movement. In addition to real-time electrophysiological recording, movement sensors might also be useful to establish the dynamic reference signal.

CONCLUSION

CL DBS was proposed to reduce energy consumption and alleviate side effects compared to continuous fixed-parameter DBS. This requires design of a suitable closed-loop system that can account for dynamic changes in the feedback signal that occur during voluntary movement. We used the beta oscillatory power of GPi model neuron spike times as a biomarker of model state, and used a PI controller to calculate the DBS frequency according to dynamic variations in the beta power. This closed-loop adjustment of stimulation frequency approach was tested in a computational model of the CTx-BG-Th network and was able to track constant as well as dynamic beta oscillatory activity.

DATA AVAILABILITY

The raw data supporting the conclusions of this manuscript will be made available by the authors, without undue reservation, to any qualified researcher.

AUTHOR CONTRIBUTIONS

All authors listed have made a substantial, direct and intellectual contribution to the work, and approved it for publication.

FUNDING

This work was supported by the US National Institutes of Health under Grant R37 NS040894 and Grant UH3 NS103468 and by the National Natural Science Foundation of China under Grant 61801273 and Grant 61701336.

REFERENCES

Arlotti, M., Marceglia, S., Foffani, G., Volkmann, J., Lozano, A. M., Moro, E., et al. (2018). Eight-hours adaptive deep brain stimulation in patients with Parkinson disease. *Neurology* 90, e971–e6. doi: 10.1212/WNL.0000000000005121

Arlotti, M., Rosa, M., Marceglia, S., Barbieri, S., and Priori, A. (2016a). The adaptive deep brain stimulation challenge. *Parkinson. Relat. Disord.* 28, 12–17. doi: 10.1016/j.parkreldis.2016.03.020

Arlotti, M., Rossi, L., Rosa, M., Marceglia, S., and Priori, A. (2016b). An external portable device for adaptive deep brain stimulation (aDBS) clinical research in advanced Parkinson's disease. *Med. Eng. Phys.* 38, 498–505. doi: 10.1016/j.medengphy.2016.02.007

Aström, K. J., and Hägglund, T. (1995). *PID Controllers: Theory Design and Tuning, 2nd Edn*. Research Triangle Park, NC: Instrument Society of America.

Birdno, M. J., and Grill, W. M. (2008). Mechanisms of deep brain stimulation in movement disorders as revealed by changes in stimulus frequency. *Neurotherapeutics* 5, 14–25. doi: 10.1016/j.nurt.2007.10.067

Brittain, J. S., and Brown, P. (2014). Oscillations and the basal ganglia: motor control and beyond. *Neuroimage* 85, 637–647. doi: 10.1016/j.neuroimage.2013.05.084

Brocker, D. T., Swan, B. D., Turner, D. A., Gross, R. E., Tatter, S. B., Miller Koop, M. M., et al. (2013). Improved efficacy of temporally non-regular deep brain stimulation in Parkinson's disease. *Exp. Neurol.* 239, 60–67. doi: 10.1016/j.expneurol.2012.09.008

Carron, R., Chaillet, A., Filipchuk, A., Pasillas-Lépine, W., and Hammond, C. (2013). Closing the loop of deep brain stimulation. *Front. Syst. Neurosci.* 7:112. doi: 10.3389/fnsys.2013.00112

Cyron, D. (2016). Mental side effects of deep brain stimulation (DBS) for movement disorders: the futility of denial. *Front. Integr. Neurosci.* 10:17. doi: 10.3389/fnint.2016.00017

Davie, C. A. (2008). A review of Parkinson's disease. *Br. Med. Bull.* 86, 109–127. doi: 10.1093/bmb/ldn013

de Hemptinne, C., Swann, N. C., Ostrem, J. L., Ryapolova-Webb, E. S., San Luciano, M., Galifianakis, N. B., et al. (2015). Therapeutic deep brain stimulation reduces cortical phase-amplitude coupling in Parkinson's disease. *Nat. Neurosci.* 18, 779–786. doi: 10.1038/nn.3997

Deuschl, G., Herzog, J., Kleiner-Fisman, G., Kubu, C., Lozano, A. M., Lyons, K. E., et al. (2006). Deep brain stimulation: postoperative issues. *Mov. Disord.* 21, S219–S237. doi: 10.1002/mds.20957

Dorval, A. D., Russo, G. S., Hashimoto, T., Xu, W., Grill, W. M., and Vitek, J. L. (2008). Deep brain stimulation reduces neuronal entropy in the MPTP-primate model of Parkinson's disease. *J. Neurophysiol.* 100, 2807–2818. doi: 10.1152/jn.90763.2008

Goldberg, J. A., Rokni, U., Boraud, T., Vaadia, E., Bergman, H. (2004). Spike synchronization in the cortex/basal-ganglia networks of Parkinsonian primates reflects global dynamics of the local field potentials. *J. Neurosci.* 24, 6003–6010. doi: 10.1523/JNEUROSCI.4848-03.2004

Gopal, M. (2002). *Control Systems: Principles and Design, 2nd Edn.* New Delhi: Tata McGraw-Hill Education.

Gorzelic, P., Schiff, S. J., and Sinha, A. (2013). Model-based rational feedback controller design for closed-loop deep brain stimulation of Parkinson's disease. *J. Neural Eng.* 10:26016. doi: 10.1088/1741-2560/10/2/026016

Grant, P. F., and Lowery, M. M. (2013). Simulation of cortico-basal ganglia oscillations and their suppression by closed loop deep brain stimulation. *IEEE Trans. Neural Syst. Rehabil. Eng.* 21, 584–594. doi: 10.1109/TNSRE.2012.2202403

Grill, W. M. (2018). Temporal pattern of electrical stimulation is a new dimension of therapeutic innovation. *Curr. Opinion. Biomed. Eng.* 8, 1–6. doi: 10.1016/j.cobme.2018.08.007

Hahn, P. J., and McIntyre, C. C. (2010). Modeling shifts in the rate and pattern of subthalamopallidal network activity during deep brain stimulation. *J. Comput. Neurosci.* 28, 425–441. doi: 10.1007/s10827-010-0225-8

Hebb, A. O., Zhang, J. J., Mahoor, M. H., Tsiokos, C., Matlack, C., Chizeck, H. J., et al. (2014). Creating the feedback loop: closed-loop neurostimulation. *Neurosurg. Clin. N. Am.* 25, 187–204. doi: 10.1016/j.nec.2013.08.006

Hoang, K. B., Cassar, I. R., Grill, W. M., and Turner, D. A. (2017). Biomarkers and stimulation algorithms for adaptive brain stimulation. *Front. Neurosci.* 11:564. doi: 10.3389/fnins.2017.00564

Holt, A. B., and Netoff, T. I. (2014). Origins and suppression of oscillations in a computational model of Parkinson's disease. *J. Comput. Neurosci.* 37, 505–521. doi: 10.1007/s10827-014-0523-7

Holt, A. B., Wilson, D., Shinn, M., Moehlis, J., and Netoff, T. I. (2016). Phasic burst stimulation: a closed-loop approach to tuning deep brain stimulation parameters for Parkinson's disease. *PLoS Comput. Biol.* 12:e1005011. doi: 10.1371/journal.pcbi.1005011

Jankovic, J. (2008). Parkinson's disease: clinical features and diagnosis. *J. Neurol. Neurosurg. Psychiatry* 79, 368–376. doi: 10.1136/jnnp.2007.131045

Jenkinson, N., and Brown, P. (2011). New insights into the relationship between dopamine, beta oscillations and motor function. *Trends Neurosci.* 34, 611–618. doi: 10.1016/j.tins.2011.09.003

Johnson, L. A., Nebeck, S. D., Muralidharan, A., Johnson, M. D., Baker, K. B., and Vitek, J. L. (2016). Closed-loop deep brain stimulation effects on Parkinsonian motor symptoms in a non-human primate-is beta enough? *Brain Stimul.* 9, 892–896. doi: 10.1016/j.brs.2016.06.051

Kita, H., and Kita, T. (2011). Cortical stimulation evokes abnormal responses in the dopamine-depleted rat basal ganglia. *J. Neurosci.* 31, 10311–10322. doi: 10.1523/JNEUROSCI.0915-11.2011

Krack, P., Batir, A., Van Blercom, N., Chabardes, S., Fraix, V., Ardouin, C., et al. (2003). Five-year follow-up of bilateral stimulation of the subthalamic nucleus in advanced Parkinson's disease. *N. Engl. J. Med.* 349, 1925–1934. doi: 10.1056/NEJMoa035275

Kühn, A. A., Trottenberg, T., Kivi, A., Kupsch, A., Schneider, G. H., and Brown, P. (2005). The relationship between local field potential and neuronal discharge in the subthalamic nucleus of patients with Parkinson's disease. *Exp. Neurol.* 194, 212–220. doi: 10.1016/j.expneurol.2005.02.010

Kumaravelu, K., Brocker, D. T., and Grill, W. M. (2016). A biophysical model of the cortex-basal ganglia-thalamus network in the 6-OHDA lesioned rat model of Parkinson's disease. *J. Comput. Neurosci.* 40, 207–229. doi: 10.1007/s10827-016-0593-9

Kuncel, A. M., and Grill, W. M. (2004). Selection of stimulus parameters for deep brain stimulation. *Clin. Neurophysiol.* 115, 2431–2441. doi: 10.1016/j.clinph.2004.05.031

Leventhal, D. K., Gage, G. J., Schmidt, R., Pettibone, J. R., Case, A. C., and Berke, J. D. (2012). Basal ganglia beta oscillations accompany cue utilization. *Neuron* 73, 523–536. doi: 10.1016/j.neuron.2011.11.032

Levy, R., Ashby, P., Hutchison, W. D., Lang, A. E., Lozano, A. M., and Dostrovsky, J. O. (2002). Dependence of subthalamic nucleus oscillations on movement and dopamine in Parkinson's disease. *Brain* 125, 1196–1209. doi: 10.1093/brain/awf128

Little, S., and Brown, P. (2012). What brain signals are suitable for feedback control of deep brain stimulation in Parkinson's disease? *Ann. N. Y. Acad. Sci.* 1265, 9–24. doi: 10.1111/j.1749-6632.2012.06650.x

Little, S., Pogosyan, A., Neal, S., Zavala, B., Zrinzo, L., Hariz, M., et al. (2013). Adaptive deep brain stimulation in advanced Parkinson disease. *Ann. Neurol.* 74, 449–457. doi: 10.1002/ana.23951

Ljung, L. (1999). *System Identification Theory for User, 2nd Edn.* Englewood Cliffs, NJ: Prentice Hall.

Mallet, N., Pogosyan, A., Márton, L. F., Bolam, J. P., Brown, P., and Magill, P. J. (2008). Parkinsonian beta oscillations in the external globus pallidus and their relationship with subthalamic nucleus activity. *J. Neurosci.* 28, 14245–14258. doi: 10.1523/JNEUROSCI.4199-08.2008

Massano, J., and Garrett, C. (2012). Deep brain stimulation and cognitive decline in Parkinson's disease: a clinical review. *Front. Neurol.* 3:66. doi: 10.3389/fneur.2012.00066

McConnell, G. C., So, R. Q., Hilliard, J. D., Lopomo, P., and Grill, W. M. (2012). Effective deep brain stimulation suppresses low-frequency network oscillations in the basal ganglia by regularizing neural firing patterns. *J. Neurosci.* 32, 15657–15668. doi: 10.1523/JNEUROSCI.2824-12.2012

McQuarrie, A. D. R., and Chih-Ling, T. (1998). *Regression and Time Series Model Selection.* Hackensack, NJ: World Scientific. doi: 10.1142/3573

Odekerken, V. J., Boel, J. A., Schmand, B. A., de Haan, R. J., Figee, M., van den Munckhof, P., et al. (2016). GPi vs. STN deep brain stimulation for Parkinson disease: three-year follow-up. *Neurology* 86, 755–761. doi: 10.1212/WNL.0000000000002401

Okun, M. S., and Foote, K. D. (2010). Parkinson's disease DBS: what, when, who and why? The time has come to tailor DBS targets. *Expert. Rev. Neurother.* 10, 1847–1857. doi: 10.1586/ern.10.156

Parastarfeizabadi, M., and Kouzani, A. Z. (2017). Advances in closed-loop deep brain stimulation devices. *J. Neuroeng. Rehabil.* 14:79. doi: 10.1186/s12984-017-0295-1

Piña-Fuentes, D., Little, S., Oterdoom, M., Oterdoom, M., Neal, S., Pogosyan, A., et al. (2017). Adaptive DBS in a Parkinson's patient with chronically implanted DBS: a proof of principle. *Mov. Disord.* 32, 1253–1254. doi: 10.1002/mds.26959

Rodriguez-Oroz, M. C., Obeso, J. A., Lang, A. E., Houeto, J. L., Pollak, P., and Rehncrona, S. (2005). Bilateral deep brain stimulation in Parkinson's disease: a multicentre study with 4 years follow-up. *Brain* 128, 2240–2249. doi: 10.1093/brain/awh571

Rosa, M., Arlotti, M., Ardolino, G., Cogiamanian, F., Marceglia, S., Di Fonzo, A., et al. (2015). Adaptive deep brain stimulation in a freely moving parkinsonian patient. *Mov. Disord.* 30, 1003–1005. doi: 10.1002/mds.26241

Rosin, B., Slovik, M., Mitelman, R., Rivlin-Etzion, M., Haber, S. N., Israel, Z., et al. (2011). Closed-loop deep brain stimulation is superior in ameliorating Parkinsonism. *Neuron* 72, 370–384. doi: 10.1016/j.neuron.2011.08.023

Rossi, P. J., Gunduz, A., Judy, J., Wilson, L., Machado, A., and Giordano, J. J. (2016). Proceedings of the third annual deep brain stimulation think tank: a review of emerging issues and technologies. *Front. Neurosci.* 10:119. doi: 10.3389/fnins.2016.00119

Sanes, J. N., and Donoghue, J. P. (1993). Oscillations in local field potentials of the primate motor cortex during voluntary movement. *Proc. Natl. Acad. Sci. U.S.A.* 90, 4470–4474. doi: 10.1073/pnas.90.10.4470

Santaniello, S., Fiengo, G., Glielmo, L., and Grill, W. M. (2011). Closed-loop control of deep brain stimulation: a simulation study. *IEEE Trans. Neural Syst. Rehabil. Eng.* 19, 15–24. doi: 10.1109/TNSRE.2010.2081377

Santaniello, S., McCarthy, M. M., Montgomery, E. B. Jr., Gale, J. T., Kopell, N., and Sarma, S. V. (2015). Therapeutic mechanisms of high-frequency stimulation in Parkinson's disease and neural restoration via loop-based reinforcement. *Proc. Natl. Acad. Sci. U.S.A.* 112, E586–595. doi: 10.1073/pnas.1406549111

So, R. Q., McConnell, G. C., August, A. T., and Grill, W. M. (2012). Characterizing effects of subthalamic nucleus deep brain stimulation on methamphetamine-induced circling behavior in hemi-Parkinsonian rats. *IEEE Trans. Neural Syst. Rehabil. Eng.* 20, 626–635. doi: 10.1109/TNSRE.2012.2197761

Stein, E., and Bar-Gad, I. (2013). β oscillations in the cortico-basal ganglia loop during parkinsonism. *Exp. Neurol.* 245, 52–59. doi: 10.1016/j.expneurol.2012.07.023

Zaepffel, M., Trachel, R., Kilavik, B. E., and Brochier, T. (2013). Modulations of EEG beta power during planning and execution of grasping movements. *PLoS ONE* 8:e60060. doi: 10.1371/journal.pone.0060060

Zaidel, A., Spivak, A., Grieb, B., Bergman, H., and Israel, Z. (2010). Subthalamic span of oscillations predicts deep brain stimulation efficacy for patients with Parkinson's disease. *Brain* 133, 2007–2021. doi: 10.1093/brain/awq144

Conflict of Interest Statement: The authors declare that the research was conducted in the absence of any commercial or financial relationships that could be construed as a potential conflict of interest.

frontiers in Neuroscience

ORIGINAL RESEARCH
published: 29 October 2019
doi: 10.3389/fnins.2019.01152

The μDBS: Multiresolution, Directional Deep Brain Stimulation for Improved Targeting of Small Diameter Fibers

*Daria Nesterovich Anderson[1,2,3], Connor Anderson[1], Nikhita Lanka[4], Rohit Sharma[4], Christopher R. Butson[1,2,3,5,6], Brian W. Baker[7] and Alan D. Dorval[1]**

[1] Department of Biomedical Engineering, College of Engineering, University of Utah, Salt Lake City, UT, United States, [2] Department of Neurosurgery, School of Medicine, University of Utah, Salt Lake City, UT, United States, [3] Scientific Computing and Imaging (SCI) Institute, University of Utah, Salt Lake City, UT, United States, [4] Department of Electrical and Computer Engineering, University of Utah, Salt Lake City, UT, United States, [5] Department of Neurology, School of Medicine, University of Utah, Salt Lake City, UT, United States, [6] Department of Psychiatry, School of Medicine, University of Utah, Salt Lake City, UT, United States, [7] Utah Nanofab, University of Utah, Salt Lake City, UT, United States

OPEN ACCESS

Edited by:
Sabato Santaniello,
University of Connecticut,
United States

Reviewed by:
Till Anselm Dembek,
University of Cologne, Germany
Peadar Grant,
Dundalk Institute of Technology,
Ireland
Faiçal Isbaine,
Emory University Hospital,
United States

***Correspondence:**
Alan D. Dorval
chuck.dorval@utah.edu

Specialty section:
This article was submitted to Neuroprosthetics, a section of the journal Frontiers in Neuroscience

Received: 23 August 2019
Accepted: 11 October 2019
Published: 29 October 2019

Citation:
Anderson DN, Anderson C, Lanka N, Sharma R, Butson CR, Baker BW and Dorval AD (2019) The μDBS: Multiresolution, Directional Deep Brain Stimulation for Improved Targeting of Small Diameter Fibers. Front. Neurosci. 13:1152. doi: 10.3389/fnins.2019.01152

Directional deep brain stimulation (DBS) leads have recently been approved and used in patients, and growing evidence suggests that directional contacts can increase the therapeutic window by redirecting stimulation to the target region while avoiding side-effect-inducing regions. We outline the design, fabrication, and testing of a novel directional DBS lead, the μDBS, which utilizes microscale contacts to increase the spatial resolution of stimulation steering and improve the selectivity in targeting small diameter fibers. We outline the steps of fabrication of the μDBS, from an integrated circuit design to post-processing and validation testing. We tested the onboard digital circuitry for programming fidelity, characterized impedance for a variety of electrode sizes, and demonstrated functionality in a saline bath. In a computational experiment, we determined that reduced electrode sizes focus the stimulation effect on small, nearby fibers. Smaller electrode sizes allow for a relative decrease in small-diameter axon thresholds compared to thresholds of large-diameter fibers, demonstrating a focusing of the stimulation effect within small, and possibly therapeutic, fibers. This principle of selectivity could be useful in further widening the window of therapy. The μDBS offers a unique, multiresolution design in which any combination of microscale contacts can be used together to function as electrodes of various shapes and sizes. Multiscale electrodes could be useful in selective neural targeting for established neurological targets and in exploring novel treatment targets for new neurological indications.

Keywords: deep brain stimulation, directional electrodes, electrode fabrication, computational modeling, neural targeting

INTRODUCTION

Deep brain stimulation (DBS) is a widely accepted therapy for several movement disorders and an emerging therapy for psychiatric disorders and additional movement disorders. From its first FDA approval for essential tremor in 1997, the physical design of DBS leads has remained largely unchanged (Eisinger et al., 2019). A cylindrical shaft with four cylindrical electrode contacts

defines the classic lead design. In this manuscript, we present a novel neurostimulation device that assembles multiresolution electrodes from microscale contacts to enable fine control of the stimulation volume and an improved capability to target small-diameter fibers.

In recent years, the FDA has approved more lead designs from major neuromodulation companies, however, these leads differ minimally from the classic quadripolar lead design. Moderate advances to the classic lead design involve contacts capable of directionally focusing stimulation, typically by having two of the four contacts subdivided into three smaller contacts each. These smaller, directional contacts allow for directional steering of the activation field to, ideally, activate the target structure while avoiding side-effect-inducing regions that might reduce the window of therapy.

Directional stimulation has already been clinically demonstrated to widen the therapeutic window by steering stimulation away from regions that may be responsible for inducing side effects (Steigerwald et al., 2016; Dembek et al., 2017). Other experimental lead designs have further subdivided contacts to allow for finer directional control and have shown promising results at widening the therapeutic window (Contarino et al., 2014; Pollo et al., 2014). However, the fundamental limitation in repeatedly subdividing contacts is enclosing enough wires for each contact within the lead shaft without increasing the width of the lead. With the technology available today, the ability to increase the number of stimulation electrodes will remain limited without further advances in lead technology.

We propose a novel directional DBS device, the μDBS, with hundreds of individually controllable contacts capable of stimulation and recording. Using onboard circuitry, the lead can stimulate using any combination of contacts at 7 independent voltage states with only 12 input wires. Multiresolution electrode sizes and complex monopolar and bipolar configurations are achievable by grouping contacts according to the desired stimulation bus lines. Such flexibility enables electrodes to scale in size from the ∼6.0 mm^2 of the classic clinical electrode down to the ∼0.02 mm^2 of a single μDBS contact. Here, we outline the design steps, fabrication, and bench testing of this novel, multi-resolution DBS device.

We aim to create a DBS device with the capability of stimulating through variously sized electrodes composed of contacts that are orders of magnitude smaller than those currently available in the clinic. In many instances, the side-effect-inducing regions comprise larger fibers than those most associated with therapeutic benefit (Lang et al., 1999; Chaturvedi et al., 2010). In this paper, we expand upon our recent computational work that smaller electrodes more efficiently activate small diameter fibers over large diameter fibers (Anderson et al., 2019). Smaller contacts may also widen the therapeutic window by preferentially activating smaller, therapeutic fibers over larger, side effect-inducing fibers. The present work supports that multiresolution stimulation devices can substantially improve neuromodulation efficiency and selectivity, and demonstrates the practicality of building one such device, the μDBS, as part of the next generation of neuromodulation therapy.

MATERIALS AND METHODS

We designed a novel DBS lead, the μDBS, as a microelectrode array appropriate for deep brain stimulation. This new lead has a similar scale to those used clinically, but comprises 864 microscale contacts instead of 4 large contacts. This design expands upon our first iteration of the μDBS (Willsie and Dorval, 2015b) with an improved fabrication process, slightly larger stimulation contacts, and increased stimulation flexibility via the incorporation of seven (cf. three) stimulation bus lines. The novel lead is fabricated using silicon wafer-based technology, and its on-board digital circuitry allows for full control to open or close any combination of the 864 contacts using only 12 input wires. The small contact size on the μDBS—0.0225 mm^2 compared to the 6 mm^2 for the clinical electrode (Lanotte et al., 2002)—allows for the μDBS to have 864 total contacts and still match the overall size of clinically available leads, having a width of 1.27 mm (**Figure 1A**). A complete lead is assembled from four silicon chips consisting of 216 contacts each: two pairs of flat chips are assembled front-to-back, and the two pairs are slid past each other to form a plus-shaped cross section (**Figure 1B**). Through our redesign of DBS lead technology, the μDBS is the first DBS lead of similar size to the clinical leads capable of stimulating through multiresolution electrodes made up of hundreds of microscale contacts.

Design and Fabrication

In order to achieve hundreds of individually controllable contacts, the μDBS must have on-board digital circuitry, unlike modern DBS leads that have a single wire to power each conductive contact. Each μDBS contact is programmable to eight possible states using three-bit digital logic ($2^3 = 8$). Seven of the eight states tie the contact to bus lines that can be used to stimulate or record, and the last state is reserved as an unconnected, floating state. Each bus line active state is independent from the others, which allows for flexibility in stimulation, frequency, pulse width, and waveform shape for each electrode used on the lead. Having these multiple independent sources allows for greater spatial and temporal flexibility in stimulation shaping since electrodes could take on various shapes, be used in complex multipolar and bipolar configurations, and deliver unique stimulation waveforms.

Programming the device requires transmitting a serial program of three-bit "words," where each word determines the bus line to which the contact will be tied. Each contact stores three bits of information across a shift register (serial cascade of three flip flops) and advances each bit during the falling phase of a clock signal until all contacts have been programmed to the intended state (**Figure 2A**). We tested whether contact states could be theoretically programmed using three-bit digital logic through the simulation of a single contact circuit prior to fabrication by X-FAB (**Figure 2B**). Given the presence of onboard circuitry and the serial nature of the circuit design, all contacts are controllable

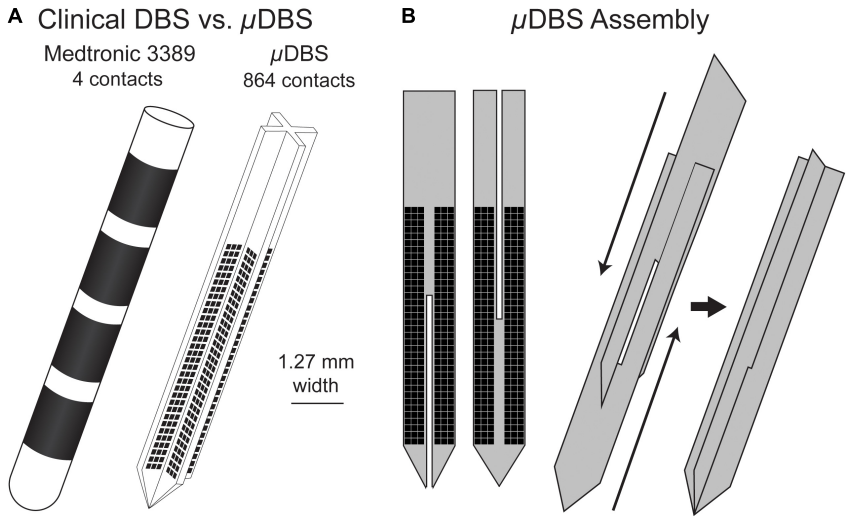

FIGURE 1 | (A) Clinical deep brain stimulation electrode (left) with four contacts, and the μDBS (right) with hundreds of contacts. **(B)** The μDBS electrode is assembled from four total flat chips, with two flat chips paired back to back. The paired chips are assembled together to form a "+" shape when viewed from above.

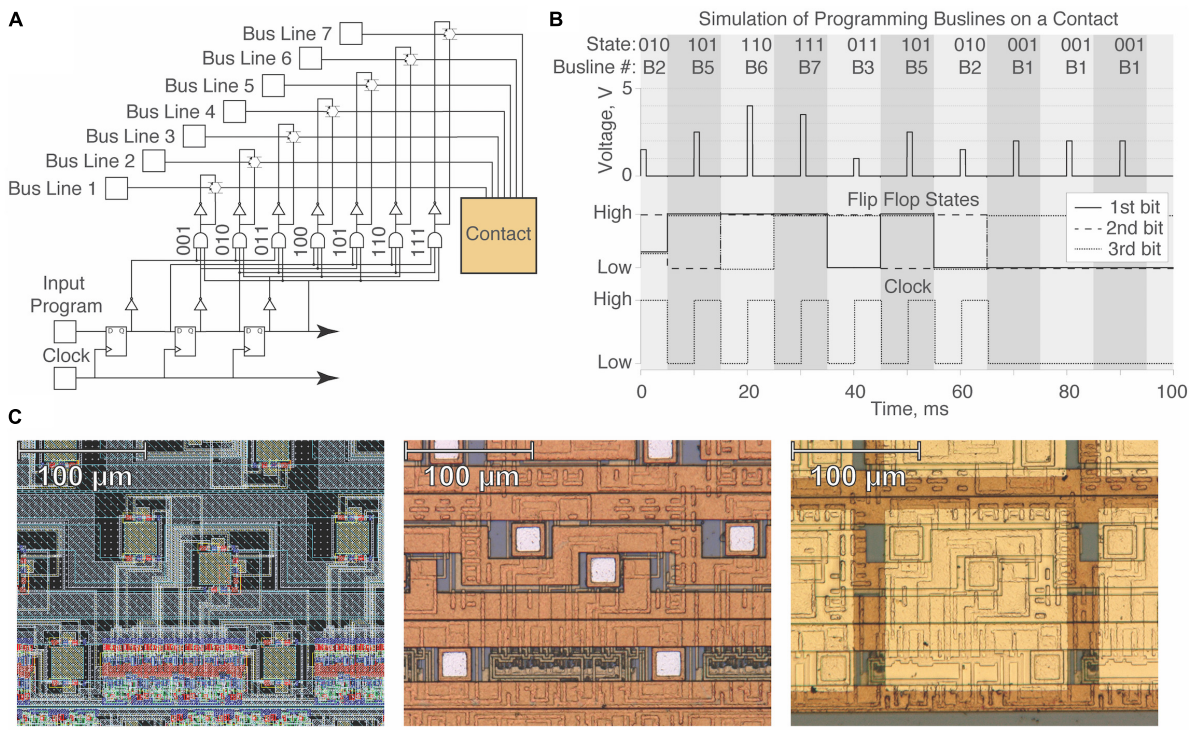

FIGURE 2 | Design and simulation of a single contact unit on the μDBS. **(A)** Single contact circuit diagram with three-bit digital logic for the gating of seven bus lines. **(B)** Simulation demonstrating programming of different bus lines on a single contact in Cadence ADE XL. With the example bit stream, 011101000, we demonstrate programming the flip flop states at the falling phase of the clock signal. **(C)** Integrated circuit layout design of a single contact used in the simulation (left), post-fabrication view of the VLSI design (middle), and view of contact after gold application in post-processing (right). Note that for any moment in time, at most 1 of the 7 bus lines can be connected to a contact (large, bright gold square at right) through one of its three subcontact conduits (small, dull white squares shown in the middle panel).

with a minimal number of wires using five inputs (input program, clock, power, ground, power switch) and up to seven different bus line inputs.

A layout design was made in Cadence Virtuoso using the XC06 (0.6 μm) technology package from X-FAB foundry (X-FAB, Erfurt, Germany). Circuitry for a single contact unit can be found

in the left panel of **Figure 2C**, and the VLSI design was validated using the Cadence ADE XL package. Images of the single contact post-fabrication and post-processing can be found in **Figure 2C**, in the middle and right panels, respectively. Circuitry associated with one contact resides within a 165 μm × 165 μm patch, enabling a total contact size of 150 μm × 150 μm with 15 μm spacing between contacts. The primary fabrication of the design was performed by X-FAB, and post-processing fabrication work was performed in the Utah Nanofab Cleanroom at the University of Utah.

The foundry-fabricated chips include three small subcontact pads per contact unit that underwent further processing to be linked into a single contact (see **Figure 2C**). Additionally, the unprocessed contact pads used Al contacts (0.5% Cu) which are not biocompatible. Chips from the foundry were sputtered with a titanium adhesion layer (∼30 nm), followed by ∼270 nm of gold, which is non-toxic and non-reactive to tissue (Merrill et al., 2005). Afterward, the chips underwent photolithography and patterning of negative photoresist (AZ nLoF 2020) in the shape of the desired contact size, at 150 μm × 150 μm (**Figure 3**). We exposed the patterned chips to a gold etch (8% I_2, 21% KI, 71% DI) and a titanium etch (20:1:1 DI:HF:H_2O_2) to clear the titanium/gold layer from non-contact areas. Afterward, we diced the test structures placed during fabrication along the edge of the chip to match the width of the clinical electrode sizing of 1.27 mm using a diamond blade saw 70 μm in width. Following the post-processing and cutting of the device, we mounted and wirebonded the chips using aluminum wire onto a custom-printed PCB to enable μDBS programming through a computer. An interface piece of silicon with gold traces was used to facilitate wirebonding from the μDBS chip to the PCB.

The design and fabrication steps discussed in this section outline novel technology necessary to build DBS leads capable of multiresolution electrode sizes for unprecedented stimulation flexibility. The onboard circuitry and three-bit programming logic enables each contact to be individually controllable, and full functionality of the device can be achieved through only twelve wires. In the following section, we demonstrate functionality of the μDBS design through a series of programming, impedance, and stimulation bench tests.

Validation

We assessed our ability to program the μDBS through a series of bench tests. In the scope of this section, we examined the functionality of the μDBS by fabricating and testing single flat chips that have 216 contacts each. The first instance of testing determined the accuracy of programming an intended contact configuration (**Figure 4A**). We measured the success rate of programming each contact state during the falling phase of the clock cycle. A numerically randomized series of 648 binary numbers (i.e., ones and zeros) was generated to program three bits on each of the 216 contacts using an Arduino programming setup, repeated five times per chip at six different clock speeds. Programming errors were quantified on a total of ten chips by comparing the fidelity of the bit program after it had passed through the chip to the series of bits that were programmed into the chip. The Arduino setup — essentially serving as the analog to an implanted pulse generator — was used to simultaneously power the device, generate the randomized programming file used to set contact states, and verify programming fidelity of the μDBS.

Additionally, we measured changes in impedances in a saline bath based on the number of contacts recruited. Increasing the number of contacts recruited to a single bus line increases the surface area of the effective electrode. The total electrode impedance was expected to vary with approximate inverse proportionality to the electrode surface area. To test proper contact recruitment, we prepared a saline solution (0.1 w/v% NaCl)—with approximately the conductivity of brain tissue (0.2 S/m)—to simulate the expected impedance of the electrode when exposed to a biological environment. Impedances were measured on a commercial electrochemical test system (Gamry Instruments PC4 Potentiostat, Warminster, PA, United States) across a Ag/AgCl reference electrode, a Pt wire counter electrode, and active contacts of the μDBS as the working electrode (**Figure 4B**). Impedances were quantified over a frequency range of 10 Hz to 10 kHz with a sinusoidal input voltage of 10 mV. The number of active contacts constituting the active μDBS electrode varied from 1 to 108, and each configuration was repeated three times for each of three chips.

Finally, we experimentally measured the stimulation field produced by the μDBS for two electrode configurations using a Ag/AgCl voltage probe manipulated by a computer numerical control (CNC) machine in a saline bath that matched the conductance of neural tissue (**Figure 4C**). The CNC machine moved the probe at a 0.5 mm resolution in a 20 mm × 10 mm grid in front of the μDBS chip in the saline solution, and voltage profiles were recorded by a separate recording Arduino setup linked to the CNC machine. The purpose of this experiment was to verify that stimulation can be done with simultaneous bus lines at different settings. The chip was functionally split in two, with 48 contacts on one half of the chip tied to bus line A and another 48 contacts on the other half tied to bus line B. For one condition, bus line A was 1.5 V and bus line B was 3.0 V with 100 μs, charge-balanced pulses; for a second condition, the bus lines were swapped. Stimulation profiles were collected for one chip in three trials for both conditions to evaluate whether the measured fields generated by the contacts were consistent with their bus line assignments.

Computational Model

To support the need for a multiresolution device with contacts as small as 150 μm × 150 μm, we simulated computational axon models to assess the influence of varying electrode sizes on neuronal activity. Each vertical column on the μDBS comprises 36 contacts. We ran bioelectric field solutions in SCIRun 4.7 (Scientific Computing and Imaging (SCI), Institute, University of Utah, Salt Lake City, UT, United States) for 1–36 adjacent contacts within a column set to −1 V each with the surrounding box set to 0 V. These configurations resulted in electrode sizes from 150 μm × 150 μm to 150 μm × 6 mm. We implemented a high-resolution submesh with 0.1 mm spacing around the electrode, as we have described previously (Anderson et al., 2018b, 2019), and we set tissue conductivity

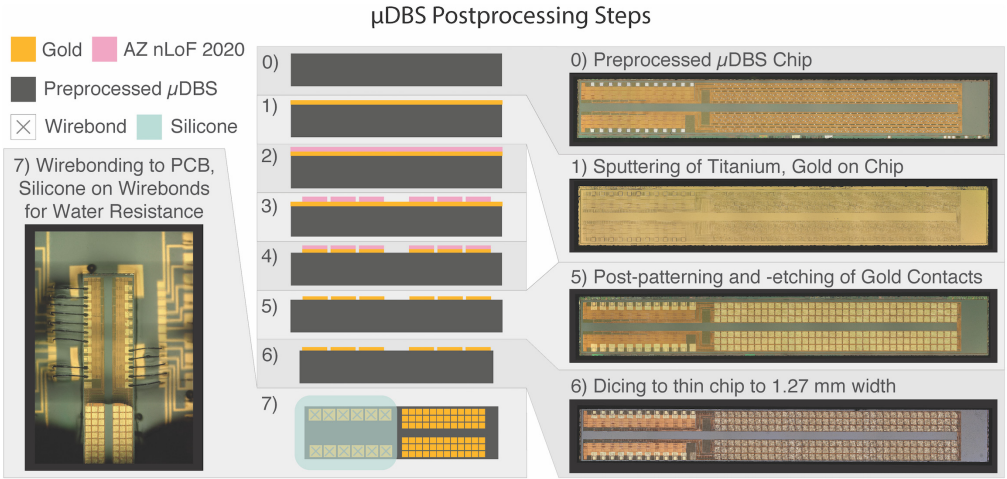

FIGURE 3 | Design architecture for μDBS post-processing. Fabricated chips (0) undergo gold deposition (1) and are covered with AZ nLoF 2020 negative photoresist (2). Photoresist is exposed to UV light according to the desired contact layout through a photolithography mask and regions of photoresist not exposed to light are removed (3). Gold and titanium layers are etched away from regions not covered by photoresist to define the gold contacts (4). Remaining photoresist is washed off (5) and the chips are diced to the appropriate size (6). Connection pads are wirebonded to test PCBs (7) to enable device programming and functionality testing. Silicone was used to insulate non-contact regions from water exposure during the validation experiments.

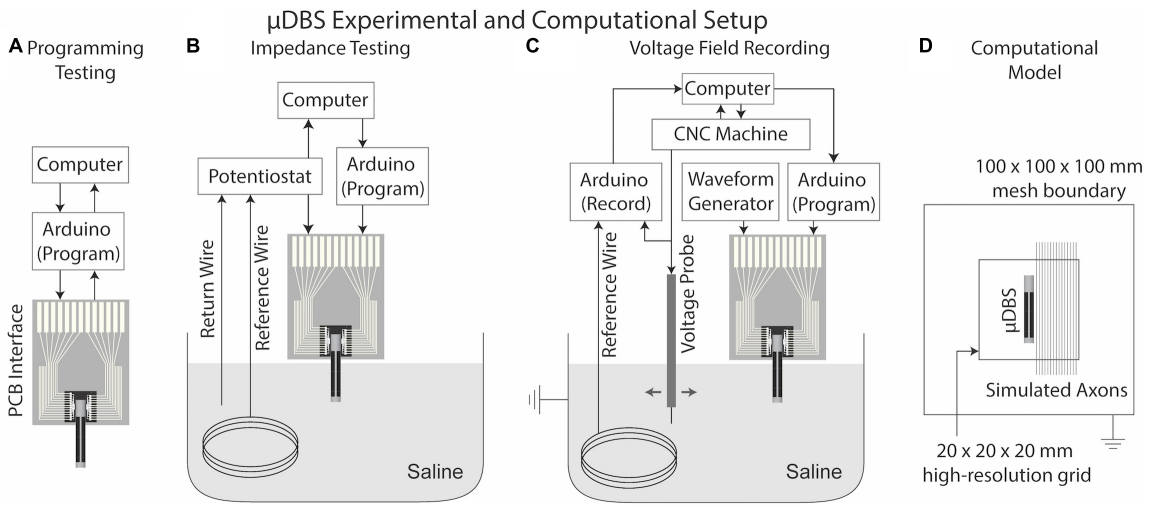

FIGURE 4 | μDBS experimental and computational setup. **(A)** Experimental setup for programming requires only input/output information from the μDBS chip interfaced with the Arduino and computer. **(B)** Impedance testing requires a potentiostat connected to one bus line of the μDBS, a Pt counter wire, and an Ag/AgCl reference wire in a saline bath. **(C)** Bath testing uses a CNC machine to move a voltage probe in the saline bath around the μDBS. Voltage recordings run through a peak detection circuit and on to the Arduino for recording. **(D)** A lead-in-the-box model was used to simulate the voltage spread; multicompartment models were used to measure the effects of contact size on activation for 2.0, 5.7, and 10.0 μm diameter axons.

to 0.2 S/m (**Figure 4D**). Non-contact regions of the μDBS were modeled as ideal insulators, and the contacts were modeled as ideal conductors. Axons of various diameters — 2.0, 5.7, and 10.0 μm — were placed parallel to the lead in 0.1 mm increments, from 0.1 to 10 mm away. The vertical axonal orientation was chosen to match that of the active electrode on the μDBS, to explore the effects of electrode size on neuron activation patterns. Simulations were run in NEURON 7.4 using the MRG neuron model (McIntyre et al., 2002), on which modeled extracellular potentials were mapped directly onto node, paranode, and internode segments. Thresholds were identified for a 90 μs charge-balanced pulse at ∼0.01 V resolution to quantify the role of electrode size on neural selectivity as a function of fiber diameter.

RESULTS

We conducted bench testing to evaluate the functionality of the fabricated and post-processed μDBS chips. We determined

whether chips met our design specifications, as well as whether contacts could be programmed and recruited into larger electrodes through programming testing and testing in a saline bath.

Design Verification

A series of sixteen chips were slated for post-processing and subsequent testing. Of those, six were irrevocably damaged, primarily at the wirebonding post-processing step. **Table 1** summarizes the design specifications and results retrieved for the ten surviving chips. Final chip widths were ∼1.29 mm, and well within 5% tolerance of 1.27 mm design specification used to match the clinical lead. Most devices (7/10) met our form-factor and bus line acceptance criteria. In the other devices (3/10), wirebonding failed to connect all seven bus lines; but note that these chips could still be used with somewhat reduced flexibility through their 4–6 functioning bus lines. We attempted gold contact patterning on eight of the ten chips, and they all met acceptance criteria. On average, the gold contact widths and heights measured slightly smaller than designed, possibly because of chemical undercutting from the gold and titanium etch during photolithography. To accommodate this undercut in future iterations, we will simply enlarge the contacts in the photolithography mask. In summary, gold contact patterning was universally successful, and the majority of chips met all acceptance criteria; for chips that did not meet acceptance criteria, wirebonding was the most common failure point.

Programming Testing

We tested ten μDBS chips for programming fidelity (**Figure 5**): chips must be programmed properly in order to stimulate properly. We randomized a series of (216 contacts × 3 bits/contact =) 648 bits for each programming trial, to give a diverse range of maximally disordered configurations. The minimal programming duration for a single chip was limited to ∼2.7 s by the maximal clock rate of the Arduino device we used for programming. Since a complete μDBS lead comprises four flat chips, programming an entire lead with this device would take ∼10.8 s in total. Programming times of 2.7–14.3 s at six different clock speeds were tested five times each, for a total of thirty programming sessions per chip. Some chips exhibited no mutation errors in any session, and there was no significant relationship between programming time and error rate (**Figure 5C**, p = 0.97, ANOVA). Thus, chips could likely be programmed in much less than 2.7 s, given appropriately high-clock rate controllers.

Figure 5A reports that three chips (#'s 8–10) did not have any errors regardless of settings, and four others (#'s 4–7) had relatively rare and/or constrained errors. In one of its thirty trials, chip #7 encountered a single deletion error, where one missed bit initiated a cascade effect resulting in many improperly set contacts in that one trial. However, most of the errors were programming mutations, where one bit was toggled inappropriately. Because individual contacts are so small and operate in parallel with the other contacts composing a shared electrode, lone mutation errors would not substantially impact functionality. Across all randomized trials, >95% of errors arose from a mutation toggling one bit from a low to a high state, which indicates possible crosstalk between programming connections. Contact errors are summarized in heat maps on each chip in panel **Figure 5B**. Most errors on any given chip recurred at similar locations — denoted with yellow-to-red coloring — which may indicate circuit damage that could have occurred during handling.

Electrode Testing

The programming tests verified that each contact received an appropriate bus line command, but verifying that the contacts successfully link to the intended bus line requires electrical testing of the electrodes. For electrical testing, we submerged μDBS chips in a saline bath and programmed them. In separate experiments, we measured the effective impedance of electrodes built from various numbers of contacts, and assessed the spatial voltage profile generated by two separate electrodes driven by two separate bus lines on the same chip.

TABLE 1 | Design verification to determine whether devices met design specifications.

	Design Specification	Median	Mean ± Standard Error	Distribution	Acceptance Criteria	Criteria Achieved
Chip width	1.27	1.2935	1.2928 ± 0.001861	1.275 1.285 1.295 1.305	(±5%)	10/10
Number of buslines	7	7	6.3 ± 0.37	0 1 2 3 4 5 6 7	(7/7)	7/10
Number of contacts	216	215	213.5 ± 1.55	200 204 208 212 216	200/216	8/8
Contact width, μm	150	142.5	141.75 ± 1.19	135 140 145 150	(±10%)	8/8
Contact height, μm	150	140.5	141.375 ± 1.28	135 140 145 150	(±10%)	8/8
I/O Contact width, μm	165	158	157.5 ± 1.9	150 155 160 165	(±10%)	8/8
I/O Contact height, μm	200	196.5	196.875 ± 1.3	190 195 200 205	(±10%)	8/8

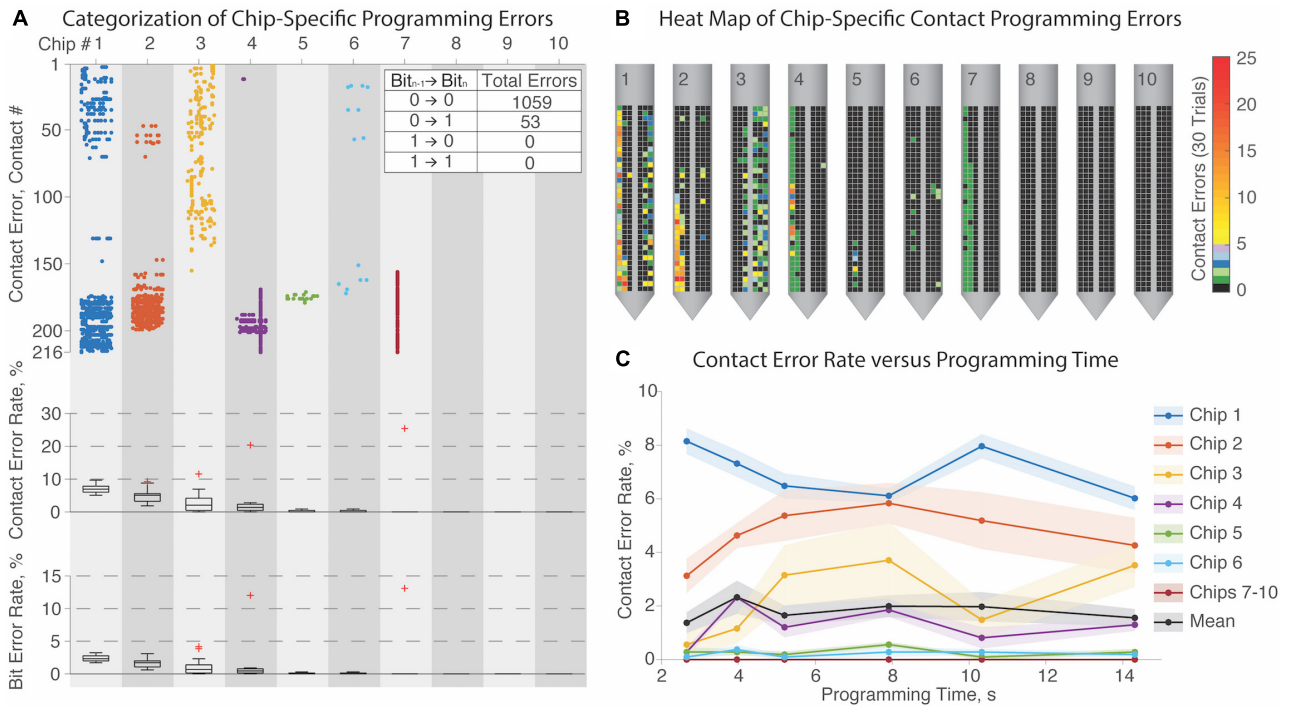

FIGURE 5 | Programming validation of μDBS chips. **(A)** Characterization of contact errors for 10 μDBS chips across 30 trials each, with incorrectly programmed contacts denoted as a dot (top), and as percentage distribution intervals (95/75/50/25/5) of contact errors (middle) and bit errors (bottom). Programming errors are largely chip-specific, with 3 chips (#'s 8–10) not displaying any programming errors. **(B)** Heatmaps of programming contact errors for each chip demonstrate that errors cluster on similar regions for each chip. **(C)** There was no significant trend that programming time affected programming error rate, indicating that chip-specific programming errors are independent of the clock rate.

Three chips were submerged into saline solution and connected to a computer for programming and a potentiostat for impedance testing according to **Figure 4B**. Impedances were recorded on each chip for electrodes programmed to range from 1 to 108 contacts, for a range of frequencies. Each recording was repeated three times, and the resulting impedance magnitude and phase spectra are shown in **Figure 6A**. Consistent with studies of other electrodes, impedances were higher at lower frequencies due to capacitance at the electrode-tissue interface.

As expected, impedance was inversely proportional to the electrode surface area — i.e., the number of active contacts— supporting that the contacts were properly programmed and linked to the appropriate bus line. **Figure 6B** summarizes impedance values at 1 kHz, the frequency most commonly used to report impedances of clinical DBS devices. At 1 kHz, a single contact has an impedance of ∼180 kΩ, yielding an effective electrode impedance of ∼180 kΩ divided by the number of constitutive contacts. Thus, an electrode comprising 90 contacts has a surface area of ∼2.0 mm^2 and an impedance of ∼2.0 kΩ, matching (to within a few percent) the corresponding parameters of clinically approved directional electrodes (Butson et al., 2006; Rebelo et al., 2018).

Finally, the field-testing experiment from **Figure 4C** was performed on one chip to validate stimulation fields generated from two simultaneously active bus lines (**Figure 6C**). Two groups of 48 contacts on each half of the chip were tied to one of the two bus lines. In the two conditions tested, either bus line A was greater than bus line B, or vice versa. The voltage probe, traveling in a 20 mm × 10 mm grid in front of the stimulation electrodes, recorded a shift in the peak voltage based on which side of the μDBS lead was tied to the larger amplitude bus line ($p < 0.00001$, two-sample t-test). Although our experimental configuration did not allow for a comprehensive mapping of the voltage field, these results demonstrate that the distinct electrodes on opposite sides of a μDBS chip are capable of properly stimulating with separate voltage signals.

Computational Experiment

Our final experiment demonstrates a possible advantage to a multiresolution device like the μDBS. We modeled individual axons in NEURON responding to voltage fields generated via μDBS electrodes as simulated in SCIRun. Initial electrodes were modeled as 9 vertically stacked contacts, or a 1.47 mm electrode height, to approximate the extent of standard cylindrical DBS electrodes. Modeling axons of three diameters—2.0, 5.7, and 10.0 μm—running parallel to the electrode, we positioned each fiber to its threshold distance at which a −1 V stimulation elicited an action potential. We then varied the number of active contacts within the electrode from 1 to 36, and determined the threshold voltage at which each axon fired (**Figure 7**).

The distance from the electrode surface at which larger axons can be activated is greater than the activation distance for

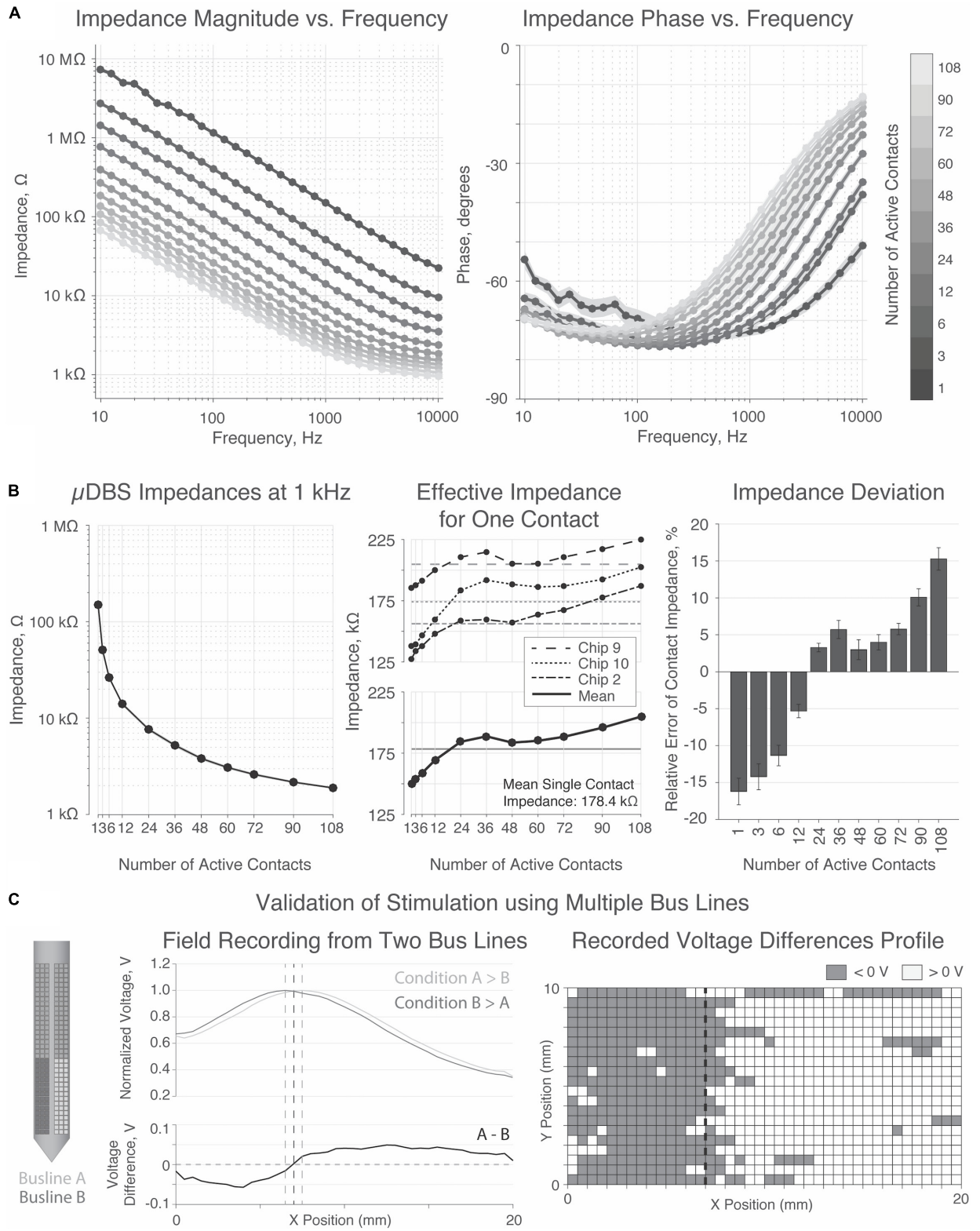

FIGURE 6 | Impedance and bath testing validation. **(A)** Magnitude and phase of impedance for 1 through 108 contacts activated. Impedance decreased at higher frequencies. **(B)** Impedance was inversely proportional to surface area. Average impedance for a single contact was 178.4 kΩ, with a trend toward increasing with the number of active contacts. **(C)** Bath testing demonstrates a directional shift in the normalized voltage field depending on the relative amplitudes of the electrode voltages.

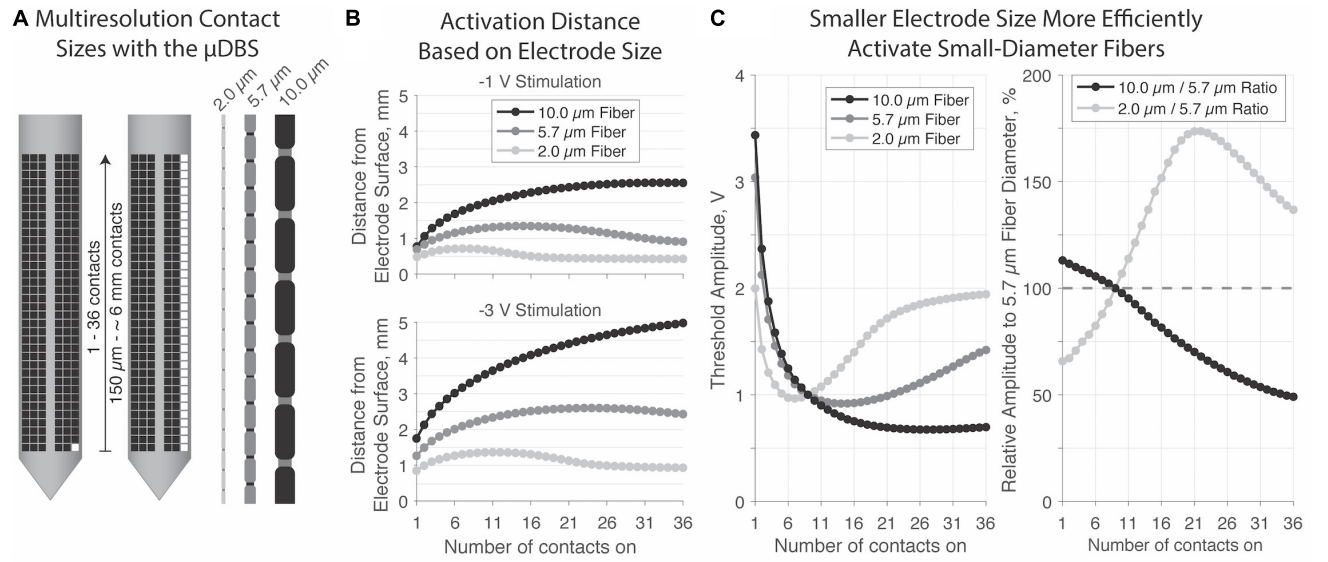

FIGURE 7 | (A) Multicompartment axon models were run with diameters of 2.0, 5,7, and 10.0 µm in response to stimulation from 1 to 36 contacts on the µDBS. **(B)** Maximum activation distance (mm) for each fiber size based on electrode size at –1 V (top) and –3 V (bottom). Large-diameter fibers can be activated at greater distances away from the electrode. For smaller diameter fibers, larger electrode sizes reduce activation spread. **(C)** Firing threshold was normalized to –1 V amplitude at 9 contacts on, which is approximately the height of classic DBS contact of 1.5 mm. A multi-resolution device may be useful to target different diameter fibers; as shown in the right panel, smaller contacts activate small diameter fibers at 65.75% efficiency over 5.7 µm fibers, and require about 113.1% additional voltage to activate the same 10.0 µm fibers. Larger contact sizes preferentially activate large diameter fibers, with about 50% lower thresholds relative to 5.7 µm fibers.

smaller axons for all electrode sizes. Initially, as the electrode size increases, activation spread increases, however, for smaller diameter fibers the extent of activation reduces as electrode size continues to increase, especially with 2.0 µm fibers. When considering relative activation across different fiber sizes, smaller electrodes preferentially excited smaller axons. In the extreme case of a single-contact electrode (i.e., 150 µm), 2.0 µm fibers were activated at 66 and 58% of the 5.7 and 10.0 µm fiber thresholds, respectively (**Figure 7C**, right). Conversely, larger electrodes preferentially excited larger axons. In the extreme case of a 36-contact electrode (i.e., ∼6 mm), 10.0 µm fibers were activated at 50 and 36% of the 5.7 and 2.0 µm fiber thresholds, respectively. Thus, the ability to use smaller electrodes may open the therapeutic window by increasing the activation of small, nearby, and likely therapeutic fibers, while decreasing the activation of large, distant, and likely side-effect inducing ones.

DISCUSSION

This manuscript discusses fabrication and testing of the µDBS device, a novel DBS lead with hundreds of individually controllable contacts. We proposed a novel approach to DBS lead design and assembly using silicon-based wafer technology that incorporates onboard circuitry capable of recruiting electrodes in essentially innumerable shapes, sizes, and configurations. A complete µDBS device is composed of four silicon chips, each with 216 contacts, assembled in a plus-shaped configuration (**Figure 1B**). The manuscript reports on validation tests on flat chips, of which four are needed for the full µDBS device. However, additional work is required to package the complete device and ensure its longevity in tissue and future tests must be conducted to quantify tissue damage during lead insertion to evaluate safety of this novel lead geometry. Assembly of the full µDBS device was not done in this manuscript, but we have previously shown mechanical stability in the 3D configuration (Willsie and Dorval, 2015b). For the chips tested, silicone was used to encase wirebonds and traces exposed on the PCB in the saline bath, but better packaging is necessary for chronic animal studies. In this manuscript, we have demonstrated feasibility of a novel DBS device design and have highlighted the benefits of leads that can stimulate through multiresolution electrodes.

The inclusion of onboard circuitry enables full control of the hundreds of contacts on the µDBS with a minimal numbers of input wires. Clinically approved devices (Medtronic, Boston Scientific, and Abbott Laboratories) require a separate wire for each contact that must fit in the lead shaft and pass under the skin to a pulse generator in the chest; such a design limits the manufacturing feasibility of increasing the number of contacts on a device. Other silicon-based neural probes, such as those created by NeuroNexus, do not use onboard circuitry and would be similarly limited in the total number of wires capable of being connected to a lead. The incorporation of onboard circuitry, however, adds possible failure modes to the lead design, as demonstrated in our programming testing, in which not all of the ten chips tested could be reliably programmed, with damage to the onboard circuitry being the likely culprit. The programming experiment in **Figure 5** demonstrates that errors, which could arise and incorrectly assign contacts to bus lines, are device dependent and cluster together on the chips, however, some

chips did not display any programming errors regardless of programming time. Specifically, we found that the transition from 0 bit to 0 bit states was the most common mutation error (95%) during randomized bit programming. It may be possible in the future to reduce these programming errors by reducing the noise in the onboard circuitry with improvements in the integrated circuit design. Finally, inclusion of onboard circuitry increases the energy demands of the lead, and in the current iteration, the μDBS must be powered during programming and stimulation. It may be possible, however, to improve circuit efficiency and explore strategies to reduce energy usage by powering the device only during stimulation pulses and not during the interpulse period.

The impedances reported for individual contacts were around 180 kΩ on average for three chips, but single contact impedances varied on a chip-by-chip basis, which may be the result of slight variations in the post-processing of chips shown in **Figure 3**. FDA safety standards of charge density would need to be followed during stimulation parameter selection, especially for small electrodes sizes. For small electrodes, resulting volumes of tissue activated would be small since very little charge could be injected into the tissue while staying within safety limits. Alternative processing techniques in future work could decrease the impedance of individual contacts to facilitate stimulation of tissue. These techniques could include the deposition of other metals, such as iridium oxide, with an increased effective contact surface area through its coral-like structure (Negi et al., 2010), or platinum iridium, as used in clinically approved devices. As shown in **Table 1**, our gold contact sizes were slightly smaller than originally intended, contributing to the higher impedance values, however, compensating for underetching by using larger contact masks in future iterations will decrease the contact impedances.

The novel design of the μDBS does not merely enable smaller electrode contacts, but also offers the ability to combine individual contacts into larger electrodes, even larger than what is clinically available. The total surface area of a stimulation electrode depends on how many contacts are tied to the same bus line, which is demonstrated in **Figures 4A,B**. Contacts grouped together function as larger electrodes and can mimic the size of clinical contacts, having similar impedances to those recorded in the clinic. The differing impedance levels recorded based on surface area demonstrates that contacts can be recruited appropriately for larger electrodes. Multiresolution stimulation contact sizing affords the μDBS an unprecedented level of flexibility, which could be useful in both research and clinical applications. Multiresolution electrodes can be especially beneficial in the customization of volumes of tissue activated based on patient-specific brain imaging and neural targets. Finally, flexibility in electrode sizes could be useful as more neurological disorders, especially psychiatric disorders with fiber tracts as targets, are being investigated for DBS therapy. Given that it would be impossible to manually choose optimal contact configurations for such a device, we have previously published an optimization algorithm that can identify optimal contact amplitudes and configurations in near real-time based on patient-specific imaging and neural structures (Anderson et al., 2018b).

The large number of electrode configurations and the seven possible voltages states through the seven bus lines on the μDBS allow for highly precise activation field shaping. We tested field shaping through recorded voltage profiles in a saline bath with two groups of contacts tied to one of two active bus lines, with one bus line set to twice the amplitude of the other. When the bus lines were swapped, there was a notable shift in the voltage field, and this demonstrates how the μDBS is able to recruit contacts to separate bus lines simultaneously (**Figure 6C**). We have previously shown through computational modeling that the μDBS is capable of precise field steering given instances where lead placement error has resulted in suboptimal lead placement off from its target by a few millimeters (Willsie and Dorval, 2015a). Our directional steering work using the μDBS corroborates other studies for different directional lead designs which have shown that smaller, directional contacts are able to activate neural structures while avoiding side-effect-inducing regions (Contarino et al., 2014; Pollo et al., 2014; Steigerwald et al., 2016; Dembek et al., 2017). Additionally, we have found that the use of smaller contacts goes beyond improved field shaping capability: smaller electrodes increase the selectivity of smaller axons compared to larger axons (**Figure 7**). Mechanistically, we believe that this selectivity is due to the smaller internode spacing of small-diameter axons which can more readily detect the spatially fine changes in the voltage field cased by smaller sized contacts. An increased selectivity for smaller diameter fibers could be used to improve therapeutic DBS since smaller fibers are typically associated with clinical benefit whereas larger fibers are more associated with side effects (Lang et al., 1999; Chaturvedi et al., 2010). For the computational selectivity experiments in this manuscript, we limited our study to vertical neurons to match the orientation of the contacts on the μDBS we studied, but as we previously have shown, different neuron orientations can change the activation profiles (Anderson et al., 2018a).

CONCLUSION

The μDBS is a novel DBS device with hundreds of microscale contacts and seven independent voltage states capable of fine control of stimulation fields through multipolar and complex bipolar configurations. This device lays the groundwork for the technology required to increase lead complexity that will allow for more stimulation contacts without the addition of more wires, and may enable the field of DBS technology to move from the initial DBS design that has been used for decades toward directional leads with a much greater number of smaller contacts. This device is the first of its kind that features multiresolution electrodes, which can be used to morph stimulation fields to the often irregular size and shape of neural targets and can offer stimulation flexibility in novel applications of DBS where stimulation targets are still being explored. Finally, we present novel evidence that smaller, directional contacts may be even more advantageous for stimulation therapy than currently thought: not only is there greater field shaping flexibility with directional contacts, but smaller contacts also improve targeting of

smaller diameter fibers, which may lead to increases in the therapeutic window.

DATA AVAILABILITY STATEMENT

The datasets generated for this study are available on request to the corresponding author.

AUTHOR CONTRIBUTIONS

AD conceived of the device design and project concept. DA executed the VLSI design, post-processed the devices, tested the devices, analyzed the data, ran the computational model, and wrote the manuscript. NL assisted in the VLSI design of the device and post-processing of the devices. CA assisted in post-processing and testing of the devices and analysis of the data. RS developed the packaging procedure. CB provided instruction on computational modeling. BB provided training and troubleshooting of the post-processing steps of the device in the Utah Nanofab cleanroom.

FUNDING

This work was supported by the National Science Foundation (NSF) NSF CAREER Award (1351112), PI AD; and the NSF Graduate Research Fellowship (1256065) awarded to DA.

REFERENCES

Anderson, C. J., Anderson, D. N., Pulst, S. M., Butson, C. R., and Dorval, A. D. (2019). Neural selectivity, efficiency, and dose equivalence in deep brain stimulation through pulse width tuning and segmented electrodes. *bioRxiv* [preprint]. doi: 10.1101/613133

Anderson, D. N., Duffley, G., Vorwerk, J., Dorval, A. C., and Butson, C. R. (2018a). anodic stimulation misunderstood: preferential activation of fiber orientations with anodic waveforms in deep brain stimulation. *J. Neural Eng.* 16, 016026. doi: 10.1088/1741-2552/aae590

Anderson, D. N., Osting, B., Vorverk, J., Dorval, A. D., and Butson, C. R. (2018b). Optimized programming algorithm for cylindrical and directional deep brain stimulation electrodes. *J. Neural Eng.* 15:026005. doi: 10.1088/1741-2552/aaa14b

Butson, C. R., Maks, C. B., and McIntyre, C. C. (2006). Sources and effects of electrode impedance during deep brain stimulation. *Clin. Neurophysiol.* 117, 447–454. doi: 10.1016/j.clinph.2005.10.007

Chaturvedi, A., Butson, C. R., Lempka, S. F., Cooper, S. E., and McIntyre, C. C. (2010). Patient-specific models of deep brain stimulation: influence of field model complexity on neural activation predictions. *Brain Stimulat.* 3, 65–77. doi: 10.1016/j.brs.2010.01.003

Contarino, M. F., Bour, L. J., Verhagen, R., Lourens, M. A. J., de Bie, R. M. A., van den Munckhof, P., et al. (2014). Directional steering: a novel approach to deep brain stimulation. *Neurology* 83, 1163–1169. doi: 10.1212/WNL.0000000000000823

Dembek, T. A., Reker, P., Visser−Vandewalle, V., Wirths, J., Treuer, H., Klehr, M., et al. (2017). Directional DBS increases side−effect thresholds—A prospective, double−blind trial. *Mov. Disord.* 32, 1380–1388. doi: 10.1002/mds.27093

Eisinger, R. S., Cernera, S., Gittis, A., Gunduz, A., and Okun, M. S. (2019). A review of basal ganglia circuits and physiology: application to deep brain stimulation. *Parkinsonism Relat. Disord.* 59, 9–20. doi: 10.1016/j.parkreldis.2019.01.009

Lang, A. E., Lozano, A. M., Ashby, P., Kumar, R., and Kim, Y. J. (1999). Neurophysiological effects of stimulation through electrodes in the human subthalamic nucleus. *Brain* 122, 1919–1931. doi: 10.1093/brain/122.10.1919

Lanotte, M. M., Rizzone, M., Bergamasco, B., Faccani, G., Melcarne, A., and Lopiano, L. (2002). Deep brain stimulation of the subthalamic nucleus: anatomical, neurophysiological, and outcome correlations with the effects of stimulation. *J. Neurol. Neurosurg. Psychiatry* 72, 53–58. doi: 10.1136/jnnp.72.1.53

McIntyre, C. C., Richardson, A. G., and Grill, W. M. (2002). Modeling the excitability of mammalian nerve fibers: influence of afterpotentials on the recovery cycle. *J. Neurophysiol.* 87, 995–1006. doi: 10.1152/jn.00353.2001

Merrill, D. R., Bikson, M., and Jefferys, J. G. (2005). Electrical stimulation of excitable tissue: design of efficacious and safe protocols. *J. Neurosci. Methods* 141, 171–198. doi: 10.1016/j.jneumeth.2004.10.020

Negi, S., Bhandari, R., Rieth, L., and Solzbacher, F. (2010). In vitro comparison of sputtered iridium oxide and platinum-coated neural implantable microelectrode arrays. *Biomed. Mater.* 5:015007. doi: 10.1088/1748-6041/5/1/015007

Pollo, C., Kaelin-Lang, A., Oertel, M. F., Stieglitz, L., Taub, E., Fuhr, P., et al. (2014). Directional deep brain stimulation: an intraoperative double-blind pilot study. *Brain* 137(Pt 7), 2015–2026. doi: 10.1093/brain/awu102

Rebelo, P., Green, A., Aziz, T., Kent, A., Schafer, D., Venkatesan, L., et al. (2018). Thalamic directional deep brain stimulation for tremor: spend less, get more. *Brain Stimulat.* 11, 600–606. doi: 10.1016/j.brs.2017.12.015

Steigerwald, F., Müller, L., Johannes, S., Matthies, C., and Volkmann, J. (2016). Directional deep brain stimulation of the subthalamic nucleus: a pilot study using a novel neurostimulation device. *Mov. Disord.* 31, 1240–1243. doi: 10.1002/mds.26669

Willsie, A. C., and Dorval, A. D. (2015a). Computational field shaping for deep brain stimulation with thousands of contacts in a novel electrode geometry. *Neuromodulation* 18, 542–551. doi: 10.1111/ner.12330

Willsie, A. C., and Dorval, A. (2015b). Fabrication and initial testing of the μDBS: a novel Deep Brain Stimulation electrode with thousands of individually controllable contacts. *Biomed. Microdevices* 17:9961.

Conflict of Interest: CB has served as a consulting for NeuroPace, Advanced Bionics, Boston Scientific, Intelect Medical, Abbott (St. Jude Medical), and Functional Neuromodulation. CB is also a shareholder of Intelect Medical and is an inventor of several patents related to neuromodulation therapy.

The remaining authors declare that the research was conducted in the absence of any commercial or financial relationships that could be construed as a potential conflict of interest.

frontiers in Neuroscience

ORIGINAL RESEARCH
published: 31 January 2020
doi: 10.3389/fnins.2020.00041

Subcortical Intermittent Theta-Burst Stimulation (iTBS) Increases Theta-Power in Dorsolateral Prefrontal Cortex (DLPFC)

J. Nicole Bentley[1†], Zachary T. Irwin[1,2†], Sarah D. Black[1], Megan L. Roach[2], Ryan J. Vaden[2], Christopher L. Gonzalez[2], Anas U. Khan[3], Galal A. El-Sayed[1], Robert T. Knight[4,5], Barton L. Guthrie[1] and Harrison C. Walker[2]*

[1] Department of Neurosurgery, University of Alabama at Birmingham, Birmingham, AL, United States, [2] Department of Neurology, University of Alabama at Birmingham, Birmingham, AL, United States, [3] School of Medicine, University of Alabama at Birmingham, Birmingham, AL, United States, [4] Department of Psychology and Neuroscience, University of California, Berkeley, Berkeley, CA, United States, [5] Department of Neurology and Neurosurgery, University of California, San Francisco, San Francisco, CA, United States

OPEN ACCESS

Edited by:
George C. McConnell,
Stevens Institute of Technology,
United States

Reviewed by:
Gordon William Arbuthnott,
Okinawa Institute of Science and Technology Graduate University, Japan
Ulrich Egert,
University of Freiburg, Germany

***Correspondence:**
J. Nicole Bentley
nbentl@uab.edu

[†] These authors have contributed equally to this work

Specialty section:
This article was submitted to Neural Technology, a section of the journal Frontiers in Neuroscience

Received: 01 October 2019
Accepted: 13 January 2020
Published: 31 January 2020

Citation:
Bentley JN, Irwin ZT, Black SD, Roach ML, Vaden RJ, Gonzalez CL, Khan AU, El-Sayed GA, Knight RT, Guthrie BL and Walker HC (2020) Subcortical Intermittent Theta-Burst Stimulation (iTBS) Increases Theta-Power in Dorsolateral Prefrontal Cortex (DLPFC). Front. Neurosci. 14:41. doi: 10.3389/fnins.2020.00041

Introduction: Cognitive symptoms from Parkinson's disease cause severe disability and significantly limit quality of life. Little is known about mechanisms of cognitive impairment in PD, although aberrant oscillatory activity in basal ganglia-thalamo-prefrontal cortical circuits likely plays an important role. While continuous high-frequency deep brain stimulation (DBS) improves motor symptoms, it is generally ineffective for cognitive symptoms. Although we lack robust treatment options for these symptoms, recent studies with transcranial magnetic stimulation (TMS), applying intermittent theta-burst stimulation (iTBS) to dorsolateral prefrontal cortex (DLPFC), suggest beneficial effects for certain aspects of cognition, such as memory or inhibitory control. While TMS is non-invasive, its results are transient and require repeated application. Subcortical DBS targets have strong reciprocal connections with prefrontal cortex, such that iTBS through the permanently implanted lead might represent a more durable solution. Here we demonstrate safety and feasibility for delivering iTBS from the DBS electrode and explore changes in DLPFC electrophysiology.

Methods: We enrolled seven participants with medically refractory Parkinson's disease who underwent DBS surgery targeting either the subthalamic nucleus (STN) or globus pallidus interna (GPi). We temporarily placed an electrocorticography strip over DLPFC through the DBS burr hole. After placement of the DBS electrode into either GPi (n = 3) or STN (n = 4), awake subjects rested quietly during iTBS (three 50-Hz pulses delivered at 5 Hz for 2 s, followed by 8 s of rest). We contrasted power spectra in DLPFC local field potentials during iTBS versus at rest, as well as between iTBS and conventional high-frequency stimulation (HFS).

Results: Dominant frequencies in DLPFC at rest varied among subjects and along the subdural strip electrode, though they were generally localized in theta (3–8 Hz) and/or beta (10–30 Hz) ranges. Both iTBS and HFS were well-tolerated and imperceptible. iTBS increased theta-frequency activity more than HFS. Further, GPi stimulation resulted in significantly greater theta-power versus STN stimulation in our sample.

Conclusion: Acute subcortical iTBS from the DBS electrode was safe and well-tolerated. This novel stimulation pattern delivered from the GPi may increase theta-frequency power in ipsilateral DLPFC. Future studies will confirm these changes in DLPFC activity during iTBS and evaluate whether they are associated with improvements in cognitive or behavioral symptoms from PD.

Keywords: deep brain stimulation, intermittent theta-burst stimulation, subthalamic nucleus, globus pallidus interna, Parkinson's disease, cognition

INTRODUCTION

Deep brain stimulation (DBS) is an established therapy for Parkinson's disease (PD) and other movement disorders (Deuschl et al., 2006; Starr et al., 2006; Baizabal-Carvallo et al., 2014). However, standard DBS is not generally considered effective for the cognitive impairments associated with PD (Cernera et al., 2019), which can be a source of overwhelming disability (Duncan et al., 2014). A small number of studies have suggested that novel DBS paradigms may address this issue in PD and other diseases. For example, theta-range (5–8 Hertz [Hz]) DBS appears to improve measures of inhibitory control and interval timing accuracy (Kelley et al., 2018; Scangos et al., 2018). DBS in other neural targets, such as the fornix, is also under investigation for the cognitive symptoms of Alzheimer's disease (Lozano et al., 2016, 2019). Support for the possibility of DBS affecting cortical cognitive networks is in part derived from studies showing DBS effects on primary motor areas. Clinically effective high-frequency DBS at subcortical targets for movement disorders [subthalamic nucleus (STN), globus pallidus interna (GPi)] results in beta-oscillation desynchronization and reduced phase-amplitude coupling (Asanuma et al., 2006; De Hemptinne et al., 2015). However, much less is known about possible interactions with prefrontal cortical areas using novel parameters. If these interactions occur, it would serve as a foundation for optimization of next-generation devices aimed at improving not only motor symptoms, but also cognitive effects of the disease as well.

Previous studies investigating the potential role of stimulation for cognition have primarily used theta-frequency pulses, which underlies many cognitive processes, especially in prefrontal cortex (Canolty et al., 2006; Cavanagh and Frank, 2014; Helfrich and Knight, 2016). Among the various prefrontal regions involved, the dorsolateral prefrontal cortex (DLPFC, Brodmann areas 9 and 46) is of special interest in PD as it is active during reward learning, set-shifting, action selection (Ridderinkhof et al., 2004), and inhibitory control (MacDonald et al., 2000; Harrison et al., 2005; Oldrati et al., 2016), which PD patients have particular difficulty with (Manza et al., 2017). The DLPFC has direct connections to the STN (Haynes and Haber, 2013) and GPi (Middleton and Strick, 2002), as well as widespread connections to the caudate nucleus and to the orbitofrontal, cingulate, pre-motor, and pre-supplementary motor cortices (Ridderinkhof et al., 2004). In PD patients, functional magnetic resonance imaging (fMRI) studies reveal reduced DLPFC activity during inhibitory control tasks, with increased activity after administration of anti-Parkinsonian medications correlating to improved inhibitory control task performance (Trujillo et al., 2019). Furthermore, EEG studies show that theta-frequency activity is decreased in PD patients performing these tasks (Singh et al., 2018).

It follows that increasing theta-power in impaired individuals may improve cognitive function. Recent studies from the transcranial non-invasive stimulation literature are providing some insight into how this might be achieved. For example, theta-frequency transcranial alternating-current stimulation (tACS) improved working memory in healthy older adults (Reinhart and Nguyen, 2019). An emerging therapy that shows promise for improving cognition that is now Food and Drug Administration (FDA) approved for depression (Blumberger et al., 2018) is intermittent theta-burst stimulation (iTBS), delivered via transcranial magnetic stimulation (TMS) to the prefrontal cortex (Hoy et al., 2016; Lowe et al., 2018). This form of therapy is thought to mimic natural brain activity, and in addition to enhancing memory in healthy adults (Hoy et al., 2016; Reinhart and Nguyen, 2019), it may also have effects on cognitive function in PD (Benninger et al., 2011; Dinkelbach et al., 2017; Trung et al., 2019). However, the effects of TMS are transient, requiring frequent re-application. Delivery of iTBS through a DBS lead implanted in subcortical sites which are already approved for therapy could represent a more durable solution. To this end, it is important to determine whether DBS at these sites can modulate DLPFC activity, whether through iTBS or standard high-frequency stimulation (HFS).

Here, we implant unilateral DBS electrodes into GPi or STN in PD patients, deliver both conventional high-frequency stimulation (>100 Hz) and iTBS, and record intracranial local field potentials (LFPs) from DLPFC with a subdural strip electrode. We report on the safety and feasibility of this approach and describe changes in theta and alpha/beta power in DLPFC between stimulation conditions, from both GPi and STN.

MATERIALS AND METHODS

Patient Selection

Participants were diagnosed with PD by a movement disorders neurologist and deemed candidates for DBS surgery after consensus review at a multi-disciplinary conference of neurologists, neurosurgeons, neuropsychologists, and nurse

practitioners. Stimulation target (STN or GPi) was chosen based on clinical features. All research procedures were approved by the University of Alabama at Birmingham Institutional Review Board with written informed consent.

Surgical Procedure

All participants underwent three Tesla MR imaging (Magnetom PRISMA, Siemens Healthcare GmbH, Erlangen, Germany) with the exception of Subject 4 who instead had high resolution CT imaging because of a contraindication to MRI (metal implant). DBS surgery was performed in the awake, off-medication state, at least 12 h following medication administration. A stereotactic headframe was placed (Cosman-Roberts-Wells, Integra LifeSciences, Plainsboro, NJ, United States), and an intraoperative 3D fluoroscopic image was obtained (O-arm 2, Medtronic, Minneapolis, MN, United States) and merged to pre-operative MRI. The prescribed target was identified according to standard techniques. To localize the DLPFC, we identified the mid-portion of the middle frontal gyrus along its longitudinal axis anterior to the pre-motor area (Trujillo et al., 2019), and designated this point as the midpoint for the subdural electrode. A radiopaque marker (18G needle) was placed at this point using the stereotactic headframe for localization.

After creating the burr hole and opening the outer dural layer but prior to DBS lead placement, we placed a 6-contact subdural strip electrode (Ad-tech Medical, Oak Creek, WI, United States) over the cortical surface, guided toward the scalp marker under X-ray fluoroscopic guidance. We then continued with the DBS procedure as routinely performed, beginning with microelectrode recordings. After defining the optimal location for the DBS, we performed 3D fluoroscopy to confirm our location. This image was merged intra-operatively to the pre-operative planning MRI to confirm subdural strip placement. We placed the DBS lead at its final position, then performed clinical testing for side effects and efficacy. Following this, the research paradigm began. After completion of the research testing (approximately 10–15 min), we removed the subdural strip electrode and proceeded with securing of the DBS lead and closure.

DLPFC Recordings

We recorded local field potentials from the subdural strip electrode over DLPFC with an actiCHamp active channel amplifier (BrainVision, Morrisville, NC, United States), sampling at 25 kHz with an analog 7.5 kHz low-pass filter and no further digital filters. We placed ground and reference EEG electrodes on the on the forehead and contralateral mastoid, respectively, and recorded muscle activity from the contralateral hand and forearm with bipolar EMG pad electrodes to screen for unwanted, incidental movements during recordings. Recordings were obtained with subjects awake, quiet, and at rest, first without stimulation, then with HFS and iTBS.

Subcortical Stimulation

Biphasic square waves were delivered through the DBS lead via an external pulse generator (STG4008, MultiChannel Systems, Reutlingen, Germany) following routine clinical macrostimulation, typically with a bipolar configuration of contacts 3 and 0, and amplitude and pulse width that conferred robust clinical benefit during behavioral testing with DBS at 160 Hz. To mark stimulus times, the STG4008 delivered a TTL pulse for each stimulus to the recording amplifier. During HFS, stimuli were delivered continuously at 125 Hz for 2 min (**Figure 1**, bottom). We delivered iTBS using standard parameters from the TMS literature (10 bursts of 3 stimulus pulses at 50 Hz, each burst separated by 200 ms [5 Hz], repeated over 2 s followed by an 8 s period of rest. This pattern was then repeated over 2 min (**Figure 1**, top). Pulse widths were based on the TMS literature for Subject 2 (300 μs) and were decreased to standard DBS pulse widths for all subsequent participants (60 μs). In one participant (Subject 4, bilateral hemispheres) we administered 4 Hz continuous stimulation for comparison to iTBS, in lieu of HFS (Kelley et al., 2018).

Post-operative Electrode Localization

We visualized DLPFC by first extracting a 3D model of the cortical surface from pre-operative MRI with FreeSurfer (Fischl, 2012). DLPFC was then identified as the combination of the rostral and caudal middle frontal regions, as labeled by FreeSurfer based on the Desikan-Killiany atlas. To localize the subdural strip electrodes, the intra-operative CT, pre-operative MRI, and 3D cortical model were imported into 3D Slicer (Fedorov et al., 2012). CT images were co-registered with the MRI and cortical model using an affine transform in the "General Registration (BRAINS)" module. Virtual fiducial markers then were manually placed in the center of the artifact of each strip contact. All contacts could be easily identified in each case and reconstructed, with the exception of Subject 4 who did not have an MRI available for reconstruction.

Signal Processing and Local Field Potential Analysis

All signal processing and statistical analyses were performed in MATLAB R2018b (MathWorks, Natick, MA, United States). Signals recorded from the subdural strip were downsampled to 400 Hz after applying a second order 1.5–75 Hz Butterworth filter. Individual channels (referenced to the contralateral mastoid) displaying high noise and/or overwhelming electrical artifacts were excluded from further analysis. The remaining channels were then re-referenced to a common average montage.

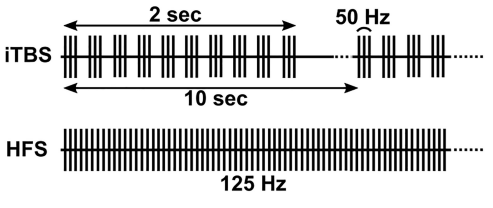

FIGURE 1 | Illustration of iTBS and HFS paradigms. iTBS consists of ten bursts of three pulses at 50 Hz (lasting 2 s), repeated at 10 s intervals. HFS consisted of a constant 125 Hz stimulation.

Power spectra were estimated as a global wavelet spectrum from each channel with and without stimulation, by averaging the continuous wavelet transform (CWT) across time during HFS and iTBS. For all analyses utilizing the CWT, the following parameters were used: complex morse wavelets, time-bandwidth product of 120, and 20 voices per octave.

To measure changes in spectral power during stimulation while allowing for inter-subject differences in frequency distributions and contact locations, ECoG contacts were first grouped into three general locations: anterior (contacts 1 and 2), middle (contacts 3 and 4), or posterior (contacts 5 and 6). The power spectra of the two component contacts in each group were then averaged together, and peaks in either the theta or alpha/beta frequency ranges were identified in the stimulation period using the "findpeaks" function in MATLAB. The width of the maximum peak was estimated as the point of half-prominence on either side, as determined by the same function. The mean power in this band was then computed by averaging the continuous wavelet transform across the band and across time. Finally, this mean power was converted to a *Z*-score by subtracting the mean of the same band during the corresponding no-stimulation baseline period and dividing by the standard deviation. Thus, we were able to quantify the impact of stimulation across subjects, DBS targets, and contact location groups.

RESULTS

Patient Demographics and Stimulation Parameters

Patient demographics and stimulation parameters are summarized in **Table 1**. Seven subjects underwent awake unilateral DBS surgery for Parkinson's disease, one of whom underwent contralateral DBS implantation in a subsequent surgery, for a total of eight DBS electrodes placed either in STN (n = 5) or GPi (n = 3). Resting DLPFC LFPs were recorded from all subjects (n = 8 hemispheres), and we delivered HFS from the DBS electrode in four participants (n = 4 hemispheres), 4-Hz continuous stimulation in 1 participant (n = 1 hemisphere) and iTBS in six participants (n = 7 hemispheres). Mean age at surgery was 69.4 years (S.D. 7.3, range 55–76 years). Mean duration of disease was 7.7 years (S.D. 3.7, range 5–15 years), with 71.4% (5/7) right-handed individuals and 1 ambidextrous subject. The right hemisphere was targeted in 62.5% of recordings. In all patients, a 6-contact subdural strip was placed over DLPFC without adverse effects. Stimulation was delivered as previously described, with HFS delivered at 125 Hz with bipolar contact pairs, at 60 μs pulse widths, and ranging from 2.0 to 6.0 milliamperes (mA), as summarized in **Table 1**. We delivered iTBS from the same bipolar contact pair, and at the same current and pulse width, that was used for HFS. In participant 2, in whom HFS was not applied, we applied the current at which clinical benefit was seen. The pulse width was the same as used in TMS studies of iTBS, though for subsequent participants we used a narrower pulse width to reduce charge density.

Resting Peak Frequencies in DLPFC Varies Across Subjects and Across Contacts

DLPFC power spectra at rest typically displayed prominent peaks in theta (3–8 Hz) (Subjects 1, 3, 4-left, 5, and 6; **Figure 2**) and/or alpha/beta range (10–30 Hz) (all subjects; **Figure 2**). Spectral power varied systematically across the subdural strip, with more prominent theta at the rostral and/or caudal extremes versus the middle contacts (e.g., subjects 1 and 3 in **Figure 2**). Alpha/beta peaks were more variably distributed across the strip, but tended to have highest power in the more caudal contacts, nearest pre-motor cortex (e.g., subjects 4-L, 4-R, and 7 in **Figure 2**). Theta and alpha/beta peaks appeared to arise from different contacts, although in two subjects the maximal peaks for these two frequency bands were in the same contacts.

iTBS From the GPi Modulates DLPFC Theta-Frequency LFP

When iTBS was delivered subcortically, temporally related changes were seen in the DLPFC (**Figure 3**). This finding was most pronounced in Subjects 2 and 3, with Subject 7 having little clear change. These increases in theta band power were delayed by approximately 30 s relative to the start of iTBS (**Figures 3A,B**). When the LFPs recorded during each set of 10 iTBS bursts within a subject were averaged together to create a mean event-related wavelet spectrogram, the increase in theta power was delayed by approximately 0.5 s and time-locked to the burst onset (**Figures 3A,B**, insets). Notably, we did not see significant activity evoked by single pulses at either target, and high-frequency stimulation did not elicit these changes (**Supplementary Figure S1**).

When comparing DLPFC changes by target, iTBS increased DLPFC theta-frequency activity to a greater extent during GPi (n = 3) versus STN (n = 4) stimulation when normalized versus rest (**Figure 4**, p = 0.0286 at the posterior contact group, Wilcoxon rank-sum test). This difference was most pronounced in the contacts over posterior DLPFC. Less pronounced changes in theta-power occurred in contacts over anterior and middle DLPFC, though theta-power still generally increased to a greater extent with GPi versus STN stimulation. Although a small effect, STN stimulation may have even decreased cortical theta power slightly in 1-2 subjects (**Figure 4D**). No clear differences in alpha/beta-power changes were observed between targets (**Figure 4**, p = 0.314 at the posterior contact group, Wilcoxon rank-sum test), though power decreased in several subjects and in several contact locations. Since only two GPi subjects underwent both HFS and iTBS, we did not similarly contrast LFPs during HFS between targets. However, in both cases, HFS increased DLPFC theta-frequency power less than did iTBS (**Supplementary Figure S2**).

DISCUSSION

New DBS technologies for movement disorders are developing at a rapid pace, with directional leads capable of current steering

TABLE 1 | Patient demographics and stimulation parameters.

Subject No.	Age at surgery* (yrs)	Disease Duration (yrs)	Target	Hemisphere	Stimulation type	Stimulation amplitude (mA)	Stimulation pulse width (us)
1	70–75	5	STN	Right	None		
2	70–75	6	GPi	Right	iTBS†	4.5	300
3	70–75	5	GPi	Left	iTBS, HFS‡	2.0	60
4§	75–80	9	STN	Left/Right	iTBS, 4-Hz	4.6/4.0	60
5	75–80	15	STN	Right	iTBS, HFS	5.0	60
6	55–60	5	STN	Left	iTBS, HFS	3.2	60
7	65–70	9	GPi	Right	iTBS, HFS	6.0	60

**Ages presented as ranges to avoid identifiable participant data. †iTBS frequency parameters: Three 50 Hz pulses at 5 Hz for 2 s, followed by 8 s of rest; repeated over 2 min. ‡HFS frequency parameters: Continuous 125 Hz. §Participant 4 initially had DBS implanted in the left STN and subsequently had the right STN implanted 2.5 months later. DLPFC recording and iTBS were performed in both surgeries. STN, subthalamic nucleus; GPi, Globus pallidus interna; iTBS, intermittent theta-burst stimulation; HFS, high-frequency stimulation; mA, milliamperes; μs, microseconds.*

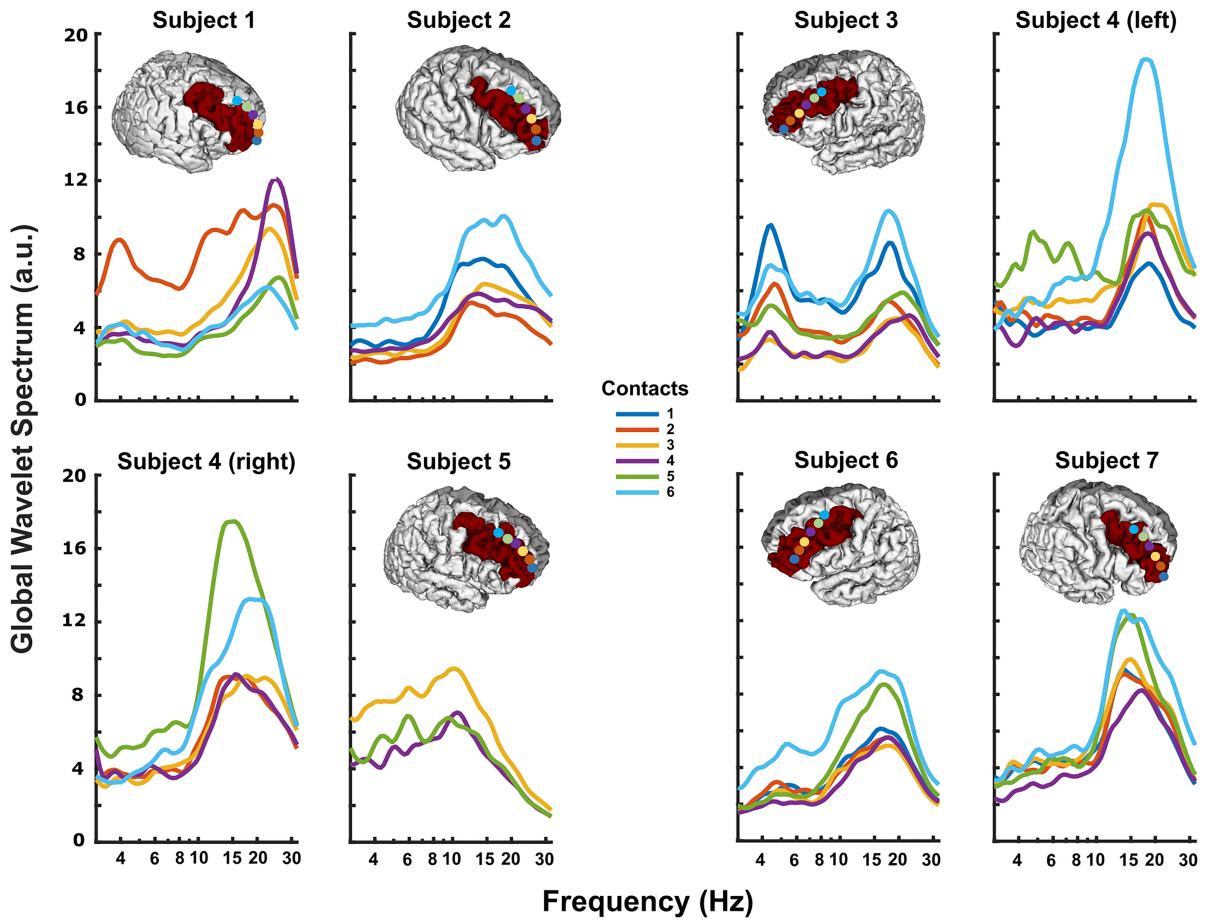

FIGURE 2 | Resting DLPFC local field potentials recorded from each subject. The 3D reconstruction of each subject's cortical surface (except Subject 4), with localized subdural strip contacts (circles colored according to contact number) and DLPFC region colored red. All subjects displayed prominent peaks in theta (3–8 Hz) and/or alpha/beta (10–30 Hz) ranges. In some subjects, particularly Subject 1, theta and alpha/beta activity had clearly different distributions along the strip, possibly indicating separate neural sources.

(Pollo et al., 2014; Dembek et al., 2017) and recording and sensing devices under investigation for closed-loop control (Rosin et al., 2011; Priori et al., 2013; Swann et al., 2018). Given this pace of device development, it may be possible that future iterations can incorporate multiple stimulation patterns addressing multiple symptoms of these diseases. In PD, non-motor cognitive symptoms are highly prevalent and disabling (Hely et al., 2008), with pronounced deficits in attention, memory, visuospatial processing, and response inhibition (Williams-Gray et al., 2009; Antonini et al., 2012;

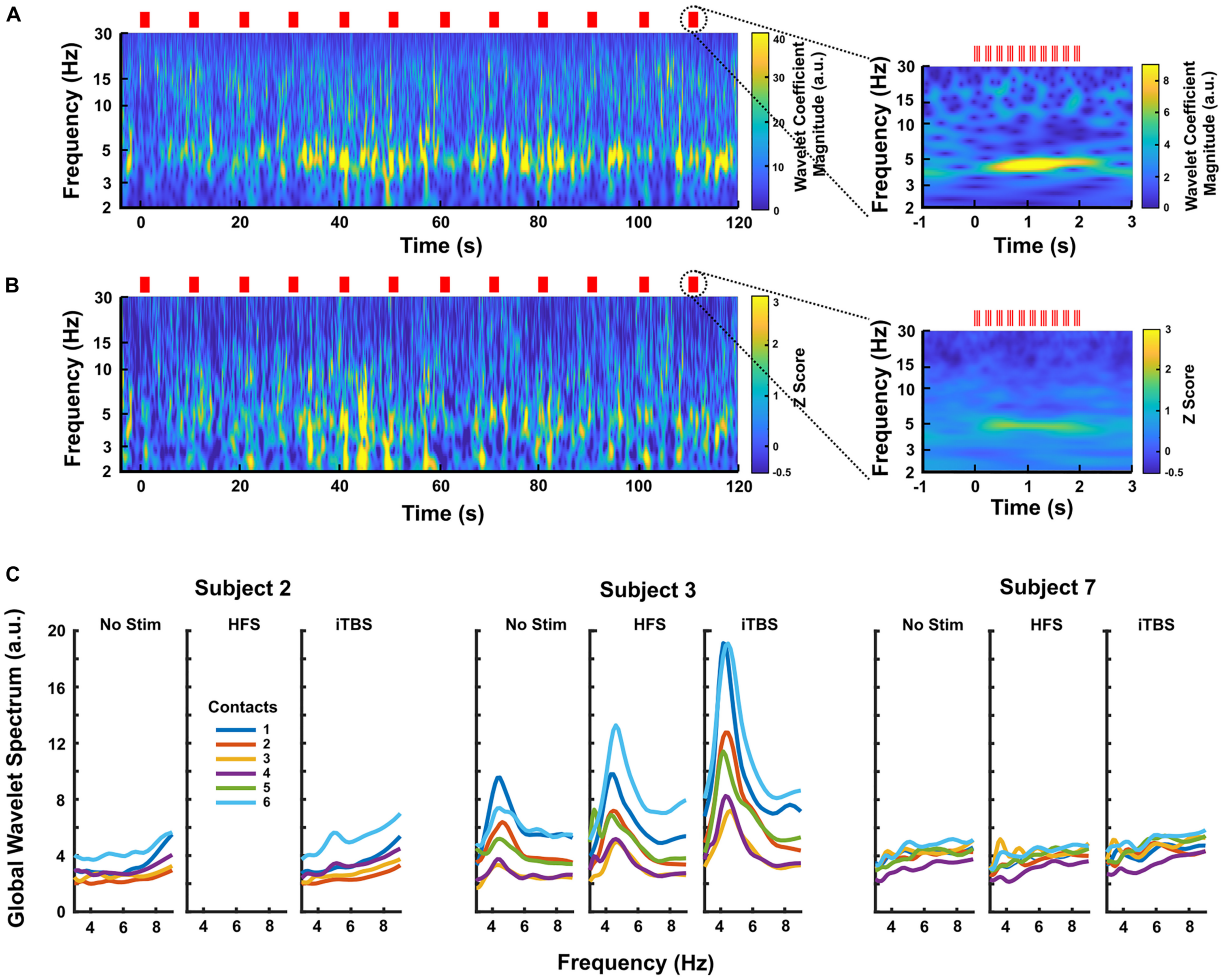

FIGURE 3 | (A) Continuous wavelet transform scalogram showing an example of the effects of iTBS on DLPFC LFPs in Subject 3 (contact 6, the most caudal contact on the subdural strip). Red lines mark stimulus times, and the start of stimulation is aligned at zero. Increased theta activity is prominent during iTBS, increasing after a delay of ∼30 s. The inset shows the LFP activity averaged across each 2 s block of theta bursts (n = 20 blocks). Here, the theta increase is clearly time-locked to the stimulation, appearing to build up over a period of ∼0.5 s. **(B)** Scalogram showing the effects of iTBS on DLPFC LFPs averaged over all three GPi subjects. Each subject's scalogram was converted to a Z-score based on that subject's baseline recordings before being averaged. The most caudal contact, contact 6, was used for each subject. Again, the inset shows the activity averaged over each 2 s block of theta bursts (n = 59 blocks), demonstrating that time-locking is preserved across subjects. **(C)** Average power spectra for all contacts in each GPi subject during no-stimulation, HFS, and iTBS periods, showing that iTBS increases theta activity more than does HFS on the same contacts. Subject 3 had the largest response to stimulation, but Subject 2 displayed a clear rise in 5 Hz activity. Subject 7 had minimal response to any stimulation condition.

Svenningsson et al., 2012; Duncan et al., 2014; Manza et al., 2017). Medical treatments fail to improve cognitive symptoms in many patients (Svenningsson et al., 2012), and cognitive outcomes following conventional high-frequency DBS are mixed (Okun et al., 2009; Combs et al., 2015; Wang et al., 2016), with a recent meta-analysis finding that STN-DBS patients experienced decrements in multiple cognitive domains compared to medically-treated controls (Cernera et al., 2019). Ideally, next-generation therapies would address both motor and cognitive aspects of the disease, but will likely require alternative patterns of stimulation.

Efficient cognitive processing likely involves coordinated signaling across multiple areas in distributed networks (Medaglia et al., 2015; Helfrich and Knight, 2016), with the prefrontal cortex acting as a major hub for many of these processes (Aron, 2007; Voytek and Knight, 2015). In particular, the DLFPC is consistently activated in cognitive tasks, including set-shifting, action selection, reward learning (Ridderinkhof et al., 2004) and tasks of inhibitory control (MacDonald et al., 2000; Harrison et al., 2005; Oldrati et al., 2016). As PD patients have deficits in several of these cognitive domains (Obeso et al., 2011; Manza et al., 2017), it is hypothesized that DLPFC function is correlated to impairment in these individuals. This is supported by both fMRI and EEG studies that reveal hypoactivity in the DLPFC of these patients (Schmiedt-Fehr et al., 2007; Singh et al., 2018; Trujillo et al., 2019).

Mechanistically, aberrant function of the DLPFC may be due to abnormal theta-frequency activity, which is thought to

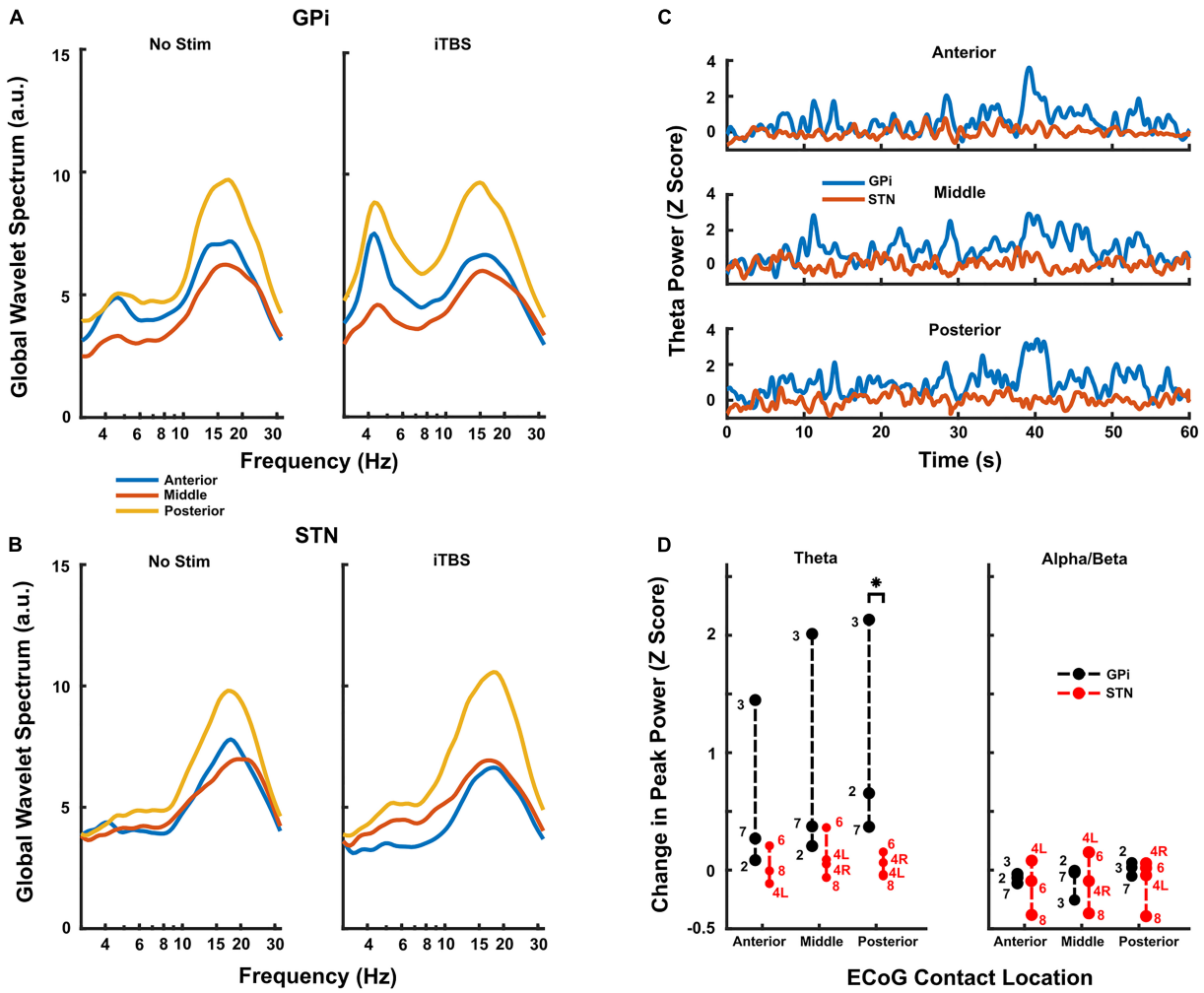

FIGURE 4 | (A,B) Resting and iTBS power spectra for each contact location group, averaged across all GPi **(A)** and STN **(B)** subjects. There was a clear trend toward higher theta facilitation caudally on the strip in the GPi subjects and there was minimal evidence of facilitation in the STN group. **(C)** Time series of theta activity in each contact location group during iTBS, averaged across GPi (blue) and STN (red) subjects. Each subject's activity was first converted to a *Z*-score based on the baseline theta activity prior to being averaged. Stimulation starts at time 0. Traces show high variability typical of neural data, but clearly show the differences in changes induced by iTBS delivered in GPi versus STN. **(D)** Group data for all subjects (n = 3 GPi; n = 4 STN) undergoing iTBS. In the posterior contact group, there was a significant difference in facilitation of theta power (compared to baseline) when iTBS was delivered in GPi versus STN (p = 0.0286, Wilcoxon rank-sum test). Conversely, the theta facilitation did not reach significance in any other contact group. There was no statistical difference in facilitation of beta activity in any contact group, and there was clearly less change overall compared to theta activity. Subject numbers appear next to each point.

underlie intact cognitive processes (Cavanagh and Frank, 2014). Notably, patients with PD have reduced theta-rhythms during cognitive tasks, particularly those involving inhibitory control (Schmiedt-Fehr et al., 2007; Singh et al., 2018). Therefore, restoring "normal" theta activity may result in improved task performance. To this end, several DBS studies have investigated subcortical delivery of continuous theta-frequency stimulation. For example, 4-Hz and 5-Hz continuous DBS is associated with improvement in interval timing (Kelley et al., 2018) and Stroop tasks (Scangos et al., 2018), respectively, and fornix stimulation is currently under investigation for memory improvement in Alzheimer's disease (Lozano et al., 2016). Non-invasive techniques are also becoming more widely studied. In transcranial magnetic stimulation (TMS), in which magnetic pulses are delivered through the scalp to interact with neural firing, several modes of theta-stimulation have been tried, including continuous and intermittent bursting patterns (Viejo-Sobera et al., 2017; Lowe et al., 2018). Theta-burst stimulation is thought to mimic naturally occurring brain rhythms (Huang and Rothwell, 2004) and in intermittent theta-burst stimulation, three pulses are delivered at 50-Hz every 200 ms for 2 s, followed by 8 s of rest (Huang et al., 2005). Initial effects were seen when delivered over motor cortex (Huang and Rothwell, 2004; Huang et al., 2005), and since then, it has been increasingly used to modulate cognitive networks (Hoy et al., 2016; Chung et al., 2018; Ji et al., 2019; Trung et al., 2019). However, a recent study of iTBS in PD showed failure to improve frontal executive function and memory when delivered via TMS, which

suggests a single session of therapy is not sufficient (Hill et al., 2020). Multiple sessions may provide benefit (Trung et al., 2019), but frequent re-application may not be logistically feasible for patients (Dinkelbach et al., 2017). In addition, the field of spread of the TMS pulse is variable due to tissue inhomogeneity, reducing the precision and predictability of this technique (Opitz et al., 2011). For these reasons, further studies of delivering iTBS patterns using deep brain stimulation are warranted.

Theta-burst patterns have previously been delivered via deep brain stimulation, primarily in the context of stimulation for memory improvement (Suthana et al., 2012; Titiz et al., 2017). Suthana et al. performed double-blinded theta-burst stimulation in the entorhinal cortex and hippocampus of 7 epilepsy patients and found improvement in a spatial learning task (Suthana et al., 2012). Similarly, in a double-blinded study of four patients, Miller et al. delivered theta-burst stimulation to the fornix of the hippocampus via depth electrodes, with overall improved performance (Miller et al., 2015), replicating prior results in animal models (Sweet et al., 2014).

In order to test the feasibility of subcortical iTBS, we delivered this pattern of stimulation in 7 PD patients undergoing routine DBS surgery. We show for the first time in humans that iTBS can be safely delivered and further show that GPi, but not STN, stimulation appears to modulate DLPFC theta activity, though responses across subjects and across anatomic areas were variable. Our results also indicate that high-frequency stimulation itself does not clearly modulate theta-power, and neither iTBS nor HFS had a substantial effect on other frequency bands. Due to the increase of theta power seen in the DLPFC of some PD patients, the implication is that subcortical iTBS may be useful for enhancing oscillatory activity and potentially correlate with cognitive improvement in impaired individuals.

Overall, this study provides evidence for the safety and feasibility of this approach, and provides some indication that iTBS may prove useful for modulating prefrontal cognitive networks. Further investigation is required to determine if increased theta-power correlates to behavioral changes in cognitive domains. If supported, this could serve as a foundation for developing next-generation DBS technologies for addressing non-motor cognitive and behavioral symptoms of Parkinson's disease and other disorders.

Limitations

Due to the small sample size, statistical tests were limited. However, placement of the strip electrode over DLPFC and iTBS were well-tolerated in all subjects, and our results reached statistical significance with regard to changes in theta-power during iTBS by stimulation target. A larger sample is required to form conclusion about connectivity between DLPFC and subcortical networks, especially given the variation in responses to stimulation within and across GPi implants. Although we did not correlate theta-activity with behavioral measures, these types of studies represent an important next step for this research. Finally, artifacts are always of consideration when interpreting recorded brain activity. It may be argued that the observed increased theta-power is an artifact of volume conduction from subcortical stimulation. However, we believe this is not the case since high-frequency stimulation did not result in analogous artifacts. Additionally, the electrical artifacts from the stimulation were limited to frequencies >100 Hz and would not have impacted theta-frequency activity.

CONCLUSION

Here, we show that iTBS, a type of patterned stimulation that is increasingly being investigated for cognitive and behavioral therapies via TMS, can be safely delivered from subcortical structures routinely targeted for DBS therapy in Parkinson's disease. As far as we are aware, this is the first demonstration of subcortical iTBS in humans. In our sample, we also show that iTBS from the GPi, but not the STN, appears to drive theta-frequency activity in the DLPFC. This is of interest since theta oscillatory activity may play a role in aberrant cognitive processing in PD. Further studies are required to confirm this result and determine if increasing theta activity in the DLPFC correlates with behavioral changes.

DATA AVAILABILITY STATEMENT

The datasets generated for this study are available on request to the corresponding author.

ETHICS STATEMENT

The studies involving human participants were reviewed and approved by the University of Alabama, Birmingham Institutional Review Board. The patients/participants provided their written informed consent to participate in this study.

AUTHOR CONTRIBUTIONS

JB, ZI, RK, BG, and HW contributed to conception and design of the study. JB, ZI, MR, CG, and HW contributed to data collection. SB performed electrode localizations. NB and ZI wrote the first draft of the manuscript. AK and GE-S wrote sections of the manuscript. All authors contributed to the manuscript revision, read, and approved the submitted version.

FUNDING

This work was supported in part by the NIH BRAIN Initiative Grant (UH3-NS100553) and the Michael J. Fox Foundation (15098). Publication costs supplemented by the University of Alabama, Birmingham internal funds.

ACKNOWLEDGMENTS

The authors would like to thank the University of Alabama, Birmingham, Department of Neurosurgery, Office of Clinical Research for their assistance with the study protocol.

SUPPLEMENTARY MATERIAL

The Supplementary Material for this article can be found online at: https://www.frontiersin.org/articles/10.3389/fnins.2020.00041/full#supplementary-material

FIGURE S1 | Power spectra for each stimulation condition performed in each subject. Contact 1 is the most anterior and contact 6 is the most posterior in all subjects.

FIGURE S2 | Comparison of iTBS versus HFS in all GPi subjects. Only Subjects 3 and 7 underwent both protocols.

REFERENCES

Antonini, A., Barone, P., Marconi, R., Morgante, L., Zappulla, S., Pontieri, F. E., et al. (2012). The progression of non-motor symptoms in Parkinson's disease and their contribution to motor disability and quality of life. *J. Neurol.* 259, 2621–2631. doi: 10.1007/s00415-012-6557-6558

Aron, A. R. (2007). The neural basis of inhibition in cognitive control. *Neuroscientist* 13, 214–228. doi: 10.1177/1073858407299288

Asanuma, K., Tang, C., Ma, Y., Dhawan, V., Mattis, P., Edwards, C., et al. (2006). Network modulation in the treatment of Parkinson's disease. *Brain* 129, 2667–2678. doi: 10.1093/brain/awl162

Baizabal-Carvallo, J. F., Kagnoff, M. N., Jimenez-Shahed, J., Fekete, R., and Jankovic, J. (2014). The safety and efficacy of thalamic deep brain stimulation in essential tremor: 10 years and beyond. *J. Neurol. Neurosurg. Psychiatry* 85:567. doi: 10.1136/jnnp-2013-304943

Benninger, D. H., Berman, B. D., Houdayer, E., Pal, N., Luckenbaugh, D. A., Schneider, L., et al. (2011). Intermittent theta-burst transcranial magnetic stimulation for treatment of Parkinson disease. *Neurology* 76, 601–609. doi: 10.1212/WNL.0b013e31820ce6bb

Blumberger, D. M., Vila-Rodriguez, F., Thorpe, K. E., Feffer, K., Noda, Y., Giacobbe, P., et al. (2018). Effectiveness of theta burst versus high-frequency repetitive transcranial magnetic stimulation in patients with depression (THREE-D): a randomised non-inferiority trial. *Lancet* 391, 1683–1692. doi: 10.1016/S0140-6736(18)30295-30292

Canolty, R. T., Edwards, E., Dalal, S. S., Soltani, M., Nagarajan, S. S., Kirsch, H. E., et al. (2006). High gamma power is phase-locked to theta oscillations in human neocortex. *Science* 313, 1626–1628. doi: 10.1126/science.1128115

Cavanagh, J. F., and Frank, M. J. (2014). Frontal theta as a mechanism for cognitive control. *Trends Cogn. Sci.* 18, 414–421. doi: 10.1016/j.tics.2014.04.012

Cernera, S., Okun, M. S., and Gunduz, A. (2019). A review of cognitive outcomes across movement disorder patients undergoing deep brain stimulation. *Front. Neurol.* 10:419. doi: 10.3389/fneur.2019.00419

Chung, S. W., Rogasch, N. C., Hoy, K. E., and Fitzgerald, P. B. (2018). The effect of single and repeated prefrontal intermittent theta burst stimulation on cortical reactivity and working memory. *Brain Stimul.* 11, 566–574. doi: 10.1016/j.brs.2018.01.002

Combs, H. L., Folley, B. S., Berry, D. T. R., Segerstrom, S. C., Han, D. Y., Anderson-Mooney, A. J., et al. (2015). Cognition and depression following deep brain stimulation of the subthalamic nucleus and globus pallidus pars internus in Parkinson's disease: a meta-analysis. *Neuropsychol. Rev.* 25, 439–454. doi: 10.1007/s11065-015-9302-9300

De Hemptinne, C., Swann, N. C., Ostrem, J. L., Ryapolova-Webb, E. S., San Luciano, M., Galifianakis, N. B., et al. (2015). Therapeutic deep brain stimulation reduces cortical phase-amplitude coupling in Parkinson's disease. *Nat. Neurosci.* 18, 779–786. doi: 10.1038/nn.3997

Dembek, T. A., Reker, P., Visser-Vandewalle, V., Wirths, J., Treuer, H., Klehr, M., et al. (2017). Directional DBS increases side-effect thresholds—A prospective, double-blind trial. *Mov. Disord.* 32, 1380–1388. doi: 10.1002/mds.27093

Deuschl, G., Schade-Brittinger, C., Krack, P., Volkmann, J., Schäfer, H., Bötzel, K., et al. (2006). A randomized trial of deep-brain stimulation for Parkinson's disease. *N Engl. J. Med.* 355, 896–908. doi: 10.1056/NEJMoa060281

Dinkelbach, L., Brambilla, M., Manenti, R., and Brem, A.-K. (2017). Non-invasive brain stimulation in Parkinson's disease: exploiting crossroads of cognition and mood. *Neurosci. Biobehav. Rev.* 75, 407–418. doi: 10.1016/j.neubiorev.2017.01.021

Duncan, G. W., Khoo, T. K., Yarnall, A. J., O'Brien, J. T., Coleman, S. Y., Brooks, D. J., et al. (2014). Health-related quality of life in early Parkinson's disease: the impact of nonmotor symptoms. *Mov. Disord.* 29, 195–202. doi: 10.1002/mds.25664

Fedorov, A., Beichel, R., Kalpathy-Cramer, J., Finet, J., Fillion-Robin, J.-C., Pujol, S., et al. (2012). 3D Slicer as an image computing platform for the quantitative imaging network. *Magn. Reson. Imaging* 30, 1323–1341. doi: 10.1016/j.mri.2012.05.001

Fischl, B. (2012). FreeSurfer. *Neuroimage* 62, 774–781. doi: 10.1016/j.neuroimage.2012.01.021

Harrison, B. J., Shaw, M., Yücel, M., Purcell, R., Brewer, W. J., Strother, S. C., et al. (2005). Functional connectivity during Stroop task performance. *Neuroimage* 24, 181–191. doi: 10.1016/j.neuroimage.2004.08.033

Haynes, W. I. A., and Haber, S. N. (2013). The organization of prefrontal-subthalamic inputs in primates provides an anatomical substrate for both functional specificity and integration: implications for basal ganglia models and deep brain stimulation. *J. Neurosci.* 33, 4804–4814. doi: 10.1523/JNEUROSCI.4674-12.2013

Helfrich, R. F., and Knight, R. T. (2016). Oscillatory dynamics of prefrontal cognitive control. *Trends Cogn. Sci.* 20, 916–930. doi: 10.1016/j.tics.2016.09.007

Hely, M. A., Reid, W. G. J., Adena, M. A., Halliday, G. M., and Morris, J. G. L. (2008). The Sydney multicenter study of Parkinson's disease: the inevitability of dementia at 20 years. *Mov. Disord.* 23, 837–844. doi: 10.1002/mds.21956

Hill, A. T., McModie, S., Fung, W., Hoy, K. E., Chung, S.-W., and Bertram, K. L. (2020). Impact of prefrontal intermittent theta-burst stimulation on working memory and executive function in Parkinson's disease: a double-blind sham-controlled pilot study. *Brain Res.* 18:146506. doi: 10.1016/j.brainres.2019.146506

Hoy, K. E., Bailey, N., Michael, M., Fitzgibbon, B., Rogasch, N. C., Saeki, T., et al. (2016). Enhancement of working memory and task-related oscillatory activity following intermittent theta burst stimulation in healthy controls. *Cereb. Cortex* 26, 4563–4573. doi: 10.1093/cercor/bhv193

Huang, Y.-Z., Edwards, M. J., Rounis, E., Bhatia, K. P., and Rothwell, J. C. (2005). Theta burst stimulation of the human motor cortex. *Neuron* 45, 201–206. doi: 10.1016/j.neuron.2004.12.033

Huang, Y.-Z., and Rothwell, J. C. (2004). The effect of short-duration bursts of high-frequency, low-intensity transcranial magnetic stimulation on the human motor cortex. *Clin. Neurophysiol.* 115, 1069–1075. doi: 10.1016/j.clinph.2003.12.026

Ji, G.-J., Wei, J.-J., Liu, T., Li, D., Zhu, C., Yu, F., et al. (2019). Aftereffect and reproducibility of three excitatory repetitive tms protocols for a response inhibition task. *Front. Neurosci.* 13:1155. doi: 10.3389/fnins.2019.01155

Kelley, R., Flouty, O., Emmons, E. B., Kim, Y., Kingyon, J., Wessel, J. R., et al. (2018). A human prefrontal-subthalamic circuit for cognitive control. *Brain* 141, 205–216. doi: 10.1093/brain/awx300

Lowe, C. J., Manocchio, F., Safati, A. B., and Hall, P. A. (2018). The effects of theta burst stimulation (TBS) targeting the prefrontal cortex on executive functioning: a systematic review and meta-analysis. *Neuropsychologia* 111, 344–359. doi: 10.1016/j.neuropsychologia.2018.02.004

Lozano, A. M., Fosdick, L., Chakravarty, M. M., Leoutsakos, J.-M., Munro, C., Oh, E., et al. (2016). A Phase II study of fornix deep brain stimulation in mild Alzheimer's disease. *J. Alzheimers Dis.* 54, 777–787. doi: 10.3233/JAD-160017

Lozano, A. M., Lipsman, N., Bergman, H., Brown, P., Chabardes, S., Chang, J. W., et al. (2019). Deep brain stimulation: current challenges and future directions. *Nat. Rev. Neurol.* 15, 148–160. doi: 10.1038/s41582-018-0128-122

MacDonald, A. W., Cohen, J. D., Stenger, V. A., and Carter, C. S. (2000). Dissociating the role of the dorsolateral prefrontal and anterior cingulate cortex in cognitive control. *Science* 288, 1835–1838. doi: 10.1126/science.288.5472.1835

Manza, P., Amandola, M., Tatineni, V., Li, C. R., and Leung, H.-C. (2017). Response inhibition in Parkinson's disease: a meta-analysis of dopaminergic medication and disease duration effects. *NPJ Parkinsons Dis.* 3:23. doi: 10.1038/s41531-017-0024-22

Medaglia, J. D., Lynall, M.-E., and Bassett, D. S. (2015). Cognitive network neuroscience. *J. Cogn. Neurosci.* 27, 1471–1491. doi: 10.1162/jocn_a_00810

Middleton, F. A., and Strick, P. L. (2002). Basal-ganglia 'Projections' to the prefrontal cortex of the primate. *Cereb. Cortex* 12, 926–935. doi: 10.1093/cercor/12.9.926

Miller, J. P., Sweet, J. A., Bailey, C. M., Munyon, C. N., Luders, H. O., and Fastenau, P. S. (2015). Visual-spatial memory may be enhanced with theta burst deep brain stimulation of the fornix: a preliminary investigation with four cases. *Brain* 138, 1833–1842. doi: 10.1093/brain/awv095

Obeso, I., Wilkinson, L., Casabona, E., Bringas, M. L., Álvarez, M., Álvarez, L., et al. (2011). Deficits in inhibitory control and conflict resolution on cognitive and motor tasks in Parkinson's disease. *Exp. Brain Res.* 212, 371–384. doi: 10.1007/s00221-011-2736-2736

Okun, M. S., Fernandez, H. H., Wu, S. S., Kirsch-Darrow, L., Bowers, D., Bova, F., et al. (2009).). Cognition and mood in Parkinson's disease in subthalamic nucleus versus globus pallidus interna deep brain stimulation: the COMPARE trial. *Ann. Neurol.* 65, 586–595. doi: 10.1002/ana.21596

Oldrati, V., Patricelli, J., Colombo, B., and Antonietti, A. (2016). The role of dorsolateral prefrontal cortex in inhibition mechanism: a study on cognitive reflection test and similar tasks through neuromodulation. *Neuropsychologia* 91, 499–508. doi: 10.1016/j.neuropsychologia.2016.09.010

Opitz, A., Windhoff, M., Heidemann, R. M., Turner, R., and Thielscher, A. (2011). How the brain tissue shapes the electric field induced by transcranial magnetic stimulation. *Neuroimage* 58, 849–859. doi: 10.1016/j.neuroimage.2011.06.069

Pollo, C., Kaelin-Lang, A., Oertel, M. F., Stieglitz, L., Taub, E., Fuhr, P., et al. (2014). Directional deep brain stimulation: an intraoperative double-blind pilot study. *Brain* 137, 2015–2026. doi: 10.1093/brain/awu102

Priori, A., Foffani, G., Rossi, L., and Marceglia, S. (2013). Adaptive deep brain stimulation (aDBS) controlled by local field potential oscillations. *Exp. Neurol.* 245, 77–86. doi: 10.1016/j.expneurol.2012.09.013

Reinhart, R. M. G., and Nguyen, J. A. (2019). Working memory revived in older adults by synchronizing rhythmic brain circuits. *Nat. Neurosci.* 22, 820–827. doi: 10.1038/s41593-019-0371-x

Ridderinkhof, K. R., van den Wildenberg, W. P. M., Segalowitz, S. J., and Carter, C. S. (2004). Neurocognitive mechanisms of cognitive control: the role of prefrontal cortex in action selection, response inhibition, performance monitoring, and reward-based learning. *Brain Cogn.* 56, 129–140. doi: 10.1016/j.bandc.2004.09.016

Rosin, B., Slovik, M., Mitelman, R., Rivlin-Etzion, M., Haber, S. N., Israel, Z., et al. (2011). Closed-loop deep brain stimulation is superior in ameliorating parkinsonism. *Neuron* 72, 370–384. doi: 10.1016/j.neuron.2011.08.023

Scangos, K. W., Carter, C. S., Gurkoff, G., Zhang, L., and Shahlaie, K. (2018). A pilot study of subthalamic theta frequency deep brain stimulation for cognitive dysfunction in Parkinson's disease. *Brain Stimul.* 11, 456–458. doi: 10.1016/j.brs.2017.11.014

Schmiedt-Fehr, C., Schwendemann, G., Herrmann, M., and Basar-Eroglu, C. (2007). Parkinson's disease and age-related alterations in brain oscillations during a Simon task. *Neuroreport* 18:277. doi: 10.1097/WNR.0b013e32801421e3

Singh, A., Richardson, S. P., Narayanan, N., and Cavanagh, J. F. (2018). Mid-frontal theta activity is diminished during cognitive control in Parkinson's disease. *Neuropsychologia* 117, 113–122. doi: 10.1016/j.neuropsychologia.2018.05.020

Starr, P. A., Turner, R. S., Rau, G., Lindsey, N., Heath, S., Volz, M., et al. (2006). Microelectrode-guided implantation of deep brain stimulators into the globus pallidus internus for dystonia: techniques, electrode locations, and outcomes. *J. Neurosurg.* 104, 488–501. doi: 10.3171/jns.2006.104.4.488

Suthana, N., Haneef, Z., Stern, J., Mukamel, R., Behnke, E., Knowlton, B., et al. (2012). Memory enhancement and deep-brain stimulation of the entorhinal area. *N. Engl. J. Med.* 366, 502–510. doi: 10.1056/NEJMoa1107212

Svenningsson, P., Westman, E., Ballard, C., and Aarsland, D. (2012). Cognitive impairment in patients with Parkinson's disease: diagnosis, biomarkers, and treatment. *Lancet Neurol.* 11, 697–707. doi: 10.1016/S1474-4422(12)70152-70157

Swann, N. C., de Hemptinne, C., Thompson, M. C., Miocinovic, S., Miller, A. M., Gilron, R., et al. (2018). Adaptive deep brain stimulation for Parkinson's disease using motor cortex sensing. *J. Neural. Eng.* 15:046006. doi: 10.1088/1741-2552/aabc9b

Sweet, J. A., Eakin, K. C., Munyon, C. N., and Miller, J. P. (2014). Improved learning and memory with theta-burst stimulation of the fornix in rat model of traumatic brain injury. *Hippocampus* 24, 1592–1600. doi: 10.1002/hipo.22338

Titiz, A. S., Hill, M. R. H., Mankin, E. A., Aghajan, Z., Eliashiv, D., Tchemodanov, N., et al. (2017). Theta-burst microstimulation in the human entorhinal area improves memory specificity. *eLife* 6:e29515. doi: 10.7554/eLife.29515

Trujillo, P., van Wouwe, N. C., Lin, Y.-C., Stark, A. J., Petersen, K. J., Kang, H., et al. (2019). Dopamine effects on frontal cortical blood flow and motor inhibition in Parkinson's disease. *Cortex* 115, 99–111. doi: 10.1016/j.cortex.2019.01.016

Trung, J., Hanganu, A., Jobert, S., Degroot, C., Mejia-Constain, B., Kibreab, M., et al. (2019). Transcranial magnetic stimulation improves cognition over time in Parkinson's disease. *Parkinson. Relat. Disord.* 9, 3–8. doi: 10.1016/j.parkreldis.2019.07.006

Viejo-Sobera, R., Redolar-Ripoll, D., Boixadós, M., Palaus, M., Valero-Cabré, A., and Marron, E. M. (2017). Impact of prefrontal theta burst stimulation on clinical neuropsychological tasks. *Front. Neurosci.* 11:462. doi: 10.3389/fnins.2017.00462

Voytek, B., and Knight, R. T. (2015). Dynamic network communication as a unifying neural basis for cognition, development, aging, and disease. *Biol. Psychiatry* 77, 1089–1097. doi: 10.1016/j.biopsych.2015.04.016

Wang, J.-W., Zhang, Y.-Q., Zhang, X.-H., Wang, Y.-P., Li, J.-P., and Li, Y.-J. (2016). Cognitive and psychiatric effects of STN versus GPi deep brain stimulation in Parkinson's Disease: a meta-analysis of randomized controlled trials. *PLoS One* 11:e0156721. doi: 10.1371/journal.pone.0156721

Williams-Gray, C. H., Evans, J. R., Goris, A., Foltynie, T., Ban, M., Robbins, T. W., et al. (2009). The distinct cognitive syndromes of Parkinson's disease: 5 year follow-up of the CamPaIGN cohort. *Brain* 132, 2958–2969. doi: 10.1093/brain/awp245

Conflict of Interest: The authors declare that the research was conducted in the absence of any commercial or financial relationships that could be construed as a potential conflict of interest.

frontiers in Neuroscience

ORIGINAL RESEARCH
published: 05 March 2020
doi: 10.3389/fnins.2020.00166

Simulation of Closed-Loop Deep Brain Stimulation Control Schemes for Suppression of Pathological Beta Oscillations in Parkinson's Disease

John E. Fleming, Eleanor Dunn and Madeleine M. Lowery*

Neuromuscular Systems Laboratory, UCD School of Electrical & Electronic Engineering, University College Dublin, Dublin, Ireland

This study presents a computational model of closed-loop control of deep brain stimulation (DBS) for Parkinson's disease (PD) to investigate clinically viable control schemes for suppressing pathological beta-band activity. Closed-loop DBS for PD has shown promising results in preliminary clinical studies and offers the potential to achieve better control of patient symptoms and side effects with lower power consumption than conventional open-loop DBS. However, extensive testing of algorithms in patients is difficult. The model presented provides a means to explore a range of control algorithms *in silico* and optimize control parameters before preclinical testing. The model incorporates (i) the extracellular DBS electric field, (ii) antidromic and orthodromic activation of STN afferent fibers, (iii) the LFP detected at non-stimulating contacts on the DBS electrode and (iv) temporal variation of network beta-band activity within the thalamo-cortico-basal ganglia loop. The performance of on-off and dual-threshold controllers for suppressing beta-band activity by modulating the DBS amplitude were first verified, showing levels of beta suppression and reductions in power consumption comparable with previous clinical studies. Proportional (P) and proportional-integral (PI) closed-loop controllers for amplitude and frequency modulation were then investigated. A simple tuning rule was derived for selecting effective PI controller parameters to target long duration beta bursts while respecting clinical constraints that limit the rate of change of stimulation parameters. Of the controllers tested, PI controllers displayed superior performance for regulating network beta-band activity whilst accounting for clinical considerations. Proportional controllers resulted in undesirable rapid fluctuations of the DBS parameters which may exceed clinically tolerable rate limits. Overall, the PI controller for modulating DBS frequency performed best, reducing the mean error by 83% compared to DBS off and the mean power consumed to 25% of that utilized by open-loop DBS. The network model presented captures sufficient physiological detail to act as a surrogate for preclinical testing of closed-loop DBS algorithms using a clinically accessible biomarker, providing a first step for deriving and testing novel, clinically suitable closed-loop DBS controllers.

Keywords: closed-loop deep brain stimulation, Parkinson's disease, beta-band activity, proportional-integral controller, computational model, control schemes, adaptive

OPEN ACCESS

Edited by:
Sabato Santaniello, University of Connecticut, United States

Reviewed by:
Georgios Detorakis, University of California, Irvine, United States
Alik Sunil Widge, University of Minnesota Twin Cities, United States

****Correspondence:***
John E. Fleming
john.fleming@ucdconnect.ie

Specialty section:
This article was submitted to Neural Technology, a section of the journal Frontiers in Neuroscience

Received: *16 December 2019*
Accepted: *14 February 2020*
Published: *05 March 2020*

Citation:
Fleming JE, Dunn E and Lowery MM (2020) Simulation of Closed-Loop Deep Brain Stimulation Control Schemes for Suppression of Pathological Beta Oscillations in Parkinson's Disease. Front. Neurosci. 14:166. doi: 10.3389/fnins.2020.00166

INTRODUCTION

In recent years, there has been growing interest on the potential offered by "closed-loop" deep brain stimulation (DBS). In a closed-loop DBS configuration, the patient's clinical state is quantified and utilized to alter stimulation parameters as necessary, so the required stimulation to minimize their disease symptoms is delivered, thus reducing potential stimulation induced side-effects while controlling symptoms. A critical step in the development of such systems is the identification of signal features or "biomarkers" which have the potential to quantify the clinical state. One of the most promising features examined for closed-loop control of DBS in PD is the level of beta-band (13 – 30 Hz) oscillatory activity within the subthalamic nucleus (STN) and cortico-basal ganglia network. Pathological exaggerated activity within this frequency band is correlated with motor impairment and its suppression, due to medication or DBS, with motor improvement (Silberstein et al., 2005a,b; Kühn et al., 2008, 2009). This oscillatory activity, however, is not continuously elevated, but rather fluctuates between long, greater than 400 ms, and short duration bursts of beta activity, with only long burst durations being positively correlated with motor impairment in PD (Tinkhauser et al., 2017a,b, 2020). These features, in combination with the potential to record LFP activity during stimulation from non-stimulating contacts on the DBS electrode, render LFP beta band activity an appealing biomarker for closed-loop DBS.

Closed-loop DBS for PD utilizing LFP derived measures of beta-band oscillatory activity has been successfully tested in small cohorts of PD patients over relatively short timescales (Little et al., 2013, 2016; Rosa et al., 2015; Arlotti et al., 2018; Velisar et al., 2019). These studies have examined amplitude modulation of the DBS waveform in response to changes in the LFP beta-band activity. "On-off" stimulation strategies, where DBS is triggered on or off as the measured oscillatory activity crosses a desired threshold value, were the first closed-loop strategies tested in patients (Little et al., 2013, 2016). Although these strategies offer benefits with respect to traditional open-loop stimulation, they rely on optimal stimulation parameters that are identified during open-loop, continuous DBS. If these stimulation parameters are no longer effective, for example, due to diurnal changes in beta activity, variations in the electrode impedance, or as the disease progresses, the controller is unable to adapt and delivers suboptimal performance. Velisar et al. (2019) proposed an alternative "dual-threshold" algorithm where the amplitude of the DBS waveform is systematically increased, decreased or kept constant as the measured LFP beta-band activity remains above, below or within a desired target range. Although the strategy can maintain the beta activity within a target range, it remains a relatively simple form of control where the DBS amplitude is varied at a fixed rate if the beta-band activity lies outside the target range. Rosa et al. (2015); Arlotti et al. (2018) investigated an alternative approach where the DBS waveform was linearly modulated in response to the measured LFP beta-band activity in freely moving PD patients. Proportional amplitude modulation stimulation strategies such as this, where the DBS amplitude is varied proportionally to the measured LFP beta-band activity, potentially offer more benefits than on-off and dual-threshold strategies, in theory, because they ideally only deliver the stimulation required to reduce beta-band LFP activity to suppress PD symptoms.

In conjunction with the amplitude modulation stimulation strategies that have been investigated so far, control theory offers a wealth of control schemes which may potentially offer better control of patient symptoms and side effects, whilst minimizing battery consumption, over the current state-of-the-art strategies. The development of novel, effective control schemes for DBS, however, is challenging and trialing in humans or animals is difficult due to its invasive nature. Computational modeling provides an alternative approach for designing and testing more complex forms of closed-loop DBS control. Although computational models have been previously used to investigate closed-loop control strategies for DBS (Santaniello et al., 2011; Carron et al., 2013; Gorzelic et al., 2013; Grant and Lowery, 2013; Pasillas-Lepine et al., 2013; Haidar et al., 2016; Liu et al., 2017a; Popovych and Tass, 2019; Su et al., 2019), they typically do not relate well to clinically relevant parameters and, in particular, rarely incorporate both simulation of the LFP and extracellular application of DBS. Simulation of the LFP is desirable for developing computational models that can be readily translated to patients as LFP derived features, such as frequency and time domain features, are currently the most accessible biomarkers for closed-loop DBS in PD (Priori et al., 2013). In addition, simulation of the electric field and extracellular application of DBS to axons and branching afferents is necessary to enable variations in DBS amplitude to be simulated. To bridge the link between computational approaches and clinically viable closed-loop approaches it is thus necessary to develop a model which captures the dynamics of the relevant neural system, the electric field generated by DBS, and the resulting LFP recording.

To address this, the aim of this study was to develop a physiologically based model of the cortico-basal ganglia network, which incorporates extracellular DBS and simulation of the STN LFP, that can be utilized to test clinically relevant closed-loop DBS control strategies. The developed model captures increased network beta-band oscillatory activity and simulates the synaptically generated STN LFP and extracellular application of DBS to STN afferent fibers, including antidromic activation of cortical pathways. The performance of on-off and dual-threshold amplitude modulation strategies are verified in the model before the feasibility of proportional (P) and proportional-integral (PI) control schemes for modulating DBS amplitude or frequency are investigated. The model provides an *in silico* testbed for developing new closed-loop DBS control strategies using STN LFP-derived features in PD.

MATERIALS AND METHODS

The structure of the network model of DBS is presented in **Figure 1** and includes the closed loop formed between the cortex, basal ganglia and thalamus (Parent and Hazrati, 1995a,b; Nambu et al., 2002; McHaffie et al., 2005). The model extends previous network models of the parkinsonian cortico-basal ganglia during

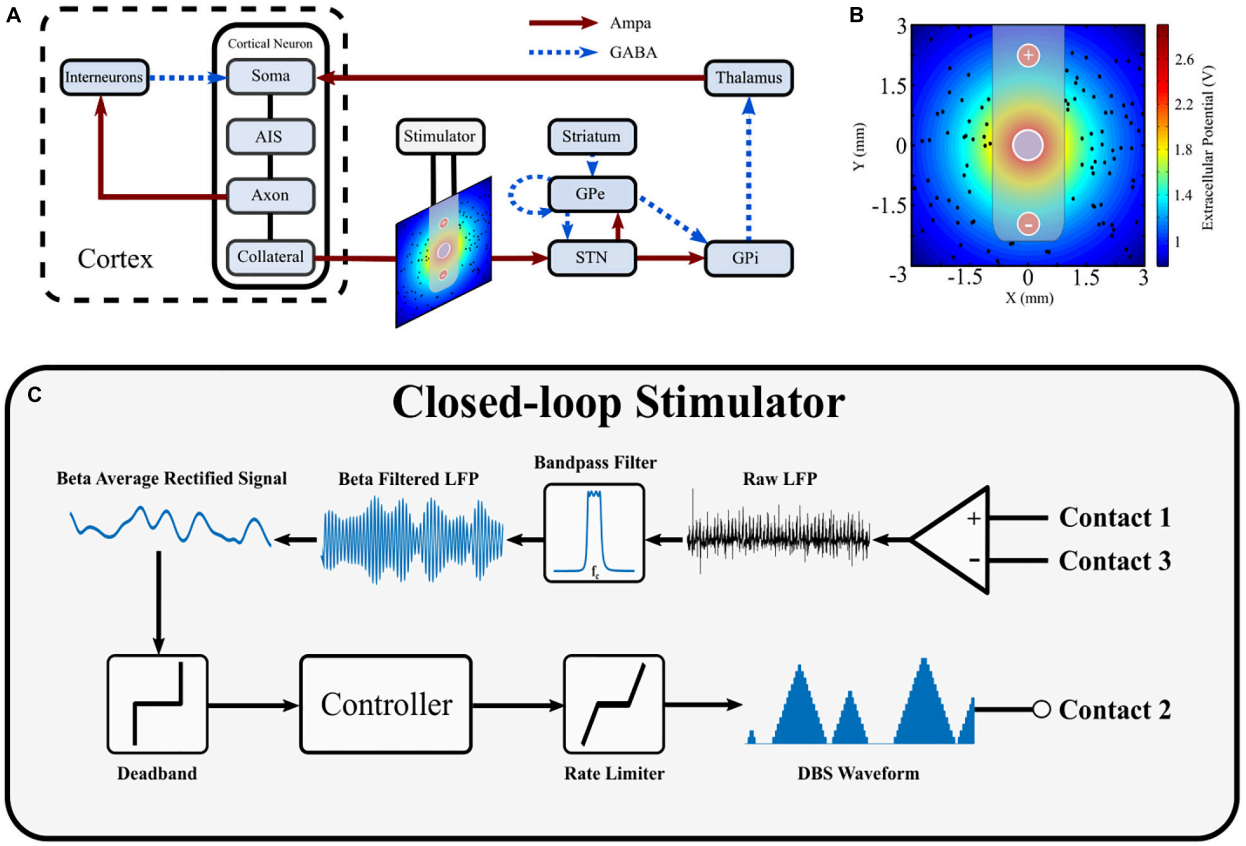

FIGURE 1 | Schematic diagram of cortical basal ganglia network model. **(A)** Network diagram of cortical basal ganglia neuron populations. Excitatory and inhibitory synaptic connections within the network are represented as solid red arrow and blue dotted arrows, respectively. **(B)** Electric field distribution due to monopolar stimulation electrode. Cortical collaterals, represented as black dots, are oriented perpendicular to the page. The electrode bipolar recording contacts are represented by + and –, respectively. **(C)** Schematic diagram of the closed-loop stimulator utilizing an LFP derived measured of network beta-band activity. Contacts 1 and 3 represent the bipolar recording electrode contacts on the DBS electrode. The recorded LFP is bandpass filtered, rectified and averaged to calculate the average rectified value of the LFP beta-band activity. The beta average rectified value is used as input to a controller which determines an updated value for the DBS parameter being modulated. The updated DBS waveform is subsequently simulated at electrode contact 2 and varies the electric field distribution.

DBS (Terman et al., 2002; Rubin and Terman, 2004; Hahn and McIntyre, 2010; Kang and Lowery, 2013, 2014; Kumaravelu et al., 2016) by (i) incorporating the extracellular DBS electric field (ii) simulating antidromic and orthodromic activation of cortical and globus pallidus efferent fibers to the STN and (iii) simulating the LFP detected at non-stimulating contacts on the DBS electrode due to STN synaptic activity and (iv) mimics temporal variation of network beta activity within the thalamo-cortico-basal ganglia loop. The model was used to investigate the performance of closed-loop amplitude and frequency modulation strategies using an LFP derived measure of the network beta-band oscillatory activity.

Network Structure

The major model components include single compartment, conductance-based biophysical models of cortical interneurons, STN, globus pallidus externa (GPe), globus pallidus interna (GPi), and thalamus neurons. Cortical Layer V pyramidal neurons, with axons projecting to the STN through the hyperdirect pathway, were simulated using multi-compartment, conductance-based biophysical models to enable extracellular application of DBS to cortical axon collaterals. The individual cell models have been validated and employed in previous modeling studies (Terman et al., 2002; Otsuka et al., 2004; Rubin and Terman, 2004; Pospischil et al., 2008; Hahn and McIntyre, 2010; Kang and Lowery, 2013, 2014; Kumaravelu et al., 2016). Six hundred cells consisting of one hundred STN, GPe, GPi, thalamic, cortical interneuron and cortical pyramidal neurons were connected through excitatory and inhibitory synapses, AMPA and GABAa, respectively, as described below, **Figure 1A**. While the type and direction of connections between the nuclei of the thalamo-cortico-basal ganglia network are well established, it is more difficult to ascertain the exact number of connections between individual neurons, and their relative strengths, in different nuclei. Input to a single neuron was therefore assumed to be from one or two neurons in each of the connected presynaptic nuclei, with the exception of the STN, which receives substantial direct cortical input (Nambu et al., 2002), with increased functional connectivity between the cortex and STN in the dopamine depleted state (Litvak et al., 2011; Moran et al.,

2011; West et al., 2018). Connections between neurons in the cortico-basal ganglia network followed a random connectivity pattern. Each STN neuron received excitatory input from five cortical neurons and inhibitory input from two GPe neurons (Smith et al., 1990; Bevan et al., 1995). Each GPe neuron received inhibitory input from one striatal neuron, and one other GPe neuron, and excitatory input from two STN neurons (Shink and Smith, 1995; Chan et al., 2004; Sadek et al., 2007). Each GPi neuron received excitatory input from a single STN neuron and inhibitory input from a single GPe neuron (Shink and Smith, 1995). Thalamic neuron received inhibitory input from a single GPi neuron (Sidibé et al., 1997). Cortical neurons received excitatory input from a single thalamic neurons and inhibitory input from ten interneurons (Kayahara and Nakano, 1996; Packer et al., 2013). Interneurons received excitatory input from ten cortical neurons (Packer et al., 2013). The values for all model parameters are provided as **Supplementary Material**.

Pathological beta oscillations in the cortico-basal ganglia network were modeled based on the hypothesis that beta activity entering the network from the cortex is enhanced locally within the reciprocally coupled STN-GPe loop and propagates through the closed-loop network from the cortex through the basal ganglia, thalamus and back to cortex (Mallet et al., 2008; Tachibana et al., 2008, 2011; Nambu and Tachibana, 2014). This hypothesis is supported by observations from primate studies, where oscillations in the STN, GPe and GPi were investigated while inputs to each population were systematically blocked (Tachibana et al., 2008, 2011). Nambu and Tachibana summarized their findings in Nambu and Tachibana (2014), where the authors articulate that oscillatory activity in the GPe and GPi were generated mainly due to glutamatergic inputs from the STN, while oscillations in the STN were mainly due to glutamatergic inputs from the cortex, with STN GABAergic inputs from the GPe potentially increasing the oscillatory activity. Furthermore, Litvak et al. (2011) observed that beta activity in the cortex led beta activity in the STN in parkinsonian patients (Litvak et al., 2011), while Sharott et al. (2005) found that in a parkinsonian rat model dopamine depletion increased the power and coherence of beta oscillations in the cerebral cortex and STN (Sharott et al., 2005). Further evidence of this hypothesis is supported by investigations of directional connectivity within the dopamine depleted cortico-basal ganglia, inversion of biophysical models using electrophysiological data from rats and patients (Moran et al., 2011; Marreiros et al., 2013; West et al., 2018), and functional imaging studies in individuals with Parkinson's disease (PD) (Lalo et al., 2008; Baudrexel et al., 2011; Fernández-Seara et al., 2015).

The strength of synaptic connections between the cortex and STN, between the STN and GPe, and the thalamus cortex were increased to induce beta oscillations within the network and the STN LFP, similar to that observed experimentally (West et al., 2018). Previous simulation studies have similarly increased the strength of connections between nuclei to simulate the effects of dopamine depletion on basal ganglia network activity in PD resulting in the emergence of oscillatory activity in conductance-based models (Rubin and Terman, 2004; Humphries et al., 2006; Hahn and McIntyre, 2010; Kang and Lowery, 2013; Kumaravelu et al., 2016) and mean-field models (Nevado-Holgado et al., 2010; Davidson et al., 2016; Liu et al., 2017b, 2020).

Neuron Models

The compartmental membrane voltage of each neuron in the network is described by

$$C_{m_{x_i}} \frac{dv_{m_{x_i}}}{dt} = -\sum_{j_x}^{J_x} I_{Ion_{x_i}} - \sum_{k_{x_i}}^{K_{x_i}} I_{syn_{x_i}}^{k_{x_i}} + \sum_{m_{x_i}}^{M_{x_i}} I_{App_{x_i}} \quad (1)$$

where x specifies the neuron population, i is the ith neuron in population x, $C_{m_{x_i}}$ is the membrane capacitance of the ith neuron in population x, $v_{m_{x_i}}$ is the membrane potential of the ith neuron in population x. The membrane potential of the ith neuron in population x was calculated as the summation of the J ionic currents of population x's neuron model, $I_{Ion_{x_i}}$, the K_x synaptic currents which project to the ith neuron in population x, $I_{syn_{x_i}}$, and the M intracellularly applied currents, $I_{App_{x_i}}$. Further details regarding the neuron models are included below, and in the **Supplementary Material**.

Cortex

The cortex was represented by a network of interneurons and cortical pyramidal neurons. The cortical neuron model, based on a layer V pyramidal tract neuron, comprised a soma, axon initial segment (AIS), main axon, and axon collateral as described by Kang and Lowery (2014). To summarize, the cortical neuron soma and interneuron models were based on the regular spiking neuron model developed in Pospischil et al. (2008), while the model used to simulate the AIS, main axon, and axon collateral was based on results from the experimental modeling study in Foust et al. (2011). The model compartments include leak, sodium, and three potassium ionic currents and an intracellular bias current for setting the neuron firing rate. The cortical soma compartment model excluded the D-type potassium current, while the AIS, main axon, and axon collateral compartments excluded the slow, voltage dependent potassium current. Cortical interneurons excluded both the D-type and slow, voltage dependent potassium currents.

Subthalamic Nucleus

The STN model incorporated a physiological representation of STN neurons developed by Otsuka et al. (2004) and implemented by Hahn and McIntyre (2010) that captures the generation of plateau potentials which have been identified as playing an important role in generating STN bursting activity that is observed during PD (Beurrier et al., 1999). The STN model included leak, sodium, three potassium, two calcium ionic currents and an intracellular bias current for setting the neuron firing rate. Further details regarding the parameter values used can be found in the **Supplementary Material** and in Otsuka et al. (2004), Hahn and McIntyre (2010), Kang and Lowery (2013, 2014).

Globus Pallidus and Thalamus

GPe, GPi, and thalamic neurons were represented using the model developed in Rubin and Terman (2004) and implemented by Hahn and McIntyre (2010). The GPe and GPi neuron models included leak, sodium, two potassium, and two calcium ionic currents and an intracellular bias current for setting the neuron firing rates. GPe neurons included an additional intracellularly injected current to simulate the application of DBS to the GPe neuron model, assuming that an equivalent proportion of GPe neurons were stimulated to the proportion of extracellularly stimulated cortical neurons during DBS. Further details on the application of DBS to GPe neurons is included below in the Application of DBS section. Thalamic neurons were modeled similarly, with the exception of excluding one of the calcium and one of the potassium currents. Striatal synaptic input to GPe neurons was modeled as a population of Poisson-distributed spike trains at 3 Hz.

Synapses

Synaptic connections between neurons were modeled by spike detectors in presynaptic neurons, coupled to synapses in postsynaptic neurons by a time delay. Individual synaptic currents, I_{syn}^{k}, were described by

$$I_{syn}^{k} = R_k \left(V_m - E_{rev}\right) \tag{2}$$

where I_{syn}^{k} is the kth synaptic current, R_k represents the kinetics of the onset decay of current following a presynaptic spike for synapse k, and E_{rev} is the reversal potential for the appropriate synapse type, excitatory AMPAergic synapses or inhibitory GABAergic synapses, respectively (Destexhe et al., 1994). The topology of synaptic connections between the network populations followed a random connectivity pattern, where the number of connections between each population and their associated synaptic transmission delay are detailed in **Table 13** of **Supplementary Material**. Full details regarding the synapse models and their parameter values can also be found in their original publication (Destexhe et al., 1994).

Application of DBS

The DBS electrode was modeled with three point source electrodes located in a homogeneous, isotropic medium of infinite extent and conductivity, σ, where a single point source was used to represent the application of extracellular DBS in a monopolar configuration, while the remaining two point source electrodes were used for simulating recording the local field potential with a bipolar, differential recording electrode. Propagation, inductive, and capacitive effects were assumed to be negligible, in accordance with the quasi-static approximation (Plonsey and Heppner, 1967; Bossetti et al., 2008).

The extracellular potential due DBS, $V_{e_i}(t)$, at each point located on the cortical collateral, i, located a distance r_i from the monopolar electrode was calculated as

$$V_{e_i}(t) = \frac{I_{DBS}(t)}{4\pi\sigma r_i} \tag{3}$$

where σ is the conductivity of gray matter, with the specified value 0.27 S/m (Latikka et al., 2001), I_{DBS} is the DBS current, simulated as a series of periodic cathodic rectangular current pulses of variable amplitude, frequency, and duration.

Cortical collaterals were randomly distributed around the monopolar electrode in a 6 mm by 6 mm square, using uniformly distributed random variables for their cartesian coordinates. The collaterals were oriented perpendicular to the cross-section, parallel to one another, and were not permitted to lie within the area covered by the cylindrical electrode lead of radius of 0.7 mm, **Figure 1B**.

The application of DBS to the model was simulated by stimulating afferent STN projections resulting in antidromic activation of the cortex and GPe and orthodromic activation of excitatory and inhibitory afferent projections to the STN. This resulted in disruption of activity in the cortex and GPe and net inhibition of the STN, consistent with experimental observations (Filali et al., 2004; Li et al., 2012; Milosevic et al., 2018). The extracellular potential due to DBS was applied to cortical collaterals projecting to the STN from descending layer V pyramidal tract fibers (Kang and Lowery, 2014). It was assumed that an equal percentage of cortical and GPe neurons were activated during stimulation. During DBS, the percentage of activated cortical neurons was calculated and an intracellular DBS current was injected to the corresponding percentage of activated GPe neurons, where cortical neurons were labeled as activated during 130 Hz DBS if their collateral firing rate increased above 60 Hz. The entrainment order of the GPe neurons was generated as a randomized sequence from the first to the hundredth neuron in the population, where ten percent activation corresponded to the intracellular DBS current being delivered to the first ten GPe neurons in the entrainment order.

Local Field Potential Simulation

The STN LFP recorded at the bipolar, recording electrode was estimated as the summation of the extracellular potentials due to the spatially distributed synaptic currents across the STN population (Rall and Shepherd, 1968; Lindén et al., 2011; Bedard and Destexhe, 2012; Einevoll et al., 2013). The x and y locations of STN neurons were randomly assigned as described previously, where the excitatory and inhibitory synapses for a given STN neuron were positioned at its x and y location, 250 μm from the bipolar electrode in the z direction. Assuming conduction within a purely resistive homogenous medium of infinite extent, the LFP at the bipolar electrode contacts was estimated as

$$LFP_i(t) = \frac{1}{4\pi\sigma}\sum_{j=1}^{M}\sum_{k=1}^{N}\frac{I_{syn_j}^{k}}{r_{ij}} \tag{4}$$

Where $LFP_i(t)$ is the LFP recorded by the ith bipolar, electrode contact at time t, $I_{syn_j}^{k}$ is the kth synaptic current of the jth STN neuron, and r_{ij} is the distance from the ith electrode contact to the kth synapse of the jth STN neuron assuming M neurons, each with N synapses.

Beta-Band LFP Activity

The average rectified value (ARV) of the beta-band LFP was calculated by full-wave rectifying the filtered LFP signal using a fourth order Chebyshev band-pass filter with an 8 Hz bandwidth, centered about the peak in the LFP power spectrum. The last 100 ms epoch of the rectified signal was discarded to remove filtering artifact before taking the mean value of the last 100 ms epoch of the resulting signal. A target value for the beta ARV was estimated as the 20th percentile of the beta ARV signal estimated for a thirty second epoch with DBS off. Cortical soma bias currents were modulated to vary the duration of beta activity within the network and simulated periods of high beta activity, or "beta bursts" periods, and low frequency activity. The duration of the beta burst periods were varied to simulate short, "healthy bursts" of beta activity, T_{HB}, and prolonged, "pathological bursts" of beta activity, T_{PB}. Healthy burst periods were defined as 100 ms in duration while the duration of pathological bursts were drawn from a uniform distribution between 600 and 1000 ms to capture variability of pathological burst durations (Tinkhauser et al., 2017a; Anidi et al., 2018). The time between beta bursts, the interburst period, was fixed at 300 ms. The beta modulation signal was generated by selecting a random number at the start of each beta burst. If the random number was less than, or equal to 0.5 the burst was labeled healthy and its duration assigned as the healthy burst duration. If the random number was greater than 0.5 it was labeled pathological and its duration was set appropriately, selecting a value from the uniform distribution of pathological burst durations. The probability of pathological burst occurrence in the model was a simplified representation of beta burst activity observed in PD. Research has observed that the probability of pathological burst occurrence is modulated in PD patients by factors such as medication and motor tasks (Tinkhauser et al., 2017a, 2020). Although not considered in this study, future studies may incorporate modulation of the burst probabilities to emulate variations in burst probabilities induced by these factors. During controller simulations, a beta ARV above the target corresponded to pathological beta activity, while a beta ARV below the target represented fluctuations of healthy beta activity. In practice, the target could be chosen based on an appropriate balance between symptom suppression and device power consumption. The controller input, e, at time t was calculated as the normalized error between the measured beta ARV, $b_{measured}$, and the target beta ARV, b_{target}, according to

$$e(t) = \frac{b_{measured}(t) - b_{target}}{b_{target}} \tag{5}$$

The controller operated with a sampling interval, T_s, of 20 ms, updating the modulated DBS parameter at each controller call. During amplitude modulation, the DBS frequency and pulse duration were fixed at 130 Hz and 60 μs, respectively, with the amplitude varying between 0 – 3 mA, where the upper amplitude bound was selected as the amplitude which minimized the beta ARV. During frequency modulation, the DBS amplitude and pulse duration were fixed at 1.5 mA and 60 μs, respectively, with the frequency varying between 0 – 250 Hz.

It has been observed in clinical studies of closed-loop DBS amplitude modulation that rapid changes in the stimulation amplitude can potentially induce stimulation induced side-effects, or paresthesia. To avoid unintentional paresthesia Little et al. (2013) ramped their DBS amplitude from its minimum to maximum value over a 250 ms period during closed-loop DBS. Following this approach, the maximum tolerable rate limit for the modulated DBS parameter during closed-loop DBS was defined as

$$R_L = \frac{u_{max} - u_{min}}{T_{Ramp}} \Rightarrow u_{\Delta_{R_L}} \cong \frac{T_s\,(u_{max} - u_{min})}{T_{Ramp}} \tag{6}$$

where R_L is the rate limit of the DBS parameter per second, T_{Ramp} is the duration of the ramping period, T_s is the controller sampling period, $u_{\Delta_{R_L}}$ is the maximum tolerable variation of the DBS parameter per controller call, and u_{max} and u_{min} are the maximum and minimum bounds of the modulated DBS parameter. Utilizing this, the maximum rate limit for DBS amplitude modulation was calculated as R_L = 0.012 A/s and R_L = 1000 Hz/s for frequency modulation.

Closed-Loop Control

On-off, dual-threshold, P and PI controllers were investigated for closed-loop control of the DBS amplitude as detailed below. P and PI control were also used to investigate closed-loop control of the DBS frequency. The closed-loop DBS methodology simulated by the model is summarized in **Figure 1C**.

On-Off Controller

The on-off controller utilized a single target and increased or decreased the stimulation amplitude toward its upper or lower bounds if the beta ARV was measured above or below the target, respectively. The on-off controller is defined as

$$u(t) = \begin{cases} u(t-1) + u_{\Delta_{R_L}} & if\ e(t) > 0 \\ u(t-1) - u_{\Delta_{R_L}} & if\ e(t) < 0 \end{cases}$$
$$where\ u_{min} \le u(t) \le u_{max} \tag{7}$$

where $u(t)$ is the modulated DBS parameter value, i.e., the stimulation amplitude, at time t, $u_{\Delta_{R_L}}$ is the rate limit of the DBS parameter at each controller call, and $e(t)$ is the controller error input signal at time t.

Dual-Threshold Controller

The dual-threshold controller utilized a target range where the upper bound of the target range was selected as the 20th percentile and the lower bound was selected as the 10th percentile of the beta ARV with DBS off. If the beta ARV was greater than the upper bound of the target range, the error was calculated with respect to the upper bound, while if it was less than the lower target range bound, the error was calculated with respect to the lower bound. The behavior of the dual-threshold controller is

defined as follows

$$u(t) = \begin{cases} u(t-1) + u_{\Delta_{R_L}} & if\ e(t) > 0 \\ u(t-1) & if\ e(t) = 0 \\ u(t-1) - u_{\Delta_{R_L}} & if\ e(t) < 0 \end{cases}$$
$$where\ u_{min} \leq u(t) \leq u_{max} \quad (8)$$

where the parameters are as described for the on-off controller.

PI and P Controllers

The PI controller utilized a single target and is defined as

$$u(t) = K_p \left(e(t) + \frac{1}{T_i} \int e(\tau)\, d\tau \right) \quad (9)$$

where $u(t)$ is the modulated DBS parameter value at time t, K_p is the controller proportional gain and T_i is the controller integral time constant. The PI proportional component contributes to the modulated DBS parameter at time t by scaling the current controller measured error while the integral component contributes to the controller output at time t by scaling the integrated history of the controller measured errors up to time t. Conditional integration of the integral component was used to prevent integral wind-up, where integration of the integral component was paused if the modulated DBS parameter reached its upper or lower parameter bounds. Inclusion of a derivative gain, which would make the controller a PID controller rather than a PI controller, was deemed undesirable because below target fluctuations in beta-band activity, which occur during healthy beta bursts, would contribute to the modulated stimulation parameter through the derivative term. The P controller was simulated by omission of the integral term in (9).

PI Controller Gain Tuning

The performance of PI controllers is heavily dependent on selection of appropriate values for the proportional gain, K_p, and integral time constant, T_i. The tuning process here is complicated by the constraint that the controller should not exceed the maximum tolerable rate limit of the modulated DBS parameter and that controller should act only on pathological beta bursts, while minimally effecting healthy beta bursts. The following tuning rules were thus designed for selecting PI controller parameters which adhere to these requirements.

Selection of Integral Time Constant

The duration of beta bursts in the model varied between healthy and pathological durations, T_{HB} and T_{PB} respectively. It was thus desirable to select the integral time constant longer than the duration of healthy bursts and shorter than the duration of pathological beta bursts. Therefore, the integral time constant, T_i, was selected as 0.2 s, so

$$T_{HB} \leq T_i \leq T_{PB} \quad (10)$$

Selection of Proportional Gain

The proportional gain, K_p, was selected so that the rate limit of the modulated DBS parameter was not exceeded. This was calculated by differentiation of Eq. (9) and setting the DBS parameter rate limit, R_L, as an inequality constraint

$$\frac{du(t)}{dt} = K_p \left(\frac{de(t)}{dt} + \frac{1}{T_i} e(t) \right) \leq R_L \quad (11)$$

Rearranging, K_p was defined as

$$K_{p_{max}} \leq \frac{R_L}{\max\left[\frac{de(t)}{dt}\right] + \frac{1}{T_i} \max\left[e(t)\right]} \quad (12)$$

The maximum value of $e(t)$ and $\frac{de(t)}{dt}$ were estimated from a 30 s simulation with no DBS. Substituting in the corresponding values allows the calculation of an upper bound value for K_p, $K_{p_{max}}$. Using these rules, the PI controller parameters were calculated as (K_p, T_i) = (0.23, 0.20) for the PI amplitude controller and (K_p, T_i) = (19.30, 0.20) for the PI frequency controller.

A parameter sweep was conducted to select the proportional gain term for the P controllers, where the gain selected minimized the resulting mean controller error. The K_p parameters were selected as 5.0 and 417 for the amplitude and frequency P controllers, respectively.

Simulation Details

The behavior of the model during continuous open-loop DBS was initially investigated with a constant level of beta activity within the network to characterize the relationship between the DBS waveform parameters and (i) the antidromic spike rate of cortical neurons detected at the cortical soma (ii) the beta-band power measured from the STN LFP and (iii) the firing rate of STN neurons. Ten simulations were conducted with initial random seeds varied between each simulation. Following this, a parameter sweep of the stimulation amplitude and frequency values was conducted to characterize the effect of parameter values on the LFP beta ARV. The parameter space was divided into 1024 linearly spaced sample points between the minimum and maximum bounds of the DBS amplitude, 0 – 3 mA, and frequency, 0 – 250 Hz. Each sample point corresponded to a 10 s simulation of open-loop DBS with the DBS parameters specified at that sample point. The performance of each closed-loop controller was then investigated in ten 30 s simulations where network beta activity was modulated as described in section 2.5. Ten independent beta modulation signals were generated, with each controller simulated for each modulation signal.

Controller performance was quantified in terms of the mean error of the half-wave rectified error signal, the mean power consumed by the controller and the controller suppression efficiency in each simulation. The mean power consumed by the controller was calculated as

$$Power\ Consumed = \frac{Z_E \int_0^{T_{sim}} I_{DBS}^2(t)\, dt}{T_{sim}} \quad (13)$$

where Z_E is the electrode impedance, assumed to be 0.5 KΩ, T_{sim} is the simulation duration and I_{DBS} is the DBS current. The suppression efficiency of the controller was quantified as the

percentage beta suppression per unit power consumed, with units %/μW. The controller suppression efficiency was thus defined as

$$\textit{Suppression Efficiency} = 100 \times \frac{\left(1 - \frac{1}{T_{sim}} \int_0^{T_{sim}} \frac{b_{DBSOff}(t) - b_{Controller}(t)}{b_{DBS\ Off}(t)} dt\right)}{\textit{Power Consumed}} \quad (14)$$

where $b_{DBS\ Off}$ is the beta ARV signal measured in the simulation when DBS was off, $b_{Controller}$ is the beta ARV signal measured from each controller simulation, and power consumed is the power consumed by the controller in the simulation, as defined in (13). The performance of the controllers was averaged over ten controller simulations, where each simulation utilized an independent cortical beta modulation signal.

A parameter sweep of the PI amplitude controller parameters was also conducted to investigate the effect of each parameter on the controller behavior. The sweep was conducted for K_p values linearly spaced between (0,6) and T_i values logarithmically spaced between (0,6). All simulations were run from the model steady state, where an initial model simulation was run for 6 s to allow the network behavior to reach steady state, before the controller performance was then evaluated on the following 10 s. The initial model parameters in steady state were saved and used as the starting point for all subsequent simulations.

The model was simulated in the NEURON simulation environment (Hines and Carnevale, 1997) and implemented in Python using the PyNN API package (Davison, 2008). The model was numerically integrated using the Crank-Nicholson method with a 0.01 ms timestep for all simulations. Simulations were run on the UCD Sonic high-performance computing cluster. Post-processing and signal analysis were done using custom scripts developed in MATLAB (The MathWorks, Inc., Natick, MA, United States).

RESULTS

The behavior of the model was first examined and compared with key features of the network behavior identified in experimental data from animal and human studies. Beta activity within the STN LFP, antidromic activation of cortical neurons and STN neural firing rates during continuous DBS with constant stimulation parameters were investigated. The firing rates of the cortical neurons were then modulated to simulate bursts of beta activity within the network and the performance of closed-loop DBS controllers to modulate either the DBS pulse amplitude or frequency were evaluated.

Network Behavior During Open-Loop DBS

Cortical desynchronization and GPe entrainment were observed in the model during open-loop stimulation, after 0 s in **Figures 2D,F**, where this behavior was qualitatively similar to these DBS effects reported in experimental studies of the parkinsonian rat model (Li et al., 2012; McConnell et al., 2012). Cortical antidromic firing rates matched well the observations of Li et al. (2012) where the rate of cortical antidromic spiking increased with increasing stimulation frequency to a maximum antidromic spike rate of 36.8 ± 0.6 Hz at a stimulation frequency of approximately 130 Hz, **Figure 2A**. Antidromic firing rate was defined as the number of successful stimulation-evoked antidromic activations detected at the soma of reliably stimulated cortical neurons where cortical collaterals were deemed to be "reliably" stimulated when they were activated by at least 90% of DBS pulses at the stimulation frequency. Further increasing the stimulation frequency resulted in a reduction in antidromic spike rate (Li et al., 2012), **Figure 2A**. In the model, DBS influenced the cortical interneurons as the antidromic activation spread through the cortical network through branching collaterals. This altered activation of inhibitory interneurons through antidromic activation of the cortical neurons is consistent with the hypothesis proposed by Li et al., where this behavior was suggested as a potential mechanism for the failure of frequency following at higher frequencies (Li et al., 2012).

Increasing the frequency of DBS resulted in a gradual reduction of the average STN neuron firing rate, **Figure 2B**. Complete suppression of STN neurons was observed in the model at 100 Hz and is consistent with STN firing rate behavior reported by Milosevic et al. (2018) during DBS in parkinsonian patients, **Figures 2B,E**. In the model, differences in the properties of excitatory, AMPAergic, and inhibitory, GABAergic, synapses leads to a net inhibition of STN neurons at higher frequencies. In experimental studies, it has been suggested that inhibitory GABAergic afferents comprising the majority of terminals on the STN soma, in combination with differing rates of synaptic depletion, may explain observations of a reduction in STN firing rates during high frequency stimulation (Milosevic et al., 2018).

The beta-band power in the LFP power spectrum decreased non-linearly with increasing DBS amplitude, **Figure 2C**. This relationship is similar to the reduction in LFP beta-band activity with increasing amplitude observed in clinical data from parkinsonian patients which can be well-described by higher order models (Davidson et al., 2016). Low stimulation amplitudes had little influence on LFP beta-band activity with amplitudes less than 1.1 mA unable to suppress beta-band power in the LFP power spectrum regardless of the stimulation frequency. Suitable stimulation amplitude and frequency values reduced the amplitude of LFP beta-band oscillations during DBS, **Figure 2G**, with the corresponding variation in the LFP power illustrated in **Figure 2H**. Prior to the application of DBS, there exists a narrowband peak in the LFP power spectrum at 25 Hz. During stimulation, the 25 Hz peak is suppressed, whilst a peak emerges in the LFP power spectrum at the 130 Hz stimulation frequency, **Figure 2H**. The sensitivity of the amplitude of beta-band oscillations to the stimulation parameters is presented in **Figure 3**, where stimulation amplitudes above 1.1 mA reduced the beta-band power in the LFP power spectrum by at least 50% for a broad range of stimulation frequencies above 40 Hz. This behavior is comparable with experimental data where Blumenfeld et al. reported the improvement of bradykinetic symptoms in freely moving parkinsonian patients during 60 Hz stimulation (Blumenfeld et al., 2016). Stimulation frequencies below 20 Hz

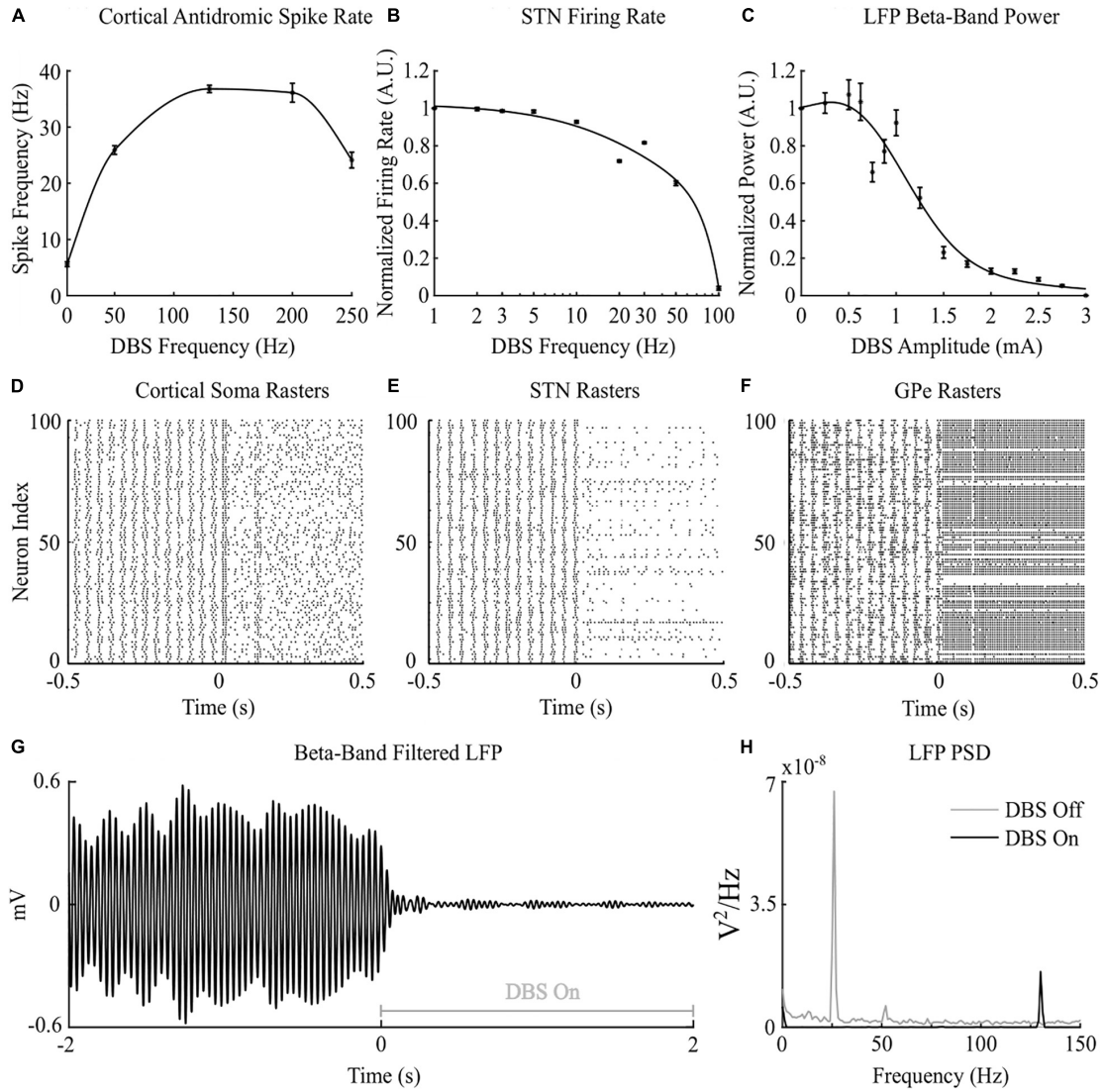

FIGURE 2 | Cortico-basal ganglia network behavior during open-loop DBS. **(A)** Antidromic cortical spike rate during DBS with 2 mA amplitude, 60 μs pulse duration and varying frequency. **(B)** Normalized STN firing rate during DBS with 3 mA amplitude, 60 μs pulse duration, and varying DBS frequency. **(C)** Normalized STN LFP beta-band (22 – 30 Hz) power during DBS with 130 Hz frequency, 60 μs pulse duration, and varying DBS amplitude. **(D–F)** Cortical soma, STN and GPe population raster plots when DBS is off and during open-loop DBS with 2.5 mA amplitude, 130 Hz and 60 μs pulse. At time 0 s, DBS is applied to the network causing desynchronization of cortical somas, STN suppression and GPe entrainment **(G)** Simulated beta-band filtered LFP before and during stimulation with 2.5 mA amplitude, 130 Hz frequency and 60 μs pulse duration. DBS is turned off prior to time 0 s and switched on at 0 s. **(H)** STN LFP power spectral densities when DBS is off (gray line) and during DBS with 2.5 mA amplitude, 130 Hz frequency and 60 μs pulse duration (black line). When DBS is off the LFP has a peak at 26 Hz in the beta frequency band. When DBS is applied to the network the 26 Hz beta-band peak is suppressed and a peak appears in the LFP power spectrum at the stimulation frequency, 130 Hz.

resulted in less than 30% reductions in beta-band power in the LFP power spectrum, indicating that low frequency stimulation is not effective at suppressing beta-band activity in the model, **Figure 3A**. Similar behavior was observed in Eusebio et al. (2008) where low frequency stimulation led to small performance improvements in a finger tapping task in PD patients if their baseline performance was below normal limits. Eusebio et al. (2008) also reported that when baseline performance was within normal limits low frequency stimulation resulted in worsened performance. This suggests that when beta-band activity is high, low frequency stimulation may not lead to a worsening of motor performance.

Closed-Loop Control of LFP Beta-Band Activity

Open-Loop DBS

Model simulations with DBS off demonstrated modulation of the STN LFP beta-band activity, with varying periods of short and prolonged beta, **Figure 4A**. The simulations without DBS were

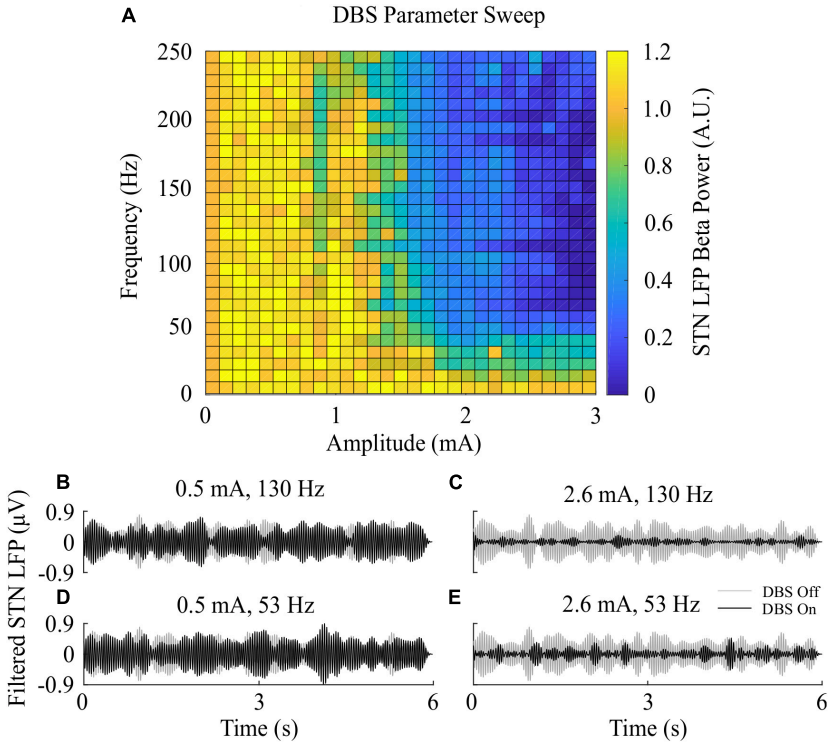

FIGURE 3 | Effect of open-loop DBS parameters on STN LFP beta-band power. **(A)** The STN LFP beta-band power was calculated during DBS with fixed 60 μs pulse duration and varying stimulation amplitude and frequency. The LFP beta-band power was normalized against the LFP beta-band power recorded when was DBS off. Stimulation amplitude and frequency values of 0 corresponded to the condition where DBS is off, resulting in an LFP beta-band power value of 1. **(B–E)** Examples of the STN LFP for varying stimulation amplitude and frequency values.

used to set a reference performance mean error value of 100% for the controller. Reference values for the mean power consumption and the suppression efficiency of the controllers were obtained from simulations with open-loop, constant DBS at 2.5 mA, 130 Hz, and 60 μs pulse duration. The mean power consumption value was used to set a reference mean power consumption value of 100%, with a corresponding mean error value of approximately zero (0.4%) and a suppression efficiency of 1.7%/μW, **Figure 4B**. These baseline performance values were used to compare the closed-loop DBS control strategies for keeping the beta ARV below the target ARV value.

Amplitude Modulation Controllers

The on-off controller resulted in a suppression efficiency of 8.3%/μW, a 63% reduction in mean error compared to the DBS off condition, and a 60% reduction in mean power consumed when compared with constant DBS. The dual-threshold controller resulted in a 5.9%/μW suppression efficiency and showed greater reduction in mean error, with a 70% decrease, but had a smaller mean power consumed reduction, with a 50% decrease, **Figures 5**, **8**.

The P controller displayed a 7.1%/μW suppression efficiency with 62% and 53% reductions in the mean error and mean power consumed, while the PI controller showed a 9.8%/μW suppression efficiency with 79% and 68% decreases in the mean error and mean power consumed respectively, **Figures 6**, **8**.

Frequency Modulation Controllers

The P controller showed a 3.5%/μW suppression efficiency, with 72% reduction in the mean error, but only a 1% decrease in the mean power consumed when compared with continuous DBS. Better performance was obtained using the PI controller with a 12.5%/μW suppression efficiency, and reductions in the mean error and mean power consumed of 83% and 75%, respectively, **Figures 7**, **8**.

The controller performances are summarized in **Figure 8**.

Effect of Varying PI Parameter Values

Having examined the PI controller using the derived parameters from the rule-tuning method, a sensitivity analysis was conducted to explore the parameters effect on controller performance. All the PI parameter value combinations tested as part of the controller parameter sensitivity analysis resulted in an approximately 55% reduction in the mean error compared to DBS off. The mean power consumed showed a reduction of at least of 40% for all combinations. A region of parameter space between K_p = (0.25, 1) and T_i = (0.02, 0.8) showed the greatest reduction in the mean error of 96% and a 60% reduction in power consumed at K_p = 0.75 and T_i = 0.19, **Figure 9**. A controller with relatively long T_i and low K_p resulted in slow performance, where the integral term slowly accumulated the error history and the modulated parameter varies slowly through the proportional term, **Figure 9C**. In comparison, a

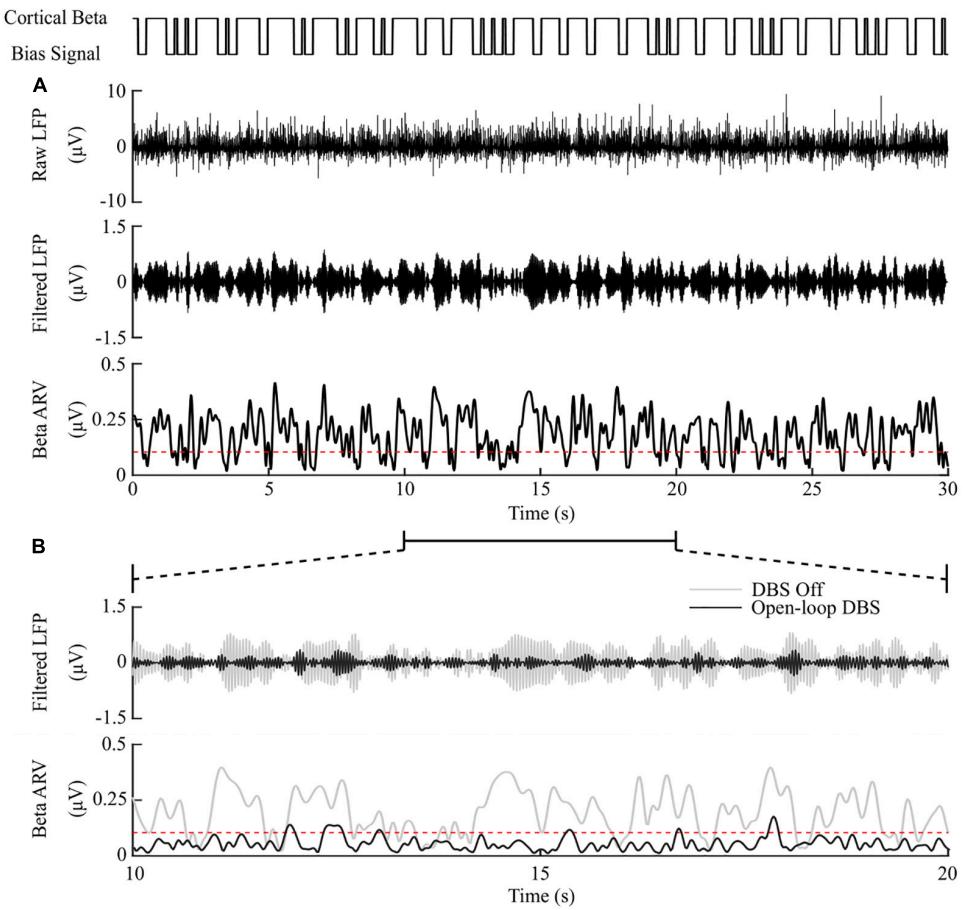

FIGURE 4 | DBS off and open-loop DBS. **(A)** Example of a 30 s simulation with DBS off. The cortical bias current signal, top panel, represents the temporal modulation of the intracellular cortical bias current applied to the cortical neuron somas to generate activity in the beta frequency band. The raw LFP, beta-band filtered LFP and beta ARV are displayed in the next three panels. The target level for the beta ARV is represented by the red dotted line in the beta ARV figure panel. **(B)** 10 s simulation period of DBS off and open-loop DBS with 2.5 mA amplitude, 130 Hz frequency and 60 μs pulse duration. The panels correspond to the 10 – 20 s simulation period from the panel **(A)**. DBS off is represented as the gray lines in the filtered LFP and beta ARV panels, while open-loop DBS is displayed in black.

controller with short T_i and relatively large K_p resulted in a fast controller response, where the error history accumulated quickly and the modulated parameter varied quickly between minimum and maximum values, **Figure 9E**. PI parameter values selected using the tuning rule presented in this study resulted in a controller response which maintained the beta activity at the target level while adhering to rate constraints on the DBS amplitude, **Figure 9D**.

DISCUSSION

A computational model is presented as an *in silico* testbed for developing and testing closed-loop DBS controllers designed to control LFP beta activity in PD. The model developed extends previous models by (i) incorporating the extracellular DBS electric field, (ii) captures both antidromic and orthodromic activation of afferent STN projections, (iii) simulates the synaptically generated STN LFPs and (iv) mimics temporal variation of network beta activity within the thalamo-cortico-basal ganglia loop. The model was first used to validate the performance of on-off and dual-threshold DBS amplitude closed-loop control schemes which have been tested clinically. P and PI controllers for modulating either the DBS amplitude or frequency were then investigated. PI controllers were found to outperform current clinically tested closed-loop controllers, displaying the greatest reductions in the controller mean error and power consumed during closed-loop DBS of the controllers examined.

Closed-Loop Control of DBS

The observed reduction in power during on-off control within the model is consistent with clinical studies which have reported a 50% reduction in mean power when compared with open-loop DBS (Little et al., 2013, 2016). This corresponded to a 6.6%/μW greater suppression efficiency value than open-loop DBS. In terms of the mean error, the dual-threshold controller performed better than on-off control, reducing the mean error by a further 7%, **Figure 8**. This resulted in a 50% reduction in

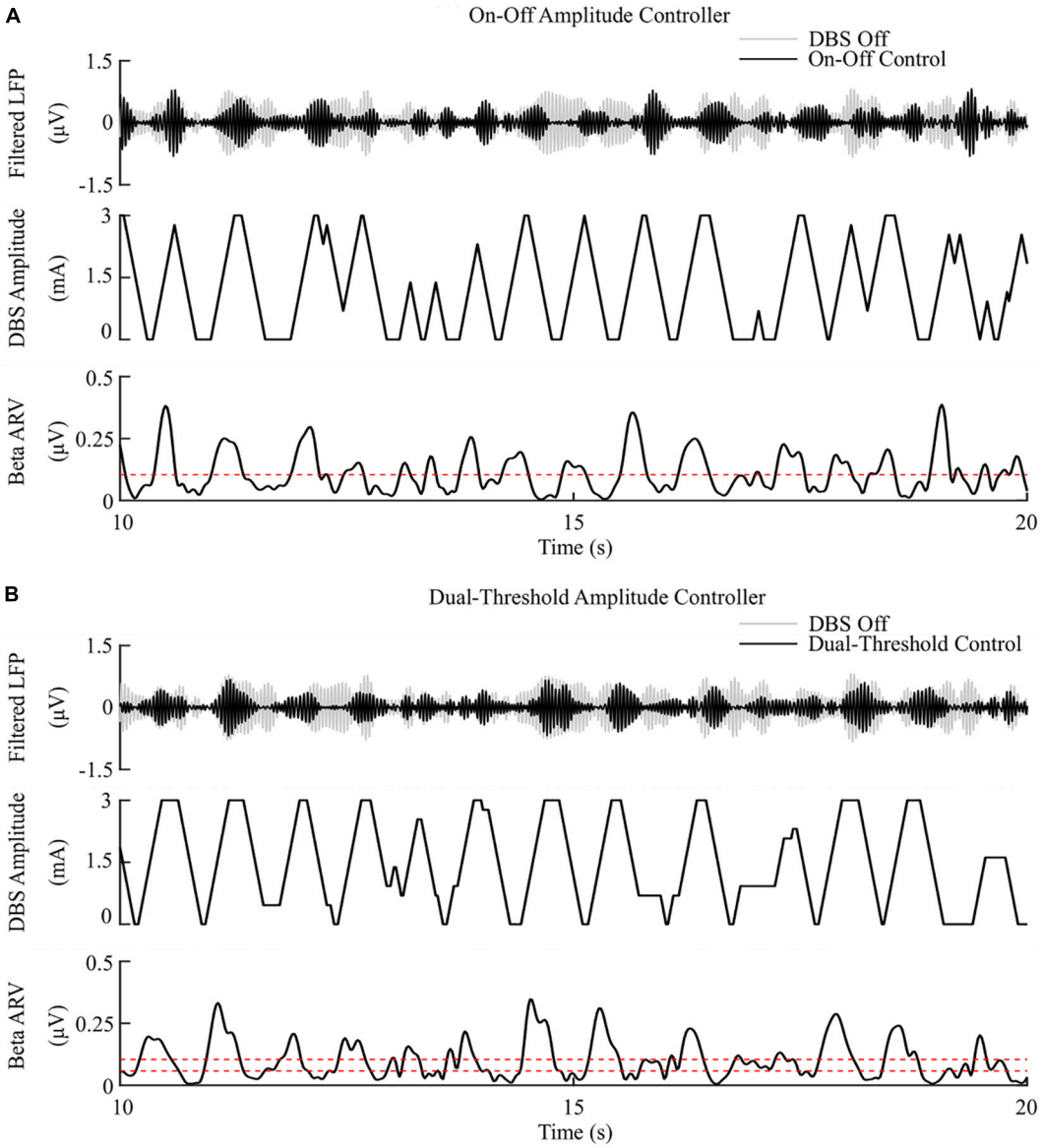

FIGURE 5 | On-off and dual-threshold amplitude control, fixed 130 Hz frequency and 60 μs pulse duration. **(A)** On-off DBS amplitude controller. During simulation, the on-off controller increases or decreases the DBS amplitude by a fixed amount at each controller call, toward its upper or lower amplitude bounds, if the beta ARV is measured above or below the target value, the dotted red line in the beta ARV panel. **(B)** Dual-threshold amplitude controller. The dual-threshold controller uses a target beta ARV range, represented by the two dotted red lines. If the beta ARV is measured above the upper target range value or below the lower target range value the stimulation amplitude is increased or decreased, respectively, by a fixed amount toward the upper or lower bounds of the stimulation amplitude. If the beta ARV lies in the target range the stimulation amplitude remains constant.

the mean power consumed compared to open-loop DBS which is again in-line with the clinically reported 56.86% reduction in energy delivered (Velisar et al., 2019). The improved performance maintaining the target beta level, at the cost of greater power consumption, resulted in a smaller suppression efficiency than on-off control and was due to the dual-threshold controller's ability to maintain a fixed stimulation amplitude when the beta ARV remained within its target bounds, **Figure 5B**. Without this, the on-off controller results in a higher error but consumes less power during stimulation, **Figures 5**, **8**.

The mean error of P amplitude control was comparable to on-off control, while its mean power consumed was comparable to that of dual-threshold control, with an intermediate suppression efficiency value between both on-off and dual threshold control, **Figures 6A**, **8**. However, to achieve this performance, the P controller exceeded the prespecified rate limit of 0.012 A/s with a maximum rate observed of 0.150 A/s, exceeding clinically recommended limits to avoid side-effects. The P controller behaved similar to on-off control without rate limiting, or "bang-bang" control, switching between its maximum and minimum

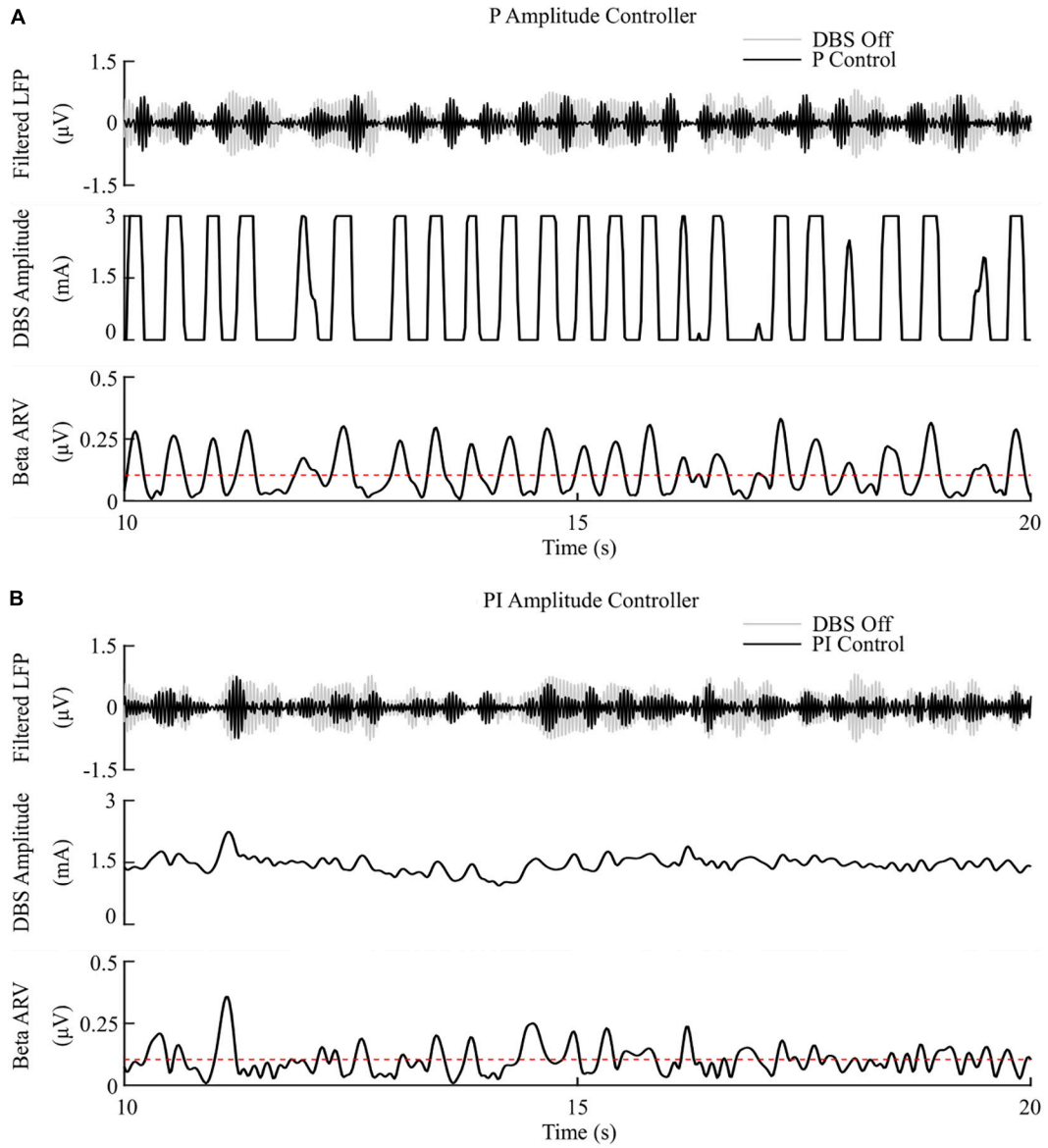

FIGURE 6 | P and PI amplitude control, fixed 130 Hz frequency and 60 μs pulse duration. **(A)** P amplitude controller. At each controller call, the stimulation amplitude is calculated as the current measured error value scaled by the controller gain, K_p. The controller stimulation amplitude is bounded between 0 – 3 mA, thus, negative error values correspond to turning DBS off. **(B)** PI amplitude controller. At each controller call, the stimulation amplitude is calculated as the summation of an integral term, i.e., the integration of the measured errors at previous controller calls, and the current measured error value, scaled by the integral time constant, T_i, and the proportional gain, K_p, respectively.

values when the beta ARV was above or below the target. If a rate limiter is implemented on the P controller, it will behave similar to the on-off controller presented in this study, where deviations of the control variable from the target result in the amplitude varying by the maximum tolerable rate at each controller call. Rosa et al. (2015) and Arlotti et al. (2018) varied the stimulation voltage linearly, or proportionally, in response to slow variations in LFP beta-band power, rather than with respect to the error between the instantaneous beta activity and a target as examined here. In that study, the control signal will not fall below zero, while the control signal in this study is negative when beta activity is below the target. Due to the controller output bound at zero, DBS switches off when the control signal is negative here, while this behavior would not be observed when directly measuring the LFP beta-band power as the control signal. This distinction between using slow variations in beta activity or the error of the instantaneous beta activity to a target is important to consider for clinical implementations of P controllers as this subtlety leads to disparate performances of the P controller.

The behavior of the P frequency controller was qualitatively similar to its amplitude counterpart, with the P frequency controller rapidly switching between its maximum and minimum

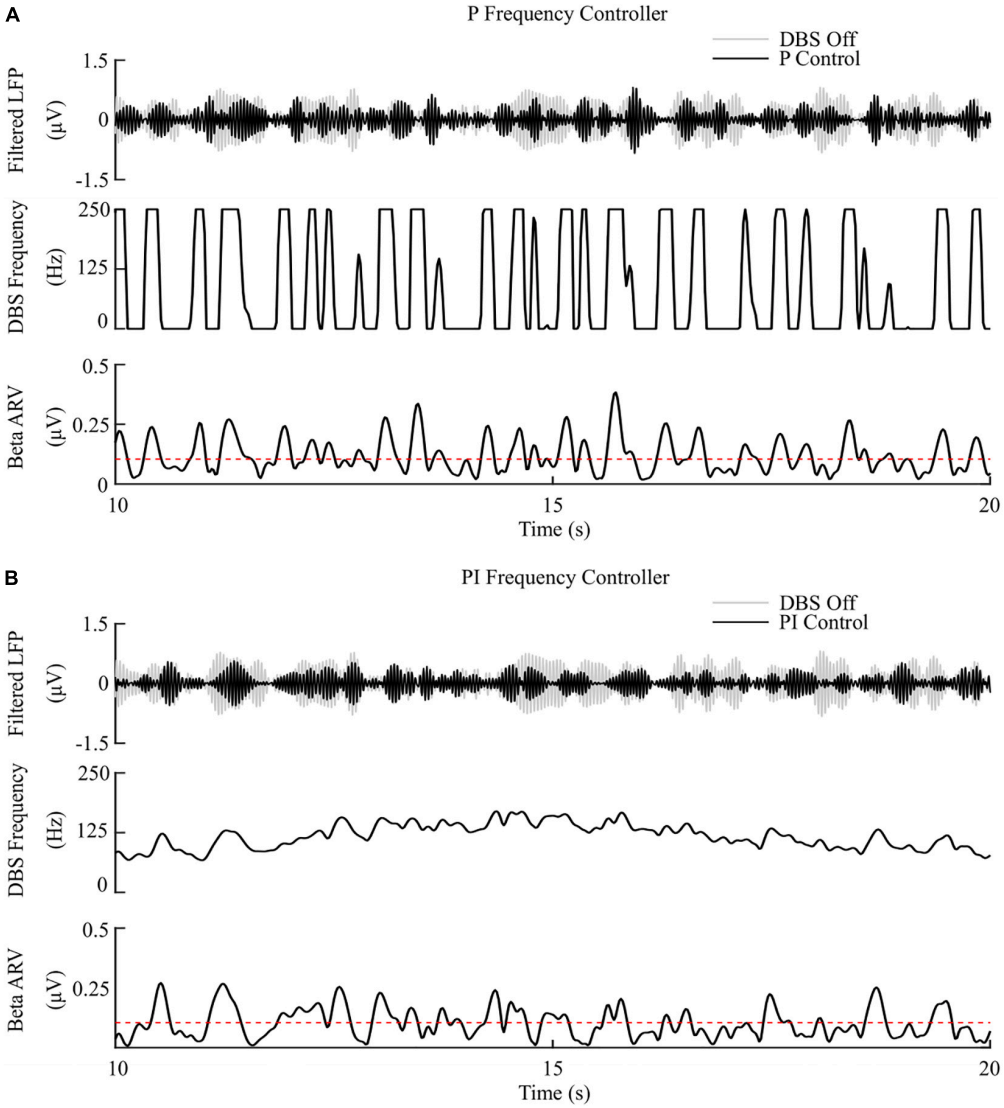

FIGURE 7 | P and PI frequency control, fixed 1.5 mA amplitude and 60 μs pulse duration. **(A)** P frequency controller. At each controller call, the stimulation frequency is calculated as the current measured error value scaled by the controller gain, K_p. The controller stimulation frequency is bounded between 0 – 250 Hz, thus, negative error values correspond to turning DBS off. **(B)** PI frequency controller. At each controller call, the stimulation frequency is calculated as the summation of an integral term, i.e., the integration of the measured errors at previous controller calls, and the current measured error value, scaled by the integral time constant, T_i, and the proportional gain, K_p, respectively.

values, **Figures 7A**, **8**. Although the P frequency controller reduced the mean error by 72%, the mean power consumed during stimulation was reduced by just 1% with only a 1.8%/μW increase in suppression efficiency when compared to open-loop DBS. The negligible change in mean power consumption was due to periods where the controller modulated the stimulation frequency between the minimum and maximum values of 0 Hz and 250 Hz. During these periods, the stimulation was either switched off or delivered close to double the number of stimulation pulses as during open-loop DBS or amplitude modulation, where the stimulation frequency was fixed at 130 Hz. With the stimulation amplitude fixed at 1.5 mA during frequency control this results in the same mean power consumed as open-loop DBS, **Figure 8**. The stimulation amplitude value selected for frequency control was chosen to allow use of the full span of stimulation frequencies, however it should be emphasized that by simply reducing this amplitude value or the controller's upper frequency bound would result in the controller consuming less power.

The PI controllers for amplitude and frequency performed with 79% and 83% reductions in mean error, and a 68 and 75% decrease in mean power consumed for amplitude and frequency modulation, respectively, **Figures 6B**, **7B**, **8**. The behaviors of both PI controllers were qualitatively similar, with the integral term increasing the modulated stimulation parameter to a value where it was effective at maintaining the beta ARV around

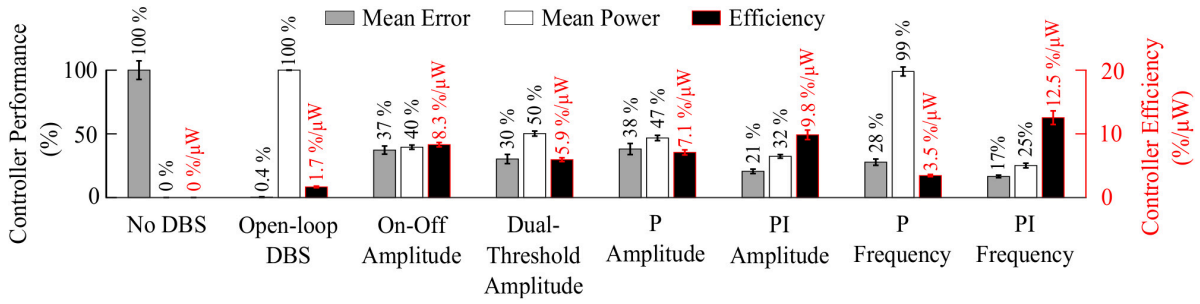

FIGURE 8 | Summary of performance of closed-loop controllers. The normalized mean error (±std), normalized mean power consumed (±std) and suppression efficiency (±std), averaged across ten 30 s simulations with ten independent beta modulation signals, of each closed-loop controller is presented. The mean error and mean power consumed are normalized against the mean error and mean power consumed when DBS is off or applied in open-loop with 2.5 mA amplitude, 130 Hz frequency and 60 μs pulse duration for each cortical beta modulation signal. The PI frequency controller performed best overall with a suppression efficiency of 12.5%/μW, reducing the mean error by 83% and the mean power consumed during stimulation by 75%.

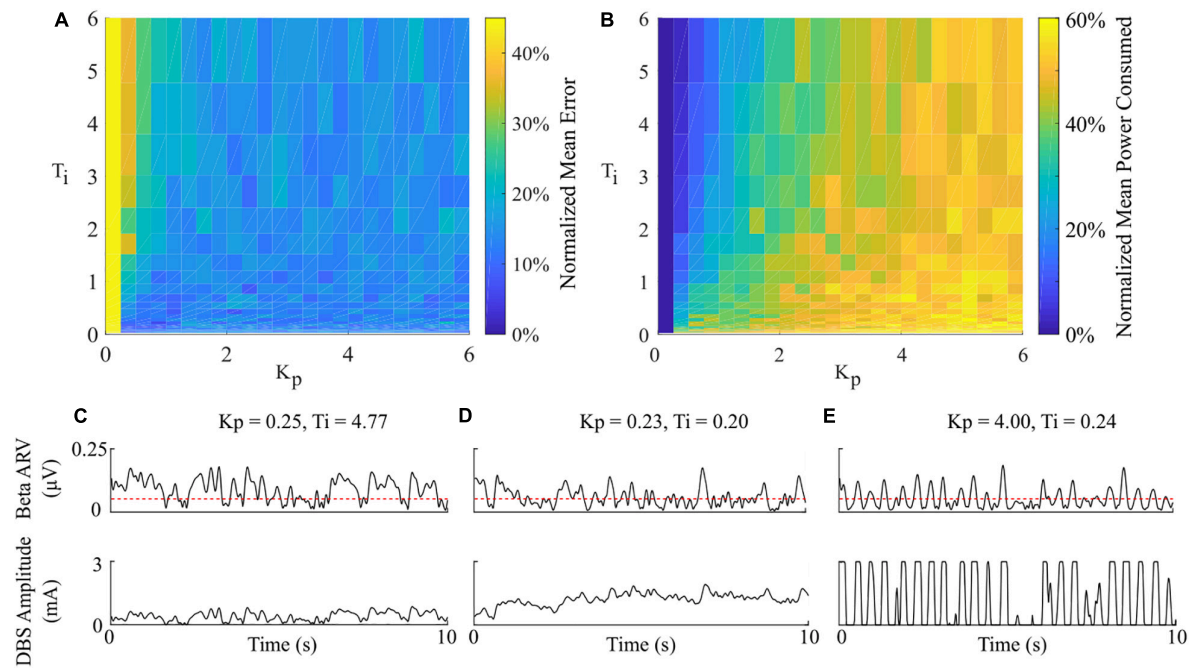

FIGURE 9 | Effect of PI parameters on amplitude controller performance. **(A)** Normalized PI controller error vs. PI parameters. **(B)** Normalized PI controller power consumed vs. PI parameters. **(C–E)** Beta ARV and DBS amplitude due to varying T_i and K_p controller parameter values.

the target level with 9.8%/μW and 12.5%/μW suppression efficiency values for the amplitude and frequency controllers respectively, **Figures 6B**, **7B**. Once at this value, fluctuations in the beta ARV resulted in proportional variation of the stimulation parameter to maintain the beta level. The integral term essentially overcomes the initial non-linearity between the DBS parameter and the beta ARV, where a minimal value must be reached before the stimulation becomes effective. This is achieved by increasing the stimulation parameter to a region of parameter space where its relationship with the beta ARV is approximately linear, **Figures 2C**, **3A**. The integral term varies the modulated stimulation parameter based on the error history in the system, whereas the on-off, dual-threshold and P controllers act only on the current error of the system at each controller call and thus have no memory of previous errors. For the on-off and dual-threshold controllers this can result in slow performance when the beta ARV exceeds the target and DBS is off. When this occurs, the DBS parameter must increase beyond the non-linear region of its parameter space before stimulation becomes effective, which may take several controller calls. The gain of each P controller was selected as the gain value which minimized the mean error in a parameter sweep over the proportional gain values. The resulting P controllers were fast and essentially avoided the non-linear region of the stimulation parameter space by quickly switching the stimulation parameter between its maximum and minimum values but did

so at a rate that may be greater than is clinically desirable, **Figures 6A**, **7A**.

Overall, the PI frequency controller performed best, yielding superior suppression efficiency and the greatest reductions in mean error and mean power consumed of the controllers examined. Interestingly, the controller settled around a mean stimulation frequency of 125 Hz, which is in line with high frequency stimulation values utilized clinically. When modulating about this point the stimulation frequency varied between 80 – 160 Hz over the course of the simulation, with DBS remaining effective throughout the simulation, **Figure 7B**. Clinical research has observed similar behavior where a 60 Hz DBS frequency was able to improve bradykinesia in PD patients (Blumenfeld et al., 2016). The authors hypothesized that 140 Hz high frequency stimulation and the lower frequency 60 Hz stimulation signals effectively decoupled the cortico-STN hyperdirect pathway during stimulation. The model presented in this study supports this hypothesis, with cortical desynchronization and STN firing rate suppression occurring during effective DBS, **Figures 2D,E**. It is again important to note however, that due to the non-linear relationship between DBS parameters and network beta activity there is a threshold stimulation amplitude value which must be reached before DBS frequency modulation becomes effective, in the model at approximately 1.1 mA, **Figure 2C**.

All closed-loop controllers tested yielded greater beta suppression efficiency values than open-loop DBS in this study. This metric suggests that closed-loop DBS provides better performance than open-loop DBS for maintaining beta-band activity in the STN LFP. However, how well this metric corresponds to actual symptom suppression would need to be examined further *in vivo* as suppression of beta-band activity in the model may not directly relate to *in vivo* symptom suppression. Another point of consideration for the controller results presented is that although the duration of LFP beta activity has been tested as a control variable for the on-off controller (Tinkhauser et al., 2017a), it has not been tested for either the dual-threshold or proportional controllers to date. Clinical studies investigating the dual-threshold and proportional controllers were limited to utilizing LFP beta band power as their control variables due to delays in the neurostimulator used during their studies (Arlotti et al., 2018; Velisar et al., 2019). This limitation is anticipated to be overcome in the next generation of neurostimulator devices and thus it will be feasible to utilize the duration of LFP beta activity as a control variable in the future (Velisar et al., 2019). With this in mind, the sampling frequency of controllers used in this study was selected so that fluctuations in the network beta band activity could be observed, with the controllers attempting to target only prolonged duration network beta activity.

PI Controller Parameters

Suitable control parameters were identified using a rule-tuning approach which takes advantage of features of the biomarker that can be readily estimated clinically to derive suitable PI controller parameters, i.e., the threshold duration of pathological beta-band activity and constraints on the rate-of-change of stimulation parameters. When clinically tuning a PI controller for closed-loop DBS, the presented tuning rule could be used initially to coarsely tune the controller, before further fine-tuning is achieved by varying the controller parameters using visual feedback of the modulated stimulation parameter. The intention here is to allow the clinician to further fine-tune the controller response if necessary, for example slowly increasing K_p to increase the speed of the controller. Identifying suitable controller parameters could also be achieved in the model by utilizing an optimization technique and a suitable objective function, where the objective function captures the clinical considerations of the system. This approach, however, would require sampling multiple points in the parameter space which may not be practical clinically. An alternative controller design approach is to linearize the input-output relationship of the system using a model and subsequently design a controller which meets the required closed-loop system response (Santaniello et al., 2011; Liu et al., 2017a; Yang et al., 2018; Su et al., 2019). This approach was used by Santaniello et al. (2011), Liu et al. (2017a), and Su et al. (2019) where autoregressive models were derived from spiking neuron models. To normalize aberrant neural activity during parkinsonian tremor, Santaniello et al. (2011) designed a minimum variance controller, while Liu et al. (2017a) implemented a generalized predictive control algorithm. In contrast, Su et al. (2019) optimized the parameters of a discrete PI controller to track a dynamic target of beta-band power which may be associated with fluctuations of the oscillatory activity during voluntary movement. Haddock et al. (2017) illustrated the potential of the approach by deriving an autoregressive model of the relationship between DBS amplitude and parkinsonian tremor from patient data, using the identified model as part of a model predictive controller for parkinsonian tremor (Haddock et al., 2017). The benefit of the autoregressive model approach is that derived models can be simulated in real-time and thus facilitate the use of advanced control techniques which require use of an internal model (Francis and Wonham, 1976). The disadvantage, however, is that it does not provide insight into the underlying physiological behavior of the system or its dynamics. Another drawback is that the identified model is valid only for the system operating region at which it was identified. Due to the dynamic, non-linear nature of the parkinsonian neuromuscular system, identified models or controller parameters which were initially suitable during controller tuning may become unsuitable or provide suboptimal performance during different tasks, times throughout the day or as the disease progresses. Advanced adaptive techniques which automatically update autoregressive model coefficients or controller gains may be required to overcome this limitation (Cameron and Seborg, 1984; Santaniello et al., 2011; Chaillet et al., 2017). Nevertheless, the PI parameter rule-tuning approach presented in this study provides improved performance over currently tested closed-loop controllers, is simple to implement in a clinical setting and adheres to clinical considerations.

Model Considerations

Previous modeling studies of closed-loop DBS have investigated LFP derived measures of network beta-band activity (Daneshzand et al., 2018; Popovych and Tass, 2019). However,

only a small number of models have simulated the coupled DBS electric field and network model during stimulation (Santaniello et al., 2011; Grant and Lowery, 2013). In the absence of a description of the electric field in the surrounding tissue during DBS, modeling studies are limited to simulating frequency modulation where the DBS waveform is injected as an intracellular current (Kang and Lowery, 2013; Holt et al., 2016; Popovych and Tass, 2019; Su et al., 2019). To develop clinically relevant closed-loop algorithms requires a model which captures modulation of the targeted networks behavior due to variations in both stimulation amplitude and frequency. The thalamocortical population model presented by Santaniello et al. (2011) incorporates both the DBS electric field and LFP simulation for investigating aberrant neural activity during parkinsonian tremor, but does not incorporate synaptic coupling between the neuron population, injecting a suprathreshold intracellular stimulus to neurons to drive spiking activity. As this modeling approach does not capture network interactions due to DBS it would, therefore, be unsuitable for modeling the full cortico-basal ganglia loop included here. Previous modeling studies of the cortico-basal ganglia during DBS have investigated network and DBS effects separately. Kang and Lowery (2013) and Kumaravelu et al. (2016) modeled the cortico-basal ganglia using networks of single compartment neuron models, however, these models did not include simulation of extracellular DBS, the LFP or antidromic stimulation of afferent STN inputs. Grant and Lowery (2013) simulated extracellular DBS and the STN LFP, where the cortico-basal ganglia was modeled using a single compartment neuron model for the STN population and neural mass type models for the remaining network neuron populations. The model thus, does not capture complex network interactions such as antidromic activation of afferent STN inputs during stimulation. Antidromic activation of cortical afferent STN inputs and extracellular DBS was captured in a network model in Kang and Lowery (2014), however, the model did not capture antidromic activation of GPe neurons during stimulation or simulation of the LFP. The model presented in this study builds on these previous modeling studies by incorporating extracellular DBS, STN LFP simulation, antidromic and orthodromic DBS effects and temporal variation of beta-band activity in a network model of the cortico-basal ganglia.

The controllers examined in this study represent the current landscape of clinically tested closed-loop DBS algorithms. The PI controller investigated is a natural extension of current state of the art closed-loop DBS research, and is the most commonly used control algorithm in industrial applications due to its robust performance in a wide range of operating conditions and its functional simplicity. PID-type controllers have been investigated in previous modeling studies of closed-loop DBS for PD (Gorzelic et al., 2013; Su et al., 2019). However, these studies utilized control variables which are not readily accessible during clinical studies, where Gorzelic et al. (2013) investigated using both thalamic reliability and GPi synaptic conductance as control variables and Su et al. (2019) used the beta-band power of GPi neuron spike times. Thus, direct comparisons between these studies and clinical research is difficult. The model presented here utilizes an LFP derived measure of network beta-band oscillatory activity analogous to that employed during clinical closed-loop DBS research, and thus facilitates a direct comparison between the performance of controllers tested in the model and in clinical research.

The purpose of the model is to provide an *in silico* testbed for developing and testing closed-loop DBS strategies which can be directly related to clinical closed-loop DBS research. Although this study focused on using an LFP derived measure of network beta-band activity for closed-loop DBS there is extensive research in identifying alternative biomarkers for PD symptoms and stimulation side-effects, such as entropy (Dorval et al., 2010; Dorval and Grill, 2014; Anderson et al., 2015; Syrkin-Nikolau et al., 2017; Fleming and Lowery, 2019), phase-amplitude coupling (de Hemptinne et al., 2013; De Hemptinne et al., 2015), coherence (Al-Fatly, 2019) and gamma-band activity (Swann et al., 2016, 2018) based measures. A restriction of the presented model is that it does not capture the neural mechanisms which lead to parkinsonian tremor, a hallmark symptom of PD, and is thus unsuited for investigating tremor-based closed-loop DBS (Hirschmann et al., 2017; Helmich, 2018). However, with this in mind, it is anticipated that future controllers which employ alternative methods or advanced techniques, such as low frequency stimulation (Fasano and Lozano, 2014; Blumenfeld et al., 2016) or phase-based (Tass, 2003; Tass et al., 2012; Holt et al., 2016, 2019), linear-delayed feedback (Popovych and Tass, 2019) and optogenetic stimulation methods (Detorakis et al., 2015), may still be applicable when alternative biomarkers are implemented as control variables.

Limitations

While the model captures several key features of the parkinsonian cortico-basal ganglia during DBS, it remains an approximation of the true system. Due to the limited access to the cortico-basal ganglia structures and data available in literature, the individual neuron models and their overall network behavior was based on parameters and observations recorded from both parkinsonian animal models and human patients from separate studies. Antidromic activation of cortical neurons and GPe neuron entrainment during DBS were fitted to data from experiments using parkinsonian rat models (Li et al., 2012; McConnell et al., 2012). Indirect evidence of antidromic activation and desynchronization of cortical neurons has also been observed in PD patients during STN DBS (Kuriakose et al., 2010; Weiss et al., 2015). The STN firing rate suppression and LFP beta-band power reduction during DBS were based observations in patient data (Davidson et al., 2016; Milosevic et al., 2018. In the model, antidromic propagation of cortical neurons was simulated and an equivalent proportion of GPe neurons were antidromically activated by the injection of an intracellular current. In practice, the level of antidromic activation of cortical and GPe neurons may differ, potentially altering DBS efficacy. In contrast to the model presented, Kumaravelu et al. (2016) used experimental data from 6-OHDA lesioned rats to parameterize their network model. In the presented model, synaptic coupling was tuned,

and the cortical population was biased to induce increased beta-band oscillatory activity within the network, with striatal input to the basal ganglia network being simplified as a population of poisson-distributed spike trains. Omission of a physiological model of the indirect pathway, and thus striatal input to the basal ganglia network, is a limitation of the presented model with research suggesting that the striatum may also play a key role in the development of pathological oscillations in the basal ganglia network during PD (McCarthy et al., 2011; Feingold et al., 2015; Corbit et al., 2016). As the primary focus of this study, however, was not the role of the striatum in the generation of network pathological oscillations, its contribution to the network was simplified. A recent study investigating the role of exogenous cortical and striatal beta inputs to the STN-GPe network using detailed multi-compartment models of STN and GPe showed that resonant beta-band oscillatory activity within the STN-GPe loop becomes phase-locked to exogenous cortical beta inputs and that this behavior can be further promoted by striatal input to the loop with the correct phase (Koelman and Lowery, 2019). The network presented here captures the exogenous cortical patterning of the STN-GPe loop but omits possible further amplification of the beta-band oscillatory activity due to the striatum. This behavior could be incorporated into the model through the inclusion of the indirect pathway.

Two consequences of the simplification of the cortical and cortico-striatal networks, and the inability to accurately capture all of the complex network interactions which lead to elevated beta-band activity in PD is that the oscillatory activity does not fully represent the activity observed in clinical studies, with this activity also reemerging relatively quickly post-stimulation in the model. In clinical studies, elevated STN beta-band power is observed as a broad peak which shows long-lasting attenuation post-stimulation, with attenuation dependent on the stimulation duration (Temperli et al., 2003; Bronte-Stewart et al., 2009). This behavior is not captured by the model, where beta-band activity appears as a narrow-band peak in the LFP power spectrum, **Figure 2H**, which reemerges quickly when DBS is off or ineffective. Finally, the electrode was simulated as a point source electrode within an ideal homogeneous resistive volume conducting medium of infinite extent. Computational studies have previously utilized the quasi-static approximation and demonstrated the point source approximation to be a valid prediction of the activation of a population of neurons during DBS when calculating the number and spatial distribution of neurons activated around the electrode (Zhang and Grill, 2010). However, in reality, the electrode geometry, its encapsulation tissue, and the capacitive and dispersive electrical properties of the tissue can have a substantial effect on the electric field distribution, on the DBS waveform shape in the surrounding tissue and the activation thresholds of target neurons during DBS (McIntyre et al., 2004; Grant and Lowery, 2010). These limitations may be mitigated by incorporating more realistic geometrical, anatomical and electrical properties of the tissues through coupling of the model to anatomically realistic finite element models. In keeping with studies regarding the spatial reach of the LFP, it was assumed that the LFP signal was dominated by synaptic currents from neurons in a plane in the vicinity of the recording electrode (Lindén et al., 2011), however, in reality these synaptic currents would be distributed as a three-dimensional cloud around the recording electrode (Lempka and McIntyre, 2013), with a contribution from more distal neurons outside of the STN network also being possible. The spatial distribution of synapses within the dendritic structures and neuron morphology can further influence the LFP, however, these were not considered here.

CONCLUSION

A computational model of closed-loop control of DBS for PD is presented that simulates (i) the extracellular DBS electric field, (ii) antidromic and orthodromic activation of STN afferent fibers, (iii) the LFP detected at non-stimulating contacts on the DBS electrode and (iv) temporal variation of beta-band activity within the cortico-basal ganglia network. The model captures experimentally reported network behavior during open-loop DBS and provides an *in silico* testbed for developing novel, clinically relevant closed-loop control strategies for updating either the amplitude or frequency of DBS. Clinically tested on-off and dual-threshold amplitude controllers were examined and exhibited reductions in power consumption comparable with their clinically reported performance. A new rule-tuning method for selecting PI controller parameters to target prolonged, pathological duration beta-band oscillatory activity whilst adhering to clinical constraints was developed. The resulting performance of both amplitude and frequency PI controllers outperformed the current clinically investigated on-off and dual-threshold closed-loop amplitude control strategies in terms of both power consumption and their ability to maintain the LFP derived measure of network beta-band activity at a target value. As the available technology progresses toward a new generation of closed-loop or adaptive stimulators, it is likely that testing novel control algorithms in computational models, such as those presented here, will become a valuable first step prior to clinical testing in patients.

DATA AVAILABILITY STATEMENT

The datasets generated for this study are available on request to the corresponding author, while the model source code will be made available from the ModelDB (https://senselab.med.yale.edu/modeldb/) upon article publication.

AUTHOR CONTRIBUTIONS

JF and ML designed the study experiments, interpreted the results of experiments, prepared the figures, and edited, revised, and approved the final version of the manuscript. JF performed the experiments, analyzed the data and drafted the manuscript.

ED and ML conceived the preliminary experiment design. All experiments were performed in the Neuromuscular Systems Laboratory in University College Dublin, Ireland.

FUNDING

This work was supported by the European Research Council (ERC) under the European Union's Horizon 2020 Research and Innovation Programme (Grant ERC-2014-CoG-646923-DBSModel).

ACKNOWLEDGMENTS

This manuscript has been released as a pre-print at BioRxiv (Fleming et al., 2019).

SUPPLEMENTARY MATERIAL

The Supplementary Material for this article can be found online at: https://www.frontiersin.org/articles/10.3389/fnins.2020.00166/full#supplementary-material

REFERENCES

Al-Fatly, B. (2019). Coherence: a unifying mechanism of deep brain stimulation. *J. Neurophysiol.* 121, 1–3. doi: 10.1152/jn.00563.2018

Anderson, C. J., Sheppard, D. T., Huynh, R., Anderson, D. N., Polar, C. A., and Dorval, A. D. (2015). Subthalamic deep brain stimulation reduces pathological information transmission to the thalamus in a rat model of parkinsonism. *Front. Neural Circ.* 9:1–11. doi: 10.3389/fncir.2015.00031

Anidi, C., O'Day, J. J., Anderson, R. W., Afzal, M. F., Syrkin-Nikolau, J., Velisar, A., et al. (2018). Neuromodulation targets pathological not physiological beta bursts during gait in Parkinson's disease. *Neurobiol. Dis.* 120, 107–117. doi: 10.1016/j.nbd.2018.09.004

Arlotti, M., Marceglia, S., Foffani, G., Volkmann, J., Lozano, A. M., Moro, E., et al. (2018). Eight-hours adaptive deep brain stimulation in patients with Parkinson disease. *Neurology* 90, e971–e976. doi: 10.1212/WNL.0000000000005121

Baudrexel, S., Witte, T., Seifried, C., von Wegner, F., Beissner, F., Klein, J. C., et al. (2011). Resting state fMRI reveals increased subthalamic nucleus–motor cortex connectivity in Parkinson's disease. *Neuroimage* 55, 1728–1738. doi: 10.1016/J.NEUROIMAGE.2011.01.017

Bedard, C., and Destexhe, A. (2012). "Modeling local field potentials and their interaction with the extracellular medium," in *Handbook of Neural Activity Measurement*, eds R. Brette, and A. Destexhe (Cambridge: Cambridge University Press).

Beurrier, C., Congar, P., Bioulac, B., and Hammond, C. (1999). Subthalamic nucleus neurons switch from single-spike activity to burst-firing mode. *J. Neurosci.* 19, 599–609. doi: 10.1523/JNEUROSCI.19-02-00599.1999

Bevan, M. D., Francis, C. M., and Bolam, J. P. (1995). The glutamate-enriched cortical and thalamic input to neurons in the subthalamic nucleus of the rat: convergence with GABA-positive terminals. *J. Comp. Neurol.* 361, 491–511. doi: 10.1002/cne.903610312

Blumenfeld, Z., Koop, M. M., Prieto, T. E., Shreve, L. A., Velisar, A., Quinn, E. J., et al. (2016). Sixty-hertz stimulation improves bradykinesia and amplifies subthalamic low-frequency oscillations. *Mov. Disord.* 32, 80–88. doi: 10.1002/mds.26837

Bossetti, C. A., Birdno, M. J., and Grill, W. M. (2008). Analysis of the quasi-static approximation for calculating potentials generated by neural stimulation. *J. Neural Eng.* 5, 44–53. doi: 10.1088/1741-2560/5/1/005

Bronte-Stewart, H., Barberini, C., Koop, M. M., Hill, B. C., Henderson, J. M., and Wingeier, B. (2009). The STN beta-band profile in Parkinson's disease is stationary and shows prolonged attenuation after deep brain stimulation. *Exp. Neurol.* 215, 20–28. doi: 10.1016/j.expneurol.2008.09.008

Cameron, F., and Seborg, D. E. (1984). "A self-tuning controller with a pid structure," in *Real Time Digital Control Application*, ed. A. Alonso-Concheiro (Amsterdam: Elsevier), 613–622. doi: 10.1016/s1474-6670(17)62721-6

Carron, R., Chaillet, A., Filipchuk, A., Pasillas-Lépine, W., and Hammond, C. (2013). Closing the loop of deep brain stimulation. *Front. Syst. Neurosci.* 7:1–18. doi: 10.3389/fnsys.2013.00112

Chaillet, A., Detorakis, G. I., Palfi, S., and Senova, S. (2017). Robust stabilization of delayed neural fields with partial measurement and actuation. *Automatica* 83, 262–274. doi: 10.1016/j.automatica.2017.05.011

Chan, C. S., Shigemoto, R., Mercer, J. N., and Surmeier, D. J. (2004). HCN2 and HCN1 channels govern the regularity of autonomous pacemaking and synaptic resetting in globus pallidus neurons. *J. Neurosci.* 24, 9921–9932. doi: 10.1523/JNEUROSCI.2162-04.2004

Corbit, V. L., Whalen, T. C., Zitelli, K. T., Crilly, S. Y., Rubin, J. E., and Gittis, A. H. (2016). Pallidostriatal projections promote β oscillations in a dopamine-depleted biophysical network model. *J. Neurosci.* 36, 5556–5571. doi: 10.1523/JNEUROSCI.0339-16.2016

Daneshzand, M., Faezipour, M., and Barkana, B. D. (2018). Robust desynchronization of Parkinson's disease pathological oscillations by frequency modulation of delayed feedback deep brain stimulation. *PLoS One* 13:1–22. doi: 10.1371/journal.pone.0207761

Davidson, C. M., de Paor, A. M., Cagnan, H., and Lowery, M. M. (2016). Analysis of oscillatory neural activity in series network models of Parkinson's disease during deep brain stimulation. *IEEE Trans. Biomed. Eng.* 63, 86–96. doi: 10.1109/TBME.2015.2475166

Davison, A. P. (2008). PyNN: a common interface for neuronal network simulators. *Front. Neuroinform.* 2:1–10. doi: 10.3389/neuro.11.011.2008

de Hemptinne, C., Ryapolova-Webb, E. S., Air, E. L., Garcia, P. A., Miller, K. J., Ojemann, J. G., et al. (2013). Exaggerated phase-amplitude coupling in the primary motor cortex in Parkinson disease. *Proc. Natl. Acad. Sci. U.S.A.* 110, 4780–4785. doi: 10.1073/pnas.1214546110

De Hemptinne, C., Swann, N. C., Ostrem, J. L., Ryapolova-Webb, E. S., San Luciano, M., Galifianakis, N. B., et al. (2015). Therapeutic deep brain stimulation reduces cortical phase-amplitude coupling in Parkinson's disease. *Nat. Neurosci.* 18, 779–786. doi: 10.1038/nn.3997

Destexhe, A., Mainen, Z. F., and Sejnowski, T. J. (1994). An efficient method for computing synaptic conductances based on a kinetic model of receptor binding. *Neural Comput.* 6, 14–18. doi: 10.1162/neco.1994.6.1.14

Detorakis, G. I., Chaillet, A., Palfi, S., and Senova, S. (2015). Closed-loop stimulation of a delayed neural fields model of parkinsonian STN-GPe network: a theoretical and computational study. *Front. Neurosci.* 9:1–16. doi: 10.3389/fnins.2015.00237

Dorval, A. D., and Grill, W. M. (2014). Deep brain stimulation of the subthalamic nucleus reestablishes neuronal information transmission in the 6-OHDA rat model of parkinsonism. *J. Neurophysiol.* 111, 1949–1959. doi: 10.1152/jn.00713.2013

Dorval, A. D., Kuncel, A. M., Birdno, M. J., Turner, D. A., and Grill, W. M. (2010). Deep brain stimulation alleviates parkinsonian bradykinesia by regularizing pallidal activity. *J. Neurophysiol.* 104, 911–921. doi: 10.1152/jn.00103.2010

Einevoll, G. T., Kayser, C., Logothetis, N. K., and Panzeri, S. (2013). Modelling and analysis of local field potentials for studying the function of cortical circuits. *Nat. Rev. Neurosci.* 14, 770–785. doi: 10.1038/nrn3599

Eusebio, A., Chen, C. C., Lu, C. S., Lee, S. T., Tsai, C. H., Limousin, P., et al. (2008). Effects of low-frequency stimulation of the subthalamic nucleus on movement in Parkinson's disease. *Exp. Neurol.* 209, 125–130. doi: 10.1016/j.expneurol.2007.09.007

Fasano, A., and Lozano, A. M. (2014). The FM/AM world is shaping the future of deep brain stimulation. *Mov. Disord.* 29:1327. doi: 10.1002/mds.25968

Feingold, J., Gibson, D. J., Depasquale, B., and Graybiel, A. M. (2015). Bursts of beta oscillation differentiate postperformance activity in the striatum and motor cortex of monkeys performing movement tasks. *Proc. Natl. Acad. Sci. U.S.A.* 112, 13687–13692. doi: 10.1073/pnas.1517629112

Fernández-Seara, M. A., Mengual, E., Vidorreta, M., Castellanos, G., Irigoyen, J., Erro, E., et al. (2015). Resting state functional connectivity of the subthalamic

nucleus in Parkinson's disease assessed using arterial spin-labeled perfusion fMRI. *Hum. Brain Mapp.* 36, 1937–1950. doi: 10.1002/hbm.22747

Filali, M., Hutchison, W. D., Palter, V. N., Lozano, A. M., and Dostrovsky, J. O. (2004). Stimulation-induced inhibition of neuronal firing in human subthalamic nucleus. *Exp. Brain Res.* 156, 274–281. doi: 10.1007/s00221-003-1784-y

Fleming, J. E., Dunn, E., and Lowery, M. M. (2019). Simulation of closed-loop deep brain stimulation control schemes for suppression of pathological beta oscillations in Parkinson ' s disease. *bioRxiv* [Preprint]

Fleming, J. E., and Lowery, M. M. (2019). Changes in neuronal entropy in a network model of the cortico-basal ganglia during deep brain stimulation. *Conf. Proc. IEEE Eng. Med. Biol. Soc.* 2019, 5172–5175. doi: 10.1109/embc.2019.8857440

Foust, A. J., Yu, Y., Popovic, M., Zecevic, D., and McCormick, D. A. (2011). Somatic membrane potential and Kv1 channels control spike repolarization in cortical axon collaterals and presynaptic boutons. *J. Neurosci.* 31, 15490–15498. doi: 10.1523/JNEUROSCI.2752-11.2011

Francis, B. A., and Wonham, W. M. (1976). The internal model principle of control theory. *Automatica* 12, 457–465. doi: 10.1016/0005-1098(76)90006-6

Gorzelic, P., Schiff, S. J., and Sinha, A. (2013). Model-based rational feedback controller design for closed-loop deep brain stimulation of Parkinson's disease. *J. Neural Eng.* 10:026016. doi: 10.1088/1741-2560/10/2/026016

Grant, P. F., and Lowery, M. M. (2010). Effect of dispersive conductivity and permittivity in volume conductor models of deep brain stimulation. *IEEE Trans. Biomed. Eng.* 57, 2386–2393. doi: 10.1109/TBME.2010.2055054

Grant, P. F., and Lowery, M. M. (2013). Simulation of cortico-basal ganglia oscillations and their suppression by closed loop deep brain stimulation. *IEEE Trans. Neural Syst. Rehabil. Eng.* 21, 584–594. doi: 10.1109/TNSRE.2012.2202403

Haddock, A., Velisar, A., Herron, J., Bronte-Stewart, H., and Chizeck, H. J. (2017). "Model predictive control of deep brain stimulation for Parkinsonian tremor," in *Int. IEEE/EMBS Conf. Neural Eng. NER* (Shanghai: IEEE), 358–362.

Hahn, P. J., and McIntyre, C. C. (2010). Modeling shifts in the rate and pattern of subthalamopallidal network activity during deep brain stimulation. *J. Comput. Neurosci.* 28, 425–441. doi: 10.1007/s10827-010-0225-8

Haidar, I., Pasillas-Lépine, W., Chaillet, A., Panteley, E., Palfi, S., and Senova, S. (2016). Closed-loop firing rate regulation of two interacting excitatory and inhibitory neural populations of the basal ganglia. *Biol. Cybern.* 110, 55–71. doi: 10.1007/s00422-015-0678-y

Helmich, R. C. (2018). The cerebral basis of Parkinsonian tremor: a network perspective. *Mov. Disord.* 33, 219–231. doi: 10.1002/mds.27224

Hines, M. L., and Carnevale, N. T. (1997). The NEURON simulation environment hines and carnevale: the NEURON simulation environment. *Neural Comput.* 9, 1–24.

Hirschmann, J., Schoffelen, J. M., Schnitzler, A., and van Gerven, M. A. J. (2017). Parkinsonian rest tremor can be detected accurately based on neuronal oscillations recorded from the subthalamic nucleus. *Clin. Neurophysiol.* 128, 2029–2036. doi: 10.1016/j.clinph.2017.07.419

Holt, A. B., Kormann, E., Gulberti, A., Pötter-Nerger, M., McNamara, C. G., Cagnan, H., et al. (2019). Phase-dependent suppression of beta oscillations in parkinson's disease patients. *J. Neurosci.* 39, 1119–1134. doi: 10.1523/JNEUROSCI.1913-18.2018

Holt, A. B., Wilson, D., Shinn, M., Moehlis, J., and Netoff, T. I. (2016). Phasic burst stimulation: a closed-loop approach to tuning deep brain stimulation parameters for parkinson's disease. *PLoS Comput. Biol.* 12:1–14. doi: 10.1371/journal.pcbi.1005011

Humphries, M. D., Stewart, R. D., and Gurney, K. N. (2006). A physiologically plausible model of action selection and oscillatory activity in the basal ganglia. *J. Neurosci.* 26, 12921–12942. doi: 10.1523/JNEUROSCI.3486-06.2006

Kang, G., and Lowery, M. M. (2013). Interaction of oscillations, and their suppression via deep brain stimulation, in a model of the cortico-basal ganglia network. *IEEE Trans. Neural Syst. Rehabil. Eng.* 21, 244–253. doi: 10.1109/TNSRE.2013.2241791

Kang, G., and Lowery, M. M. (2014). Effects of antidromic and orthodromic activation of STN afferent axons during DBS in Parkinson's disease: a simulation study. *Front. Comput. Neurosci.* 8:32. doi: 10.3389/fncom.2014.00032

Kayahara, T., and Nakano, K. (1996). Pallido-thalamo-motor cortical connections: an electron microscopic study in the macaque monkey. *Brain Res.* 706, 337–342. doi: 10.1016/0006-8993(95)01338-5

Koelman, L. A., and Lowery, M. M. (2019). Beta-band resonance and intrinsic oscillations in a biophysically detailed model of the subthalamic nucleus-globus pallidus network. *Front. Comput. Neurosci.* 13:77. doi: 10.3389/FNCOM.2019.00077

Kühn, A. A., Kempf, F., Brücke, C., Doyle, L. G., Martinez-Torres, I., Pogosyan, A., et al. (2008). High-frequency stimulation of the subthalamic nucleus suppresses oscillatory β activity in patients with Parkinson's disease in parallel with improvement in motor performance. *J. Neurosci.* 28, 6165–6173. doi: 10.1523/JNEUROSCI.0282-08.2008

Kühn, A. A., Tsui, A., Aziz, T., Ray, N., Brücke, C., Kupsch, A., et al. (2009). Pathological synchronisation in the subthalamic nucleus of patients with Parkinson's disease relates to both bradykinesia and rigidity. *Exp. Neurol.* 215, 380–387. doi: 10.1016/J.EXPNEUROL.2008.11.008

Kumaravelu, K., Brocker, D. T., and Grill, W. M. (2016). A biophysical model of the cortex-basal ganglia-thalamus network in the 6-OHDA lesioned rat model of Parkinson's disease. *J. Comput. Neurosci.* 40, 207–229. doi: 10.1007/s10827-016-0593-9

Kuriakose, R., Saha, U., Castillo, G., Udupa, K., Ni, Z., Gunraj, C., et al. (2010). The nature and time course of cortical activation following subthalamic stimulation in parkinson's disease. *Cereb. Cortex* 20, 1926–1936. doi: 10.1093/cercor/bhp269

Lalo, E., Thobois, S., Sharott, A., Polo, G., Mertens, P., Pogosyan, A., et al. (2008). Patterns of bidirectional communication between cortex and basal ganglia during movement in patients with Parkinson disease. *J. Neurosci.* 28, 3008–3016. doi: 10.1523/JNEUROSCI.5295-07.2008

Latikka, J., Kuurne, T., and Eskola, H. (2001). Conductivity of living intracranial tissues. *Phys. Med. Biol.* 46, 1611–1616. doi: 10.1088/0031-9155/46/6/302

Lempka, S. F., and McIntyre, C. C. (2013). Theoretical analysis of the local field potential in deep brain stimulation applications. *PLoS One* 8:e59839. doi: 10.1371/journal.pone.0059839

Li, Q., Ke, Y., Chan, D. C. W., Qian, Z.-M., Yung, K. K. L., Ko, H., et al. (2012). Therapeutic deep brain stimulation in parkinsonian rats directly influences motor cortex. *Neuron* 76, 1030–1041. doi: 10.1016/J.NEURON.2012.09.032

Lindén, H., Tetzlaff, T., Potjans, T. C., Pettersen, K. H., Grün, S., Diesmann, M., et al. (2011). Modeling the spatial reach of the LFP. *Neuron* 72, 859–872. doi: 10.1016/j.neuron.2011.11.006

Little, S., Beudel, M., Zrinzo, L., Foltynie, T., Limousin, P., Hariz, M., et al. (2016). Bilateral adaptive deep brain stimulation is effective in Parkinson's disease. *J. Neurol. Neurosurg. Psychiatry* 87, 717–721.

Little, S., Pogosyan, A., Neal, S., Zavala, B., Zrinzo, L., Hariz, M., et al. (2013). Adaptive deep brain stimulation in advanced Parkinson disease. *Ann. Neurol.* 74, 449–457. doi: 10.1002/ana.23951

Litvak, V., Jha, A., Eusebio, A., Oostenveld, R., Foltynie, T., Limousin, P., et al. (2011). Resting oscillatory cortico-subthalamic connectivity in patients with Parkinson's disease. *Brain* 134, 359–374. doi: 10.1093/brain/awq332

Liu, C., Wang, J., Li, H., Lu, M., Deng, B., Yu, H., et al. (2017a). Closed-loop modulation of the pathological disorders of the basal ganglia network. *IEEE Trans. Neural Netw. Learn. Syst.* 28, 371–382. doi: 10.1109/TNNLS.2015.2508599

Liu, C., Zhou, C., Wang, J., Fietkiewicz, C., and Loparo, K. A. (2020). The role of coupling connections in a model of the cortico-basal ganglia-thalamocortical neural loop for the generation of beta oscillations. *Neural Netw.* 123, 381–392. doi: 10.1016/j.neunet.2019.12.021

Liu, C., Zhu, Y., Liu, F., Wang, J., Li, H., Deng, B., et al. (2017b). Neural mass models describing possible origin of the excessive beta oscillations correlated with Parkinsonian state. *Neural Netw.* 88, 65–73. doi: 10.1016/j.neunet.2017.01.011

Mallet, N., Pogosyan, A., Márton, L. F., Bolam, J. P., Brown, P., and Magill, P. J. (2008). Parkinsonian beta oscillations in the external globus pallidus and their relationship with subthalamic nucleus activity. *J. Neurosci.* 28, 14245–14258. doi: 10.1523/JNEUROSCI.4199-08.2008

Marreiros, A. C., Cagnan, H., Moran, R. J., Friston, K. J., and Brown, P. (2013). Basal ganglia–cortical interactions in Parkinsonian patients. *Neuroimage* 66, 301–310. doi: 10.1016/J.NEUROIMAGE.2012.10.088

McCarthy, M. M., Moore-Kochlacs, C., Gu, X., Boyden, E. S., Han, X., and Kopell, N. (2011). Striatal origin of the pathologic beta oscillations in Parkinson's

disease. *Proc. Natl. Acad. Sci. U.S.A.* 108, 11620–11625. doi: 10.1073/pnas.1107748108

McConnell, G. C., So, R. Q., Hilliard, J. D., Lopomo, P., and Grill, W. M. (2012). Effective deep brain stimulation suppresses low-frequency network oscillations in the basal ganglia by regularizing neural firing patterns. *J. Neurosci.* 32, 15657–15668. doi: 10.1523/JNEUROSCI.2824-12.2012

McHaffie, J. G., Stanford, T. R., Stein, B. E., Coizet, V., and Redgrave, P. (2005). Subcortical loops through the basal ganglia. *Trends Neurosci.* 28, 401–407. doi: 10.1016/j.tins.2005.06.006

McIntyre, C. C., Mori, S., Sherman, D. L., Thakor, N. V., and Vitek, J. L. (2004). Electric field and stimulating influence generated by deep brain stimulation of the subthalamic nucleus. *Clin. Neurophysiol.* 115, 589–595. doi: 10.1016/j.clinph.2003.10.033

Milosevic, L., Kalia, S. K., Hodaie, M., Lozano, A. M., Fasano, A., Popovic, M. R., et al. (2018). Neuronal inhibition and synaptic plasticity of basal ganglia neurons in Parkinson's disease. *Brain* 141, 177–190. doi: 10.1093/brain/awx296

Moran, R. J., Mallet, N., Litvak, V., Dolan, R. J., Magill, P. J., Friston, K. J., et al. (2011). Alterations in brain connectivity underlying beta oscillations in parkinsonism. *PLoS Comput. Biol.* 7:e1002124. doi: 10.1371/journal.pcbi.1002124

Nambu, A., and Tachibana, Y. (2014). Mechanism of parkinsonian neuronal oscillations in the primate basal ganglia: some considerations based on our recent work. *Front. Syst. Neurosci.* 8:74. doi: 10.3389/fnsys.2014.00074

Nambu, A., Tokuno, H., and Takada, M. (2002). Functional significance of the cortico–subthalamo–pallidal 'hyperdirect' pathway. *Neurosci. Res.* 43, 111–117. doi: 10.1016/s0168-0102(02)00027-5

Nevado-Holgado, A. J., Terry, J. R., and Bogacz, R. (2010). Conditions for the generation of beta oscillations in the subthalamic nucleus-globus pallidus network. *J. Neurosci.* 30, 12340–12352. doi: 10.1523/JNEUROSCI.0817-10.2010

Otsuka, T., Abe, T., Tsukagawa, T., and Song, W.-J. (2004). Conductance-based model of the voltage-dependent generation of a plateau potential in subthalamic neurons. *J. Neurophysiol.* 92, 255–264. doi: 10.1152/jn.00508.2003

Packer, A. M., McConnell, D. J., Fino, E., and Yuste, R. (2013). Axo-dendritic overlap and laminar projection can explain interneuron connectivity to pyramidal cells. *Cereb. Cortex* 23, 2790–2802. doi: 10.1093/cercor/bhs210

Parent, A., and Hazrati, L.-N. (1995a). Functional anatomy of the basal ganglia. I. The cortico-basal ganglia-thalamo-cortical loop. *Brain Res. Rev.* 20, 91–127. doi: 10.1016/0165-0173(94)00007-C

Parent, A., and Hazrati, L. N. (1995b). Functional anatomy of the basal ganglia: the place of the subthalamic nucleus and external pallidum in basal ganglia circuitry. *Brain Res. Rev.* 20, 128–154. doi: 10.1016/0165-0173(94)00008-D

Pasillas-Lepine, W., Haidar, I., Chaillet, A., and Panteley, E. (2013). "Closed-loop deep brain stimulation based on firing-rate regulation," in *Proceedings 6th IEEE EMBS Conference on Neural Engineering* (San Diego, CA: IEEE), 166–169.

Plonsey, R., and Heppner, D. B. (1967). Considerations of quasi-stationarity in electrophysiological systems. *Bull. Math. Biophys.* 29, 657–664. doi: 10.1007/BF02476917

Popovych, O. V., and Tass, P. A. (2019). Adaptive delivery of continuous and delayed feedback deep brain stimulation – A computational study. *Sci. Rep.* 9, 1–17.

Pospischil, M., Toledo-Rodriguez, M., Monier, C., Piwkowska, Z., Bal, T., Frégnac, Y., et al. (2008). Minimal Hodgkin–Huxley type models for different classes of cortical and thalamic neurons. *Biol. Cybern.* 99, 427–441. doi: 10.1007/s00422-008-0263-8

Priori, A., Foffani, G., Rossi, L., and Marceglia, S. (2013). Adaptive deep brain stimulation (aDBS) controlled by local field potential oscillations. *Exp. Neurol.* 245, 77–86. doi: 10.1016/j.expneurol.2012.09.013

Rall, W., and Shepherd, G. M. (1968). Theoretical reconstruction of field potentials and dendrodendritic synaptic interactions in olfactory bulb. *J. Neurophysiol.* 31, 884–915. doi: 10.1152/jn.1968.31.6.884

Rosa, M., Arlotti, M., Ardolino, G., Cogiamanian, F., Marceglia, S., Di Fonzo, A., et al. (2015). Adaptive deep brain stimulation in a freely moving parkinsonian patient. *Mov. Disord.* 30, 1003–1005. doi: 10.1002/mds.26241

Rubin, J. E., and Terman, D. (2004). High frequency stimulation of the subthalamic nucleus eliminates pathological thalamic rhythmicity in a computational model. *J. Comput. Neurosci.* 16, 211–235. doi: 10.1023/B:JCNS.0000025686.47117.67

Sadek, A. R., Magill, P. J., and Bolam, J. P. (2007). A single-cell analysis of intrinsic connectivity in the rat globus pallidus. *J. Neurosci.* 27, 6352–6362. doi: 10.1523/JNEUROSCI.0953-07.2007

Santaniello, S., Fiengo, G., Glielmo, L., and Grill, W. M. (2011). Closed-loop control of deep brain stimulation: a simulation study. *IEEE Trans. Neural Syst. Rehabil. Eng.* 19, 15–24. doi: 10.1109/TNSRE.2010.2081377

Sharott, A., Magill, P. J., Harnack, D., Kupsch, A., Meissner, W., and Brown, P. (2005). Dopamine depletion increases the power and coherence of β-oscillations in the cerebral cortex and subthalamic nucleus of the awake rat. *Eur. J. Neurosci.* 21, 1413–1422. doi: 10.1111/j.1460-9568.2005.03973.x

Shink, E., and Smith, Y. (1995). Differential synaptic innervation of neurons in the internal and external segments of the globus pallidus by the GABA- and glutamate-containing terminals in the squirrel monkey. *J. Comp. Neurol.* 358, 119–141. doi: 10.1002/cne.903580108

Sidibé, M., Bevan, M. D., Bolam, J. P., and Smith, Y. (1997). Efferent connections of the internal globus pallidus in the squirrel monkey: I. Topography and synaptic organization of the pallidothalamic projection. *J. Comp. Neurol.* 382, 323–347. doi: 10.1002/(SICI)1096-9861(19970609)382:3<323::AID-CNE3<3.3.CO;2-6

Silberstein, P., Oliviero, A., Di Lazzaro, V., Insola, A., Mazzone, P., and Brown, P. (2005a). Oscillatory pallidal local field potential activity inversely correlates with limb dyskinesias in Parkinson's disease. *Exp. Neurol.* 194, 523–529. doi: 10.1016/j.expneurol.2005.03.014

Silberstein, P., Pogosyan, A., Kühn, A. A., Hotton, G., Tisch, S., Kupsch, A., et al. (2005b). Cortico-cortical coupling in Parkinson's disease and its modulation by therapy. *Brain* 128, 1277–1291. doi: 10.1093/brain/awh480

Smith, Y., Bolam, J. P., and Krosigk, M. (1990). Topographical and synaptic organization of the GABA-containing pallidosubthalamic projection in the rat. *Eur. J. Neurosci.* 2, 500–511. doi: 10.1111/j.1460-9568.1990.tb00441.x

Su, F., Kumaravelu, K., Wang, J., and Grill, W. M. (2019). Model-based evaluation of closed-loop deep brain stimulation controller to adapt to dynamic changes in reference signal. *Front. Neurosci.* 13:1–13. doi: 10.3389/fnins.2019.00956

Swann, N. C., de Hemptinne, C., Miocinovic, S., Qasim, S., Wang, S. S., Ziman, N., et al. (2016). Gamma oscillations in the hyperkinetic state detected with chronic human brain recordings in Parkinson's disease. *J. Neurosci.* 36, 6445–6458. doi: 10.1523/JNEUROSCI.1128-16.2016

Swann, N. C., De Hemptinne, C., Thompson, M. C., Miocinovic, S., Miller, A. M., Gilron, R., et al. (2018). Adaptive deep brain stimulation for Parkinson's disease using motor cortex sensing. *J. Neural Eng.* 15, 046006. doi: 10.1088/1741-2552/aabc9b

Syrkin-Nikolau, J., Koop, M. M., Prieto, T., Anidi, C., Afzal, M. F., Velisar, A., et al. (2017). Subthalamic neural entropy is a feature of freezing of gait in freely moving people with Parkinson's disease. *Neurobiol. Dis.* 108, 288–297. doi: 10.1016/j.nbd.2017.09.002

Tachibana, Y., Iwamuro, H., Kita, H., Takada, M., and Nambu, A. (2011). Subthalamo-pallidal interactions underlying parkinsonian neuronal oscillations in the primate basal ganglia. *Eur. J. Neurosci.* 34, 1470–1484. doi: 10.1111/j.1460-9568.2011.07865.x

Tachibana, Y., Kita, H., Chiken, S., Takada, M., and Nambu, A. (2008). Motor cortical control of internal pallidal activity through glutamatergic and GABAergic inputs in awake monkeys. *Eur. J. Neurosci.* 27, 238–253. doi: 10.1111/j.1460-9568.2007.05990.x

Tass, P. A. (2003). Letter to the Editor A model of desynchronizing deep brain stimulation with a demand-controlled coordinated reset of neural subpopulations. *Biol. Cybern.* 88, 81–88. doi: 10.1007/s00422-003-0425-7

Tass, P. A., Qin, L., Hauptmann, C., Dovero, S., Bezard, E., Boraud, T., et al. (2012). Coordinated reset has sustained aftereffects in Parkinsonian monkeys. *Ann. Neurol.* 72, 816–820. doi: 10.1002/ana.23663

Temperli, P., Ghika, J., Villemure, J. G., Burkhard, P. R., Bogousslavsky, J., and Vingerhoets, F. J. G. (2003). How do parkinsonian signs return after discontinuation of subthalamic DBS? *Neurology* 60, 78–81. doi: 10.1212/WNL.60.1.78

Terman, D., Rubin, J. E., Yew, A. C., and Wilson, C. J. (2002). Activity patterns in a model for the subthalamopallidal network of the basal ganglia. *J. Neurosci.* 22, 2963–2976. doi: 10.1523/JNEUROSCI.22-07-02963.2002

Tinkhauser, G., Pogosyan, A., Little, S., Beudel, M., Herz, D. M., Tan, H., et al. (2017a). The modulatory effect of adaptive deep brain stimulation on beta

bursts in Parkinson's disease. *Brain* 140, 1053–1067. doi: 10.1093/brain/aw x010

Tinkhauser, G., Pogosyan, A., Tan, H., Herz, D. M., Kühn, A. A., and Brown, P. (2017b). Beta burst dynamics in Parkinson's disease off and on dopaminergic medication. *Brain* 140, 2968–2981. doi: 10.1093/brain/aw x252

Tinkhauser, G., Torrecillos, F., Pogosyan, A., Mostofi, A., Bange, M., Fischer, P., et al. (2020). The cumulative effect of transient synchrony states on motor performance in Parkinson ' s disease. *J. Neurosci.* 40, 1571–1580. doi: 10.1523/jneurosci.1975-19.2019

Velisar, A., Syrkin-Nikolau, J., Blumenfeld, Z., Trager, M. H., Afzal, M. F., Prabhakar, V., et al. (2019). Dual threshold neural closed loop deep brain stimulation in Parkinson disease patients. *Brain Stimul.* 12, 868–876. doi: 10.1016/j.brs.2019.02.020

Weiss, D., Klotz, R., Govindan, R. B., Scholten, M., Naros, G., Ramos-Murguialday, A., et al. (2015). Subthalamic stimulation modulates cortical motor network activity and synchronization in Parkinson's disease. *Brain* 138, 679–693. doi: 10.1093/brain/awu380

West, T. O., Berthouze, L., Halliday, D. M., Litvak, V., Sharott, A., Magill, P. J., et al. (2018). Propagation of beta/gamma rhythms in the cortico-basal ganglia circuits of the parkinsonian rat. *J. Neurophysiol.* 119, 1608–1628. doi: 10.1152/jn.00629.2017

Yang, Y., Connolly, A. T., and Shanechi, M. M. (2018). A control-theoretic system identification framework and a real-time closed-loop clinical simulation testbed for electrical brain stimulation. *J. Neural Eng.* 15:066007. doi: 10.1088/1741-2552/aad1a8

Zhang, T. C., and Grill, W. M. (2010). Modeling deep brain stimulation: point source approximation versus realistic. 18, 1199–1216. doi: 10.1088/1741-2560/7/6/066009.Modeling

Conflict of Interest: The authors declare that the research was conducted in the absence of any commercial or financial relationships that could be construed as a potential conflict of interest.

frontiers in Neuroscience

BRIEF RESEARCH REPORT
published: 29 April 2020
doi: 10.3389/fnins.2020.00367

Intraoperative Microelectrode Recordings in Substantia Nigra Pars Reticulata in Anesthetized Rats

*Hanyan Li and George C. McConnell**

Department of Biomedical Engineering, Stevens Institute of Technology, Hoboken, NJ, United States

The Substantia Nigra pars reticulata (SNr) is a promising target for deep brain stimulation (DBS) to treat the gait and postural disturbances in Parkinson's disease (PD). Positioning the DBS electrode within the SNr is critical for the development of preclinical models of SNr DBS to investigate underlying mechanisms. However, a complete characterization of intraoperative microelectrode recordings in the SNr to guide DBS electrode placement is lacking. In this study, we recorded extracellular single-unit activity in anesthetized rats at multiple locations in the medial SNr (mSNr), lateral SNr (lSNr), and the Ventral Tegmental Area (VTA). Immunohistochemistry and fluorescently dyed electrodes were used to map neural recordings to neuroanatomy. Neural recordings were analyzed in the time domain (i.e., firing rate, interspike interval (ISI) correlation, ISI variance, regularity, spike amplitude, signal-to-noise ratio, half-width, asymmetry, and latency) and the frequency domain (i.e., spectral power in frequency bands of interest). Spike amplitude decreased and ISI correlation increased in the mSNr versus the lSNr. Spike amplitude, signal-to-noise ratio, and ISI correlation increased in the VTA versus the mSNr. ISI correlation increased in the VTA versus the lSNr. Spectral power in the VTA increased versus: (1) the mSNr in the 20–30 Hz band and (2) the lSNr in the 20–40 Hz band. No significant differences were observed between structures for any other feature analyzed. Our results shed light on the heterogeneity of the SNr and suggest electrophysiological features to promote precise targeting of SNr subregions during stereotaxic surgery.

Keywords: deep brain stimulation, Parkinson's disease, intraoperative microelectrode recordings, action potentials, Substantia Nigra pars reticulata

OPEN ACCESS

Edited by:
Reinhold Scherer,
University of Essex, United Kingdom

Reviewed by:
Adolfo Ramirez-Zamora,
University of Florida Health, United States
Chadwick Boulay,
The Ottawa Hospital, Canada

***Correspondence:**
George C. McConnell
george.mcconnell@stevens.edu

Specialty section:
This article was submitted to Neuroprosthetics, a section of the journal Frontiers in Neuroscience

Received: *26 September 2019*
Accepted: *25 March 2020*
Published: *29 April 2020*

Citation:
Li H and McConnell GC (2020) Intraoperative Microelectrode Recordings in Substantia Nigra Pars Reticulata in Anesthetized Rats. Front. Neurosci. 14:367. doi: 10.3389/fnins.2020.00367

INTRODUCTION

Deep brain stimulation (DBS) is an effective treatment for tremor, rigidity, and bradykinesia in Parkinson's disease (PD). Although these distal symptoms are reliably treated by DBS and dopaminergic medication, the axial symptoms of gait and postural disturbances continue to worsen 5 years after implant (St George et al., 2010). The gait and postural disturbances are difficult to treat by either medication (Curtze et al., 2016) or DBS at the Subthalamic Nucleus (STN) (St George et al., 2010). Substantia Nigra pars reticulata (SNr) is a promising DBS target to treat the gait and postural disturbances in PD (Chastan et al., 2009; Weiss et al., 2011, 2013; Brosius et al., 2015; Scholten et al., 2017; Valldeoriola et al., 2019). Location of the DBS electrode within the SNr may play a crucial role in effective treatment, but the neural mechanisms for the location dependence of SNr DBS are not clear. Studies in rats (McConnell and Grill, 2013), cats (Takakusaki et al., 2003), and humans (Scholten et al., 2017) suggest that stimulation at lateral SNr (lSNr) sites is less effective at treating the gait disturbances of PD compared to stimulation at medial SNr (mSNr) sites.

The lateralization of SNr DBS may stem from the anatomical and functional heterogeneity of the SNr. The mSNr and lSNr receive different projections from the sensorimotor and limbic striatum, respectively (Deniau et al., 1996; Mailly et al., 2001). GABAergic neurons of mSNr and lSNr have a differential change of firing activity in PD (Wang et al., 2010). Ablation of the mSNr results in contralateral turning behavior, while ablation of the lSNr results in ipsilateral turning behavior in rats (Franklin and Wolfe, 1987).

Intraoperative microelectrode recordings (MERs) are commonly used to verify and refine targeting of DBS electrode placement during STN DBS surgery for PD. MERs employ extracellular recordings of action potentials along preplanned trajectories (Benazzouz et al., 2002) to minimize misplacement of the DBS electrode, which may result in unwanted side effects (Chan et al., 2009; Valsky et al., 2017). We hypothesized that the waveform shape and neuronal firing patterns of spikes detected from MERs within the SNr differ depending on the location of the electrode within SNr subregions. In addition to characterizing MERs in the mSNr and the lSNr, we investigated the capability of MERs to define structures surrounding the SNr including the Substantia Nigra pars compacta (SNc; dorsal to SNr) and Ventral Tegmental Area (VTA; medial to SNr). We recorded the subregions and surroundings of the SNr, namely the mSNr, the lSNr, the SNc and the VTA, in an anesthetized healthy rat model. MERs in anesthetized healthy rats is consistent with the future application of SNr DBS or SNr electrophysiology in parkinsonian rats by chronically implanting a cannula for 6-hydroxydopamine (6-OHDA) infusion to later render the rats parkinsonian (McConnell et al., 2016). Each recording site was confirmed postmortem by identification of the electrode track and immunohistochemistry to compare electrophysiological features of action potentials recorded in the mSNr, the lSNr, and the VTA.

METHODS

Electrode Preparation

Each tungsten microelectrode (MicroProbes; diameter = 75 μm; impedance = 0.5 MΩ) was oriented vertically, dipped 10 times into DiI (Molecular Probes, 50 mg/ml solution concentration) and allowed to dry in air 5 s between dips (DiCarlo et al., 1996). Following the dip-coating procedure, each electrode was inspected under a microscope to confirm that it was undamaged and uniformly coated to the tip of the electrode.

Surgery

All animal care and experimental procedures were approved by the Stevens Institute of Technology Institutional Animal Care and Use Committee. Stereotaxic (Stoelting) surgery was conducted in anesthetized Long-Evans female rats (250–300 g) (n = 13). Anesthesia was induced at 7% Sevoflurane (Piramal Petrem) and maintained under 4% Sevoflurane. A craniotomy was made over the SNr and the electrode was lowered into the brain at the coordinates: anterior/posterior: 5.5 mm; medial/lateral (ML) 1.5 mm from the midline for mSNr and ML 2.3 mm from the midline for lSNr. Data were recorded from 6.0 to 9.0 mm from the cortical surface in 0.1 mm steps for 30 s at each location for a total of 31 recordings per insertion track. One mSNr and one lSNr insertion track was made in each brain hemisphere. The recorded anatomical structure was confirmed by postmortem histology. A Grapevine Scout neural recording system (Ripple) was used to record the raw data, which was sampled at 30 kHz.

Immunohistochemistry

Immediately following the surgery, rats were intracardially perfused with Phosphate-buffered saline prewash followed by 10% formalin. Following perfusion, brains were extracted and fixed in 10% formalin overnight, followed by 30% sucrose solution until the brain sank to the bottom. The left side of the cortical surface was marked with green dye (Triangle Biomedical Science) to determine the left and right hemispheres under bright field microscopy. The brain samples were cryoprotected with Optimal Cutting Temperature (O.C.T.) compound and stored in −80°C overnight. Samples were then sectioned using a cryostat (Thermo Scientific CryoStar NX50) at −23°C (thickness = 40 μm). Tissue sections containing the SNr were immunostained for Tyrosine Hydroxylase (TH) (Sigma-Aldrich) for dopaminergic neurons and cover-slipped using DAPI Fluoromount-G (Southern- Biotech) for all cell nuclei. TH immunostaining confirmed the microelectrode tip location by visualizing the SNc to aid in identification of the SNr (McConnell et al., 2012, 2016; So et al., 2017). Only recordings of tracks confirmed to pass through the SNr and/or the VTA were further analyzed.

Data Analysis

Spike Sorting

Action potentials were obtained by 4th order Butterworth bandpass filtering the raw neural data from 300–5000 Hz and sorted using the Wave_clus toolbox (Quiroga et al., 2004) in MATLAB (Mathworks). The detection threshold was set within the background noise (threshold type: negative, minimal threshold for detection STD = 5, maximal threshold for detection STD = 50, minimal size of cluster = 60, sampling rate = 30 kHz) in order to include the background noise as one sorted cluster and facilitate visualization of a spike cluster. Background noise was defined as the amplitude of the noise cluster after spike sorting. While Principal Component Analysis (PCA) is more generally applied for spike sorting, wavelet transform can outperform PCA in some datasets (Pavlov et al., 2007). Therefore, wavelet transform was used as the spike sorting method to identify spikes for feature extraction.

Feature Extraction

Following spike sorting, single-unit activity was analyzed using custom MATLAB software to extract features in both the time and frequency domains. Action potentials recorded in the VTA, the mSNr, and the lSNr, based on histology, were analyzed for feature extraction. In the time domain, firing temporal features and waveform shape features were investigated. Firing temporal features included: (1) firing rate – number of

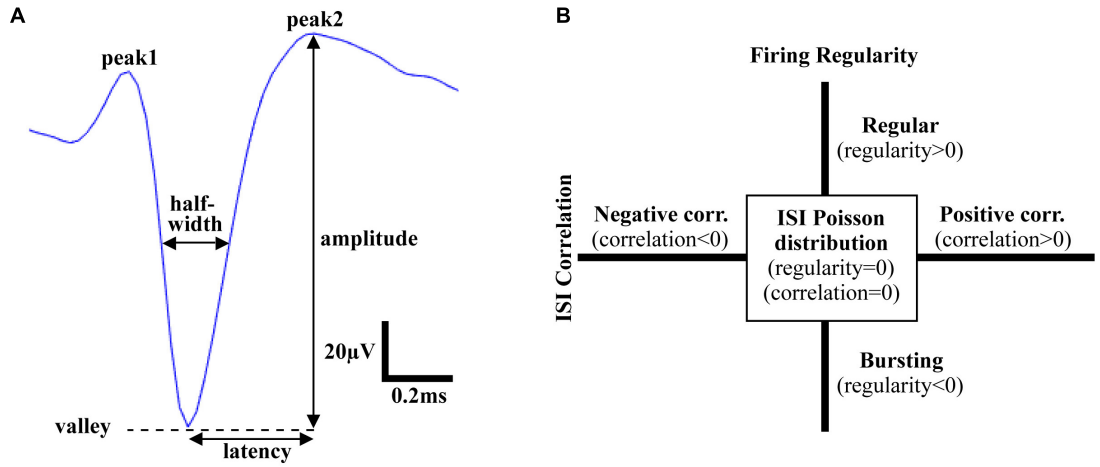

FIGURE 1 | Time domain features of action potentials. **(A)** Waveform shape features. Amplitude: voltage from valley to peak; Latency: time from valley to the 2nd peak; Half-width: width at half amplitude; Asymmetry: ratio of amplitude of the 1st peak and the 2nd peak. **(B)** Firing pattern features. Firing regularity: the logarithm of the shape factor κ of the gamma distribution fitted to the interspike intervals (ISIs). A spike train was considered Poisson random if its ISIs were exponentially distributed (κ = 1 or log κ = 0), whereas it was considered regular if log κ > 0 or bursting if log κ < 0; ISI correlation: the Spearman's rank-order correlation calculated for sequentially paired ISIs indicated whether consecutive ISIs were positively correlated or negatively correlated.

spikes per second [Hz]; (2) ISI correlation – the Spearman's rank-order correlation computed for sequentially paired ISIs indicates whether consecutive ISIs are positively correlated or negatively correlated; (3) ISI variance – the variance of ISIs; (4) firing regularity – logarithm of the shape factor of the gamma distribution fitted to the ISIs resulting in classification of spike trains as Poisson random if its ISIs are exponentially distributed (i.e., regularity = 0), regular (i.e., regularity >0), or bursting (i.e., regularity <0) (Mochizuki et al., 2016; **Figure 1B**). Waveform shape features included: (5) spike amplitude - measured from the negative peak to the positive peak of the spike waveform [μV]; (6) signal-to-noise ratio – spike amplitude divided by background noise amplitude; (7) half-width – width when amplitude equals to half of the amplitude [ms]; (8) asymmetry – the ratio of the amplitude of 2nd positive peak and the 1st positive peak; (9) latency – time from negative peak to the 2nd positive peak [ms] (**Figure 1A**). For each electrode track, density was calculated as percentage of recording locations with spiking activity compared with the total number of recording locations [%]. In the frequency domain, the power of spike trains was evaluated by Chronux with sampling rate = 30 kHz, win = 5 s, tapers = [3 5], pad = 0, and frequency calculation band = [0 200] (Mitra and Pesaran, 1999). Band power was calculated as the sum of the spectral power over frequencies in the bands of interest: delta (1.5–4 Hz), theta (4–10 Hz), low beta (10–20 Hz), high beta (20–30 Hz), Gamma (30–40 Hz, 40–50 Hz, 50–60 Hz, 60–70 Hz, and 70–80 Hz).

Feature Comparison

Time domain: After each time domain feature was extracted, firing temporal features (firing rate, amplitude, ISI correlation, ISI variance, firing regularity) and waveform shape features (amplitude, signal-to-noise ratio, half-width, asymmetry, latency) from the mSNr, the lSNr and the VTA were compared.

Frequency domain: After power spectrum at each depth was calculated, power of each frequency was calculated and compared between the mSNr, the lSNr and the VTA. Contiguous frequencies with statistically significant differences in power were considered as a frequency band of interest.

Statistical Analysis

Statistical inferences were made between differing conditions using one-way ANOVA. When we found a significant factor, we performed the Fisher's protected least significant difference (PLSD) *post hoc* test to identify pairwise differences. Student's *t*-test were used where indicated. All results are presented as the mean ± SEM and were considered significant at $p < 0.05$.

RESULTS

Histology

Thirteen rats were recorded with 28 electrode insertions spanning the mSNr, the lSNr, and the VTA. Six insertions using bare electrodes confirmed that the quality of recordings was not altered by the DiI coating (data not shown). Twenty two tracks were made by DiI coated electrodes. DiI remained intact after insertion (**Figures 2A,B**). Sixteen out of the 22 DiI coated electrode tracks could be visualized by fluorescence microscopy. Dopaminergic neurons in the SNc and the VTA were visualized by TH immunohistochemistry. The dorsal border of the SNr was defined by an absence of TH staining and immediately ventral to the SNc. The midline in the medial/lateral direction within SNr was defined as the border line of the mSNr and the lSNr (**Figure 2C**). Out of 16 tracks, 8 tracks passed through mSNr, 5 tracks passed through the lSNr, and 4 tracks passed through the VTA (**Figure 3A**). One out of the 4 tracks that passed through the VTA also passed through the mSNr (**Figure 3A**). The

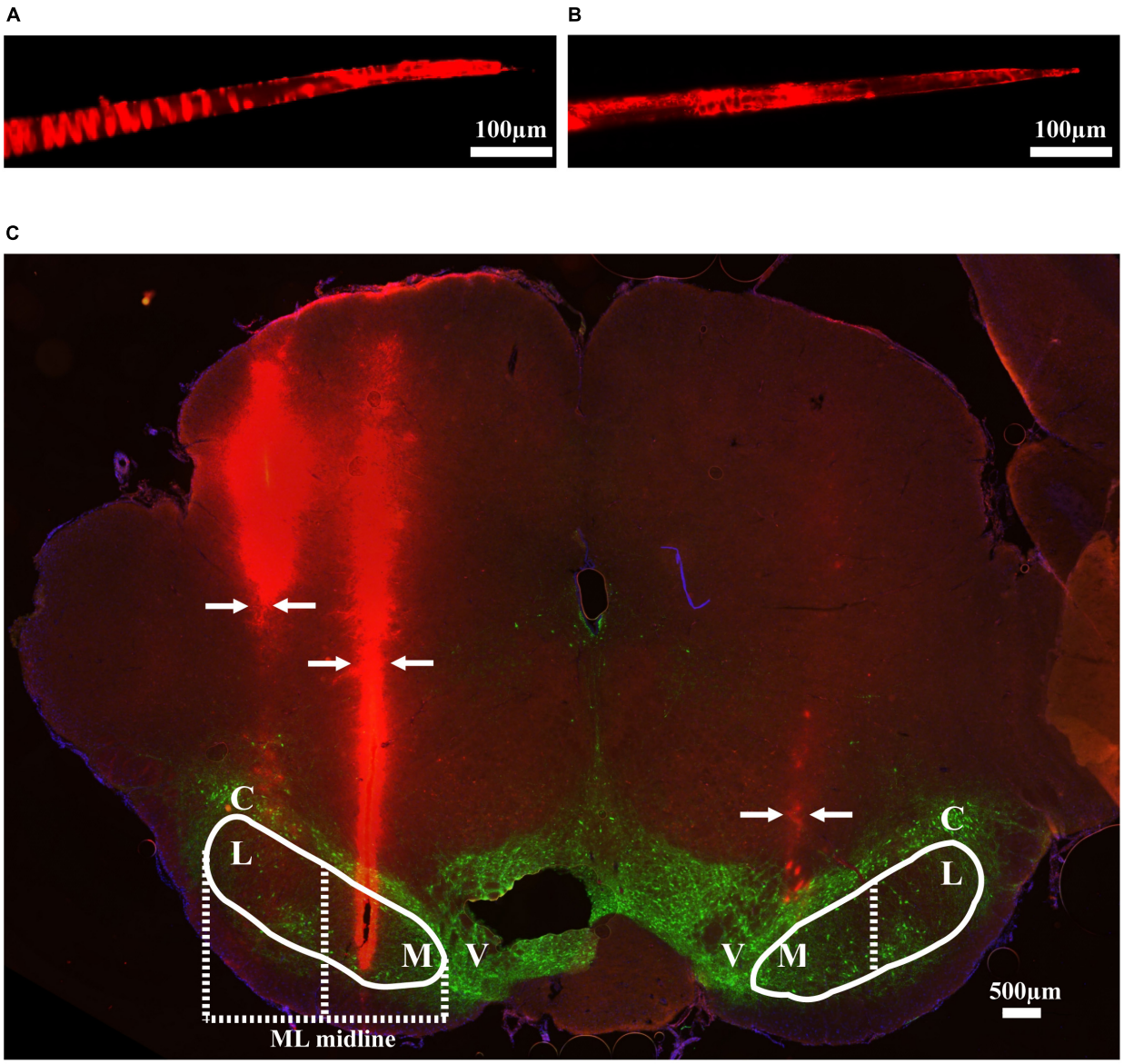

FIGURE 2 | Methods used to validate electrode location. **(A)** An example of DiI coated electrode before brain insertion. **(B)** The same electrode after brain insertion. **(C)** Coronal brain section showing DiI coated electrodes in mSNr and lSNr. Red indicates electrode tracks coated with DiI; green indicates dopaminergic neurons in SNc and VTA stained by anti-tyrosine hydroxylase. Borders of SNr are indicated by the white solid line. mSNr and lSNr (separated by dashed white line) were defined by evenly dividing the SNr in the medial/lateral direction. Arrows indicate locations of the electrode tracks. Abbreviations: M, medial Substantia Nigra pars reticulata (mSNr); L, lateral Substantia Nigra pars reticulata (lSNr); C, Substantia Nigra pars compacta (SNc); V, ventral tegmental area (VTA).

mSNr dorsal border was approximately 6.4 mm from the cortical surface according to histology compared to 8.0 mm according to the stereotaxic atlas (Paxinos and Watson, 2007). The lSNr border was approximately 6.1 mm from the cortical surface according to histology compared to 7.3 mm according to the stereotaxic atlas (Paxinos and Watson, 2007).

Spike Sorting

Neural recordings from electrode tracks confirmed by histology were further analyzed. The total number of recordings with histological confirmation was 496 (**Figure 3**). Following spike sorting, the total recordings with isolated single-unit activity was 72 with the remainder of recordings containing multi-unit activity and/or background noise. Fluorescent images were overlayed with the corresponding atlas panel (Paxinos and Watson, 2007), and all recording sites with single-unit activity were marked (**Figure 3**). Thirty out of 72 recording sites were in the mSNr, 26 out of 72 recording sites were in the lSNr, and 16 out of 72 recording sites were in the VTA. Single-unit activity was observed only in VTA, mSNr and lSNr; no spikes were detected dorsal or ventral to the VTA, dorsal to the SNc, or within the SNc.

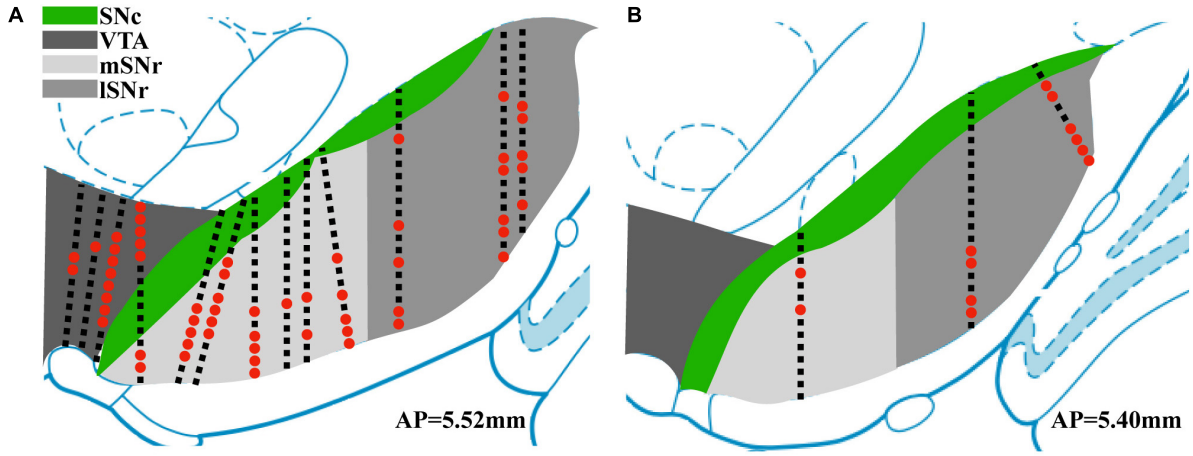

FIGURE 3 | Summary of position of electrode tracks based on histology. **(A)** Electrode tracks in coronal section corresponding to AP 5.52 mm (Paxinos and Watson, 2007). **(B)** Electrode tracks in coronal section corresponding to AP 5.40 mm. Black squares indicate recording sites with no sorted single units. Red dots indicate recording sites with sorted single units.

Feature Comparison

VTA vs. mSNr

In the time domain, the significantly different features between VTA and mSNr were spike amplitude, signal-to-noise ratio (**Figures 4A,B**). Amplitude was significantly greater in the VTA compared to the mSNr ($p = 0.0007$) (**Figure 4A**). Signal-to-noise ratio was significantly greater in the VTA compared to the mSNr ($p = 0.0028$) (**Figure 4B**). In the frequency domain, the 20–30 Hz band was significantly decreased in the mSNr compared to the VTA ($p = 0.0197$) (**Figures 4D,E**). Thus, the VTA and the mSNr differed in waveform shape and neuronal firing pattern. No significant differences were observed between the VTA and the mSNr for any other feature analyzed (**Supplementary Table S1**).

VTA vs. lSNr

In the time domain, the significantly different feature between the VTA and the lSNr was ISI correlation (**Figures 4A,C**). The ISI correlation was positive in VTA but negative in lSNr ($p = 0.0156$) (**Figure 4C**). In the frequency domain, the 20–40 Hz band was significantly decreased in the lSNr compared to the VTA ($p = 0.0118$) (**Figures 4D,E**). Thus, the VTA and lSNr differed only in measures of neuronal firing pattern, with no significant differences were observed between the VTA and the lSNr for any other feature analyzed (**Supplementary Table S1**).

mSNr vs. lSNr

In the time domain, the significantly different features between the mSNr and the lSNr were spike amplitude and ISI correlation (**Figures 4A,C**). The spike amplitude in the mSNr decreased compared to the lSNr ($p = 0.0224$) (**Figure 4A**). The ISI correlation of mSNr increased compared to the lSNr ($p = 0.0338$) (**Figure 4C**). In the frequency domain, there were no significant differences between brain regions in any continuous frequency band (**Figures 4D,E** and **Supplementary Table S1**). Thus, the mSNr and the lSNr differed only in the time domain, for both waveform shape and neuronal firing pattern features. No significant differences were observed between the mSNr and lSNr for any other feature analyzed (**Supplementary Table S1**).

DISCUSSION

SNr DBS is a promising approach to treat the gait and postural disturbances of PD, but the neural basis is not clear. The position of the electrode within the SNr appears to play a role in effectively treating gait regularity in PD (McConnell and Grill, 2013; Scholten et al., 2017). In this study, we characterized intraoperative MERs of the SNr as an approach to improve the accuracy and precision of the stereotaxic placement of SNr DBS electrodes to study the underlying neural mechanisms. We characterized MERs across the SNr spanning medial and lateral subregions to compare both temporal and spectral features in the medial and lateral SNr, and the nearby VTA. Fluorescently labeled microelectrodes were used to map neuroanatomical position to MERs. Our results suggest that spike amplitude, signal-to-noise ratio and firing pattern differ depending on brain regions. These electrophysiological features may be useful markers to guide either SNr recording or stimulation microelectrode array placement in healthy rats, which could later be rendered parkinsonian via infusion of 6-OHDA in the medial forebrain bundle (Dorval and Grill, 2014). In this way, our results could improve the reliability of a parkinsonian rat model of SNr DBS for behavioral studies to investigate stimulation parameters and underlying neural mechanisms.

The location dependence of SNr DBS on the efficacy of treating gait may be attributed to several factors. Connections with Pedunculopontine Nucleus (PPN) of the brainstem suggest that SNr DBS modulates the descending network linking the SNr to the PPN (Pahapill and Lozano, 2000), which support the involvement of the SNr in gait and postural disturbances of PD. Also, it is possible that SNr DBS may increase SNc neuronal activity, because SNc is dorsal to, and interdigitated among the

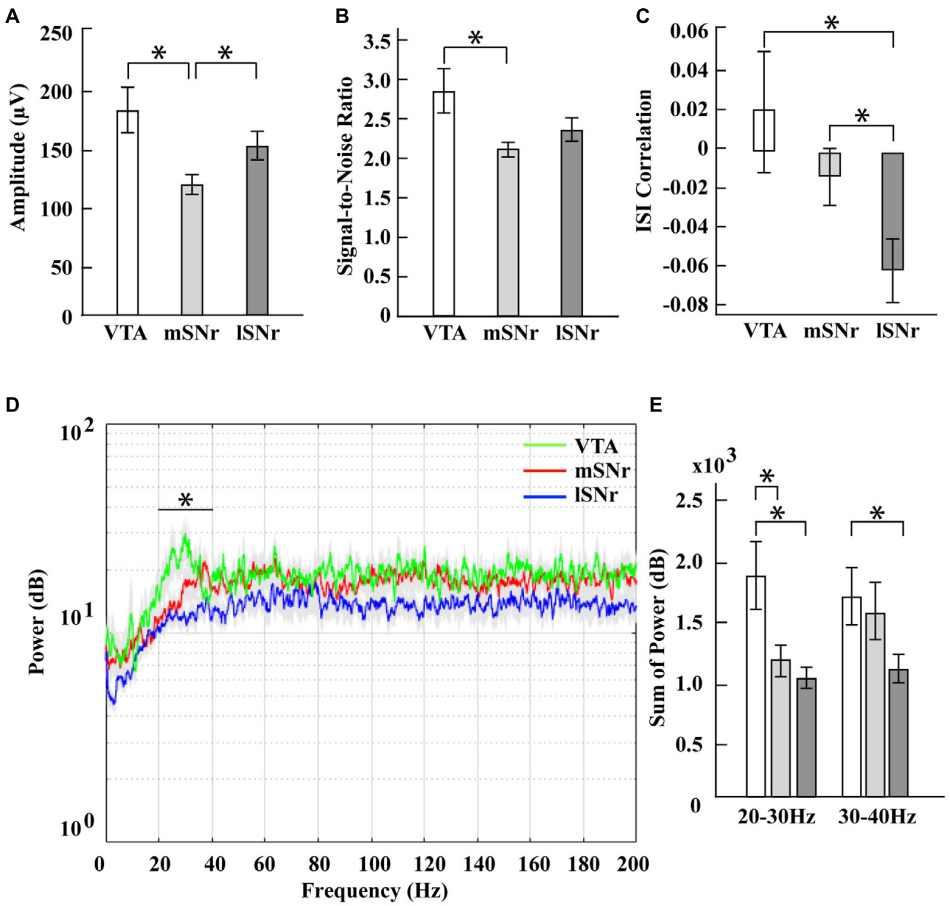

FIGURE 4 | Electrophysiological results in mSNr, lSNr and VTA. **(A)** Spike amplitudes in mSNr, lSNr and VTA. **(B)** Signal-to-noise ratio in mSNr, lSNr and VTA. **(C)** ISI correlation in mSNr, lSNr and VTA. **(D)** Spectral power in mSNr, lSNr and VTA. Mean (colored lines) ± SEM (gray filled area surrounding colored lines) are shown. **(E)** Sum of power in 20–30 Hz and 30–40 Hz frequency bands. Mean ± SEM (SEM indicated by gray filled area surrounding lines) are shown. Features that showed statistically significant differences are indicated with $^*p < 0.05$.

SNr. If so, high frequency stimulation induced excitation of SNc axons could induce dopaminergic release in the striatum and thereby improve PD symptoms (McIntyre et al., 2004; Zheng et al., 2011). In addition to the effects of SNr DBS location, frequency is another parameter that warrants more careful attention regarding mechanisms. Low stimulation SNr DBS (63 Hz) combined with high frequency STN DBS (130 Hz) was reported to improve freezing of gait in humans with PD (Valldeoriola et al., 2019). The mechanisms for these observed location and frequency effects of SNr DBS warrant further study in animal models of PD.

Although PPN is another promising DBS target for gait and postural disturbances in PD, PPN is a small midbrain region in comparison to the spatial extent of the stimulation effect produced by the microelectrode (Hamani et al., 2011). The lack of clarity of PPN contributes to the difficulty in targeting and determining the exact localization of the electrodes. It is likely that DBS in the PPN region affects neighbor structures. In humans the PPN overlaps with the posterior part of the Substantia Nigra (SN), so that it is presumably impossible to constrain stimulation to the PPN without also altering the SN. Hence, the observed effects on discrimination performance may at least to some degree stem from a modulation of activity in the SN (Strumpf et al., 2016). Because of the location, PPN DBS poses additional risk compared to other DBS surgeries (Welter et al., 2015). Stimulation-related adverse events during LFS PPN DSB include paresthesia, pain and temperature sensation, and some patients develop oscillopsia (a visual disturbance) during LFS PPN DBS (Fraix et al., 2010; Moro et al., 2010). One study reported that two out of six patients that received PPN DBS developed several adverse effects (Welter et al., 2015). For these reasons, there is growing interest in alternative DBS targets for gait and postural disturbances including the SNr.

Our results highlight the increased accuracy for electrode placement when using intraoperative MERs compared to stereotaxic coordinates from a rat brain atlas to localize deep brain structures. Previous studies of STN DBS in rodents reported a discrepancy between the dorsal/ventral coordinate predicted by MERs compared to the stereotaxic atlas (Gradinaru et al., 2009; McConnell et al., 2012, 2016). Here, the location of mSNr

and lSNr according to histology and MERs was approximately 0.5–1.0 mm dorsal to the stereotaxic atlas coordinates. Thus, MERs may be advantageous for targeting compared to using a stereotaxic atlas alone. Future stereotaxic surgeries may consider adding intraoperative recordings in tandem with the traditional atlas to target deep brain structures with higher accuracy. It is common that during stereotaxic surgeries edema occurs due to drilling, which could contribute to the decreased accuracy the dorsal/ventral stereotaxic coordinates. The maximum swelling or denting of the cortex we observed was approximately 0.5 mm, which could result in missed targeting of a deep brain structure in the absence of MERs.

Our rationale for recording single-unit activity was to confine the measurement of extracellular potentials to the immediate vicinity of the microelectrode given the small dimensions of the SNr subregions in the rat. One limitation of single-unit recordings, however, is that sorted spikes are not observed at all depths along an electrode track. In some instances, single-unit activity was observed at only one recording site along the dorsal-ventral direction of an insertion track and the majority of the recordings we collected were excluded from this study due to an absence of sorted spikes. Local field potential (LFPs) to target SNr and its subregions could provide an alternative measure or additional measure to spiking activity relevant to SNr position (Li and McConnell, 2019). Unlike action potentials in SNr, LFPs can be measured at every recording site and thereby provide a more consistent measure but at a lower spatial resolution compared to single-unit recordings. Because a complete analysis of LFPs was beyond the scope of this study, we are at this time unable to correlate our histological results to features of LFPs. An additional limitation was the use of anesthetized healthy rats and not awake or parkinsonian rats. The 6-OHDA lesion model is the most commonly used pre-clinical parkinsonian rat model to investigate PD. The procedure to study DBS in 6-OHDA rats typically is to implant the electrode and cannula in anesthetized healthy rat brain (McConnell et al., 2016). Following a period of baseline healthy recordings, the cannula is then used to infuse 6-OHDA. In this way, longitudinal studies of DBS are possible with healthy and parkinsonian behavior and neural recordings from the same animal. Another limitation is that although each electrode was dye coated before surgery, with the same amount times of dipping and drying, only 16 out of 22 tracks were able to be visualized from histology. It is possible that the brain sections containing the electrode tracks were not saved during the sectioning procedure or torn during the immunohistochemistry protocol.

No spiking activity dorsal or ventral to the SNr suggests that it is feasible to use intraoperative recordings to delineate the dorsal and ventral borders of the SNr when using anesthetized healthy rat model. Electrophysiological features that showed significant differences between mSNr and VTA in the time domain were amplitude and signal-to-noise ratio. ISI correlation in VTA was positive while it was negative in both the mSNr and the lSNr. More specifically, the consecutive ISIs in VTA were positively correlated but the ISIs in mSNr and lSNr were negatively correlated. This suggests that VTA has a different firing pattern than either subregion of SNr. When targeting SNr, amplitude, signal-to-noise ratio, and ISI correlation could minimize misplacement in the medial direction. The power of spikes in mSNr and VTA were significantly different in the high beta band (20–30 Hz), which could be an additional electrophysiological marker to distinguish mSNr and VTA in the frequency domain. Extracellular recording features that differed between mSNr and lSNr in the time domain were spike amplitude and ISI correlation. The difference in amplitude may be due to the density of neurons, thereby reducing the distance between the electrode tip and a nearby neuron. A difference in ISI correlation indicates a difference in firing pattern between the mSNr and lSNr. Interestingly, no changes in firing rate were observed between the mSNr and lSNr despite changes in firing pattern. Taken together, these results support a model of heterogeneity within the SNr due to differences not in in firing rate, but rather in firing pattern.

We speculate that differences in neuronal type may explain the lack of single-unit activity in SNc, but some in the VTA, even though electrode tracks did penetrate the SNc prior to passing through the mSNr and the lSNr. Dopaminergic neurons are highly heterogeneous and not always spontaneously active both *in vivo* and *ex vivo* (Dai and Tepper, 1998; Marinelli and McCutcheon, 2014). The VTA is composed of dopaminergic and GABAergic neurons (Merrill et al., 2015), in comparison to the SNc comprised entirely of dopaminergic neurons. The SNr contains dopaminergic neurons and GABAergic neurons with GABAergic the predominant neuronal type (Zhou and Lee, 2011). Our finding of differential firing patterns and waveform shapes in the mSNr and the lSNr parallel previous studies showing the SNr contains distinct GABAergic subpopulations (Yung et al., 1999).

There exists a paucity of studies in the literature using SNr recordings in animal models. In healthy rats, SNr neurons fired at 19.4 ± 1.2 spikes/s, while 71% of neurons had a tonic discharge, 29% fired randomly, and 0% showed a bursting firing pattern (Breit et al., 2008). One study specifically recorded from the subregions of the SNr and isolated the GABAergic neurons (Wang et al., 2010). The mean firing rate was 21.98 ± 1.27 spikes/s in the lSNr and 23.15 ± 1.33 spikes/s in the mSNr. In the lSNr, the firing pattern distribution was 54.00% regular, 40.00% irregular, and 6.00% bursting neurons. In the mSNr, the firing pattern distribution was 58.97% regular, 33.33% irregular, and 7.70% bursting neurons. Similar to our findings, no differences were observed in firing rate between the mSNr and the lSNr. In contrast to our results, however, no significant difference was found in neuronal firing patterns between the mSNr and the lSNr in healthy rats (Wang et al., 2010). These contradictory results may be explained by differences in the sex of the rats, the type of anesthesia delivered, spike sorting methodology, standard for excluding data points, and the features used to classify firing pattern. It is important that future studies reporting MERs in the SNr include the medial/lateral atlas coordinates used to allow investigators to properly interpret and reproduce the results.

In summary, changes in spike amplitude and firing pattern may be useful measures for the analysis of MERs to more reliably locate the SNr and its subregions. These findings suggest

that mapping MERs to electrode position using the combined fluorescently dyed microelectrode and immunohistochemistry technique described can facilitate targeting of other deep brain targets, rather than relying on stereotaxic atlas coordinates *per se*. We suggest that LFPs in tandem with spiking activity may further facilitate MERs to promote precise targeting of microelectrodes.

DATA AVAILABILITY STATEMENT

The datasets generated for this study are available on request to the corresponding author.

ETHICS STATEMENT

The animal study was reviewed and approved by the Stevens Institute of Technology Institutional Animal Care and Use Committee.

AUTHOR CONTRIBUTIONS

HL and GM designed the research and wrote the manuscript. HL performed the research and analyzed the data.

FUNDING

This study was supported by grants from the NIH R21-NS-085539 to GM and the Branfman Family Foundation to GM. HL received a fellowship from the Office of Innovation and Entrepreneurship at Stevens Institute of Technology.

SUPPLEMENTARY MATERIAL

The Supplementary Material for this article can be found online at: https://www.frontiersin.org/articles/10.3389/fnins.2020.00367/full#supplementary-material

REFERENCES

Benazzouz, A., Breit, S., Koudsie, A., Pollak, P., Krack, P., and Benabid, A. L. (2002). Intraoperative microrecordings of the subthalamic nucleus in Parkinson's disease. *Movement Disord.* 17, 145–149. doi: 10.1002/mds.10156

Breit, S., Martin, A., Lessmann, L., Cerkez, D., Gasser, T., and Schulz, J. B. (2008). Bilateral changes in neuronal activity of the basal ganglia in the unilateral 6-hydroxydopamine rat model. *J. Neurosci. Res.* 86, 1388–1396. doi: 10.1002/jnr.21588

Brosius, S. N., Gonzalez, C. L., Shuresh, J., and Walker, H. C. (2015). Reversible improvement in severe freezing of gait from Parkinson's disease with unilateral interleaved subthalamic brain stimulation. *Park. Relat. Disord.* 21, 1469–1470. doi: 10.1016/j.parkreldis.2015.09.047

Chan, D. T. M., Zhu, X. L., Yeung, J. H. M., Mok, V. C. T., Wong, E., Lau, C., et al. (2009). Complications of deep brain stimulation: a collective review. *Asian J. Surg.* 32, 258–263. doi: 10.1016/S1015-9584(09)60404-8

Chastan, N., Westby, G. W. M., Yelnik, J., Bardinet, E., Do, M. C., Agid, Y., et al. (2009). Effects of nigral stimulation on locomotion and postural stability in patients with Parkinson's disease. *Brain* 132, 172–184. doi: 10.1093/brain/awn294

Curtze, C., Nutt, J. G., Carlson-Kuhta, P., Mancini, M., and Horak, F. B. (2016). Levodopa Is a double-edged sword for balance and gait in people with Parkinson's disease. *Mov. Disord.* 30, 1361–1370. doi: 10.1002/mds.26269

Dai, M., and Tepper, J. M. (1998). Do silent dopaminergic neurons exist in rat substantia nigra in vivo? *Neuroscience* 85, 1089–1099. doi: 10.1016/S0306-4522(97)00615-5

Deniau, J. M., Menetrey, A., and Charpier, S. (1996). The lamellar organization of the rat substantia nigra pars reticulata: segregated patterns of striatal afferents and relationship to the topography of corticostriatal projections. *Neuroscience* 73, 761–781. doi: 10.1016/0306-4522(96)00088-7

DiCarlo, J. J., Lane, J. W., Hsiao, S. S., and Johnson, K. O. (1996). Marking metal microelectrode penetrations with fluorescent dyes. *J. Neurosci. Methods* 64, 75–81.

Dorval, A. D., and Grill, W. M. (2014). Deep brain stimulation of the subthalamic nucleus reestablishes neuronal information transmission in the 6-OHDA rat model of parkinsonism. *J. Neurophysiol.* 111, 1949–1959. doi: 10.1152/jn.00713.2013

Fraix, V., Goetz, L., Ardouin, C., Yelnik, J., Henry-Lagrange, C., Seigneuret, E., et al. (2010). Effects of pedunculopontine nucleus area stimulation on gait disorders in Parkinson's Disease. *Brain* 133, 204–214. doi: 10.1093/brain/awp229

Franklin, K. B. J., and Wolfe, J. (1987). Opposed locomotor asymmetries following lesions of the medial and lateral substantia nigra pars compacta or pars reticulata in the rat. *Physiol. Behav.* 40, 741–745. doi: 10.1016/0031-9384(87)90277-0

Gradinaru, V., Mogri, M., Thompson, K. R., Henderson, M. J., and Deisseroth, K. (2009). Optical deconstruction of parkinsonian neural circuitry. *Science* 324, 354–359. doi: 10.1126/science.1167093

Hamani, C., Moro, E., and Lozano, A. M. (2011). The pedunculopontine nucleus as a target for deep brain stimulation. *J. Neural Transm.* 118, 1461–1468. doi: 10.1007/s00702-010-0547-8

Li, H., and McConnell, G. C. (2019). Proceedings #8: microstimulation evoked neuronal activity in the substantia nigra pars reticulata in anesthetized rats. *Brain Stimul.* 12, e66–e68. doi: 10.1016/j.brs.2018.12.177

Mailly, P., Charpier, S., Mahon, S., Menetrey, A., Thierry, A. M., Glowinski, J., et al. (2001). Dendritic arborizations of the rat substantia nigra pars reticulata neurons: spatial organization and relation to the lamellar compartmentation of striato-nigral projections. *J. Neurosci.* 21, 6874–6888. doi: 10.1523/jneurosci.21-17-06874.2001

Marinelli, M., and McCutcheon, J. E. (2014). Heterogeneity of dopamine neuron activity across traits and states. *Neuroscience* 282, 176–197. doi: 10.1016/j.neuroscience.2014.07.034

McConnell, G. C., and Grill, W. M. (2013). "Stimulation location within the substantia nigra pars reticulata differentially modulates gait in hemiparkinsonian rats," in *International IEEE/EMBS Conference on Neural Engineering, NER*, Francisco, CA, 1210–1213.

McConnell, G. C., So, R. Q., and Grill, W. M. (2016). Failure to suppress low-frequency neuronal oscillatory activity underlies the reduced effectiveness of random patterns of deep brain stimulation. *J. Neurophysiol.* 115, 2791–2802. doi: 10.1152/jn.00822.2015

McConnell, G. C., So, R. Q., Hilliard, J. D., Lopomo, P., and Grill, W. M. (2012). Effective deep brain stimulation suppresses low-frequency network oscillations in the basal ganglia by regularizing neural firing patterns. *J. Neurosci.* 32, 15657–15668. doi: 10.1523/JNEUROSCI.2824-12.2012

McIntyre, C. C., Savasta, M., Kerkerian-Le Goff, L., and Vitek, J. L. (2004). Uncovering the mechanism(s) of action of deep brain stimulation: activation, inhibition, or both. *Clin. Neurophysiol.* 115, 1239–1248. doi: 10.1016/j.clinph.2003.12.024

Merrill, C. B., Friend, L. N., Newton, S. T., Hopkins, Z. H., and Edwards, J. G. (2015). Ventral tegmental area dopamine and GABA neurons: physiological properties and expression of mRNA for endocannabinoid biosynthetic elements. *Sci. Rep.* 5:16176. doi: 10.1038/srep16176

Mitra, P. P., and Pesaran, B. (1999). Analysis of dynamic brain imaging data. *Biophys. J.* 76, 691–708.

Mochizuki, Y., Onaga, T., Shimazaki, H., Shimokawa, T., Tsubo, Y., Kimura, R., et al. (2016). Similarity in neuronal firing regimes across mammalian

species. *J. Neurosci.* 36, 5736–5747. doi: 10.1523/JNEUROSCI.0230-16.2016

Moro, E., Hamani, C., Poon, Y.-Y., Al-khairallah, T., Dostrovsky, O., Hutchison, W. D., et al. (2010). Unilateral pedunculopontine stimulation improves falls in Parkinson's Disease. *Brain* 133, 215–224. doi: 10.1093/brain/awp261

Pahapill, P. A., and Lozano, A. M. (2000). The pedunculopontine nucleus and Parkinson's disease. *Brain* 123, 1767–1783. doi: 10.1093/brain/123.9.1767

Pavlov, A., Makarov, V. A., Makarova, I., and Panetsos, F. (2007). Sorting of neural spikes: when wavelet based methods outperform principal component analysis. *Nat. Comput.* 6, 269–281. doi: 10.1007/s11047-006-9014-8

Paxinos, G., and Watson, C. (2007). *The rat Brain in Stereotaxic Coordinates*, 6th Edn. San Diego, CA: Academic Press.

Quiroga, R. Q., Nadasdy, Z., and Ben-Shaul, Y. (2004). Unsupervised spike detection and sorting with wavelets and superparamagnetic clustering. *Neural Comput.* 16, 1661–1687. doi: 10.1162/089976604774201631

Scholten, M., Klemt, J., Heilbronn, M., Plewnia, C., Bloem, B. R., Bunjes, F., et al. (2017). Effects of subthalamic and nigral stimulation on gait kinematics in Parkinson's disease. *Front. Neurol.* 8:543. doi: 10.3389/fneur.2017.00543

So, R. Q., McConnell, G. C., and Grill, W. M. (2017). Frequency-dependent, transient effects of subthalamic nucleus deep brain stimulation on methamphetamine-induced circling and neuronal activity in the hemiparkinsonian rat. *Behav. Brain Res.* 320, 119–127. doi: 10.1016/j.bbr.2016.12.003

St George, R. J., Nutt, J. G., and Burchiel, K. J. (2010). A meta-regression of the long-term effects of deep brain stimulation on balance and gait in PD. *Neurology* 75, 1292–1299. doi: 10.1212/WNL.0b013e3181f61329

Strumpf, H., Noesselt, T., Schoenfeld, M. A., Voges, J., Panther, P., Kaufmann, J., et al. (2016). Deep brain stimulation of the pedunculopontine tegmental nucleus (PPN) influences visual contrast sensitivity in human observers. *PLoS One* 11:e0155206. doi: 10.1371/journal.pone.0155206

Takakusaki, K., Habaguchi, T., Ohtinata-Sugimoto, J., Saitoh, K., and Sakamoto, T. (2003). Basal ganglia efferents to the brainstem centers controlling postural muscle tone and locomotion: a new concept for understanding motor disorders in basal ganglia dysfunction. *Neuroscience* 119, 293–308. doi: 10.1016/S0306-4522(03)00095-2

Valldeoriola, F., Muñoz, E., Rumià, J., Roldán, P., Cámara, A., Compta, Y., et al. (2019). Simultaneous low-frequency deep brain stimulation of the substantia nigra pars reticulata and high-frequency stimulation of the subthalamic nucleus to treat levodopa unresponsive freezing of gait in Parkinson's disease. *Park. Relat. Disord.* 60, 153–157. doi: 10.1016/j.parkreldis.2018.09.008

Valsky, D., Marmor-Levin, O., Deffains, M., Eitan, R., Blackwell, K. T., Bergman, H., et al. (2017). Stop! border ahead: automatic detection of subthalamic exit during deep brain stimulation surgery. *Mov. Disord.* 32, 70–79. doi: 10.1002/mds.26806

Wang, Y., Zhang, Q. J., Liu, J., Ali, U., Gui, Z. H., Hui, Y. P., et al. (2010). Changes in firing rate and pattern of GABAergic neurons in subregions of the substantia nigra pars reticulata in rat models of Parkinson's disease. *Brain Res.* 1324, 54–63. doi: 10.1016/j.brainres.2010.02.008

Weiss, D., Wächter, T., Meisner, C., Fritz, M., Gharabaghi, A., Plewnia, C., et al. (2011). Combined STN/SNr-DBS for the treatment of refractory gait disturbances in Parkinson's disease: study protocol for a randomized controlled trial. *Trials* 12:222. doi: 10.1186/1745-6215-12-222

Weiss, D., Walach, M., Meisner, C., Fritz, M., Scholten, M., Breit, S., et al. (2013). Nigral stimulation for resistant axial motor impairment in Parkinson's disease? A randomized controlled trial. *Brain* 136, 2098–2108. doi: 10.1093/brain/awt122

Welter, M.-L., Demain, A., and Ewenczyk, C. (2015). PPNa-DBS for gait and balance disorders in Parkinson's Disease: a double-blind, randomised study. *J. Neurol.* 262, 1515–1525. doi: 10.1007/s00415-015-7744-1

Yung, K. K. L., Ng, T. K. Y., and Wong, C. K. C. (1999). Subpopulations of neurons in the rat neostriatum display GABABR1 receptor immunoreactivity. *Brain Res.* 830, 345–352.

Zheng, F., Lammert, K., Nixdorf-Bergweiler, B. E., Steigerwald, F., Volkmann, J., and Alzheimer, C. (2011). Axonal failure during high frequency stimulation of rat subthalamic nucleus. *J. Physiol.* 589, 2781–2793. doi: 10.1113/jphysiol.2011.205807

Zhou, F. M., and Lee, C. R. (2011). Intrinsic and integrative properties of substantia nigra pars reticulata neurons. *Neuroscience* 198, 69–94. doi: 10.1016/j.neuroscience.2011.07.061

Conflict of Interest: The authors declare that the research was conducted in the absence of any commercial or financial relationships that could be construed as a potential conflict of interest.

frontiers in Neuroscience

ORIGINAL RESEARCH
published: 19 May 2020
doi: 10.3389/fnins.2020.00397

The Appearance Order of Varying Intervals Introduces Extra Modulation Effects on Neuronal Firing Through Non-linear Dynamics of Sodium Channels During High-Frequency Stimulations

Lvpiao Zheng[1], Zhouyan Feng[1], Hanhan Hu[1], Zhaoxiang Wang[1], Yue Yuan[1] and Xuefeng Wei[2]*

[1] Key Laboratory of Biomedical Engineering for Ministry of Education, College of Biomedical Engineering and Instrument Science, Zhejiang University, Hangzhou, China, [2] Department of Biomedical Engineering, The College of New Jersey, Ewing, NJ, United States

OPEN ACCESS

Edited by:
Caleb Kemere,
Rice University, United States

Reviewed by:
Martin Han,
University of Connecticut, United States
Daniel Llewellyn Rathbun,
Henry Ford Health System, United States

***Correspondence:**
Zhouyan Feng
fengzhouyan@zju.edu.cn;
fengzhouyan@139.com

Specialty section:
This article was submitted to Neuroprosthetics, a section of the journal Frontiers in Neuroscience

Received: *29 August 2019*
Accepted: *30 March 2020*
Published: *19 May 2020*

Citation:
Zheng L, Feng Z, Hu H, Wang Z, Yuan Y and Wei X (2020) The Appearance Order of Varying Intervals Introduces Extra Modulation Effects on Neuronal Firing Through Non-linear Dynamics of Sodium Channels During High-Frequency Stimulations. Front. Neurosci. 14:397. doi: 10.3389/fnins.2020.00397

Electrical pulse stimulation in the brain has shown success in treating several brain disorders with constant pulse frequency or constant inter-pulse interval (IPI). Varying IPI may offer a variety of novel stimulation paradigms and may extend the clinical applications. However, a lack of understanding of neuronal responses to varying IPI limits its informed applications. In this study, to investigate the effects of varying IPI, we performed both rat experiments and computational modeling by applying high-frequency stimulation (HFS) to efferent axon fibers of hippocampal pyramidal cells. Antidromically evoked population spikes (PSs) were used to evaluate the neuronal responses to pulse stimulations with different IPI patterns including constant IPI, gradually varying IPI, and randomly varying IPI. All the varying IPI sequences were uniformly distributed in the same interval range of 10 to 5 ms (i.e., 100 to 200 Hz). The experimental results showed that the mean correlation coefficient of PS amplitudes to the lengths of preceding IPI during HFS with random IPI (0.72 ± 0.04, $n = 7$ rats) was significantly smaller than the corresponding correlation coefficient during HFS with gradual IPI (0.92 ± 0.03, $n = 7$ rats, $P < 0.001$, t-test). The PS amplitudes induced by the random IPI covered a wider range, over twice as much as that induced by the gradual IPI, indicating additional effects induced by merely changing the appearance order of IPI. The computational modeling reproduced these experimental results and provided insights into these modulatory effects through the mechanism of non-linear dynamics of sodium channels and potassium accumulation in the narrow peri-axonal space. The simulation results showed that the HFS-induced increase of extracellular potassium ($[K^+]_o$) elevated the membrane potential of axons, delayed the recovery course of sodium channels that were repeatedly activated and inactivated during HFS, and resulted in intermittent neuronal firing. Because of non-linear membrane dynamics, random IPI recruited more neurons to fire together following specific sub-sequences of

pulses than gradual IPI, thereby widening the range of PS amplitudes. In conclusion, the study demonstrated novel HFS effects of neuronal modulation induced by merely changing the appearance order of the same group of IPI of pulses, which may inform the development of new stimulation patterns to meet different demands for treating various brain diseases.

Keywords: high-frequency stimulation, inter-pulse interval, *in vivo* experiment, computational modeling, hippocampal pyramidal cell, membrane dynamics, non-linearity, population spike

INTRODUCTION

Deep brain stimulation (DBS) generally refers to utilizing sequences of electrical pulses to treat neurological and psychiatric disorders in the brain (Lozano and Lipsman, 2013). In theory, electrical stimulations on the neuronal membrane could generate various modulation effects on neuronal activity to treat various brain diseases. However, current DBS therapy has only been popularized in treating a few diseases such as movement disorders and refractory epilepsy (Bergey, 2013; Wichmann and DeLong, 2016; Cury et al., 2017). Besides the lack of understanding of the exact pathophysiological mechanisms of many brain diseases, extending DBS treatment to other diseases is limited by a lack of versatility in stimulation paradigms, as well as a lack of understanding of various stimulation effects on neurons and their mechanisms.

Major parameters involved in the design of pulse stimulation paradigms include pulse amplitude, pulse width, and pulse repetition rate (frequency). In particular, the efficiency and efficacy of DBS therapy are strongly dependent on the pulse frequency [or inter-pulse interval (IPI)]. Common DBS therapy utilizes pulse sequences with a constant frequency of around 130 Hz (Cagnan et al., 2017; Dandekar et al., 2018), termed as high-frequency stimulation (HFS). For example, a frequency in 90–185 Hz was proven effective in suppressing tremor of Parkinson's disease in clinic (Rizzone et al., 2001; Bittar et al., 2005; Dayal et al., 2017). Frequencies in a similar range have also been applied to control epileptic seizures (Cukiert et al., 2011; Fisher and Velasco, 2014; Laxpati et al., 2014).

Besides constant IPI, irregular temporal patterns of stimulation (i.e., sequences with varying IPI) have been exploited to improve the DBS therapies as well as to probe the underlying mechanisms of DBS (Grill, 2018). For example, stimulations with random IPI have emerged as a strategy to suppress the epileptic activity of neural networks (Cota et al., 2009; Mesquita et al., 2011; Medeiros et al., 2012; Santos-Valencia et al., 2019) and to affect central nervous system arousal (Quinkert et al., 2010; Quinkert and Pfaff, 2012; Tabansky et al., 2014). These studies demonstrated a significant effect of temporally random IPI on behavioral outcomes of seizure suppression or CNS arousal evaluated on experimental animals. Also, stimulations with varying IPI of different patterns have been used to suppress tremor (Birdno et al., 2007; Kuncel et al., 2012; Swan et al., 2016). However, the effects of stimulations and mechanisms of action with varying IPI are uncertain yet, limiting the application and development of irregular HFS in clinic.

Previous studies have shown that HFS with constant IPI can only intermittently generate action potentials in neurons because the HFS-induced depolarization block on the neuronal membrane prevents the neurons from firing in response to each stimulation pulse (Jensen and Durand, 2009; Feng et al., 2013; Rosenbaum et al., 2014). Intermittent activation of individual neurons may generate asynchronous firing in neuronal populations (Popovych and Tass, 2014; Feng et al., 2017; Wang et al., 2018). Pulses with a higher frequency (i.e., a shorter IPI) cause a deeper depolarization block, allowing less neurons to be recruited to fire by every pulse, as indicated by smaller evoked population spikes (PSs) during steady-state period of HFS (Feng et al., 2013, 2014). However, a recent study has shown that even with higher instantaneous frequencies for all pulses, stimulations of varying IPI with a random order can occasionally recruit more, rather than less, neurons to fire simultaneously than stimulations with constant IPI (Feng et al., 2019). This suggests that the recruitment of neuronal firing could be affected not only by pulse frequencies but also by the temporal orders of varying IPI. However, the underlying mechanisms are not clear. The purpose of this study is to unveil the cellular mechanisms of neuronal responses to HFS with different temporal orders of varying IPI, which may promote the development of novel stimulation paradigms of DBS for treating more diseases.

Membrane dynamics of ionic channels, such as Na^+ and K^+ channels, change non-linearly with time and with transmembrane potential (Hodgkin and Huxley, 1952). We hypothesize that a random arrangement of varying IPI could introduce additional effects of stimulation on neuronal population due to non-linear responses of the neuronal membrane to stimulation. To investigate the relationship between dynamic responses of neurons and instantaneous IPI lengths, we performed both rat experiments *in vivo* and computational modeling on stimulations of efferent axon fibers of hippocampal pyramidal cells with HFS of gradually varying and randomly varying IPI. Antidromically evoked unit spikes and PSs were used to evaluate the neuronal responses directly to pulse stimulations without involving synaptic transmission.

Hippocampal structure contains high density of neurons with clear lamellar organization of neuronal elements, allowing manipulation of distinct stimulation and recording from local cells and their axons as well as evaluation of responses of neuronal populations. Additionally, the hippocampus plays an important role in brain diseases such as epilepsy and Alzheimer's disease (Fisher and Velasco, 2014; Deeb et al., 2019). Therefore, the responses of hippocampal neurons to electric stimulation have gained increasing attention in DBS research and in clinic. In

addition, we investigated the neuronal responses initiated from axons because axons are more prone to excitation by extracellular pulses than other structural elements of neurons (Nowak and Bullier, 1998). The results of this study provide new clues to design effective novel stimulation paradigms with temporal arrangement of IPI for extending the application of DBS.

MATERIALS AND METHODS

Animal Experiments

The animal experiment was approved by the Institutional Animal Care and Ethics Committee, Zhejiang University. Seven adult Sprague-Dawley rats (250–350 g) were anesthetized with urethane (1.25 g/kg, i.p.) and placed in a stereotaxic apparatus (Stoelting Co., United States). Details of surgical procedures and electrode placements have been reported previously (Feng et al., 2013, 2014). Briefly, a 16-channel array of recording electrodes (#Poly2, NeuroNexus Technologies, United States) was inserted into the hippocampal CA1 region [anterior–posterior, −3.5; medio-lateral, 2.7; dorso-ventral, 2.5]. A stimulation electrode (#CBCSG75, a concentric bipolar electrode, FHC Inc., United States) was inserted in the CA1 alveus [anterior–posterior, −4.8; medio-lateral, 2.7; dorso-ventral, 2.3] for antidromically activating the neurons upstream in the recording site. Based on the clear lamellar organizations of neuronal structures in the hippocampus, the recordings of both unit activity and the specific waveforms of evoked potentials along the 16 channels were used to correct the final positions of the two electrodes. The channel closest to the pyramidal layer that was able to record an evoked-PS with a maximum amplitude was used to analyze the changes of evoked potential during HFS.

Electrical signals collected by the recording electrode were amplified by a 16-channel extracellular amplifier (Model 3600, A-M Systems Inc., United States) with a frequency range of 0.3–5000 Hz. The amplified signals were then sampled by an ML880 Powerlab 16/30 data acquisition system (ADInstruments Inc., Australia) at a sampling rate of 20 kHz/channel. PSs were extracted by a high-pass digital filter with a cutoff of 50 Hz.

Stimulations were sequences of biphasic current pulses with a strength of 0.3 mA and a width of 0.1 ms per phase. To compare the steady-state neuronal responses with those of two temporal arrangements of varying IPI, we utilized two patterns of pulse sequences: a same prelude 20-s period of 100-Hz HFS with constant IPI of 10 ms allowing the neuronal responses to reach steady state, followed by a 10-s period of 100–200 Hz varying IPI either quasi-linearly decreasing from 10 to 5 ms or randomly varying in the range of 5–10 ms. The mean frequency of varying IPI was 133 Hz, similar to the most used DBS frequency 130 Hz. The deceasing IPI was "quasi-linear" because it was designed to have a uniform distribution of IPI counts but not with an exact linear relationship between IPI lengths and time course.

The 10-s sequences of gradually varying IPI and randomly varying IPI were composed of the same set of 1,334 IPIs in the range of 5–10 ms with a sampling resolution of 0.05 ms, that is, 20 kHz, same as the sampling rate of the signal recordings in the experiments. Under this resolution, the 5- to 10-ms range was divided into 101 different lengths of IPI. With a uniform distribution, each IPI length was repeated 13 times in the sequences with an addition of one IPI in every five IPI lengths to get a total of 1,334 IPIs ($101 \times 13 + 21$) with a duration of 10.005 s. The 1,334 IPIs were arranged from the longest to the shortest in the sequence of gradual IPI or were randomized by the MATLAB function randperm() to get the sequence of random IPI. Four different sequences of random IPI were used in the rat experiments, and one of the sequences was used in the computational simulation.

Simulation Models

The computational model includes a population of pyramidal neurons in hippocampus with the mechanisms of potassium ion accumulation and clearance in the narrow peri-axonal space, distributed application of stimulation currents induced by a bipolar electrode, and recording of extracellular potential. The simulation was performed by using the NEURON simulation package (Hines and Carnevale, 1997).

Model of Pyramidal Neurons

Morphology

The pyramidal neuron consisted of a cell body, an axonal initial segment (AIS), dendrites, and a long myelinated axon (**Figure 1A**). The cell body was an asymmetric spindle with a length of 20 μm (Migliore et al., 1999), consisting of 10 cylinder segments with a maximum diameter of 20 μm in the center that linearly decreased to 5 μm to the dendrite side and to 1.7 μm to the AIS side. The AIS was 50 μm long with a diameter of 1.22 μm (Hu et al., 2009). The dendrites were simplified as five separate cylinder segments, each with 20-μm length and 5-μm diameter. The myelinated axon consisted of 20 Ranvier nodes (abbreviated as Node) and 20 internode segments with detailed structures similar to those of a previous axon model (Bellinger et al., 2008; Guo et al., 2018). The outside diameter of axon was ∼1 μm wrapped by 15 layers of myelin membranes. The internode segments were made up of paranodal junction (PNJ), juxtaparanode (JXP), and internode (IND). Details of sizes and morphologic parameters of each neuronal element are shown in **Table 1**.

Electrical properties

The neuronal membrane consisted of both passive and active electrical properties. The parameters of passive electrical properties include membrane capacitance, leakage conductance, leakage reverse potential, and intracellular resistivity. The capacitance and leakage conductance were distributed on the entire membrane of the neuron including the myelin. The intracellular resistivity was 300 Ω cm in cell body and 70 Ω cm in axon (McIntyre et al., 2004). The details of the passive electrical parameters are shown in **Table 2**.

The parameters of active electrical properties including sodium, potassium, and calcium channels are distributed in different membrane sections (**Table 2** and **Figure 1A**). The ion channels distributed on the neuronal membrane include the followings: voltage-gated Na^+, non-inactivating K^+ (M current) channel, voltage-gated K^+ channel, Ca^{2+}-dependent K^+ channel, and high-voltage activated Ca^{2+} channel for cell body

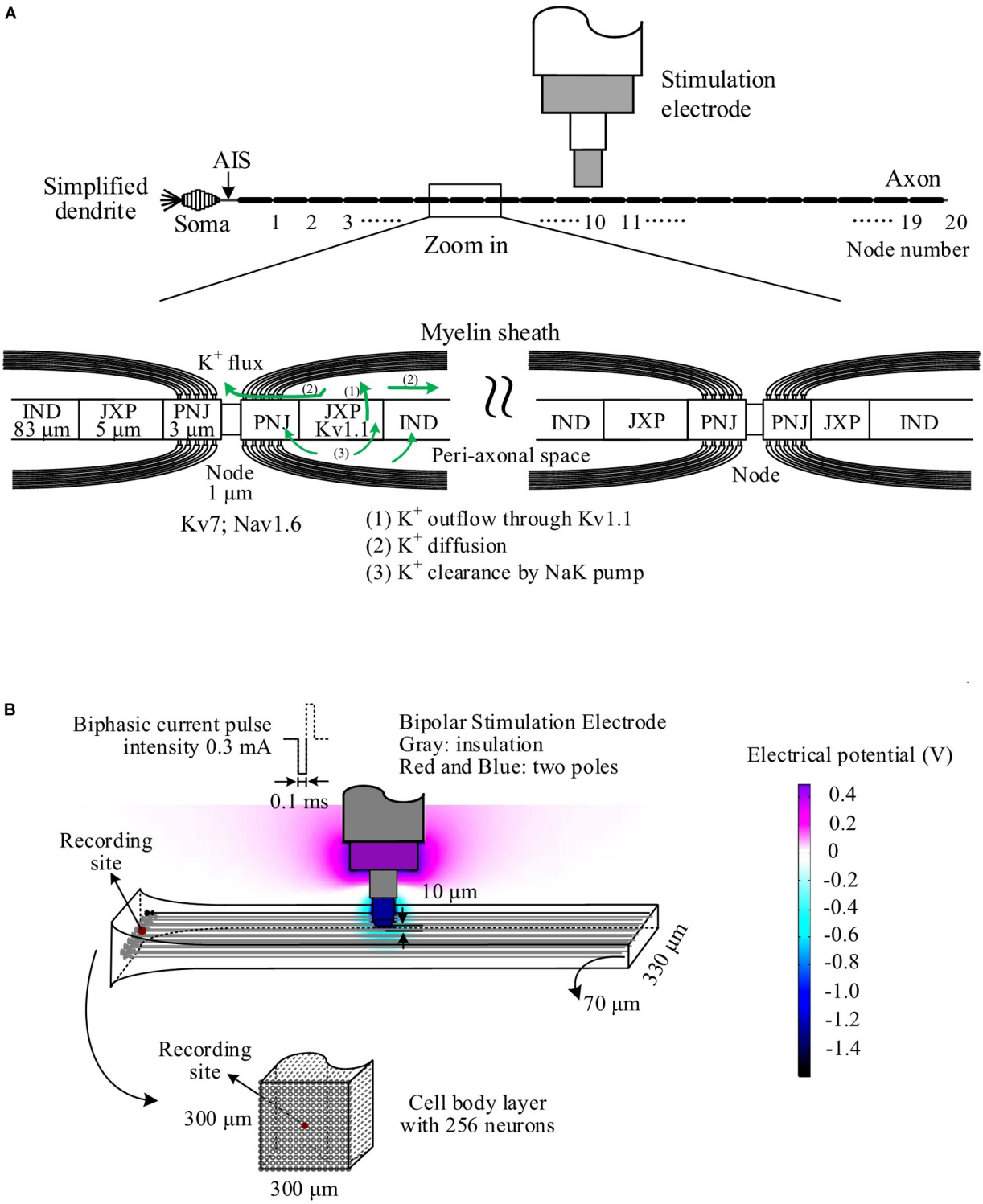

FIGURE 1 | Schematic diagram of the simulation model. **(A)** The neuron consisting of a cell body, simplified dendrites, an axonal initiation segment (AIS) and a long myelinated axon. The axon consisted of 20 Ranvier nodes (Node) and 20 internode sections including paranodal junction (PNJ), juxtaparanode (JXP), and internode (IND). Voltage-gated channels of K^+ (Kv7) and Na^+ (Nav1.6) are on the membrane of Node, whereas fast K^+ channels (Kv1.1) are on the JXP membrane. The green lines denote the outwards flow of K^+ through Kv1.1 channels, accumulating in the peri-axonal space, back through NaK pump, and diffusing to the outside of Node. **(B)** Simulation of the electric field generated by the negative phase of a stimulation pulse in COMSOL. A layer of 256 neurons are arranged in parallel with small axial shifts randomly distributed within 20 μm. The stimulation electrode is located 10 μm over the surface of neuronal layer above the central node ($Node_{10}$) of all neurons, delivering biphasic current pulses (0.1 ms, 0.3 mA). A mimic recording electrode is set at the center of cell body end.

TABLE 1 | Morphologic parameters of the neuron model.

Parameter	Value
Cell body	
Soma length	20 μm
Soma maximum diameter	20 μm
Axonal initial segment (AIS) length	50 μm
Axonal initial segment diameter	1.22 μm
Dendrites	
Dendritic (five segments) length	100 μm
Dendritic diameter	5 μm
Myelinated axon	
Axon diameter	1 μm
Number of myelin lamella	15
Node length	1 μm
Node diameter	0.7 μm
Internode segment length	100 μm
PNJ length and diameter	3 and 1 μm
JXP length and diameter	5 and 1 μm
IND length and diameter	83 and 1 μm
Peri-axonal space width outside PNJ	0.004 μm
Peri-axonal space width outside JXP and IND	0.012 μm

PNJ, paranodal junction; JXP, juxtaparanode; IND, internode.

TABLE 2 | Electrical parameters of the cell body, dendrite, and axon.

Parameter	Value
General	
Membrane capacitance	1 μF/cm^2
Leakage reversal potential	−65 mV
Na^+ Nernst potential	45 mV
K^+ Nernst potential (without K^+ accumulation)	−90 mV
Ca^{2+} Nernst potential	140 mV
Soma and dendrite	
Max voltage-gated Na^+ conductance	80 pS/μm^2
Max slow non-inactivating K^+ conductance	0.3 pS/μm^2
Max fast voltage-gated K^+ conductance	20 pS/μm^2
Max Ca^{2+}-dependent K^+ conductance	3 pS/μm^2
Max high-voltage activated Ca^{2+} conductance	0.3 pS/μm^2
Leakage conductance	0.5 pS/μm^2
Axonal initial segment (AIS)	
Max fast voltage-gated Na^+ conductance	1,100–3,200 pS/μm^2
Max fast voltage-gated K^+ conductance	200–1,000 pS/μm^2
Leakage conductance	0.5 pS/μm^2
Axon internode section	
Myelin conductance	10 pS/μm^2
Myelin capacitance	0.1 μF/cm^2
PNJ leakage conductance	1 pS/μm^2
JXP leakage conductance	1 pS/μm^2
JXP max fast K^+ conductance	300 pS/μm^2
IND leakage conductance	1 pS/μm^2
Axon node	
Max voltage-gated Na^+ conductance	6,000 pS/μm^2
Max slow voltage-gated K^+ conductance	150 pS/μm^2
Leakage conductance	1 pS/μm^2

PNJ, paranodal junction; JXP, juxtaparanode; IND, internode.

and dendrites; voltage-gated K^+ channel (Kv) and voltage-gated Na^+ channel (Nav1.2 and Nav1.6) for the AIS (Hu et al., 2009); fast K^+ channel (i.e., Kv1.1) for the membrane of JXP in the internode sections; and voltage-gated Na^+ channel (Nav1.6) and slow K^+ channel (Kv7) for the Node. Specifically, the Nav1.2 subunit was present in proximal AIS, whereas Nav1.6, although present in proximal AIS, was dominant in distal AIS and the axonal Node. The Kv density increased linearly with distance in the AIS to a maximum value of 1,000 pS/μm^2. A previous model (Hu et al., 2009) may be referred to for the detailed distribution of Na^+ and K^+ channels in the AIS. On the Node membrane, the density of Nav1.6 channels was about 6,000 pS/μm^2 (Lorincz and Nusser, 2010) and the K^+ channel density was 150 pS/μm^2 (Röper and Schwarz, 1989; Battefeld et al., 2014).

Accumulating and Clearing Mechanisms of Potassium Ions in the Model

Potassium accumulated in the narrow peri-axonal space during stimulation because of the outflow of K^+ from the intracellular space through K^+ channels in JXP (Bellinger et al., 2008; Guo et al., 2018). The accumulated K^+ was cleared by NaK pumps distributed uniformly on the membrane of internode sections and by axial diffusion of K^+ from the peri-axonal space to the extracellular space outside Nodes (indicated by the green arrow in **Figure 1A**). The axial diffusion of K^+ followed the Fick law:

$$J = D \times A \times \frac{\mathrm{d}[K^+]_o}{\mathrm{d}x} \quad (1)$$

where J is the diffusion flux; D is the diffusion coefficient (1.85 μm^2/ms); A is the cross-sectional area of the peri-axonal space of 0.025, 0.076, and 0.076 μm^2 outside PNJ, JXP, and IND, respectively; $[K^+]_o$ is the K^+ concentration in peri-axonal space; and x is the diffusion distance. The concentration of potassium ion outside the Node (extracellular concentration) was 3 mM.

The clearance of K^+ by NaK pump, which pumped out three Na^+ and pumped in two K^+ per ATP hydrolyzed, was described as follows:

$$I_{\mathrm{NaK}} = I_{\mathrm{NaK\,max}} \left(\frac{[K^+]_o}{[K^+]_o + \mathrm{KmK}} \right) \times \left(\frac{[Na^+]_i^{1.5}}{[Na^+]_i^{1.5} + \mathrm{KmNa}^{1.5}} \right) \left(\frac{V + 150}{V + 200} \right) \quad (2)$$

where V is the membrane potential; $[Na^+]_i$ is intracellular Na^+ concentration; I_{NaKmax} is the maximum transport current per unit area, set as 2.46 μA/cm^2; and KmK and KmNa are the equilibrium binding constants of K^+ and Na^+, set as 5.3 and 27.9 mM, respectively.

Models of Stimulation and Recording

Pulse sequences were applied by a stimulation electrode located 10 μm above the top surface of the axial center of an axon layer or approximately over the center Nodes ($Node_{10}$) of axons (**Figure 1A**). The layer included 256 axons distributed uniformly in an array of 8 × 32 in a cross section of 70 μm × 310 μm with an inter-axon distance of 10 μm in both spatial orientations (**Figure 1B**). The axial positions of the parallel axons shifted

randomly within a range of −10 to +10 μm, mimicking the lamellar organization of alveus axons. The cell bodies of the neurons were distributed uniformly in an array of 16 × 16 in a cross section of 300 μm × 300 μm and in random one-to-one correspondence with the 256 axons.

The electrical field generated by biphasic pulses was simulated with finite element software COMSOL Multiphysics 5.3 (COMSOL Inc., Sweden), thereby determining the stimulation potentials imposing immediately outside every Ranvier node (Node) of the axonal fibers. Both the electrode parameters (size and material) and stimulation parameters (current biphasic pulses) used in COMSOL simulation were consistent with experimental settings. The stimulation sequences applied in the model were similar to those used in rat experiments, that is, following a prelude of 100-Hz HFS with constant IPI by 100–200 Hz varying IPI of either gradual IPI or random IPI. A recording site was located in the center of the cell body layer to record extracellular potential (Ep) including the extracellular action potentials either from a specific single neuron (i.e., unit spike, abbreviated as spike) or from a population of neurons (i.e., PS). The equation for Ep was as follows (Varona et al., 2000; Guo et al., 2018):

$$\mathrm{Ep} = \frac{1}{4\pi\sigma}\sum\frac{I}{r} \tag{3}$$

where σ is the extracellular conductivity (0.286 S/m), I is the transmembrane current, and r is the distance between the recording site and each neuronal element generating I, including the compartments of cell body and AISs. Although the transmembrane currents from dendrites may contribute to the shape of the PS waveforms (Varona et al., 2000), we did not take into account the dendrite currents because the exact PS waveform was not critical for the study. We only utilized the PS amplitude, especially the relative changes of PS amplitudes during an HFS sequence, to estimate the relative changes in the number of firing neurons. The major contributions from cell body and AIS were adequate.

Other signals such as intracellular membrane potentials (V_m), concentration of K^+ in peri-axonal spaces ($[K^+]_o$), and dynamics of Na^+ channels (e.g., inactivation variable of Na^+ channel, h_Na) were extracted directly from simulation results in NEURON.

Data Analyses for Both Rat Experiments and Modeling

The amplitude of PS was used to evaluate the number of neurons simultaneously generating action potentials (Kloosterman et al., 2001). The PS amplitude was normalized by the mean PS amplitude induced during steady-state of HFS with constant IPI of 10 ms. The mean value of normalized PS amplitudes induced by each pulse during varying IPI was calculated by dividing the sum of PS amplitudes by the pulse number. The range (maximum–minimum) of normalized PS amplitudes was used to describe the variation of PS amplitudes. Because the history of IPIs plays a role in how many neurons are recruited in the PS, the two IPIs immediately preceding a stimulus ("1-back IPI" and "2-back IPI," termed as IPI_1 and IPI_2, respectively) were examined. Correlation analysis was implemented to analyze the relationships between the PS amplitude and the preceding IPIs (including IPI_1 and $\Delta IPI = IPI_1 - IPI_2$). Student t-test was used to show the statistical significance of the difference between data groups. Additionally, in simulation, the threshold of h_Na at the center node ($Node_{10}$) for a specific neuron was defined as the minimal value of h_Na at the onset of a pulse that was able to induce an action potential successfully propagating to the cell body.

RESULTS

Different Neuronal Responses to High-Frequency Stimulation With Gradually and Randomly Varying Inter-Pulse Interval in Rat Hippocampus *in vivo*

Stimulations applied in the alveus of hippocampal CA1 region can antidromically excite a population of CA1 pyramidal neurons without involving synaptic transmissions (**Figure 2A1**). A single pulse evoked a large PS (**Figure 2A2**) with a short latency of 1.27 ± 0.09 ms and an amplitude 9.1 ± 1.9 mV (n = 7 rats), just as that evoked by the very first pulse in any pulse sequences. However, after seconds of prolonged 100-Hz HFS with constant IPI, during the steady state, each pulse only evoked a small PS with an amplitude ∼20% of the original amplitude. Afterward, when the IPI gradually decreased from 10 ms (100 Hz) to 5 ms (200 Hz) in a 10-s period, the PS amplitude decreased further to ∼6% of the original amplitude (**Figure 2B1**). The PS amplitudes induced by gradual IPI were compared with those with constant IPI in a 10-s period immediately before the gradual IPI (**Figure 2B2**, the switch moment of the two IPI patterns is set as time "0," with the time duration of −10 to 0 s for constant IPI and 0–10 s for gradual IPI). The normalized PS amplitude decreased from 1 to 0.3 during the 10-s period of gradual IPI. During this period, the IPI decreased quasi-linearly and distributed uniformly in the range of 5–10 ms (**Figure 2B3**). The PS amplitude significantly correlated with its 1-back IPI (IPI_1) with a correlation coefficient of 0.94 (**Figure 2B4**). When the above stimulation was followed by a pulse sequence with a reverse change of IPI from 5 to 10 ms, a reverse change of PS increase was observed, as expected. For simplicity, the data are not repeatedly presented here.

When the varying IPI of a gradual order was replaced by a random order, the normalized amplitudes of evoked PS varied randomly in a much wider range from 0 (no PS) to ∼2.4 (**Figures 2C1,C2**), as compared with the range of 0.3–1 induced by gradual IPI. Although the random IPI was in the same range of 5–10 ms and with the same uniform distribution (**Figure 2C3**), the correlation coefficient (0.73) between the PS amplitudes and the preceding IPI_1 of random IPI was smaller than that of gradual IPI. The less correlation was caused by a lot of small PSs appearing following the longer IPIs (**Figure 2C4**). However, the correlation coefficient between the PS amplitudes and ΔIPI ($=IPI_1 - IPI_2$) increased to 0.88 (**Figure 2C4**), indicating that a longer IPI_1 accompanied by a short IPI_2 (2-back IPI) would result in a larger PS with a higher probability.

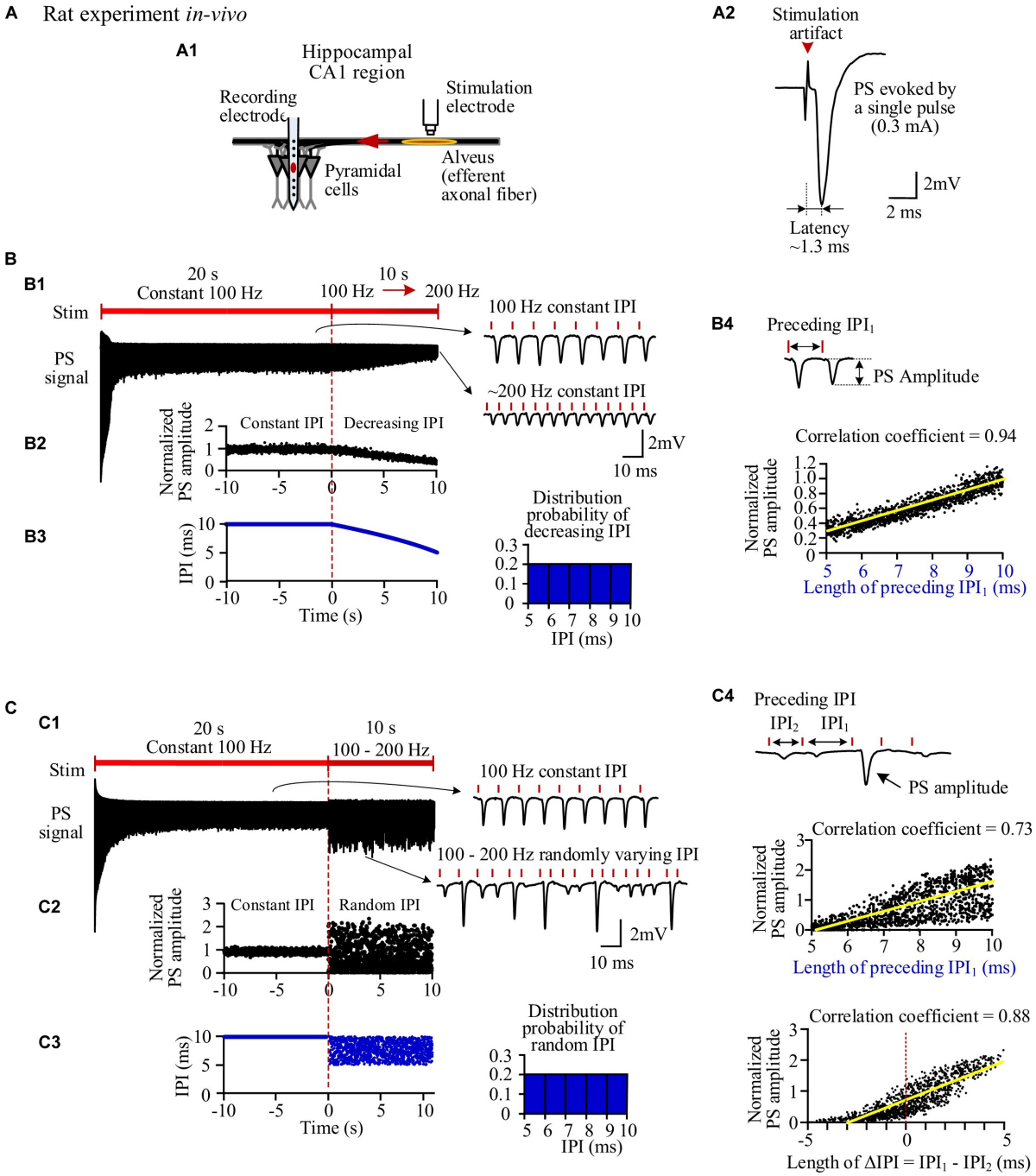

FIGURE 2 | Neuronal responses to stimulations with different inter-pulse interval (IPI) sequences in rat hippocampal CA1 region *in vivo*. **(A)** A1: Schematic diagram of the locations of a recording electrode in pyramidal layer and a stimulation electrode at alveus to antidromically activate the pyramidal cells. A2: A population spike (PS) evoked by a single pulse (0.3 mA). **(B)** PS evoked by pulses with gradually decreasing IPI. B1: A typical PS recording during 30-s HFS consisted of 20 s of constant IPI (10 ms, 100 Hz) followed by 10 s of gradually decreasing IPI (10 to 5 ms, i.e., 100 to 200 Hz). B2: Changes of normalized PS amplitudes during 10 s of constant IPI and 10 s of gradual IPI. The switch moment from constant IPI to gradual IPI is set as time "0." B3: IPI curve along stimulation time (*left*) and distribution probability of gradual IPI (*right*). B4: Correlation between normalized PS amplitude and preceding IPI during 10-s period with gradual IPI. **(C)** PS evoked by pulses with random IPI. C1–C4: Corresponding to B1–B4. *Bottom of* C4: Correlation between the normalized PS amplitude and the difference of IPI_1–IPI_2.

Statistical data (n = 7 rats) showed that the mean normalized PS amplitude during 10-s period of random IPI was similar to that of gradual IPI (**Table 3**), whereas the range of normalized PS amplitude with random IPI was significantly greater than the value with gradual IPI. However, because of the same pulse number and similar mean of normalized PS amplitude, the sums

TABLE 3 | Normalized PS amplitudes distribution during gradually and randomly varying IPI.

IPI patterns	Normalized PS amplitude		Correlation coefficient (PS amplitude vs. IPI)	
	Range	Mean	Preceding IPI_1	Preceding IPI_1-IPI_2
Experiment (*n* = 7 rats)				
Gradual	0.92 ± 0.05	0.72 ± 0.06	0.92 ± 0.03	–
Random	2.49 ± 0.43**	0.77 ± 0.06	0.72 ± 0.04**	0.84 ± 0.03##
Simulation				
Gradual	1.12	0.62	0.92	–
Random	2.95	0.73	0.73	0.8

*PS, population spike; IPI, inter-pulse interval. **P < 0.001, gradual IPI vs. random IPI, t-test, n = 7 rats. ##P < 0.001, random IPI_1-IPI_2 vs. random IPI_1, t-test, n = 7 rats.*

of normalized PS amplitude during gradual IPI and random IPI were approximately equal, indicating similar amounts of total neuronal firing. Additionally, the mean correlation coefficient between the PS amplitude and the preceding IPI_1 (or IPI_1-IPI_2) was significantly smaller with random IPI than with gradual IPI. The results of large PS indicated that pulses with random order of varying IPI could occasionally recruit a larger fraction of neurons to fire together.

Previous studies with constant IPI have shown that prolonged HFS can extend the refractory periods of the neuronal membranes owing to accumulation of extracellular potassium, leading to the intermittent firing of individual neurons and a decrease of PS amplitude with higher frequency (i.e., shorter IPI) (Feng et al., 2014; Guo et al., 2018). We hypothesize that the same mechanism of potassium accumulation in the narrow peri-axonal space together with non-linear dynamics of ionic channels may generate the irregular neuronal responses with simultaneous recruitment of a larger fraction of neurons by pulses with random order of varying IPI. Because current techniques of *in vivo* experiments have limitations in simultaneous intracellular recordings of individual axons, we next tested the hypothesis by a modeling study.

Simulated Neuronal Responses to High-Frequency Stimulation With Varying Inter-Pulse Interval of Gradual and Random Orders

The simulated evoked PS (**Figure 3**) closely matched the experimental recordings (**Figure 2**). At the onset of a pulse sequence, the evoked PS was also as large as a PS evoked by a single pulse (**Figures 3A,B1**). Following seconds of prolonged 100-Hz HFS, during the steady-state period, the PS amplitude decreased to ∼20% of the original amplitude. Afterward, when IPI gradually decreased from 10 to 5 ms in a 10-s period, the PS amplitude further decreased to ∼4% of the original amplitude (**Figure 3B1**). The normalized PS amplitude decreased from ∼1 at the start (corresponding to 10-ms IPI) to ∼0.2 at the end (corresponding to 5-ms IPI) during the 10-s period with gradual IPI (**Figure 3B2**). In addition, the PS amplitude was significantly correlated with its preceding IPI with a correlation coefficient of 0.92 (**Figure 3B3** and **Table 3**).

Similar to the experimental results, when the varying IPI in a gradually decreasing order was replaced with a random order, the normalized PS amplitude varied in a much wider range from 0 to 2.95 (**Figures 3C1,C2**), more than double of the value with gradual IPI (2.95 vs. 1.12, **Table 3**). However, the mean normalized PS amplitudes during the periods with two different orders of varying IPI were relatively close (0.62 vs. 0.73). Additionally, the correlation coefficient between the PS amplitude and the preceding IPI_1 was smaller with random order IPI than with gradual IPI (0.73 vs. 0.92); but the correlation coefficient between the PS amplitude and the ΔIPI increased to 0.8 (**Figures 3C3,C4** and **Table 3**).

The PS only reflects the summation of firing from a population of neurons. To investigate the underlying mechanisms, we next examined unit spike firing of individual neurons.

Simulated Membrane Dynamics of Individual Neurons During High Frequency Stimulation With Different Inter-Pulse Interval Patterns

Neurons at different distances from the stimulation electrode had different periodical firing patterns because they received different stimulation intensities (Guo et al., 2018). We took one neuron as an example, with its middle axonal node ($Node_{10}$) located at a distance 104.4 μm (30 μm below and 100 μm left) from the stimulation center (**Figure 4A**). During the steady state of 100 Hz of constant HFS, the inter-spike interval (ISI) of the neuronal firing kept constant at two times the IPI as the neuron fired a spike at every other pulses (**Figure 4B**). During the period of gradually decreasing IPI, the firing ISI exhibited two alternating stages: gradually decreasing stage and jumping stage (**Figure 4C**). At a gradually decreasing stage, the ISI decreased gradually following the decrease of IPI as the neuron fired steadily at every *n*-th pulses. The stage was interrupted by sporadic and short jumping stages when the ISI increased by one or more IPI. Therefore, during most of the stimulation period with gradual IPI, the firing of individual neurons was similar to the firing under constant IPI. However, during the entire 10-s stimulation period with random IPI, the firing ISI changed randomly in a wider range (14.5–64.5 ms) (**Figure 4D**).

To analyze the mechanisms underlying the behaviors of individual neurons during HFS with gradual IPI and random IPI, we extracted the following variables from the simulation results: the accumulated $[K^+]_o$ in peri-axonal space near $Node_{10}$, the membrane potential (V_m) on $Node_{10}$, the inactivation variable

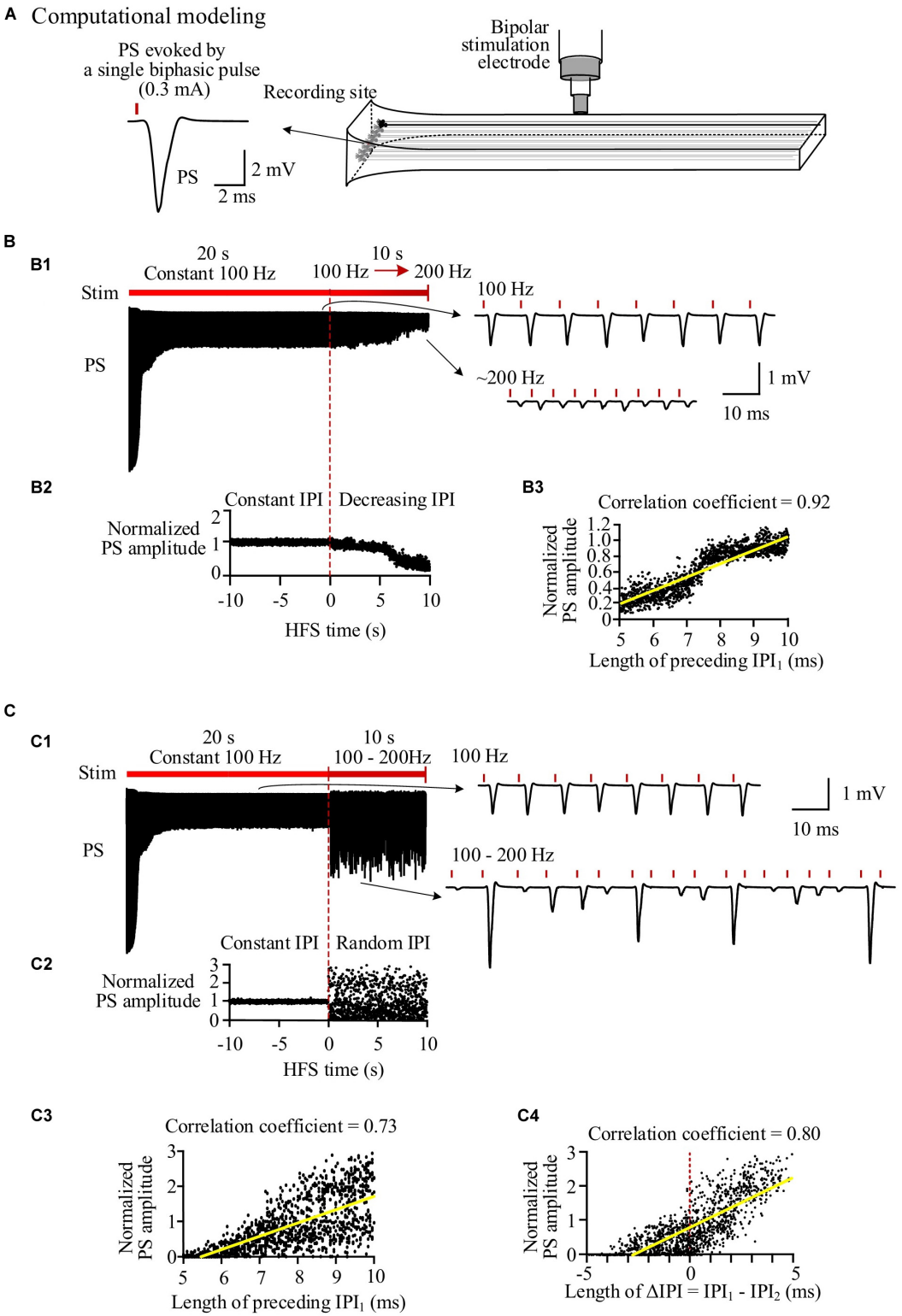

FIGURE 3 | Simulation of neuronal responses to stimulations with different inter-pulse interval (IPI) sequences. **(A)** Schematic diagram of the locations of stimulation electrode and recording electrode together with a population spike (PS) waveform evoked by a single pulse. **(B)** Simulated PS evoked by pulses with gradual IPI. B1: Simulated PS signal during 30-s HFS including 20 s of constant IPI (10 ms, 100 Hz) followed by 10 s of gradually decreasing IPI (10 to 5 ms, i.e., 100 to 200 Hz). B2: Changes of normalized PS amplitudes during 10 s of constant IPI and 10 s of gradual IPI. The switch moment from constant IPI to gradual IPI is set as time "0." B3: Correlation between normalized PS amplitude and its preceding IPI during 10-s period with gradual IPI. **(C)** Simulated PS evoked by pulses with random IPI. C1–C3: Corresponding to B1–B3. C4: Correlation between the normalized PS amplitude and the difference of IPI_1–IPI_2.

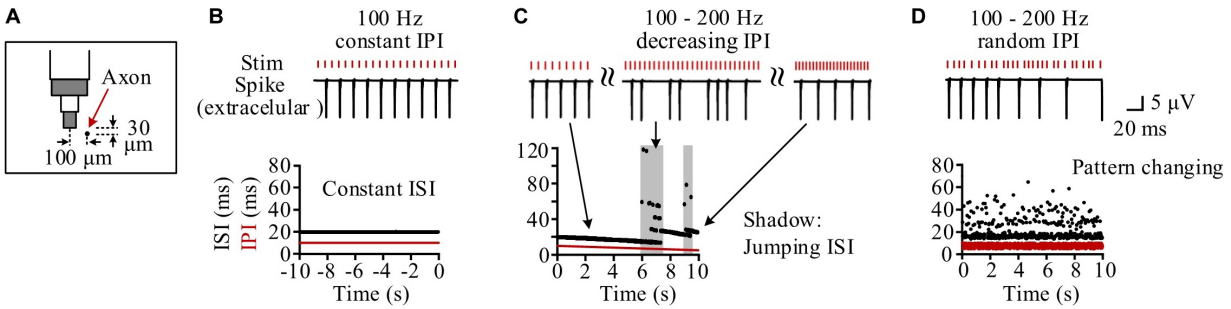

FIGURE 4 | Simulation of the response firing of a typical neuron to different pulse sequences. **(A)** Schematic diagram of the neuron's location with its axon center ($Node_{10}$) 104.4 μm (30 μm below and 100 μm left) from the bottom center of the stimulation electrode. **(B)** During the steady-state period of constant inter-pulse interval (IPI) of 10 ms, the neuron fires with a constant inter-spike interval (ISI) of 20 ms. **(C)** During the stimulation period with gradual IPI, the ISI of neuronal firing gradually decreases along with the decrease of IPI in most time except several jumping stages (denoted by shadows) to elevate the ISI in stairs by adding one or more IPI into ISI. **(D)** During the stimulation period with random IPI, the ISI of neuronal firing changes irregularly all the time.

(h_Na) of Na^+ channel on $Node_{10}$, and the extracellular spike signal of the soma (**Figure 5A**).

Following the prelude 20-s period of 100-Hz HFS with constant IPI of 10 ms, the $[K^+]_o$ had increased from original 3 to above 12 mM. The accumulated K^+ elevated V_m from original −70 to around −60 mV, thereby inactivating Na^+ channel as h_Na declining from baseline value 0.95 to below 0.5. Nodal membrane depolarized upon each incoming pulse and repolarized during the interval before the incoming of next pulse.

During most of the period with gradual IPI, pulses of HFS changed the membrane dynamics of the neuron periodically. **Figure 5B1** shows an episode of gradually decreasing IPI of ∼10 ms. At every other pulse, an action potential (AP) was generated and then resulted in a pronounced elevation of $[K^+]_o$ as well as a pronounced decline of h_Na, consequently. Accordingly, the V_m, $[K^+]_o$ and h_Na changed periodically. At the onset moment of each pulse, V_m on $Node_{10}$ was either −59.0 or −60.6 mV, $[K^+]_o$ 12.9 or 12.4 mM, and h_Na 0.330 or 0.454, respectively corresponding to a subthreshold state or a suprathreshold state of firing. The alternation between the two states gave rise to an intermittent and regular firing of spikes with an ISI of ∼20 ms, two times the IPI.

In contrast, HFS with random IPI (5–10 ms) induced irregular firing of spikes in the same neuron owing to the non-linear dynamics of the membrane excitation. Because the inactivation of Na^+ channel (h_Na) has a much longer time constant than the activation of Na^+ channel (Hodgkin and Huxley, 1952), the excitability of Na^+ channels during HFS was mainly determined by the recovery of h_Na. A small difference in h_Na could change the membrane excitability and flip its state from subthreshold to suprathreshold or vice versa, thereby drastically changing the firing pattern of the neuron (**Figure 5B2**). For instance, for the three firing patterns of type 1, type 2, and type 3 illustrated in **Figures 5B2,C1**, one, three, and four pulses failed to activate spikes in soma and resulted in an ISI of 16.0, 27.1, and 34.8 ms, respectively. Failed pulses still caused the membrane depolarization that delayed the recovery course of h_Na. In this case, the h_Na threshold for generating a spike at soma was 0.386 (**Figure 5B2**). For the type 2 firing pattern shown in **Figure 5C1**, with a preceding pulse P2 (a failed pulse), a recovery of h_Na to 0.370 at the onset moment of pulse P3 only allowed the pulse to generate an AP at $Node_{10}$, but the AP failed to activate the soma to fire a spike. Otherwise, in a case without the preceding failed pulse P2, the h_Na would have recovered to 0.421 to exceed the threshold, thereby driving the soma to fire a spike (**Figure 5C2**).

It should be noted that a fraction of AP induced at axonal nodes were not strong enough to travel to the soma and generate an AP (i.e., a spike) at soma (see **Figures 5B2,C1**). Nevertheless, the failed AP would decrease h_Na substantially, delaying the recovery of h_Na and possibly preventing the next pulse from generating a spike (denoted by hollow triangles in **Figures 5B2,C1**). The repeated delays of h_Na recovery resulted in a prolonged interval between two adjacent spikes (**Figure 5C3**).

These simulation results indicated that stimulations with regular IPI (including most of the period with gradually varying IPI) can generate AP with regular ISI in individual neurons. However, stimulations with a random order of varying IPI can postpone the firing of individual neurons and generate AP with various ISI. The different patterns of ISI could result in different numbers of neurons to fire spikes simultaneously. Therefore, we next investigated the firing of neuron populations by modeling.

Comparing Firing of Neuronal Population Induced by High-Frequency Stimulation With Regular and Random Inter-Pulse Interval

During episodes of stimulation with gradually varying IPI, individual neurons fired spikes in a fixed periodical pattern. For example, five neurons with different distances (at $Node_{10}$) to the stimulation center of 28, 70, 104, 117, and 130 μm had different periodical patterns of spike firing (**Figure 6A1**). Neurons located nearer to the stimulation electrode received a greater stimulation intensity and had a lower h_Na threshold for firing. Because of the overstimulation received, the nearest neuron (Neuron-1) was not able to fire spike, with its h_Na at $Node_{10}$ only fluctuating below the firing threshold at the onset of each incoming pulse.

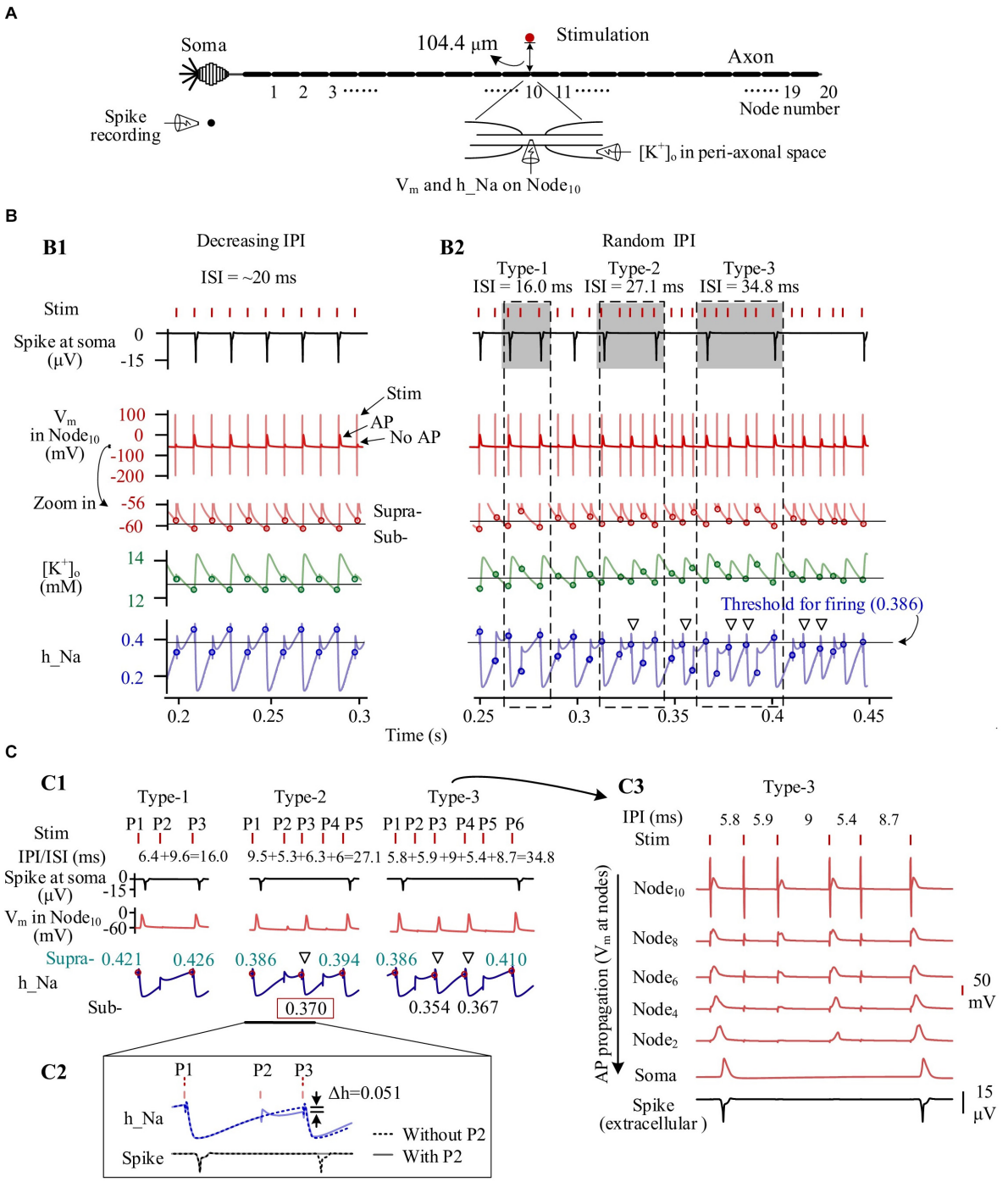

FIGURE 5 | Simulated dynamics of neuronal membrane during high-frequency stimulation (HFS) with different patterns of inter-pulse interval (IPI). **(A)** Schematic diagram of simulated signals collected from a neuron, including K^+ concentration in peri-axonal space near $Node_{10}$ ($[K^+]_o$), membrane potentials of $Node_{10}$ (V_m), inactivation variable of Na^+ channels on $Node_{10}$ (h_Na), and spike recording near soma. **(B)** Dynamics of four signals during stimulations with gradually varying IPI (B1) and randomly varying IPI (B2). Circles on the curves of V_m, $[K^+]_o$ and h_Na denote the values at the onset of stimulation pulses. Thin horizontal lines on the three curves denote thresholds for neuronal firing. Three typical IPI sequences (shadowed) generate different lengths of inter-spike interval (ISI) of 16.0, 27.1, and 34.8 ms. **(C)** Generation of different ISI. C1: The three examples of IPI sequences from B2 show that the levels of inactivation variable h_Na at the onset of pulses determine whether AP can be induced at $Node_{10}$ and whether the AP can successfully propagate to soma. The red dots and cyan numbers on the h_Na curves denote h_Na values at the onset of pulses inducing AP at $Node_{10}$. C2: A pulse (P2) failing to induce AP can decrease h_Na and delay the recovery course of h_Na, thereby causing no spike at soma following the next pulse (P3). A spike would otherwise be evoked by P3 in the situation without P2. C3: Even an AP is induced on $Node_{10}$ immediately under the stimulation electrode, due to an inadequate recovery of h_Na, the AP may not be strong enough to propagate along the axon to generate a spike at soma. Hollow triangles in B2 and C1 denote that the APs of $Node_{10}$ fail to generate a somata spike but can cause a substantial decrease of h_Na.

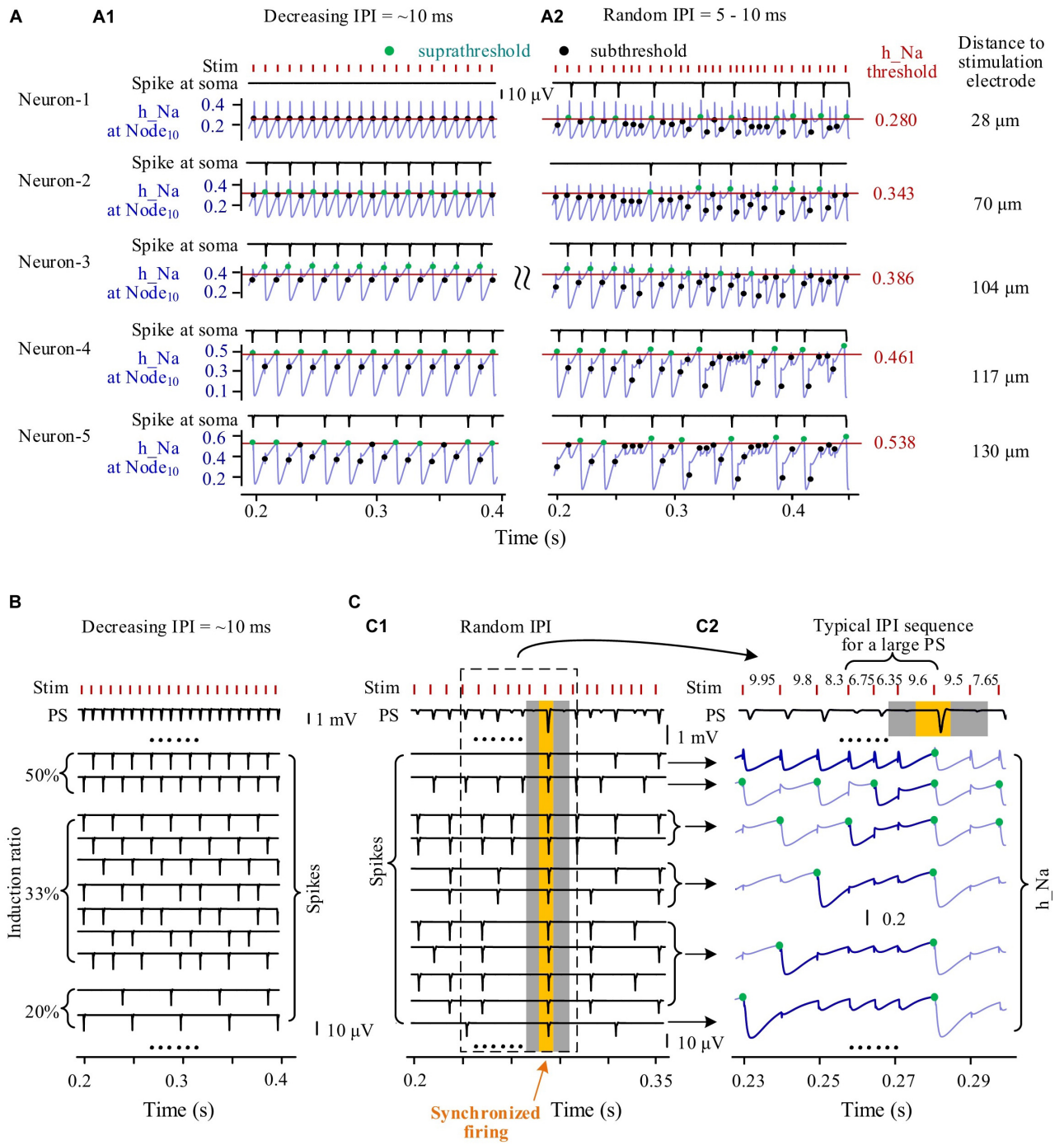

FIGURE 6 | Simulated responses of multiple neurons to form population spikes (PSs) during stimulations with different patterns of inter-pulse interval (IPI). **(A)** Somata spikes and inactivation variable h_Na curves of five neurons with different distances (28–130 μm) from the stimulation electrode. Thin horizontal lines on the h_Na curves denote spike thresholds of individual neurons (0.280–0.538). A1: During an episode of stimulation with gradually decreasing IPI, except that Neuron-1 does not fire spikes, the other four neurons generate spikes regularly with h_Na regularly switching between suprathreshold and subthreshold levels (denoted by green and black dots, respectively) upon a pulse incoming. A2: During stimulation with random IPI, all of the five neurons generate spikes irregularly with h_Na surpassing threshold occasionally upon a pulse incoming. **(B)** During an episode of stimulation with gradually decreasing IPI, regular firing of individual neurons with different induction ratios (ratio of spike number to pulse number) produces uniform PS. **(C)** During stimulation with random IPI, a large PS formed by synchronous neuronal firing is induced by a typical IPI sequence. C1: Different spike sequences of individual neurons integrate into PS sequences with various PS amplitudes including a large PS (yellow zone) with surrounding silent periods of no PS (gray zones). C2: Inactivation variable h_Na curves show the recovery course of h_Na before synchronous firing of neurons following an IPI sequence including two shorter IPI (6.75 and 6.35 ms) and one longer IPI (9.6 ms). The thickening and dark-blue segments of h_Na curves show that the series of preceding pulses fail to generate somata spikes in individual neurons before the generation of the large PS.

The three neurons at other distances, Neuron-2, Neuron-3, and Neuron-4 fired spikes at a same induction ratio of 50% (i.e., every other pulse induced a spike), but Neuron-2 and Neuron-3 followed the same pulses whereas Neuron-4 followed the others. The farthest neuron (Neuron-5) had an induction ratio of 33%.

However, during the stimulation with random IPI, the five neurons all fired spikes irregularly with their h_Na at $Node_{10}$ exceeding respective threshold occasionally (**Figure 6A2**). Interestingly, Neuron-1 changed from no firing with gradual IPI into intermittent firing with random IPI.

The differences in spike firing of individual neurons resulted in different responses of a neuronal population to different patterns of varying IPI. During an episode of stimulation with gradually varying IPI (**Figure 6B**), the periodical spikes of individual neuron firing were integrated to form PSs with similar amplitudes following every pulse. However, during stimulation with random IPI, owing to the irregular firing of individual neurons, the amplitudes of integrated PS varied randomly in a large range (**Figure 6C1**). Repeatedly decreasing h_Na by several successive pulses with shorter IPI could postpone the time for h_Na to recover to its threshold (**Figure 6C2**, thick blue lines in h_Na curves), finally giving rise to simultaneous firing of a large number of neurons to form a large PS following a longer IPI (the yellow zone in **Figure 6C**). The large PS was accompanied by very small PS induced by neighboring pulses (the two gray zones in **Figure 6C**). The mean PS amplitudes induced by gradual IPI and by random IPI were similar (**Table 3** simulation), indicating that randomization of IPI could only redistribute the firing timing of neurons but not significantly change their firing amount.

These simulation results indicated that the stimulation pulses with random IPI could recruit neurons to fire at specific moments because of the occasional occurrence of specific sub-sequences of pulses, thereby generating extremely large and extremely small PS events.

DISCUSSION

The novel finding of the present study with experiments and computation is that the HFS pulses with varying IPI in random order had additional recruitment effects on the firing of neuronal population. Possible mechanisms underlying the experimental finding are unveiled by our simulation study and analyzed below.

Possible Cellular Mechanisms Underlying the Firing Patterns of Neurons Induced by Different Patterns of Varying Inter-Pulse Interval

Previous experiment studies both *in vitro* and *in vivo* have shown that HFS with a constant frequency over 50 Hz can induce partial depolarization block of axons in the brain regions such as the hippocampus and subthalamus (Jensen and Durand, 2009; Zheng et al., 2011; Rosenbaum et al., 2014). Our previous study has shown that with a substantial decrease of antidromic PS induced by HFS applied to efferent fibers of CA1 neurons as shown in the present study, the neuronal somata preserved the capacity to respond to an orthodromic stimulus with large PS (Feng et al., 2013), thereby confirming the HFS-caused failures in the axons, not in the soma. *In vitro* studies have shown that repeated pulse stimulation can elevate $[K^+]_o$, thereby causing a decreased speed of axonal conduction until a complete block. Artificially increasing $[K^+]_o$ can also lead to axonal block (Förstl et al., 1982; Poolos et al., 1987). Computational models on HFS with constant IPI suggest the underlying mechanisms of the block: the outflow of K^+ during stimulations may be trapped in the narrow peri-axonal space and increasing $[K^+]_o$, thereby prolonging depolarization of membrane and inactivation of Na^+ channels and leading to intermittent depolarization block (Bellinger et al., 2008; Guo et al., 2018). HFS at the commonly used frequency range (∼100–200 Hz) for DBS can only induce partial but not complete axonal block. The axons can still intermittently generate action potentials to form PS events (Jensen and Durand, 2009; Feng et al., 2013, 2014). During an HFS sequence with a higher frequency (i.e., shorter IPI), each pulse can recruit fewer neurons to fire, thereby only generating a smaller PS (Guo et al., 2018).

The above mechanisms may explain the IPI-dependent PSs evoked by pulses with gradually varying IPI in the present study, as shown by the highly linear correlation between PS amplitudes and lengths of immediate preceding IPI (1-back IPI) in both the experiment and simulation results (**Figures 2B**, **3B** and **Table 3**). Based on these mechanisms, it seems reasonable to speculate that the IPI-dependent PSs would have also appeared with IPI arrangements in any other orders as long as the IPI set was the same. However, our study shows that even with the same set of IPI varying only in a small range of 5–10 ms (i.e., 200–100 Hz), substantially different responses of population neurons appeared during HFS with random IPI (**Figures 2C**, **3C** and **Table 3**). Here, we reveal the mechanisms of these different neuronal responses by the recovery course of Na^+ channel with non-linear dynamics.

Owing to the much longer time constant of Na^+ channel inactivation than that of Na^+ activation (Hodgkin and Huxley, 1952), under the situation of intermittent depolarization block, the excitability of Na^+ channels in response to HFS pulses would be mainly determined by the non-linear recovery of Na^+ inactivation (h_Na). An IPI in the range of 5–10 ms was not long enough for a complete recovery of h_Na after a firing spike under the situation of HFS. It took several IPIs for h_Na to recover to a suprathreshold level. In addition, each failed pulse would also lower the h_Na and postpone the recovery of h_Na (**Figures 5**, **6**). The firing history of a neuron, the lengths of several preceding IPIs, and the pulse impulses following the previous firing affect the non-linear recovery course of h_Na, hence the next firing of the neuron.

During HFS periods with regular IPI (e.g., gradually varying IPI or constant IPI), although the number of IPI cycles needed for the h_Na recovery varied for neurons at various distances from the stimulation point, the firing of individual neurons was regular at most time because of the approximately fixed IPI length within a relative short episode. The integration of regular firing from a large population of neurons remained steady over time (**Figures 6A1,B**). However, when the varying IPI appeared randomly, the number of IPI cycles as well as the sum of IPI lengths for h_Na to recover to suprathreshold was uncertain,

and the firing of individual neurons became irregular, thereby occasionally generating extremely large and extremely small PSs as a result of the firing integration of a neuronal population (**Figures 6A2,C**).

Taken together, through the mechanisms of intermittent $[K^+]_o$ elevation and Na^+ channel inactivation induced by HFS, as well as the non-linear recovery course of Na^+ channel, HFS with different patterns of varying IPI in a small range can modulate the firing of neuronal populations differently. To our knowledge, this is the first simulation study addressing the effect of irregular pulse patterns on the neuronal firing by incorporating the mechanism of submyelin K^+ accumulation and non-linear gating dynamics of Na^+ channel activation.

Implications of the Neuronal Firing Induced by Different Patterns of Varying Inter-Pulse Interval

Pulse frequency is the most commonly used parameter to adjust the effects of DBS applications. For example, different temporal patterns of stimulation with varying frequency (IPI) have been investigated to modulate central nervous system arousal in intact mice (Quinkert et al., 2010; Quinkert and Pfaff, 2012) and in mice with traumatic brain injury (Tabansky et al., 2014) and to suppress epileptogenesis (Santos-Valencia et al., 2019). Irregular temporal patterns of stimulation clearly offer the opportunity to improve the efficacy and efficiency of DBS therapies (Grill, 2018). However, the vast design space for arbitrary sequences of varying IPI poses a clear challenge in designing irregular temporal patterns of stimulation. It is not clear how patterns of stimulation should be selected for therapeutic advantage in treating various diseases. In this study, we find that even rearranging the order of the same set of varying IPI can change the effect of stimulation pulses substantially. Notably, the IPIs need to vary only in a small range such as 5–10 ms (i.e., 200–100 Hz) with a mean pulse frequency of ∼130 Hz, a commonly used frequency in DBS therapy. In addition, the changes in the orders of varying IPI did not significantly change the total amount of neuronal firing during HFS (**Table 3**) but only redistributed the firing timing of individual neurons.

Furthermore, our investigation of the neuronal responses to specific IPI episodes in a random IPI sequence provides clues to designing novel temporal patterns of stimulation. The salient changes in the ability of a pulse sequence to recruit a population of neurons by the specific IPI episodes (several shorter IPIs followed by a longer IPI as in **Figure 6C**) may exert stronger effects on neurons than regular and mild impulses from stimulation with constant IPI. This suggests that adjusting the amount of such IPI episodes may quantitatively regulate the stimulation effect, which acts as a "dose" of stimulation. The recruitment of a large population of neurons may be beneficial for treating diseases caused by excessive suppression of neuronal activity, such as disorders of consciousness after traumatic brain injury. In another perspective, the enhanced effects by random IPI suggest a potential to lower the electrical energy consumption, because only a decreased strength of stimulation may be needed to obtain a similar level of effect as constant IPI. Therefore, the present study with random IPI may inform the design of novel temporal patterns of stimulation that provide therapeutic advantage, less energy consumption, and more safety over regular stimulation for extending DBS applications in treating more brain diseases.

Limitations of the Study

In the study, the effects of varying IPI were generated from the direct action of stimulation on the neuronal membrane, not involving specific synaptic transmission or neuronal network. Because the mechanisms of action involving the non-linear dynamics of ion channels are universal to the membrane of various neurons in brain, the effects of varying IPI may also apply to neurons in other brain regions directly activated by stimulations. However, synaptic and network involvements may complicate these effects and impose additional modulation to projection neurons in orthodromic propagations, which needs further investigations. Furthermore, even for the antidromic situation, in addition to the depolarization block of axons investigated here, sustained HFS might induce changes in other features along the axon to soma. Also, the stochastic network activity received by soma and the complexity of axonal structures might affect soma's responses to the axonal HFS. Therefore, more accurate modeling with considerations of these factors is needed to further confirm the results of the present study.

In addition, the rat experiments were performed under anesthesia. The anesthetic urethane could reduce the synaptic responses, elevate the threshold of action potential firing, and decrease the firing rate of neurons (Mercer et al., 1978; Shirasaka and Wasterlain, 1995). Although the antidromic activation paradigm used in the present study did not involve synaptic transmissions, the excitability of soma may be changed by the anesthetic, thereby possibly affecting the responses of neurons to the stimulation. Therefore, further studies are needed to duplicate the results in awake animals.

CONCLUSION

The present study suggests that with the same amount of pulses together with the same distribution of IPI, only changing the order of varying IPI can introduce substantial changes in neuronal responses to HFS. Non-linear recovery course of membrane excitability might be the underlying cellular mechanisms resulting in the differences in neuronal responses. The finding provides a new strategy for developing novel stimulation paradigms to modulate the firing patterns of neuron populations, which may improve the DBS efficacy and extend the application of DBS therapy to more brain diseases.

DATA AVAILABILITY STATEMENT

The original contributions presented in the study are included in the article, further inquiries can be directed to the corresponding author.

ETHICS STATEMENT

The animal study was reviewed and approved by the Institutional Animal Care and Ethics Committee, Zhejiang University, Hangzhou, China.

AUTHOR CONTRIBUTIONS

ZF and LZ designed the study. HH and ZW performed the animal experiments. LZ, HH, and YY analyzed the experimental data. LZ created the computational model, and XW contributed to the model modification. LZ performed the simulations. ZF, LZ, and XW interpreted the results and wrote the manuscript. All authors approved the final version for submission.

FUNDING

This work was supported by the National Natural Science Foundation of China (No. 30970753).

REFERENCES

Battefeld, A., Tran, B. T., Gavrilis, J., Cooper, E. C., and Kole, M. H. (2014). Heteromeric Kv7.2/7.3 channels differentially regulate action potential initiation and conduction in neocortical myelinated axons. *J. Neurosci.* 34, 3719–3732. doi: 10.1523/JNEUROSCI.4206-13.2014

Bellinger, S. C., Miyazawa, G., and Steinmetz, P. N. (2008). Submyelin potassium accumulation may functionally block subsets of local axons during deep brain stimulation: a modeling study. *J. Neural Eng.* 5, 263–274. doi: 10.1088/1741-2560/5/3/001

Bergey, G. K. (2013). Neurostimulation in the treatment of epilepsy. *Exp. Neurol.* 244, 87–95. doi: 10.1016/j.expneurol.2013.04.004

Birdno, M. J., Cooper, S. E., Rezai, A. R., and Grill, W. M. (2007). Pulse-to-pulse changes in the frequency of deep brain stimulation affect tremor and modeled neuronal activity. *J. Neurophysiol.* 98, 1675–1684. doi: 10.1152/jn.00547.2007

Bittar, R. G., Burn, S. C., Bain, P. G., Owen, S. L., Joint, C., Shlugman, D., et al. (2005). Deep brain stimulation for movement disorders and pain. *J. Clin. Neurosci.* 12, 457–463. doi: 10.1016/j.jocn.2004.09.001

Cagnan, H., Pedrosa, D., Little, S., Pogosyan, A., Cheeran, B., Aziz, T., et al. (2017). Stimulating at the right time: phase-specific deep brain stimulation. *Brain* 140, 132–145. doi: 10.1093/brain/aww286

Cota, V. R., Medeiros, D. D. C., Doretto, M. C., and Moraes, M. F. D. (2009). Distinct patterns of electrical stimulation of the basolateral amygdala influence pentylenetetrazole seizure outcome. *Epilepsy Behav.* 14, 26–31. doi: 10.1016/j.yebeh.2008.09.006

Cukiert, A., Cukiert, C. M., Argentoni-Baldochi, M., Baise, C., Forster, C. R., Mello, V. A., et al. (2011). Intraoperative neurophysiological responses in epileptic patients submitted to hippocampal and thalamic deep brain stimulation. *Seizure* 20, 748–753. doi: 10.1016/j.seizure.2011.07.003

Cury, R. G., Fraix, V., Castrioto, A., Pérez Fernández, M. A., Krack, P., Chabardes, S., et al. (2017). Thalamic deep brain stimulation for tremor in Parkinson disease, essential tremor, and dystonia. *Neurology* 89, 1416–1423. doi: 10.1212/WNL.0000000000004295

Dandekar, M. P., Fenoy, A. J., Carvalho, A. F., Soares, J. C., and Quevedo, J. (2018). Deep brain stimulation for treatment-resistant depression: an integrative review of preclinical and clinical findings and translational implications. *Mol. Psychiatry* 23, 1094–1112. doi: 10.1038/mp.2018.2

Dayal, V., Limousin, P., and Foltynie, T. (2017). Subthalamic nucleus deep brain stimulation in parkinson's disease: the effect of varying stimulation parameters. *J. Parkinsons Dis.* 7, 235–245. doi: 10.3233/JPD-171077

Deeb, W., Salvato, B., Almeida, L., Foote, K. D., Amaral, R., Germann, J., et al. (2019). Fornix-region deep brain stimulation-induced memory flashbacks in Alzheimer's Disease. *N. Engl. J. Med.* 381, 783–785. doi: 10.1056/NEJMc1905240

Feng, Z., Ma, W., Wang, Z., Qiu, C., and Hu, H. (2019). Small changes in inter-pulse-intervals can cause synchronized neuronal firing during high-frequency stimulations in rat hippocampus. *Front. Neurosci.* 13:36. doi: 10.3389/fnins.2019.00036

Feng, Z., Wang, Z., Guo, Z., Zhou, W., Cai, Z., and Durand, D. M. (2017). High frequency stimulation of afferent fibers generates asynchronous firing in the downstream neurons in hippocampus through partial block of axonal conduction. *Brain Res.* 1661, 67–78. doi: 10.1016/j.brainres.2017.02.008

Feng, Z., Yu, Y., Guo, Z., Cao, J., and Durand, D. M. (2014). High frequency stimulation extends the refractory period and generates axonal block in the rat hippocampus. *Brain Stimul.* 7, 680–689. doi: 10.1016/j.brs.2014.03.011

Feng, Z., Zheng, X., Yu, Y., and Durand, D. M. (2013). Functional disconnection of axonal fibers generated by high frequency stimulation in the hippocampal CA1 region in-vivo. *Brain Res.* 1509, 32–42. doi: 10.1016/j.brainres.2013.02.048

Fisher, R. S., and Velasco, A. L. (2014). Electrical brain stimulation for epilepsy. *Nat. Rev. Neurol.* 10, 261–270. doi: 10.1038/nrneurol.2014.59

Förstl, J., Galvan, M., and Ten, B. G. (1982). Extracellular K+ concentration during electrical stimulation of rat isolated sympathetic ganglia, vagus and optic nerves. *Neuroscience* 7, 3221–3229. doi: 10.1016/0306-4522(82)90244-5

Grill, W. M. (2018). Temporal pattern of electrical stimulation is a new dimension of therapeutic innovation. *Curr. Opin. Biomed. Eng.* 8, 1–6. doi: 10.1016/j.cobme.2018.08.007

Guo, Z., Feng, Z., Wang, Y., and Wei, X. (2018). Simulation study of intermittent axonal block and desynchronization effect induced by high-frequency stimulation of electrical pulses. *Front. Neurosci.* 12:858. doi: 10.3389/fnins.2018.00858

Hines, M. L., and Carnevale, N. T. (1997). The NEURON simulation environment. *Neural Comput.* 9, 1179–1209. doi: 10.1162/neco.1997.9.6.1179

Hodgkin, A. L., and Huxley, A. F. (1952). A quantitative description of membrane current and its application to conduction and excitation in nerve. *J. Physiol.* 117, 500–544. doi: 10.1007/bf02459568

Hu, W., Tian, C., Li, T., Yang, M., Hou, H., and Shu, Y. (2009). Distinct contributions of Na(v)1.6 *and Na(v)*1.2 in action potential initiation and backpropagation. *Nat. Neurosci.* 12, 996–1002. doi: 10.1038/nn.2359

Jensen, A. L., and Durand, D. M. (2009). High frequency stimulation can block axonal conduction. *Exp. Neurol.* 220, 57–70. doi: 10.1016/j.brainres.2017.02.008

Kloosterman, F., Peloquin, P., and Leung, L. S. (2001). Apical and basal orthodromic population spikes in hippocampal CA1 in vivo show different origins and patterns of propagation. *J. Neurophysiol.* 86, 2435–2444. doi: 10.1152/jn.2001.86.5.2435

Kuncel, A. M., Birdno, M. J., Swan, B. D., and Grill, W. M. (2012). Tremor reduction and modeled neural activity during cycling thalamic deep brain stimulation. *Clin. Neurophysiol.* 123, 1044–1052. doi: 10.1016/j.clinph.2011.07.052

Laxpati, N. G., Kasoff, W. S., and Gross, R. E. (2014). Deep brain stimulation for the treatment of epilepsy: circuits. *Targets Trials Neurotherap.* 11, 508–526. doi: 10.1007/s13311-014-0279-9

Lorincz, A., and Nusser, Z. (2010). Molecular identity of dendritic voltage-gated sodium channels. *Science* 328, 906–909. doi: 10.1126/science.1187958

Lozano, A. M., and Lipsman, N. (2013). Probing and regulating dysfunctional circuits using deep brain stimulation. *Neuron* 77, 406–424. doi: 10.1016/j.neuron.2013.01.020

McIntyre, C. C., Grill, W. M., Sherman, D. L., and Thakor, N. V. (2004). Cellular effects of deep brain stimulation: model-based analysis of activation and inhibition. *J. Neurophysiol.* 91, 1457–1469. doi: 10.1152/jn.00989.2003

Medeiros, D. C., Cota, V. R., Vilela, M. R. S. P., Mourão, F. A. G., Massensini, A. R., and Moraes, M. F. D. (2012). Anatomically dependent anticonvulsant properties of temporally-coded electrical stimulation. *Epilepsy Behav.* 23, 294–297. doi: 10.1016/j.yebeh.2012.01.004

Mercer, L. F. Jr., Remley, N. R., and Gilman, D. P. (1978). Effects of urethane on hippocampal unit activity in the rat. *Brain Res. Bull.* 3, 567–570. doi: 10.1016/0361-9230(78)90089-8

Mesquita, M. B. S., Medeiros, D. C., Cota, V. R., Richardson, M. P., Williams, S., and Moraes, M. F. D. (2011). Distinct temporal patterns of electrical stimulation influence neural recruitment during PTZ infusion: an fMRI study. *Prog. Biophys. Mol. Biol.* 105, 109–118. doi: 10.1016/j.pbiomolbio.2010.10.005

Migliore, M., Hoffman, D. A., Magee, J. C., and Johnston, D. (1999). Role of an A-Type K + conductance in the back-propagation of action potentials in the dendrites of hippocampal pyramidal neurons. *J. Comput. Neurosci.* 7, 5–15. doi: 10.1023/a:1008906225285

Nowak, L. G., and Bullier, J. (1998). Axons, but not cell bodies, are activated by electrical stimulation in cortical gray matter I. Evidence from chronaxie measurements. *Exp. Brain Res.* 118, 477–488. doi: 10.1007/s002210050304

Poolos, N. P., Mauk, M. D., and Kocsis, J. D. (1987). Activity-evoked increases in extracellular potassium modulate presynaptic excitability in the CA1 region of the hippocampus. *J. Neurophysiol.* 58, 404–416. doi: 10.1152/jn.1987.58.2.404

Popovych, O. V., and Tass, P. A. (2014). Control of abnormal synchronization in neurological disorders. *Front. Neurol.* 5:268. doi: 10.3389/fneur.2014.00268

Quinkert, A. W., and Pfaff, D. W. (2012). Temporal patterns of deep brain stimulation generated with a true random number generator and the logistic equation: effects on CNS arousal in mice. *Behav. Brain Res.* 229, 349–358. doi: 10.1016/j.bbr.2012.01.025

Quinkert, A. W., Schiff, N. D., and Pfaff, D. W. (2010). Temporal patterning of pulses during deep brain stimulation affects central nervous system arousal. *Behav. Brain Res.* 214, 377–385. doi: 10.1016/j.bbr.2010.06.009

Rizzone, M., Lanotte, M., Bergamasco, B., Tavella, A., Torre, E., Faccani, G., et al. (2001). Deep brain stimulation of the subthalamic nucleus in Parkinson's disease: effects of variation in stimulation parameters. *J. Neurol. Neurosurg. Psychiatry* 71, 215–219. doi: 10.1136/jnnp.71.2.215

Röper, J., and Schwarz, J. R. (1989). Heterogeneous distribution of fast and slow potassium channels in myelinated rat nerve fibres. *J. Physiol.* 416, 93–110. doi: 10.1113/jphysiol.1989.sp017751

Rosenbaum, R., Zimnik, A., Zheng, F., Turner, R. S., Alzheimer, C., Doiron, B., et al. (2014). Axonal and synaptic failure suppress the transfer of firing rate oscillations, synchrony and information during high frequency deep brain stimulation. *Neurobiol. Dis.* 62, 86–99. doi: 10.1016/j.nbd.2013.09.006

Santos-Valencia, F., Almazan-Alvarado, S., Rubio-Luviano, A., Valdes-Cruz, A., Magdaleno-Madrigal, V. M., and Martinez-Vargas, D. (2019). Temporally irregular electrical stimulation to the epileptogenic focus delays epileptogenesis in rats. *Brain Stimul.* doi: 10.1016/j.brs.2019.07.016

Shirasaka, Y., and Wasterlain, C. G. (1995). The effect of urethane anesthesia on evoked potentials in dentate gyrus. *Eur. J. Pharmacol.* 282, 11–17. doi: 10.1016/0014-2999(95)00244-f

Swan, B. D., Brocker, D. T., Hilliard, J. D., Tatter, S. B., Gross, R. E., Turner, D. A., et al. (2016). Short pauses in thalamic deep brain stimulation promote tremor and neuronal bursting. *Clin. Neurophysiol.* 127, 1551–1559. doi: 10.1016/j.clinph.2015.07.034

Tabansky, I., Quinkert, A. W., Rahman, N., Muller, S. Z., Lofgren, J., Rudling, J., et al. (2014). Temporally-patterned deep brain stimulation in a mouse model of multiple traumatic brain injury. *Behav. Brain Res.* 273, 123–132. doi: 10.1016/j.bbr.2014.07.026

Varona, P., Ibarz, J. M., López-Aguado, L., and Herreras, O. (2000). Macroscopic and subcellular factors shaping population spikes. *J. Neurophysiol.* 83, 2192–2208. doi: 10.1152/jn.2000.83.4.2192

Wang, Z., Feng, Z., and Wei, X. (2018). Axonal stimulations with a higher frequency generate more randomness in neuronal firing rather than increase firing rates in rat hippocampus. *Front. Neurosci.* 12:783. doi: 10.3389/fnins.2018.00783

Wichmann, T., and DeLong, M. R. (2016). Deep brain stimulation for movement disorders of basal ganglia origin: restoring function or functionality? *Neurotherapeutics* 13, 264–283. doi: 10.1007/s13311-016-0426-6

Zheng, F., Lammert, K., Nixdorf-Bergweiler, B. E., Steigerwald, F., Volkmann, J., and Alzheimer, C. (2011). Axonal failure during high frequency stimulation of rat subthalamic nucleus. *J. Physiol.* 589(Pt 11), 2781–2793. doi: 10.1113/jphysiol.2011.205807

Conflict of Interest: The authors declare that the research was conducted in the absence of any commercial or financial relationships that could be construed as a potential conflict of interest.

frontiers in Neuroscience

ORIGINAL RESEARCH
published: 12 June 2020
doi: 10.3389/fnins.2020.00611

Randomized, Double-Blind Assessment of LFP Versus SUA Guidance in STN-DBS Lead Implantation: A Pilot Study

*Musa Ozturk[1], Ilknur Telkes[2], Joohi Jimenez-Shahed[3], Ashwin Viswanathan[4], Arjun Tarakad[5], Suneel Kumar[5], Sameer A. Sheth[4] and Nuri F. Ince[1]**

[1] Department of Biomedical Engineering, University of Houston, Houston, TX, United States, [2] Department of Neuroscience and Experimental Therapeutics, Albany Medical College, Albany, NY, United States, [3] Department of Neurology, Icahn School of Medicine at Mount Sinai, New York, NY, United States, [4] Department of Neurosurgery, Baylor College of Medicine, Houston, TX, United States, [5] Department of Neurology, Baylor College of Medicine, Houston, TX, United States

Background: The efficacy of deep brain stimulation (DBS) therapy in Parkinson's disease (PD) patients is highly dependent on the precise localization of the target structures such as subthalamic nucleus (STN). Most commonly, microelectrode single unit activity (SUA) recordings are performed to refine the target. This process is heavily experience based and can be technically challenging. Local field potentials (LFPs), representing the activity of a population of neurons, can be obtained from the same microelectrodes used for SUA recordings and allow flexible online processing with less computational complexity due to lower sampling rate requirements. Although LFPs have been shown to contain biomarkers capable of predicting patients' symptoms and differentiating various structures, their use in the localization of the STN in the clinical practice is not prevalent.

Methods: Here we present, for the first time, a randomized and double-blinded pilot study with intraoperative online LFP processing in which we compare the clinical benefit from SUA- versus LFP-based implantation. Ten PD patients referred for bilateral STN-DBS were randomly implanted using either SUA or LFP guided targeting in each hemisphere. Although both SUA and LFP were recorded for each STN, the electrophysiologist was blinded to one at a time. Three months postoperatively, the patients were evaluated by a neurologist blinded to the intraoperative recordings to assess the performance of each modality. While SUA-based decisions relied on the visual and auditory inspection of the raw traces, LFP-based decisions were given through an online signal processing and machine learning pipeline.

Results: We found a dramatic agreement between LFP- and SUA-based localization (16/20 STNs) providing adequate clinical improvement (51.8% decrease in 3-month contralateral motor assessment scores), with LFP-guided implantation resulting in greater average improvement in the discordant cases (74.9%, $n = 3$ STNs). The selected tracks were characterized by higher activity in beta (11–32 Hz) and high-frequency (200–400 Hz) bands ($p < 0.01$) of LFPs and stronger non-linear coupling between these bands ($p < 0.05$).

OPEN ACCESS

Edited by:
Caleb Kemere,
Rice University, United States

Reviewed by:
Xin Liu,
University of California, San Diego, United States
Matthew N. Petrucci,
Stanford University, United States
Amir H. Faraji,
University of Pittsburgh Medical Center, United States

***Correspondence:**
Nuri F. Ince
nfince@uh.edu

Specialty section:
This article was submitted to Neural Technology, a section of the journal Frontiers in Neuroscience

Received: 27 February 2020
Accepted: 18 May 2020
Published: 12 June 2020

Citation:
Ozturk M, Telkes I, Jimenez-Shahed J, Viswanathan A, Tarakad A, Kumar S, Sheth SA and Ince NF (2020) Randomized, Double-Blind Assessment of LFP Versus SUA Guidance in STN-DBS Lead Implantation: A Pilot Study. Front. Neurosci. 14:611. doi: 10.3389/fnins.2020.00611

Conclusion: Our pilot study shows equal or better clinical benefit with LFP-based targeting. Given the robustness of the electrode interface and lower computational cost, more centers can utilize LFP as a strategic feedback modality intraoperatively, in conjunction to the SUA-guided targeting.

Keywords: Parkinson's disease, subthalamic nucleus, single unit activity, local field potentials, electrophysiological targeting

INTRODUCTION

Deep brain stimulation (DBS) is an effective treatment option for patients suffering from various neurological disorders such as Parkinson's disease (PD) (Benabid et al., 2008; Groiss et al., 2009; Schiefer et al., 2011; Hariz, 2012, 2014; Odekerken et al., 2013; Gunduz et al., 2017; Lee et al., 2018). Although the exact mechanism of DBS remains to be explored, it is well-established that stimulation of the subthalamic nucleus (STN) alleviates the cardinal symptoms of PD (Limousin et al., 1998; Krack et al., 2003; Herzog et al., 2004; Benabid et al., 2009). However, stimulation can also result in side effects arising from unintended activation of structures surrounding the STN (Krack et al., 2001; Okun et al., 2003; Deuschl et al., 2006; Guehl et al., 2006; Wojtecki et al., 2007; Benabid et al., 2009; Groiss et al., 2009; Richardson et al., 2009; Zhang et al., 2016). Moreover, a multi-center study has reported that the sub-optimal positioning of DBS electrodes accounts for 46% of cases with inadequate clinical improvement postoperatively (Okun et al., 2005). Thus, the clinical efficacy of DBS therapy depends critically on accurate localization of the STN (Zonenshayn et al., 2000; Sterio et al., 2002; Amirnovin et al., 2006; Gross et al., 2006; Campbell et al., 2019).

Precise placement of the DBS lead can be challenging due to the small size and the anatomical variability in the human STN (Patel et al., 2008; Richardson et al., 2009). While MRI-guided asleep DBS is being performed by some centers (Aziz and Hariz, 2017; Brodsky et al., 2017; Chen et al., 2018; Ho et al., 2018; Wang et al., 2019; Liu et al., 2020), intraoperative electrophysiology remains to be an important technique for localizing the STN, despite the variations in the surgical procedure between medical centers (Zonenshayn et al., 2000; Sterio et al., 2002; Amirnovin et al., 2006; Gross et al., 2006; Abosch et al., 2013; Campbell et al., 2019). A worldwide survey involving 143 DBS centers reported that 83% of them use single unit activity (SUA) recordings for DBS lead implantation (Abosch et al., 2013). Typically, up to five microelectrodes are advanced toward the target structure to obtain a 3-dimensional perspective (Gross et al., 2006; Benabid et al., 2009; Abosch et al., 2013). SUA is used to identify cells with firing characteristics consistent with STN neurons and response characteristics confirming the motor sub-territory of the STN based on a variety of visual and auditory cues (Hutchison et al., 1998; Magnin et al., 2001; Rodriguez-Oroz et al., 2001; Abosch et al., 2002; Benazzouz et al., 2002). This procedure is subjective, heavily experience-based and depends critically on the neurosurgeon's or electrophysiologist's ability to recognize the STN (Benazzouz et al., 2002; Benabid et al., 2009; Marceglia et al., 2010; Abosch et al., 2013). Aside from difficulties in interpreting the data and small number of neurons sampled by 1–5 microelectrodes, challenges in interface stability (e.g., necessity of turning lights or other devices off in the operating room) and high bandwidth/sampling frequency requirements may complicate the collection and real-time analysis of SUA (Novak et al., 2011; Rouse et al., 2011; Thompson et al., 2014).

Local field potentials (LFPs), which represent the aggregated synaptic potentials of a population of neurons (Priori et al., 2004; Gross et al., 2006; Buzsáki et al., 2012), can be obtained from the shaft of the same microelectrode used for SUA recordings. Although LFPs have been shown to contain biomarkers capable of predicting Parkinsonian symptoms (Foffani et al., 2003; Ray et al., 2008; Lopez-Azcarate et al., 2010; Özkurt et al., 2011; Little and Brown, 2012; Oswal et al., 2013; Priori et al., 2013; Brittain and Brown, 2014; Ozturk et al., 2019) and differentiating basal ganglia structures (Chen et al., 2006; Telkes et al., 2016; Kolb et al., 2017) only a handful of centers around the world rely on LFPs for the localization of the STN (Abosch et al., 2013).

Here, we present, for the first time, a randomized, double-blinded study comparing the targeting performance of SUA- vs LFP-based implantation. While SUA was interpreted by visual and auditory inspection of the raw traces as done in clinical practice, we employed real-time intraoperative processing of LFPs to facilitate the selection of the implantation track.

Patients and Methods

Patients

Ten patients (four females, six males) with PD undergoing bilateral STN-DBS implantation at Baylor St. Luke's Medical Center were included in the study. Their ages ranged between 40 to 64 (mean ± standard deviation = 55 ± 8.8) with disease duration ranging from 4 to 16 years (mean ± standard deviation = 9 ± 3.9). Nine patients were implanted with Medtronic lead model 3389, and one was with model 3387 (Medtronic, Ireland). The study protocol was approved by the Institutional Review Boards of Baylor College of Medicine and University of Houston. All patients provided written informed consent.

Study Design

This study investigates the functional utility of LFP versus SUA in targeting the STN with an online processing pipeline (**Figure 1A**) and compares both modalities in terms of clinical outcomes postoperatively. The implantation modality for each hemisphere (SUA vs. LFP) was randomly identified prior to the surgery. If one hemisphere was implanted using LFP, the

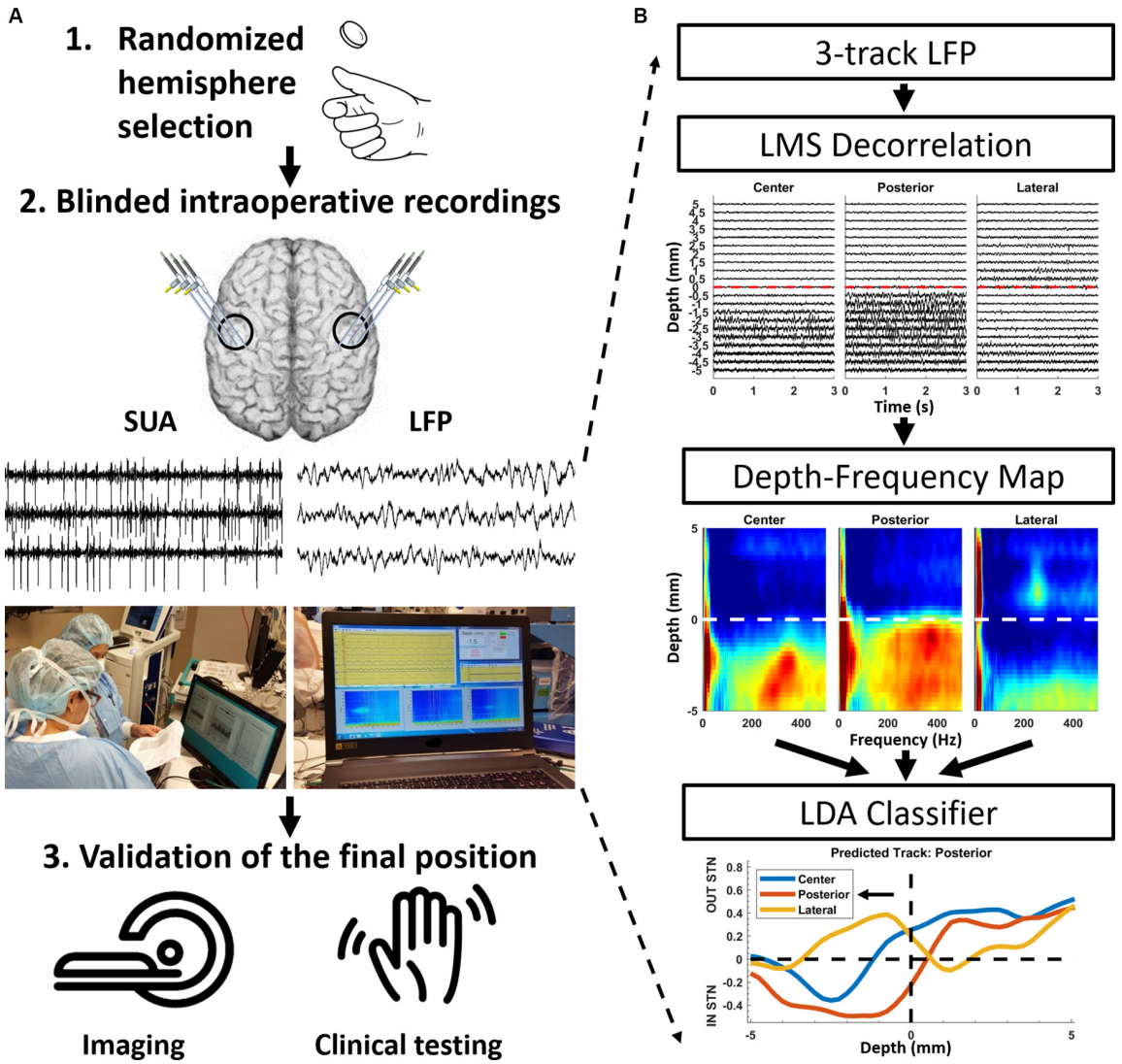

FIGURE 1 | Randomized double-blinded paradigm and the processing pipeline for LFPs. **(A)** The decision modality for each hemisphere was determined in the beginning of the operation randomly. Intraoperative recordings included both SUA and LFP activity. However, only the decision modality, either SUA or LFP, was made available to the electrophysiologist. After the implantation site was selected, the final position was confirmed with intraoperative imaging and clinical testing for motor improvement and side effects, which was performed by a neurologist blinded to the electrophysiological recordings. **(B)** Signal processing and machine learning pipeline for LFP-based decision making. The raw traces are de-correlated using least mean square (LMS) algorithm with the steepest descent update. Then, the LFP traces were analyzed in the spectral domain using modified Welch periodogram with a 1 s Hamming window and 50% overlap. Individual spectra across depths were combined to generate a 2D depth-frequency map (DFM) representing the depth-varying power spectrum of the LFPs. The track selection was performed automatically using a linear discriminant analysis (LDA) classifier developed by Telkes et al. (2016), using the power in beta and HFO bands as input features.

other one was implanted using SUA. Three track MER was performed with only the guiding waveform provided to the electrophysiologist for decision making, while the other signal was recorded in the background (blinded recordings) for off-line comparison. After DBS lead placement in the selected track, an intraoperative computed tomography (CT) fused with preoperative magnetic resonance imaging (MRI) was used to verify lead location. Finally, a neurologist blinded to the recordings tested the patients for clinical benefit and side effects intraoperatively and 3-months postoperatively (blinded testing). To prevent possible interference induced by inter-rater variability on the paired statistics performed in this study, the rating neurologists (authors JS and AT, both MDS-UPDRS certified) performed the clinical assessment for each patient consistently (the same rater performed both OFF and ON assessments of a patient, for both the left and right hemispheres). The systematic testing done at 3-months postoperatively was used to assess the clinical improvement by stimulation (medication OFF/DBS ON). The clinical scores were computed as the sum of Movement Disorders Society Unified Parkinson's Disease Rating Scale (MDS-UPDRS) Part-III items 3.3–3.8, 3.15–3.17 of the side contralateral to the implant.

Intraoperative Recordings

Patients were requested to stop medication at least 12 h prior to surgery and all recordings were obtained in the awake state using local anesthesia. On the morning of the surgery, all patients obtained a head CT after application of the stereotactic head frame. The stereotactic coordinates and trajectories to the STN were identified by fusing preoperative MRI and CT scans on a neuro-navigational platform (StealthStation, Medtronic, Ireland). In each hemisphere, awake recordings were performed using a set of three parallel microelectrodes separated by 2 mm (center-to-center) using the 5-cannula BenGun with "+" configuration. The preoperative planning using direct targeting methods determined the "center" track. Among "anterior, posterior, lateral and medial" tracks, two other tracks were selected by the neurosurgeon on a patient specific basis by taking into account the subject's anatomy. The microelectrodes (NeuroProbe, AlphaOmega, Israel) were initially placed at least 15 mm above the stereotactic target and advanced deeper with 0.5–1 mm steps using NeuroOmega drive (AlphaOmega, Israel), in order to refine the radiographic target. At each depth, by using the cannula as reference, at least 20 s of SUA from the high-impedance tungsten tip (0.6–0.8 MΩ) and LFP from the low impedance stainless-steel ring (<10 KΩ, 3 mm above the tip) on the shaft were obtained simultaneously. The entire data was recorded with Grapevine Neural Amplifier (Ripple Neuro, UT) at 30 KHz and 16-bit A/D resolution, and LFPs were down-sampled to 2 KHz before further processing.

Signal Processing

The signals were recorded and visualized in real-time with an in-house built Simulink model and processed with custom MATLAB scripts using version R2014a (Mathworks, Natick, MA, United States) and gHiSys high-speed online processing library (gTec, Austria). The entire online processing was performed on a 17" laptop with quad-core (2.4 GHz) processor and 12 GB memory. The SUA data were high-pass filtered at 300 Hz with a second order infinite-impulse response filter and presented to the electrophysiologist in visual and auditory format, similar to the commercially available devices. After the mapping was completed, the SUA traces were plotted depth by depth from all three tracks for reviewing and final decision. The entry to and exit from the STN was determined by an experienced neurophysiologist by listening to and visually observing the firing patterns of neurons. The entry to the STN was identified with a prominent increase in the background activity and discharge rates (**Figure 2A**), as reported previously (Hutchison et al., 1998; Novak et al., 2007). Among three, the track with the longest span of cell firing and background activity was selected for the chronic DBS electrode implantation (Abosch et al., 2002; Benazzouz et al., 2002; Gross et al., 2006). In those hemispheres where the implantation was performed based on LFPs, the same procedures were used to process SUA data offline, following the implantation of the DBS electrode.

The LFPs were processed intraoperatively with the real-time implementation of the signal processing pipeline (**Figure 1B**) provided by Telkes et al. (2016). Specifically, LFP raw traces were visualized initially and it was noted that tracks were difficult to distinguish, due to common activity coming from the reference contact (cannula) masking spatially localized patterns. In order to eliminate the common activity without affecting the localized neural activity, the LFP from tracks were de-correlated using a least mean square (LMS) algorithm with the steepest descent update. Explicitly, each track was predicted by using a linear weighted combination of other two channels and the residual was used for the further processing. With this adaptive approach, the common activity was eliminated across tracks and only spatially specific information was preserved (Telkes et al., 2016). LFP traces were then analyzed in the spectral domain using a modified Welch periodogram. A fast Fourier transform was computed at each depth with a 1 s Hamming window and 50% overlap and presented to the electrophysiologist in near real-time in the form of online spectrograms (**Supplementary Video S1**). After the mapping was completed, a median spectrum was calculated from the spectra to eliminate localized artifacts at each depth. Then, spectra across depths were combined to generate a 2D depth-frequency map (DFM) representing the depth-varying power spectrum of the LFPs of each track (Telkes et al., 2016, 2018). The maps were then normalized with the average baseline of three tracks and transformed into log scale (**Figure 1B**). The tracks were not normalized by their own baseline but by the mean of all three tracks in order to compare the signal power between them. The baseline used for normalization was selected as the highest depths which are assumed to be in the white matter. The STN was identified by distinct LFP activity in beta (11–32 Hz) and HFO (200–400 Hz, high-frequency oscillations) ranges. The track containing the largest beta and HFO bandpower for the longest span was selected as the implantation site for the DBS electrode (Zaidel et al., 2010; Wang et al., 2014; Telkes et al., 2016; van Wijk et al., 2017). This selection was performed automatically using a linear discriminant analysis (LDA) classifier developed by Telkes et al. (2016). Specifically, after obtaining the normalized depth-frequency maps, the beta and HFO sub-band powers were extracted for each track and depth from these maps. Then, the sub-band power features were normalized between zero and one with a Min-Max normalization method for the minimization of inter-subject variability in LFP power, and a binary LDA classifier was applied for classification. This classifier was trained by contrasting the LFP sub-band features coming from selected and non-selected tracks using the data from the 24 PD patients analyzed in Telkes et al. (2016). During online classification, the neural data in each track and at each depth were fed to the classifier. Therefore, each electrode trajectory received a vote at each depth from the classifier. The decision distance of the LDA classifier was plotted to give visual feedback regarding the votes and related confidence of the classifier (**Figure 1B**). The track that received the longest span of decision distances voting for in-STN was selected for the final DBS electrode implantation (**Figure 1B**). Once again, in those hemispheres where the implantation was performed based on SUA, the same signal processing pipeline was executed offline to process LFPs, following the implantation of the DBS electrode.

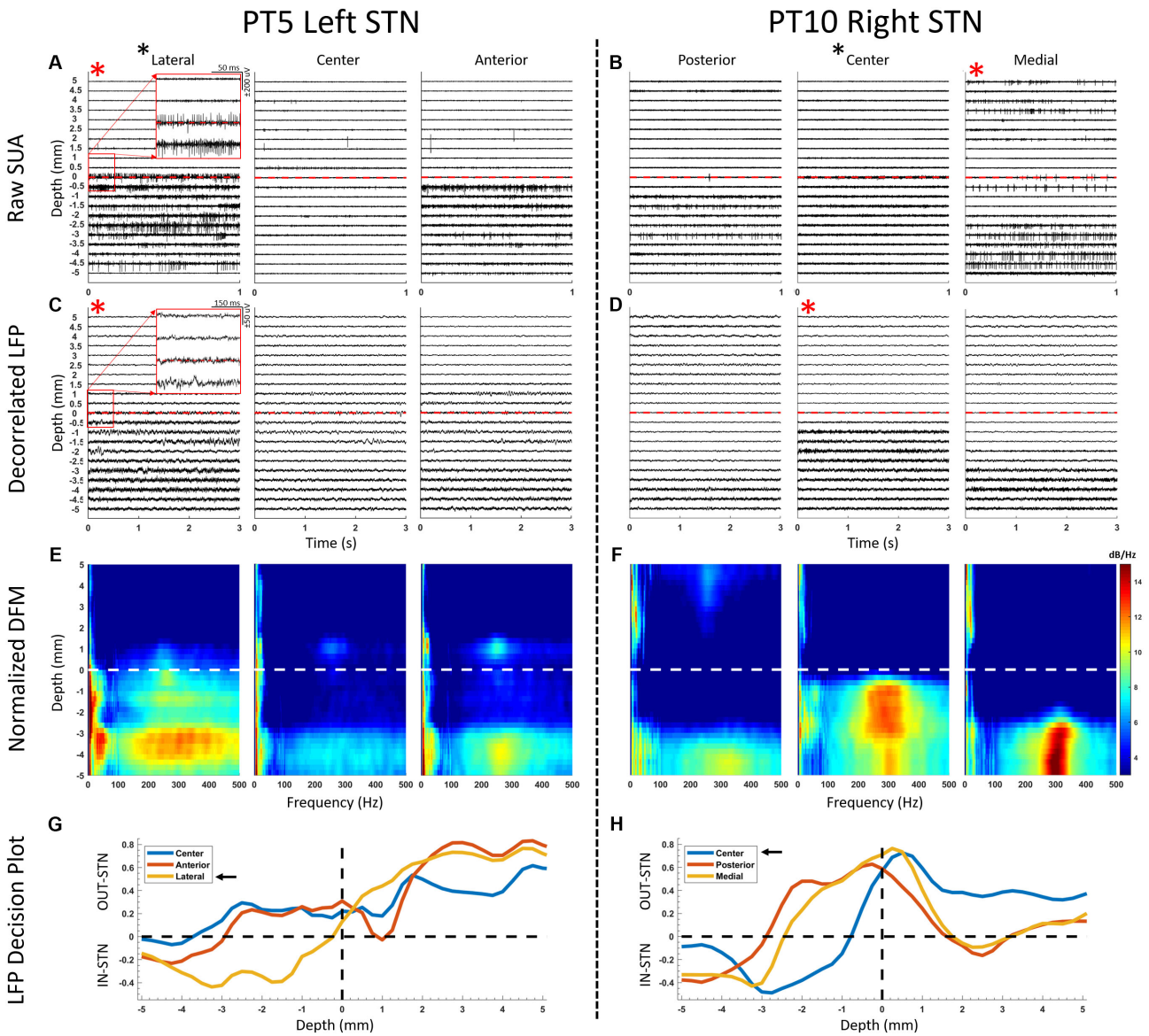

FIGURE 2 | Representative SUA and LFP raw traces and depth-frequency maps (DFM) from two STNs where the suggested track by SUA and LFP overlapped (left panel) and did not overlap (right panel). **(A,B)** SUA raw traces presented from 5 mm above down to 5 mm below the dorsal border of the STN, with 0.5 mm steps. The dorsal border is marked by an increased spiking and background activity. Red asterisks denote suggested track by the corresponding modality and black asterisk next to the track name denotes the implanted track. **(C,D)** The decorrelated LFP traces are provided in a similar fashion to SUA traces. Although it can be observed that the oscillatory activity increases after crossing the dorsal border, the nature of the change can be visualized better in the spectral domain where **(E,F)** DFMs of the corresponding LFPs are presented. The entry to STN is characterized with increased activity in both beta and HFO ranges. **(G,H)** Decision plots of the classifier voting whether each track is in- or out-STN at each traversed depth. The track with the longest in-STN vote is selected as the implanted track, as indicated with the black arrows. The SUA activity was stronger in the lateral track **(A)** and the corresponding LFPs agreed **(G)** in the left panel. On the right panel, SUA **(B)**, which was the decision modality, suggested the medial track. However, after intraoperative imaging validation the lead was placed in the center track, which agreed with the LFP-based decision **(H)**.

Additional offline analysis was performed postoperatively to investigate the cross-frequency coupling (CFC) between beta and HFO bands. The comodulograms representing CFC were computed using the phase-locking principle (Penny et al., 2008) with amplitude frequency axis from 150 to 450 Hz with 10 Hz steps and 50 Hz filter bandwidth, and phase frequency axis from 6 to 40 Hz with 1 Hz steps and 3 Hz filter bandwidth.

Statistics

Normality of all distributions was tested using Anderson-Darling test and it was found that most of them are non-normal ($p < 0.05$). Statistical tests were performed in a paired fashion using non-parametric Wilcoxon signed rank test to compare the clinical scores in the OFF- and ON- DBS states, the beta and HFO bandpowers and the coupling strength between them. The

sample size and significance levels are provided throughout the text, when referred.

RESULTS

A total of 60 microelectrode tracks from 20 STNs were included in this study. **Figure 2** illustrates offline comparison of representative LFP and SUA data from two STNs, where both modalities suggested the same track in one (Pt5, left hemisphere) and different tracks in another (Pt10, right hemisphere). The SUA-predicted tracks were determined by the longest span of background and spiking activity (**Figures 2A,B**) whereas the longest span of in-STN votes of the classifier were considered in LFP-based selection (**Figures 2C–F**). The decision distance (y-axis of **Figures 2G,H**) represented the confidence of the classifier which used the power in beta and HFO bands of LFP as input features. Note that, although the randomized decision modality was SUA for the right hemisphere of patient 10 (**Figure 2**, right panel) suggesting implantation in the medial track, intraoperative CT favored the center track as the target, which was used as the final implantation location. The offline analysis of LFPs agreed with the radiographic decision as well.

Distribution of decisions for all hemispheres given by each modality as well as their randomization is provided in **Figure 3A**. In 16/20 hemispheres, the SUA and LFP recordings were concordant in their prediction of implantation track. In those four discordant hemispheres, the LFP was the decision modality in only one of them and the final implantation validated by intraoperative CT and clinical testing agreed with LFP-suggested track. In remaining three STNs where SUA was the decision modality, the lead had to be repositioned based on intraoperative CT validation and/or stimulation testing. For two STNs (Pt6, left; Pt10 right), the track suggested by the SUA, did not agree with the track residing within the target confirmed radiographically (according to intraoperative CT scans merged with preoperative MRI). Therefore, the DBS electrode was placed into the most likely track suggested by the radiography. Interestingly, for these two STNs, the track suggested by the imaging agreed with LFPs. In one STN (Pt1, left), the lead was moved to posterior track due to stimulation side-effects during intraoperative testing and imaging considerations, without the use of microelectrode recordings. This STN was excluded from further analysis. The repositioned hemispheres are marked with a star on **Figure 3A**. Overall, the track favored by SUA was implanted in a total of 16 chronic lead placements whereas LFP-favored track was used in 19. In addition to intraoperative radiographic validation, all 20 implantations were visualized postoperatively by merging the preoperative MRI and postoperative CT images using LeadDBS (Horn and Kühn, 2015). It was observed that at least one contact of the DBS lead was within the STN (**Figure 3B**).

The mean lateralized MDS-UPDRS part III improvement for 19 STNs was 51.8% at 3-month postoperative programming (mean ± standard deviation OFF score = 16.3 ± 5.4, ON score = 6.5 ± 4.6, **Figure 3C**). When the track decisions were compared across modalities in terms of outcome measures, the 16 STNs where both modalities agreed had average clinical improvement of 55.5%. Of the tracks with LFP-SUA mismatch, the mean improvement in three LFP-concordant implantations was 74.9% (**Figure 3D**).

The average DFMs and CFC comodulograms of selected vs other tracks from 19 STNs are presented in **Figure 4**. The left hemisphere of patient 1 was excluded since the electrode was repositioned due to side effects observed during intraoperative stimulation testing without neural recordings. The STN was characterized by exaggerated activity in the beta and HFO ranges in the selected track while the average map of the non-selected tracks contained weaker beta and HFO activity, as presented in **Figure 4A**. The power of these two bands were significantly higher in the selected track, both in dorsal and ventral regions (**Figure 4B**, $p < 0.01$, $n = 19$). Although three patients had localized HFO activity above the STN border (see representative DFMs in **Figures 2E,F**), there was no significant difference in HFO bandpower between selected and other tracks at this depth range. The dorsal half of STN demonstrated CFC between the phase of beta and the amplitude of slow HFO (200–280 Hz) oscillations whereas the ventral half was coupled with fast HFO (280–400 Hz) band as illustrated in **Figure 4C**. Amongst all selected tracks, the beta-HFO coupling strength was significantly higher in both dorsal and ventral territories, when compared to other tracks (**Figure 4D**, $p < 0.05$, $n = 19$).

DISCUSSION

In this blinded study, we compared the functional utility of LFPs for the implantation of DBS electrode against the widely used method, SUA (Benabid et al., 2009; Przybyszewski et al., 2016; Valsky et al., 2017). We observed an overall agreement in track prediction between both modalities (16/20 hemispheres) with adequate clinical benefit (55.5%) from chronic DBS, comparable to previous reports (Limousin et al., 1998; Krack et al., 2003; Walter and Vitek, 2004). In the three discordant cases, our findings suggest that the mean improvement in motor symptoms with LFP guided implantation may be greater.

The large overlap between optimal tracks predicted by both SUA and LFP is not a surprise as firing activity and field potentials have shown to be linked (Kühn et al., 2005; Buzsáki et al., 2012; Telkes et al., 2016; Meidahl et al., 2019), and supports the use of LFP-guided lead placement. A possible explanation for the mismatched hemispheres could be the stability issues in the electrode tip - tissue interface (Amirnovin et al., 2006; Hill et al., 2011; Harris et al., 2016). In one STN presented in **Figure 2B**, although the background activity in center track SUA increases after the border (0 mm), a potential tip failure (i.e., bending or damage to the fine tip of microelectrode that could reduce the high impedance, which is essential to capture SUA) could have prevented the isolation of individual neurons. Since the LFP traces (**Figure 2D**) and DFM (**Figure 2F**) of the same STN show strong activity correlated with intraoperative CT, a technical or hardware issue specific to the tip of the microelectrode is a distinct possibility. Even without any damage, the SUA tip may not necessarily isolate single neurons at every site (Benazzouz et al., 2002; Weinberger et al., 2006; Sharott et al., 2014) by

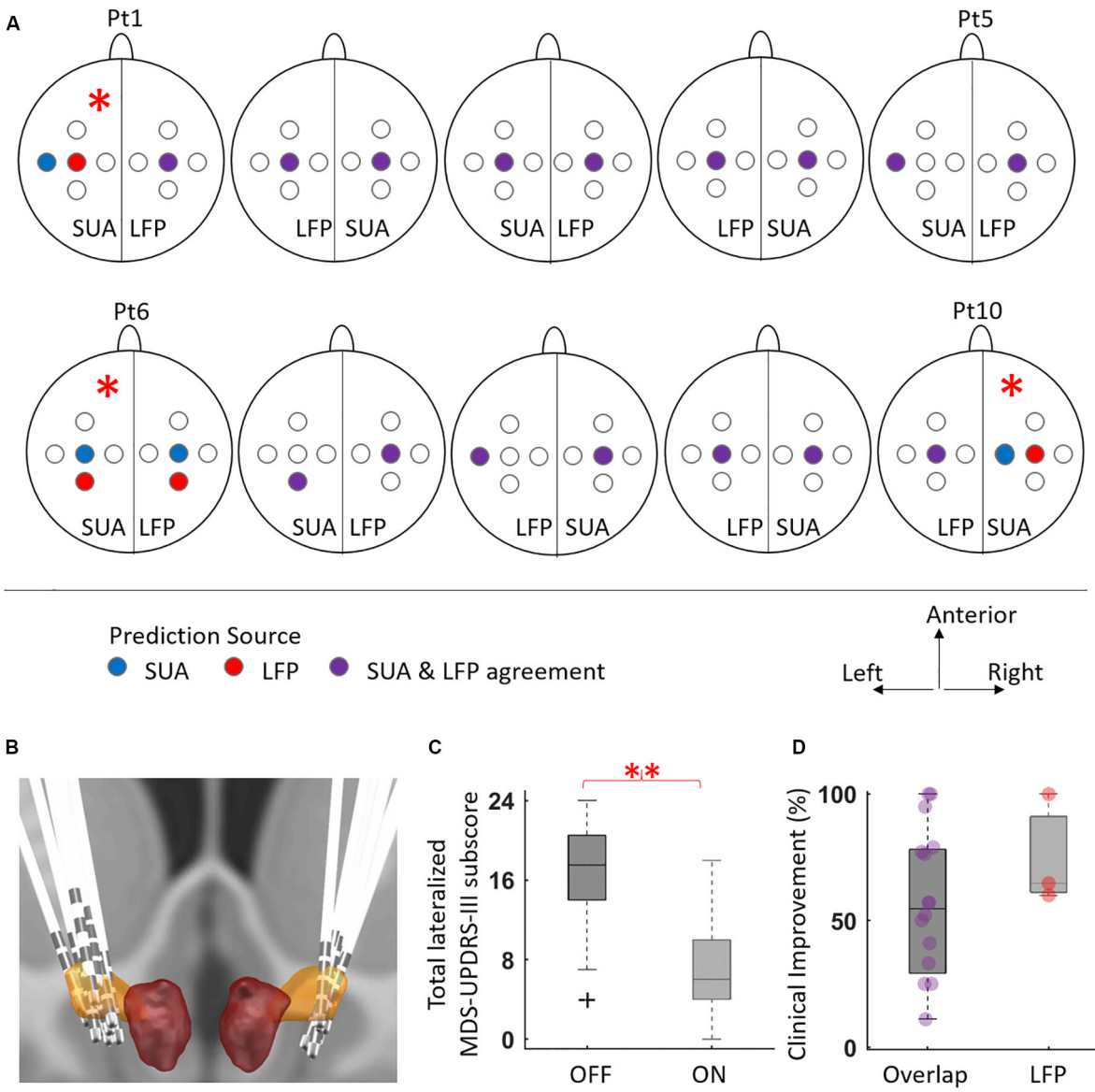

FIGURE 3 | The distribution of selected tracks by SUA and LFP, and the corresponding motor improvement. **(A)** The BenGun representation of suggested and implanted tracks for individual STNs. For each hemisphere, the randomized implantation modality is written at the bottom. There were three cases where the decision modality was SUA, but the lead had to be repositioned (denoted by asterisk): left hemisphere of patient 1 moved to posterior track due to intraoperative stimulation side effects, without use of electrophysiology (excluded from further analysis); left hemisphere of patient 6 and right hemisphere of patient 10 repositioned due to discrepancy with the intraoperative imaging. In the latter two cases, the LFP suggested track agreed with the final decision. **(B)** The illustration of implanted DBS leads generated by merging preoperative MRI and intraoperative CT using Lead DBS toolbox (Horn and Kühn, 2015). In all hemispheres, at least one contact was observed to be in STN. **(C)** The distribution of total contralateral motor UPDRS scores in the DBS OFF and DBS ON states for 19 hemispheres. There was a significant clinical motor improvement (51.8%) after DBS treatment ($p < 0.01$, $n = 19$). **(D)** The tracks suggested by SUA and LFP overlapped for 16 STNs, with average improvement of 55.5%. When there was a disagreement and the implant location agreed with LFP ($n = 3$), the average improvement was 74.9%. Individual data points are presented with circles to emphasize the unequal sample size between groups.

being too far to the cells or by damaging them (Buzsáki, 2004; Harris et al., 2016). In such instances, the electrophysiologist faces the uncertainty of missing the target or missing the neurons. By contrast, the stainless-steel ring on the shaft where LFPs are recorded has more structural integrity, larger surface and smaller impedance (Lenz et al., 1988; Gross et al., 2006), and captures the oscillatory activity from a population of neurons (Priori et al., 2004; Gross et al., 2006; Buzsáki et al., 2012), thereby limiting the chances of missing the electrophysiological activity (Buzsáki et al., 2012; Priori et al., 2013; Thompson et al., 2014). Supporting the favorability of LFP recordings, we found that among three cases where SUA was the deciding modality but the implantation track had to be modified, two of the final locations agreed with the LFP-based track selection (**Figure 3A**).

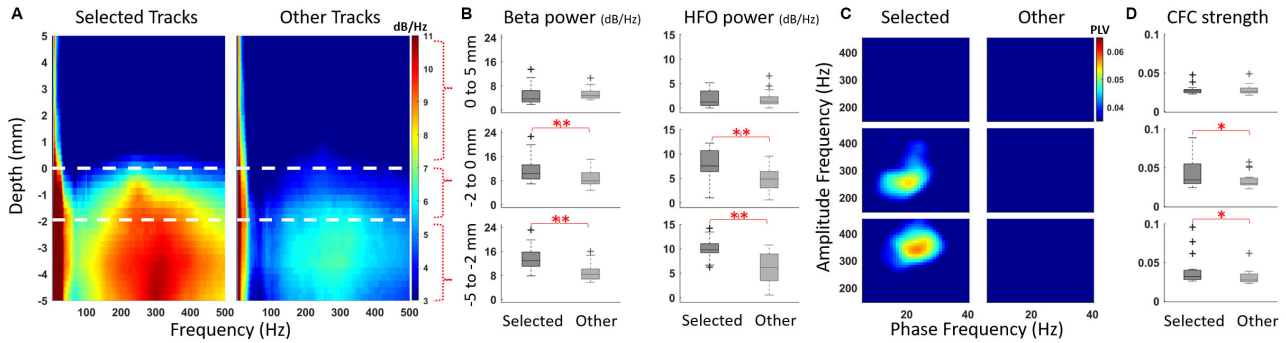

FIGURE 4 | LFP patterns of selected and non-selected (other) tracks. **(A)** DFM averages of LFPs recorded from selected and other tracks 5 mm above and below the dorsal border of 19 STNs. One hemisphere which was repositioned due to side effects without recordings was excluded from the electrophysiological averages. The white dashed lines represent the dorsal border and, the dorsal and ventral regions of STN. Upon entry to the STN, there was a marked increase in the beta and HFO activity. The dorsal half was dominated with slow HFOs (200–280 Hz) whereas the ventral half had HFOs in the 280–400 Hz range. **(B)** The beta and HFO bandpowers are contrasted between selected and other tracks in three spatial regions: above (5–0 mm), dorsal (0 to -2 mm) and ventral (-2 to -5 mm) STN. There was significant difference in both beta and HFO bandpower in dorsal and ventral regions ($p < 0.01$, $n = 19$). **(C)** The CFC patterns contrasted from the same depth regions revealed beta-slow HFO coupling in the dorsal territory, whereas there was beta-fast HFO coupling in the ventral territory of the selected track. **(D)** The mean beta-HFO coupling strength was significantly higher in both dorsal and ventral territories ($p < 0.05$, $n = 19$).

Intraoperative electrophysiological recordings for the accurate localization of STN have been a vital step for DBS electrode implantation (Zonenshayn et al., 2000; Sterio et al., 2002; Amirnovin et al., 2006; Gross et al., 2006; Abosch et al., 2013; Campbell et al., 2019). SUA has been the most commonly used electrophysiological signal for targeting (Gross et al., 2006; Abosch et al., 2013; Campbell et al., 2019), which strongly relies on subjective interpretation of single unit firings (Benazzouz et al., 2002; Benabid et al., 2009; Marceglia et al., 2010; Abosch et al., 2013). Recently, there have been reports to ameliorate this disadvantage by identifying and clustering firing types (Kaku et al., 2019, 2020) or by detecting entry and exit of the STN automatically (Wong et al., 2009; Zaidel et al., 2009; Pinzon-Morales et al., 2011; Valsky et al., 2017; Thompson et al., 2018). However, the volatile interface stability and increased computational power requirement arising from higher sampling rates might still favor LFPs (Rouse et al., 2011; Buzsáki et al., 2012; Priori et al., 2013; Thompson et al., 2014). Growing literature supports the utility of LFPs in intraoperative mapping (Chen et al., 2006; Przybyszewski et al., 2016; Telkes et al., 2016; Kolb et al., 2017; Lu et al., 2019). Our results also support the use of LFPs intraoperatively for DBS lead implantation. The processing pipeline and real-time visualization tool (**Supplementary Video S1**) presented here can facilitate this process.

The exploration of disease biomarkers for the development of novel technologies such as closed loop DBS have been of great interest lately (Little and Brown, 2012; Priori et al., 2013; Meidahl et al., 2017; Hell et al., 2019). In this regard, LFPs can provide variety of non-binary patterns including power of distinct oscillatory bands and their nonlinear interactions. There is an abundance of studies reporting the response of LFP-derived biomarkers to medication (Foffani et al., 2003; Priori et al., 2004; Marceglia et al., 2006; Kane et al., 2009; Lopez-Azcarate et al., 2010; Özkurt et al., 2011; Ozturk et al., 2019) and DBS (Kühn et al., 2008; Eusebio et al., 2011; McConnell et al., 2012) therapies, as well the correlation between these biomarkers and cardinal symptoms of PD (Kühn et al., 2006; Weinberger et al., 2006; Ray et al., 2008; Lopez-Azcarate et al., 2010; Oswal et al., 2013; Brittain and Brown, 2014; Ozturk et al., 2019). We and others have previously shown that these patterns can provide utility in contact selection (Ince et al., 2010; Connolly et al., 2015) or targeting the optimal location for DBS implantation (Chen et al., 2006; Thompson et al., 2014; Telkes et al., 2016; Kolb et al., 2017; Lu et al., 2019). Specifically, oscillations in the beta and HFO range and their cross-frequency interactions have been used to pinpoint the "sweet spot" for DBS (Wang et al., 2014; Connolly et al., 2015; Telkes et al., 2016; Horn et al., 2017; van Wijk et al., 2017; Hell et al., 2019). When comparing the selected track with others, we have observed that the bandpowers of beta and HFO oscillations were significantly higher in both dorsal and ventral parts of the STN. Postoperative analyses revealed that the coupling pattern between phase of beta and amplitude of HFO differed in dorsal and ventral territories, similar to previous reports distinguishing both regions with electrophysiology (Rodriguez-Oroz et al., 2001; Theodosopoulos et al., 2003; Zaidel et al., 2009; Telkes et al., 2018). This difference is expected as the dorsolateral STN has been associated with motor functions and exhibited distinct oscillatory/bursting single unit firings whereas ventromedial STN is associated with limbic functions and tonic firings (Abosch et al., 2002; Gross et al., 2006; Zaidel et al., 2010; Thompson et al., 2018; Campbell et al., 2019; Kaku et al., 2020). Interestingly, we also noted HFOs above STN in three patients (see **Figure 2E**). This activity could be originating from other structures such as thalamus or zona incerta (ZI) (Thompson et al., 2014; Yang et al., 2014; Lu et al., 2019; Meidahl et al., 2019). Previous work has shown that dorsolateral STN and ZI stimulation provides the greatest improvement in PD motor symptoms (Gourisankar et al., 2018), which correlates with our observation. However, lack of activity

in the bulk of our recordings begs for further investigation regarding the out-of-STN oscillatory activity in more patients.

CONCLUSION

In this report, we assessed the functional utility of LFP-based lead implantation against the gold standard SUA method using intraoperative online signal processing and compared these modalities in terms of clinical outcomes. Our results suggest that the LFP oscillations can be a more stable, less processing-intensive method that can be integrated in the intraoperative workflow together with SUA-based mapping, without affecting the surgical procedure. In addition to the functional role of LFPs in intraoperative target mapping, the fact that LFPs can also be recorded from the chronic DBS lead after the surgery is another potential advantage that might guide therapeutic programming to a higher efficacy and efficiency. Here, we provided results of a pilot study with ten patients. Future clinical trials with more subjects will be needed to establish if LFPs can become the standard of care for intraoperative mapping.

DATA AVAILABILITY STATEMENT

The data that support the findings of this study are available on a reasonable request from the corresponding author. The raw data are not publicly available as the data might contain potentially identifying or sensitive information that could compromise the privacy of the research participants.

ETHICS STATEMENT

The studies involving human participants were reviewed and approved by University of Houston and Baylor College of Medicine. The patients/participants provided their written informed consent to participate in this study. Written informed consent was obtained from the individual(s) for the publication of any potentially identifiable images or data included in this article.

AUTHOR CONTRIBUTIONS

AV, NI, and JJ-S conceived and designed the experiments. MO, IT, and AV performed the experiments. JJ-S and AT performed clinical testing. MO and NI analyzed the data. MO, IT, and NI wrote the manuscript. MO, IT, JJ-S, AT, AV, SS, SK, and NI reviewed and revised the manuscript and approved the final manuscript as submitted.

FUNDING

This research was supported, in part, by the National Science Foundation, award CBET-1067488, and by an investigator-initiated grant from Medtronic (to AV, JJ-S, and NI).

ACKNOWLEDGMENTS

We would like to thank the patients for their participation. We acknowledge the OR supervisor Carolle Daniel and the rest of the operating room personnel at Baylor St Luke's Medical Center for their help in data collection and Texas Institute for Measurement, Evaluation, and Statistics (TIMES) for the resources and support they provided. The "coin flipping," "cat scan" and shaking "hand" icons in **Figure 1A** are downloaded from nounproject.com under CC-BY licence with credits to Oleksandr Panasovskyi, Sergey Demushkin, and Gregor Cresnar respectively.

SUPPLEMENTARY MATERIAL

The Supplementary Material for this article can be found online at: https://www.frontiersin.org/articles/10.3389/fnins.2020.00611/full#supplementary-material

VIDEO S1 | The soft real-time processing of the LFP activity from 3-track microelectrode recordings (playback accelerated by x50). The traces of ECG, upper limb EMG and LFP signals are provided at the top. The time-evolving frequency spectrum in the low (0–60 Hz) and high (60–500 Hz) frequency ranges of each LFP track is provided at the bottom. As the time passes, the electrodes are inserted deeper towards the target.

REFERENCES

Abosch, A., Hutchison, W. D., Saint-Cyr, J. A., Dostrovsky, J. O., and Lozano, A. M. (2002). Movement-related neurons of the subthalamic nucleus in patients with Parkinson disease. *J. Neurosurg.* 97, 1167–1172. doi: 10.3171/jns.2002.97.5.1167

Abosch, A., Timmermann, L., Bartley, S., Rietkerk, H. G., Whiting, D., Connolly, P. J., et al. (2013). An international survey of deep brain stimulation procedural steps. *Stereotact. Funct. Neurosurg.* 91, 1–11. doi: 10.1159/000343207

Amirnovin, R., Williams, Z. M., Cosgrove, G. R., and Eskandar, E. N. (2006). Experience with microelectrode guided subthalamic nucleus deep brain stimulation. *Neurosurgery* 58, 96–102. doi: 10.1227/01.NEU.0000192690.45680.C2

Aziz, T. Z., and Hariz, M. (2017). To sleep or not to sleep during deep brain stimulation surgery for Parkinson disease? *Neurology* 89, 1938–1939. doi: 10.1212/WNL.0000000000004635

Benabid, A. L., Benazzouz, A., Hoffmann, D., Limousin, P., Krack, P., and Pollak, P. (2008). Long-term electrical inhibition of deep brain targets in movement disorders. *Mov. Disord.* 13, 119–125. doi: 10.1002/mds.870131321

Benabid, A. L., Chabardes, S., Mitrofanis, J., and Pollak, P. (2009). Deep brain stimulation of the subthalamic nucleus for the treatment of Parkinson's disease. *Lancet Neurol.* 8, 67–81.

Benazzouz, A., Breit, S., Koudsie, A., Pollak, P., Krack, P., and Benabid, A. L. (2002). Intraoperative microrecordings of the subthalamic nucleus in Parkinson's disease. *Mov. Disord.* 17, 145–149. doi: 10.1002/mds.10156

Brittain, J.-S., and Brown, P. (2014). Oscillations and the basal ganglia: motor control and beyond. *Neuroimage* 85, 637–647. doi: 10.1016/j.neuroimage.2013.05.084

Brodsky, M. A., Anderson, S., Murchison, C., Seier, M., Wilhelm, J., Vederman, A., et al. (2017). Clinical outcomes of asleep vs awake deep brain stimulation for Parkinson disease. *Neurology* 89, 1944–1950. doi: 10.1212/WNL.0000000000004630

Buzsáki, G. (2004). Large-scale recording of neuronal ensembles. *Nat. Neurosci.* 7, 446–451. doi: 10.1038/nn1233

Buzsáki, G., Anastassiou, C. A., and Koch, C. (2012). The origin of extracellular fields and currents – EEG, ECoG, LFP and spikes. *Nat. Rev. Neurosci.* 13, 407–420. doi: 10.1038/nrn3241

Campbell, B. A., Machado, A. G., and Baker, K. B. (2019). *Electrophysiologic Mapping for Deep Brain Stimulation for Movement Disorders*, 1st Edn. Amsterdam: Elsevier B.V, doi: 10.1016/B978-0-444-64032-1.00022-9

Chen, C. C., Pogosyan, A., Zrinzo, L. U., Tisch, S., Limousin, P., Ashkan, K., et al. (2006). Intra-operative recordings of local field potentials can help localize the subthalamic nucleus in Parkinson's disease surgery. *Exp. Neurol.* 198, 214–221. doi: 10.1016/j.expneurol.2005.11.019

Chen, T., Mirzadeh, Z., Chapple, K. M., Lambert, M., Shill, H. A., Moguel-Cobos, G., et al. (2018). Clinical outcomes following awake and asleep deep brain stimulation for Parkinson disease. *J. Neurosurg.* 130, 109–120. doi: 10.3171/2017.8.JNS17883

Connolly, A. T., Kaemmerer, W. F., Dani, S., Stanslaski, S. R., Panken, E., Johnson, M. D., et al. (2015). "Guiding deep brain stimulation contact selection using local field potentials sensed by a chronically implanted device in Parkinson ' s disease patients," in *Proceedings of the 2015 7th International IEEE/EMBS Conference on Neural Engineering (NER)* (Montpellier: IEEE), 22–24.

Deuschl, G., Schade-Brittinger, C., Krack, P., Volkmann, J., Schäfer, H., Bötzel, K., et al. (2006). A randomized trial of deep-brain stimulation for Parkinson's disease. *N. Engl. J. Med.* 355, 896–908. doi: 10.1056/NEJMoa060281

Eusebio, A., Thevathasan, W., Doyle Gaynor, L., Pogosyan, A., Bye, E., Foltynie, T., et al. (2011). Deep brain stimulation can suppress pathological synchronisation in parkinsonian patients. *J. Neurol. Neurosurg. Psychiatry* 82, 569–573. doi: 10.1136/jnnp.2010.217489

Foffani, G., Priori, A., Egidi, M., Rampini, P., Tamma, F., Caputo, E., et al. (2003). 300-Hz subthalamic oscillations in Parkinson's disease. *Brain* 126, 2153–2163. doi: 10.1093/brain/awg229

Gourisankar, A., Eisenstein, S. A., Trapp, N. T., Koller, J. M., Campbell, M. C., Ushe, M., et al. (2018). Mapping movement, mood, motivation and mentation in the subthalamic nucleus. *R. Soc. Open Sci.* 5:171177. doi: 10.1098/rsos.171177

Groiss, S. J., Wojtecki, L., Südmeyer, M., and Schnitzler, A. (2009). Deep brain stimulation in Parkinson's disease. *Ther. Adv. Neurol. Disord.* 2, 20–28. doi: 10.1177/1756285609339382

Gross, R. E., Krack, P., Rodriguez-Oroz, M. C., Rezai, A. R., and Benabid, A.-L. (2006). Electrophysiological mapping for the implantation of deep brain stimulators for Parkinson's disease and tremor. *Mov. Disord.* 21, S259–S283. doi: 10.1002/mds.20960

Guehl, D., Cuny, E., Benazzouz, A., Rougier, A., Tison, F., Machado, S., et al. (2006). Side-effects of subthalamic stimulation in Parkinson's disease: clinical evolution and predictive factors. *Eur. J. Neurol.* 13, 963–971. doi: 10.1111/j.1468-1331.2006.01405.x

Gunduz, A., Foote, K. D., and Okun, M. S. (2017). Reengineering deep brain stimulation for movement disorders: emerging technologies. *Curr. Opin. Biomed. Eng.* 4, 97–105. doi: 10.1016/j.cobme.2017.09.001

Hariz, M. (2012). Twenty-five years of deep brain stimulation: celebrations and apprehensions. *Mov. Disord.* 27, 930–933. doi: 10.1002/mds.25007

Hariz, M. (2014). Deep brain stimulation: new techniques. *Parkinsonism Relat. Disord.* 20, S192–S196. doi: 10.1016/S1353-8020(13)70045-2

Harris, K. D., Quiroga, R. Q., Freeman, J., and Smith, S. L. (2016). Improving data quality in neuronal population recordings. *Nat. Neurosci.* 19, 1165–1174. doi: 10.1038/nn.4365

Hell, F., Palleis, C., Mehrkens, J. H., Koeglsperger, T., and Bötzel, K. (2019). Deep brain stimulation programming 2.0: future perspectives for target identification and adaptive closed loop stimulation. *Front. Neurol.* 10:314. doi: 10.3389/fneur.2019.00314

Herzog, J., Fietzek, U., Hamel, W., Morsnowski, A., Steigerwald, F., Schrader, B., et al. (2004). Most effective stimulation site in subthalamic deep brain stimulation for Parkinson's disease. *Mov. Disord.* 19, 1050–1054. doi: 10.1002/mds.20056

Hill, D. N., Mehta, S. B., and Kleinfeld, D. (2011). Quality metrics to accompany spike sorting of extracellular signals. *J. Neurosci.* 31, 8699–8705. doi: 10.1523/JNEUROSCI.0971-11.2011

Ho, A. L., Ali, R., Connolly, I. D., Henderson, J. M., Dhall, R., Stein, S. C., et al. (2018). Awake versus asleep deep brain stimulation for Parkinson's disease: a critical comparison and meta-analysis. *J. Neurol. Neurosurg. Psychiatry* 89, 687–691. doi: 10.1136/jnnp-2016-314500

Horn, A., and Kühn, A. A. (2015). Lead-DBS: a toolbox for deep brain stimulation electrode localizations and visualizations. *Neuroimage* 107, 127–135. doi: 10.1016/j.neuroimage.2014.12.002

Horn, A., Neumann, W.-J., Degen, K., Schneider, G.-H., and Kühn, A. A. (2017). Toward an electrophysiological "sweet spot" for deep brain stimulation in the subthalamic nucleus. *Hum. Brain Mapp.* 3390, 3377–3390. doi: 10.1002/hbm.23594

Hutchison, W. D., Allan, R. J., Opitz, H., Levy, R., Dostrovsky, J. O., Lang, A. E., et al. (1998). Neurophysiological identification of the subthalamic nucleus in surgery for Parkinson's disease. *Ann. Neurol.* 44, 622–628. doi: 10.1002/ana.410440407

Ince, N. F., Gupte, A., Wichmann, T., Ashe, J., Henry, T., Bebler, M., et al. (2010). Selection of optimal programming contacts based on local field potential recordings from subthalamic nucleus in patients with Parkinson's disease. *Neurosurgery* 67, 390–397. doi: 10.1227/01.NEU.0000372091.64824.63

Kaku, H., Ozturk, M., Viswanathan, A., Jimenez-Shahed, J., Sheth, S., and Ince, N. F. (2019). "Grouping neuronal spiking patterns in the subthalamic nucleus of Parkinsonian patients," in *Proceedings of the 2019 41st Annual International Conference of the IEEE Engineering in Medicine and Biology Society (EMBC)* (Berlin: IEEE), 4221–4224. doi: 10.1109/EMBC.2019.8857418

Kaku, H., Ozturk, M., Viswanathan, A., Shahed, J., Sheth, S. A., Kumar, S., et al. (2020). Unsupervised clustering reveals spatially varying single neuronal firing patterns in the subthalamic nucleus of patients with Parkinson's disease. *Clin. Park. Relat. Disord.* 3:100032. doi: 10.1016/j.prdoa.2019.100032

Kane, A., Hutchison, W. D., Hodaie, M., Lozano, A. M., and Dostrovsky, J. O. (2009). Dopamine-dependent high-frequency oscillatory activity in thalamus and subthalamic nucleus of patients with Parkinson's disease. *Neuroreport* 20, 1549–1553. doi: 10.1097/WNR.0b013e32833282c8

Kolb, R., Abosch, A., Felsen, G., and Thompson, J. A. (2017). Use of intraoperative local field potential spectral analysis to differentiate basal ganglia structures in Parkinson's disease patients. *Physiol. Rep.* 5, 1–14. doi: 10.14814/phy2.13322

Krack, P., Batir, A., Van Blercom, N., Chabardes, S., Fraix, V., Ardouin, C., et al. (2003). Five-year follow-up of bilateral stimulation of the subthalamic nucleus in advanced Parkinson's disease. *N. Engl. J. Med.* 349, 1925–1934. doi: 10.1056/NEJMoa035275

Krack, P., Kumar, R., Ardouin, C., Dowsey, P. L., McVicker, J. M., Benabid, A.-L., et al. (2001). Mirthful laughter induced by subthalamic nucleus stimulation. *Mov. Disord.* 16, 867–875. doi: 10.1002/mds.1174

Kühn, A. A., Kempf, F., Brucke, C., Gaynor Doyle, L., Martinez-Torres, I., Pogosyan, A., et al. (2008). High-frequency stimulation of the subthalamic nucleus suppresses oscillatory activity in patients with Parkinson's disease in parallel with improvement in motor performance. *J. Neurosci.* 28, 6165–6173. doi: 10.1523/JNEUROSCI.0282-08.2008

Kühn, A. A., Kupsch, A., Schneider, G. H., and Brown, P. (2006). Reduction in subthalamic 8-35 Hz oscillatory activity correlates with clinical improvement in Parkinson's disease. *Eur. J. Neurosci.* 23, 1956–1960. doi: 10.1111/j.1460-9568.2006.04717.x

Kühn, A. A., Trottenberg, T., Kivi, A., Kupsch, A., Schneider, G. H., and Brown, P. (2005). The relationship between local field potential and neuronal discharge in the subthalamic nucleus of patients with Parkinson's disease. *Exp. Neurol.* 194, 212–220. doi: 10.1016/j.expneurol.2005.02.010

Lee, D., Dallapiazza, R., De Vloo, P., and Lozano, A. (2018). Current surgical treatments for Parkinson's disease and potential therapeutic targets. *Neural Regen. Res.* 13, 1342–1345. doi: 10.4103/1673-5374.235220

Lenz, F. A., Dostrovsky, J. O., Kwan, H. C., Tasker, R. R., Yamashiro, K., and Murphy, J. T. (1988). Methods for microstimulation and recording of single neurons and evoked potentials in the human central nervous system. *J. Neurosurg.* 68, 630–634. doi: 10.3171/jns.1988.68.4.0630

Limousin, P., Krack, P., Pollak, P., Benazzouz, A., Ardouin, C., Hoffmann, D., et al. (1998). Electrical stimulation of the subthalamic nucleus in advanced Parkinson's disease. *N. Engl. J. Med.* 339, 1105–1111. doi: 10.1056/NEJM199810153391603

Little, S., and Brown, P. (2012). What brain signals are suitable for feedback control of deep brain stimulation in Parkinson's disease? *Ann. N. Y. Acad. Sci.* 1265, 9–24. doi: 10.1111/j.1749-6632.2012.06650.x

Liu, Z., He, S., and Li, L. (2020). General anesthesia versus local anesthesia for deep brain stimulation in Parkinson's disease: a meta-analysis. *Stereotact. Funct. Neurosurg.* 97, 381–390. doi: 10.1159/000505079

Lopez-Azcarate, J., Tainta, M., Rodriguez-Oroz, M. C., Valencia, M., Gonzalez, R., Guridi, J., et al. (2010). Coupling between beta and high-frequency activity in the human subthalamic nucleus may be a pathophysiological mechanism in Parkinson's disease. *J. Neurosci.* 30, 6667–6677. doi: 10.1523/JNEUROSCI.5459-09.2010

Lu, C. W., Malaga, K. A., Chou, K. L., Chestek, C. A., and Patil, P. G. (2019). High density microelectrode recording predicts span of therapeutic tissue activation volumes in subthalamic deep brain stimulation for Parkinson disease. *Brain Stimul.* 13, 412–419. doi: 10.1016/j.brs.2019.11.013

Magnin, M., Jetzer, U., Morel, A., and Jeanmonod, D. (2001). Microelectrode recording and macrostimulation in thalamic and subthalamic MRI guided stereotactic surgery. *Neurophysiol. Clin.* 31, 230–238. doi: 10.1016/S0987-7053(01)00261-1

Marceglia, S., Foffani, G., Bianchi, A. M., Baselli, G., Tamma, F., Egidi, M., et al. (2006). Dopamine-dependent non-linear correlation between subthalamic rhythms in Parkinson's disease. *J. Physiol.* 571, 579–591. doi: 10.1113/jphysiol.2005.100271

Marceglia, S., Mrakic-Sposta, S., Tommasi, G., Bartolomei, L., Foresti, C., Valzania, F., et al. (2010). Multicenter study report: electrophysiological monitoring procedures for subthalamic deep brain stimulation surgery in Parkinson's disease. *Neurol. Sci.* 31, 449–457. doi: 10.1007/s10072-010-0254-0

McConnell, G. C., So, R. Q., Hilliard, J. D., Lopomo, P., and Grill, W. M. (2012). Effective deep brain stimulation suppresses low-frequency network oscillations in the basal ganglia by regularizing neural firing patterns. *J. Neurosci.* 32, 15657–15668. doi: 10.1523/JNEUROSCI.2824-12.2012

Meidahl, A. C., Moll, C. K. E., van Wijk, B. C. M., Gulberti, A., Tinkhauser, G., Westphal, M., et al. (2019). Synchronised spiking activity underlies phase amplitude coupling in the subthalamic nucleus of Parkinson's disease patients. *Neurobiol. Dis.* 127, 101–113. doi: 10.1016/j.nbd.2019.02.005

Meidahl, A. C., Tinkhauser, G., Herz, D. M., Cagnan, H., Debarros, J., and Brown, P. (2017). Adaptive deep brain stimulation for movement disorders: the long road to clinical therapy. *Mov. Disord.* 32, 810–819. doi: 10.1002/mds.27022

Novak, P., Daniluk, S., Ellias, S. A., and Nazzaro, J. M. (2007). Detection of the subthalamic nucleus in microelectrographic recordings in Parkinson disease using the high-frequency (>500 Hz) neuronal background. *J. Neurosurg.* 106, 175–179. doi: 10.3171/jns.2007.106.1.175

Novak, P., Przybyszewski, A. W., Barborica, A., Ravin, P., Margolin, L., and Pilitsis, J. G. (2011). Localization of the subthalamic nucleus in Parkinson disease using multiunit activity. *J. Neurol. Sci.* 310, 44–49. doi: 10.1016/j.jns.2011.07.027

Odekerken, V. J. J., van Laar, T., Staal, M. J., Mosch, A., Hoffmann, C. F. E., Nijssen, P. C. G., et al. (2013). Subthalamic nucleus versus globus pallidus bilateral deep brain stimulation for advanced Parkinson's disease (NSTAPS study): a randomised controlled trial. *Lancet Neurol.* 12, 37–44. doi: 10.1016/S1474-4422(12)70264-8

Okun, M. S., Green, J., Saben, R., Gross, R., Foote, K. D., and Vitek, J. L. (2003). Mood changes with deep brain stimulation of STN and GPi: results of a pilot study. *J. Neurol. Neurosurg. Psychiatry* 74, 1584–1586. doi: 10.1136/jnnp.74.11.1584

Okun, M. S., Tagliati, M., Pourfar, M., Fernandez, H. H., Rodriguez, R. L., Alterman, R. L., et al. (2005). Management of referred deep brain stimulation failures. *Arch. Neurol.* 62:1250. doi: 10.1001/archneur.62.8.noc40425

Oswal, A., Brown, P., and Litvak, V. (2013). Synchronized neural oscillations and the pathophysiology of Parkinson's disease. *Curr. Opin. Neurol.* 26, 662–670. doi: 10.1097/WCO.0000000000000034

Özkurt, T. E., Butz, M., Homburger, M., Elben, S., Vesper, J., Wojtecki, L., et al. (2011). High frequency oscillations in the subthalamic nucleus: a neurophysiological marker of the motor state in Parkinson's disease. *Exp. Neurol.* 229, 324–331. doi: 10.1016/j.expneurol.2011.02.015

Ozturk, M., Abosch, A., Francis, D., Wu, J., Jimenez−Shahed, J., and Ince, N. F. (2019). Distinct subthalamic coupling in the ON state describes motor performance in Parkinson's disease. *Mov. Disord.* 35, 91–100. doi: 10.1002/mds.27800

Patel, N. K., Khan, S., and Gill, S. S. (2008). Comparison of atlas- and magnetic-resonance-imaging-based stereotactic targeting of the subthalamic nucleus in the surgical treatment of Parkinson's disease. *Stereotact. Funct. Neurosurg.* 86, 153–161. doi: 10.1159/000120427

Penny, W. D., Duzel, E., Miller, K. J., and Ojemann, J. G. (2008). Testing for nested oscillation. *J. Neurosci. Methods* 174, 50–61. doi: 10.1016/j.jneumeth.2008.06.035

Pinzon-Morales, R. D., Orozco-Gutierrez, A. A., and Castellanos-Dominguez, G. (2011). Novel signal-dependent filter bank method for identification of multiple basal ganglia nuclei in Parkinsonian patients. *J. Neural Eng.* 8:036026. doi: 10.1088/1741-2560/8/3/036026

Priori, A., Foffani, G., Pesenti, A., Tamma, F., Bianchi, A. M., Pellegrini, M., et al. (2004). Rhythm-specific pharmacological modulation of subthalamic activity in Parkinson's disease. *Exp. Neurol.* 189, 369–379. doi: 10.1016/j.expneurol.2004.06.001

Priori, A., Foffani, G., Rossi, L., and Marceglia, S. (2013). Adaptive deep brain stimulation (aDBS) controlled by local field potential oscillations. *Exp. Neurol.* 245, 77–86. doi: 10.1016/j.expneurol.2012.09.013

Przybyszewski, A. W., Ravin, P., Pilitsis, J. G., Szymanski, A., Barborica, A., and Novak, P. (2016). Multi-parametric analysis assists in STN localization in Parkinson's patients. *J. Neurol. Sci.* 366, 37–43. doi: 10.1016/j.jns.2016.04.043

Ray, N. J., Jenkinson, N., Wang, S., Holland, P., Brittain, J. S., Joint, C., et al. (2008). Local field potential beta activity in the subthalamic nucleus of patients with Parkinson's disease is associated with improvements in bradykinesia after dopamine and deep brain stimulation. *Exp. Neurol.* 213, 108–113. doi: 10.1016/j.expneurol.2008.05.008

Richardson, R. M., Ostrem, J. L., and Starr, P. A. (2009). Surgical repositioning of misplaced subthalamic electrodes in Parkinson's disease: location of effective and ineffective leads. *Stereotact. Funct. Neurosurg.* 87, 297–303. doi: 10.1159/000230692

Rodriguez-Oroz, M. C., Rodriguez, M., Guridi, J., Mewes, K., Chockkman, V., Vitek, J., et al. (2001). The subthalamic nucleus in Parkinson's disease: somatotopic organization and physiological characteristics. *Brain* 124, 1777–1790. doi: 10.1093/brain/124.9.1777

Rouse, A. G., Stanslaski, S. R., Cong, P., Jensen, R. M., Afshar, P., Ullestad, D., et al. (2011). A chronic generalized bi-directional brain–machine interface. *J. Neural. Eng.* 8:036018. doi: 10.1088/1741-2560/8/3/036018

Schiefer, T. K., Matsumoto, J. Y., and Lee, K. H. (2011). Moving forward: advances in the treatment of movement disorders with deep brain stimulation. *Front. Integr. Neurosci.* 5:69. doi: 10.3389/fnint.2011.00069

Sharott, A., Gulberti, A., Zittel, S., Tudor Jones, A. A., Fickel, U., Munchau, A., et al. (2014). Activity parameters of subthalamic nucleus neurons selectively predict motor symptom severity in Parkinson's disease. *J. Neurosci.* 34, 6273–6285. doi: 10.1523/jneurosci.1803-13.2014

Sterio, D., Zonenshayn, M., Mogilner, A. Y., Rezai, A. R., Kiprovski, K., Kelly, P. J., et al. (2002). Neurophysiological refinement of subthalamic nucleus targeting. *Neurosurgery* 50, 58–69. doi: 10.1097/00006123-200201000-00012

Telkes, I., Jimenez-Shahed, J., Viswanathan, A., Abosch, A., and Ince, N. F. (2016). Prediction of STN-DBS electrode implantation track in Parkinson's disease by using local field potentials. *Front. Neurosci.* 10:198. doi: 10.3389/fnins.2016.00198

Telkes, I., Viswanathan, A., Jimenez-Shahed, J., Abosch, A., Ozturk, M., Gupte, A., et al. (2018). Local field potentials of subthalamic nucleus contain electrophysiological footprints of motor subtypes of Parkinson's disease. *Proc. Natl. Acad. Sci. U.S.A.* 115:201810589. doi: 10.1073/pnas.1810589115

Theodosopoulos, P. V., Marks, W. J., Christine, C., and Starr, P. A. (2003). Locations of movement-related cells in the human subthalamic nucleus in Parkinson's disease. *Mov. Disord.* 18, 791–798. doi: 10.1002/mds.10446

Thompson, J. A., Lanctin, D., Ince, N. F., and Abosch, A. (2014). Clinical implications of local field potentials for understanding and treating movement disorders. *Stereotact. Funct. Neurosurg.* 92, 251–263. doi: 10.1159/000364913

Thompson, J. A., Oukal, S., Bergman, H., Ojemann, S., Hebb, A. O., Hanrahan, S., et al. (2018). Semi-automated application for estimating subthalamic nucleus boundaries and optimal target selection for deep brain stimulation implantation surgery. *J. Neurosurg.* 130, 1–10. doi: 10.3171/2017.12.JNS171964

Valsky, D., Marmor-Levin, O., Deffains, M., Eitan, R., Blackwell, K. T., Bergman, H., et al. (2017). Stop! border ahead: automatic detection of subthalamic exit during deep brain stimulation surgery. *Mov. Disord.* 32, 70–79. doi: 10.1002/mds.26806

van Wijk, B. C. M., Pogosyan, A., Hariz, M. I., Akram, H., Foltynie, T., Limousin, P., et al. (2017). Localization of beta and high-frequency oscillations within the subthalamic nucleus region. *Neuroimage Clin.* 16, 175–183. doi: 10.1016/j.nicl.2017.07.018

Walter, B. L., and Vitek, J. L. (2004). Surgical treatment for Parkinson's disease. *Lancet Neurol.* 3, 719–728. doi: 10.1016/S1474-4422(04)00934-2

Wang, J., Hirschmann, J., Elben, S., Hartmann, C. J., Vesper, J., Wojtecki, L., et al. (2014). High-frequency oscillations in Parkinson's disease: spatial distribution and clinical relevance. *Mov. Disord.* 29, 1265–1272. doi: 10.1002/mds.25962

Wang, J., Ponce, F. A., Tao, J., Yu, H., Liu, J., Wang, Y., et al. (2019). Comparison of awake and asleep deep brain stimulation for Parkinson's disease: a detailed analysis through literature review. *Neuromodulation Technol. Neural Interface* doi: 10.1111/ner.13061 [Epub ahead of print].

Weinberger, M., Mahant, N., Hutchison, W. D., Lozano, A. M., Moro, E., Hodaie, M., et al. (2006). Beta oscillatory activity in the subthalamic nucleus and its relation to dopaminergic response in Parkinson's disease. *J. Neurophysiol.* 96, 3248–3256. doi: 10.1152/jn.00697.2006

Wojtecki, L., Nickel, J., Timmermann, L., Maarouf, M., Südmeyer, M., Schneider, F., et al. (2007). Pathological crying induced by deep brain stimulation. *Mov. Disord.* 22, 1314–1316. doi: 10.1002/mds.21266

Wong, S., Baltuch, G. H., Jaggi, J. L., and Danish, S. F. (2009). Functional localization and visualization of the subthalamic nucleus from microelectrode recordings acquired during DBS surgery with unsupervised machine learning. *J. Neural. Eng.* 6:026006. doi: 10.1088/1741-2560/6/2/026006

Yang, A. I., Vanegas, N., Lungu, C., and Zaghloul, K. A. (2014). Beta-coupled high-frequency activity and beta-locked neuronal spiking in the subthalamic nucleus of Parkinson's disease. *J. Neurosci.* 34, 12816–12827. doi: 10.1523/JNEUROSCI.1895-14.2014

Zaidel, A., Spivak, A., Grieb, B., Bergman, H., and Israel, Z. (2010). Subthalamic span of β oscillations predicts deep brain stimulation efficacy for patients with Parkinson's disease. *Brain* 133, 2007–2021. doi: 10.1093/brain/awq144

Zaidel, A., Spivak, A., Shpigelman, L., Bergman, H., and Israel, Z. (2009). Delimiting subterritories of the human subthalamic nucleus by means of microelectrode recordings and a Hidden Markov Model. *Mov. Disord.* 24, 1785–1793. doi: 10.1002/mds.22674

Zhang, S., Zhou, P., Jiang, S., Wang, W., and Li, P. (2016). Interleaving subthalamic nucleus deep brain stimulation to avoid side effects while achieving satisfactory motor benefits in Parkinson disease: a report of 12 cases. *Medicine (Baltimore)* 95:e5575. doi: 10.1097/MD.0000000000005575

Zonenshayn, M., Rezai, A. R., Mogilner, A. Y., Beric, A., Sterio, D., and Kelly, P. J. (2000). Comparison of anatomic and neurophysiological methods for subthalamic nucleus targeting. *Neurosurgery* 47, 282–294. doi: 10.1097/00006123-200008000-00005

Conflict of Interest: The authors declare that this study received funding from Medtronic. The funder was not involved in the study design, collection, analysis, interpretation of the data, the preparation of this manuscript or the decision to submit for publication.

frontiers in Neuroscience

ORIGINAL RESEARCH
published: 30 June 2020
doi: 10.3389/fnins.2020.00639

Self-Tuning Deep Brain Stimulation Controller for Suppression of Beta Oscillations: Analytical Derivation and Numerical Validation

John E. Fleming[1†], *Jakub Orłowski*[2†], *Madeleine M. Lowery*[1*] *and Antoine Chaillet*[2,3]

[1] *Neuromuscular Systems Laboratory, UCD School of Electrical & Electronic Engineering, University College Dublin, Dublin, Ireland,* [2] *Laboratoire des Signaux et Systèmes, Université Paris-Saclay, CNRS, CentraleSupélec, Gif-sur-Yvette, France,* [3] *Institut Universitaire de France, Paris, France*

Closed-loop control strategies for deep brain stimulation (DBS) in Parkinson's disease offer the potential to provide more effective control of patient symptoms and fewer side effects than continuous stimulation, while reducing battery consumption. Most of the closed-loop methods proposed and tested to-date rely on controller parameters, such as controller gains, that remain constant over time. While the controller may operate effectively close to the operating point for which it is set, providing benefits when compared to conventional open-loop DBS, it may perform sub-optimally if the operating conditions evolve. Such changes may result from, for example, diurnal variation in symptoms, disease progression or changes in the properties of the electrode-tissue interface. In contrast, an adaptive or "self-tuning" control mechanism has the potential to accommodate slowly varying changes in system properties over a period of days, months, or years. Such an adaptive mechanism would automatically adjust the controller parameters to maintain the desired performance while limiting side effects, despite changes in the system operating point. In this paper, two neural modeling approaches are utilized to derive and test an adaptive control scheme for closed-loop DBS, whereby the gain of a feedback controller is continuously adjusted to sustain suppression of pathological beta-band oscillatory activity at a desired target level. First, the controller is derived based on a simplified firing-rate model of the reciprocally connected subthalamic nucleus (STN) and globus pallidus (GPe). Its efficacy is shown both when pathological oscillations are generated endogenously within the STN-GPe network and when they arise in response to exogenous cortical STN inputs. To account for more realistic biological features, the control scheme is then tested in a physiologically detailed model of the cortical basal ganglia network, comprised of individual conductance-based spiking neurons, and simulates the coupled DBS electric field and STN local field potential. Compared to proportional feedback methods without gain adaptation, the proposed adaptive controller was able to suppress beta-band oscillations with less power consumption, even as the properties of the controlled system evolve over time due to alterations in the target for beta suppression, beta fluctuations and variations in the electrode impedance.

Keywords: deep brain stimulation, self-tuning, Parkinson's disease, beta-band oscillations, closed-loop, adaptive control

OPEN ACCESS

Edited by:
Sabato Santaniello, University of Connecticut, United States

Reviewed by:
Pierre Sacré, Johns Hopkins University, United States
Clayton Bingham, University of Southern California, Los Angeles, United States

***Correspondence:**
Madeleine M. Lowery
madeleine.lowery@ucd.ie

[†]These authors have contributed equally to this work

Specialty section:
This article was submitted to Neural Technology, a section of the journal Frontiers in Neuroscience

Received: *31 March 2020*
Accepted: *25 May 2020*
Published: *30 June 2020*

Citation:
Fleming JE, Orłowski J, Lowery MM and Chaillet A (2020) Self-Tuning Deep Brain Stimulation Controller for Suppression of Beta Oscillations: Analytical Derivation and Numerical Validation. Front. Neurosci. 14:639. doi: 10.3389/fnins.2020.00639

1. INTRODUCTION

Deep brain stimulation (DBS) is a clinically effective treatment used in patients with advanced Parkinson's disease (PD) to supplement or replace pharmacological treatment of symptoms. It consists of high-frequency stimulation of neurons within the basal ganglia, with the subthalamic nucleus and globus pallidus being the most common targets, using a chronically implanted electrode and a subcutaneous pulse generator. At present, DBS is delivered clinically in an open-loop fashion where stimulation parameters remain fixed over time. This approach, however, may lead to overstimulation, inducing side effects and shortening battery life. Regular retuning of parameters is also required, involving a time-consuming trial and error process (Lozano et al., 2019).

The search for new approaches to improve the attenuation of patient symptoms and minimize side effects while increasing battery life has motivated a growing interest in closed-loop DBS over the last several years (Santaniello et al., 2010; Rosin et al., 2011; Santos et al., 2011; Carron et al., 2013; Beuter et al., 2014; Shah et al., 2018; Eitan et al., 2019). In a closed-loop paradigm, the stimulation waveform is modified based on specific biomarkers which are used as a surrogate measure of symptom severity. To date, beta-band (13–30 Hz) activity in the STN local field potential (LFP) has been one of the most widely investigated biomarkers for closed-loop DBS during Parkinson's disease (Parastarfeizabadi and Kouzani, 2017). Increased beta-band power in the STN LFP is correlated with motor impairment symptoms in Parkinson's disease, and its suppression, due to medication or high frequency DBS, with improved motor performance (Kühn et al., 2006, 2008; Hammond et al., 2007; Eusebio et al., 2011).

Closed-loop stimulation utilizing LFP beta-band power has been experimentally validated in patients for short periods (Rosin et al., 2011; Little et al., 2013, 2016; Rosa et al., 2015; Arlotti et al., 2018; Velisar et al., 2019), however, longer term investigations have yet to be conducted. The improvement in symptoms has been comparable to that with conventional open-loop DBS while the energy required has been substantially reduced. In a number of studies, the stimulation signal has been delivered in an "on-off" fashion, switching the stimulation on or off depending on whether or not the biomarker exceeded a specified threshold (Little et al., 2013, 2016). Using this approach, suitable stimulation parameters must be first identified, as in the case of open-loop DBS. Using two thresholds, Velisar et al. (2019) increased or decreased stimulation amplitude to maintain the biomarker within a given range. Proportional feedback approaches, where the stimulation amplitude is proportional to the measured biomarker, have also shown potential in both clinical (Rosa et al., 2015; Arlotti et al., 2018) and computational studies (Tukhlina et al., 2007; Chaillet et al., 2017; Popovych and Tass, 2019). Clinical studies in patients have confirmed that proportional stimulation responding to slowly changing beta-band LFP activity is not only effective and well-tolerated by patients, but might also help avoid stimulation-induced dyskinesia when patients are on medication (Rosa et al., 2015; Arlotti et al., 2018).

Similar to on-off strategies, which utilize fixed stimulation parameters, proportional feedback requires a fixed controller gain parameter to be identified where the stimulation amplitude at a given time is controlled by this gain and an estimated biomarker value. Identification of the controller gain parameter is a potentially complicated and time-consuming postoperative process. Furthermore, although the selected gain may be suitable for the operating point at which it was initially set, it may provide suboptimal performance and require retuning when properties of the system change, for example in response to disease progression or changes in the properties of the electrode-tissue interface.

To address this problem, we propose a self-tuning control strategy inspired by adaptive control theory, where the value of the controller gain evolves based on the measured pathological activity. The controller gain automatically increases until the detected pathological oscillations are sufficiently suppressed and then begins to dissipate when the oscillation amplitude is low enough. In this manner, the proportional controller self-adapts its gain to the lowest value that guarantees suppression of the oscillations to the desired level. Using tools from control theory, namely Lyapunov-Krasovskii analysis, we mathematically show in a firing-rate model that the proposed controller guarantees disruption of the pathological oscillations provided that the internal coupling within the GPe is sufficiently weak. The controller is derived first under the assumption of endogenously generated oscillations, arising from increased coupling within the STN-GPe network, and is then extended to the case where oscillatory activity arises in the STN-GPe loop due to exogenous cortical inputs.

While firing-rate models provide a means to represent the activity of the network in a mathematically tractable manner, they lack the physiological detail that enables them to be easily related to the underlying processes at the cellular level. To overcome this limitation, we computationally test its performance in a more physiologically relevant context, by implementing it in a network of conductance-based neuron models. We first demonstrate through simulations that the firing-rate and conductance-based network models studied here have similar characteristics in terms of the emergence of oscillations as a function of connection strength between STN and GPe, and that both models have similar qualitative frequency responses. Firing-rate model parameters are then identified based on data obtained from simulations of the conductance-based model to link the two models and demonstrate that the latter fulfills the theoretical criterion of low internal GPe connectivity. Finally, the ability of the adaptive controller to "self-tune" to maintain the suppression of pathological oscillations is assessed numerically in three different scenarios: changing the target suppression level, modifying the background beta activity in the network, and varying the electrode impedance.

2. MATERIALS AND METHODS

2.1. Firing-Rate Model

The firing-rate model, which we derive the self-tuning DBS strategy and mathematically prove its efficacy, is inspired by the STN-GPe loop model originally proposed in Nevado-Holgado

et al. (2010) to study the emergence of pathological beta oscillations observed in the parkinsonian basal ganglia. The model is defined as follows:

$$\tau_1 \dot{x}_1(t) = -x_1(t) + S_1\big(c_{11}x_1(t-\delta_{11}) - c_{12}x_2(t-\delta_{12}) + b_1u_1(t)\big) \tag{1a}$$

$$\tau_2 \dot{x}_2(t) = -x_2(t) + S_2\big(c_{21}x_1(t-\delta_{21}) - c_{22}x_2(t-\delta_{22}) - b_2u_2(t)\big). \tag{1b}$$

The instantaneous firing activities (in pulses per second) of the STN and GPe, are respectively represented by $x_1(t)$ and $x_2(t)$. $\tau_1, \tau_2 > 0$ are time constants. For each $i,j \in \{1,2\}$, the constant $c_{ij} \geq 0$ represents the synaptic connection strength from population j to population i and $\delta_{ij} \geq 0$ is a time delay that occurs due to finite velocity of axonal and synaptic transmission from population j to population i. u_1 and u_2 represent the influence of cortical (into STN) and striatal (into GPe) inputs to the system, respectively, modulated by the synaptic weights $b_1 \geq 0$ and $b_2 \geq 0$. All the coupling constants c_{ij} and b_j being non-negative, the sign represents whether the neurons in the presynaptic population have excitatory (STN and cortex) or inhibitory (GPe and striatum) effect on the postsynaptic one. The activation functions S_1 and S_2 encode the response of the neuronal populations to their input. Although they were considered in Nevado-Holgado et al. (2010) as sigmoids, the theoretical analysis provided below allows them to be any increasing function with bounded derivative.

2.1.1. Self-Tuning Controller Derivation

It was shown in Nevado-Holgado et al. (2010) and Pasillas-Lépine (2013) that if the coupling weights c_{12} and c_{21} between STN and GPe are sufficiently high, the model exhibits sustained endogenous oscillations, which fall in the beta frequency band for appropriate values of the model parameters. The controller is first derived and assessed under that assumption and is then further explored in the case where oscillations within the loop arise from exogenous inputs to the STN-GPe network.

Under the assumption that the cortical and striatal inputs are constant ($u(t) = (u_1(t), u_2(t))^T = \bar{u}$), consider the change of variables $u \leftarrow u - \bar{u}$, and $x \leftarrow x - \bar{x}$, where $\bar{x}$ is an equilibrium value of $x = (x_1, x_2)^T$ for the input $\bar{u}$, whose existence is guaranteed by Pasillas-Lépine (2013). Adding a feedback $\mu(t)$ representing the influence of artificial stimulation (DBS) on STN and shifting the activation functions S_j such that $S_j(0) = 0$ for $j \in \{1,2\}$, we obtain the following dynamics:

$$\tau_1 \dot{x}_1(t) = -x_1(t) + S_1\big(c_{11}x_1(t-\delta_{11}) - c_{12}x_2(t-\delta_{12}) + \mu(t)\big) \tag{2a}$$

$$\tau_2 \dot{x}_2(t) = -x_2(t) + S_2\big(c_{21}x_1(t-\delta_{21}) - c_{22}x_2(t-\delta_{22})\big). \tag{2b}$$

The model described by (2) has been studied by Pasillas-Lépine et al. (2013) and Haidar et al. (2016), who showed that a proportional feedback acting only on STN is capable of disrupting exaggerated oscillations and stabilizing the system. More precisely, assuming that the inner GPe interconnections are sufficiently weak, namely:

$$c_{22}\ell_2 < 1, \tag{3}$$

where ℓ_2 denotes the maximum slope of the GPe activation function S_2, it was demonstrated in those papers that the system (2) is asymptotically stable under proportional feedback from the STN to itself, namely:

$$\mu(t) = -\theta x_1(t), \tag{4}$$

where the proportional gain $\theta > 0$ should be chosen to be sufficiently large.

The original result was obtained using linearization techniques. Since then, it has been extended to take full account of the nonlinear effects induced by the activation functions S_j (Chaillet et al., 2017, 2019). In particular, it was shown in Chaillet et al. (2019), using Lyapunov-Krasovskii methodology, that the network described in (2) in closed loop with (4) is globally exponentially stable, provided that θ is above some minimum value $\theta^* > 0$ and condition (3) is satisfied. Global exponential stability of the origin means that there exist $\eta, \gamma > 0$ such that the solutions of (2) satisfy

$$|x(t)| \leq \eta \|x_0\| e^{-\gamma t}, \quad \forall t \geq 0, \tag{5}$$

for any initial state x_0. The model being a delay differential equation, the state here is not a point in $\mathbb{R}^2$, but rather a history function defined as $x_t(s) = x(t+s)$ for all $s \in [-\delta, 0]$, where δ denotes the maximum delay δ_{ij} involved in the dynamics. This state (hence, the initial state) belongs to the set of all continuous functions from $[-\delta, 0]$ to $\mathbb{R}^2$ and we employ the norm $\|x_t\| = \max_{s\in[-\delta,0]} |x(t+s)|$ on this functional set. Global exponential stability is thus a very strong stability property, as it imposes an exponential convergence to the equilibrium and a transient overshoot proportional to the magnitude of the initial state, no matter where the system initially lies. Imposing such a property on the firing-rate model (2) impedes the existence of steady-state pathological oscillations. Global exponential stability is also known to induce robustness properties with respect to exogenous inputs for a wide class of systems (Yeganefar et al., 2008), which may prove useful for the problem considered here due to the inherent imprecision and variability of biological models.

One of the major limitations of the stimulation strategy proposed above is that we do not know a priori the value of the minimum effective gain θ^*. In Chaillet et al. (2019), the following estimate of θ^* was proposed:

$$\theta^* \leq 8\left(c_{11}^2 + \frac{4c_{21}^2c_{12}^2}{(1-c_{22})^2}\right),$$

but it is a conservative approximation. Moreover, this value depends on the connection parameters c_{ij} that would be very hard to estimate accurately in practical applications, due to the high level of abstraction of the considered model.

The alternative to pure proportional control that we propose here is inspired from adaptive control theory and involves updating the gain parameter θ based on the measured state of the system, namely:

$$\mu(t) = -\theta(t)x_1(t) \tag{6a}$$

$$\tau_\theta \dot{\theta}(t) = |x_1(t)| - \sigma\theta(t), \tag{6b}$$

where $\sigma, \tau_\theta > 0$ are control parameters governing how fast the control gain reacts to changes in the system.

First note that, similar to (4), this control law requires recording of the STN activity only. In the same way, it involves only stimulation of the STN. In practice, these constitute important features in terms of limited insertion of measurement and stimulation electrodes.

The idea behind the adaptive law (6) is simple. As long as x_1 is not at zero (meaning that STN activity has not reached its equilibrium), the term $|x_1(t)| \geq 0$ increases the proportional gain θ. With that, $\theta(t)$ will eventually overpass θ^* (no matter what its precise value is) and cause the state to converge to zero exponentially. On the other hand, the dissipation (or leakage) term $-\sigma\theta(t)$ decreases the value of θ whenever $\sigma\theta(t) \geq |x_1(t)|$, due to either a too high value reached by the gain θ or because x_1 has reached a sufficiently low value (as desired). These balanced effects are designed in such a way that the control law automatically adjusts its gain around the (unknown) value θ^*.

The dissipation term $-\sigma\theta(t)$ present in (6b) is in the spirit of what is known in the control theory literature as the "σ-modification" (Ioannou and Kokotovic, 1984). It was introduced to increase robustness of adaptive control to external disturbances and unmodeled dynamics. It has been shown to guarantee that all the closed-loop signals are bounded and that their mean values converge to a residual set, whose size can be made arbitrarily small with an appropriate choice of σ (Ioannou and Fidan, 2006), even for certain classes of nonlinear systems (Fradkov et al., 1999). Until recently, this methodology was confined to delay-free systems but, for the purpose of the present study, we have extended it to nonlinear time-delay systems (Orłowski, 2019). More precisely, we have the following result (the interested reader is referred to Orłowski, 2019 for more details on the mathematical aspects of this result).

Proposition. *Let ℓ_i denote the maximum slope of the activation functions S_i and let $\tilde{\theta}_0 = \theta_0 - \theta^*$. Under the condition that $\ell_2 c_{22} < 1$, there exists $q > 0$ such that, for any $\sigma \geq 0$ small enough and any initial conditions x_0 and θ_0, the solution of system (2) in closed loop with (6) is bounded and satisfies the following property for all $t, T \geq 0$:*

$$\frac{1}{T}\int_t^{t+T} |x(\tau)|\mathrm{d}\tau \leq \frac{q}{T}\left(\|x_0\| + \min\{\tilde{\theta}_0; 0\}\tilde{\theta}_0 + 1\right) + q\sigma.$$

This statement ensures that solutions are bounded and the system is "stable in the mean." This latter property guarantees that the mean value of the solution, taken over a sufficiently long time window T, converges to a neighborhood proportional to σ, regardless of the initial state. Since σ is a tunable parameter in our controller, this means we can arbitrarily decrease the average amplitude of steady-state oscillations by picking a sufficiently small σ (picking σ as zero would annihilate steady-state oscillations, but would impede the ability to decrease the proportional gain θ whenever possible). The key assumption under which this stabilization is made possible is that $\ell_2 c_{22} < 1$, meaning that the GPe self-coupling should be reasonably low. More discussion on this assumption and its biological meaning is provided in section 4.2.

In order to selectively attenuate pathological oscillations, with moderate effect on other frequency bands, we propose the following frequency-sensitive version of (6):

$$\mu(t) = -\theta(t)x_1(t) \tag{7a}$$

$$\tau_\theta\dot{\theta}(t) = \beta(x_{1t}) - \sigma\theta(t), \tag{7b}$$

where $\beta(x_{1t}) \geq 0$ is a biomarker detection function. β is implemented as the peak-to-peak amplitude of a bandpass-filtered signal (Butterworth filter, order 5, 15–30 Hz) from $t-500$ ms to t.

This version is similar in spirit to the self-tuning controller (6), but the increase of the gain θ depends only on the STN activity within the targeted frequency band (beta). In a situation when no beta activity is present in the STN, the leakage term $-\sigma\theta(t)$ would cause the gain $\theta(t)$ to converge to zero, in which case no DBS signal would be delivered.

2.1.2. Endogenous and Exogenous Generation of Beta Oscillations

The mathematical derivations in section 2.1.1 assume that external inputs into the STN-GPe loop are constant and pathological oscillations arise in an endogenous manner due to too strong synaptic coupling between STN and GPe (Plenz and Kital, 1999; Nevado-Holgado et al., 2010; Pavlides et al., 2012). However, the origin of beta oscillations is still a subject of much debate and there is increasing evidence supporting a role for an exogenous mechanism in which oscillations originating in the cortex or striatum are transmitted to the STN-GPe network and amplified within the network (Magill et al., 2001; Sharott et al., 2005; Mallet et al., 2008; Tachibana et al., 2011; Corbit et al., 2016).

To simulate oscillations arising due to exogenous inputs to the STN, the synaptic coupling between STN and GPe were taken as sufficiently low such that the firing-rate model is not only stable but also incrementally stable (Chaillet et al., 2013) which implies that its steady-state solutions in response to any T-periodic inputs are themselves T-periodic. Thus, any oscillatory input (from cortex or striatum) can entrain the STN-GPe network and cause it to oscillate at the same frequency. This observation enables us to identify the frequency characteristics of the STN-GPe network (despite its nonlinear nature) and which frequency bands, if any, are preferably amplified (see section 3.1.2).

In the firing-rate model, the exogenous and endogenous hypotheses of beta oscillations generation thus correspond to two distinct dynamical behaviors: instability for the former and incremental stability (entrainment) for the latter. Both mechanisms are studied in the simulations presented in this paper (**Figures 2–5**), using the parameter values presented in **Table 1**. Additionally, the time constants of the populations were set to $\tau_1 = 6$ ms, $\tau_2 = 14$ ms, and the delays in the system were set to $\delta_{12} = \delta_{21} = 6$ ms and $\delta_{22} = 4$ ms. The functions S_i were implemented as sigmoids with slope 1

$$S_i(x) = \frac{M_i B_i}{B_i + \exp(-4x/M_i)(M_i - B_i)}, \tag{8}$$

TABLE 1 | Parameters of the firing-rate model (1) used in numerical simulations to obtain **Figures 2A**, **3A**, **4**, **5**.

	c_{12}	c_{21}	c_{22}	b_1	b_2
Figure 2A (endogenous)	0–4	0–32	4	8	139.4
Figure 3A (exogenous)	1.12	19	0.9	2.42	15.1
Figure 4 (endogenous)	3	10	0.9	5	139.4
Figure 5 (exogenous)	1.12	19	0.9	2.42	15.1

where the constants were set to $M_1 = 300$, $M_2 = 400$, $B_1 = 17$, $B_2 = 75$.

2.2. Conductance-Based Model

2.2.1. Model and Controller Implementation

In view of its self-tuning capacities, induced robustness and limited requirements in terms of recording and stimulation electrodes, the proposed adaptive closed-loop DBS strategy is promising. Nevertheless, the strong abstraction of the model considered, which summarizes the activity of an entire neuronal population by a unique variable (its firing rate), makes it difficult to assess whether this strategy would be effective clinically. To address this, the performance of the proposed controller was assessed in a biophysically realistic network model of the cortical basal ganglia network comprised of conductance-based neurons. The model is presented in Fleming et al. (2020) and consists of a population of multicompartment cortical pyramidal neurons and single compartment models of cortical interneurons as well as STN, GPe, GPi, and thalamic neurons which have been previously validated and used in other modeling studies (Terman et al., 2002; Otsuka et al., 2004; Rubin and Terman, 2004; Pospischil et al., 2008; Hahn and McIntyre, 2010; Foust et al., 2011; Kang and Lowery, 2013, 2014; Kumaravelu et al., 2016). Each population was comprised of 100 neurons, where synaptic connections between neurons were modeled by spike detectors in presynaptic neurons coupled to synapses in postsynaptic neurons by a time delay. Synaptic connections in the model were either excitatory (AMPAergic) or inhibitory (GABAergic) depending on the synapse type (Destexhe et al., 1994). Striatal input to the network was represented as Poisson-distributed spike trains to GPe neurons with a mean firing rate of 3 Hz. An overview of the model structure is presented in **Figure 1**.

The model captures key features of the cortical basal ganglia network required for simulating clinical implementations of closed-loop DBS including: (i) the extracellular DBS electric field, which is required to accurately model changes in the DBS amplitude, (ii) antidromic and orthodromic activation of STN afferent fibers, and (iii) the STN LFP detected at non-stimulating contacts of the DBS electrode. In Fleming et al. (2020), the model parameters were tuned to match key features observed during experimental investigations of DBS including cortical desynchronization (Li et al., 2012), GPe entrainment (McConnell et al., 2012), and a gradual suppression of beta-band power detected in the STN LFP for increasing stimulation amplitude (Davidson et al., 2016). The model is described in full detail in its original publication (Fleming et al., 2020) and available to download from ModelDB (https://senselab.med.yale.edu/modeldb/) at ascension number 262046.

The oscillatory properties of the model's STN-GPe network were first examined to explore the duality between its oscillatory behavior and that of the firing-rate model. Beta-band activity was then configured to remain fixed, or was varied according to the three numerical scenarios detailed below which may require controller adaptation *in vivo*.

In line with (7), the proposed self-tuning controller was implemented in the conductance-based model to adapt the amplitude of the stimulation waveform as follows:

$$\mu(t) = \theta(t)x_1(t) \tag{9a}$$

$$\tau_\theta \dot{\theta}(t) = |e(t)| - \sigma\theta(t), \tag{9b}$$

where $\mu(t)$ is the controller output and represents the instantaneous stimulation amplitude, $\theta(t)$ is the controller gain, $x_1(t)$ is the biomarker measurement [i.e., the average rectified value (ARV) of a 100 ms epoch from the beta-band filtered STN LFP, which was filtered using a fourth order Chebyshev band-pass filter with an 8 Hz bandwidth, centered on 25 Hz as described in Fleming et al., 2020], $|e(t)|$ is the half-wave rectified error signal calculated as the difference between the measured biomarker and the desired target suppression level, and τ_θ and σ represent tuning parameters which were fixed at 100 ms and 0.00875, respectively, for all controller simulations in the conductance-based model.

A key difference with (7) is that the DBS in (9) is delivered as a positive feedback on the biomarker [as indicated by the positive sign in $\mu(t)$]. This difference is due to the implementation of DBS in the conductance-based model, whereby increasing DBS amplitude results in a stronger suppression of pathological oscillations.

The model was simulated in the NEURON simulation environment (Hines and Carnevale, 1997) and implemented in Python using the PyNN API package (Davison et al., 2009). The model was numerically integrated using the Crank-Nicholson method with a 0.01 ms timestep for all simulations. Simulations were run on the UCD Sonic high-performance computing cluster.

2.2.2. Numerical Scenarios

The self-tuning controller (9) was tested in three independent scenarios to simulate practical situations in which adaptation of controller parameters *in vivo* may be required to maintain the biomarker (the ARV of LFP beta activity) at a target value. All scenarios were simulated for a 130 s duration.

In the first scenario, background beta-band activity in the model was set to its maximum value for the duration of the simulation while the target level for beta suppression was varied. The beta-band activity (prior to DBS activation) was set by fixing the firing rates of cortical neurons to 26 pulses per second, which resulted in a peak in the LFP power spectrum at 26 Hz. Target values of 10, 0.2, 0.05, 0.15, and 10 μV were then considered over the time intervals 0–10, 10–40, 40–70, 70–100, and 100–130 s, respectively.

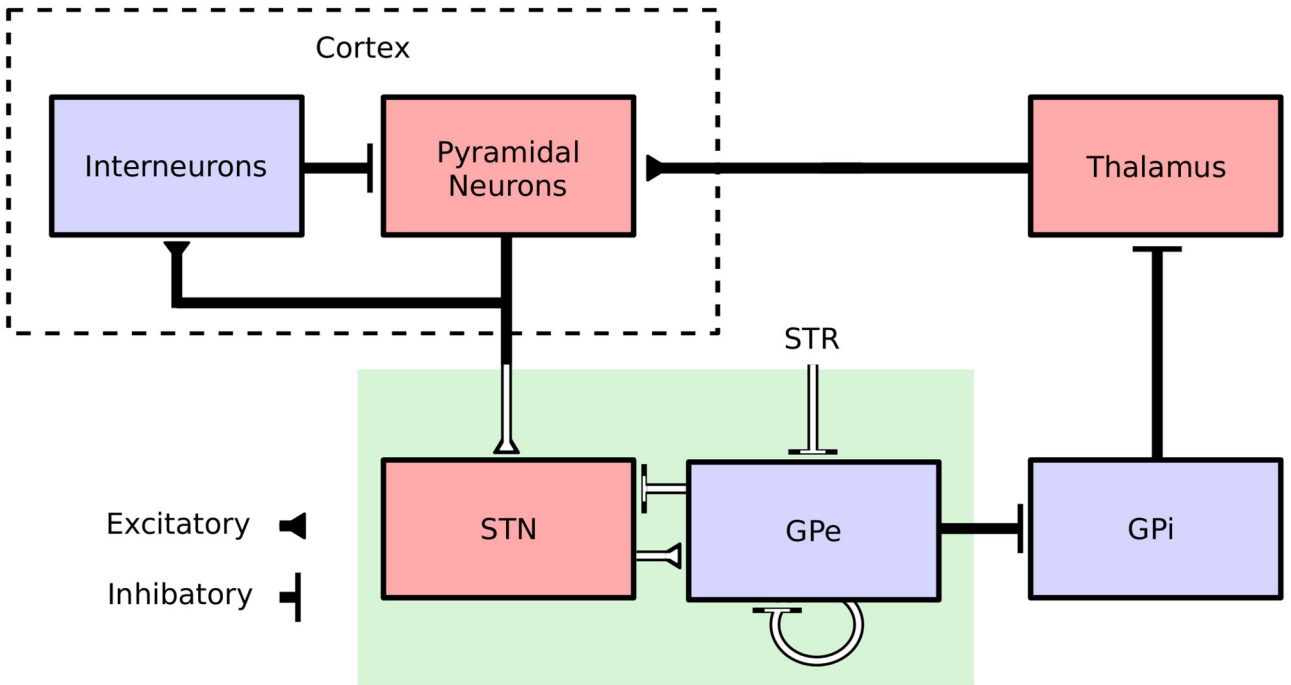

FIGURE 1 | Cortical Basal ganglia network structure. Excitatory and inhibitory populations in the network model are represented in red and blue, respectively. Synaptic connections in the population model are represented by solid black lines. The firing-rate model, representing only a subnetwork of the population model, is highlighted by a green box. White lines correspond to connections which are common to both the population and the firing-rate model.

In the second scenario, the target value for the LFP biomarker was fixed at 0.1 μV for the duration of the simulation while background beta-band activity in the model was modulated to be low during the 0–10, 40–70, and 100–130 s time intervals and high during the 10–40 and 70–100 s time intervals. The intracellular cortical neuron bias current was varied to shift the mean cortical neuron firing rate between 14 and 26 pulses per second during the low and high beta-band activity periods, respectively. Thus, beta-band activity in the model was modulated to display a 14 Hz peak in the LFP power spectrum during the low beta-band activity periods, which shifted to 26 Hz during the high beta-band activity periods. As the bandwidth of the biomarker filter was centered at 25 Hz, modulation of the background beta-band activity in this manner led to lower beta ARV measurements during the low beta-band activity periods.

The third scenario considered a linear variation of the electrode impedance over the simulation period, while background beta-band activity in the model was fixed at its maximum value and the beta ARV target value remained constant at 0.1 μV. In the simulation, the electrode impedance remained constant at 0.5 kΩ up to $t = 30$ s, after which it was linearly increased to a maximum value of 2.5 kΩ at $t = 130$ s.

2.2.3. Performance Measures

Controller performance was quantified using two measures: the error while tracking the target value and the mean power consumption. The mean squared error (MSE) was utilized to measure the controller's ability to track the target level. It is defined as

$$\mathrm{MSE} = \frac{1}{T_{sim}} \int_0^{T_{\mathrm{sim}}} e(t)^2 \, dt, \tag{10}$$

where T_{sim} is the simulation duration ($T_{\mathrm{sim}} = 130$ s) and $e(t)$ is the normalized error signal between the measured LFP beta ARV and the target value, as used in (9). For simplicity, the MSE value for the controllers in each scenario are reported as a percentage of the MSE value that was measured in each respective scenario when DBS was off. Power consumption (PC) was measured as

$$\mathrm{PC} = \frac{1}{T_{\mathrm{sim}}} \int_0^{T_{\mathrm{sim}}} Z_E(t) I_{\mathrm{DBS}}(t)^2 \, dt, \tag{11}$$

where Z_E is the electrode impedance, assumed to be 0.5 kΩ in the non-varying electrode impedance scenarios, and I_{DBS} is the delivered DBS current.

2.3. Parameter Identification

One of the necessary conditions for practical stabilization using the adaptive controller, as recalled in section 2.1.1, is that the internal connections within GPe are weak, as expressed by $c_{22}\ell_2 < 1$ in the firing-rate model. It was, therefore, first checked whether this condition was fulfilled in the conductance-based model.

The value of c_{22} from the firing-rate model is related to the maximum conductance of the GPe-GPe synapses $\bar{g}_{\mathrm{GPeGPe}}$, in the conductance-based model, which was set to 0.015 μS. ℓ_2 is the

maximum slope of the GPe activation function S_2. Thus, in order to verify the stabilizability criterion, we need to identify the slope of the GPe activation function in the conductance-based model, as well as the value of c_{22} corresponding to the value of $\bar{g}_{\text{GPeGPe}}$ used in the conductance-based model.

To that aim, the GPe neurons of the conductance-based model were disconnected from the rest of the network, the only remaining connections being the excitatory projections from STN to GPe. In the firing-rate model, this translates in the following dynamics:

$$\tau_2 \dot{x}_2(t) = -x_2(t) + S_2\big(u(t) + c_{22}x_2(t-\delta_{22})\big), \qquad (12)$$

where $u(t)$ represents synaptic inputs to GPe from STN. Setting $\bar{g}_{\text{GPeGPe}} = 0$ in the conductance-based model leads to $c_{22} = 0$ in the firing-rate model, thus yielding

$$\tau_2 \dot{x}_2(t) = -x_2(t) + S_2(u(t)). \qquad (13)$$

We conducted a series of simulations for different values of cortical input to STN and we estimated the firing rate $u(t)$ of STN and the firing rate $x_2(t)$ of GPe. We have rescaled the data to obtain a slope 1, by fitting a linear function and dividing the values by the obtained slope $a = 1.29$. We then fitted a sigmoid of the form (8) to the obtained data and rescaled it by the same factor a, to obtain an estimate of the activation function S_2.

Next, we obtained a similar set of data for $\bar{g}_{\text{GPeGPe}} = 0.015\,\mu$S. Using the activation function S_2 determined in the previous step, we found the equilibrium of (12) for different values of c_{22} and constant STN input u using a numerical solver. We compared the curves obtained for the different values of c_{22} with the steady-state data from the conductance-based model, to identify the value that minimized the normalized square error:

$$\text{nLSQ}(c_{22}; \text{STN}, \text{GPe}) = \frac{\sum_i \left(f_{c_{22}}(\text{STN}[i]) - \text{GPe}[i]\right)^2}{\sum_i \text{GPe}[i]^2}, \qquad (14)$$

where STN$[i]$ and GPe$[i]$ represent the firing rate of STN and GPe taken from simulation i, and $f_{c_{22}}(\text{STN}[i])$ is the solution of

$$x = S_2(u + c_{22}x)$$

for a given c_{22} with $u = \text{STN}[i]$, meaning the steady-state solution of (12) for these generated inputs from STN. The best fit was reached for $c_{22} = 0.35$. Since the GPe activation S_2 identified in (8) has maximum slope $\ell_2 = 1.29$, the stabilizability criterion (3) is satisfied.

3. RESULTS

3.1. Qualitative Comparison Between the Two Models

3.1.1. Endogenous Oscillations

For constant striatal and cortical inputs, beta-band oscillations emerged in the firing-rate model when the STN-GPe and GPe-STN connectivity strength was sufficiently increased (**Figure 2A**). In the conductance-based model, the intensity of beta power in the spectra of the cumulative STN and GPe population spike trains similarly increased with increasing STN-GPe and GPe-STN connectivity strengths (**Figure 2B**). The increase in beta power within the STN and GPe was accompanied by an increase in synchronization of the two populations within the beta band. The beta-band coherence of the STN and GPe neural spike trains increased similarly with increased connectivity strengths (**Supplementary Figure 1**).

Both models exhibited beta-band oscillations as STN-GPe and GPe-STN connectivity increased, indicating that the firing-rate abstraction well captures the oscillatory dynamics of the conductance-based model. Differences between the two models are, however, observed. In particular, in the firing-rate model, the transition from non-oscillatory to oscillatory behavior occurs more abruptly than in the conductance-based model and oscillatory conditions are associated with a relatively stronger coupling from STN to GPe than from GPe to STN. Also, in the conductance-based model, fluctuations in the frequency and amplitude of the beta oscillations are apparent as GPe-STN connectivity increases. Nevertheless, the overall behavior of the models is qualitatively similar with oscillations emerging in both models as STN-GPe connectivity and GPe-STN connectivity increase.

3.1.2. Exogenous Oscillations

When synaptic coupling between STN and GPe is sufficiently low, the firing-rate model of the STN-GPe loop is not only stable but also entrainable, meaning that any T-periodic input (whether cortical or striatal) generates T-periodic steady-state solutions (Chaillet et al., 2013). While this feature is guaranteed for stable linear systems, the nonlinear nature of the firing-rate model makes it less straightforward. This entrainability is a fundamental requirement for constructing frequency profiles of the STN-GPe network. By considering a sinusoidal input at a given frequency, it is indeed possible to measure the magnitude of the resulting steady-state oscillations, and thus the amplification of the network at this specific frequency (Pavlov et al., 2007). Repeating this procedure across a range of input frequencies, we obtained the nonlinear Bode plots depicted as solid lines in **Figure 3A**.

When DBS is off (solid curves), a clear resonance is observed in the beta frequency band, thus indicating that the network preferably amplifies beta components of the cortical input. This resonance can therefore be interpreted as the beta generation mechanism in the exogenous hypothesis. Due to the nonlinear nature of the firing-rate model, this resonance strength depends on the amplitude of the applied cortical input with more pronounced resonance occurring for stronger mean cortical input.

Akin to the resonance behavior in the firing-rate model, the influence of an external cortical oscillatory input to the STN-GPe network was investigated in the conductance-based model. The connectivity strengths between the STN and GPe populations were selected to lie below the threshold for which the network generated endogenous beta-band oscillations (at 0.11 μS for both), analogous to the entrainable state in the firing-rate model. The frequency of cortical inputs to the STN were varied from 3 to 100 pulses per second, while striatal input to the network remained fixed at 3 pulses per second.

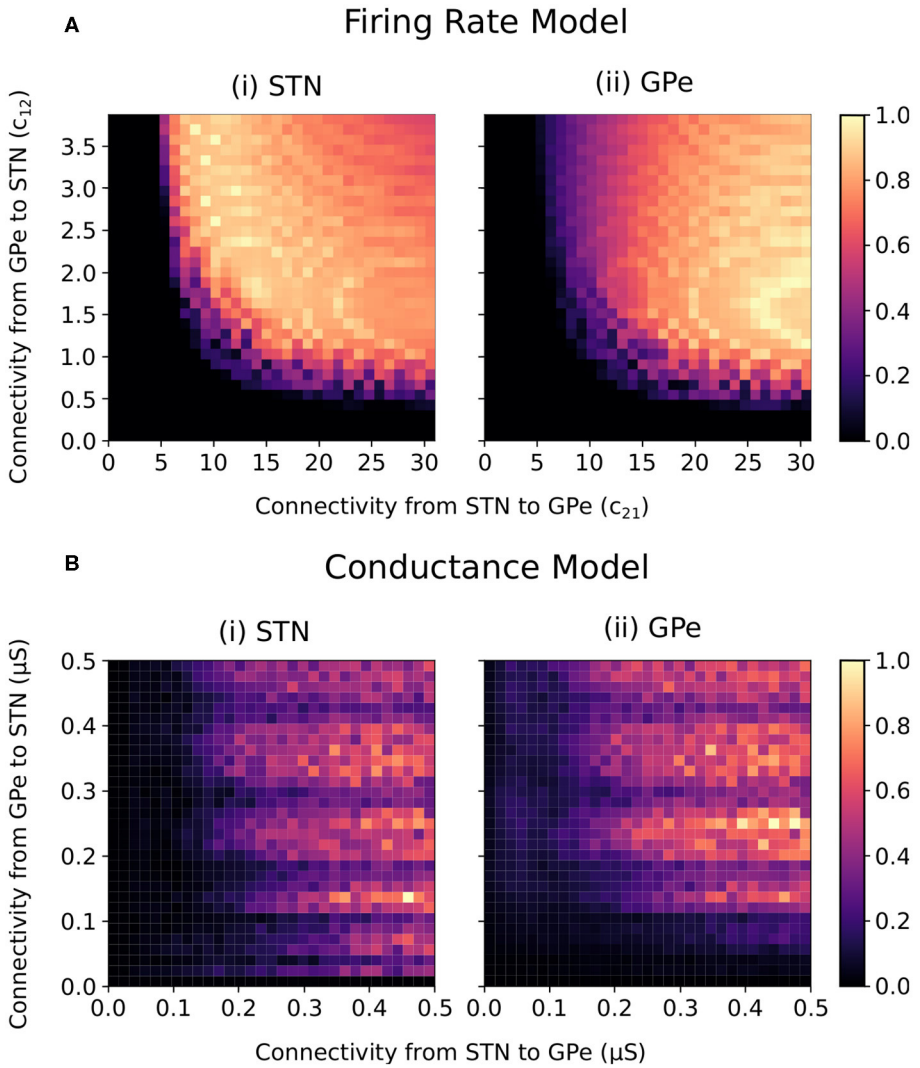

FIGURE 2 | Normalized endogenous beta-band activity in the firing rate and conductance-based models for varying STN and GPe coupling strengths. **(A)** Beta-band oscillation amplitude in the (i) STN and (ii) GPe of the firing rate model. The beta-band oscillation amplitude in each population was estimated for each combination of connectivity parameters (c_{12} and c_{21}) by band-pass filtering the firing rate signals using a fifth order Butterworth filter with 8 Hz bandwidth centered on 20 Hz. The oscillation amplitude in each population was normalized between 0 and 1 in each panel separately. **(B)** Beta-band activity of the (i) STN and (ii) GPe populations in the conductance-based model. Beta-band activity was quantified in each population by integrating the power spectra of the cumulative spike trains for each population between 16 and 24 Hz. The power for each population was normalized between 0 and 1 in each panel separately.

The frequency response of the STN-GPe network due to synchronous cortical inputs through the hyperdirect pathway was examined by estimating the power of the cumulative population spike trains and the spike train coherence between STN and GPe populations within a 4 Hz window centered on the mean frequency of the cortical input. Additionally, resonant network activity was calculated by estimating the power in the simulated STN LFP at the cortical input frequency. Resonance effects were examined as the strength of cortical connectivity to the STN was systematically increased from 0.03 to 0.12 μS (**Figure 3B**).

As the strength of the hyperdirect pathway was increased, a beta-band resonance emerged in the STN and GPe populations and in the power spectrum of the STN LFP. This was accompanied by synchronization across the STN and GPe populations, as evidenced by a peak in the coherence between STN and GPe spike trains for cortical inputs in the beta frequency range (**Figure 3B**). Further strengthening of the hyperdirect pathway led to a broadening of the frequency band at which resonance occurred in the cumulative spike trains of the STN and GPe populations and the STN LFP, extending beyond the beta-band. Synchronous cortical inputs to the STN at low connectivity strengths in the beta band and at frequencies outside this range resulted in coherent activity in the subnetwork, but with relatively low power (**Figure 3B**). Consistent with the firing-rate model (**Figure 3A**), the beta-band resonance was more pronounced for stronger cortical inputs.

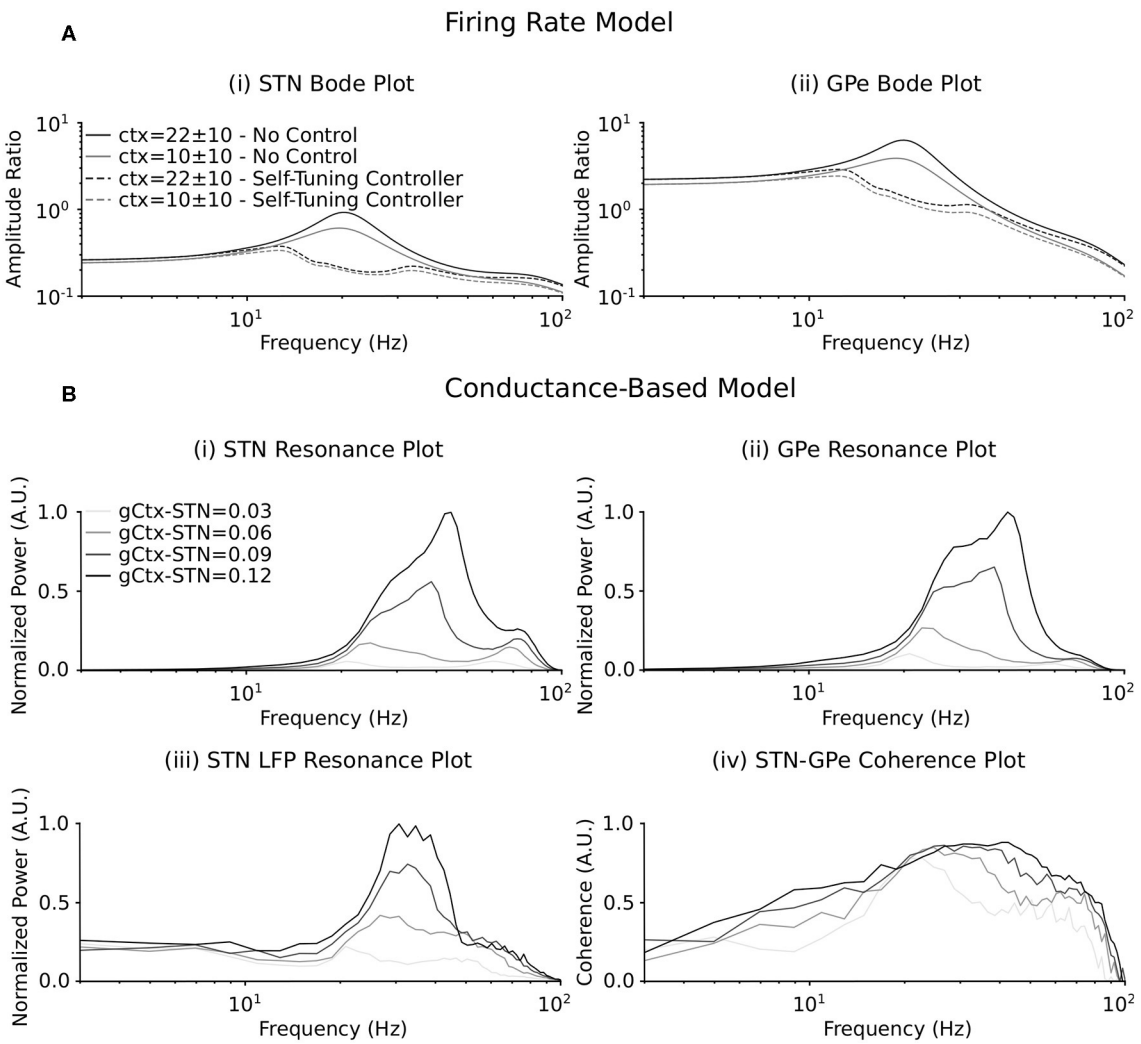

FIGURE 3 | Resonance behavior of the firing rate and conductance-based models in response to synchronous cortical drives. **(A)** Bode plot illustrating amplification of cortical input signals of varying frequency by the (i) STN and (ii) GPe populations in the firing rate model. The amplitude ratio is defined as the amplitude of the input oscillation (the cortical input signal) to the amplitude of the steady state oscillation in the (i) STN and (ii) GPe populations at each cortical input frequency. Solid lines represent the frequency response of each population when DBS is off. Dashed lines represent the frequency response of each population when the self-tuning DBS (7) is implemented with $\sigma = 0.1$ and $\tau_\theta = 50$ ms. Two mean values of the cortical input signal are represented. **(B)** Resonance plot of the power centered at the cortical input frequency in the (i) STN and (ii) GPe cumulative spike trains, (iii) the STN LFP power spectrum and (iv) the coherence between the STN and GPe populations for varying cortical input frequencies. Power at the cortical input frequency was estimated in the cumulative spike trains and LFP power spectra by integrating the power in a 4 Hz window centered on the input frequency in the respective power spectra. The coherence between the STN and GPe populations at the cortical input frequency was estimated from pairs of composite spike trains randomly chosen from the STN and GPe populations (Farina et al., 2014; McManus et al., 2019). The spike trains in the STN and GPe were summed to obtain two composite spike trains. The magnitude squared coherence between the two composite spike trains was then calculated with 1 s overlapping Hamming windows. This was repeated for 200 randomly chosen combinations of spike trains from the STN and GPe populations, as each combination will generate a slightly different coherence estimate. The coherence between the populations was then estimated as the median coherence spectrum over all 200 combinations. The coherence at the cortical input frequency was determined by integrating the resulting coherence spectrum in the 4 Hz window centered on the input frequency. Four cortical to STN connectivity strengths are represented, where the resonance responses are normalized between 0 and 1 in each panel separately.

3.2. Self-Tuning Controller Assessment

3.2.1. Firing-Rate Model

3.2.1.1. Endogenous oscillations with beta-band activity variation

Suppression of endogenous beta oscillations during DBS was assessed first in the firing-rate model, with synaptic weights c_{12} and c_{21} between STN and GPe increased to generate beta oscillations within the network. A performance comparison between self-tuning DBS (6) and proportional DBS (4) is presented in **Figure 4**. Both strategies successfully disrupt pathological oscillations between 200 and 750 ms. At $t = 750$ ms, an additional increase of the cortical input to STN was artificially

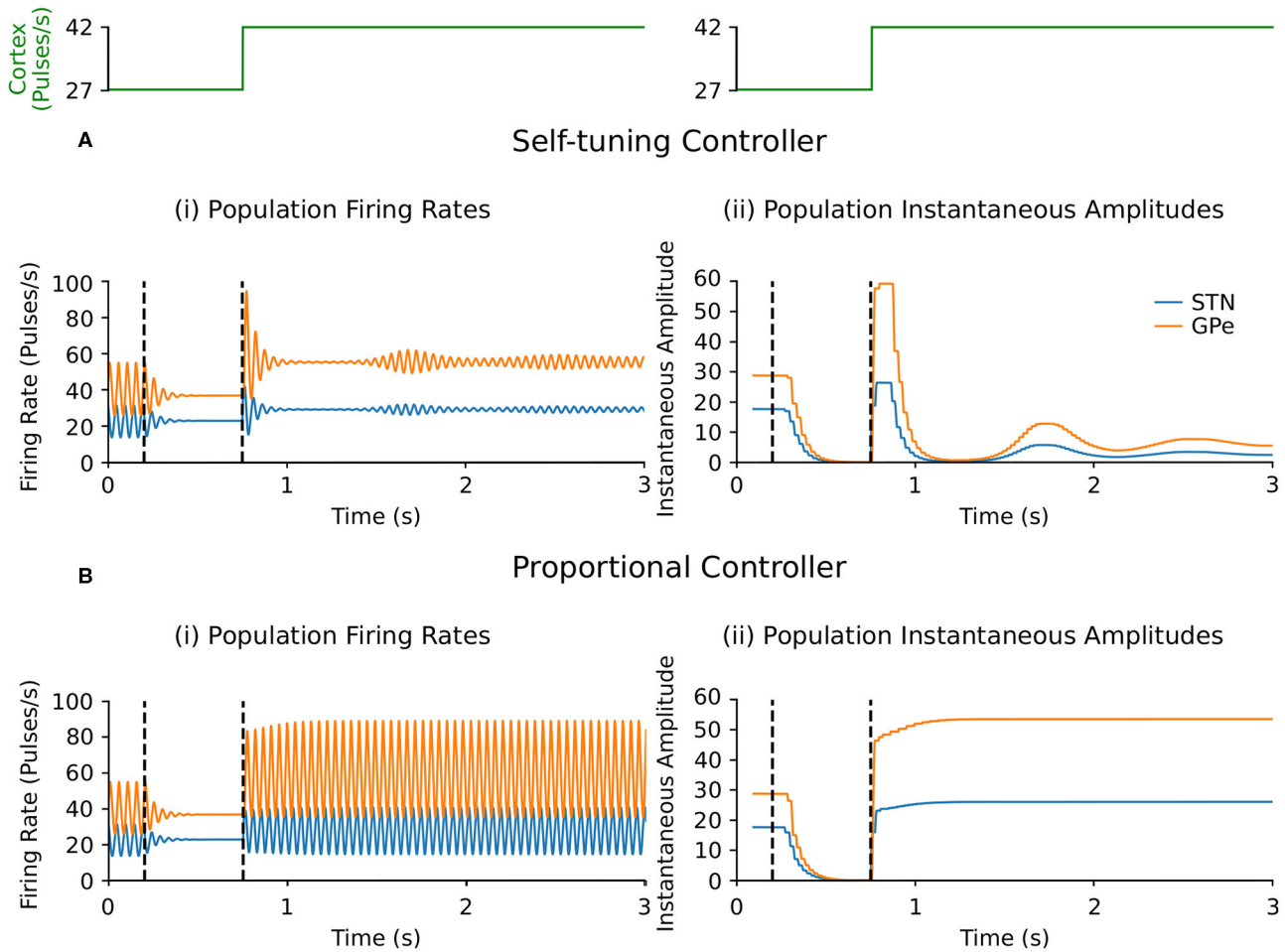

FIGURE 4 | Performance comparison of self-tuning and proportional controllers on endogenous oscillations in the firing-rate model. During simulation, DBS was initially off and then switched on at $t = 200$ ms, where either the **(A)** self-tuning controller or **(B)** proportional controller was implemented. At $t = 750$ ms, the magnitude of the constant cortical input to STN was artificially increased by from 27 to 42, amplifying the endogenous oscillations present in the STN and GPe. The cortical input is presented in green at the top of the figure, aligned with respect to the simulation time with the plots underneath. Left panels illustrate the firing rate behavior of the STN and GPe populations and the right panels correspond to the instantaneous peak-to-peak oscillation amplitude of each population (measured with a sliding window of 100 ms) due to either **(A)** the self-tuning controller (7) with $\tau_\theta = 75$ ms and $\sigma = 0.19$ or **(B)** the proportional controller (4) with $\theta = 2$.

introduced to simulate an increase in beta oscillations. While the self-tuning DBS automatically adapts the proportional gain θ to maintain the attenuation of beta oscillations, pure proportional DBS is unable to do so, resulting in strong beta oscillations that cannot be counteracted without manual tuning of the proportional gain. The self-tuning controller thus outperforms the proportional controller in terms of robustness to disease evolution in the simulated endogenous mechanism scenario.

3.2.1.2. Exogenous oscillations with beta-band activity variation

Selective disruption of pathological beta oscillations generated through exogenous inputs to the STN using the self-tuning controller (7) was then confirmed. With the self-tuning DBS (dashed curves) (**Figure 3A**) the beta-band resonance was eliminated in the firing-rate model, while the frequency profile of the STN-GPe network remained essentially unaltered in other frequency bands, as DBS remains off when beta activity is not detected within the STN. **Figure 5** illustrates that, similar to the endogenous case, self-tuning DBS (6) outperforms proportional DBS (4) when faced with changes in the exogenous oscillations. After the stimulation is turned on at $t = 200$ ms, both controllers successfully decrease the amplitude of the pathological oscillations. After the mean level of the cortical input as well as the amplitude of oscillations is increased at $t = 750$ ms, the self-tuning controller achieves higher damping of the oscillations than the proportional controller.

3.2.2. Conductance-Based Model

3.2.2.1. Scenario 1: beta-band target variation

The self-tuning controller maintained the LFP beta ARV around the desired target values between 10 and 100 s,

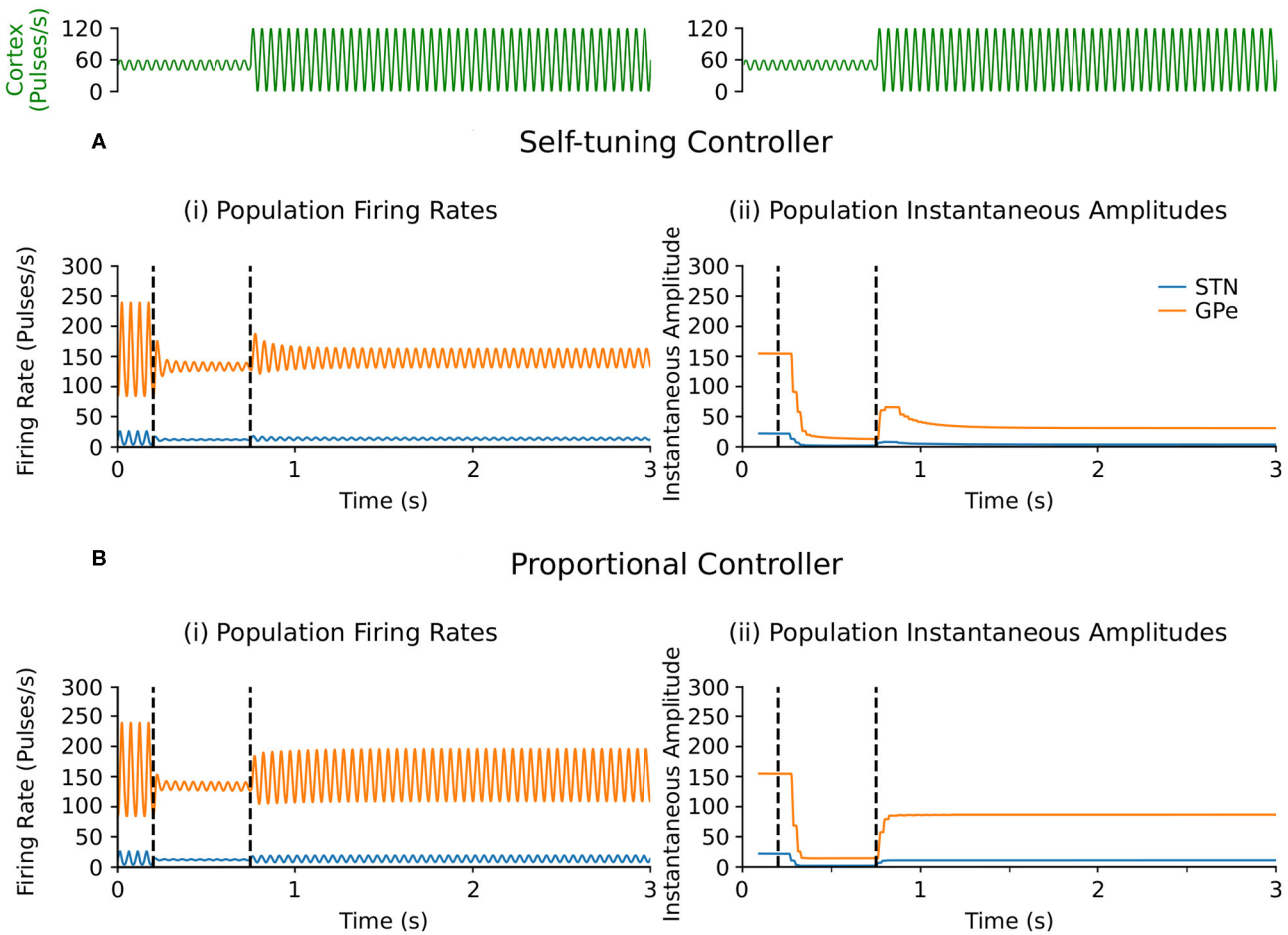

FIGURE 5 | Performance comparison of self-tuning and proportional controllers on exogenous 20 Hz oscillations in the firing-rate model. During simulation, DBS was initially off and then switched on at $t = 200$ ms, where either the **(A)** self-tuning controller or **(B)** proportional controller was implemented. At $t = 750$ ms, the amplitude of the cortical oscillations was increased from 10 to 60 and the mean level of the oscillations is raised from 50 to 60, amplifying the exogenous oscillations present in the STN and GPe. The cortical input is presented in green at the top of the figure, aligned with respect to the simulation time with the plots underneath. Left panels illustrate the firing rate behavior of the STN and GPe populations and the right panels correspond to the instantaneous peak-to-peak oscillation amplitude of each population (measured with a sliding window of 100 ms) due to either **(A)** the self-tuning controller (7) with $\tau_\theta = 5$ ms and $\sigma = 0.01$ or **(B)** the proportional controller (4) with $\theta = 25$.

and turned off from 0 to 10 and 100 to 130 s, where the target value was high and stimulation was not required (**Figure 6A**). The self-tuning controller resulted in a mean power consumption of 11.0 μW and a 82.1% reduction in the MSE. Proportional controllers with fixed gain were able to maintain beta ARV at a single target value, however they were unsuitable for target values other than the one for which they were tuned and resulted in either under or over stimulation when attempting to maintain beta ARV (**Figures 6B–D**). Proportional controllers with fixed gains at 7, 10 and 26 resulted in mean power consumption values of 6.9, 9.3, and 28.2 μW and reductions in the MSE of 79.4, 85.1, and 81.1%, respectively.

3.2.2.2. Scenario 2: beta-band activity variation

The LFP beta ARV was maintained at the target value by the self-tuning controller as the background beta activity was varied between low and high activity periods (**Figure 7A**). The self-tuning controller consumed 17.9 μW and resulted in a 91.4 % reduction of the MSE. The proportional controller with a fixed gain value of 10 was able to maintain the LFP beta ARV at the target value during low background beta activity periods, but did not provide sufficient stimulation to suppress to the target value during periods of high background beta activity (**Figure 7B**). The proportional controller with a fixed gain value of 40 maintained the LFP beta ARV at the target value during both low and high background beta activity periods (**Figure 7C**). The proportional controllers with fixed gain values of 10 and 40 resulted in MSE reductions of 73.4 and 95.0 % and power consumption values of 6.6 and 34.8 μW, respectively. When maintaining the LFP beta activity at the target value, the proportional controller with a fixed gain value of 40 resulted in over stimulation during the low background activity periods, consuming more power than necessary to maintain the LFP beta ARV.

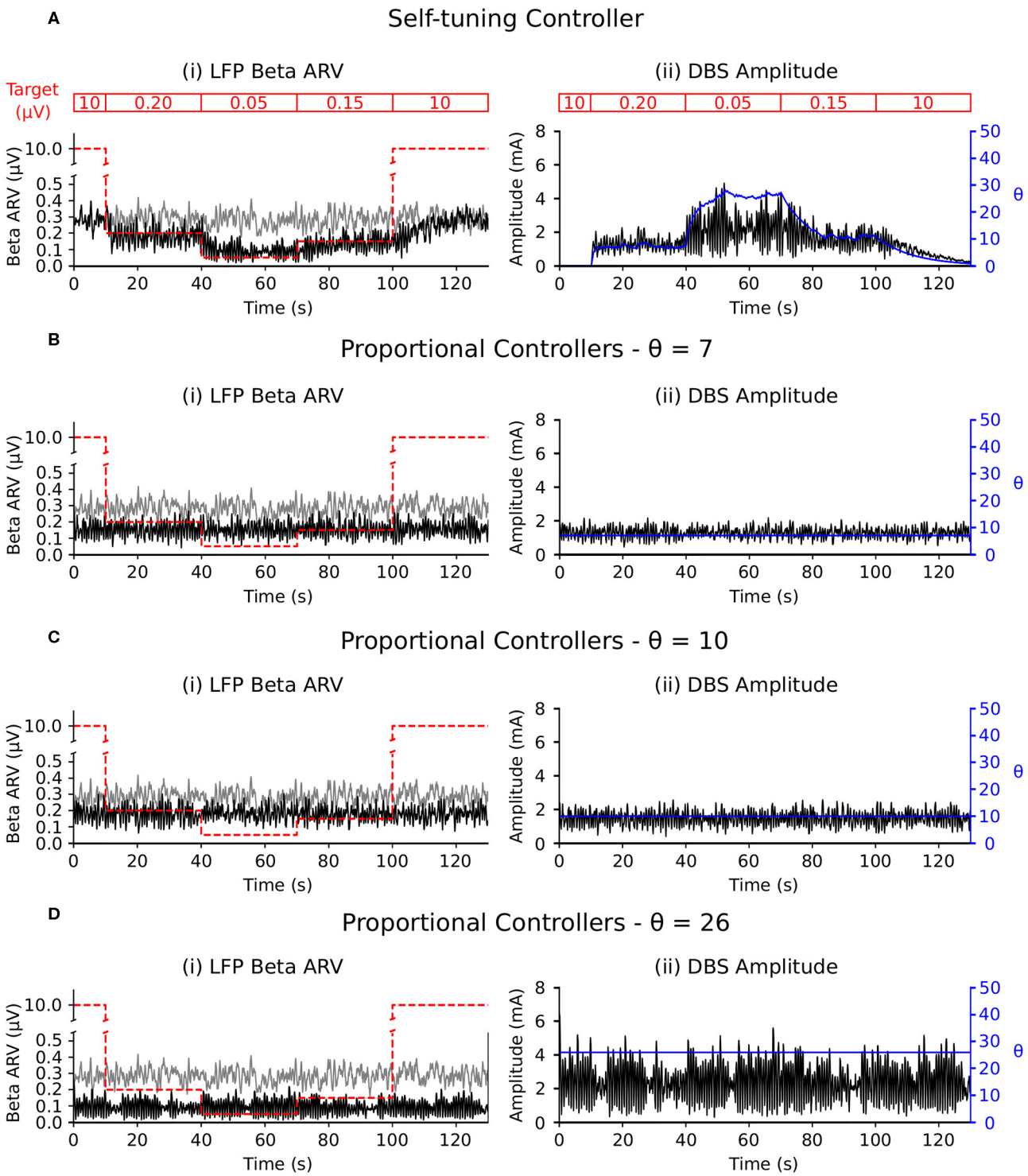

FIGURE 6 | Performance comparison of self-tuning and proportional controllers in response to beta ARV target variations in the conductance-based model. Background beta-band activity in the model was fixed to its maximum value for the duration of the simulation while the target value was modulated to 10, 0.20, 0.05, 0.15, and 10 μV during the 0–10, 10–40, 40–70, 70–100, and 100–130 s time periods, respectively. The target value for each time period is highlighted by the red segmented bar at the top of the figure. Left panels illustrate the target value (dashed red), the beta ARV measured from the STN LFP when DBS was off (gray) or on (black), where the DBS amplitude is modulated by the corresponding controller. Right panels illustrate the time evolution of the DBS amplitude (black) and controller gain θ (blue) during simulation. **(A)** Self-tuning DBS controller with $\tau_\theta = 100$ ms and $\sigma = 0.00875$. **(B)** Proportional controller with a fixed gain value of $\theta = 7$. **(C)** Proportional controller with a fixed gain value of $\theta = 10$. **(D)** Proportional controller with a fixed gain value of $\theta = 26$.

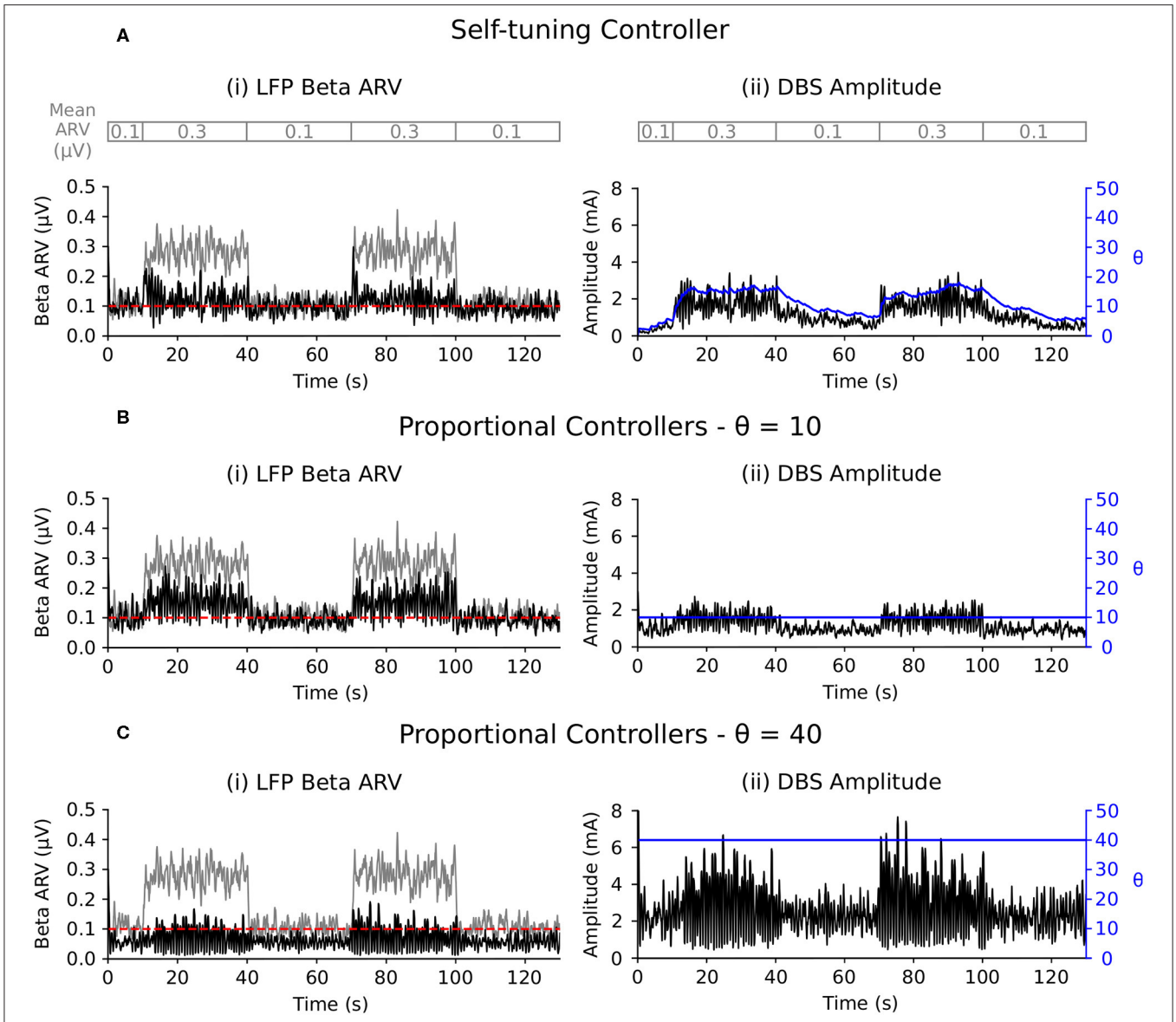

FIGURE 7 | Performance comparison of self-tuning and proportional controllers in response to background beta-band activity variations in the conductance-based model. The beta ARV target value was fixed to 0.1μV for the duration of the simulation while the background beta-band activity was modulated to be at its maximum value during the 10–40 and 70–100 s time periods and at its minimum value during the 0–10, 40–70, and 100–130 s time periods, respectively. The mean ARV of the background beta-band activity measured in the LFP when DBS was off is highlighted by the gray segmented bar at the top of the figure. Left panels illustrate the target value (dashed red), the beta ARV measured from the STN LFP when DBS was off (gray) or on (black), where the DBS amplitude was modulated by the corresponding controller. Right panels illustrate the time evolution of the DBS amplitude (black) and controller gain θ (blue) during simulation. **(A)** Self-tuning DBS controller with $\tau_\theta = 100$ ms and $\sigma = 0.00875$. **(B)** Proportional controller with a fixed gain value of $\theta = 10$. **(C)** Proportional controller with a fixed gain value of $\theta = 40$.

3.2.2.3. Scenario 3: electrode impedance variation

The self-tuning controller maintained the LFP beta ARV at the target level as the electrode impedance was linearly increased over the course of the simulation to five times its initial impedance value, i.e., from an initial value of 0.5–2.5 kΩ (**Figure 8A**). Background beta activity and the target value of 0.1 μV remained fixed over the course of the simulation. The self-tuning controller resulted in a MSE reduction of 93.5% and a power consumption of 11.2 μW. Proportional controllers with fixed gain values of 10 and 40 lead to MSE reductions of 77.0 and 96.0 % while consuming 6.2 and 27.7 μW, respectively. Similar to scenarios 1 and 2, the self-tuning controller was able to tune its gain to the required level to maintain beta ARV at the target level. Proportional control with fixed gain of 10 became less effective over the course of the simulation, while proportional control with fixed gain of 40 was effective throughout the simulation, but consumed more power than necessary (**Figures 8B,C**). A summary of the controller performance under the different scenarios considered is presented in **Table 2**.

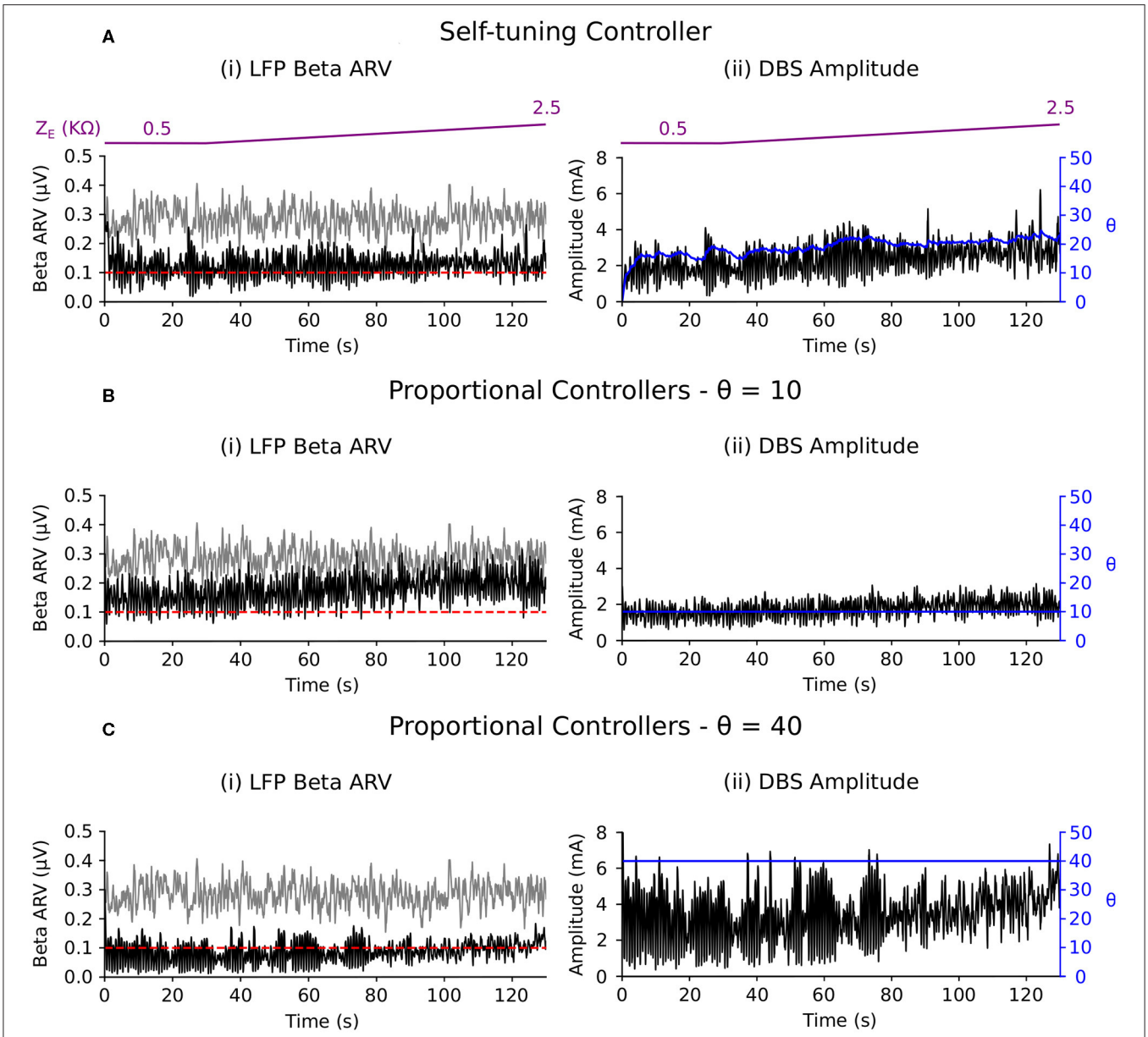

FIGURE 8 | Performance comparison of self-tuning and proportional controllers in response to electrode impedance variations in the conductance-based model. The beta ARV target value was fixed to 0.1μV and the background beta-band activity was fixed to its maximum value for the duration of the simulation. The electrode impedance was fixed at 0.5 KΩ during the 0–30 s period and was then linearly increased from 0.5 to 2.5 KΩ over the 30–130 simulation period. The electrode impedance variation is illustrated by the purple bar at the top of the figure. Left panels illustrate the target value (dashed red), the beta ARV measured from the STN LFP when DBS was off (gray) or on (black), where the DBS amplitude was modulated by the corresponding controller. Right panels illustrate the time evolution of the DBS amplitude (black) and controller gain θ (blue) during simulation. **(A)** Self-tuning DBS controller with $\tau_\theta = 100$ ms and $\sigma = 0.00875$. **(B)** Proportional controller with a fixed gain value of $\theta = 10$. **(C)** Proportional controller with a fixed gain value of $\theta = 40$.

4. DISCUSSION

4.1. Firing-Rate and Conductance-Based Models

The proposed firing-rate model facilitated the derivation of a robust control law capable of disrupting pathological beta-band oscillations in the STN-GPe network in Parkinson's disease and the analytic establishment of its efficiency. Firing-rate models capture the average behavior of neural populations and facilitate tractable mathematical analysis of network behavior (Destexhe and Sejnowski, 2009). These models, however, summarize the neuronal population to a single variable: the number of spikes it emits per unit time. They are thus unable to capture cellular-level features such as sub-threshold activity, LFP activity, specific responses induced by bursting, antidromic activation of STN afferent inputs or the interaction between neurons and

TABLE 2 | Summary of controller performance in the three considered scenarios.

Target variation:	**MSE (%)**	**Power consumed (μW)**
DBS Off	100	0
Self-tuning controller	7.9	11.0
Proportional controller ($\theta = 7$)	20.6	6.9
Proportional controller ($\theta = 10$)	14.9	9.3
Proportional controller ($\theta = 26$)	18.9	28.2
Beta variation:	**MSE (%)**	**Power consumed (μW)**
DBS Off	100	0
Self-tuning controller	8.6	17.9
Proportional controller ($\theta = 10$)	26.6	6.6
Proportional controller ($\theta = 40$)	5.0	34.8
Electrode impedance variation:	**MSE (%)**	**Power consumed (μW)**
DBS Off	100	0
Self-tuning controller	6.5	11.2
Proportional controller ($\theta = 10$)	23.0	6.2
Proportional controller ($\theta = 40$)	4.0	27.7

In each scenario, the MSE value is reported as a percentage of the DBS Off case, where the DBS Off case corresponds to a 100% MSE.

the induced extracellular potential. In contrast, networks of conductance-based neuron models offer the ability to capture more complex network dynamics and interactions, but are usually too complex to analyze mathematically.

While recent approaches have attempted to bridge the gap between these two types of models (di Volo et al., 2019), we have empirically assessed the similarities and discrepancies between them and shown that key features needed to analyze and control pathological oscillations in Parkinson's disease are indeed captured by both models (**Figures 2**, **3**). We also demonstrated in section 2.3 the possibility to check the theoretical stabilization condition (3), derived on the firing-rate model, using observations from the conductance-based model. By utilizing both modeling approaches, the limitations of each model are complemented by the strengths of the other. The joint analysis of these two models also supports the relevance of abstract firing-rate models for the derivation of advanced DBS strategies aiming at counteracting a targeted brain oscillation, which can then be validated in computationally detailed models before preclinical investigations.

4.2. Physiological Interpretation of the Stabilizability Condition

The theoretical condition obtained on the firing-rate model to ensure stabilizability by the self-tuning DBS signal reads $\ell_2 c_{22} < 1$ (see Proposition). In other words, the synaptic weights from GPe to itself should be sufficiently low. This condition ensures that the GPe does not act as a pacemaker on its own, as low internal coupling is a standard sufficient condition for stability of a neuronal population (see for instance Faye and Faugeras, 2010). The necessity to impose that GPe does not generate pathological oscillations on its own is quite reasonable: considering the extreme case when STN is not connected to the GPe, it would be impossible to attenuate self-generated GPe oscillations by stimulating STN only.

It is worth noting that the proposed condition precludes GPe self-oscillatory activity no matter the value of its internal delay. This constitutes a noteworthy feature of our mathematical result as this delay does not need to be estimated. Nevertheless, for realistic values of internal GPe delays (of the order of few milliseconds), no such self-oscillatory GPe activity is observed even if the condition is violated, at least for reasonable values of the striatal input. This was confirmed in numerical simulations of the conductance-based model in which the internal GPe synaptic weights were artificially increased by two orders of magnitude. Even in that case, GPe was unable to autonomously generate oscillations and the proposed self-tuning DBS successfully disrupted network beta oscillations (data not shown).

4.3. Endogenous and Exogenous Generation of Oscillations

Beyond employing two modeling approaches of the structures involved, the paper also investigated two possible mechanisms of pathological oscillations generation: the emergence of endogenous oscillations, in which the STN-GPe network acts as a pacemaker, and the generation of oscillations through the interaction of the network with inputs originating from other structures such as the cortex.

The ability of the STN-GPe network to endogenously generate beta-band oscillations was consistent across both the firing-rate and conductance-based models (**Figure 2**). The STN-GPe network has been proposed as a potential source of pathologically increased beta-band oscillations in Parkinson's disease, where connectivity changes in the reciprocally connected network leads to the endogenous generation of beta-band oscillations. This behavior has been previously explored in modeling studies utilizing firing-rate models where the progression of Parkinson's disease is represented as an increase in the synaptic coupling strengths between the STN and GPe neuron populations (Nevado-Holgado et al., 2010; Pavlides et al., 2012; Pasillas-Lépine, 2013). The firing-rate model presented here is consistent with these previous studies in which a Hopf bifurcation occurs and leads to beta-band oscillations in the network when the synaptic coupling strengths are sufficiently increased (**Figure 2A**). This behavior is well-matched in the conductance model, where increases in the synaptic coupling strengths between the two populations also leads to the endogenous emergence of beta-band oscillations in the network (**Figure 2B**).

Although modeling studies support the hypothesis that the reciprocally connected STN-GPe network is capable of generating the beta-band oscillatory activity, investigations of isolated STN-GPe cell cultures *in vitro* have observed the emergence of endogenous oscillations at much lower frequencies (Plenz and Kital, 1999). Furthermore, increasing evidence from experimental studies in patients and animal models suggest that external inputs to the STN-GPe loop may play a key role in the generation of elevated beta-band oscillations in the parkinsonian cortex and basal ganglia. The STN-GPe network occupies a crucial location in the cortical basal ganglia network

receiving inputs from both cortical and striatal structures through the hyperdirect and indirect pathways, respectively. Due to connectivity changes in the STN-GPe loop during Parkinson's disease, it is thus hypothesized that exogenous beta oscillations are locally amplified by the loop, with subsequent oscillations then propagating throughout the full cortical basal-ganglia network (Magill et al., 2001; Mallet et al., 2008; Corbit et al., 2016; West et al., 2018). Consistent with this, Sharott et al. (2005) observed that the power and coherence of beta oscillations in the cortex and STN were elevated during dopamine depletion in a parkinsonian rat model, while Litvak et al. (2011) observed cortical beta activity leading to STN beta activity in parkinsonian patients. In primate studies, oscillatory activity in the GPe was observed to be mainly due to excitatory activity from the STN, while oscillatory activity in the STN was primarily due to excitatory cortical input (Tachibana et al., 2008, 2011).

Both the firing-rate and conductance-based models in the present study demonstrated the STN-GPe network's ability to entrain to an external cortical rhythm (**Figure 3**). A Bode plot of the input-output relationship in the firing-rate model showed a marked peak in the beta frequency band, with this peak increasing in magnitude and broadening with increasing strength of the inputs to the STN (**Figure 3A**). This behavior was consistent with the conductance-based model behavior, where the STN-GPe network displayed a resonant peak in the beta frequency band for low connectivity strength between the cortex and STN (**Figure 3B**). Increasing the strength of the hyperdirect pathway led to increased resonance in the model and also to a widening of the frequency bands where resonance was observed (**Figure 3B**). This observed resonance is consistent with other modeling investigations of the STN-GPe network, where firing-rate models (Nevado-Holgado et al., 2014; Detorakis and Chaillet, 2017; Liu et al., 2017, 2020) and conductance-based neuron models (Ahn et al., 2016; Shouno et al., 2017; Koelman and Lowery, 2019) were used to investigate the behavior of STN-GPe network in response to external drives. Although those studies have illustrated the resonant capabilities of the STN-GPe network of both firing-rate and conductance-based models separately, this study is the first to demonstrate that both modeling approaches lead to comparable results (**Figure 3**).

4.4. Self-Tuning DBS Controller

Having established qualitative consistency in the behavior of the firing-rate and conductance-based models, the performance of the proposed self-tuning DBS controller was first proven mathematically and validated in the firing-rate model where the controller was capable of disrupting both exogenously and endogenously generated beta-band activity in the STN-GPe network (**Figures 3A**, **4**, **5**). The simulations confirmed that the self-tuning controller autonomously adapts its gain value to the minimal value required to counteract pathological oscillations, thus avoiding over-stimulation and allowing for adaptation to possible changes in the system properties associated with disease progression (**Figures 4**, **5**).

The performance of the controller to maintain network beta-band oscillations at a target level was then assessed in the conductance-based model in three example conditions, which emulated practical situations in which gain adaptation may be required *in vivo*: modification of the beta-level target, variation of the beta oscillations intensity, and alteration of the electrode impedance.

4.4.1. Adaptation to Target-Level Changes

The self-tuning controller adapted the controller gain in response to changes in the target value (**Figure 6A**). For each target value, the controller identified the necessary gain to maintain the biomarker at the target level. In contrast, proportional controllers with fixed gain were unable to track target changes and resulted in less reduction in the MSE than the self-tuning controller (**Figures 6B–D**, **Table 2**). The self-tuning controller consumed more power than the controllers with low fixed gain and less power than the controller with high fixed gain, but was able to maintain low error as the target changed (**Table 2**).

Similar issues were identified by Su et al. (2019) who investigated the ability of a proportional-integral controller to modulate DBS frequency to track dynamic changes in a target signal during closed-loop DBS using a conductance-based model. While the proportional-integral controller considered in that study was able to successfully track dynamic changes in the target beta signal, it required different controller gain values for each beta-band target level considered. The adaptive controller proposed here overcomes this issue as the controller self-tunes its gain value to find the gain necessary for maintaining the beta ARV at the target values (**Figure 6A**).

4.4.2. Adaptation to Beta Oscillation Fluctuations

The self-tuning controller was able to maintain the biomarker at the target level while beta activity in the network varied (**Figure 7A**). Between $t = 0$ and $t = 10$ s, the self-tuning controller adapted its gain value to the low beta activity. Once beta activity in the network increased, during the 10–40 s period, the controller increased its gain to suppress the beta activity to the target level. The proportional controller with low fixed gain value ($\theta = 10$) was able to maintain the biomarker at the target level during low beta activity periods, but was unable to during high beta periods (**Figure 7B**). In contrast, the proportional controller with a high fixed gain value ($\theta = 40$) was able to maintain the biomarker close to the target during both low and high beta activity periods (**Figure 7C**), but at the cost of increased power consumption (**Table 2**).

In line with the power consumption in scenario 1, the controllers with low and high fixed gain resulted in the lowest and highest power consumption, respectively, and the power consumption of the self-tuning controller lay between these values (**Table 2**). Essentially, the self-tuning controller identified the gain required to maintain the beta ARV at the target level in both the high and low beta activity periods and consumed the necessary power to maintain beta at the target.

Clinical investigations of proportional control strategies in patients with Parkinson's disease (Rosa et al., 2015; Arlotti et al., 2018), have observed attenuation of DBS when subjects were on and off medication, motivating the need for self-tuning in response to varying background beta activity. Arlotti et al. (2018) investigated proportional control over an 8 h period and showed

a 30–45 % improvement in patient UPDRS III motor scores. Although these clinical studies showed promising results, we hypothesize that additional benefits may result from using the self-tuning controller proposed here. The proportional control scheme implemented in Rosa et al. (2015) and Arlotti et al. (2018) utilized a fixed gain value, and thus may lead to under or over stimulation if a suitable gain is not selected.

4.4.3. Adaptation to Electrode Impedance Variations

Clinical measurements of electrode impedance usually vary between 0.5 and 1.5 kΩ (Obeso et al., 2001; Volkmann et al., 2002). However, many factors contribute to the electrode impedance, and its variability between subjects. These factors include the surface properties of the electrodes, electrical double layer, conductivity of the bulk tissue medium and thickness of the surrounding encapsulation layer (Butson et al., 2006). The electrode impedance plays a crucial role in determining the current delivered to tissue during voltage-controlled stimulation. Clinical investigations of closed-loop DBS have not yet investigated the impact of electrode impedance variations on DBS efficiency as the timescales at which these variations take place are much longer than the current timescales at which closed-loop DBS has been investigated clinically. For closed-loop DBS to remain effective when chronically implemented, it is necessary to utilize controllers which can accommodate such changes and avoid a need for clinical retuning of the controller parameters. This third scenario, therefore, aimed to assess this robustness to electrode impedance variations. In response to the simulated changes, the self-tuning controller gradually increased the controller gain to maintain the biomarker at the target level (**Figure 8A**).

In contrast, the proportional controller with low fixed gain was able to maintain the beta ARV at the target up until $t = 60$ s, but became less effective thereafter (**Figure 8B**). With a higher fixed gain value, the proportional controller was able to accommodate changes in the electrode impedance and remained effective at suppressing the beta ARV to the target for whole the duration of the simulation (**Figure 8C**).

In line with the other examples, the power consumption of the self-tuning controller was greater than that of the proportional controller with low fixed gain and less than the proportional controller with the high fixed gain (**Table 2**). Although both the proportional controller with high fixed gain and the self-tuning controller successfully maintained beta activity at its target level, more power consumption was needed for the former than for the latter.

4.5. Clinical Implementation of the Self-Tuning DBS

The self-tuning controller presented here offers several advantages for experimental implementation. First, it relies only on data from the STN, no additional recording electrodes in other brain structures are required. Moreover, although the firing-rate model utilized the number of STN pulses per second, the simulations conducted in the conductance-based model showed the efficiency of the approach when only STN LFP is accessible. More importantly, the self-tuning controller relies on very limited information regarding the system parameters. The theoretical result of Proposition simply requires that the GPe internal synaptic weights are sufficiently low. This condition, also present in theoretical investigations on fixed-gain proportional DBS (Chaillet et al., 2017), does not require precise knowledge on the exact shape of activation functions, or the values of the time constants, synaptic weights, or delays.

Nonetheless, experimental validation of the self-tuning controller also comes with challenges. First, both the stimulation and the recording are assumed to be within the STN. This would lead to stimulation artifacts that should be removed. Several techniques are available to address this issue (Rossi et al., 2007; Stanslaski et al., 2012; Basir-Kazeruni, 2017) The proposed controller also requires some embedded computational capabilities in order to filter the STN LFP and implement the control law (7). While more demanding than classical open-loop DBS, the required computational power is comparable to the algorithms employed for proportional or on-off stimulation. In addition, the upper and lower bounds on the applied current or voltage would be the same as those used during conventional stimulus parameter setting.

Despite its self-tuning nature, the control law (7) requires two parameters to be chosen: the time constant τ_θ and the dissipation parameter σ. Both these parameters have a strong impact on the beta attenuation performance. For the sake of illustration, these parameters have been chosen here to demonstrate quick adaptation of the gain over the simulation duration. In an experimental setting, τ_θ should be chosen on the order of the timescale at which the targeted variations occur. Generally speaking, a large value of τ_θ is more convenient for adaptation to slow variations. σ should be chosen as a compromise between rapid decrease of the gain when the beta level is low (high σ) and limited gain overshoot in response to an increase of the beta level (low σ). In practice, the controller parameters could also be obtained through an optimization process, such as the dual-loop framework outlined in Grado et al. (2018), though an optimization approach would itself also require the identification of appropriate objective functions which may be non-trivial.

In summary, the proposed self-tuning DBS controller offers increased robustness to variations in system properties including changes in the strength of beta oscillations and or the electrode-tissue interface, and can accommodate alterations in the desired beta level. Compared to fixed-gain proportional control, it provides a better compromise between power consumption and efficient attenuation of beta oscillations, with little additional computational complexity or technological requirements.

DATA AVAILABILITY STATEMENT

The models presented in this study can be found in online repositories. The names of the repository/repositories and accession number(s) can be found below: The firing-rate model

is available to download from GitHub (https://github.com/silvanx/self-tuning-control). The conductance-based model is available to download from ModelDB (https://senselab.med.yale.edu/modeldb/) at ascension number 262046.

AUTHOR CONTRIBUTIONS

JO has developed and implemented the firing-rate model. JF has developed and implemented the conductance-based model. JO and AC have established the Proposition in Section 2.1.1. AC and ML have coordinated and supervised the study. All authors have contributed to the paper writing.

FUNDING

This research has received support from the Joint Irish Research Council—Campus France Research Program PHC Ulysses and the European Research Council (ERC) under the European Union's Horizon 2020 Research and Innovation Programme (Grant ERC-2014-CoG-646923-DBSModel).

SUPPLEMENTARY MATERIAL

The Supplementary Material for this article can be found online at: https://www.frontiersin.org/articles/10.3389/fnins.2020.00639/full#supplementary-material

REFERENCES

Ahn, S., Zauber, S. E., Worth, R. M., and Rubchinsky, L. L. (2016). Synchronized beta-band oscillations in a model of the globus pallidus-subthalamic nucleus network under external input. *Front. Comput. Neurosci.* 10:134. doi: 10.3389/fncom.2016.00134

Arlotti, M., Marceglia, S., Foffani, G., Volkmann, J., Lozano, A. M., Moro, E., et al. (2018). Eight-hours adaptive deep brain stimulation in patients with Parkinson disease. *Neurology* 90, e971–e976. doi: 10.1212/WNL.0000000000005121

Basir-Kazeruni, S. (2017). *Energy-efficient DSP solutions for simultaneous neural recording and stimulation* (Ph.D. thesis). ProQuest Dissertations Publishing, Ann Arbor, MI.

Beuter, A., Lefaucheur, J.-P., and Modolo, J. (2014). Closed-loop cortical neuromodulation in Parkinson's disease: an alternative to deep brain stimulation? *Clin. Neurophysiol.* 125, 874–885. doi: 10.1016/j.clinph.2014.01.006

Butson, C. R., Maks, C. B., and McIntyre, C. C. (2006). Sources and effects of electrode impedance during deep brain stimulation. *Clin. Neurophysiol.* 117, 447–454. doi: 10.1016/j.clinph.2005.10.007

Carron, R., Chaillet, A., Filipchuk, A., Pasillas-Lepine, W., and Hammond, C. (2013). Closing the loop of deep brain stimulation. *Front. Syst. Neurosci.* 7:112. doi: 10.3389/fnsys.2013.00112

Chaillet, A., Detorakis, G. I., Palfi, S., and Senova, S. (2017). Robust stabilization of delayed neural fields with partial measurement and actuation. *Automatica* 83, 262–274. doi: 10.1016/j.automatica.2017.05.011

Chaillet, A., Orłowski, J., and Pepe, P. (2019). "A relaxed Lyapunov-Krasovskii condition for global exponential stability of Lipschitz time-delay systems," in *58th IEEE Conference on Decision and Control (CDC)* (Nice).

Chaillet, A., Pogromsky, A., and Rüffer, B. (2013). "A Razumikhin approach for the incremental stability of delayed nonlinear systems," in *52nd IEEE Conference on Decision and Control (CDC)* (Florence).

Corbit, V. L., Whalen, T. C., Zitelli, K. T., Crilly, S. Y., Rubin, J. E., and Gittis, A. H. (2016). Pallidostriatal projections promote β oscillations in a dopamine-depleted biophysical network model. *J. Neurosci.* 36, 5556–5571. doi: 10.1523/JNEUROSCI.0339-16.2016

Davidson, C. M., de Paor, A. M., Cagnan, H., and Lowery, M. M. (2016). Analysis of oscillatory neural activity in series network models of Parkinson's disease during deep brain stimulation. *IEEE Trans. Biomed. Eng.* 63, 86–96. doi: 10.1109/TBME.2015.2475166

Davison, A. P., Brüderle, D., Eppler, J. M., Kremkow, J., Muller, E., Pecevski, D., et al. (2009). PyNN: a common interface for neuronal network simulators. *Front. Neuroinformatics* 2:11. doi: 10.3389/neuro.11.011.2008

Destexhe, A., Mainen, Z., and Sejnowski, T. (1994). An efficient method for computing synaptic conductances based on a kinetic model of receptor binding. *Neural Comput.* 6, 14–18. doi: 10.1162/neco.1994.6.1.14

Destexhe, A., and Sejnowski, T. J. (2009). The Wilson–Cowan model, 36 years later. *Biol. Cybern.* 101, 1–2. doi: 10.1007/s00422-009-0328-3

Detorakis, G. I., and Chaillet, A. (2017). "Incremental stability of spatiotemporal delayed dynamics and application to neural fields," in *56th IEEE Conference on Decision and Control (CDC)* (Melbourne, QLD).

di Volo, M., Romagnoni, A., Capone, C., and Destexhe, A. (2019). Biologically realistic mean-field models of conductance-based networks of spiking neurons with adaptation. *Neural Comput.* 31, 653–680. doi: 10.1162/neco_a_01173

Eitan, R., Bergman, H., and Israel, Z. (2019). "Closed-loop deep brain stimulation for Parkinson's disease," in *Surgery for Parkinson's Disease*, ed R. R. Goodman (Cham: Springer), 131–149.

Eusebio, A., Thevathasan, W., Doyle, G. L., Pogosyan, A., Bye, E., Foltynie, T., et al. (2011). Deep brain stimulation can suppress pathological synchronisation in parkinsonian patients. *J. Neurol. Neurosurg. Psychiatry* 82, 569–573. doi: 10.1136/jnnp.2010.217489

Farina, D., Negro, F., and Dideriksen, J. (2014). The effective neural drive to muscles is the common synaptic input to motor neurons. *J. Physiol.* 592, 3427–3441. doi: 10.1113/jphysiol.2014.273581

Faye, G., and Faugeras, O. (2010). Some theoretical and numerical results for delayed neural field equations. *Phys. D* 239, 561–578. doi: 10.1016/j.physd.2010.01.010

Fleming, J., Dunn, E., and Lowery, M. (2020). Simulation of closed-loop deep brain stimulation control schemes for suppression of pathological beta oscillations in Parkinson's disease. *Front. Neurosci.* 14:166. doi: 10.3389/fnins.2020.00166

Foust, A., Yu, Y., Popovic, M., Zecevic, D., and McCormick, D. (2011). Somatic membrane potential and kv1 channels control spike repolarization in cortical axon collaterals and presynaptic boutons. *J. Neurosci.* 31, 15490–15498. doi: 10.1523/JNEUROSCI.2752-11.2011

Fradkov, A. L., Miroshnik, I. V., and Nikiforov, V. O. (1999). *Nonlinear and Adaptive Control of Complex Systems*. Dordrecht: Springer Science & Business Media.

Grado, L. L., Johnson, M. D., and Netoff, T. I. (2018). Bayesian adaptive dual control of deep brain stimulation in a computational model of parkinson's disease. *PLoS Comput. Biol.* 14:e1006606. doi: 10.1371/journal.pcbi.1006606

Hahn, P., and McIntyre, C. (2010). Modeling shifts in the rate and pattern of subthalamopallidal network activity during deep brain stimulation. *J. Comput. Neurosci.* 28, 425–441. doi: 10.1007/s10827-010-0225-8

Haidar, I., Pasillas-Lépine, W., Chaillet, A., Panteley, E., Palfi, S., and Senova, S. (2016). Closed-loop firing rate regulation of two interacting excitatory and inhibitory neural populations of the basal ganglia. *Biol. Cybern.* 110, 55–71. doi: 10.1007/s00422-015-0678-y

Hammond, C., Bergman, H., and Brown, P. (2007). Pathological synchronization in Parkinson's disease: networks, models and treatments. *Trends Neurosci.* 30, 357–364. doi: 10.1016/j.tins.2007.05.004

Hines, M. L., and Carnevale, N. T. (1997). The NEURON simulation environment. *Neural Comput.* 9, 1179–1209. doi: 10.1162/neco.1997.9.6.1179

Ioannou, P., and Fidan, B. (2006). *Adaptive Control Tutorial*. Advances in Design and Control. Philadelphia, PA: SIAM.

Ioannou, P., and Kokotovic, P. V. (1984). Instability analysis and improvement of robustness of adaptive control. *Automatica* 20, 583–594. doi: 10.1016/0005-1098(84)90009-8

Kang, G., and Lowery, M. (2013). Interaction of oscillations, and their suppression via deep brain stimulation, in a model of the cortico-basal ganglia network. *IEEE Trans. Neural Syst. Rehabil. Eng.* 21, 244–253. doi: 10.1109/TNSRE.2013.2241791

Kang, G., and Lowery, M. (2014). Effects of antidromic and orthodromic activation of STN afferent axons during dbs in parkinson's disease: a simulation study. *Front. Comput. Neurosci.* 8:32. doi: 10.3389/fncom.2014.00032

Koelman, L. A., and Lowery, M. M. (2019). Beta-band resonance and intrinsic oscillations in a biophysically detailed model of the subthalamic nucleus-globus pallidus network. *Front. Comput. Neurosci.* 13:77. doi: 10.3389/fncom.2019.00077

Kühn, A. A., Kempf, F., Brücke, C., Doyle, L. G., Martinez-Torres, I., Pogosyan, A., et al. (2008). High-frequency stimulation of the subthalamic nucleus suppresses oscillatory β activity in patients with Parkinson's disease in parallel with improvement in motor performance. *J. Neurosci.* 28, 6165–6173. doi: 10.1523/JNEUROSCI.0282-08.2008

Kühn, A. A., Kupsch, A., Schneider, G. H., and Brown, P. (2006). Reduction in subthalamic 8-35 Hz oscillatory activity correlates with clinical improvement in Parkinson's disease. *Eur. J. Neurosci.* 23, 1956–1960. doi: 10.1111/j.1460-9568.2006.04717.x

Kumaravelu, K., Brocker, D., and Grill, W. (2016). A biophysical model of the cortex-basal ganglia-thalamus network in the 6-ohda lesioned rat model of parkinson's disease. *J. Comput. Neurosci.* 40, 207–229. doi: 10.1007/s10827-016-0593-9

Li, Q., Ke, Y., Chan, D., Qian, Z., Yung, K., Ko, H., et al. (2012). Therapeutic deep brain stimulation in Parkinsonian rats directly influences motor cortex. *Neuron* 76, 1030–1041. doi: 10.1016/j.neuron.2012.09.032

Little, S., Beudel, M., Zrinzo, L., Foltynie, T., Limousin, P., Hariz, M., et al. (2016). Bilateral adaptive deep brain stimulation is effective in Parkinson's disease. *J. Neurol. Neurosurg. Psychiatry* 87, 717–721. doi: 10.1136/jnnp-2015-310972

Little, S., Pogosyan, A., Neal, S., Zavala, B., Zrinzo, L., Hariz, M., et al. (2013). Adaptive deep brain stimulation in advanced Parkinson disease. *Ann. Neurol.* 74, 449–457. doi: 10.1002/ana.23951

Litvak, V., Jha, A., Eusebio, A., Oostenveld, R., Foltynie, T., Limousin, P., et al. (2011). Resting oscillatory cortico-subthalamic connectivity in patients with Parkinson's disease. *Brain* 134, 359–374. doi: 10.1093/brain/awq332

Liu, C., Zhou, C., Wang, J., Fietkiewicz, C., and Loparo, K. A. (2020). The role of coupling connections in a model of the cortico-basal ganglia-thalamocortical neural loop for the generation of beta oscillations. *Neural Netw.* 123, 381–392. doi: 10.1016/j.neunet.2019.12.021

Liu, C., Zhu, Y., Liu, F., Wang, J., Li, H., Deng, B., et al. (2017). Neural mass models describing possible origin of the excessive beta oscillations correlated with parkinsonian state. *Neural Netw.* 88, 65–73. doi: 10.1016/j.neunet.2017.01.011

Lozano, A. M., Lipsman, N., Bergman, H., Brown, P., Chabardes, S., Chang, J. W., et al. (2019). Deep brain stimulation: current challenges and future directions. *Nat. Rev. Neurol.* 15, 148–160. doi: 10.1038/s41582-018-0128-2

Magill, P. J., Bolam, J. P., and Bevan, M. D. (2001). Dopamine regulates the impact of the cerebral cortex on the subthalamic nucleus-globus pallidus network. *Neuroscience* 106, 313–330. doi: 10.1016/S0306-4522(01)00281-0

Mallet, N., Pogosyan, A., Márton, L. F., Bolam, J. P., Brown, P., and Magill, P. J. (2008). Parkinsonian beta oscillations in the external globus pallidus and their relationship with subthalamic nucleus activity. *J. Neurosci.* 52, 14245–14258. doi: 10.1523/JNEUROSCI.4199-08.2008

McConnell, G., So, R., Hilliard, J., Lopomo, P., and Grill, W. M. (2012). Effective deep brain stimulation suppresses low-frequency network oscillations in the basal ganglia by regularizing neural firing patterns. *J. Neurosci.* 32, 15657–15668. doi: 10.1523/JNEUROSCI.2824-12.2012

McManus, L., Flood, M., and Lowery, M. (2019). Beta-band motor unit coherence and nonlinear surface emg features of the first dorsal interosseous muscle vary with force. *J. Neurophysiol.* 122, 1147–1162. doi: 10.1152/jn.00228.2019

Nevado-Holgado, A. J., Mallet, N., Magill, P. J., and Bogacz, R. (2014). Effective connectivity of the subthalamic nucleus-globus pallidus network during parkinsonian oscillations. *J. Physiol.* 592, 1429–1455. doi: 10.1113/jphysiol.2013.259721

Nevado-Holgado, A. J., Terry, J. R., and Bogacz, R. (2010). Conditions for the generation of beta oscillations in the subthalamic nucleus-globus pallidus network. *J. Neurosci.* 30, 12340–12352. doi: 10.1523/JNEUROSCI.0817-10.2010

Obeso, J., Olanow, C., Rodriguez-Oroz, M., Krack, P., Kumar, R., and Lang, A. (2001). Deep-brain stimulation of the subthalamic nucleus or the pars interna of the globus pallidus in Parkinson's disease. *New Engl. J. Med.* 345, 956–963. doi: 10.1056/NEJMoa000827

Orłowski, J. (2019). *Adaptive control of time-delay systems to counteract pathological brain oscillations* (Ph.D. thesis). Université Paris-Saclay, Saint-Aubin.

Otsuka, T., Abe, T., and Song, W. (2004). Conductance-based model of the voltage-dependent generation of a plateau potential in subthalamic neurons. *J. Neurophysiol.* 92, 255–264. doi: 10.1152/jn.00508.2003

Parastarfeizabadi, M., and Kouzani, A. Z. (2017). Advances in closed-loop deep brain stimulation devices. *J. Neuroeng. Rehabil.* 14:79. doi: 10.1186/s12984-017-0295-1

Pasillas-Lépine, W. (2013). Delay-induced oscillations in Wilson and Cowan's model: an analysis of the subthalamo-pallidal feedback loop in healthy and parkinsonian subjects. *Biol. Cybern.* 107, 289–308. doi: 10.1007/s00422-013-0549-3

Pasillas-Lépine, W., Haidar, I., Chaillet, A., and Panteley, E. (2013). "Closed-loop deep brain stimulation based on firing-rate regulation," in *6th International IEEE/EMBS Conference on Neural Engineering (NER)* (San Diego, CA), 166–169.

Pavlides, A., John Hogan, S., and Bogacz, R. (2012). Improved conditions for the generation of beta oscillations in the subthalamic nucleus-globus pallidus network. *Eur. J. Neurosci.* 36, 2229–2239. doi: 10.1111/j.1460-9568.2012.08105.x

Pavlov, A., van de Wouw, N., and Nijmeijer, H. (2007). Frequency response functions for nonlinear convergent systems. *IEEE Trans. Autom. Control* 52, 1159–1165. doi: 10.1109/TAC.2007.899020

Plenz, D., and Kital, S. T. (1999). A basal ganglia pacemaker formed by the subthalamic nucleus and external globus pallidus. *Nature* 400, 677–682. doi: 10.1038/23281

Popovych, O. V., and Tass, P. A. (2019). Adaptive delivery of continuous and delayed feedback deep brain stimulation - a computational study. *Sci. Rep.* 9, 1–17. doi: 10.1038/s41598-019-47036-4

Pospischil, M., Toledo-Rodriguez, M., Monier, C., Piwkowska, Z., Bal, T., Frégnac, Y., et al. (2008). Minimal hodgkin–huxley type models for different classes of cortical and thalamic neurons. *Biol. Cybern.* 99, 427–441. doi: 10.1007/s00422-008-0263-8

Rosa, M., Arlotti, M., Ardolino, G., Cogiamanian, F., Marceglia, S., Di Fonzo, A., et al. (2015). Adaptive deep brain stimulation in a freely moving parkinsonian patient. *Mov. Disord.* 30, 1003–1005. doi: 10.1002/mds.26241

Rosin, B., Slovik, M., Mitelman, R., Rivlin-Etzion, M., Haber, S. N., Israel, Z., et al. (2011). Closed-loop deep brain stimulation is superior in ameliorating parkinsonism. *Neuron* 72, 370–384. doi: 10.1016/j.neuron.2011.08.023

Rossi, L., Foffani, G., Marceglia, S., Bracchi, F., Barbieri, S., and Priori, A. (2007). An electronic device for artefact suppression in human local field potential recordings during deep brain stimulation. *J. Neural Eng.* 4, 96–106. doi: 10.1088/1741-2560/4/2/010

Rubin, J., and Terman, D. (2004). High frequency stimulation of the subthalamic nucleus eliminates pathological thalamic rhythmicity in a computational model. *J. Comput. Neurosci.* 16, 211–235. doi: 10.1023/B:JCNS.0000025686.47117.67

Santaniello, S., Fiengo, G., Glielmo, L., and Grill, W. M. (2010). Closed-loop control of deep brain stimulation: a simulation study. *IEEE Trans. Neural Syst. Rehabil. Eng.* 19, 15–24. doi: 10.1109/TNSRE.2010.2081377

Santos, F. J., Costa, R. M., and Tecuapetla, F. (2011). Stimulation on demand: closing the loop on deep brain stimulation. *Neuron* 72, 197–198. doi: 10.1016/j.neuron.2011.10.004

Shah, S. A., Tinkhauser, G., Chen, C. C., Little, S., and Brown, P. (2018). "Parkinsonian tremor detection from subthalamic nucleus local field potentials for closed-loop deep brain stimulation," in *Proceedings of the Annual International Conference of the IEEE Engineering in Medicine and Biology Society, EMBS* (Honolulu, HI), 2320–2324.

Sharott, A., Magill, P. J., Harnack, D., Kupsch, A., Meissner, W., and Brown, P. (2005). Dopamine depletion increases the power and coherence of β-oscillations in the cerebral cortex and subthalamic nucleus of the awake rat. *Eur. J. Neurosci.* 21, 1413–1422. doi: 10.1111/j.1460-9568.2005.03973.x

Shouno, O., Tachibana, Y., Nambu, A., and Doya, K. (2017). Computational model of recurrent subthalamo-pallidal circuit for generation of parkinsonian oscillations. *Front. Neuroanat.* 11:21. doi: 10.3389/fnana.2017.00021

Stanslaski, S., Afshar, P., Cong, P., Giftakis, J., Stypulkowski, P., Carlson, D., et al. (2012). Design and validation of a fully implantable, chronic, closed-loop neuromodulation device with concurrent sensing and stimulation. *IEEE Trans. Neural Syst. Rehabil. Eng.* 20, 410–421. doi: 10.1109/TNSRE.2012.2183617

Su, F., Kumaravelu, K., Wang, J., and Grill, W. M. (2019). Model-based evaluation of closed-loop deep brain stimulation controller to adapt to dynamic changes in reference signal. *Front. Neurosci.* 13:956. doi: 10.3389/fnins.2019.00956

Tachibana, Y., Iwamuro, H., Kita, H., Takada, M., and Nambu, A. (2011). Subthalamo-pallidal interactions underlying parkinsonian neuronal oscillations in the primate basal ganglia. *Eur. J. Neurosci.* 34, 1470–1484. doi: 10.1111/j.1460-9568.2011.07865.x

Tachibana, Y., Kita, H., Chiken, S., Takada, M., and Nambu, A. (2008). Motor cortical control of internal pallidal activity through glutamatergic and gabaergic inputs in awake monkeys. *Eur. J. Neurosci.* 27, 238–253. doi: 10.1111/j.1460-9568.2007.05990.x

Terman, D., Rubin, J., Yew, A., and Wilson, C. (2002). Activity patterns in a model for the subthalamopallidal network of the basal ganglia. *J. Neurosci.* 22, 2963–2976. doi: 10.1523/JNEUROSCI.22-07-02963.2002

Tukhlina, N., Rosenblum, M., Pikovsky, A., and Kurths, J. (2007). Feedback suppression of neural synchrony by vanishing stimulation. *Phys. Rev. E* 75:11918. doi: 10.1103/PhysRevE.75.011918

Velisar, A., Syrkin-Nikolau, J., Blumenfeld, Z., Trager, M., Afzal, M., Prabhakar, V., et al. (2019). Dual threshold neural closed loop deep brain stimulation in Parkinson disease patients. *Brain Stimul.* 12, 868–876. doi: 10.1016/j.brs.2019.02.020

Volkmann, J., Herzog, J., Kopper, F., and Deuschl, G. (2002). Introduction to the programming of deep brain stimulators. *Mov. Disord.* 17, S181–S187. doi: 10.1002/mds.10162

West, T. O., Berthouze, L., Halliday, D. M., Litvak, V., Sharott, A., Magill, P. J., et al. (2018). Propagation of beta/gamma rhythms in the cortico-basal ganglia circuits of the parkinsonian rat. *J. Neurophysiol.* 119, 1608–1628. doi: 10.1152/jn.00629.2017

Yeganefar, N., Pepe, P., and Dambrine, M. (2008). Input-to-State Stability of time-delay systems: a link with exponential stability. *IEEE Trans. Autom. Control* 53, 1526–1531. doi: 10.1109/TAC.2008.928340

Conflict of Interest: The authors declare that the research was conducted in the absence of any commercial or financial relationships that could be construed as a potential conflict of interest.

Advantages of publishing in Frontiers

OPEN ACCESS
Articles are free to read for greatest visibility and readership

FAST PUBLICATION
Around 90 days from submission to decision

HIGH QUALITY PEER-REVIEW
Rigorous, collaborative, and constructive peer-review

TRANSPARENT PEER-REVIEW
Editors and reviewers acknowledged by name on published articles

Frontiers
Avenue du Tribunal-Fédéral 34
1005 Lausanne | Switzerland

Visit us: www.frontiersin.org
Contact us: frontiersin.org/about/contact

REPRODUCIBILITY OF RESEARCH
Support open data and methods to enhance research reproducibility

DIGITAL PUBLISHING
Articles designed for optimal readership across devices

FOLLOW US
@frontiersin

IMPACT METRICS
Advanced article metrics track visibility across digital media

EXTENSIVE PROMOTION
Marketing and promotion of impactful research

LOOP RESEARCH NETWORK
Our network increases your article's readership